

**APPENDIX E
ATTACHMENT E-2**

HYDROTHERMAL MODELING PROGRAM

**SPONSOR: DR. E. ERIC ADAMS
PSE&G RENEWAL APPLICATION
SALEM GENERATING STATION
PERMIT NO. NJ0005622
4 MARCH 1999**

APPENDIX E
ATTACHMENT E-2
HYDROTHERMAL MODELING PROGRAM

TABLE OF CONTENTS

LIST OF TABLES	2
LIST OF FIGURES	2
INTRODUCTION.....	16
I.DESCRPTION OF THE STATION'S DISCHARGE AND THERMAL PLUME PROCESSES	17
I.A.Salem Generating Station	17
I.B.Artificial Island and the Delaware Estuary	18
I.C.Hydrothermal Plume Processes.....	19
II.PRIOR HYDROTHERMAL AND HYDRODYNAMIC MODELING PROGRAMS	19
II.A.Physical Modeling In Support of PSE&G's Initial §316(a) Demonstration...20	
II.B.Thermal Monitoring Program One-Unit Operation (1977-1978).....20	
II.C.Thermal Monitoring Program Two-Unit Operation (1982-1985).....21	
II.D.1991 Hydrothermal Studies	21
II.E.1993 Hydrothermal Modeling Program.....	22
II.F.1995 Hydrodynamic Field Data Collection and Modeling Program	22
III.DESCRPTION OF HYDROTHERMAL MODELING METHODS	23
III.A.Ambient Temperature Model (ATM).....	26
III.A.1.Description of ATM.....	26
III.A.2.Methodology.....	27
III.A.3.Set-Up.....	28
III.A.4. Calibration	28
III.A.5. Verification	29
III.B.Near-field Modeling: CORMIX	30
III.B.1.CORMIX Objectives	30
III.B.2.CORMIX Description	30
III.B.2.a.CORMIX Origin	31
III.B.2.b.CORMIX Features	31
III.B.3.CORMIX Modeling Approach for Salem Station	31
III.B.4.Methodology.....	32
III.B.5.CORMIX Set-up	34
III.B.5.a.CORMIX Input Data.....	34
III.B.5.b.CORMIX Output Data	34
III.B.6.CORMIX One-Unit Validation	35
III.B.7.CORMIX Two-Unit Validation	35
III.B.8.CORMIX Model Improvements	36
III.B.8.a.General Improvements to CORMIX	36
III.B.8.a.i.Error Correction to the Dilution Equation	36

III.B.8.a.ii.Improvements to the Dilution Equation	37
<i>III.B.8.b.Site-specific CORMIX Improvements</i>	<i>37</i>
III.B.8.b.i.Adjustment to Logic Structure	38
III.B.8.b.ii.Distinction Between Plume Surfacing and End of Near-Field Plume Momentum	38
III.B.8.b.iii.Non-linear Interpolation and Heat Conservation within CORMIX Modules.....	41
III.B.8.b.iv.Final Synthesis of Actual and Virtual Discharge Simulations	41
III.B.9.CORMIX Calibration	42
<i>III.B.9.a.Two-Unit Plume Trajectory and Width Calibration</i>	<i>42</i>
<i>III.B.9.b.Two-Unit Centerline Plume Temperature Calibration</i>	<i>45</i>
<i>III.B.9.c.Two-Unit Transverse Surface Temperature Calibration.....</i>	<i>46</i>
III.B.10.CORMIX Verification	48
<i>III.B.10.a.One-Unit Plume Trajectory and Width Verification</i>	<i>48</i>
<i>III.B.10.b.One-Unit Centerline Plume Temperature Verification</i>	<i>49</i>
<i>III.B.10.c.One-Unit Transverse Surface Temperature Verification.....</i>	<i>49</i>
<i>III.B.10.d.Two-Unit Plume Verification Using Infrared Images</i>	<i>49</i>
<i>III.B.10.e.Two-Unit Plume Vertical Distribution Verification Using Dye Data ..</i>	<i>49</i>
<i>III.B.10.f.Two-Unit Plume Temperature Verification Using Mooring Data</i>	<i>50</i>
III.C.Far-field Model: RMA-10.....	50
III.C.1.RMA-10 Objectives	51
III.C.2.RMA-10 Description.....	51
<i>III.C.2.a.RMA-10 Model Selection.....</i>	<i>52</i>
<i>III.C.2.b.RMA-10 Theory.....</i>	<i>54</i>
<i>III.C.2.c.RMA-10 Improvements Since the 1993 Permit Renewal.....</i>	<i>54</i>
III.C.3.General RMA-10 Modeling Procedure.....	56
III.C.4.RMA-10 Set-up	57
<i>III.C.4.a.RMA-10 Finite Element Grid</i>	<i>57</i>
<i>III.C.4.b.Model Input Parameters.....</i>	<i>58</i>
<i>III.C.4.c.Boundary Conditions.....</i>	<i>58</i>
<i>III.C.4.d.Initial Conditions</i>	<i>59</i>
<i>III.C.4.e.External Point Sources</i>	<i>59</i>
III.C.5.RMA-10 Calibration	60
<i>III.C.5.a.Input Data Sets for RMA-10 Calibration</i>	<i>60</i>
<i>III.C.5.a.i.Boundary Conditions for RMA-10 Calibration</i>	<i>61</i>
<i>III.C.5.a.ii.Initial Conditions for RMA-10 Calibration</i>	<i>63</i>
<i>III.C.5.a.iii.Point Source Discharges of Heat for RMA-10 Calibration</i>	<i>63</i>
<i>III.C.5.a.iv.Spin-Up Time</i>	<i>64</i>
<i>III.C.5.b.Data Available to Evaluate the Performance of RMA-10.....</i>	<i>65</i>
<i>III.C.5.c.RMA-10 Calibration Process</i>	<i>67</i>
<i>III.C.5.c.i.RMA-10 Estuary-Wide Calibration Process.....</i>	<i>67</i>
<i>III.C.5.c.ii.RMA-10 Plume Calibration Process.....</i>	<i>67</i>
<i>III.C.5.d.Finite Element Grid and Coefficients for the Calibrated Model</i>	<i>69</i>
<i>III.C.5.e.RMA-10 Estuary-wide Calibration Results</i>	<i>72</i>
<i>III.C.5.e.i.Tides</i>	<i>73</i>

III.C.5.e.ii. Currents	74
III.C.5.e.iii. Salinity.....	76
III.C.5.e.iv. Water Temperature	78
<i>III.C.5.f. RMA-10 Plume Calibration Results.....</i>	<i>80</i>
III.C.5.f.i. Numerical Experiments for Conservation of Mass.....	80
III.C.5.f.ii. Factors Considered in the Comparison of Observations with Simulation Results	81
III.C.5.f.iii. Observed versus Simulated Surface Water Temperature	82
III.C.5.f.iv. Observed versus Simulated Water Temperature at the Salem Intake	86
III.C.5.f.v. Comparisons of ΔT for the Calibration Period.....	86
<i>III.C.5.g. Tidal Marshes.....</i>	<i>88</i>
III.C.6. Verification	89
<i>III.C.6.a. Input Data Sets for RMA-10 Verification for the One-Unit Survey.....</i>	<i>90</i>
<i>III.C.6.b. Data Available to Evaluate the Performance of RMA-10.....</i>	<i>94</i>
III.C.6.b.i. One-Unit Survey.....	94
III.C.6.b.ii. Dye Measurements from the Two-Unit Survey	95
III.C.6.c. Estuary-Wide Verification Results	95
<i>III.C.6.d. RMA-10 Plume Verification Results</i>	<i>98</i>
III.C.6.d.i. Observed Versus Simulated Water Temperature	99
III.C.6.d.ii. Comparisons of ΔT for the Verification Period	101
III.C.6.d.iii. Observed versus Simulated Water Temperature at the Salem Intake	102
III.C.6.d.iv. Two-Unit Dye Verification	103
III.D. Linkage of CORMIX and RMA-10	106
<i>III.D.1. Methodology</i>	<i>107</i>
<i>III.D.2. Application.....</i>	<i>109</i>
III.E. Total Temperature Model.....	111
<i>III.E.1. Description of the Total Temperature Model (TTM).....</i>	<i>111</i>
<i>III.E.2. Methodology.....</i>	<i>112</i>
<i>III.E.3. Set-Up.....</i>	<i>112</i>
<i>III.E.4. Validation.....</i>	<i>113</i>
IV. CONCLUSIONS AND COMPARISONS TO FAR-FIELD MODEL.....	117
IV.A. Consistency with Historical Data and Observations.....	117
IV.B. Consistency of Data and Simulations.....	118
IV.B.1. Tidal Hydrodynamics.....	120
<i>IV.B.1.a. Tidal Hydrodynamics in RMA-10.....</i>	<i>120</i>
<i>IV.B.1.b. Model versus Observed Tidal Variability.....</i>	<i>121</i>
<i>IV.B.1.c. Conclusions from Tidal Hydrodynamics Comparison.....</i>	<i>126</i>
IV.B.2. Ambient Temperature and Salinity	127
<i>IV.B.2.a. Stratification in RMA-10.....</i>	<i>127</i>
<i>IV.B.2.b. Mean Longitudinal Temperature and Salinity Structure.....</i>	<i>128</i>
<i>IV.B.2.c. Mean Cross-River Temperature and Salinity Structure</i>	<i>130</i>
<i>IV.B.2.d. Spatial Salinity Patterns</i>	<i>131</i>
<i>IV.B.2.e. Temporal Variability of Temperature and Salinity South of the Station</i>	<i>131</i>
<i>IV.B.2.f. Conclusions Regarding Stratification and Mixing.....</i>	<i>132</i>
IV.B.3. Thermal Discharge Plume Dynamics	133

<i>IV.B.3.a. Thermal Plume Dynamics in RMA-10</i>	133
<i>IV.B.3.b. Slack Current Plume Shape</i>	134
<i>IV.B.3.c. Flood and Ebb Current Plume Shape</i>	136
<i>IV.B.3.d. Conclusions Regarding RMA-10's Thermal Plume Structure</i>	138
<i>IV.B.4. Tidal Marsh Exchange Processes</i>	139
<i>IV.B.4.a. Tidal Marsh Heat Exchange in RMA-10</i>	139
<i>IV.B.4.b. Heat Exchange with Nearby Marshes</i>	140
<i>IV.B.4.c. Heat Transfer From Marshes North of the Station</i>	141
<i>IV.B.4.d. Conclusions Regarding Tidal Marsh Processes</i>	142
<i>IV.B.5. Exchange with Chesapeake Bay via the C&D Canal</i>	143
<i>IV.B.5.a. The C&D Canal in the RMA-10 Model</i>	144
<i>IV.B.5.b. Instantaneous Flow Response to Slope Forcing in the RMA-10 Model</i>	144
<i>IV.B.5.c. Mean Flow and Mean Slope</i>	145
<i>IV.B.5.d. Peak Flow and Slope</i>	146
<i>IV.B.5.e. Conclusions Regarding the Model's Representation of Flow in the C&D Canal</i>	146
IV.C. Adequacy of Data and Models Towards Understanding of River Processes at the Station	147
<i>IV. C. 1. Tidal Hydrodynamics</i>	147
<i>IV. C. 2. Ambient Temperature and Salinity</i>	148
<i>IV. C. 3. Thermal Discharge Plume Dynamics</i>	148
<i>IV. C. 4. Tidal Marsh Heat Exchange</i>	149
<i>IV. C. 5. Exchange with Chesapeake Bay via the C&D Canal</i>	150
V CHARACTERIZATION OF THE THERMAL PLUME AND BIOLOGICAL THERMAL EXPOSURE	151
REFERENCES	153

**APPENDIX E
ATTACHMENT E-2
HYDROTHERMAL MODELING PROGRAM**

LIST OF TABLES

Table No.	Title
Table III-1	Synthesis of the Basic Components of the Modified CORMIX Approach (in sequential order of application).
Table III-2	Overview of CORMIX Inputs for the Two-Unit Survey Model Calibration (29 May 1998).
Table III-3	Overview of CORMIX Inputs for the One-Unit Survey Model Verification (27 October 1997).
Table III-4	Boundary Conditions for the Calibration of RMA-10 May 1998.
Table III-5	Names and Drainage Areas of Ungauged Tributaries Used in RMA-10.
Table III-6	Major Point Source Discharges of Heat for Calibration (May 1998).
Table III-7	Data for Evaluating the Performance of RMA-10 for Calibration (May 1998).
Table III-8	Coefficients Used in the Calibration of RMA-10 Model (May 1998).
Table III-9	Figures for Comparing Observed and Modeled Distributions of Surface Water Temperature for Calibration (May 1998).
Table III-10	Boundary Conditions for the Verification of RMA-10 (October 1997).
Table III-11	Major Point Source Discharges of Heat for Verification (October 1997).
Table III-12	Data for Evaluating the Performance of RMA-10 for Verification (October 1997).
Table IV-1	Volume conservation in RMA-10 through exterior model boundaries over a 75-hour period (6 complete tidal cycles) during 24-26 May 1998.

LIST OF FIGURES

Figure No.	Title
Figure III-1a	Components of the Total Temperature Model where T represents T_{ambient} .
Figure III-1b	General numerical modeling procedure.
Figure III-1c	Schematic showing how the hydrothermal models are used to define the thermal exposure.
Figure III-2	Ambient temperature model calibration comparison.
Figure III-3	CORMIX modeling procedure for the Salem plume.
Figure III-4	Sample of CORMIX Two-Unit Validation; 29 May 1998 temperature contours & CORMIX predicted plume dimensions at the surface ebb phase (06:40 - 08:40).
Figure III-5	Schematic of the CORMIX version 3.2 treatment of the Salem thermal plume (not to scale).

- Figure III-6 Plan view: Triangular Irregular Network (TIN) of bathymetry at the Salem discharge. The approximate location of the discharge pipes, and the surface upwelling measured on a flood tide is shown.
- Figure III-7 CORMIX Two-Unit Calibration 29 May 1998; velocity and direction of ambient flow at bottom ADCP, depth = 9 to 10 feet (mid-depth).
- Figure III-8 Schematic of the improved CORMIX treatment of the Salem thermal plume (not to scale).
- Figure III-9 CORMIX model coordinate system for a representative ebb tidal phase.
- Figure III-10 CORMIX Two-Unit Calibration 29 May 1998; Temperature contours & CORMIX predicted plume dimensions at the surface, ebb phase (06:40 - 08:40).
- Figure III-11 CORMIX Two-Unit Calibration 29 May 1998; Temperature contours & CORMIX predicted plume dimensions at the surface, flood phase (11:40 - 13:40).
- Figure III-12 CORMIX Two-Unit Calibration 29 May 1998; Temperature contours & CORMIX predicted plume dimensions at the surface, end-of-ebb phase (09:10 - 11:10).
- Figure III-13a CORMIX Two-Unit Calibration 29 May 1998; Temperature contours & CORMIX predicted plume dimensions at the surface, end-of-flood phase (14:25 - 16:25). Expanded area.
- Figure III-13b CORMIX Two-Unit Calibration 29 May 1998; Temperature contours & CORMIX predicted plume dimensions at the surface, end-of-flood phase (14:25 - 16:25).
- Figure III-14 CORMIX Two-Unit Calibration 29 May 1998; Observed vs. CORMIX Predicted Surface Temperatures Ebb Phase [Approach Temperature = 21.72°C].
- Figure III-15 CORMIX Two-Unit Calibration 29 May 1998; Observed vs. CORMIX predicted surface temperatures flood phase [approach temperature = 22.50°C].
- Figure III-16 CORMIX Two-Unit Calibration 29 May 1998; Observed vs. CORMIX predicted surface temperatures end-of-ebb phase [approach temperature = 22.13°C].
- Figure III-17 CORMIX Two-Unit Calibration 29 May 1998; Observed vs. CORMIX predicted surface temperatures end-of-flood phase [approach temperature = 22.53°C].
- Figure III-18 CORMIX Two-Unit Calibration 29 May 1998; Comparison of model predicted vs. observed lateral temperature distributions, ebb phase.
- Figure III-19 CORMIX Two-Unit Calibration 29 May 1998; Comparison of model predicted vs. observed lateral temperature distributions, flood phase.

- Figure III-20 CORMIX Two-Unit Calibration 29 May 1998;
Comparison of model predicted vs. observed lateral temperature distributions, end of ebb phase.
- Figure III-21 CORMIX Two-Unit Calibration 29 May 1998;
Comparison of model predicted vs. observed lateral temperature distributions, end of flood phase.
- Figure III-22 CORMIX One-Unit Verification 28 October 1997;
Temperature contours & CORMIX predicted plume dimensions at the surface, ebb phase (12:25 - 14:25).
- Figure III-23 CORMIX One-Unit Verification 28 October 1997;
Temperature contours & CORMIX predicted plume dimensions at the surface, flood phase (06:30 - 08:30).
- Figure III-24 CORMIX One-Unit Verification 28 October 1997;
Observed vs. CORMIX predicted surface temperatures at ebb phase [approach temperature = 14.0°C].
- Figure III-25 CORMIX One-Unit Verification 28 October 1997;
Observed vs. CORMIX predicted surface temperatures at flood phase [approach temperature = 13.8°C].
- Figure III-26 CORMIX One-Unit Verification 28 October 1997;
Comparison of model predicted vs. observed lateral temperature distributions, ebb phase.
- Figure III-27 CORMIX One-Unit Verification 28 October 1997;
Comparison of model predicted vs. observed lateral temperature distributions, flood phase.
- Figure III-28 Infrared imaging contours 29 May 1998; Ebb phase (18:07 - 18:10).
- Figure III-29 Infrared imaging contours 29 May 1998; Flood phase (12:39 - 12:41).
- Figure III-30 Infrared imaging contours 29 May 1998; End-of-ebb phase (10:31 - 10:34).
- Figure III-31 Infrared imaging contours 29 May 1998; End-of-flood phase (14:50 - 14:52).
- Figure III-32a Measured dye at locations of shipboard verticals north of the Station during an ebb phase on May 29, 1998.
- Figure III-32b Measured dye at locations of shipboard verticals south of the Station during an ebb phase on May 29, 1998.
- Figure III-33a Measured dye at locations of shipboard verticals north of the Station during a slack phase (end-of-ebb) on May 29, 1998.
- Figure III-33b Measured dye at locations of shipboard verticals south of the Station during a slack phase (end-of-ebb) on May 29, 1998.
- Figure III-34a Measured dye at locations of shipboard verticals north of the Station during a flood phase on May 29, 1998.
- Figure III-34b Measured dye at locations of shipboard verticals south of the Station during a flood phase on May 29, 1998.
- Figure III-35a Measured dye at locations of shipboard verticals north of the Station during a slack phase (end-of-flood) on May 29, 1998.

- Figure III-35b Measured dye at locations of shipboard verticals south of the Station during a slack phase (end-of-flood) on May 29, 1998.
- Figure III-36a Locations of shipboard vertical profiles measured during an ebb phase on May 29, 1998.
- Figure III-36b Locations of shipboard vertical profiles measured during a slack phase (end-of-ebb) on May 29, 1998.
- Figure III-36c Locations of shipboard vertical profiles measured during a flood phase on May 29, 1998.
- Figure III-36d Locations of shipboard vertical profiles measured during a slack phase (end-of-flood) on May 29, 1998.
- Figure III-37 Observed near-field surface mooring temperature vs. model predicted plume surface temperature, 29 May 1998.
- Figure III-38 RMA-10 work plan.
- Figure III-39 RMA element types.
- Figure III-40a Model spinup based on upstream plume lengths.
- Figure III-40b Model spinup based on downstream plume lengths.
- Figure III-41 Model grid showing element types and dimensional classifications (i.e., 1-D, 2-D, and 3-D regions).
- Figure III-42 Model grid in the vicinity showing intake and discharge elements.
- Figure III-43 Locations of tide gages for One-Unit Survey (21-31 October 1997) and Two-Unit Survey (19 May - 4 June 1998).
- Figure III-44a Comparison of modeled and measured tides in the Estuary for the calibration period (19 May - 4 June 1998).
- Figure III-44b Comparison of modeled and measured tides at the west side of the Bay mouth (Lewes, DE) and the western end of the C&D Canal for the calibration period (19 May - 4 June 1998).
- Figure III-45a Comparison of modeled and measured tides in the Estuary for 29 May 1998.
- Figure III-45b Comparison of modeled and measured tides at the west side of the Bay mouth (Lewes, DE) and the western end of the C&D Canal for 29 May 1998.
- Figure III-46 Variation in tide range and tidal delay along the axis of the Estuary for the calibration period (22 May - 4 June 1998).
- Figure III-47 Comparison of the magnitude of the modeled and measured current velocities at the fixed-station ADCP located offshore of the discharge for the calibration period (22 May - 4 June 1998).
- Figure III-48 Comparison of the magnitude of the modeled and measured current velocities at the fixed-station ADCP located offshore of the discharge for 29 May 1998.
- Figure III-49 Comparison of modeled and measured current directions at the fixed-station ADCP located offshore of the discharge for 29 May 1998.
- Figure III-50 Comparison of measured and modeled flow through three transects located 6 miles north of the Station, at the Station, and 6 miles south of the Station for 29 May 1998.

- Figure III-51a Measured current speeds along three transects located 6 miles north of the Station, at the Station, and 6 miles south of the Station for a flood phase on 29 May 1998.
- Figure III-51b Modeled current speeds along three transects located 6 miles north of the Station, at the Station, and 6 miles south of the Station for a flood phase on 29 May 1998.
- Figure III-52 Comparison of measured and modeled depth-averaged salinity along the shipping channel for 21 May, 27 May, and 2 June 1998.
- Figure III-53 Locations of shipboard vertical profiles collected along the axis of the Estuary on 2 June 1998.
- Figure III-54a Comparison of modeled and measured salinities along the axis of the Estuary for 2 June 1998 (RM 130 to 90).
- Figure III-54b Comparison of modeled and measured salinities along the axis of the Estuary for 2 June 1998 (RM 80 to 45).
- Figure III-54c Comparison of modeled and measured salinities along the axis of the Estuary for 2 June 1998 (RM 40 to 10).
- Figure III-55 Delaware Bay tide gauge locations, mobile ADCP transects, and the fixed-point ADCP.
- Figure III-56a Comparison of modeled and measured salinities at the locations of shipboard verticals north of the Station during a flood phase on 29 May 1998.
- Figure III-56b Comparison of modeled and measured salinities at the locations of shipboard verticals south of the Station during a flood phase on 29 May 1998.
- Figure III-57 Location of moored instruments for the calibration period.
- Figure III-58a Comparison of modeled and measured salinity at Mooring 5, which is located offshore of the Station near the shipping channel, for the calibration period (19 May - 4 June 1998).
- Figure III-58b Comparison of modeled and measured salinity at Mooring 2, which is located 6 miles north of the Station near the shipping channel, for the calibration period (19 May - 4 June 1998).
- Figure III-58c Comparison of modeled and measured salinity at Mooring 4, which is located towards the northern end of Artificial Island near the shipping channel, for the calibration period (19 May - 4 June 1998).
- Figure III-58d Comparison of modeled and measured salinity at Mooring 7, which is located 3 miles south of the Station, for the calibration period (19 May - 4 June 1998).
- Figure III-58e Comparison of modeled and measured salinity at Mooring 9, which is located 6 miles south of the Station near the shipping channel, for the calibration period (19 May - 4 June 1998).
- Figure III-58f Comparison of modeled and measured salinity at Mooring 6, which is located near the Station on the western side of the shipping channel, for the calibration period (19 May - 4 June 1998).

- Figure III-58g Comparison of modeled and measured salinity at Mooring 1, which is located 6 miles north of the Station on the western side of the shipping channel, for the calibration period (19 May - 4 June 1998).
- Figure III-58h Comparison of modeled and measured salinity at Mooring 10, which is located 6 miles south of the Station on the eastern side of the shipping channel, for the calibration period (19 May - 4 June 1998).
- Figure III-58i Comparison of modeled and measured salinity at Mooring M9, which is located 9 miles south of the Station near the shipping channel, for the calibration period (19 May - 4 June 1998).
- Figure III-58j Comparison of modeled and measured salinity at Mooring M12, which is located 12 miles south of the Station near the shipping channel, for the calibration period (19 May - 4 June 1998).
- Figure III-59a Comparison of modeled and measured temperatures along the axis of the Estuary for 27 May 1998 (RM 130 to 90).
- Figure III-59b Comparison of modeled and measured temperatures along the axis of the Estuary for 27 May 1998 (RM 80 to 145).
- Figure III-59c Comparison of modeled and measured temperatures along the axis of the Estuary for 27 May 1998 (RM 40 to 0).
- Figure III-60a Comparison of modeled and measured temperatures along the axis of the Estuary for 2 June 1998 (RM 130 to 90).
- Figure III-60b Comparison of modeled and measured temperatures along the axis of the Estuary for 2 June 1998 (RM 80 to 45).
- Figure III-60c Comparison of modeled and measured temperatures along the axis of the Estuary for 2 June 1998 (RM 40 to 10).
- Figure III-61a Comparison of modeled and measured temperature at Mooring M9, which is located 9 miles south of the Station near the shipping channel, for the calibration period (19 May - 4 June 1998).
- Figure III-61b Comparison of modeled and measured temperature at Mooring 9M, which is located 9 miles north of the Station near the shipping channel, for the calibration period (19 May - 4 June 1998).
- Figure III-61c Comparison of modeled and measured temperature at the Hope Creek mooring, for the calibration period (19 May - 4 June 1998).
- Figure III-61d Comparison of modeled and measured temperature at Mooring 6, which is located near the Station on the western side of the shipping channel, for the calibration period (19 May - 4 June 1998).
- Figure III-62a Contours of measured surface temperatures with boat trackings for an ebb phase on 29 May 1998.
- Figure III-62b Contours of measured surface temperatures with boat trackings for an ebb phase on 29 May 1998 (close-up view).
- Figure III-63a Contours of measured surface temperatures with boat trackings for a slack (end-of-ebb) phase on 29 May 1998.
- Figure III-63b Contours of measured surface temperatures with boat trackings for a slack (end-of-ebb) phase on 29 May 1998 (close-up view).
- Figure III-64a Contours of measured surface temperatures with boat trackings for a flood phase on 29 May 1998.

- Figure III-64b Contours of measured surface temperatures with boat trackings for a flood phase on 29 May 1998 (close-up view).
- Figure III-65a Contours of measured surface temperatures with boat trackings for a slack (end-of-flood) phase on 29 May 1998.
- Figure III-65b Contours of measured surface temperatures with boat trackings for a slack (end-of-flood) phase on 29 May 1998 (close-up view).
- Figure III-66a Contours of modeled surface temperatures for an ebb phase on 29 May 1998.
- Figure III-66b Contours of modeled surface temperatures for an ebb phase on 29 May 1998 (close-up view).
- Figure III-67a Contours of modeled surface temperatures for a slack phase (end-of-ebb) on 29 May 1998.
- Figure III-67b Contours of modeled surface temperatures for a slack phase (end-of-ebb) on 29 May 1998 (close-up view).
- Figure III-68a Contours of modeled surface temperatures for a flood phase on 29 May 1998.
- Figure III-68b Contours of modeled surface temperatures for a flood phase on 29 May 1998 (close-up view).
- Figure III-69a Contours of modeled surface temperatures for a slack phase (end-of-flood) on 29 May 1998.
- Figure III-69b Contours of modeled surface temperatures for a slack phase (end-of-flood) on 29 May 1998 (close-up view).
- Figure III-70 Comparison of modeled Station intake and discharge temperatures to measured intake (TIN1 and TIN2) and discharge (Unit 1 and Unit 2) temperatures for the calibration period (21 May - June 4 1998).
- Figure III-71 Comparison of modeled surface delta temperatures for an ebb phase on 29 May 1998.
- Figure III-72 Contours of modeled surface delta temperatures for a slack phase (end-of-ebb) on 29 May 1998.
- Figure III-73 Comparison of modeled surface delta temperatures for a flood phase on 29 May 1998.
- Figure III-74 Contours of modeled surface delta temperatures for a slack phase (end-of-flood) on 29 May 1998.
- Figure III-75 Contours of measured surface delta temperatures for an ebb phase on 29 May 1998 (based on an ambient temperature of 71.42°F.).
- Figure III-76 Contours of measured surface delta temperatures for a slack phase (end-of-ebb) on 29 May 1998 (based on an ambient temperature of 71.42°F.).
- Figure III-77 Contours of measured surface delta temperatures for a flood phase on 29 May 1998 (based on an ambient temperature of 71.42°F.).
- Figure III-78 Contours of measured surface delta temperatures for a slack phase (end-of-flood) on 29 May 1998 (based on an ambient temperature of 71.42°F.).
- Figure III-79a Comparison of modeled and measured tides in the Estuary for the verification period (21-31 October 1997).

- Figure III-79b Comparison of modeled and measured tides at the west side of the Bay mouth (Lewes, DE) and the western end of the C&D Canal for the verification period (21-31 October 1997).
- Figure III-80a Comparison of modeled and measured tides in the Estuary for 28 October 1997.
- Figure III-80b Comparison of modeled and measured tides at the west side of the Bay mouth (Lewes, DE) and the western end of the C&D Canal for 28 October 1997.
- Figure III-81 Variation in tide range and tidal delay along the axis of the Estuary for the verification period (21-31 October 1997).
- Figure III-82 Comparison of the measured and modeled flow through three transects located 6 miles north of the Station, at the Station and 6 miles south of the Station for 28 October 1997.
- Figure III-83 Measured current speed along three transects located 6 miles north of the Station, at the Station, and 6 miles south of the Station for a flood phase on 28 October 1997.
- Figure III-84 Modeled current speeds along three transects located 6 miles north of the Station, at the Station, and 6 miles south of the Station for a flood phase on 28 October 1997.
- Figure III-85 Locations of shipboard vertical profiles during a flood phase on 28 October 1997.
- Figure III-86 Comparison of modeled and measured salinities at locations of shipboard verticals near the limits of the sampling region during a flood phase on 28 October 1997.
- Figure III-87 Comparison of modeled and measured salinities at locations of shipboard verticals in the vicinity of the Station during a flood phase on 28 October 1997.
- Figure III-88a Comparison of modeled and measured salinity at Mooring 5, which is located offshore of the Station near the shipping channel, for the verification period (21-31 October 1997).
- Figure III-88b Comparison of modeled and measured salinity at Mooring 9, which is located 6 miles south of the Station near the shipping channel, for the verification period (21-31 October 1997).
- Figure III-88c Comparison of modeled and measured temperature at Mooring 2, which is located 6 miles north of the Station near the shipping channel, for the verification period (21-31 October 1997).
- Figure III-88d Comparison of modeled and measured temperature at Mooring 9, which is located 6 miles south of the Station near the shipping channel, for the verification period (21-31 October 1997).
- Figure III-88e Comparison of modeled and measured temperature at the Hope Creek mooring, for the verification period (21-31 October 1997).
- Figure III-88f Comparison of modeled and measured temperature at Mooring 5, which is located offshore of the Station near the shipping channel, for the verification period (21-31 October 1997).

- Figure III-88g Comparison of modeled and measured temperature at Mooring 6, which is located near the Station on the western side of the shipping channel, for the verification period (21-31 October 1997).
- Figure III-89a Contours of measured surface temperatures with boat trackings for an ebb phase on 28 October 1997.
- Figure III-89b Contours of measured surface temperatures with boat trackings for an ebb phase on 28 October 1997 (close-up view).
- Figure III-90a Contours of measured surface temperatures with boat trackings for a slack phase (end-of-ebb) on 28 October 1997.
- Figure III-90b Contours of measured surface temperatures with boat trackings for a slack phase (end-of-ebb) on 28 October 1997 (close-up view).
- Figure III-91a Contours of measured surface temperatures with boat trackings for a flood phase on 28 October 1997.
- Figure III-91b Contours of measured surface temperatures with boat trackings for a flood phase on 28 October 1997 (close-up view).
- Figure III-92a Contours of measured surface temperatures with boat trackings for a slack phase (end-of-flood) on 28 October 1997.
- Figure III-92b Contours of measured surface temperatures with boat trackings for a slack phase (end-of-flood) on 28 October 1997 (close-up view).
- Figure III-93a Contours of modeled surface temperatures for an ebb phase on 28 October 1997.
- Figure III-93b Contours of modeled surface temperatures for an ebb phase on 28 October 1997 (close-up view).
- Figure III-94a Contours of modeled surface temperatures for a slack phase (end-of-ebb) on 28 October 1997.
- Figure III-94b Contours of modeled surface temperatures for a slack phase (end-of-ebb) on 28 October 1997 (close-up view).
- Figure III-95a Contours of modeled surface temperatures for a flood phase on 28 October 1997.
- Figure III-95b Contours of modeled surface temperatures for a flood phase on 28 October 1997 (close-up view).
- Figure III-96a Contours of modeled surface temperatures for a slack phase (end-of-flood) on 28 October 1997.
- Figure III-96b Contours of modeled surface temperatures for a slack phase (end-of-flood) on 28 October 1997 (close-up view).
- Figure III-97a Comparison of modeled and measured temperature at Mooring H, which is located approximately ½ mile southeast of the Station, for the verification period (21-31 October 1997).
- Figure III-97b Comparison of modeled and measured temperature at Mooring N, which is located approximately 1 mile southeast of the Station, for the verification period (21-31 October 1997).
- Figure III-97c Comparison of modeled and measured temperature at Alloway Creek mooring for the verification period (21-31 October 1997).
- Figure III-98 Location of shipboard vertical profiles measured during an ebb phase on 28 October 1997.

- Figure III-99 Comparison of modeled and measured temperatures at locations of shipboard verticals in the vicinity of the Station during an ebb phase on 28 October 1997.
- Figure III-100 Location of shipboard vertical profiles measured during a flood phase on 28 October 1997.
- Figure III-101 Comparison of modeled and measured temperatures at locations of shipboard verticals in the vicinity of the Station during a flood phase on 28 October 1997.
- Figure III-102a Contours of modeled surface delta temperatures for an ebb phase on 28 October 1997 (based on an ambient run).
- Figure III-102b Contours of modeled surface delta temperatures for a slack phase (end-of-ebb) on 28 October 1997 (based on an ambient run).
- Figure III-102c Contours of modeled surface delta temperatures for a flood phase on 28 October 1997 (based on an ambient run).
- Figure III-102d Contours of modeled surface delta temperatures for a slack phase (end-of-flood) on 28 October 1997 (based on an ambient run).
- Figure III-103a Contours of measured surface delta temperatures for an ebb phase on 28 October 1997 (based on an ambient temperature of 56°F).
- Figure III-103b Contours of measured surface delta temperatures for a slack phase (end-of-ebb) on 28 October 1997 (based on an ambient temperature of 56°F).
- Figure III-103c Contours of measured surface delta temperatures for a flood phase on 28 October 1997 (based on an ambient temperature of 56°F).
- Figure III-103d Contours of measured surface delta temperatures for a slack phase (end-of-flood) on 28 October 1997 (based on an ambient temperature of 56°F).
- Figure III-104 Comparison of measured and modeled Station intake and discharge temperatures for the verification period (21-31 October 1997).
- Figure III-105a Contours of measured surface dye with boat trackings for an ebb phase on 29 May 1998.
- Figure III-105b Contours of measured surface dye with boat trackings for an ebb phase on 29 May 1998 (close-up view).
- Figure III-106a Contours of measured surface dye with boat trackings for a slack phase (end-of-ebb) on 29 May 1998.
- Figure III-106b Contours of measured surface dye with boat trackings for a slack phase (end-of-ebb) on 29 May 1998 (close-up view).
- Figure III-107a Contours of measured surface dye with boat trackings for a flood phase on 29 May 1998.
- Figure III-107b Contours of measured surface dye with boat trackings for a flood phase on 29 May 1998 (close-up view).
- Figure III-108a Contours of measured surface dye with boat trackings for a slack phase (end-of-flood) on 29 May 1998.
- Figure III-108b Contours of measured surface dye with boat trackings for a slack phase (end-of-flood) on 29 May 1998 (close-up view).
- Figure III-109a Contours of modeled surface dye for an ebb phase on 29 May 1998.

- Figure III-109b Contours of modeled surface dye for an ebb phase on 29 May 1998 (close-up view).
- Figure III-110a Contours of modeled surface dye for a slack phase (end-of-ebb) on 29 May 1998.
- Figure III-110b Contours of modeled surface dye for a slack phase (end-of-ebb) on 29 May 1998 (close-up view).
- Figure III-111a Contours of modeled surface dye for a flood phase on 29 May 1998.
- Figure III-111b Contours of modeled surface dye for a flood phase on 29 May 1998 (close-up view).
- Figure III-112a Contours of modeled surface dye for a slack phase (end-of-flood) on 29 May 1998.
- Figure III-112b Contours of modeled surface dye for a slack phase (end-of-flood) on 29 May 1998 (close-up view).
- Figure III-113 Comparison of modeled and measured Station intake and discharge dye concentrations for the calibration period (27-30 May 1998).
- Figure III-114 Linkage results for the ebb tidal phase (29 May 1998 model calibration period).
- Figure III-115 Linkage results for the floor tidal phase (29 May 1998 model calibration period).
- Figure III-116 Linkage results for the end of ebb tidal phase (29 May 1998 model calibration period).
- Figure III-117 Linkage results for the end of flood tidal phase (29 May 1998 model calibration period).
- Figure III-118 Comparison of TTM results with observed mid-depth water temperatures at Mooring 24 (4 October 1998 through 17 October 1998).
- Figure III-119 Comparison of TTM results with observed surface water temperatures at Mooring 23 (4 October 1998 through 17 October 1998).
- Figure III-120 Comparison of TTM results with observed surface water temperatures at Mooring 22 (4 October 1998 through 17 October 1998).
- Figure III-121 Comparison of TTM results with observed bottom water temperatures at Mooring 21 (4 October 1998 through 17 October 1998).
- Figure IV-1 Map of Delaware Bay showing moored instrument station locations occupied during the Two-Unit Survey May-June 1998 (Exhibit E-1-3).
- Figure IV-2a Longitudinal variation of tidal harmonic constituents and nonlinear component along Delaware Bay: amplitudes.
- Figure IV-2b Longitudinal variation of tidal harmonic constituents and nonlinear component along Delaware Bay: phases.
- Figure IV-3a Current time-series at near-surface, mid-depth, and near-bottom levels measured with an ADCP at mooring V (red), compared with model-predicted currents (black); a: current speed. Sea level measured at the Salem Barge Slip is also shown.

- Figure IV-3b Current time-series at near-surface, mid-depth, and near-bottom levels measured with an ADCP at mooring V (red), compared with model-predicted currents (black); b: current direction. Sea level measured at the barge slip is also shown.
- Figure IV-4 Comparison of modeled and observed flow on 29 May 1998 at three cross-river transects located six miles upstream and downstream of the Station and at the Station. The curves show smoothed model predictions, and plotted points are observed volume transport measurements from the vessel ADCP surveys (Exhibit E-1-3).
- Figure IV-5 Observed (upper panel) and modeled (lower panel) mean longitudinal salinity structure of Delaware Bay. Mile 0 on this plot represents the location of the Station. The moorings shown are located at the east side of the main channel.
- Figure IV-6 Observed and modeled mean longitudinal temperature structure of Delaware Bay. Mile 0 on this plot represents the location of the Station. The moorings shown are located at the east side of the main channel.
- Figure IV-7 Observed (red) and modeled (black) time-series of surface, mid-depth and bottom temperature at Mooring M5, also showing tide height at Salem Barge Slip and ADCP current speed and direction.
- Figure IV-8 Observed and modeled cross river structure of mean temperature and salinity. The bottom observed temperature at Mooring M9 is extrapolated from the mid-depth observation (due to lack of moored data).
- Figure IV-9 Tidally averaged surface salinity predicted by RMA-10 during 12.5 hour period centered on 1200 hrs., 29 May 1998, also showing tidally averaged mean salinities measured with moored instruments.
- Figure IV-10 Observed (red) and modeled (black) temperature time-series observed at station M9 at surface, mid-depth and bottom levels, also showing modeled tide height at Woodland Beach, solar insolation and air temperature.
- Figure IV-11 Observed (red) and modeled (black) salinity time-series at mooring M9 at surface, mid-depth and bottom levels, also showing modeled tide height at Woodland Beach, solar insolation and air temperature.
- Figure IV-12 Observed (red) and modeled (black) surface temperature time-series along a line extending offshore through the Station is discharge. From east to west, the moorings plotted are 21, 22, V, and 5. Also shown is tide height at the nearest point, the Salem Barge Slip.
- Figure IV-13 Peak observed (upper panel) and modeled (lower panel) temperatures at surface, mid-depth and bottom at stations 21, 22, V, 5, and 6 on a cross-shore line through the Station is discharge. Shown on the upper panel (solid line) is observed surface temperature from a vessel survey following the plume. Shown on the lower panel (solid line) is the combined model-predicted temperature following the centerline of the predicted plume.

- Figure IV-14 Observed surface plume temperatures during the EOF slack period from the Two-Unit Survey, 29 May 1998 (Exhibit E-1-3), overplotted with CORMIX model results.
- Figure IV-15 Observed (red) and modeled (black) surface temperature time-series along a shore-parallel line through the Station discharge. From south to north, the moorings plotted are H, 24, 21, 23 and E. Also shown is tide height at the nearest point, the Salem Barge Slip.
- Figure IV-16 Peak observed (upper panel) and modeled (lower panel) temperatures at surface, mid-depth and bottom at stations H, 24, 23, and E on an along-shore line through the Station's discharge.
- Figure IV-17 Observed surface plume temperature during flood phase from the Two-Unit Survey, 29 May 1998 (Exhibit E-1-3), overplotted with CORMIX model results.
- Figure IV-18 Observed surface plume temperature during ebb phase from the Two-Unit Survey, 29 May 1998 (Exhibit E-1-3), overplotted with CORMIX model results.
- Figure IV-19 Observed (red) and modeled (black) temperature time-series at Alloway Creek. Also shown: tide height at Alloway Creek, current direction from the bottom-mounted ADCP near the Station, and solar insolation and air temperature at the Station.
- Figure IV-20 Observed (red) and modeled (black) temperature time-series at Hope Creek. Also shown: tide height at Hope Creek, current direction from the bottom-mounted ADCP near the Station, and solar insolation and air temperature at the Station.
- Figure IV-21 Observed (red) and modeled (black) temperature time-series at Mad Horse Creek. Also shown: tide height at Mad Horse Creek, current direction from the bottom-mounted ADCP near the Station, and solar insolation and air temperature at the Station.
- Figure IV-22 Observed (red) and modeled (black) time series of surface temperature at moorings 9G and 9R, located 9 miles north of the Station off the Salem River. Also shown are Reedy Point tide height, current direction from the bottom-mounted ADCP near the Station, and solar insolation and air temperature at the Station.
- Figure IV-23 Observed (red) and modeled (black) time series of surface temperature at moorings 12G and 12R, located 12 miles north of the Station off the Salem River. Also shown are Reedy Point tide height, current direction from the bottom-mounted ADCP near the Station, and solar insolation and air temperature at the Station.
- Figure IV-24 Time-series of water surface slope along the C&D Canal (upper trace) and modeled flow in the Canal (lower trace) for sample Simulation E.
- Figure IV-25 Relationship of flow to slope in modeled C&D Canal for projection sample Simulations A-E. Data points are hourly values; lines are linear least squares regressions.

- Figure V-1 Plume Surface Delta-T Contours Ebb Tidal Phase, 2 June 1998, 0830 hrs. Discharge Delta-T = 22.7 deg. F (Relative to Ambient Temperature).
- Figure V-2 Plume Centerline Delta-T (degrees F) Ebb Tidal Phase, 2 June 1998, 0830 hrs. Discharge Delta-T = 22.7 deg. F (Relative to Ambient Temperature).
- Figure V-3 Plume Centerline Velocity (feet per second) Ebb Tidal Phase, 2 June 1998, 0830 hrs. Ambient Velocity = 1/85 ft/s.
- Figure V-4 Plume Bottom Contact Velocity (feet per second) Ebb Tidal Phase, 2 June 1998, 0830 hrs.
- Figure V-5 Sample Time-Delta-Temperature History, Ebb Phase (2 June 1998, 0830 hrs.).
- Figure V-6 Surface ΔT isotherms for Salem's longest plume at end-of-flood on 5 May 1998.
- Figure V-7 Bottom ΔT isotherms for Salem's longest plume at end-of-flood on 5 May 1998.
- Figure V-8 Cross-section locations for the Delaware Estuary in the vicinity of the Salem Thermal Discharge
- Figure V-9 Delaware River Delta-T Cross Section Looking Down-river at End of ZIM on Ebb Tide on 2 June 1998, 0830 hrs..
- Figure V-10 Locations of Delaware River cross-sections at mouths of tributaries.
- Figure V-11 Cross section of ΔT : Delaware River at Alloway Creek on ebb, 2 June 1998, 08:30.
- Figure V-12 Example of Time Series of Shoreline ΔT Along Artificial Island (5 May 1998 - 4 June 1998).
- Figure V-13 Weekly Mean Observed Water Temperature at plant Intake 1992-1998 Plant at or above 90% Thermal Power for 7 or More Consecutive Days.
- Figure V-14 Ranked Weekly Average Temperatures.
- Figure V-15 20-Year Average Weekly Ambient Water Temperatures (1978-1997) from ATM Modeling.

APPENDIX E ATTACHMENT E-2 HYDROTHERMAL MODELING PROGRAM

INTRODUCTION

Attachment E-2 describes the numerical models and methods that were applied in the 1999 Hydrothermal Modeling Program conducted for this 316(a) Demonstration. The numerical models were implemented to characterize the process of thermal plume formation as the discharge water from the Salem Generating Station enters and mixes with the receiving water in the Delaware Bay Estuary.

The purpose of the 1999 Hydrothermal Modeling Program is to apply a set of computer models that can be used to approximate the behavior of the Salem plume in accordance with government environmental regulations, such as §316(a) of the federal Clean Water Act. These regulations provide that a §316(a) variance will be granted if the Station's thermal effluent is protective of the Balanced Indigenous Community (BIC). Hydrothermal models are applied to determine the potential extent of the plume under reasonable worst-case biological scenarios (Appendix E Section V.F), and to provide work products that support a biothermal assessment for this 316(a) Demonstration.

For the purposes of this assessment, the models have been developed with the capability to predict several characteristics of the thermal plume including its size, trajectory, and temperature variations. The hydrothermal modeling work products derived from these models for the biothermal assessment are provided in Appendix E Section V.F., and the biothermal assessment is presented in Appendix E Section VI. of. The biothermal assessment demonstrates compliance with the requirement that the thermal effluent be protective of the BIP.

Section I. provides a brief description of the 1999 Hydrothermal Modeling Program in the context of Station operations, the hydrodynamics of the Estuary, and generally established thermal plume dynamics. Section II. reviews the methods previously used to support investigations and permit applications for the Station.

Section III. describes the 1999 modeling methods, including the selection process for the particular models used as well as any modifications that were required to tailor them for site-specific application in this evaluation of the Station. Section III. also documents the implementation of the models which was consistent with the Modified Thermal Monitoring Program (Modified TMP). This section describes how field data were used as input to the models as well as for model calibration, verification, and/or validation to ensure an accurate simulation of the natural processes associated with the Salem plume.

Sections IV. and V. describe how the model results were processed and interpreted to produce the statistical and graphical output necessary for the biothermal assessment. Actual model results and detailed descriptions are provided in Section V.

I. DESCRIPTION OF THE STATION'S DISCHARGE AND THERMAL PLUME PROCESSES

The size, shape, and dynamics of the Salem plume are dependent on the design of the cooling water discharge outfall, the local bathymetry around the outfall, the characteristics of the thermal discharge, and the hydrodynamic conditions in the Estuary. The interaction of these factors can be evaluated using mathematical models that accurately simulate the transport and mixing processes that take place in the vicinity of Salem and throughout the Estuary. The following Sections summarize established information that was relied upon in the development of the 1999 Hydrothermal Modeling Program.

I.A. Salem Generating Station

Previous modeling studies (Section II) of the Station's thermal discharge have shown consistently that the dynamics of the near-field region of the plume are strongly dependent on the configuration of the discharge structure, the characteristics of the thermal discharge, the local currents, and the local bathymetry. At greater distances from the discharge structure, the primary operational variable affecting the plume is the Station's heat rejection rate over time. This section summarizes those characteristics of the Station that were pertinent to the modification of the numerical models used for the 1999 Hydrothermal Modeling Program. A detailed description of the Station is provided in Appendix B of this submittal.

Two of the three electric generating units (Units 1 and 2) at the Station use a once-through cooling water system. These units withdraw water from the Estuary to condense the steam from the Station's turbines, then discharge this water to the Estuary at an elevated temperature. The intake structure is located along the shoreline of Artificial Island, and spans the entire water column. The heated water is returned to the Delaware Estuary through six adjacent pipes that are 10 feet in diameter and spaced 15 feet apart on center. The pipes are buried for most of their length between the Station and the discharge location, approximately 500 feet offshore, where they are exposed to the receiving water body. At mean tidal level the depth of the discharge centerline is approximately 31 feet. The discharge is horizontal and approximately perpendicular to the prevailing currents at the discharge point. Features of the local bathymetry at the discharge site help mix the plume throughout the water column relatively quickly. Details of the diffuser and surrounding bathymetry are provided in Exhibit E-1-4.

The two operational variables that affect the size, shape and structure of the Salem plume are its cooling water discharge rate ($Q_{\text{condenser}}$) and the difference between the temperatures of its discharge and intake waters ($\Delta T_{\text{condenser}}$). A related variable, the heat rejection rate, is equal to the product of the specific heat of water (c_p), $Q_{\text{condenser}}$ and $\Delta T_{\text{condenser}}$. Based on the design of Units 1 and 2, the Station's maximum expected heat rejection rate is approximately $15,600 \times 10^6$ Btu/hr.

$Q_{\text{condenser}}$ varies with the number of operating circulating pumps, pump efficiency, and fouling of condenser tubes. Based on analyses of the hydraulic design of Salem's cooling

water system, manufacturer's curves for the circulating water pumps (Exhibit B-1-1) and Station data, the average circulating pump flow rate is expected to range from 140,000 gpm to 175,000 gpm. Accordingly, when Salem discharges at the maximum heat rejection rate, $\Delta T_{\text{condenser}}$ is 14.8°F when the average circulating pump flow rate is 175,000 gpm, and 18.6°F when the average circulating pump flow rate is 140,000 gpm.

I.B. Artificial Island and the Delaware Estuary

This section provides a brief overview of the Estuary in the vicinity of Salem to highlight elements most pertinent to the hydrothermal modeling. A detailed description of the Estuary is provided in Appendix C to this submittal, and Appendix E Section IV summarizes those elements most pertinent to this 316(a) Demonstration. Detailed field data and analyses describing estuarine processes are provided in Attachment E-1, including accompanying Exhibits.

The Estuary is a tidal water body that extends from the mouth of Delaware Bay, where it meets the Atlantic Ocean (RM 0), upstream to the head-of-tide at Trenton, New Jersey (RM 133). Tides from the Atlantic Ocean propagate throughout the Estuary. The mean tide range at the mouth of the Estuary is approximately 4.8 feet; it increases to more than 8 feet at Trenton due to the funnel-shaped geometry of the Estuary that amplifies the tide. Other tidal forcing is introduced to the Estuary through the C&D Canal that connects the Delaware River Estuary with the Chesapeake Bay Estuary. Freshwater inflows to the Delaware Estuary also affect the Salem Station thermal plume. The freshwater inflows include the Delaware River at Trenton, major tributaries such as the Schuylkill River, other minor tributaries, and extensive marsh plains.

Currents in the Estuary adjacent to the Station are tidally reversing, with speeds dependent on both tidal stage and freshwater inflows. Tidal currents flow generally south-to-north on the flood tide, and north-to-south on the ebb tide. Currents can reach speeds of up to 4 feet per second (ft/sec) in the navigational channel, but are typically lower in the shallows adjacent to the Station. The average cross-sectional velocity measured in the vicinity of the Station is 1.2 ft/sec, with typical ebb and flood current speed maxima of 3.2 and 2.5 ft/sec, respectively. Slack tides are relatively brief, and last less than one hour.

Currents also are affected by the salinity- and temperature-based density variations within the Estuary. Generally, increasing salinity and/or decreasing temperature increases water density. Current patterns are affected as denser water tends to sink and less dense water tends to float.

The salinity at the Station can range from nearly zero to up to 20 ppt. During periods of low freshwater inflow in summer, the salinity is typically above 6 ppt. The Delaware Estuary in the vicinity of the Station typically displays little salinity stratification, meaning that there is little variation in salinity from the surface to the bottom of the water column. Periods of significant freshwater inflow can on occasion cause some salinity stratification.

Water temperature in the Estuary is dependent upon a variety of factors, including temperature of the tidal water flowing through from the Atlantic Ocean and the C&D Canal, freshwater inflow, water depth, and other sources of heat such as the Station. Meteorological factors, including solar radiation, wind speed, and dewpoint, affect water temperature by influencing heat exchange rates at the water's surface.

I.C. Hydrothermal Plume Processes

Appendix E Section V.B.3 provides a detailed description of the Salem plume processes. A brief summary of the plume processes is provided here as a basis for further discussions of the hydrothermal modeling program.

The thermal plume may be described as the portion of the Estuary in which water temperature is affected by the Salem discharge. The thermal plume typically is characterized by an applicable legal discharge-induced increase in temperature (i.e., the excess temperature or ΔT) as measured against an ambient or background temperature. The boundary within which all ΔT values are equal to or greater than a given ΔT is called an isopleth of ΔT . Thus, the thermal plume is defined as the volume of water bounded by a specified ΔT isopleth.

Due to the tidal character of the Estuary, the Salem plume is dynamic, moving alternately up-estuary for approximately five hours during incoming flood flow, then down-estuary for approximately seven hours during ebb flow. Slack tides are brief and occur only for a period of minutes between floods and ebbs.

The processes by which the plume ΔT isopleths are established occur in several steps that can generally be characterized as near-field and far-field. Near-field processes occur in a region where the momentum primarily and, to a lesser extent, the buoyancy of the discharged water dominate the factors influencing plume transport and dilution. This near-field includes the zone of initial mixing (ZIM). The temperature of the plume reduces rapidly in the near-field as the discharged water mixes with receiving water.

The transport of the diluted plume is governed primarily by ambient tidal currents in the Estuary. Plume temperature generally decreases more slowly in the far-field as heat dissipates through mechanisms such as buoyant spreading, passive diffusion, and surface heat exchange. The characteristics of the thermal plume in the far-field vary as the prevailing meteorological and receiving water conditions change.

II. PRIOR HYDROTHERMAL AND HYDRODYNAMIC MODELING PROGRAMS

Between 1968 and 1995, various studies were completed to develop an understanding of the Salem plume characteristics. Appendix E Section V.C. provides a detailed summary of these previous studies, which incorporated a range of methods, including physical modeling, field measurements, and numerical modeling.

These methods varied in both ease of implementation and in the type and accuracy of the information they produced. To provide a background for the 1999 Hydrothermal Modeling Program, the methods employed in the previous studies are reviewed in this section, with a summary of the advantages and limitations of each. The complexity of these studies has increased through the years as science and technology have advanced. As a result, more detailed information about the Salem plume has been gathered recently. Despite the improvements to these studies, the general description of the Salem plume has not been modified significantly since the initial physical model of the system was constructed in 1968. The current predictions and measurements of the excess water temperature (ΔT) and the overall extent of the plume are consistent with the predictions presented even before the Station was constructed.

Currently, the best methodology for simulating plume dynamics combines field measurements with numerical modeling. This approach was used for the 1999 Demonstration (methods are described in detail in Section III.).

II.A. Physical Modeling In Support of PSE&G's Initial §316(a) Demonstration

The methodology employed for the initial Salem Section 316(a) Demonstration was based on a physical model of the Delaware Estuary. The physical modeling was completed by Pritchard and Carpenter (1968) at the United States Army Corps of Engineers Waterways Experiment Station in Vicksburg, Mississippi. The physical model was capable of simulating the thermal plume caused by the Salem discharge in the Estuary. As with any physical model, there were limitations associated with scale; however, the model was robust and simulated various discharge alternatives and estuarine flow conditions, including those at which heat exchange was expected to be minimal, thus simulating a worst-case plume in the Estuary.

II.B. Thermal Monitoring Program One-Unit Operation (1977-1978)

Following the Pritchard and Carpenter (1968) physical modeling study, a number of field data collection programs were undertaken to help characterize the Salem plume. The first field data collection program was performed in 1977-1978, and included monthly and semi-monthly shipboard monitoring surveys, as well as a number of shorter studies. These surveys were conducted to describe the extent of the thermal plume, its effect on the thermal regime of the Estuary, and the dispersion and circulation characteristics of the receiving water body. The following field data were collected: temperature, salinity, current velocity, dye concentration, and infrared imagery.

In addition to the routine monitoring program described above, two additional studies were conducted in 1977. A "Special Recirculation Study" was performed in July to determine if the heat discharged was being recirculated upstream to the cooling water intake. A second study, the "Special Heat Flux Study," was conducted in October 1977 to assess heat inputs of Alloway, Hope, and Mad Horse creeks into the Delaware River in the vicinity of the Station (Appendix E Section V.C).

These field measurements were valuable because they provided a direct measure of conditions in the receiving water, as opposed to forecast conditions predicted in a laboratory by the physical model. The primary limitation of such field data for characterizing the Salem Station plume is that the data are necessarily specific to the conditions that prevail during the survey period; prevailing conditions are not typically worst-case conditions. Another limitation of the 1977-1978 surveys was that the measurements were representative of single-unit operation only (Unit 2 was not yet in operation). They were further limited by the accuracy and extent of the measurement technology available.

II.C. Thermal Monitoring Program Two-Unit Operation (1982-1985)

In 1982, additional field data were collected to characterize the Salem plume (Appendix E, Section V.C.3). Two major thermal plume studies were conducted and included the following data: fixed station thermographs, continuous temperature recording mobile mapping, real-time fixed station water column temperature measurements, and aircraft-carried infrared thermal remote sensing imagery. The first survey was conducted on 15-16 June 1982, during relatively high freshwater inflow conditions; the second survey (which did not include infrared imagery) was conducted on 24 August 1982, during low freshwater inflow conditions.

The primary advantage of the 1982 surveys is that the data provide a direct measure of water temperature during two-unit operation. As described below, these data proved useful for future investigations in calibrating a numerical model that simulated near-field plume dynamics. The 1982 far-field data also were interpreted to help characterize the extent of the two-unit plume under the conditions that prevailed during the measurement periods. These measurement periods did not, however, include any instances of worst-case conditions.

II.D. 1991 Hydrothermal Studies

The 1991 §316(a) Variance Demonstration for Salem included the first application of a numerical model, UDKHDEN, to characterize the near-field region of the Salem plume. UDKHDEN is a three-dimensional steady-state mathematical plume model that was used to estimate ΔT s in the near-field only. In 1991, UDKHDEN was state-of-the-art with respect to three-dimensional near-field models. However, UDKHDEN had certain inherent limitations. In particular, it did not account for the interaction between the predicted plume and its physical boundaries (such as the water surface and bottom). It was therefore necessary to apply engineering judgment to interpret the UDKHDEN model results. Specifically, interpretation was required to characterize the interaction of the plume with the bottom near the point of discharge.

The UDKHDEN model was run using data from the field surveys performed in 1982. For the UDKHDEN model, the $\Delta T_{\text{condenser}}$ across the Station's condenser (observed during the 1982 field survey) and the Station's design maximum flow rate were used. Combining the 1982 $\Delta T_{\text{condenser}}$ with the maximum flow rate was conservative because the coupling of

the two inputs yielded higher Station heat rejection rates than can actually occur. This conservative approach therefore overestimated the near-field extent of the Salem plume.

The primary advantage of the 1991 computer modeling methodology over previous studies was in the information it furnished characterizing the near-field, which could not have been measured in the field due to the limitations of field equipment technology. The concern about using the computer surrounded its ability to accurately simulate natural processes. To address this concern, the model was applied for a time frame in which field data were collected.

Since UDKHDEN only simulated the near-field, the far-field plume was characterized based on the 1982 field data. These estimates of the far-field plume were restricted by the discharge, tidal, and meteorological conditions that prevailed during the measurement period. The Pritchard and Carpenter physical model (1968) remained the only method that had been used to forecast the far-field extent of the worst-case Salem plume.

II.E. 1993 Hydrothermal Modeling Program

For the NJPDES permit renewal of 1993, the mathematical modeling methods were improved so that they could accurately model both the near-field and the far-field. It was determined that a new state-of-the-art near-field model would eliminate many limitations of the UDKHDEN model implemented in 1991. Accordingly, the Cornell Mixing Zone Expert System, Version 2 (CORMIX-2) was applied to model the near-field. To model the far-field, RMA-10, a state-of-the-art, three-dimensional, time-variable mathematical model was applied. Because these models were implemented successfully in the 1993 modeling, refined versions are also being used for the 1999 permit renewal. A detailed description of CORMIX and RMA-10 is provided in Attachment E-2 Section III.

The major advantage of the 1993 modeling study was that it provided the first set of mathematical models that could be used to forecast worst-case conditions. Prior to 1993, only the Pritchard and Carpenter physical modeling study provided this capability. Generally, numerical models are more adaptable than physical models for this purpose, because the physical models are limited by scaling factors and physical constraints. The numerical models employed in 1993 allowed for the plume to be forecast under a variety of discharge, estuarine, and meteorological conditions.

II.F. 1995 Hydrodynamic Field Data Collection and Modeling Program

Although not applied to characterize the Salem plume, an additional extensive study involving field data collection and computer modeling applications was completed in 1995 (Exhibit E-1-1). The 1995 modeling program also utilized RMA-10, but focused on hydrodynamic processes only. Its purpose was the identification of the physical processes contributing to the accumulation of detritus in the Estuary near Salem. RMA-10 was calibrated and verified through the extensive collection of hydrodynamic data, including tide, current, and salinity measurements. The 1995 hydrodynamic calibration and verification of RMA-10 produced a more detailed representation of current patterns in the vicinity of Salem than had previously existed, specifically at Sunken Ships Cove and

Hope Creek Jetty. This information was provided based on a comprehensive hydrodynamic data set and a numerical grid with a higher degree of resolution. Portions of the enhanced grid resolution developed to simulate these current patterns in the 1995 study were adopted for the 1999 hydrothermal modeling study.

III. DESCRIPTION OF HYDROTHERMAL MODELING METHODS

The discharge of once-through cooling water from Salem increases water temperatures in the Estuary near the Station. These increases are relative to the ambient water temperature (T_{ambient}), which would exist in the absence of Salem's thermal discharge, and are called excess temperatures (or ΔT). The spatial distribution of ΔT over time defines the Station's thermal plume, which includes a region exhibiting strong spatial gradients in ΔT (the near-field including the Zone of Initial Mixing (ZIM)) where the discharge rapidly mixes with the Estuary water, and a region with much weaker temperature gradients (the far-field) where more passive mixing occurs. Temperatures within the thermal plume at any point and time can be estimated by adding the appropriate ΔT to T_{ambient} .

Numerical hydrothermal models were used to calculate seasonal variations in water temperatures and to characterize the thermal plume. These models produce estimates of T_{ambient} , a near-field component of ΔT ($\Delta T_{\text{near-field}}$), and a far-field ΔT ($\Delta T_{\text{far-field}}$). Other measures of ΔT that are referenced in this Attachment are:

- ΔT_{intake} : the ΔT relative to T_{ambient} at the Station's intake.
- ΔT_{eop} : the ΔT relative to T_{ambient} at the end of the discharge pipe,
- $\Delta T_{\text{approach}}$: ΔT relative to T_{ambient} just outside the near-field,
- $\Delta T_{\text{condenser}}$: the ΔT introduced by the Station as the cooling water condenses the steam from the turbines,
- ΔT_{CORMIX} : the ΔT relative to T_{approach} computed by near-field model, CORMIX,
- $\Delta T_{\text{RMA-10}}$: the ΔT relative to T_{ambient} computed by the far-field model, RMA-10, and
- ΔT_{ZIM} : the ΔT relative to T_{ambient} at the end of the zone of initial mixing (ZIM).

The procedure for combining the output from these models is conceptually illustrated in Figure III-1a, where three dimensions of temperature are presented. The top left plot shows the water temperature along a line that spans the Estuary from the mouth of Delaware Bay to Trenton, NJ, assuming the line passes over the discharge. The water temperature at any point in the plume near-field (ZIM) is the sum of T_{ambient} , the far-field component of ΔT ($\Delta T_{\text{RMA-10}}$), and the near-field component of ΔT (ΔT_{CORMIX}). Thus, ΔT at a point in the near-field of the thermal plume is the sum of the near-field and far-field components. By contrast, ΔT at a point in the far-field thermal plume is equal to the far-field component only. This approach is summarized below. Specific details are provided in Sections III.A through III.E.

T_{ambient} varies mainly over time and secondarily in space within the Estuary. The bottom plot on Figure III-1a shows that T_{ambient} varies naturally by 50°F (approximately 28°C)

over the course of a year. Consequently, the natural variation of T_{ambient} governs the water temperature in the Estuary. For instance, the dotted line on the bottom plot on Figure III-1a represents the thermal influence of the Station's plume at the end of the ZIM T_{ambient} , and demonstrates the Station's influence, even at this point close to the discharge, is small compared to the seasonal temperature variability. The top right plot on Figure III-1a focuses on the temporal variability of ΔT . It is apparent that a large percentage of the Station's thermal influence is reduced after approximately one hour.

Tidal marshes are natural sources of heat as well, and can contribute large spatial variations of T_{ambient} . Exhibit E-1-5 discusses the thermal significance of tidal marshes as heat sources. It shows that a single marsh can contribute significantly more heat than the Station, and can contribute a ΔT exceeding 7°F (4°C). Other spatial variations result from non-uniform natural heating and cooling of the Estuary, tidal mixing, tidal exchanges with marshes, and distant anthropogenic sources.

Given the relative importance of T_{ambient} , a long-term record of T_{ambient} is needed to reliably estimate the effect of the thermal plume on temperatures within the Estuary. The only long-term record of water temperature in the immediate vicinity of Artificial Island is the Reedy Island U.S. Geological Survey (USGS) data set. The Reedy Island USGS station is located near the western shore of the Delaware River, about 3.5 miles north of Salem. The Reedy Island data set contains limited information on T_{ambient} , because it is influenced by the Salem discharge. While the Reedy Island station is outside the Salem plume (i.e., the region enclosed by the 1.5°F isopleth of ΔT), Reedy Island experiences some thermal influence from the Station. The magnitude of the influence varies with tide conditions, Station operating conditions, and other factors. Consequently, there is no measured estimate of the Station's influence (ΔT) at Reedy Island that could be subtracted from the temperature data observed when Salem was operating to produce a time series of ambient water temperature. Water temperatures were recorded at Reedy Island for about seven years prior to Station operation and for the approximately two-year Station shutdown period. These data sets are not long enough to reliably project ambient temperatures that occur less often than about one year in seven. Also, the older data are not necessarily representative of present-day ambient conditions. Finally, there are gaps in the Reedy Island data set, and it is not certain whether measurements 3.5 miles from the Station are truly representative of ambient water temperatures at the Station, due to natural spatial variations of water temperature in the Estuary.

In the absence of complete, long-term observed ambient temperature data from the pre-operational period, a numerical model is required. The Ambient Temperature Model (ATM) was developed for this purpose. It was possible to simulate the long-term ambient water temperatures that would exist in the absence of a thermal discharge from Salem using this numerical model. The model was calibrated specifically to estimate ambient water temperature at the Salem intake, based on field data collected when the Station was not operating for 26 months. The calibrated and verified model was applied to provide a 50-year time history of ambient water temperature at the Station. This estimated ambient water temperature is equal to the sum of a "response temperature", a

seasonal adjustment for the buffering effect of the Atlantic Ocean on local water temperatures in the vicinity of Salem, and a site-specific adjustment that incorporates such factors as other anthropogenic sources of heat. The response temperature (T_r) is the temperature that a fully-mixed column of water reaches in response to meteorological and solar conditions alone. T_{ambient} was estimated using the Ambient Temperature Model (ATM) which sums T_r , the adjustment for the buffering effect of the Atlantic Ocean, and the site-specific adjustment for each day of a 50-year period. ATM provides estimates of daily average T_{ambient} at a single point (Section III.A. for the details of the ATM).

The far-field component of ΔT varies primarily with space, due to tidal transport and mixing, and secondarily with season, due to such factors as stratification and seasonal variation in surface heat exchange. Temperature changes (ΔT) in Salem's far-field thermal plume range from low to moderate (i.e., about 1.5°F to about 4°F), and reflect the mixing and transport of Salem's thermal discharge by tidal action. A state-of-the-art, three-dimensional hydrodynamic and transport model (RMA-10) was used to calculate the spatial distributions of ΔT in the far-field and their temporal variation over a tidal cycle (Section III.C. for the details of RMA-10).

The near-field component of ΔT varies almost exclusively in space for a given time in the tidal cycle, because near-field mixing is determined primarily by momentum effects of the discharge and water currents. Buoyancy is a secondary factor. Any temporal variations result primarily from changes in the magnitude and direction of water currents induced by tidal action. The near-field component of ΔT during ebb and flood running tides is confined to the immediate vicinity of Salem's discharge (approximately 1000 feet), but may extend farther during periods of slack water. A state-of-the-art, near-field mixing model (CORMIX) was used to calculate the near-field spatial distributions of ΔT for tidal currents at times of maximum flood and ebb, and at end-of-ebb and end-of-flood near-slack currents (Section III.B. for details on CORMIX).

The three models (i.e., ATM, CORMIX, and RMA-10) were linked to form a Total Temperature Model (TTM), which can be used to compute spatial distributions of water temperatures in the Estuary over time. The temporal variations include those that occur during a tide cycle, as well as seasonally. The following sections provide descriptions of ATM, CORMIX, RMA-10, and TTM; the methodology and data used to develop each model; and the procedures used to calibrate, verify, and /or validate each model and their linkages.

Figure III-1b illustrates the general approach implemented for the numerical models. Once a model was selected, it was calibrated and verified and/or validated before being applied to generate products that were used to support the Biothermal Assessment. Model calibration was a step that involved modifications to a model to ensure it had the capability to simulate observed data. Model verification was a step implemented after calibration to ensure the calibrated model could simulate an observed process independent of the calibration. Model validation was a step implemented to test an already calibrated and verified model for its ability to simulate a site-specific observed

process. The calibration, verification, and validation steps all required comprehensive monitoring data.

After the models were selected and calibrated, verified, and/or validated, the models were applied to represent four types of thermal exposure for the Biothermal Assessment. Figure III-1c illustrates that the models were applied to characterize the seasonality of exposure, the exposure duration, the spatial extent of thermal exposure, and the frequency of exposure. Graphical output from the hydrothermal models designed to support the Biothermal Assessment is provided in Appendix E Section V.F.

III.A. Ambient Temperature Model (ATM)

III.A.1. Description of ATM

The Ambient Temperature Model (ATM) is required because there is no long-term data set available to represent ambient water temperatures near the Station (Section III). ATM calculates an estimate of daily average T_{ambient} for the vicinity of Salem as the sum of a daily average T_r , a daily average adjustment for the Atlantic Ocean's influence ($\alpha \cdot \cos[2\pi(d - \tau)/365]$), and a site-specific adjustment (β) for such factors as other anthropogenic heat sources, or:

$$T_{\text{ambient}} \approx T_r + (\alpha \cdot \cos[2\pi(d - \tau)/365]) + \beta$$

where:

α = amplitude (°F) of the daily average adjustment for the buffering effect of the Atlantic Ocean

τ = phase lag (days) for the daily average buffering effect of the Atlantic Ocean

d = day of the year (Julian day)

T_r is the daily average temperature that a fully-mixed column of water reaches in response to meteorological and solar conditions. T_r is computed by solving the following equation that relates the change in the temperature of a fully-mixed column of water of depth, D , due to meteorological and solar inputs:

$$dT_r/dt = H_n / (\rho c_p D)$$

where:

T_r = response temperature

ρ = density of water

c_p = specific heat of water

D = depth of water column

dT_r/dt = rate of change in response temperature with time

H_n = net rate of surface heat exchange = $(H_s + H_a - H_{sr} - H_{ar}) - (H_b + H_e + H_c)$

H_s = short-wave solar radiation

H_a = long-wave atmospheric radiation

H_{sr} = reflected short-wave radiation

H_{ar} = reflected long-wave atmospheric radiation

H_b = back-radiation from the water column
 H_e = evaporative heat loss from the water column
 H_c = conductive heat exchange with the water column

Approximations for calculating H_s , H_a , H_{sr} , H_{ar} , H_b , H_e , and H_c are identical to those incorporated in RMA-10 (Section III.C.).

For this Demonstration, the equation for T_r is solved at hourly intervals. The hourly values of T_r over a 24-hour period are then averaged to obtain a daily average T_r .

The daily average T_{ambient} is calculated by adding the daily average T_r to the contribution by the Atlantic Ocean ($\alpha \cdot \cos[2\pi(d - \tau)/365]$) and the site-specific factor (β).

The seasonal buffering effect of the Atlantic Ocean is expressed as a cosinusoidal function having amplitude (α), a period of 365 days, and phase lag (τ) which accounts for the time required for the Atlantic Ocean's effect to occur in the vicinity of Salem. For example, when " $d - \tau$ " equals 0 days, the cosine term equals 1 and the Atlantic Ocean has the effect of increasing the local water temperature by an amount " α ." When " $d - \tau$ " is about 182 days, the cosine term equals -1 , and the Atlantic Ocean has the effect of decreasing the local water temperature by an amount " α ." The contribution of the Atlantic Ocean is zero when " $d - \tau$ " is about 90 days or 270 days, because the cosine term equals 0 at these times. This is a reflection of the seasonal affect of the ocean on water temperature.

The site-specific adjustment factor (β) accounts for other contributions to T_{ambient} that are not taken into account either by T_r or the adjustment for the buffering effect of the Atlantic Ocean. Examples include differences in water depth and influence of other heat sources.

Since ATM is a semi-empirical model, it must first be calibrated and then verified before it can be used to predict T_{ambient} . Once calibrated, the ATM can be used to create a long-term record of estimated daily average values of T_{ambient} for the vicinity of Salem. The methods for calibrating, verifying, and applying the ATM are described below.

III.A.2. Methodology

There are no long-term field data on T_{ambient} that can be used to estimate temperatures within Salem's plume (TRA et al. 1993). Instead, as described above, the ATM was applied to construct a long-term record of estimated T_{ambient} that reasonably represents the daily, seasonal, and annual variations in T_{ambient} .

The ATM is a semi-empirical model that includes four coefficients (α , τ , β , and D) whose values must be determined based on actual observations. As a result, ATM must be calibrated and verified before it can be used to construct a long-term estimated record. Input data for calibration and verification are described in Section III.A.3. The calibration

and verification methodology and results are summarized in Sections III.A.4 and III.A.5, respectively.

After the calibration and verification processes are completed, the ATM is used to calculate a long-term (50-year) record of estimated T_{ambient} . This record can then be used to derive statistics showing how often the average T_{ambient} on any day of the year is equaled or exceeded, and to derive similar statistics for longer (e.g., weekly) averaging periods. These statistics are used to quantify the year-to-year variability in T_{ambient} for any day or week and to quantify the seasonal variability in T_{ambient} over the year. When combined with estimates of ΔT , these statistics provide the basis for establishing the daily, seasonal, and annual variation in total water temperatures within the Salem plume. The results of the application of the ATM are presented in Appendix E Section V and VI.

III.A.3. Set-Up

Daily averages of water temperatures measured at the Salem Circulating Water Intake Structure (CWIS) (see Appendix B for a detailed description of the CWIS), and hourly meteorological observations from 1 July 1995 through 31 August 1997 were used to calibrate the ATM. The temperatures at Salem's intake provided an appropriate measure of T_{ambient} , because there was no thermal discharge from Salem during this period due to Station shutdown. Meteorological data from the National Weather Service (NWS) station at Wilmington, Delaware (Appendix C) were used in lieu of meteorological data collected at Salem, because the NWS data were available for a much longer period and a long-term meteorological record was needed to compute a long-term record of estimated T_{ambient} . The procedure used to determine values for the four empirical coefficients and to complete the calibration as discussed in Section III.A.4.

Once the four empirical coefficients were determined, the verification process involved testing the calibrated version of the ATM using data set that was not used previously for calibration. The data that were used to verify the accuracy of ATM's calculations were collected at the USGS Reedy Island station during the period 1 July 1995 through 31 August 1997, for the same period above when there was no thermal discharge from Salem. The Reedy Island station is near the western shore of the Delaware River, approximately 3.5 miles north of Salem.

III.A.4. Calibration

The calibration process for ATM requires determining appropriate values for α , τ , β and D . Appropriate values were selected by serially comparing calculated and measured water temperatures over time. The coefficients were elected such that the best correlation and smallest Root Mean Square (RMS) difference could be produced between ATM calculations and measured data.

The RMS difference between the observed daily average water temperatures at the Salem intake and the calculated daily averages of T_{ambient} is a measure of the confidence level that can be placed in any given estimate of daily average T_{ambient} . This difference is not constant and varies from day to day. The best comparison between ATM's calculations

and measured data is achieved when the values for the four empirical coefficients result in a minimum RMS difference. Since the site-specific correction (β) is removed before calculating the RMS difference, the RMS difference is essentially a measure of the variance in the differences.

Figure III-2 compares the time-series of computed and measured T_{ambient} at the Salem intake based on the final calibration of ATM which uses $\alpha = 2.0^{\circ}\text{F}$, $\tau = 52$ days, $\beta = 0.96^{\circ}\text{F}$, and $D = 18$ feet. Thus, the equation for estimating the daily average T_{ambient} is:

$$T_{\text{ambient}} \approx T_r + (2.0 \cos[2\pi(d - 52)/365]) + 0.96 (^{\circ}\text{F})$$

The computed time-series of T_{ambient} shows agreement with the time-series of measured intake temperatures at Salem. The RMS difference between the computed and observed temperatures was 1.15°F , during a period when the seasonal temperature varied by nearly 50°F . This RMS difference is not significantly greater than the accuracy of the measurements, indicating acceptable agreement.

III.A.5. Verification

The verification process involved comparing the results of the ATM with an independent (i.e., not used for calibration) set of water temperature observations from a site near Salem unaffected by the thermal discharge. The model can be considered verified if the RMS difference between the two series (after removal of any site-specific offset) is similar to the RMS difference achieved during calibration.

The data used for the verification of the ATM were observed at the USGS gauging station at Reedy Island during the period 1 July 1995 through 31 August 1997. The Reedy Island station is approximately 3.5 miles north of Salem, and is expected to have similar ambient temperatures for the period when the Station was not operating.

The verification comparison resulted in a mean difference of 0.62°F (Reedy Island had a slightly higher ambient temperature) and an RMS difference (after adjustment for the mean difference) of 1.35°F . These values provided acceptable verification when compared with the 1.15°F RMS difference found during the calibration. The mean difference appears to be related to prevailing spatial variation in ambient temperatures. During the Ambient Survey (Exhibit E-1-1) the typical standard deviation of cross-channel temperature measurements in the vicinity of Reedy Island ranged from about 0.3°F to about 1.1°F .

Verification of the ATM shows that the model can be used to estimate the ambient temperature for the region near the Station discharge.

III.B. Near-field Modeling: CORMIX

III.B.1. CORMIX Objectives

The CORMIX model was applied (1) to characterize the near-field thermal discharge dynamics at Salem; (2) to provide a calibrated and verified near-field model linked with the far-field model for simulating a continuous ΔT field, as described in Section III.D.; (3) to verify the Total Temperature Model (TTM), as described in Section III.E.; and (4) to provide work products required for the biothermal assessment.

To achieve these objectives the CORMIX model was modified. The subsequent modified and improved model provided a better simulation of the site-specific near-field temperature and velocity distribution in time and space, and a more refined method of calculating intra-modular CORMIX predictions. These modifications were discussed with and approved by staff who maintain the CORMIX model (Doneker 1998 and 1999).

In this section, reference is frequently made to the near-field "plume." This refers to the recently discharged plume, that is, the excess temperature field that is directly traceable to the thermal discharge within one tidal phase. The recently discharged plume is a sub-component of the total plume, which includes the accumulated excess temperature contributions beyond the near-field region from previous tidal cycles. Also, the term "ambient" is used in association with the receiving water hydrodynamics (e.g., current speed and direction), and does not imply that the water is at "ambient temperature," as defined by DRBC.

III.B.2. CORMIX Description

The hydrothermal modeling requires a near-field model to simulate conditions in the near vicinity of the thermal discharge, where the distribution of the plume is dominated by the momentum and, to a lesser extent, the buoyancy of the discharge. The model used to simulate these conditions is the CORnell MIXing Zone Expert System (CORMIX).

CORMIX is a synthesis of software subsystems used for the analysis, prediction, and design of aqueous discharges into water-courses. Emphasis is placed on the geometry and dilution characteristics of the near-field (Akar and Jirka 1990). The model assumes steady-state flow conditions for both the thermal discharge and the approaching receiving water conditions (flow rate, temperature field, salinity). The application of this steady-state model to simulate the thermal discharge characteristics into the dynamic tidal environment at Salem is described in Section III.B.4.

CORMIX's near-field formulation is based on a technique called "asymptotic analysis," which considers three flow regions where the plume dynamics are determined by three different aspects of the discharge: geometry, initial kinematic momentum flux, and buoyant flux (Fischer 1979 pp. 377-389; Akar and Jirka 1990). Asymptotic analysis uses the predominant factor (geometry, momentum, or buoyancy) to characterize each region. Thereafter, CORMIX uses flow-class categories that tailor the solution technique to the particular combination of receiving water and discharge conditions being modeled.

III.B.2.a. CORMIX Origin

Since its development in 1985, CORMIX has been continually refined and improved. The most current version of the CORMIX model (CORMIX 3.2) was used to simulate the Salem thermal plume. CORMIX is the recommended analysis tool in several key guidance documents regarding the permitting of industry discharges into receiving waters. The EPA recommends CORMIX in the Technical Support Document for Water Quality-based Toxics Control (1990; pp. 121-181).

III.B.2.b. CORMIX Features

CORMIX was selected for this application based on its wide acceptance and use as an industry standard, as well as its technical strengths. The major advantages of CORMIX are that the model:

- is supported and maintained by the USEPA;
- is flexible, with a built-in logic structure that allows it to select the most appropriate computational scheme depending on the conditions being modeled;
- has the ability to provide a three-dimensional characterization of the plume centerline position;
- is applicable to shallow and deep water;
- is applicable to both stratified and unstratified water;
- accounts, to a limited extent, for the interaction of the plume with the Estuary bottom; and
- was previously applied to simulate the near-field processes for the Salem thermal plume for the 1993 permit renewal application.

For the reasons outlined above, CORMIX is particularly well-suited to the Salem situation. In addition, certain modifications were implemented to improve the site-specific simulation of the especially complex near-field processes (Section III.B.8.).

III.B.3. CORMIX Modeling Approach for Salem Station

The procedure that was implemented to develop CORMIX to simulate the near-field thermal plume is outlined in E-2 Figure III-3. The first step was the One-Unit validation, which tested the ability of CORMIX 3.2, in its unmodified form, to simulate the complex near-field processes that were observed and measured during the One-Unit Survey at Salem (Exhibit E-I-2.). The One-Unit validation also revealed how the Two-Unit Survey could be tailored to support the near-field modeling.

The second step in the CORMIX modeling process was the Two-Unit validation. Here again, CORMIX 3.2 was applied in its original form to test its ability to simulate complex near-field processes observed and measured during the Two-Unit Survey (Exhibit E-I-3). This survey revealed additional complexity in the near-field plume characteristics. Differences between CORMIX results and the One- and Two-Unit Survey field observations were determined.

The third step was then to modify CORMIX to ensure it had the capability to simulate the site-specific complex near-field thermal plume processes at the Station. These

modifications resulted in markedly improving the near-field thermal plume dynamics simulation, and were made iteratively in combination with the fourth step in the CORMIX application to Salem: the Two-Unit calibration. The Two-Unit calibration successfully demonstrated that the improved CORMIX model accurately and properly simulated the thermal plume. The calibrated model then was verified against the One-Unit, and additional Two-Unit Survey field observations; this verification process was the fifth and last CORMIX step.

The improved, calibrated, and verified CORMIX model provided the near-field modeling capabilities to accurately estimate near-field temperature and velocity distributions in time and space, and areas and volumes of water within various ranges of velocity and temperature that comprise the near-field. As detailed in Section III.D, the subsequent CORMIX near-field projection results were then integrated with far-field RMA-10 model (i.e., model Linkage) to produce a continuous ΔT field.

III.B.4. Methodology

CORMIX was applied to simulate the mixing of the heated discharge water with the receiving water in the Estuary. Two especially complex areas were addressed in developing the CORMIX model for the Station discharge. One was related to the dynamic tides in the Estuary, and the other was related to the far-field heat build-up resulting from continued Station operations. CORMIX simulates the plume with a uniform lateral and vertical distribution of temperature within the region where the plume is dominated by its momentum. Methodological details are presented below.

CORMIX is a steady-state model, and assumes time-invariant flow conditions in the approaching receiving water. In reality, currents in the Estuary are dynamic and change with the tides (Attachment E-1 Section III.). This apparent contradiction was resolved by applying CORMIX for four representative phases or discrete points of the tide. The four representative phases of the tide, measured during the One- and Two-Unit surveys, were ebb, end-of-ebb, flood, and end-of-flood. Each of these tidal phases was treated as a separate steady-state condition. This treatment is appropriate because the time scale for the near-field mixing processes is on the order of minutes, whereas, with the exception of conditions near slack tide, the tidal conditions persist for longer time periods. Therefore, it is reasonable to assume that the uniform flow field as described in the CORMIX model has sufficient time to become established in the receiving water environment. In tidally dominated waters, it is important to limit the spatial application of CORMIX to the near-field region, because other numerical models (e.g., RMA-10) are superior to CORMIX in representing far-field conditions (i.e., dynamic tidal currents).

This treatment of each tidal phase as a separate steady-state condition is more appropriate for running tides than for slack tides. Slack tides are shorter in duration than flood tides (about 30 minutes for slack water versus hours for running tides). The CORMIX model tends to significantly overestimate the spatial extent of the Zone of Initial Mixing (ZIM) during a pure slack tide when the discharge momentum carries the ZIM an excessive distance from the discharge. Such slack conditions are not characteristic of tidal flows in

the Estuary, though. In the Estuary, slack water refers to velocities at the peak of the change in tidal direction between flood and ebb. Velocities rarely are zero, but instead represent minimum values. Therefore, for the Salem application of CORMIX, the end-of-ebb and end-of-flood tidal phases were treated as near-slack conditions, with relatively small ambient currents.

The build-up of heat due to continuous Station operation over multiple tidal cycles is not a near-field process and thus requires input from the far-field RMA-10 model. For instance, heat from a flood tide that is carried up-estuary and then back down-estuary through the discharge area on a subsequent ebb tide is not simulated by CORMIX. The model considers heat input only directly from the thermal discharge, no heat from other areas or time is considered. Therefore, rather than simulating the mixing of heated discharge water into purely ambient temperature water (i.e., local water temperatures without Station operations); the model used here simulated the mixing of discharge water into receiving water with a slightly elevated temperature due to localized heat build-up.

The elevated temperature of this receiving water is termed the approach temperature (T_{approach}), because it represents the temperature of the water as it is approaching the near-field into which the heated water is discharged. When temperature measurements are available (i.e., such as during the Two-Unit Survey), T_{approach} is simply obtained from moored measurements. Mooring E (approximately 1,000 feet north of the discharge) is used for the ebb and end-of-ebb tides, and Mooring H (approximately 1,000 feet south of the discharge) is used for the flood and end-of-flood tides (for locations, refer to E-1-3). When the mooring data are not available, such as during projection simulations, T_{approach} is provided by the far-field model at a location near the moorings. CORMIX then predicts the mixing between the discharge water and receiving water, with the simulated dilution referred to as "S". The discharge water temperature (ΔT_{eop} ; end of pipe) is equal to the sum of the intake temperature plus a $\Delta T_{\text{condensers}}$ introduced by the Station. The receiving water temperature is equal to T_{approach} . Thus, for the model calibration process discussed herein, the ΔT values input into the CORMIX model were equal to $T_{\text{discharge}} - T_{\text{approach}}$. The following equation shows how the model-predicted dilution was compared to the observed ambient temperature field data (T_{observed}):

$$T_{\text{observed}} = ((T_{\text{eop}} - T_{\text{approach}})/S) + T_{\text{approach}}$$

For each of the four tidal phases, appropriate values are selected for T_{approach} as discussed above. CORMIX then simulates the mixing of the discharge water with the approach waters.

The modules used by CORMIX for the Salem Station application depict a plume having uniform temperature normal to the plume centerline (width and thickness). Therefore, the near-field is simulated as a completely well-mixed plume, with a rectangular cross-section. It is accurate to characterize the plume as well-mixed over depths along its centerline, but it is a simplification of characteristics near its lateral margins. Observations show the near-field plume's temperature is vertically stratified near its

lateral margins; i.e., surface temperatures can be higher than bottom temperatures due to complex near-field plume dynamics (E-2-IV) which can give the actual plume cross-section a trapezoidal shape (i.e., wider at the surface than at the bottom). Consequently, the CORMIX depiction of the near-field plume may slightly underestimate the plume width at the surface and overestimate the plume width at the bottom. However, the CORMIX model conserves heat (Section E-2 III.B.8.b.iii). As a result, the model simulates a near-field plume with the correct amount of heat, even if, in nature, the heat distribution is more complex than in the model. This also introduces a measure of conservatism to the near-field modeling, since the area of bottom contact is overestimated.

III.B.5. CORMIX Set-up

III.B.5.a. CORMIX Input Data

CORMIX requires a variety of input parameters to characterize the discharge, including the geometry of the discharge as well as the characteristics of the effluent. The input parameters also characterize the receiving water properties. Input parameters associated with the discharge include the simulated diffuser line length, outfall separation from the shoreline, horizontal angle of the diffuser line with respect to current direction, vertical angle of ports, number of port openings, port diameter, configuration, and effluent flow and density. Receiving water parameters include the width and depth of the receiving water body, current speed, and water density, which is based on approach temperature and salinity.

III.B.5.b. CORMIX Output Data

Output from CORMIX 3.2 includes the following:

- Plume dilution: a ratio of the total water volume in the plume to the discharge volume. This ratio increases as more receiving water is entrained in the plume;
- Plume width: the plan form width of the plume is symmetric about its centerline, i.e., the plume spans the same distance on each side of the centerline;
- Plume vertical thickness: the vertical thickness of the plume also is symmetric, perpendicular to its centerline. The plume's contact with the bottom or surface may vary along its centerline; and
- Trajectory: the centerline trajectory of the plume is linearly-interpolated from the CORMIX output as a post-processing step. Section III.B.8. below describes how CORMIX was modified for the Salem Station application to produce a nonlinear trajectory.

The following model outputs were added via the CORMIX model improvements (Section III.B.8.):

- Travel time along plume centerline (post-processing calculation); and
- Plume velocity along plume centerline (post-processing calculation).

Together these model outputs or results allowed for three-dimensional and temporal definition of the temperature and velocity distributions for the near-field plume.

III.B.6. CORMIX One-Unit Validation

The initial step in the Salem application of the CORMIX model was the One-Unit validation (Figure III-3). The One-Unit validation consisted of applying CORMIX 3.2 in its original form for times corresponding to the One-Unit Survey (Exhibit E-1-2). This survey was designed based on prior data collection and modeling efforts to specifically support this validation process. Specifically, CORMIX was applied to simulate four phases of the tide on 28 October 1997. The four phases of the tide that were simulated, and the corresponding time periods when field data were collected, are listed below:

- Ebb: 1225 through 1425 hours (EST)
- End-of-ebb: 1615 through 1815 hours
- Flood: 0630 through 0830 hours
- End-of-flood: 0910 through 1110 hours

CORMIX results were compared to data measured during the One-Unit Survey to assess the model's performance. The CORMIX One-Unit Validation revealed differences between CORMIX predictions of the plume's surfacing location and temperature. Generally, the CORMIX results were too conservative. The dilution was too low, resulting in temperatures that exceeded the field observations. Also, CORMIX overpredicted the offshore extension of the plume, and its surfacing location.

Due to the apparent differences between the CORMIX predictions and the One-Unit data, it was decided that a more comprehensive validation was required to assure CORMIX provided accurate near-field simulations.

Additionally, the One-Unit Validation demonstrated ways of designing the Two-Unit Survey to improve the near-field modeling. Therefore, for the Two-Unit Survey, a cluster of optimally-spaced moorings was placed in the near-field, and more intensive near-field shipboard measurements were collected.

III.B.7. CORMIX Two-Unit Validation

Following the One-Unit Validation, CORMIX 3.2 was applied in its original form for four times in the tidal cycle corresponding to the Two-Unit Survey. The purpose of the Two-Unit validation was to test the ability of CORMIX to simulate the near-field processes measured during the Two-Unit Survey. As noted above, the Two-Unit Survey was designed to provide more refined measurement of near-field behavior. The four phases of the tide on 29 May 1998, that were modeled, along with corresponding field observation periods are listed below:

- Ebb: 0640 through 0840 hours (EDT)
- End-of-ebb: 0910 through 1110 hours
- Flood: 1140 through 1340 hours
- End-of-flood: 1425 through 1625 hours

Figure III-4 provides a sample comparison between the CORMIX predictions and measured data on an ebb tide during the Two-Unit Survey. The contours represent surface water temperatures interpolated from actual measurements (locations indicated by the lightly shaded + symbols). The blue dashed line represents the observed centerline of the plume at the surface, which describes the path of highest observed surface water temperatures. The blue dashed line begins at the discharge surfacing location (approximately 50 feet in front of the discharge), as defined by the maximum surface temperatures and visual observations from a survey vessel. The brown line represents the location of the discharge, with arrows showing the initial discharge trajectory.

The model results are represented by the red and green lines. The red line is the plume centerline predicted by CORMIX. The green line shows the plume width predicted by CORMIX. The beginning of the red and green lines indicates the modeled surfacing location.

Figure III-4 reveals significant differences between the measured and modeled surfacing location and plume trajectory. These differences are generally due to the following two reasons (1) the discharge ports comprise a large portion of the ambient water column (approximately one-third), which is an atypical discharge configuration for the CORMIX model, and (2) complex interactions appear to occur between the near-field plume and the uneven bottom bathymetry. Because of these significant differences, it was decided to modify the CORMIX code to accurately model the complex site-specific processes characteristic of the Salem thermal plume.

III.B.8. CORMIX Model Improvements

As noted above, when applied in its original form, CORMIX 3.2 could not accurately simulate the complex near-field thermal plume processes and the atypical discharge configuration. Both general and site-specific improvements were incorporated to make CORMIX appropriate for modeling the Salem application.

III.B.8.a. General Improvements to CORMIX

Two general improvements were made to CORMIX based on a review of the model's source code and supporting theory.

III.B.8.a.i. Error Correction to the Dilution Equation

A correction was made to the equation that computes the plume dilution in CORMIX caused by ambient cross-flow in the receiving water. This dilution is dependent upon the angle between the discharge and the direction of the ambient current. In this equation, a cosine function had been used where a sine function should have been used. This correction reconstituted the effect of the cross-flow on the near-field plume, such as its

tendency to compress the plume width and thus reduce dilution. The CORMIX authors will incorporate this correction in the next version of the model (Doneker 1998 and 1999).

III.B.8.a.ii. Improvements to the Dilution Equation

The dilution equation in the original CORMIX module is most often applied for conditions where the dilution is much greater than one. At lower dilution conditions, such as one at Salem, the equation periodically resulted in a predicted surface plume dilution less than one (<1). Because it is not physically possible to have negative entrainment, (i.e., a situation where the temperature increases following discharge), a correction needed to be made. This correction was a logical extension to the existing formulation which was based on a paper by Adams (1982).

In addition, under conditions for which the modified CORMIX predicts a dilution less than one, dilution was assigned the value of 1.41 (square root of 2), consistent with the top hat lateral temperature distribution in CORMIX. The rationale for this minimum dilution value of 1.41 is that, in the absence of model-predicted momentum induced mixing, there will be at least some nominal dilution via lateral entrainment. Therefore, for those instances where the calculated dilution was less than 1.41, this minimum dilution value would be applied.

The second improvement to the CORMIX dilution (S) equation addressed an assumption in the original derivation (Adams 1982), which assumed that $S \approx S-1$ (i.e., the applied dilutions would be relatively large). Given that the dilutions for this application are on the order of 2:1, this assumption was re-evaluated. Based on a re-derivation without the above assumption (i.e., $S \neq S-1$), a dilution correction constant of +0.27 was determined and applied. This correction constant is valid for low or high dilutions, but is particularly relevant at low dilutions when the percent error can be significant (i.e., the correction represents an approximate 13% increase for an originally calculated dilution of 2:1). These modifications were discussed and approved by staff who maintain CORMIX (Doneker 1998 and 1999).

III.B.8.b. Site-specific CORMIX Improvements

Site-specific improvements were made to CORMIX for this application. The information provided from the One- and Two-Unit Surveys revealed complex near-field plume processes that had not been observed previously. CORMIX 3.2 did not have the capability to simulate these complex processes, and thus modifications were made to certain modules of CORMIX 3.2 to remove these limitations. These modifications represent significant advances in techniques for modeling the Station's near-field thermal plume processes.

Modifications were made to CORMIX, then model results were compared to field data. Depending on the success of the model/data comparisons, additional improvements were made until the near-field physics were approximated accurately. As a result of this

iterative approach, the CORMIX site-specific modifications and the CORMIX calibration processes were interrelated.

III.B.8.b.i. Adjustment to Logic Structure

An adjustment was made to the CORMIX logic structure to assure that CORMIX made its dilution calculations using the most appropriate module. For the Salem Station application, it was necessary to change CORMIX to assure it considered the cross-flow effect on the plume of ambient currents in the receiving water for all tidal phases. The cross-flow effect essentially compresses the width (e.g., cross-sectional area) of the discharge plume, thereby reducing dilution. In its original form, CORMIX version 3.2 was coded to make a determination regarding which module to apply when computing plume characteristics. This determination was based on the "jet/cross-flow length scale," which is the ratio of discharge momentum flux over the ambient velocity squared. Based on this dimensionless parameter, CORMIX version 3.2 was originally coded to select between a module that considered the cross-flow effect of ambient currents (Module 273, the MU4 flow class) and one that did not (Module 274, the MU3 flow class). The dilution equation applied by CORMIX for module 273 is universally acceptable for high, low ambient flow, and even slack conditions. Module 274 does not consider the cross-flow effect of ambient currents, as it calculates a near-field plume dilution for a discharge into a stagnant water body, a condition rarely representative of the Station's tidal estuary receiving waters. Hence, the logic structure was "hard-wired" to ensure that the appropriate module (i.e., number 273) was employed during this application of a discharge into a cross-flowing ambient current.

III.B.8.b.ii. Distinction Between Plume Surfacing and End of Near-Field Plume Momentum

The second site-specific improvement distinguished the location where the near-field plume surfaces from the location where the discharge momentum ends. The discharge momentum ends where its velocities become negligible relative to the receiving water. At this point, its trajectory is dominated by the ambient tidal currents in the Estuary. The original CORMIX 3.2 model assumed that the plume loses its momentum when it surfaces. It also assumed that the receiving water can be characterized as a flat-bottomed, rectangular channel. Figure III-5 illustrates this schematically. At the point (x_f, y_f) where the plume surfaces, it begins to lift off the bottom and its trajectory is dominated by the ambient currents. Although this process may occur under certain ideal conditions, it is not characteristic of the Station's thermal plume.

Instead, field observations from the One- and Two-Unit Surveys indicate that the thermal plume surfaces before it loses its momentum. Water surface temperature data and visual observations from a survey vessel show the plume surfaces 50 to 100 feet offshore from the discharge location (Figure III-4; see Section III.B.8.b.ii. (a) for more details). The measurements also indicate the surfacing location is essentially independent of tidal phase, and, therefore, surfacing is not dependent upon the ambient currents in the receiving water. Rather, the plume surfacing is dependent primarily upon the discharge momentum. Bathymetry measurements surrounding the discharge show there are features

of the bottom that cause the plume to surface at a relatively constant location. Figure III-6 shows a depression and a ridge fronting the discharge that cause the plume to mix throughout the water column and surface relatively quickly (less than 10 seconds) (Exhibit E-1-4 provides details of the bathymetric survey methods and results). Although CORMIX 3.2 includes some discharge/bottom interaction, it cannot simulate this deflection of the plume off the bottom.

Although the plume surfaces rapidly, it still possesses substantial momentum. For instance, Figure III-7 shows plume-induced velocities 1,000 feet after discharge (and approximately 900 feet after surfacing) for certain phases of tidal near-slack conditions. The data shown on Figure III-7 were derived from an Acoustic Doppler Current Profiler (ADCP) that was deployed during the Two-Unit Survey approximately 1,000 feet offshore from the discharge location (Exhibit E-1-3). Figure III-13 shows the location of the ADCP. The arrow in the figure points to a time when measured velocities are dominated by the discharge. Thus, the field data clearly indicated a difference between where the plume surfaces and where it loses its momentum. CORMIX was modified to simulate these processes.

Figure III-8 presents a schematic of how these improvements were made. The point where the plume surfaces is defined as (x_s, y_s) , and the point where the discharge momentum ends is defined as (x_f, y_f) . For CORMIX to simulate these processes, it was necessary to implement two CORMIX simulations for each phase of the tide: One simulation for the actual discharge to predict plume characteristics up to the surfacing location, and a second simulation for a virtual discharge to predict plume characteristics at the endpoint of discharge momentum. An interpolation was then performed from the surfacing location to the virtual discharge endpoint of X_f, Y_f (Section III.B.8.b.iv.).

III.B.8.b.ii. (a) Actual Discharge

The CORMIX simulation representing the actual discharge provided plume characteristics between the discharge point and the surfacing point. Input parameters for these simulations characterized the actual geometry of the discharge. This configuration provided a realistic description of the plume, such as centerline velocities, water temperatures, and plume size, between the discharge and the surfacing location (x_s, y_s) . Characteristics of the plume between the discharge point and the surfacing location were then interpolated. The interpolation method represents another improvement to CORMIX that is discussed in Section III.B.8.b.iv. below.

In the original CORMIX code, the offshore or y-component was defined as the intercept where the ambient cross-flow momentum equals two times the discharge momentum. This is an empirical approximation of the point offshore where the discharge momentum is fully dissipated. As shown in Figure III-4, the field data shows that the discharge momentum was not dissipated at the point of surfacing, as the discharge trajectory still continues offshore. Theory (Adams 1982) shows that a diffuser of the type employed by Salem provides dilution by inducing an entrainment water flow from behind the diffuser, much like a propeller. As the water is accelerated across the diffuser, it contracts. The

maximum contraction has been shown both experimentally and theoretically to be located a distance $L_d/2$ downstream from the diffuser (where L_d is the length of the simulated diffuser line) (Lee et al. 1977, pp. 89-116). The high plume velocity interacting around $L_d/2$ produce bottom scour with irregularities, and the associated unevenness in bottom bathymetry causes the plume to surface.

The downstream or x-component in the original CORMIX code was empirically defined as $L_d/2 + (5 \text{ times the water depth})$. Again, this formulation was developed to approximate the end-point of discharge momentum, and thus is inappropriate for the prediction of the x-component of the plume's surfacing location. Hence, this formulation was modified to better represent the actual hydrodynamics observed during the field survey, as the x-component was approximated in the model as the plume travel time (to the point of surfacing) times the ambient current speed. This yields a downstream plume deflection that was directly related to the applied ambient current velocity.

In addition, it is relevant to note that the CORMIX code solves for the predicted plume width via the conservation of flow/heat flux equations. Thus, plume width was originally solved using the equation (dilution at surface \times discharge flow)/(water depth \times ambient current speed). But at the point of surfacing the plume still possesses momentum and thus, the plume velocity is greater than the ambient current speed. Therefore, an approximation of the plume velocity at the point of surfacing (termed U_2) was required to properly calculate the surfacing plume width. This velocity approximation is provided in the original derivation of the dilution equations (Adams 1982) discussed in Section III.B.8.a.ii. Termed as U_2 or the velocity at the end of the contraction zone (which has been observed to be approximate $L_d/2$), it is defined as follows:

$$U_2 = ((2 \times Q_o \times U_o \times \cos(\theta))/H_d \times L_d)^{0.5}$$

Where:

Q_o = discharge flow

U_o = discharge velocity

Theta = vertical angle of the discharge above the horizontal plane

H_d = height of the water column

L_d = diffuser length

Thus, plume width for this modified actual discharge CORMIX application was determined using the equation (dilution at surface \times discharge flow)/(water depth \times *plume velocity at the surfacing location [or U_2]*). This modification maintained the principle of flow/heat flux conservation and provided for an approximation of the plume width at the surfacing location that corresponded to the observed plume dynamics (i.e., plume velocity \neq ambient current speed at the surfacing location).

III.B.8.b.ii. (b) Virtual Discharge

A virtual diffuser was applied because CORMIX could not be expected to properly simulate the effect of the uneven bathymetry caused by plume scour. These effects were a reduction in plume velocity and an increase in plume width. Therefore, a virtual

diffuser was employed with a somewhat slower discharge velocity (U_o) and longer width than the real diffuser (L_d). This is the reason the simulation was termed "virtual discharge," as the two major CORMIX input parameters were adjusted (via multiplicative correction factors) to account for the interaction between the uneven bottom bathymetry and discharge plume. The adjustments to U_o and L_d were selected by comparing observed and predicted plume trajectories, and by compiling observed and predicted plume velocities during slack tide. The observed velocities were recorded by the bottom mounted Acoustic Doppler Current Profiler (ADCP) located 1,000 feet offshore from the discharge.

The CORMIX simulation with the virtual discharge provided information at the point where the discharge momentum ends. This simulation was performed from the discharge location up to the end-point of discharge momentum. The results from the actual and virtual discharge simulations, were synthesized to provide one continuous simulation of the Station's plume from discharge to surfacing, and through to the end of discharge momentum. A summary of the basic components of the modified CORMIX approach for both the actual and virtual discharge simulations is provided in Table III-1. As a supplement to this table, Figure III-9 details the CORMIX model coordinate system for a representative ebb tidal phase.

For the virtual discharge simulation, the offshore or y-component was defined (as per the original CORMIX code) as the intercept where the ambient cross-flow momentum equals two times the discharge momentum (Table III-1). The solution for this parameter was effected by the selection of the correction factors. Similarly, the downstream or x-component was approximated as the plume travel time (to the end of discharge momentum) times the ambient current speed. The plume width was determined using the original CORMIX formulation of (dilution at surface \times discharge flow)/(water depth \times ambient current speed), since at the end of the momentum region the plume velocity is, by definition, equal to the ambient current velocity.

III.B.8.b.iii. Non-linear Interpolation and Heat Conservation within CORMIX Modules

In its original form, CORMIX applies a linear interpolation of plume trajectory. A nonlinear intra-module interpolation scheme was implemented to allow a curvilinear plume trajectory. Additionally, the nonlinear interpolation scheme allowed for plume velocity to vary within a module. This nonlinear interpolation scheme was implemented so that heat was conserved within and between the different modules. Details of this analysis are provided in Table III-1, specifically item numbers 3-5 and 11-13.

III.B.8.b.iv. Final Synthesis of Actual and Virtual Discharge Simulations

The above actual and virtual discharge simulations yielded two sets of predictions from the point of discharge to their respective end-points (X_s, Y_s or X_f, Y_f). While the maximum departure between the two predicted plume trajectories was small (approximately 1 meter), a last step of integrating the two results into one continuous prediction of the

plume flow path was carried out. Thus, the real diffuser results were used until the surfacing location. The final interpolation was then performed from the surfacing location to the virtual discharge endpoint of X_j, Y_j . Within this interpolated area (X_s, Y_s to X_j, Y_j), the plume was assumed to be fully mixed in the water column, as supported by both the observed near-field mooring temperature data, and measured plume velocities at the bottom ADCP during slack tides. Between the surfacing location and end of momentum, the resultant quadratic interpolation of plume dilution and velocity again conserved both volume and heat.

III.B.9. CORMIX Calibration

The improved CORMIX model was calibrated using the Two-Unit Survey surface temperature and ADCP current velocity data. The calibration was achieved through an iterative process while the implementation of the model improvements described in Section E-2 III.B.8 and comparison with observations were carried out alternatively. As noted above, the calibration process included a review of various combinations of L_d and U_o multiplication factors (all of which maintained agreement with the measured ADCP data) to achieve an optimal match to the measured plume characteristics. The selected multiplicative correction factors, 3.30 and 0.65 for L_d and U_o , respectively, were employed throughout this application. Input parameters to the calibrated model are provided for the actual and virtual discharge simulations in Table III-2. The model was calibrated for the same four phases of the tide used for the Two-Unit Validation on 29 May 1998 (Section III.B.7).

The calibrated model produced results that matched the field observations. Graphical comparisons of model results with data are presented in this Section, with an emphasis on the plume trajectory and width, centerline plume surface temperature, and cross-plume surface temperature.

III.B.9.a. Two-Unit Plume Trajectory and Width Calibration

Figures III-10 through III-13 illustrate a plan view of the water surface, and compare CORMIX results to field observations. Information representing the field observations is presented by the blue contours and the blue dashed line. The blue contours on these figures represent measured surface temperature. These contours were generated based on unevenly spaced surface temperature measurements collected during the shipboard surveys. The measurements are assumed to be synoptic, i.e., collected at the same time; however, they were collected over a period of approximately one hour. Consequently, the contoured data are not truly synoptic, and include water temperature variations over a period of approximately one hour. The blue dashed line is an estimate of the observed plume centerline drawn to trace the maximum observed surface water temperatures.

CORMIX results are presented by the red and green lines. The red line represents the modeled plume centerline, which begins where CORMIX predicted the plume surfacing location. The green line represents the margins of the plume based on the plume width predicted by CORMIX. CORMIX predictions of water temperature are not shown on these plots.

Other features of these figures are as follows:

- The thick brown line represents the location and length of the submerged discharge structure; with arrows indicating the initial discharge trajectory.
- The brown numbered circles are the mooring locations from the Two-Unit Survey.
- The gray arrow is the ambient current direction input to CORMIX. The ambient current speed is provided in the figure title.
- The yellow lines indicate the location of cross-sections that are referenced in Section III.B.9.c. The yellow line nearest to the discharge is located at the estimated center of the measured surfacing location, and the second yellow line is the location where CORMIX predicted the end of discharge momentum.
- The axes on the coordinate system are New Jersey State Plane Coordinates in feet (NAD '27).

Figure III-10 compares the model and the data for ebb tide, as measured between 0640 and 0840 hours 29 May 1998. The trajectory of the plume is non-linear, curving toward the southeast direction of the ambient ebb tidal currents. The modeled plume width increases from approximately 50 feet at its surfacing location to nearly 225 feet at the end of discharge momentum. The modeled (red line) and measured (blue dashed line) plume trajectories match extremely well, typically differing by less than 10 feet to the end of discharge momentum (second yellow line). The region between the discharge and the end of discharge momentum was the focus of the calibration because the transition to the far-field model begins at this point (Section III.D.).

The surfacing locations match well, as the distance between the start of the red line (where CORMIX predicted that the plume centerline surfaced) and the center of the measured surface location (the small white circle of 27°C (80.6°F) is the highest measured surface water temperature) is small. The modeled and measured surfacing locations differ by approximately 25 feet: the surfacing location is approximately 50 feet west-southwest of the discharge, and the measured surfacing location is approximately 75 feet southwest of the discharge mid-point.

The offshore margin of the plume in the model, represented by the green line on the left-hand side of the plot, compares well with data. The green line is near the measured edge of the plume (the sharp measured surface water temperature gradient is indicated by the closely spaced temperature contours). The landward edge of the plume predicted by CORMIX (green line on right-hand side of plot) does not match the data as closely (as evidenced by the elevated measured surface temperatures landward of the CORMIX predicted plume extent). This difference between the modeled and measured plume width is discussed in more detail in Section III.B.9.c. below.

Figure III-11 compares CORMIX results with measurements for the flood tide, (1140 to 1340 hours on 29 May 1998). On the flood tide, the plume is carried northeast by the

tidal currents. The plume trajectory and width compare well out to the edge of discharge momentum. The measured surfacing location was approximately 100 feet away from the discharge, and the modeled surfacing location was approximately 50 feet from the discharge.

Figure III-12 compares the model and data for the end-of-ebb tide, as measured between 0910 and 1110 hours on 29 May 1998. The plume is carried northeast on this end-of-ebb phase by the tidal currents. The end-of-ebb measurements were made slightly after slack tide; when the flood tidal currents had begun to increase. The modeled plume trajectory and width are similar to the measurements, and the surfacing location was predicted within approximately 75 feet.

Figure III-13 compares the model with measurements collected near the end-of-flood tide between 1425 and 1625 hours on May 1998. The ambient velocity for this near-slack time period was only 0.37 fps, a factor of four lower than the ambient current speed measured during the other tide phases. Consequently, the end-of-flood calibration period was close to a slack tide, and the plume was carried almost directly offshore under its own momentum. Because the ambient currents were weak, CORMIX predicted that the plume would be carried far offshore by its momentum (Figure III-13a). The CORMIX results for end-of-flood match observed data out to a distance of approximately 1,000 feet offshore of the discharge (Figure III-13). Beyond this distance, CORMIX overpredicted the extent of the discharge momentum. In CORMIX, the plume maintained its momentum to approximately 3,300 feet offshore, which is very conservative. This discrepancy between the model and the data for end-of-flood is addressed in Section III.D. below, where the integration of CORMIX with the far-field model is described. The CORMIX results are truncated at 1,000 feet for such near slack conditions, as supported by the end-of-flood infrared image presented in Section III.B.10.d. (Figure III-31) and Section III-D.

For this near-slack period, special consideration was given to the determination of the model input ambient current speed (U_a), as U_a varied with time over the measurement period. The averaging time-interval to determine U_a was calculated as follows:

1. As discussed above, Y_f for the virtual discharge is defined as the intercept where the ambient cross-flow momentum equals two times the discharge momentum (Table III-1; Item 3). Since Y_f is inversely proportional to U_a^2 , it is very sensitive to small changes in the value of input ambient velocity during the near-slack condition (where velocity ranges from approximately 0.15 to 3.3 ft/sec). For this end-of-flood calibration an increase in the U_a averaging time interval from 10 to 20 minutes yields a decrease in the predicted Y_f from 9,000 to 5,500 feet. Thus, as the averaging interval increases around slack, Y_f decreases.
2. As shown in Table III-1 (Item 4), the y-component velocity is equal to travel time (or averaging time interval) $\times U_y$ (average; as defined by the integral of U_y from T_o to T_f). Thus, as the averaging interval increases around slack, the resultant y-

component also increases. Also, by definition, the end-point of the y-component should be equal to Y_f .

3. Therefore, there must be a unique value of the applied averaging time interval that defines an intercept of both Y_f and the y-component. Thus, through an iterative process, an averaging time interval of 31 minutes was selected to provide a consistent plume trajectory end-point of approximately 3,300 feet for the above two equations. The resultant value of U_a was 0.37 ft/sec, which was then applied to the end-of-flood virtual discharge simulation. This refined approach was not necessary for the other tidal phases because U_a (average) is relatively constant over time. Hence, the computed values of the offshore or y-component for the virtual discharge simulation would be insensitive to small changes in the averaging time interval.

Overall, the improved CORMIX model compared well with data within the region where the discharge is carried by its momentum as intended. Plume centerline surfacing location, plume trajectory, and margins of the near-field plume were also simulated well. These results provide a substantial improvement to the original Two-Unit validation presented in Section III.B.7.

III.B.9.b. Two-Unit Centerline Plume Temperature Calibration

Figures III-14 through III-17 provide graphical comparisons of the modeled and measured water temperature as a function of distance along the plume centerline. The solid line on these figures is the centerline plume temperature predicted by CORMIX. The first diamond on the left hand side of the plot represents the measured discharge temperature at the end of the discharge pipes. The remaining diamonds represent measured surface water temperatures along the estimated plume centerline (i.e., the measured surface water temperature along the blue dashed line on Figures III-10 through III-13). There are no plume temperature measurements depicted on these figures between the discharge point and the location where the plume surfaced.

Figure III-14 compares the model with data for the ebb tidal phase. The plume temperature decreases substantially within the first 50 feet of the discharge (i.e., the modeled surfacing location). A temperature reduction of 4.1°C (7.38°F) is experienced at the surfacing location, which represents 50 percent of the ΔT input into the CORMIX model (e.g., $T_{eop} - T_{approach}$). The plume temperature then reduces less rapidly to the end of discharge momentum at a distance of approximately 350 feet from the discharge. After the endpoint of discharge momentum, as shown in Figure III-14, the next CORMIX module applied was "buoyant ambient spreading." Generally, the CORMIX predictions and measured centerline plume temperatures compare well in this region. CORMIX predicts a plume that "lifts off" the Estuary bottom (Figure III-8), and thus becomes sharply vertically stratified. As a vertically well-mixed plume was observed during the Two-Unit Survey (Section III.B.10.e.), the application of CORMIX beyond the predicted endpoint of discharge momentum would improperly characterize the observed vertical plume distribution. Therefore, as detailed in Section III.D., the CORMIX results are not used beyond the predicted endpoint of discharge momentum (i.e., the near-field region).

Figure III-15 compares the model and data for the flood tide. CORMIX predicted plume temperatures within 0.5°C (0.9°F). The measured surface temperature is correctly reproduced by the model for the flood tide. At distances beyond the surfacing location, CORMIX predictions are conservative for the flood tide, as the modeled temperature is slightly greater than the measurements.

CORMIX results for the end-of-ebb tide condition are compared with the measured plume temperatures in Figure III-16. This end-of-ebb tidal phase is better characterized as an early flood as the near-field data collection was performed just after slack. This tidal phase was more complex than the ebb and flood tides. CORMIX reproduced measured surface temperatures well. The plume surfacing temperature is underpredicted by approximately 1°C (1.8°F), but the model matches the data at the end of discharge momentum (approximately 300 feet from the discharge). The model is conservative beyond the end of discharge momentum, as it consistently overpredicts the plume temperature by 0.5° to 1.0°C ($0.9 - 1.8^{\circ}\text{F}$). However, as described in Section III.D., the far-field model is applied to this region.

Figure III-17 compares the CORMIX results with the data for the end-of-flood tide. The measurements collected during the end-of-flood tide were most representative of near-slack conditions, and, therefore, it is difficult to accurately simulate these relatively short duration conditions using the steady-state CORMIX model. However, the CORMIX predictions still compare well with measurements between the discharge approximately 1,000 feet offshore from the discharge. The field observations indicate variability, as the mixing processes are complex under these low ambient current conditions. CORMIX predicts the surfacing temperature to within 0.5°C (0.9°F). Between the surfacing location and 1,000 feet offshore, CORMIX predictions are 0° to 1.5°C (0 to 2.7°F) higher than data so the model was conservative for the end-of-flood tide. One exception was at approximately 900 feet offshore from the discharge, where CORMIX underpredicts plume temperature by approximately 0.1°C (0.18°F). Beyond 1,000 feet, CORMIX significantly overpredicts the plume temperature on the end-of-flood tide, and is very conservative. Section III.D. describes how a transition was made to the far-field to provide a more realistic simulation of the plume. The end-of-flood tide is the only calibration scenario where CORMIX results are not used to the end of discharge momentum, as it is representative of a slack tide.

Figures III-14 through III-17 show that CORMIX reproduces observed centerline plume temperatures well, particularly between the discharge and the end of discharge momentum. At locations where CORMIX predictions differ from measurements, the model tends to overpredict measured plume temperatures, adding a measure of conservatism to the near-field modeling results.

III.B.9.c. Two-Unit Transverse Surface Temperature Calibration

Transverse surface water surface temperatures are shown in Figures III-18 through III-21. Water surface temperature is plotted as a function of lateral distance perpendicular to the

modeled plume centerline. The right side of figures corresponds to the side of the plume closest to the discharge (i.e., looking at the figure is equivalent to facing the oncoming plume). Two transects of the surface of the plume are plotted per tidal phase at the locations indicated by the yellow lines on Figures III-10 through III-13. One transect is at the mid-point of the measured surfacing location; the other transect is at the location where CORMIX predicts the end of discharge momentum. CORMIX predictions are shown by the solid lines, and field observations are represented by dots.

Figure III-18 compares the model results to data collected during the ebb tide. Although this figure portrays significant differences between the model and the observations, these differences are characteristic of the limitations of CORMIX. CORMIX predicts the maximum plume temperatures; however, the lateral span of these temperatures at the surface is not predicted accurately. This is illustrated by the right hand side of Figure III-18, where the CORMIX plume temperature drops to background temperature approximately ± 25 feet from the plume centerline at the surfacing location (top plot) and ± 120 feet from the plume centerline at the end of discharge momentum (bottom plot). In contrast, the observations show the plume surface temperature remains elevated for a longer distance perpendicular to the plume centerline. This difference between the model and the observations is revealed in Figure III-10, where the surface temperatures are elevated beyond the CORMIX predicted extent of the plume shown by the green line on the right side of the plot.

This difference can be explained by the CORMIX assumption of uniform lateral and vertical distribution of temperature in the region where the plume transport is dominated by momentum (Section III.B.4). Although observations show the plume is well-mixed along its centerline at the surfacing location, there is a vertical variation in plume temperature (higher temperatures at the surface) at the lateral margins of the plume, that CORMIX cannot reproduce. As described in Section III.B.4., where the plume has a vertical variation in temperature along its lateral margin, CORMIX underpredicts plume width at the surface and overpredicts plume width at the bottom, while conserving heat (Section III.B.8.b.iii). This simplification adds a measure of conservatism to the near-field prediction of the area of bottom contact of the plume. Similar comparisons of model and observed temperatures are presented for the other three tidal phases (Figure III-19 to III-21). The elevated temperatures beyond the landward edge of the CORMIX predicted plume could be an artifact of the plume's deflection/reflection off the river bottom and the water surface. These site-specific processes can yield complex plume characteristics, such as surface plume width, that CORMIX cannot simulate accurately.

Additionally, there is some evidence that for a horizontal discharge into a cross-flow, strong interactions can occur to produce a "trailing eddy," in which a portion of the discharge heat is re-entrained in the vicinity of the discharge (Fischer 1979). Local re-entrainment can occur if the total induced re-entrained water (i.e., the portion of the receiving water that is drawn into and dilutes the discharge (Q_{approach}) is greater than the amount of flow that normally passes through the region between the discharge and the shoreline (Lee et al. 1977). For the approximate 2:1 dilution at the plume surfacing

location. Q_{approach} is approximately equal to the discharge flow (Q_{saalem} ; where dilution (S) = $Q_{\text{saalem}} + Q_{\text{approach}} / Q_{\text{saalem}}$). Furthermore, the amount of flow that normally passes between the discharge and the shoreline is approximately equal to the distance offshore \times average depth $\times U_a$. Using the discharge flow and geometry from the CORMIX calibration simulations, a receiving water velocity (U_a) of approximately 0.3 feet per second would "supply" sufficient entrainment water to avoid local re-entrainment. As shown in Figure III-7, the receiving water currents typically exceed 0.3 feet per second and thus re-entrainment is unlikely. Furthermore, a similar model versus observed comparison shown for the end-of-flood slack tide (when the cross-flow effect is minimal $U_a = 0.37$ feet per second), it suggests that plume re-entrainment is not a primary issue in explaining the disparity shown between the model and predicted temperatures in Figures III-18 to III-21.

III.B.10. CORMIX Verification

The improved and calibrated CORMIX model was verified using the One-Unit Survey data, as well as information from the Two-Unit Survey that were independent from the data used for the calibration. Water surface temperature data from the One-Unit Survey were utilized for verification. Input parameters for the verification model run are provided in Table III-3. The model was verified for the two running tides that occurred during the One-Unit Survey on 28 October 1997. Measured and predicted plume properties at slack conditions were also reviewed, but lacking the requisite high resolution ambient current measurements, a rough approximation was required. Since the plume trajectory is very sensitive to current speed (Section III.B.9.a), the comparison of model and observed plume trajectories is not representative of the model formulation accuracy.

Graphical comparisons for the One-Unit Verification are presented in this section for plume trajectory and width, centerline plume temperature, and cross-plume surface temperature. The graphical comparisons portray a robust CORMIX model, capable of simulating the Salem plume under both One- and Two-Unit operating conditions. This is a rigorous test of the near-field model because the same input parameters selected through the iterative model improvement/Two-Unit calibration process were applied in the One-Unit verification process. Only the thermal discharge flow and ΔT were changed to reflect the One-Unit Station operating conditions.

In addition to the One-Unit Verification, CORMIX was verified against the infrared images and mooring temperature data collected during the Two-Unit Survey. These data sets were not utilized in the calibration process; therefore, they provide independent verification of the model. CORMIX results compared well with the synoptic infrared images and the mooring data.

III.B.10.a. One-Unit Plume Trajectory and Width Verification

Figures III-22 and III-23 compare CORMIX results with field observations for the ebb and flood tides, respectively. In both cases, CORMIX reproduces the plume surfacing location and trajectory. As in the calibration run, CORMIX underpredicted the plume

width at the surface, due to the uniform lateral and vertical temperature distribution inherent in CORMIX.

III.B.10.b. One-Unit Centerline Plume Temperature Verification

The temperature along the centerline of the plume as a function of distance offshore from the discharge is shown on Figures III-24 and III-25. For both the ebb and flood tides, CORMIX simulates the rate of temperature decrease well. Both, the model results and observations shows that the temperature decreases rapidly from the point of discharge to the surface. CORMIX underpredicts the surface temperature by approximately 1°C (1.8°F). Beyond the surfacing point, CORMIX is generally conservative, overpredicting centerline temperature by 0° to 1°C (0°-1.8°F).

III.B.10.c. One-Unit Transverse Surface Temperature Verification

CORMIX reproduces the observed surface temperature well, but underpredicts the width of the plume at the surface. Figures III-26 and III-27 compare the model results with the observed plume surface temperatures. The CORMIX predicted surface plume width is less than the observed width for the reasons outlined in Section III.B.9.c.

III.B.10.d. Two-Unit Plume Verification Using Infrared Images

Figures III-28 through III-31 compare the CORMIX predicted plume centerline trajectory and width with the infrared data collected during the Two-Unit Survey. The isotherms on these figures depict relative temperature gradients based on infrared imagery; the values do not represent actual ΔT fields. The comparison of CORMIX results with infrared images is particularly informative, and different from comparisons of water surface temperature measurements made by shipboard surveys, because the infrared images are synoptic, whereas the near-field shipboard surveys made the measurements over a period of approximately one hour.

The infrared model/data comparisons reveal the ability of CORMIX to reproduce the trajectory and shape of the plume at the surface. There is agreement for all tidal phases. Even in the complex end-of-flood phase, which is a near-slack condition, good agreement between CORMIX and observations for a distance approximately 1,000 feet offshore of the discharge was seen (Section III.D. describes a transition made to the far-field model beyond 1,000 feet for the end-of-flood tide).

III.B.10.e. Two-Unit Plume Vertical Distribution Verification Using Dye Data

The vertical dye profiles measured during the Two-Unit Mobile Survey on 29 May 1998 are consistent with the vertically well-mixed plume predicted by CORMIX in the near-field. The observed vertical profiles are shown in Figures III-32a and b for ebb phase, Figures III-33a and b for end-of-ebb phase, Figures III-34a and b for flood phase, and Figures III-35a and b for end-of-flood phase (detailed description is presented in Exhibit E-1-3). The corresponding locations for the vertical profiles are shown in Figures III-36a, b, c, and d, respectively. But during the running tides (ebb and flood), vertical profiles, both in close proximity of the discharge (near-field) and in the more distant transects,

display nearly uniform dye concentrations over depth. During the periods of tidal current reversal (end-of-ebb and end-of-flood), many profiles display non-uniform vertical dye concentrations. This vertical variability could be due to far-field effects during the preceding running tide. (In reviewing the figures, it should be remembered that the end-of-ebb figures correspond to a period that is better characterized as "early flood".) These results are consistent with the vertically well-mixed CORMIX prediction of the Station's discharge plume.

III.B.10.f. Two-Unit Plume Temperature Verification Using Mooring Data

The final verification of the improved CORMIX model was performed by comparing model predictions to the temperature data collected at the near-field moorings during the Two-Unit Survey. The four near-field mooring locations are illustrated on Figure III-13. Inspection of Figures III-10 through III-13 shows that as the plume is moved by the changing tidal currents, it "sweeps" through different moorings. For instance, Figure III-10 shows that Mooring 24 was in the plume during the observed ebb tide on 29 May 1998; Figures III-11 and III-12 shows that Mooring 23 was in the plume during the observed flood and end-of-ebb tides on 29 May 1998; Figure III-13 shows that Moorings 21 and 22 were in the plume during the observed near-slack end-of-flood tide on 29 May 1998. Figure III-37 compares the CORMIX results with the near-field mooring temperature data. The lines on this plot are measured near-surface temperatures from the moorings. The squares in the figure are CORMIX predictions of plume temperature for times corresponding to the four simulated tide phases. The model predictions were in good agreement with the observed mooring temperature data during all the phases of the tides to within 0.1°C. Figure III-37 also shows that both data and model predictions relatively constant values for the four tidal phases (i.e., approximately 26.0 to 26.8°C [78.8° to 80.2°F]). This suggests that near-field temperatures (and thus dilution) are relatively insensitive to the range of ambient current speeds encountered over the four tidal phases. This supports the use of approximate ambient currents values from the far-field model (RMA-10) for input to CORMIX for the projection runs to predict plume temperatures.

III.C. Far-field Model: RMA-10

In addition to the near-field model described in the previous section (Section III.B), a properly calibrated and verified far-field numerical model was used to provide accurate delineation of far-field ΔT . Delineation of far-field plume ΔT fields are required for the biothermal assessment, which addresses the protection of the Balanced Indigenous Community (BIC) (Appendix E Section VI).

This delineation is accomplished through simulations of hydrodynamic and transport processes within the Estuary. RMA-10 was selected as the far-field model for the Salem application (King 1985). The far-field model is used to evaluate the Salem thermal plume (ΔT) over a range of tidal current phases, atmospheric conditions, and Station operations. Once the model was calibrated and verified as an appropriate tool to simulate the Salem thermal plume, it was applied to simulate the plume under prevailing

conditions determined to be reasonable worst-case from a biological perspective (Appendix E Section V.F).

This section describes the application of the far-field model to simulate the distribution of the thermal plume in the Delaware Estuary. E-2 Section III.C.1. lists the objectives of the far-field modeling. E-2 Section III.C.2. describes the far-field model, including the basis for selecting RMA-10 as the appropriate model for this application, a brief summary of the scientific theory governing RMA-10, and a summary of the improvements made to RMA-10 for the Salem application. As a preface to the more detailed sections that follow, E-2 Section III.C.3. summarizes the general approach implemented for the Salem thermal plume far-field modeling.

Building on the background information about the far-field modeling provided by E-2 Section III.C.1. through III.C.3, E-2 Section III.C.4. discusses how RMA-10 was set-up for the Salem application. E-2 Sections III.C.5. then follows with a detailed description of how the far-field model was calibrated, including a summary of the model inputs and extensive model results and data comparisons. Qualitative model results and data comparisons are presented graphically in the calibration section. A more detailed and quantitative assessment of the model's ability to simulate observed physical processes is provided in Section IV. Finally, E-2 Section III.C.6. presents the approach and results implemented to verify RMA-10.

III.C.1. RMA-10 Objectives

The objectives of the far-field modeling were:

- to delineate far-field ΔT contours, relative to ambient;
- to provide a far-field model that can be integrated with the near-field model to provide a continuous distribution of ΔT contours associated with the Salem thermal plume;
- to provide far-field ΔT contours necessary to verify the Total Temperature Model (TTM), as described in E-2 Section III.E; and
- to provide work products required for the biothermal assessment.

These objectives are accomplished by simulating the Estuary-wide processes governing the transport of the Salem thermal plume.

III.C.2. RMA-10 Description

RMA-10 was developed by Resource Management Associates (RMA) as part of a continual enhancement process since the development of the depth-averaged version (i.e., RMA-2) in the early 1970s (Norton et al. 1973). The main support for this process is from the United States Army Corps of Engineers (USACE) which included the original depth-averaged development, the peer-reviewed application to the Columbia River Estuary (McAnally et al. 1984), and the update for three-dimensional applications (King 1985; King and Rachiele 1989a). Other developmental support for the model is derived through RMA's many clients as well as consultants which have supported improvements.

such as the addition of temperature modeling and water quality modeling to RMA-10 (TRA et al. 1993, LMS 1995, LMS 1996). Particle tracking was added to RMA-10 as part of a graduate thesis and following work which provides the user with the ability to quantify the exposure of passive organisms over time. Model documentation for a recent version, and an additional report on its application for the USACE, can be found in LMS (1996) and King and Rachiele (1989b).

RMA-10 can be used to simulate flow characteristics of a water body in three dimensions; the two horizontal dimensions and at depth. It simulates current velocity in three directions, water pressure, and the distribution of salinity, temperature, and suspended sediment throughout the water body of interest. It is a density stratified, three-dimensional hydrodynamic/hydrothermal numerical model.

RMA-10 is a finite element model that solves the governing hydrodynamic equations at various points within the region being modeled (the model "domain"). The points in the network where the model provides its numerical output (i.e. computed tidal elevations, currents, temperatures, and salinities) are termed *nodes*, and nodes are joined to form *elements*. The finite element network provides the user with the flexibility to vary grid size from element to element so as to provide appropriate resolution. The RMA-10 finite element method uses Gaussian quadrature which provides a continuous inter-element distribution. The density of nodes and elements depends upon the needs of the specific application, and is generally increased where more detailed information is required. Elements can be one-, two-, or three-dimensional, depending upon the level of resolution required and other factors.

The model computes solutions within its domain based on conditions prescribed at its external boundaries, including the ocean entrance, the C&D Canal, tributary mouths, and the water surface. An example of a boundary condition is the specification of tidal height, temperature, and salinity measurements at the ocean boundary. Another example is the specification of tributary inflows and inflow temperatures. These extremal conditions regulate the hydrodynamic/hydrothermal response of the Estuary.

Additional measurements are used to test the accuracy of the model computations within its domain. The process whereby model parameters are adjusted to achieve an acceptable match with measured data is termed *calibration*. The process whereby the calibrated model is tested against a second, independent data set is termed *verification*. Calibrated and verified models are widely accepted practice in engineering and sciences as appropriate analysis tools that can be used to evaluate various conditions where empirical data can not be obtained

III.C.2.a. RMA-10 Model Selection

RMA-10 was selected to simulate the distribution of the Salem thermal plume within the Estuary because:

- RMA-10 has been applied successfully at Salem for previous applications. The far-field plume was characterized using RMA-10 for the 1993 permit renewal (TRA et al. 1993), and for the 1995 DRBC Docket renewal (PSE&G 1995). Also RMA-10 was used in 1995 for a hydrodynamic study to investigate processes that are likely to contribute to the accumulation of detritus in the vicinity of the Station (Exhibit E-1-1).
- In addition to previous applications at Salem, RMA-10 has been used extensively by consulting firms, universities, and government agencies in the U.S., Canada, Europe, Asia, and Australia. These applications include a hydrodynamic and salinity intrusion study of the Delaware Estuary sponsored by the U.S. EPA (DiLorenzo et al. 1993). Subsequently, RMA-10 was applied to the Delaware Estuary as a localized, three-dimensional model nested within a large-scale, two-dimensional model (Ramsey et al. 1995). RMA-10 was used in conjunction with an RMA dissolved oxygen (DO) module to simulate temperature and its effects on DO (LMS 1995a). Also, the model was adapted to the Chambers Point region of the Delaware Estuary (LMS 1990). Recent applications of this model to outfall plumes include Boyle et al. (1993), King et al. (1994), and Pierson and King (1995). King (1999) summarizes many of the RMA-10 users, which include seven government agencies, nine universities, five research organizations, and twenty consulting groups. The USACE alone has applied RMA-10 for more than 60 applications.
- RMA-10 has a re-circulation module that was developed specifically for Salem as part of the (TRA et al. 1993) 1993 Permit Renewal. The module simulates the withdrawal of water through the intake, adds a Station-specific heat load, and discharges the same amount of heat and volume of water through the discharge structure at the elevated temperature. In this manner, both water mass and heat are conserved.
- RMA-10 has the ability to simulate surface heat exchange based on a heat budget method.
- RMA-10's finite-element structure is flexible, allowing the specification of varying element sizes, shapes, and dimensions (one-, two-, and three-dimensional elements). This flexibility allows the user to simulate effects of the Estuary's irregular shoreline configuration and bathymetry. Also, relatively coarse grid spacing can be used away from the area of interest and where spatial gradients are weak. Moreover, unlike finite-difference models, the finite-element structure allows any section of the grid to be modified without making changes to other areas. Thus, the flexibility of the finite-element structure provides convenience, economy, and spatial refinement.
- The depth-averaged version of RMA provides an advanced marsh module which may be implemented RMA-10. It has the capability to simulate alternately wet and dry marsh areas while maintaining model stability by using an algorithm that maintains the dry areas in its computations (King and Roig 1988; MacArthur et al. 1990).

- The depth-averaged version of RMA-10's implicit solution scheme allows for the use of relatively long time steps. This then allows computations to be performed where and when resolution is necessary.
- RMA-10 is continually maintained and well-supported by its developers. Also, the model source code is readily available. A companion three-dimensional water quality model (RMA-11; King and DeGeorge 1995) has been added to the RMA suite of models, and a new cohesive sediment transport module has been reported in the literature (Shrestha and Orlob 1996). The source code availability provides advanced users with the ability to interact, test, understand, and improve the model's performance, as opposed to the alternative "black box" approach.

III.C.2.b. RMA-10 Theory

A detailed summary of RMA-10's governing equations and numerical solution techniques is provided in LMS (1996). The following paragraphs provide a brief overview of the model theory.

RMA-10 solves the full, nonlinear Navier-Stokes equations for three dimensions, and incorporates the hydrostatic assumption. The model simulates the three-dimensional distribution of salinity and temperature using the advection-diffusion equation. Heat transfer across the air-water interface is modeled using the heat budget method (EPA 1985). The governing hydrodynamic equations are coupled to density through an equation of state. Thus, RMA-10 is capable of simulating density-induced currents (i.e., circulation patterns resulting from temperature and/or salinity variations).

RMA-10 is constructed using quadratic basis (interpolation) functions for velocity and salinity, and linear basis functions for water depth. A Galerkin, weighted-residuals approach (Abraham 1991) is used to formulate the model's finite-element integrals. The model equations are transformed to a constant vertical grid to facilitate automatic solution of the free-surface problem. A Newton-Raphson iterative method is used to solve the resulting set of simultaneous, nonlinear equations. A nearly implicit, Crank-Nicholson scheme is used to integrate over time (the actual implicit/explicit weighting for the calibration run was 0.54, compared with the 0.5 fully implicit and the 1.0 fully explicit solution).

III.C.2.c. RMA-10 Improvements Since the 1993 Permit Renewal

RMA-10 version 4.3 was used as the far-field model for the permit renewal submitted in 1993 (TRA et al. 1993). Since 1993, several improvements have been incorporated into RMA-10. For instance, LMS incorporated several improvements to version 4.3, and labeled this version 4.3 LMS (LMS 1996). These improvements consisted of:

- Simplifying the input of boundary condition information: The RMA-10 computer program was improved to ease the procedure for supplying boundary condition information. For instance, for a tidal boundary, a separate file can be created with columns of input data, such as time, water surface elevation, temperature, and salinity. The name of this file is simply typed into the header of the RMA-10

input file, and the model automatically accesses the file and extracts appropriate boundary condition information corresponding to the time step specified in the model. The same method applies to other boundary conditions, such as freshwater inflow, Station heat input, and meteorology. Previous versions of the model required that actual boundary condition data be specified at every time step within the RMA-10 input file (block input). The previous method was time consuming and introduced a potential source of user error. The other benefit of this improvement is the ability to change the time step in the model without changing the boundary condition file. The model will automatically select the coincident boundary condition information. If the exact time step does not exist in the input file, the model will linearly interpolate an appropriate value.

- Debugging capabilities: Error-checking capabilities were added to RMA-10 to help the user troubleshoot problems during the model set-up and calibration processes. For instance, statements were added that print messages to the screen that help the user identify the error when RMA-10 terminates unexpectedly. The types of problems that are identified include input data errors, as well as run time errors associated with model instability.
- Open boundary condition improvement: The specification of the open boundary conditions was improved so that on an incoming tide the temperature, salinity, and suspended sediment concentration are derived from model input data. On an outgoing tide, the model is given the flexibility to compute these parameters based on the characteristics of the water flowing out of the water body.
- Surface heat exchange formulation improvement: The method RMA-10 uses to calculate surface heat exchange was improved. Version 4.3 used the linearized equilibrium temperature approach, which is better suited for longer-term temperature simulations (EPA 1985). The more complete surface heat budget approach was incorporated into RMA-10 in 1994. EPA (1985) provides a detailed description of the heat budget method for computing surface heat exchange.

Other model improvements have been implemented since 1993 by the RMA-10 developers, and have been distributed as RMA-10 version 6.4. Between version 4.3 and version 6.4, the RMA developments include:

- improved calculation of surface density gradients (version 4.4);
- revised input data structure to ease data input (versions 5.0, 6.0, 6.2, and 6.3);
- an alternative equilibrium-temperature-based surface heat exchange computation (version 6.1); and
- included the Smagorinsky turbulence closure model (version 6.3).

RMA-10 version 6.6 was used for this 1999 permit renewal request. This version, which was assembled by the RMA-10 developers, combines the improvements incorporated in previous versions 4.3LMS and 6.4. An improved marsh module was added to RMA-10 version 6.6 based on a wetting and drying formulation that was previously incorporated in the depth-averaged model RMA-2 (King and Roig 1988).

Although not an improvement to the RMA-10 model source code, another improvement to the RMA-10 modeling procedure for the 1999 permit renewal is the development of a new Graphical User Interface (GUI). The GUI is an external program developed by LMS to ease input data preparation procedures, review data (numerically and graphically), and generally improve quality control. The GUI reduces the time required to set-up model runs by converting raw input data into more complex requisite RMA-10 input data formats. Also the GUI automatically creates the directory structure and initial raw data files for a new run based on previous runs. The GUI serves as a measure of quality control because it reduces the chance for input errors. For instance, if the user desires to change one model parameter for a subsequent model run, the GUI can be used to modify a previous simulation rather than having the user create a completely new set of input files. This eliminates the chance of user error when compiling input files.

Another measure of quality control implemented to test RMA-10 version 6.6 was a comparison of the 1993 model run using source code versions 4.3 and 6.6. The improvements made to the RMA-10 code were not of the type that would change the results from the previous model but rather would improve the model's potential and overall reliability. For instance, the improvement to the open boundary condition was not expected to change results since the boundary was far enough away from the area of interest. Also, the improved marsh module would not change the results from 1993 because no marshes were incorporated in that model grid. Consequently, the characterization of the plume produced by version 6.6 was expected to match the results from version 4.3 under the same set of input conditions. Differences would provide reason to suspect that errors were made when incorporating the model improvements.

A test was conducted by running RMA-10 version 6.6 with the same finite-element grid and input parameters that were used for the 1993 permit renewal. Also, the 1993 model was resurrected and run with the same parameters so the two models could be compared graphically, based on the extent and shapes of the 1.5°F and higher isopleths. No difference between the two models was observed. Their extents and shapes were very similar, thereby confirming that the changes were implemented correctly to RMA-10. This test also confirmed the accuracy of the previous modeling, and ensured that the 1993 model was an appropriate starting point for the 1999 modeling.

III.C.3. General RMA-10 Modeling Procedure

Figure III-38 illustrates the RMA-10 modeling procedure. The first step is model set-up, which involves: (1) identification of all data and other information required to run the model; and (2) the generation of model input files. E-2 Section III.C.4 provides a general overview of the information required for model set-up. The RMA-10 model grid and parameters used for the 1993 permit renewal served as the starting point. The 1993 model was set-up to run using RMA-10 version 6.6. Once set-up, the model was run to ensure the improvements made to RMA-10 were made correctly, as described in Section III.C.2.c.

After RMA-10 version 6.6 was determined to be accurate, the calibration process was initiated. Section III.C.5 describes the calibration process and results in detail, including model results and data comparisons. Numerous project-specific improvements were made to RMA-10 to ensure the model was capable of simulating the detailed and complex processes measured during the Two-Unit Survey. The calibration process first demonstrated that the model could simulate observed Estuary-wide processes (Section III.C.5.e. for a description of the Estuary-wide calibration). Next, the calibration was focused to ensure the model could simulate the far-field distribution of the Salem thermal plume (Section III.C.5.f. for a description of the plume calibration). The plume calibration required modifications to RMA-10 to ensure its output could be integrated with results from the near-field model, CORMIX. Through the calibration process, information was gathered about the marshes in the vicinity of Artificial Island. Section III.C.5.g. describes the model results for a grid with a refined marsh schematization. Though informative, this schematization was not incorporated into the calibrated model.

Once RMA-10 was calibrated for the Two-Unit Survey, it was verified using the One-Unit Survey data (Section III.C.6). The calibrated and verified RMA-10 model provided the far-field modeling tool that was:

- integrated with CORMIX to produce a continuous field of ΔT fields (Section III.D);
- combined with the ATM to estimate the total water temperature (Section III.E); and
- used to produce work products for the biothermal assessment (Section III.F. for methods used to produce the work products and Appendix E Section V.F for the actual work products).

III.C.4. RMA-10 Set-up

RMA-10 is a numerical hydrodynamic and transport model that must be adapted (or set-up) to a specific application. For the Salem application, RMA-10 is used to simulate the hydrodynamic, transport and surface heat exchange processes in the Estuary from the mouth of Delaware Bay to the head of tide at Trenton, New Jersey (the model domain). Setting-up RMA-10 involves compiling data on the physical and hydrodynamic features of the Estuary, and assembling coincident ("synoptic") data on processes or conditions that affect tidal elevations, currents, salinity concentrations, and temperatures (the dependent variables) in the Estuary. The set-up also requires characterization of point source discharges that have some significant relationship to the application. This section presents a brief discussion on the types of information required to set-up RMA-10.

III.C.4.a. RMA-10 Finite Element Grid

The physical features and hydrodynamic characteristics of the Estuary are provided as input to RMA-10 in the form of a computational grid that extends over the entire model domain. The computational grid is a network of discrete points ("nodes") that are joined to form "elements." RMA-10 uses the nodes and elements to solve the governing hydrodynamic and transport equations. The model computes values for all dependent

variables (tidal elevations, currents, salinities and temperatures) at each node for each time step. The user selects appropriate locations for the nodes and joins them with line segments to form triangular, quadrilateral or linear elements (small sub-regions of the Estuary). The user also specifies the number of layers at corner nodes which yields the third (vertical) dimension.

The mesh is designed considering the tradeoffs between spatial resolution, computational capabilities, and finite-element properties. Nodal spacing must be sufficiently small to characterize salient features in shoreline and channel morphology, such as the shoreline shape and variation in water depths. In addition, a fine mesh is needed in areas where the computed dependent variables exhibit sharp spatial variations (gradients), such as near a thermal discharge. Furthermore, consideration is given towards avoiding numerical errors associated with highly acute angles within the finite elements and irregular shoreline boundary angles (Abraham 1991). However, the overall density of nodal points is limited by computational constraints (i.e., mainly computer speed and to a lesser extent disk space). A mesh that is too fine may require an inordinately long simulation time (typically up to several days of real time). Thus, user judgement is required to balance these conflicting constraints.

Within the computational mesh, linear (one-dimensional) elements may be used in relatively narrow and shallow reaches that do not exhibit significant lateral or vertical variability. Two-dimensional (triangular and quadrilateral) elements are constructed in vertically well-mixed regions where dependent variables do not exhibit significant vertical variability. Three-dimensional elements, consisting of triangular and quadrilateral elements that can have multiple layers (and vertical nodes), are used where one or more dependent variables may exhibit significant variability in any direction. Elements have computational nodes at the corners and at the midpoints of their sides. For instance, a one-dimensional element has 3 nodes, a two-dimensional quadrilateral element has eight nodes, and a three-dimensional brick element has twenty nodes, as shown on Figure III-39. The resulting three-dimensional discretization of the model domain is referred to as the computational grid or model domain.

III.C.4.b. Model Input Parameters

Specific data on the physical features and hydrodynamic characteristics of an element are provided at the element's nodes. This information includes the local elevation of the river bottom relative to a reference datum and the spatial coordinates relative to a defined reference point (origin). Elements are grouped by type, and each type of element is assigned empirical coefficients that are used to calculate energy dissipation (turbulent exchange and friction coefficients), hydrodynamic dispersion (diffusion coefficients), and surface heat exchange (for the surface).

III.C.4.c. Boundary Conditions

RMA-10 computes the hydrodynamic, temperature, and salinity responses of an estuary to various external influences (forcings), including:

- the rise and fall of sea levels at all open boundaries;
- variations in boundary salinities and temperatures;
- tributary inflows;
- surface heat exchange processes; and
- point sources of heat.

Boundary conditions are applied where the computational grid cuts across waterbodies that adjoin the model domain and at the air-water interface. In this case, the "external waterbodies" are the Atlantic Ocean, the C&D Canal, the Schuylkill River, the Delaware River beyond Trenton, the Salem River, Hope Creek, Mad Horse Creek, and other smaller tributaries. The boundary conditions are the tidal elevations at the mouth of the Delaware Bay and C&D Canal; the freshwater inflows from tributaries; and the salinity concentrations and temperatures of the flows entering the Estuary from the external waterbodies.

The boundary condition for the water surface is the surface heat exchange rate, which is computed by RMA-10 using solar insolation input and meteorological conditions required for the heat budget method. This boundary condition controls the natural heating and cooling of the Estuary, including the dissipation of Salem's heat to the atmosphere. The boundary conditions, as well as the solar inputs and meteorological conditions, are expressed as time-series with coincident starting and ending times. The starting and ending times define the period for the particular application (namely, calibration, verification, or predictive analyses).

III.C.4.d. Initial Conditions

In addition to the boundary conditions, the dependent variables at all the nodes in the model domain must be assigned an initial value. Generally, the closer the prescribed initial conditions are to actual conditions, the faster RMA-10 simulation will converge on the actual hydrodynamic state of the Estuary. However, the initial conditions are usually estimated from sparse field measurements, and, therefore, accurately quantified for every node. Therefore, for a period of time, the RMA-10 solutions are dependent on the initial values and may not be sufficiently reliable for a particular application. However, this dependence decreases, and eventually is lost, as the natural physical processes that occur in the Estuary (namely, energy dissipation, hydrodynamic dispersion, flushing, and surface heat exchange) remove any significant influence of the initial values on the solution. The time for the numerical solutions to become practically independent of the initial values is referred to as the "spin-up time," which decreases as the accuracy of the initial conditions increased. After the spin-up time, the solutions can be used for the particular application. Model spin-up time for the Salem application of RMA-10 is discussed in Section III.C.5.a.iv.

III.C.4.e. External Point Sources

Water temperatures and currents conditions in the Estuary also may be affected by major point source discharges. Data that characterize the discharges must be provided for those sources that are pertinent to an application. For the Salem thermal study, the major point

sources are the Station and other power plants whose thermal plumes might affect the calibration or verification of RMA-10. Data for the Station includes discharge flow and heat rejection rates expressed as a time-series. Data for other point sources are specified as time-series of the discharge flow rate and temperature. The starting and ending times of these time-series are coincident with those for the boundary conditions.

III.C.5. RMA-10 Calibration

RMA-10 requires inputs for the physical attributes of the Estuary, and values of empirical coefficients that are needed to solve the governing hydrodynamic and transport equations. Although reasonable approximations for these inputs can be made based on previous studies, or information in the literature, these RMA-10 inputs must be refined (or calibrated) for the present application to ensure that the model predictions are consistent with the field observations. RMA-10 was calibrated for the period between 21 May and 4 June 1998. The primary calibration data set was the Two-Unit Survey performed according to the Modified TMP (Exhibit E-1-3).

For this application calibration is an iterative and systematic process of modifying the inputs to RMA-10 until: (1) the model reproduces the observed tidal elevations, currents, and salinities; and (2) reproduces the observed temperature distributions associated with Salem's discharge (plume calibration). The modifications made to RMA-10 to achieve calibration include reconfigurations of the computational grid, and the assignment of new values to the empirical coefficients at the computational elements. Reconfigurations to the grid involved changing the number, sizes, types, and interconnections of elements. These types of changes are made to obtain better spatial resolution, to enhance (or remove) some physical feature, or to improve mass conservation. Values of empirical coefficients that affect vertical and lateral dispersion and mixing are also adjusted to achieve better comparison between observed data and RMA-10 predictions. Similarly, values of empirical parameters that affect energy loss may be changed to improve the modeled hydrodynamics.

III.C.5.a. Input Data Sets for RMA-10 Calibration

RMA-10 was calibrated using published information on the physical features of the Estuary; hydrodynamic water quality, and point source-discharge data collected from 21 May 1998 through 4 June 1998. Data on the physical features of the Estuary were taken primarily from nautical charts prepared by the National Oceanic and Atmospheric Administration (NOAA) and a bathymetric survey performed in 1995 by Aubrey Consulting, Inc. (ACI) (Exhibit E-1-1). All the other data were obtained from the Modified TMP (Exhibit E-1-3), the Station, and various state and federal agencies. These data were used to construct the boundary and initial conditions, quantify heat loads from major point-source dischargers, and evaluate the performance of RMA-10. The following section summarizes the data used to calibrate RMA-10, and the sources of the data according to their application to the calibration.

III.C.5.a.i. Boundary Conditions for RMA-10 Calibration

Table III-4 summarizes the data and data sources for each open boundary of the model domain. The following paragraphs briefly explain the boundary conditions, and the procedures that were used to estimate boundary conditions for which direct observations were not available.

III.C.5.a.i. (a) Tidal Boundaries

The entrance to the Estuary is the southern boundary of the model domain, where the periodic rise and fall of sea level drives water level changes and the tidal flows in the Estuary. The boundary conditions specified in the model across this boundary are time-series of sea levels, and the temperature and salinity of water flowing into the Estuary during flood tides. The model computes salinity and temperature at the ocean boundary on the ebb tide. The time-series of sea levels at two locations near this boundary are recorded by NOAA (1998) at Cape May, NJ and Lewes, DE. Since the measurements are recorded just inside the ocean boundary, the records must be adjusted using time corrections and amplification factors developed by NOAA (Thomas Reed Publication, Inc. 1998) to approximate the sea level at two points on opposite sides of the ocean boundary. Between these points, the estimated tidal elevations at any time are linearly interpolated. This linear interpolation is appropriate because the width of the Bay is small compared to the length of the tide wave.

RMA-10 computes water temperature and salinity across the ocean boundary during ebb tides, but implements user-specified values on flood tides. Input data for the RMA-10 boundary condition are provided by measurements of temperature and salinity collected at three locations across the ocean boundary during flood tide as part of the Modified TMP. These measurements indicated that it is appropriate to prescribe a spatially constant salinity and temperature at the ocean boundary. Measured water temperatures and salinity concentrations at Cape May, NJ and Lewes, DE (NOAA 1998) during the flood intervals were relatively constant at 60°F and 22 ppt (parts per thousand), respectively, over the calibration period. Therefore, the constant values of salinity and temperature prescribed at the ocean boundary on the flood tide are averages of the measured water temperatures (57.69°F) and salinity concentrations (27.65 ppt on May 22, 1998).

A tidal boundary condition is also prescribed at the C&D Canal. Tidal elevations, water temperature and salinity were recorded at Courthouse Point, DE as part of the Modified TMP. Similar to the ocean boundary, temperature and salinity were specified on the flood tide at the C&D Canal, while RMA-10 computed water temperature and salinity on the ebb tide.

III.C.5.a.i. (b) Freshwater Inflow

Freshwater inflow and water temperature were specified at the Delaware River in Trenton, New Jersey, the Schuylkill River in Philadelphia, Pennsylvania, and other tributaries. Daily-averaged time-series of freshwater inflow from the Delaware and Schuylkill Rivers were obtained from the United States Geological Survey (USGS). Time-series of the hourly water temperature for the inflow at Trenton, NJ also were

obtained from the USGS. The water temperature of the Schuylkill River inflow was assumed to be the same as the Delaware River in Trenton, NJ. This was justified based on recorded water temperatures at Trenton, NJ and Fort Mifflin on the Schuylkill River south of Philadelphia, which were compared and found to be similar.

Numerous other tributaries were included in the model. Each tributary's daily average inflow rate was estimated by multiplying the daily average flow of the Schuylkill River by the ratio of the tributaries' to the Schuylkill River's drainage areas. The water temperature of the flows from the ungauged tributaries and the Schuylkill River were assumed to be equal. Table III-5 lists the names and drainage areas of the ungauged tributaries for which inflows were provided to RMA-10.

III.C.5.a.i. (c) Surface Heat Exchange

The surface-heat exchange process is simulated by RMA-10 using computed water temperatures and hourly measurements of meteorological conditions. Meteorological inputs to RMA-10 include short- and long-wave solar radiation, dew point, wind speed, and air temperature. All of these data were recorded at the Station, except for dew point, which was obtained from the National Weather Service (NWS) for Wilmington, DE.

RMA-10 incorporates the following formulation for heat transfer across the air-sea interface (EPA, 1985):

$$H = Q_{sn} + Q_{an} + Q_{br} + Q_e + Q_c$$

where:

- H = net surface heat flux (in units of BTU/ft²/day in this analysis)
- Q_{sn} = net short-wave solar radiation (incident minus reflected)
- Q_{an} = net long-wave atmospheric radiation (incoming minus reflected)
- Q_{br} = back radiation emitted by the body of water
- Q_e = energy removed from the waterbody by evaporation
- Q_c = energy convected to or from the waterbody

Like most numerical models, RMA-10 calculates these terms based on semi-theoretical relations, empirical equations, and basic meteorological data (EPA 1985). These data include atmospheric pressure, cloud cover, wind speed and direction, wet and dry bulb air temperatures, dew point temperature, short-wave solar radiation, relative humidity, and water temperature. Most of the equations derived for heat transfer simulations rely heavily on empirical coefficients (EPA 1985).

The total heat budget for a waterbody combines the surface heat exchange with changes in heat content due to tributary inflows, advection, thermal discharges and other sources/sinks (e.g., marshes). However, the dominant process controlling the heat budget is, typically, the atmospheric heat exchange (EPA 1985).

Representative heat transfer data for ambient conditions are tabulated below, based on the modeling approach employed in this study. As indicated, dominant atmospheric heat inputs include both net short-wave and net long-wave radiation. Both back radiation and evaporative heat flux comprise dominant loss terms. The average conductive term is small air-water temperature differences during this period. In each case, the representative ambient data fall within the range of published values.

Heat Transfer Term (BTU/ft ² /day)	Simulated Average 21 May - 4 June, 1998 (BTU/ft ² /day)	Expected Range* (BTU/ft ² /day)
Net Short-Wave	1,878	44 to 2,611
Net Long-Wave	2,416	1,858 to 3,142
Back	-3,095	-1,947 to -3,053
Evaporative	-892	-221 to -7,965
Conductive	-19	-310 to 442
Net	288	

* From EPA (1985)

III.C.5.a.ii. Initial Conditions for RMA-10 Calibration

Initial estimates of the spatial distributions of tidal elevation, velocity, water temperature and salinity concentration throughout the Estuary were derived using data collected during the 21 May 1998 initial conditions survey component of the Modified TMP, and a RMA-10 "hot-start simulation" (explained later in this Section). The initial conditions survey measured vertical profiles of water temperature and conductivity (salinity) at discrete points in or near the shipping channel from the ocean boundary to Trenton, New Jersey. The hot-start simulation was a preliminary, two-day simulation that was used to derive hydrodynamic initial conditions for each node. The purpose of the hot-start simulation was to generate the hydrodynamic information necessary to start the calibration run on 21 May with tidally consistent velocities and water surface elevations. By starting the calibration simulation with the Estuary in motion, the model spin-up time (time required to establish the Salem thermal plume) is reduced. The hot-start simulation was conducted for two model days to generate requisite hydrodynamic initial conditions. In summary, the initial conditions specified for the calibration run on May 21, 1998 consisted of the longitudinal (axial) distribution of salinity and temperature measured during the initial conditions survey and the hydrodynamic conditions generated by the RMA-10 hot-start run. Values for salinity, temperature, velocity, and water surface elevation were prescribed at each node at the beginning of the calibration period.

III.C.5.a.iii. Point Source Discharges of Heat for RMA-10 Calibration

A power plant boundary condition was applied to simulate the once-through cooling water system (CWS) at the Station. The model requires intake and discharge flow rates, and a change in water temperature caused by the Station ($\Delta T_{\text{condenser}}$) for this boundary condition. The $\Delta T_{\text{condenser}}$ was calculated from measured intake and discharge temperatures at the Station. The flow rate from the cooling water system was calculated

from the $\Delta T_{\text{condenser}}$ and heat discharge rate from the Station. The sum of the cooling water and service water system flows was used as the total discharge flow rate from the Station, except during the dye study period (27 May 1998 through 29 May 1998) when discharge flow rate was measured directly, so the measured flow values were used. Time series of the total discharge and intake flow rates, and the discharge ΔT from the Station were input into the model.

Similar information for other major point source discharges of heat to the Estuary was obtained from state and federal agencies, including the New Jersey Department of Environmental Protection (NJDEP), Pennsylvania Department of Environmental Protection (PADEP), and Delaware Department of Natural Resources and Environmental Conservation (DNREC). Permitted discharges other than the Station with heat or temperature inputs below certain limits were not considered. Also, other discharges were not considered based on relative heat loading and proximity to the Station. Table III-6 lists the names and discharge characteristics of the major point sources of heat. These other point sources of heat were input to RMA-10 as volumetric element inflows with an elevated water temperature.

III.C.5.a.iv. Spin-Up Time

RMA-10 requires both initial conditions (Section C.4.d) and boundary conditions (Section C.4.c) as input data. At the beginning of the RMA-10 simulation, the results are dependent upon the limited initial condition data. Since it is not possible to specify accurate initial condition data throughout the model domain (i.e., it is not possible to measure everything everywhere initially), RMA-10 must be run long enough to achieve independence from the initial conditions before RMA-10 results can be used reliably. For this application, the model was run long enough to ensure the plume was not influenced by the initial conditions. Since the model prediction of the farthest extent of the plume needs the longest spin-up time the upstream and downstream plume lengths were used to evaluate the spin-up time required. Extent of plume was defined as the edge of the 24-hour averaged 1.5°F isopleth of $\Delta T_{\text{far-field}}$.

The spin-up time was defined as the time required for RMA-10 to develop a plume with constant length. When the model run was initiated, a period of time was required for the heat from the discharge to evolve into a plume of stable and constant length. Further, since the plume length is dependent upon changing tide, meteorology, freshwater inflow, Station operating conditions, and other input data, the spin-up test was performed using constant input data. A repeating sinusoidal tide was specified at the C&D Canal and at the Atlantic Ocean boundaries. Other input parameters, such as climatological parameters and freshwater inflow, were specified as the average over the calibration period (May 21 through June 5, 1998). Low-flow, high $\Delta T_{\text{condenser}}$ Station operating conditions, which were consistent with the reasonable worst-case for the Biothermal Assessment were used.

Figures 40a and 40b illustrate the results of the spin-up analysis. Based on these figures, it is clear that the plume is increasing in length for the first four days. After four days, the

upstream plume stabilizes to a length of approximately 18,000 to 21,000 feet, and the downstream plume stabilizes to a length of approximately 14,000 to 16,000 feet under these conditions. The 2,000- to 3,000- ft oscillation in plume length is due to the fact that a 24-hour average was computed, whereas two tidal cycles actually span 24.8 hours. Based on the spin-up analysis, it was concluded that RMA-10 must be run for at least four days before reliable plume simulation results can be obtained. This guideline was adhered to for all calibration, verification, and other (e.g., reasonable worst-case) RMA-10 simulations:

III.C.5.b. Data Available to Evaluate the Performance of RMA-10

The Modified TMP produced most of the data that were needed to evaluate the performance of RMA-10. Additional data used included tidal elevations that were obtained from NOAA and the USGS at the following locations: Burlington, NJ; Philadelphia, PA; and Woodland Beach, DE. Table III-7 lists an inventory of the types and sources of data, and summarizes how the data were used to calibrate RMA-10. It also lists the periods for which data were available, and the frequencies of data collection.

The Modified TMP consisted of the following six components: (1) a network of instrumented moorings; (2) a shipboard survey; (3) a dye-tracer study in both the near-field and far-field; (4) an infrared survey in the near-field; (5) a hydrodynamic survey of tidal elevations and currents; and (6) a marsh survey. The Modified TMP produced a high-quality, comprehensive data set that exceeded typical requirements for calibrating a hydrodynamic and transport model, such as RMA-10. Although the objectives were met, a few of the components did not produce all the data that were originally intended. Exhibit E-1-3 presents the Modified TMP data that passed the final quality assurance process. Section V.D. of Appendix E discusses the success of the Modified TMP's data collection program. The remainder of this section briefly summarizes how the available data were used to calibrate RMA-10 according to the Modified TMP.

The moorings and shipboard surveys were designed to complement each other. The moorings provided data that primarily captured temporal variability, whereas the shipboard surveys provided data that captured spatial variability. The moorings recorded time-series of water temperatures, conductivity (salinity), and dissolved oxygen concentrations within the near- and far-fields of the Salem thermal plume and beyond. The shipboard surveys measured the surface distribution of water temperatures and vertical profiles of temperature and conductivity (salinity) over the region of the Estuary that could be potentially occupied by the Salem thermal plume and beyond. The shipboard measurements were taken on 29 May 1998 at four phases of the tidal cycle (approximately at maximum flood, end-of-flood, maximum ebb and end-of-ebb). For the RMA-10 calibration, the data from the moorings and shipboard surveys were primarily used to calibrate the shape of the Salem thermal plume by adjusting the diffusion coefficients used in the transport calculations for heat, and salinity. Data from the shipboard surveys in the near-field were also used to guide refinements to the configuration of computational elements.

A dye-tracer study was performed in tandem with the shipboard surveys. Rhodamine WT dye was discharged at a constant mass rate from the Station over a three day period. Dye concentrations were measured along various transects of the Estuary and along the boundaries of the near-field at four phases of a tidal cycle. Also, the spatial distributions of dye concentration were used to adjust the diffusion coefficients used in the RMA-10 transport calculations.

The infrared images provided synoptic views of surface water temperatures over the near-field and the surrounding region at four phases of a tidal cycle. These photographs showed where changes in the spatial distribution of surface temperature were the greatest, where the momentum of the discharge has a significant effect on the near-field mixing processes, and how the warmest regions of the Salem thermal plume change shape over a tidal cycle. Results of these surveys were used to guide refinements to the computational elements that were used to approximate the near-field, and to refine the diffusion coefficients in the immediate vicinity of Salem.

A bottom-mounted Acoustic Doppler Current Profiler (ADCP) measured the vertical profile of current speed and direction at a point approximately 1,000 feet offshore from the discharge over a two-week period. In addition, vertical profiles of current speeds across several transects in the Estuary and at four phases of a tidal cycle, were measured using mobile (towed) ADCPs during the shipboard surveys. The current measurements, plus the observations of tidal elevations, were used to adjust the friction and energy loss coefficients to ensure RMA-10 accurately simulates the tidal hydrodynamics of the Estuary, and correctly calculates the flux of water over cross sections of the Estuary.

The marsh surveys were designed to estimate the potential contribution of heat to the Estuary from the marshes. The large tidal marshes in the vicinity of the Station store significant volumes of water during flood tides, and release that water back to the Estuary during ebb tides. Natural heating and cooling processes may significantly alter the temperature of the water between the time it enters and leaves the marshes. The temperature alterations may approach or exceed ΔT values due to the Station in some regions of the Estuary. The results of the marsh survey were used to better understand the natural heating and cooling processes that occur in tidal marshes, to estimate the contribution (either the gain or loss) of heat by the tidal marshes to the Estuary, and to understand the potential compounding effects of these contributions on the calibration/verification of RMA-10. Marshes were ultimately approximated as shallow storage basins in the calibrated model. Exhibit E-1-5 provides an evaluation of the marsh data.

III.C.5.c. RMA-10 Calibration Process

RMA-10 was calibrated to simulate the tidal hydrodynamics of the Estuary (the "Estuary-wide" calibration) and to simulate the transport and mixing of the discharge in the Estuary (the "plume" calibration). The Estuary-wide calibration was completed first since the transport and mixing calculations for the Salem thermal plume require accurate estimates of ambient currents, which are available only after the Estuary-wide calibration is completed. This section summarizes the processes used to complete both phases of the calibration, and elaborates on those components of the "plume" calibration that are unique to the discharge.

III.C.5.c.i. RMA-10 Estuary-Wide Calibration Process

The procedure for the Estuary-wide calibration is standard for tidal hydrodynamic models, such as RMA-10. The sizes and arrangements of elements over sub-regions of the entire model domain, or for specific features of the Estuary, were modified, and friction and turbulent energy loss coefficients were adjusted until RMA-10 reproduced the observed tidal hydrodynamics of the Estuary with an acceptable level of agreement. RMA-10 was calibrated for Estuary-wide processes using the following comparisons of observed data and model predictions:

- Tides: Observed time series of tidal elevations were compared to modeled time series at five locations within the Estuary.
- Currents: Observed current speed and direction were compared to model results at a location in the near-vicinity of the Station. Observed current speed and direction, as well as the flux of water across these transects of the Estuary, were compared to model results for four phases of the tide.
- Salinity: Vertical salinity profile data collected throughout the Estuary, as well as time series of salinity recorded at moorings deployed within a 24-mile stretch of the Estuary (centered on the Station), were compared to model results.
- Water Temperature: Observations of temperature from vertical profiles, moorings, and shipboard surveys were compared to model results.

The Estuary-wide calibration was completed when the simulated tidal hydrodynamics on-balance showed good agreement with the observations. A graphical presentation of the model results and data comparisons is provided in Section III.C.5.e. An assessment of RMA-10's ability to simulate the Estuary's tidal hydrodynamic processes is provided in Section IV.

III.C.5.c.ii. RMA-10 Plume Calibration Process

The procedure for the plume calibration included a basic component that is common to most transport calculations, and more complex components that addressed unique aspects of RMA-10's adaptation to the Salem discharge and the Estuary. The basic component of the plume calibration involved making refinements to the computational grid to improve spatial resolution where sharp gradients in temperature or salinity existed, and adjusting vertical and horizontal diffusion coefficients to control the vertical and horizontal distributions of salinity and water temperature. The more complex components of the

plume calibration dealt with the RMA-10 schematization of the near-field, the recirculation of heat in the vicinity of Salem, RMA-10's ability to budget the mass of a dye tracer, and the effect of tidal marshes on water temperatures in the vicinity of Salem. The following paragraphs describe each of the complex components, and their relevance to the plume calibration.

Although RMA-10 is not expected to produce accurate calculations of the plume distribution in the near-field, it is necessary to calibrate the near-field region of the model domain to achieve a transition to the near-field model, (Section III.B) simulations.

An important component of the plume calibration is the design of these discharge element (Section III.C.5.d). The discharge is approximated as a "volume heat source" with a discharge flow rate and ΔT that combine to equal the heat flux of the Salem discharge. The volume of water with elevated temperature is distributed throughout several elements. RMA-10 was not setup to characterize the discharge momentum. RMA-10 mixes the discharge volume with the surrounding Estuary water according to the governing hydrodynamic and transport equations. The mixed flow is advected and dispersed into the far-field by the ambient currents. Suitable dimensions for the volume heat source and the distribution of heat within the volume were derived as part of the plume calibration process. The size of the volume is constrained by practical considerations and the numerical properties of RMA-10. If the volume is too large, Salem's heat is artificially dispersed over too large a region, and the modeled water temperatures just outside the volume are underestimated significantly. If the volume is too small, RMA-10 does not properly solve the governing hydrodynamic and transport equations. Relatively high coefficients of vertical and horizontal diffusion were needed to approximate the vigorous near-field mixing associated with the discharge while retaining numerical stability. The dimensions of the discharge elements and model parameters that govern mixing characteristics (diffusion coefficients) that were used to approximate the near-field were based on: (1) input data from the Modified TMP (Section III.C.5.a); (2) the trajectory and width of the near-field region that were calculated for (four) specific phases of a tidal cycle using the calibrated version of CORMIX (Section III.B); and (3) stability and convergence limitations of RMA-10.

The plume calibration also considered effects of recirculation. Also, the size of the volume heat source and the sizes and arrangements of the elements in the vicinity of Salem's intake and discharge, affect how much of Salem's heat is recirculated in the once-through cooling water. Temperatures in the immediate vicinity of Salem increase with the amount of heat that is recirculated. Thus, the plume calibration also included adjusting the configuration of the elements in the vicinity of Salem until the measured and computed water temperatures at Salem intake were in reasonable agreement.

Another key component of the plume calibration was conducting a test to ensure that RMA-10 conserved mass. Finite-element models, such as RMA-10, conserve water mass over the model domain, but the model may not conserve water mass locally. Local gains and losses in water mass affect the budgeting of constituents (such as heat and dye)

that are included in transport calculations. An appropriate step in calibration is to provide assurance that RMA-10 adequately accounts for the mass of a constituent that is discharged from Salem. Consequently, numerical simulations for the release of a conservative dye from Salem were performed to measure the rate of gain or loss of the mass of dye over time. The results of these experiments were used to refine the shapes and bottoms of elements to minimize local gains or losses of water and, hence, maximize the budgeting of dye (and therefore Salem's heat). The results of the dye balance are presented in Section III.C.5.f.i. This dye balance was simply a numerical experiment designed to ensure the model does not introduce unacceptable levels of numerical inaccuracy. The dye balance did not include comparisons to dye survey data, which was reserved for model verification.

The plume calibration considered the effect of nearby marshes on the plume. There are extensive tidal marshes that can affect water temperatures in the Estuary. Natural cooling and heating processes occur in the tidal marshes, and can affect water temperatures in the Estuary and the dissipation of the heat from the Station (Exhibit E-1-5). Several modifications were made to the detailed computational grid to include specific tidal marshes that could affect the dissipation of Salem's heat including: Alloway Creek, Hope Creek, and Mad Horse Creek. At one point in the plume calibration process, a detailed computational grid was constructed that allowed RMA-10 to accurately simulate the flow rates through the marsh channels. The detailed marsh grid also simulated the exchange of heat through the marsh channels, but had some limitations for simulating natural inputs of heat to the marshes. This grid included many of the tidal marsh tributaries and accurately depicted many of the finer topographic details of tidal marsh. When RMA-10 was tested for mass conservation, however, this grid was found to artificially increase the total of amount of dye relative to what was discharged. The model's artificial accumulation of dye indicated the model also accumulated heat. Consequently, a simpler representation of the tidal marshes was adopted for the final calibration to ensure the accuracy of plume simulation. The simplified marsh scheme conserved marsh surface area to ensure surface heat exchange processes were appropriately represented.

The RMA-10 plume calibration was evaluated using comparisons of model results with measured data. The plume calibration was completed when the modeled and observed distributions of water temperatures were in reasonable agreement, considering the goal of RMA-10 is to simulate ΔT far-field. The modifications made to achieve the plume calibration had little effect on the Estuary-wide calibration. A detailed presentation of the model/data comparisons for the plume calibration is provided in Section III.C.5.f. An assessment of RMA-10's ability to simulate the transport processes governing the distribution of the Salem plume is presented in Section IV.

III.C.5.d. Finite Element Grid and Coefficients for the Calibrated Model

The finite element grid described in this section is the final grid that resulted from the calibration process. The grid is presented in advance of the calibration results so that features of the grid can be referenced in these later sections.

The computational grid used to characterize Salem's thermal plume in 1993 (TRA et al. 1993) provided the starting point for the 1999 calibration. Therefore, the initial mesh of nodes and elements, including the discharge, was based on the previous modeling. Initial values for empirical coefficients for calculating energy dissipation, mixing, and hydrodynamic dispersion were taken from the 1993 model. Also, the initial regions characterized by one-, two-, and three-dimensional elements were utilized initially for the new grid. This included the two-layer, three-dimensional region where the top element encompassed 20% of the water column, and the bottom element encompassed the bottom 80% of the water column.

The 1993 computational grid underwent significant revisions during the calibration process for the 1999 model. These modifications were motivated by new data and information obtained since 1993, the joint calibration of CORMIX and RMA-10, and improvements to RMA-10 for simulating the tidal marshes.

Initial modifications to the computational grid were based on water depths, shorelines, and other physical features of the Estuary that are shown on National Oceanic and Atmospheric Administration (NOAA) Nautical Charts 12277 (28th Ed.), 12304 (39th Ed.), 12311 (38th Ed.), 12312 (48th Ed.), 12313 (45th Ed.), 12314 and (29th Ed.). A bathymetry survey, also was used to refine the computational grid. The survey was performed in 1995 (Exhibit E-1-1), and provided detailed depth information in the vicinity of Artificial Island and across the Estuary from a southern limit at Hope Creek Jetty to a northern limit at the northern tip of Artificial Island.

Local refinements to the computational grid in the immediate vicinity of the Salem discharge and intake were made as calibration progressed. The 1995 detritus study (Exhibit E-1-1) provided data on currents and circulation patterns in the vicinity of Salem that identified where improved spatial resolution was warranted in the vicinity of the Salem outfall and Hope Creek Jetty. The joint calibration of CORMIX and RMA-10 established the need for more numerous and smaller elements in the vicinity of the discharge. These smaller elements enhanced the spatial resolution and improved RMA-10's ability to properly conserve mass of constituents input through the discharge. Finally, the computational grid was expanded in the vicinity of the Station to include tidal marshes that affect the dissipation of Salem's heat to the atmosphere.

Figure III-41 is a plan view of the computational grid following calibration. The shoreline of the Estuary at mean low water (MLW) defines the landward boundaries of the computational grid for all but the marsh regions where the mean high water (MHW) line was used to establish the limits of the model grid. The horizontal size of elements increases with distance from the Station where less resolution is required.

With respect to vertical resolution, the regions with one-dimensional, two-dimensional and three-dimensional elements are largely the same as in the 1993 computational grid. Two-dimensional elements were used for the lower portion of Delaware Bay from RM 34

to the Atlantic Ocean, and north of Artificial Island from RM 57 to RM 80. Vertical salinity or temperature stratification in the lower Delaware Bay does not have a significant effect on the transport of the Salem thermal plume; therefore, it was not necessary to model these processes. The use of two-dimensional elements above RM 57 is appropriate since there is no evidence of vertical stratification there. Farther up-estuary, one-dimensional elements are used north of RM 80 where the Estuary is characterized as a long and narrow river and is well-mixed in the vertical and cross-channel dimensions.

The finite element grid in the vicinity of the Station is three-dimensional. Between RM 34 and 57, the grid is composed of two layers of three-dimensional elements, which provides five points (nodes) over depth at which calculations are made. The purpose of the three-dimensional grid is to give the model the capability to simulate vertical stratification of the plume if it occurs. Simplified numerical experiments were conducted that showed two layers are adequate to simulate stratification, depending upon the temperature (density) difference between the discharge and receiving water, and upon the mixing characteristics of the receiving water. The three-dimensional grid is not designed to simulate depth stratification associated with ambient salinity and/or temperature in the Estuary. Although there can be some salinity stratification in the shipping channel offshore from the Station, it is not significant in terms of plume transport and mixing. For the purposes of simulating the transport and mixing of Salem's thermal plume, the Estuary can be treated as well-mixed over depth.

The computational grid includes specific elements that withdrawal and discharge the cooling water. The elements that withdrawal the cooling water are located on the grid adjacent to the Station's intake. The inclusion of these elements allows RMA-10 to calculate the recirculation of heat resulting from the operation of Salem's once-through cooling operations. RMA-10's power plant boundary condition was designed specifically for the Salem application.

Figure III-42 shows an enlargement of the grid in the immediate vicinity of the Station including a region of small elements around the discharge. The numbers and sizes of these small elements were based on design drawings of the Salem outfall, the joint calibration of RMA-10 and CORMIX, and numerical properties of RMA-10 that affect the conservation of Salem's discharged heat. The horizontal and vertical dimensions of these elements are small compared to the width of the Estuary. For example, the horizontal dimension of the elements just offshore of the discharge are approximately 200 feet (60 meters) whereas the Estuary is approximately 2.5 miles wide. This enhanced horizontal resolution was provided so that RMA-10 could resolve changes in water temperature over small distances in the vicinity of the Salem discharge.

Although RMA-10 cannot simulate the momentum of the discharge jet, an attempt was made to incorporate this effect. The momentum of the discharge transports the plume farther offshore during the brief slack tides. This effect was incorporated into RMA-10 by using different discharge elements during slack tides as opposed to running tides as

shown in Figure III-42. The discharge water is distributed over nine elements surrounding the end of the discharge pipes during running tides. The cooling water is distributed evenly over depth, based on field observations and CORMIX that show the plume is well-mixed in the near-field (Section III.B). Also, these nine elements were moved slightly offshore (approximately 100 feet) from the end of the pipe location to simulate the effect of discharge momentum during running tides. For slack tides, the cooling water is distributed over the seven elements indicated on Figure III-42. This simulates the effect of momentum during slack tides that transports the discharged water farther offshore, as determined from field observations and CORMIX (Section III.B).

As shown by Figures III-41 and III-42, the grid is subdivided into 14 (type 10 was not used) element types. Each element type is characterized by a unique set of RMA-10 coefficients. These include turbulent exchange coefficients, turbulent diffusivities, and friction factors. In the calibration process, these coefficients are adjusted repeatedly until the model reproduces observed features of the tidal regime, salinity distribution, and temperature patterns. Table III-8 summarizes the values of model coefficients used in the calibrated model by element type. These are the resulting coefficients that were "tuned".

The overall strategy used to select these coefficients builds on previous model studies and reflects on physical characteristics of the Estuary. Following Walters (1991), relatively high friction factors were applied in the Tidal River Zone (element types 5, and 6); where larger friction can be expected due to bottom roughness, lateral constrictions, sinuous channel geometry, and the presence of islands. In contrast, smaller friction factors that are typical of a coastal plain estuary were selected in the Delaware Bay Zone (element types 1, 3 and 9).

RMA-10 computes the horizontal turbulent exchange coefficient for an element by multiplying a user-specified value by a nominal element length. Consequently, relatively large exchange coefficients are applied in regions where the mesh is coarse (e.g., element types 3, 5 and 6). For example, larger horizontal turbulent exchange coefficients were applied for elements in the Delaware Bay Zone (Type 3), the Northern 2-D extent (Type 2), and the 1-D region (Type 5 and 6) than for the fine-mesh elements near the Station (Type 4).

Also, relatively large turbulent diffusion coefficients were selected in the far-field region where the model is one-dimensional. This selection was based on numerical stability concerns and on the distance of these regions from the Station. Relatively high diffusion coefficients were selected in the vicinity of the discharge to account for mixing induced by the Station's discharge momentum, which was not incorporated directly into the RMA-10 model. Additional element types were specified to characterize the near-field areas, marshes, Sunken Ship Cove, and Hope Creek Jetty (element types 7, 8, 11, and 12).

III.C.5.e. RMA-10 Estuary-wide Calibration Results

RMA-10 was calibrated for the time period corresponding to the Two-Unit Survey between May 21 and June 4, 1998. This section presents graphical comparisons between

model results and field observations for the final calibrated model. The Estuary-wide calibration preceded the plume calibration (Section III.C.5.f) and was designed to ensure RMA-10 had the capability to simulate the dominant Estuary-wide processes that are relevant to the transport of the Salem thermal plume. The graphical model/data comparisons presented in this section are generally visual and qualitative. Section IV provides a more quantitative assessment of the model's performance with regard to simulating observed physical processes.

The Estuary-wide calibration focused on tides, currents, salinity, and water temperature. These processes were selected based on their potential effect on plume transport. The Modified TMP (Exhibit E-1-3) provided appropriate data for the model calibration. It was important to ensure the model appropriately simulated large-scale processes that affect the plume before focusing on the local plume transport and mixing processes (i.e., the plume calibration). The Estuary-wide calibration consisted of numerous iterative model simulations and refinements, designed to produce a robust RMA-10 model of the Delaware Estuary.

Although the model/data comparisons illustrate good agreement, some of the comparisons reveal differences which need to be put in perspective. All numerical models incorporate assumptions that limit their ability to simulate nature. For instance, the high quality and comprehensive data set produced for this application according to the Modified TMP revealed numerous complex processes that RMA-10 cannot simulate. In most cases, though, these differences between the model and data are not pertinent to this application. The differences are not associated with processes that significantly affect the model's ability to simulate the transport and mixing of the Salem thermal plume (ΔT). Model/data comparisons that reveal the model's limitations are presented in the following sections to put the model's capabilities in perspective.

III.C.5.e.i. Tides

Since tides are the dominant process in the Estuary, RMA-10 was calibrated to achieve the best match between observed and simulated tides. Modeled tides were compared to measurements at five locations within the Estuary (Figure III-43: Woodland Beach (RM 42), Salem Barge (RM 50), Reedy Point (RM 59), Philadelphia (RM 99) and Burlington (RM125). Tide gages record the time-varying rise and fall of the water surface elevation. Based on these comparisons, friction and turbulent exchange coefficients were adjusted to match the RMA-10 predictions to the measured tides. The results of these comparisons for the calibrated model are presented below.

Figures III-44a and III-44b compare modeled (thin line) and measured tides (thick line) for the two-week calibration period. Figures III-45a and III-45b show the tide measurements on May 29, 1998. Additionally, Figure III-46 illustrates the variation of tide range and tidal time delay as a function of distance (RM) along the axis of the Estuary. Average modeled tide height over the two-week calibration period is illustrated by the solid line, and is bracketed by thin lines that represent the maximum and minimum modeled tide height during that time. Model results were extracted from nodes near the

shipping channel. Average observed tide heights from the gages are represented by the squares, and are bracketed by the maximum and minimum tide height observed during the calibration period.

Based on an examination of these figures, the following observations were made regarding RMA-10's ability to simulate measured tides:

- Tidal range: The modeled water surface elevation reproduces the observed semi-diurnal (twice-daily) tidal oscillations reasonably well, along with the spring/neap tidal cycle. The spring/neap cycle causes the tide range, i.e., vertical distance between successive low and high tides, to vary over a fourteen day period. The highest tides corresponding to the near-spring tides occur between May 25 and 28.
- Tidal amplification: The modeled tide range is amplified from the mouth of the Bay up to Burlington in similar fashion as the observations. The tidal amplification occurs primarily due to the funnel shape of the Estuary, and is well-represented by the model.
- Tidal asymmetry: The modeled tide curves reproduce the characteristics of the observed tidal curves; namely, short, steep flood tides and longer, more shallow ebb tides. This distortion of the tide curve strengthens as the tide propagates up-estuary, and is a nonlinear process that occurs as the tide responds to the friction and the changing geometry of the Estuary.
- Tidal phase: The modeled times of high and low tides are nearly coincident with observations, particularly from the mouth of Delaware Bay up to Salem Barge and Reedy Point, which best represent the tide in the vicinity of the Station. At Philadelphia (RM99) and Burlington (RM 125), the modeled and measured times of high and low tide differ by approximately one hour. The calibration process showed this difference can be reduced by increasing bottom friction, i.e., slowing the tide down; however, increasing friction also reduces the tide height, which is not preferred. A high priority was placed on modeling the observed tide height to simulate correct tidal exchange.

Overall, the graphical comparisons demonstrate the tides predicted by RMA-10 compare reasonably well with observations. Section IV provides an assessment of RMA-10's ability to simulate tidal processes.

III.C.5.e.ii. Currents

Since currents govern transport processes in the Estuary, RMA-10 was calibrated to match observed currents. No significant parameter adjustments were required to calibrate the model for currents. The calibration of tides combined with the accurate representation of the Estuary geometry (i.e., shoreline and depth) produced a reasonable match between observed and modeled currents. Current data were collected using Acoustic Doppler Current Profilers (ADCPs). A fixed-station ADCP was deployed approximately 1,000 feet offshore of the discharge (Figure III-43) to measure the time-varying vertical variation of currents at a fixed point. Also, vessel-mounted, mobile ADCPs were used to measure currents along three cross-sections (Figure III-43) of the

Estuary for four tidal phases. One cross-section is located at the Station. The other two cross-sections are location six miles up- and down-estuary, respectively. A description of the ADCP survey methods and observations is provided in Exhibit E-1-3.

Figure III-47 compares the magnitude of the modeled and measured current velocities during the two-week calibration period at the fixed-station ADCP located offshore of the discharge. Current data are shown by the thick line for four depth intervals: surface to one foot (upper panel), four to five feet, nine to ten feet, and fourteen to fifteen feet. Model results are presented by the thin dashed line, and were output from the node nearest to the ADCP location. Figure III-48 provides the time-series of currents for 29 May 1998. Modeled and measured current directions for the 29 May are compared on Figure III-49. Current direction is represented on the vertical axis in degrees ($^{\circ}$) based on a clockwise compass reading, such that north is 0° , east is 90° , etc. To put current direction in perspective spatially, flood and ebb tidal currents are directed approximately 320° and 140° , roughly northeast and southeast, respectively, and the discharge flow is directed approximately 220° (roughly southwest).

Inspection of these figures reveals the following regarding currents at the fixed-station ADCP:

- The modeled and measured current velocities exhibit similar tidal oscillations. Maximum modeled and measured current velocities are approximately 2.5 to 3 feet per second.
- There is almost no difference between modeled and measured current directions for the running ebb and flood tides.
- During slack tides, the observations reveal velocities oriented in-line with the discharge. These are discharge-induced velocities that cannot be included in RMA-10, and, therefore, are not represented by the model.
- Observed short-duration motions are superimposed on the tides that are not reproduced by the model. These high frequency motions, which may represent turbulent fluctuations, were not expected to be simulated by the model, and are not expected to affect plume transport.
- There is little depth-variation of current speed and direction.

The model/data comparisons demonstrate that the model predictions of receiving water velocity and direction in the vicinity of the discharge are well-represented by the model.

In addition to the fixed-station ADCP data, the mobile ADCP cross-section data are compared with model predictions. The location of the three ADCP cross-sections are shown on Figure III-43. The ADCP data were post-processed to estimate total flow through the three measured cross-sections and modeled flow (line) of the Estuary. Figure III-50 compares the observed flow (dots) and modeled flow (line) through each of the three transects. The observed data are available for the four phases of the tide during which the vessels traversed each Estuary transect. There is excellent agreement between the model results and the observations.

A more detailed comparison of modeled and measured currents based on the mobile ADCP cross-sections is provided by Figures III-51a and III-51b. These figures illustrate the variation of current speed along the three cross-sections where ADCP data were collected for a flood tide. Positive values are typical of flood tides and represent currents oriented up-estuary. The New Jersey (east) side of the Estuary is on the right-hand side of the page; therefore, positive currents are directed into the page.

Inspection of these figures shows that generally the modeled currents agree with the observed currents best on the east (New Jersey) side of the Estuary, in the vicinity of Artificial Island. This region is generally characterized by currents that are uniform over depth. Across the Estuary as a whole, though, there are more cross-Estuary and depth variation in the observed current patterns than in the model. That is, the model simulates a smoother horizontal distributions of currents. However, there is a tendency for higher simulated velocities over the deep channel, as in the observed distributions.

To summarize the model/data comparisons for currents, the modeled currents match observations reasonably well. The modeled current patterns at the location of the fixed-Station ADCP match observations extremely well. Additionally, the modeled and measured volumetric flow through cross-sections of the Estuary match extremely well. Although there are some detailed observed cross-estuary and depth-varying current patterns that are not reproduced by the model, the modeled and observed currents were generally higher over the navigation channel. Thus, the model has the capability to simulate the overall advective transport of the plume. Section IV provides an assessment of RMA-10's ability to simulate currents and their relationship to plume transport processes.

III.C.5.e.iii. Salinity

The variation of salinity in the Estuary is an indicator of large-scale transport processes. Higher saline water from the Atlantic Ocean is mixed with freshwater input to the Estuary via various tributaries and other sources, as well as nearly freshwater from the C&D Canal. Significant variations in salinity, either over depth or across the Estuary, could potentially generate circulation patterns due to differences in water density. Although such density-driven currents are not expected in the Delaware Estuary because it is well-mixed, particularly in the vicinity of the Station, it is still important to evaluate the model's performance with regard to Estuary-wide salinity distributions. Adjustments made to RMA-10 for the Estuary-wide salinity calibration were limited to horizontal diffusion coefficients in order to match the observed variation of salinity along the shipping channel.

Data available for comparison to the modeled salinity include vertical profiles and mooring time series. Vertical profiles were taken at various locations and times. On three occasions (21 May, 27 May, and 2 June 1998), vertical profiles were collected, along the shipping channel from the mouth of Delaware Bay to Trenton, NJ. Other vertical profiles were collected during the shipboard surveys on 29 May 1998, closer to

the Station. Moorings recorded salinity at near-surface, near-middle, and near-bottom depths in May and June, 1998. Exhibit E-1-3 describes the methods and results of the salinity data collection program in detail.

Figure III-52 summarizes the depth-averaged results of the vertical salinity profiles collected along the shipping channel, and compares the observations to model predictions. The diamonds represent depth-averaged observed salinity along the shipping channel. These values were calculated from the vertical profiles taken at the locations shown on Figure III-53. The circles depict corresponding values of depth-averaged modeled salinity. Multiple values are plotted for RM 40 and RM 50 that represent cross-Estuary variability. Figure III-52 demonstrates that RMA-10 reproduces the observed axial variation in salinity reasonably well. On 21 May (top plot on Figure III-52, the modeled salinity is generally lower than the observed salinity up to RM 50 because the model did not have time to equilibrate to its initial conditions. By 27 May, though, there is excellent agreement between modeled and observed salinity. Except for RM 40, a similar level of agreement exists on 2 June.

A closer comparison of the model with data for salinity variations along the shipping channel is provided in plots showing the actual vertical profiles against modeled salinity. Figures III-54a, III-54b and III-54c illustrate the vertical variation of salinity for each vertical profile location sampled on May 27, 1998 (locations of vertical profiles are shown on Figure III-55). Observations are shown as dots, and model results are indicated as a thin line. Salinity is less than 2 ppt from RM 130 down to RM 55 (just north of Artificial Island). In this region, the model and data match almost perfectly with no vertical stratification. Between RM 50 and RM 20, observed salinity increases significantly. The model reproduces the increase in salinity toward the ocean boundary well.

Figures III-54a, b, and c also show that there can be vertical stratification of salinity in the shipping channel, and that RMA-10 does not reproduce this feature well. This limitation of the model is not of particular concern for this application, though, because these depth variations of salinity have a limited effect on the mixing of the Salem thermal plume. Further, there is little to no depth variation of salinity on the channel margins where the Salem thermal plume exists, as supported by a review of the vertical salinity profiles collected during the shipboard surveys (locations shown on Figure III-55). Generally, there is little vertical variation of salinity within the region sampled, with few exceptions near the shipping channel (Figures III-56a and III-56b). The model was not implemented to simulate vertical variations in salinity in the lower Bay Zone. For instance, as shown in Figure III-41, the three-dimensional domain of the model does not extend throughout the Bay Zone. RMA-10 was implemented in this case specifically to simulate the Salem thermal plume $\Delta T_{\text{far-field}}$, and the small vertical variation of salinity are not a relevant feature in this well-mixed estuary.

An additional comparison between modeled and measured salinity was made based on the mooring data. The mooring locations are shown on Figure III-57). Generally, the

model simulates the range and tidal fluctuation of salinity reasonably well. For instance, Figure III-58a illustrates a good comparison with salinity at Mooring 5, which is located offshore of the Station near the shipping channel. A similarly good comparison between modeled and measured salinity exists for the moorings in the vicinity of the Station, such as Moorings 2, 4, and 7 (Figures III-58b, III-58c and III-58d). A good comparison was achieved also for Mooring 9 (Figure III-58e), which is approximately six miles south of the Station and near the shipping channel. These comparisons indicate that transport processes are well-represented by the model in the vicinity of Salem.

There are fewer similarities between measured and modeled salinity at some locations on the opposite side of the shipping channel (e.g., Moorings 6 and 1 illustrated by Figures III-58f and III-58g), and at the southern limits of the mooring array (e.g., Moorings 10, M9, and M12 shown on Figures III-58h, III-58i, and III-58j, respectively). Achieving a match at these locations was less important than for locations near the Station, though, given that the model is intended to characterize the Salem thermal plume, which is marginally affected by salinity at remote locations.

Overall, the modeled salinity distribution along the shipping channel, is similar to the observations. The observed variation in salinity along the shipping channel, from the mouth of Delaware Bay up to RM 130, is well-represented by the model. The distribution of salinity produced by the model in the vicinity of the Station also compares well with data. Although there are observed depth-variations of salinity that the model does not represent, particularly near the shipping channel, these variations are not expected to influence significantly the transport processes governing the plume. A more detailed assessment of the RMA-10's ability to simulate observed salinity and related transport processes is provided in Section IV.

III.C.5.e.iv. Water Temperature

The Estuary-wide calibration also focused on the variation of water temperature throughout the Estuary. Water temperature in the Estuary is controlled by a number of factors, including mixing of the Atlantic Ocean water and surface heat exchange processes. Although not expected in this well-mixed Estuary, large gradients in water temperature could potentially generate currents within the Estuary due to density differences. Therefore, as with salinity, the ability of the RMA-10 to reproduce observed water temperature gradients is a measure of the model's ability to simulate large-scale transport and mixing processes. It also provides assurance that the surface heat exchange processes are modeled accurately. Limited adjustment of diffusion coefficients was required for the Estuary-wide calibration of water temperature.

For the RMA-10 Estuary-wide calibration, modeled water temperatures were compared to vertical profiles and mooring data. Vertical temperature profiles were collected along the shipping channel from the mouth of Delaware Bay up to RM 130. Other vertical profiles were collected during the shipboard surveys.

Model/data comparisons of the variation in temperature along the shipping channel are illustrated by Figures III-59a, b and c; and III-60a, b, and c. These vertical profiles were collected in concert with the salinity profiles described above. The locations of the profiles are shown by Figure III-53, and the data were collected on 21 May, 27 May, and 2 June 1998.

Again, when assessing the model's performance, it is important to recognize where the model performs three-dimensional calculations and where it is depth-averaged (Figure III-41). The observations differ substantially between these three sampling periods. For instance, there were significant depth-variations in water temperature on May 21 and June 2 that did not exist on May 27. When/where depth-variations of temperature exist, they are primarily confined to the shipping channel and do not extend farther up-estuary than Artificial Island. The model performs well at simulating the variation of temperature along the shipping channel from the Ocean boundary to RM 130, but has limited ability to reproduce observed vertical variations. As with salinity, the limited ability of the model to reproduce vertical temperature variations in the Bay and channel is not expected to limit its ability to simulate dominant plume transport and mixing processes, which occur on the east side of the Estuary near Artificial Island where the water column is more well-mixed and well-represented by RMA-10.

Model/data comparisons at the mooring locations shown on Figure III-57 are provided by Figures III-61a, b, and c. These moorings were identified as important for the Estuary-wide calibration. Other model/data comparisons for moorings within the region occupied by the plume are discussed in the plume calibration (Section III.C.5.f). The temperatures predicted by RMA-10 throughout the mooring array compare well against data, with few exceptions that are generally far from the Station. For example, Figures III-61a and III-61b show RMA-10 simulates observed temperatures closely for two locations nine miles up- and down-estuary from the Station. Additionally, Figure III-61c demonstrated excellent agreement between the modeled temperatures and observations collected at the Hope Creek mooring. By contrast, Figure III-61d illustrates a less exact agreement between the model and data. This comparison is for Mooring 6, though, which is on the opposite side of the Estuary.

Overall, the model simulates the balance of water temperature throughout the Estuary quite well. There are some observed depth-variations in water temperature that the model does not simulate. In the Bay, the model cannot reproduce depth variations in water temperature because the model is two-dimensional there. This limitation is not relevant to the dominant transport processes governing the Salem thermal plume, which RMA-10 was implemented to simulate. A detailed assessment of the model's ability to simulate Estuary-wide temperature gradients is presented in Section IV. The model's ability to simulate water temperature in the region occupied by the Salem thermal plume is discussed in the plume calibration section that follows.

III.C.5.f. RMA-10 Plume Calibration Results

This section presents the results of the RMA-10 plume calibration, which was completed after the Estuary-wide calibration. It consisted of a series of iterative refinements to the computational grid and model parameters that were guided by direct comparisons of observed and modeled water temperatures and dye concentrations. The refinements were implemented to improve RMA-10's ability to simulate transport and mixing of the thermal plume. Localized changes were made to diffusion coefficients to achieve the best match possible between modeled and observed water temperatures. The Modified TMP (Exhibit E-1-3) provided a comprehensive data set that provided the basis to improve RMA-10's representation of the plume. Numerical experiments that tested RMA-10's ability to account for the mass of a conservative dye tracer injected at the Salem discharge also were incorporated in the plume calibration. The plume calibration was completed when the simulated temporal and spatial distributions of water temperature and the transport process were determined to be (on-balance) in reasonable agreement with field observations, and when RMA-10 budgeted Salem's heat within an acceptable level of accuracy. Subjective judgements were required to determine whether the plume calibration was satisfactory, based on model/data comparisons. To make these judgements, it is necessary to consider some factors that complicate model/data comparisons in the region occupied by the plume (Section III.C.5.f.ii).

This section presents the results of the numerical experiments for mass conservation first. Then, a brief discussion on factors considered in the subjective decisions is provided. Finally, various comparisons of observed and modeled water temperatures for the calibrated model are discussed. The comparisons generally are presented as qualitative narratives that identify the similarities and differences between the observations and model results. Where appropriate, the potential impacts of the more significant differences on the accuracy of subsequent calculations for ΔT are discussed. A more detailed and quantitative assessment of RMA-10's ability to simulate the general transport and mixing in the Estuary is provided in Section IV.

III.C.5.f.i. Numerical Experiments for Conservation of Mass

Finite element models, such as RMA-10, can be susceptible to mass conservation problems if not implemented appropriately. Constituents within the water, such as dye or heat, can be gained or lost due to numerical approximations encountered when solving the governing equations using finite elements. Sharp element corners and/or rapidly varying bathymetry can introduce spurious numerical gains or losses of constituents. Therefore, numerical experiments were performed to verify that this application of RMA-10 adequately conserves Salem's heat. If the total amount of Salem's heat is not conserved by the model, then the ΔT fields computed using output from RMA-10 will be affected. ΔT fields will be overestimated or underestimated if the model simulates too much heat or too little heat, respectively. The numerical experiment was conducted using a conservative dye tracer in lieu of Salem's heat. The substitution was made because Salem's heat is a small component of the Estuary's larger total heat budget, which includes the marshes (Exhibit E-1-5). The total heat budget includes components for all the natural heat exchange processes (e.g., marshes) and the flux of heat across the mouth

of Delaware Bay. Due to the large volume of water in the Estuary and large associated total heat, a variance in the total budget for the natural heat exchange processes would exceed a variance in the heat budget for Salem. On the other hand, performing the test on dye isolates the model's capability to conserve a constituent discharged by the Station. Additionally, variances in the mass balance for dye overestimate the corresponding variance for heat because dye is conservative (i.e., it all remains in the system), so more can be lost. Alternatively, heat is lost to the atmosphere through surface heat exchange processes.

The numerical experiment to test the conservation of dye was run for the calibration period starting immediately after the spin-up time. The duration of the dye balance experiment was approximately 250 simulated hours. The total mass of dye in the model domain, expressed as a percentage of the simulated amount of dye discharged, was tracked over time. At the end of the experiment, the amount of dye in the model domain was approximately 16 % greater than the amount of dye that was discharged. This mild accumulation of dye, hence heat, is analogous to losing less heat through surface heat exchange processes. On average, it was determined that the gain in heat due to the numerical gain in dye is equivalent to an average increase in far-field ΔT of about 0.1°F. This indicated that the thermal plume derived using output from the calibrated version of RMA-10 is slightly conservative, in that it is slightly larger and warmer than the actual thermal plume.

III.C.5.f.ii. Factors Considered in the Comparison of Observations with Simulation Results

The model/data comparisons presented in this section on the plume calibration require subjective interpretation to evaluate the performance of the model. Two items, in particular, that affect these subjective comparisons are discussed below. One is related to the size of the elements in the model. In a physical system as large as the Estuary, computation constraints severely limit the number of small elements that can be used to capture all the spatial gradients which may occur as the Salem thermal discharge is dispersed by tidal mixing. Where an observed sharp gradient exists within the location of an element, RMA-10 will smooth the distribution of water temperature (reduce the gradient) by "averaging" the higher and lower temperature across the element. This occurs when the size of the element exceeds the spatial scale of the measured phenomenon. The observed differences in the maximum temperatures and the regions over which they occur, however, are not sufficient to warrant further refinement of the computational grid since the locations of the observed gradients varies rapidly in time and space. The grid would have to be refined to an unreasonable level to attempt to simulate the observed small-scale temperature gradients. Even still, these small-scale phenomena would be difficult to simulate, and are more refined than the ΔT distributions required for this application.

The other factor considered when making model/data comparisons for the plume calibration concerns the time periods over which data are collected versus the "snapshot in time" represented by the model results. The comparison of a non-synoptic (i.e. not

measured all at once) set of measured water temperatures and a truly synoptic (i.e. model results are calculated at one time step) set of modeled water temperatures may exaggerate differences between observations and simulations. The spatial distributions of measured water temperatures were constructed using measurements taken over a two-hour period during four tidal phases. Since the measurements are not entirely synoptic, they include some temporal distortion due to movement of the Salem thermal plume. The greatest distortions occur at the times of slack water when the reversal of tidal current causes the Salem thermal plume to change direction rapidly. In contrast, the corresponding modeled spatial distributions are based on RMA-10 output for targeted times in the simulation and are truly synoptic. The time that model results are output for comparison to data is the model time step closest to the mid-point of the two-hour survey period. The temporal variability of the computed spatial distributions from one time step before to one time step after the targeted time was evaluated to determine the effect of comparing non-synoptic measurements with a synoptic calculation. This temporal variability was found to be significant only for the times of slack water and sufficiently accounted for the more significant differences between the observed (non-synoptic) and computed (synoptic) distributions of surface water temperature.

III.C.5.f.iii. Observed versus Simulated Surface Water Temperature

The effect of the Salem discharge on water temperatures in the Estuary is partially evident from plots showing lines of constant temperature (or isotherms) across the water surface. Figures III-62 through III-65 show the observed isotherms based on data from the shipboard surveys. Water temperatures over a 12-mile length of the Estuary that is centered around the Station discharge in this region exhibit significant spatial variability. These temperatures are highest in the immediate vicinity of the Salem discharge, and progressively decrease with distance from Salem until an apparent minimum is reached where the spatial gradient becomes nearly flat or non-uniform.

It is important to distinguish observed water temperatures from the thermal plume (ΔT). As a first approximation, the isotherms for the higher water temperatures are near the discharge are reasonably coincident with lines of constant ΔT (isopleths of ΔT). At greater distances from the discharge, where the spatial gradient of isotherms is nearly flat, ΔT has decreased to a level that is indistinguishable from the background temperature fluctuations. Natural background temperature fluctuations are due to non-uniform heating/cooling of the Estuary, exchanges with tidal marshes, and tidal mixing of water with varying temperature. Since at these distances, the background fluctuations equal or exceed the ΔT that defines the perimeter of the Salem thermal plume (namely 1.5°F for the summer months and the 4.0 °F for the non-summer months), the isotherms for the lower temperatures are not applicable for resolving characteristics of the Salem thermal plume. The distribution of Salem's heat at these distances is better defined by the distribution of dye concentrations, which is discussed in the verification Section III.C.6.

The spatial distribution of observed water temperature isotherms for the higher temperatures (namely, greater than 21.5°C) locates the warmest regions of the Salem thermal plume. These isotherms are a useful reference for identifying features of the

Salem thermal plume and characterizing the transport and mixing of the Salem heat before it becomes too diluted and indistinguishable from background heat sources and fluctuations. For example, the trajectory of the Salem thermal plume is discernable and generally coincides with the path of maximum water temperature in the direction of the ambient current. In addition, the redistribution of Salem's heat with distance is manifest in the relatively steep spatial gradients in temperature across this path. Thus, one component in the evaluation of the plume calibration is RMA-10's ability to simulate the discernable trajectory of the Salem thermal plume with distance from the Salem discharge. Other components evaluated are the lateral and longitudinal distributions of temperatures along the plume's trajectory.

Observed and modeled spatial distributions of surface water temperatures were compared for four phases of a tidal cycle on 29 May 1998. The comparisons discussed herein focus on isotherms for which the water temperature is 21.5 °C or greater since the pattern of isotherms exhibits at least some structure and degree of spatial variability that is likely attributable to the Salem discharge (i.e., dissimilar from natural background temperature influences). The Salem thermal plume (ΔT) extends beyond these isotherms, but natural fluctuations in water temperature obscure further characterizations of the distribution of Salem's heat. Table III-9 lists the phases of the tidal cycle, the distance over which each comparison is made, the figure number for the observed surface water, and the figure number for the modeled water temperature.

For the ebb phase (Figures III-62a and III-66a), the observed and calculated distributions of surface isotherms are similar. The regions of water with temperatures greater than 22.0°C occur in long and relatively narrow bands that are comparable in size and aligned with the general direction of flow. The simulated centerline trajectory of the Salem thermal plume is oriented slightly away from the east shore, whereas the observed trajectory parallels the shore. Figure III-14 shows the temperature variation along the observed and simulated centerline of the Salem thermal plume. Between 1,000 ft and 3,000 ft down-estuary from the Salem discharge, the maximum measured temperatures range from 24.0°C to 25.0°C which are 1.0°C to 1.5°C warmer than the simulated water temperatures.

Within 3,000 ft and 10,000 ft south of the discharge of the Salem discharge, the observed lateral gradients in water temperatures are much steeper than the modeled isotherms. Because the steep lateral gradient occurs over distances that are comparable to the lateral dimensions of the computational elements, RMA-10 cannot reproduce the gradients and compensates by locally reducing the peak temperatures and elevating the lower temperatures. The differences in the maximum temperatures and the regions over which they occur are not sufficient to warrant further refinement of the computational grid since the regions are small and their location varies rapidly in time and space. An unreasonable level of refinement would be required to attempt to simulate these small-scale temperature variations. Even with substantial refinement, these complex processes would not likely be simulated by the model.

Between approximately 3,000 feet and 10,000 feet south of the discharge, there is a gap in the survey data and no model/data comparison can be made. Beyond 10,000 feet, the bands of isotherms for measured water temperatures between 21.0°C to 22.5°C extend farther down-estuary than the corresponding bands based on simulated water temperatures.

The fact that the measured isotherms extend farther south than the modeled isotherms does not indicate the model underestimates the southern extent of the plume on an ebb tide. Rather, there are other natural sources of heat, such as Hope Creek and Mad Horse Creek Marshes, that elevate water temperature south of the Station on an ebb tide (e.g., the marshes are draining heated water from the shallow marsh plains). This process was included in the field observations, but not in the model results, because the model does not simulate heat derived from the marshes well. Consequently, at relatively far distances from the discharge, observed water temperatures exceed modeled water temperatures. This apparent discrepancy between the model and data is further explained through model/data comparisons for dye presented in the verification (Section III.C.6) which eliminates the bias associated with natural sources of heat (i.e., dye is only defined from the Station during the dye survey).

Inspection of modeled water temperature gradients suggests RMA-10 focuses heat in the vicinity of Hope Creek Jetty on the ebb tide. Although field data are sparse at this location, the pattern of the gradient suggests the model over-predicts water temperature which introduces a measure of conservatism to the RMA-10 modeling.

For the end-of-ebb phase, there is no apparent order to the isotherms of observed water temperatures (Figure III-63a and III-63b). In the immediate vicinity of the Salem discharge, pools of water with elevated water temperatures (22.0°C to 24.0°C) exist within larger volumes of milder temperature water on both sides of the Salem discharge. This indicates that rapid changes in the direction and magnitude of flow field are disturbing the structure of the Salem thermal plume. The affect of the changing flow field is exaggerated since the measurements were taken over a two-hour period. In the immediate vicinity of the Salem discharge, pools of water with elevated water temperatures (22.0°C to 24.0°C) exist within larger volumes of milder temperature water on both sides of the Salem discharge. RMA-10 is not expected to reproduce these small pools of warmer water because they are in the immediate vicinity of the near-field (RMA-10 is a far-field model), and because the pools have which is approximated as a volume source and have sizes close to the horizontal dimensions of the elements.

The 22°C and 23°C isotherms indicate the Salem thermal plume is predominately to the south of the Salem discharge from the previous ebb tide, but that it is less structured and beginning to be transported north by the developing flood tide. Pools of warm water are apparent from the observations near the mouths of tidal creeks. The absence of comparable dye concentrations (Figure 106a) indicates that these localized regions of warmer water are likely due to flows from the tidal marshes. Exhibit E-1-5 discusses the heat input to the Estuary by marshes in detail.

The simulation results for the end-of-ebb (Figures III-67a and III-67b) are consistent with the observations considering that a modeled synoptic picture is being compared to a picture from non-synoptic measurements. The maximum modeled water temperatures (approximately 24 °C) occur in pools along Artificial Island and are comparable to the observed maximum temperatures. While the spatial distribution of modeled isotherms is more continuous, they also show a thermal plume that is in transition. About the time of low water slack, the Salem thermal plume is down-estuary of the Salem discharge. As the tidal currents are redirected up-estuary, the Salem thermal plume appears to redevelop along Artificial Island and to dissipate south of the Salem discharge. The dissipation appears as an uneven breakup in the bands of higher temperature water and expansion in the size of the lower temperature water.

The patterns of isotherms based on RMA-10 (Figures III-68a and III-68b) and data from the Modified TMP (Figures III-64a and III-64b) compare extremely well during the flood phase. North of the Salem discharge, the waters with the highest temperatures are along Artificial Island. Starting at 1,000 ft up-estuary from the Salem discharge, the simulated water temperature is approximately 0.5°C warmer than the measured water temperature; therefore, the model is conservative. The observed and calculated isotherms remain parallel to the shoreline, and the distances between the shore and a given isotherm tend to be slightly greater for the simulation than for the observation. Consequently, the model overestimates the width of the flood tide plume. At the northern tip of Artificial Island, the 23 °C isotherm for measured water temperatures extends approximately 5,000 ft more northward than in the model. The modeled 23°C isotherm wraps around the tip of Artificial Island, and is overestimated there. The simulated flow into the simplified tidal marshes during the time of flood likely contributes to the concentration of temperature north of Artificial Island. South of Artificial Island, the field data and RMA-10 show elevated water temperatures (typically between 22 °C and 23 °C). The more concentrated pattern of the isotherms for temperatures above 22 °C based on RMA-10, indicates that Salem's heat is more dispersed in the Estuary than what is simulated by RMA-10. Again, the model is conservative, because it overestimates water temperature in this region.

For the end-of-flood, the patterns of isotherms based on RMA-10 (Figure III-69a and III-69b) and the shipboard survey (Figures III-65a and III-65b) are also consistent, and show a thermal plume that is in transition. The maximum temperatures are along Artificial Island, with the modeled maximum temperature being approximately 1°C greater than the observed. The 22°C isotherms based on observations and simulations indicate that a portion of the Salem thermal plume remains south of Artificial Island over a tidal cycle. The tighter grouping of isotherms with temperatures in excess of 21°C based on the RMA-10 suggest that the simulated dispersal of Salem's heat is not as much as what occurs naturally. This is because RMA-10 does not include the discharge momentum, which transports the heat offshore at near slack conditions. The change in the direction of tidal current to the ebbing direction is evident from the redevelopment of the Salem thermal plume just south of the Salem discharge, and the down-estuary folding of the

22.0°C and 22.5°C isotherms at several miles north of the northern tip of Artificial Island. This is caused by the change from flood to ebb tide currents.

RMA-10 and the results of the Modified TMP provide consistent depictions of the distribution of Salem's heat within the survey region. The comparisons suggest that the dispersion of Salem's heat in the Estuary may be slightly greater than what is modeled. Consequently, the heat tends to be more focused in RMA-10, which is conservative in that modeled temperatures are slightly overestimated. At farther distances from the discharge, it is difficult to discern Salem's heat from natural heat (e.g., marshes) based on the measurements. Comparisons of ΔT (Section III.C.5.f.v) and dye (Section III.C.6) eliminate some of this natural bias. When used to calculate the affect of the Salem discharge on water temperature, this would result in overestimates of ΔT in some areas, and underestimates of ΔT in other areas.

III.C.5.f.iv. Observed versus Simulated Water Temperature at the Salem Intake

The water that is withdrawn from the Estuary for once-through cooling includes residual heat that remains in the vicinity of Salem. Heat from the discharge is circulated back into the intake during slack water. The recirculation of heat is important because it potentially adds to the increase in water temperature in the immediate vicinity of Salem (i.e., the ΔT across the Station's condensers is added to the intake temperature before it is discharged back to the Estuary). The plume calibration included refinements to the local grid that allowed this process to be represented adequately in the simulation. Too much recirculation would erroneously increase discharge temperatures, and, hence, increase the water temperature in the plume. The assessment of RMA-10's ability to simulate this process was based on comparisons of measured and computed water temperature at the Salem intake and discharge.

Figure III-70 compares observed and modeled water temperatures, starting at the end of the hydrodynamic spin-up time and ending on June 5, 1998, which is the last day of the calibration period. The observed water temperature is plotted as a daily average of the intake and discharge temperatures at Salem Unit 1 and Unit 2, which is consistent with the use of daily average heat loads and flows as input to RMA-10. The modeled water temperature is plotted for every time step, and represents the intake temperature computed by the model. Figure III-70 demonstrates that the modeled time-series of water temperature over each day is consistent with the daily averages of measured temperatures for the two Salem units. This result indicates that RMA-10 simulates accurately the recirculation of Salem's heat.

III.C.5.f.v. Comparisons of ΔT for the Calibration Period

The primary purpose of RMA-10 is to provide a numerical model to estimate $\Delta T_{\text{far-field}}$. $\Delta T_{\text{far-field}}$ is defined as the increase in water temperature, above ambient water temperature (i.e., water temperature in the absence of the Estuary), caused by the Station's thermal discharge. $\Delta T_{\text{far-field}}$ must be modeled because it can not be measured directly in the field due to the fact that coincident ambient temperatures can not be measured while the

Station is operating. ΔT far-field is modeled using two RMA-10 simulations: a with-Station simulation and a without-station (or ambient) simulation. Each simulation produces a time series of water temperature at each node comprising the finite element grid. The difference between the temperatures computed by these two model simulations (with-Station minus without-Station) produces a time series of ΔT at each node. The modeled ΔT contours then can be mapped for a point in time to illustrate the temperature and extent of the Salem thermal plume.

This section provides contour maps of ΔT for the RMA-10 calibration run. Additionally, some conceptual model/data comparisons are presented. The comparisons are conceptual because ΔT can not be measured directly in the field; however, rough estimates of ΔT can be estimated based on the field data. The values of ΔT estimated from the observations are not expected to be precise, but can be used to evaluate the ability of RMA-10 to simulate the general shape and extent of ΔT fields. These comparisons also provide the basis for some of the comparisons presented in the RMA-10 verification Section III.C.6.

Figures III-71 to III-74 provide contour maps of modeled ΔT in $^{\circ}\text{F}$ for four phases of the tide (ebb, end-of-ebb, flood, and end-of-flood, respectively) during the calibration simulation on May 29, 1998. Some general observations about the tidal behavior of the plume are extracted from these figures. On the ebb tide (Figure III-71), the plume is transported southeast, and the highest temperatures are separated from the shoreline. As the tide changes to end-of-ebb (Figure III-72), residual heat from the ebb tide remains southeast from the discharge; however, heat begins to pool in the vicinity of the discharge for this near-slack tide. On the flood tide (Figure III-73), the plume is carried north along the Artificial Island shoreline. The flood tide plume is relatively narrow, and wraps around the northern tip of Artificial Island. Even on the flood tide, residual heat remains southeast from the discharge. On the end-of-flood tide (Figure III-74), heat again begins to pool in the vicinity of the discharge because the tidal currents are near-slack. Significant heat remains north of Artificial Island on the end-of-flood tide.

The gradients in ΔT contours provide additional information about the shape of the plume. Generally, gradients are sharpest near the discharge, which is expected since temperature decreases most rapidly near the discharge point. The sharpest gradients exist in the vicinity of the discharge during near-slack tides. Farther from the discharge, gradients are relatively mild along the trajectory of the plume. Cross-plume gradients are relatively sharp, though, which shows the plume is generally narrow compared to its length.

To compare these general modeled characteristics of the plume to field data, Figures III-75 to III-78 provide surface contour maps of estimated ΔT based on the shipboard surveys. This estimate of surface water ΔT was calculated by subtracting an estimated value of ambient surface water temperature from the surface water temperatures measured during the shipboard surveys. For simplicity, the ambient temperature was assumed to be the minimum temperature recorded at Reedy Island during the tidal cycle. This estimate of ΔT is not expected to be precise since Reedy Island is not truly

representative of an ambient temperature. There is some influence from the Station at Reedy Island; therefore, the estimate of T_{ambient} is high and the estimated ΔT is low. Additional uncertainty is introduced to the estimate of ΔT because the ambient temperatures actually vary in space throughout the survey region, whereas the Reedy Island estimate of ambient was applied as if it were spatially constant. Nonetheless, the ΔT estimated from the field observations is useful to evaluate the general shape and extent of the ΔT modeled by RMA-10. On Figures III-71 to III-78, survey track lines are shown by the "x" symbols.

Visual comparisons between Figures III-71 to III-74 (modeled ΔT) and III-75 to III-78 (estimated ΔT from the shipboard surveys) indicate the shape and extent of the modeled ΔT are representative of measured processes in the field. The actual values of ΔT do not compare exactly, nor are they expected to. The ebb and flood pattern of the plume is confirmed by the estimated ΔT . The estimated ΔT has a similar narrow plume shape with the sharpest gradients of ΔT in the vicinity of the discharge and at the cross-plume limits. This shows that RMA-10 simulates plume temperature gradients well. The measurements also reveal more complex plume features, such as scattered small puddles of elevated temperature, that the model can not be expected to reproduce, particularly in the vicinity of the discharge where the momentum of the plume can not be simulated by RMA-10.

RMA-10 was developed and applied specifically to produce far-field ΔT . The $\Delta T_{\text{far-field}}$ are required to characterize thermal exposure for the Biothermal Assessment. ΔT is valuable because they isolate the influence of the Station, by identifying the temperature, shape, and extent of the Salem thermal plume. Although the estimates of ΔT computed from the field data are not intended to be precise, they help confirm that the modeled ΔT is reasonable. Similar plots of ΔT and comparisons to estimated ΔT from the field data are used to verify RMA-10 in Section III.C.6.

III.C.5.g. Tidal Marshes

RMA-10 Version 6.6 incorporated improvements compared with previous versions (Section V.E.3). One of these improvements was the representation of marshes and marsh processes. The observational program carried out as part of the Modified TMP included components that addressed the influence of marshes on the Estuary as a whole, and or the Station's thermal plume.

Exhibit E-1-5 addresses the effects of marshes on the Estuarine heat balance. Marshes contribute large amounts of heat on ebbing tides, which dwarfs the Station's thermal discharge during certain portions of the year, including the summer. Station effects on the protection of the balanced indigenous community must be assessed in the context of the marsh effects on the River surrounding the Station.

Attachment E-3 addresses the dissolved oxygen dynamics of the Estuary, in the context of interactive effects of the Station's thermal discharge on pollutants. One finding from this study was that the marshes can provide a large oxygen contribution to the River

surrounding the Station. During certain portions of the year, marshes can exert a large oxygen demand on the River, with deficits of up to 4.5 mg/L in dissolved oxygen.

These observations helped achieve the Modified TMP goal to investigate marsh interactions with the Estuary near the Station. Experimental simulations of marsh hydrodynamics showed the marshes could be represented by RMA-10. However, for the purposes of characterizing the Station's thermal plume and thermal exposures, the simulations and observations showed proper marsh area representation was important to characterize thermal exchange between the River and marshes. Consequently, the marsh areas were incorporated in all subsequent simulations.

III.C.6. Verification

The verification of RMA-10 was performed using data from the One-Unit Survey, data that were provided by Salem Generating Station and various state and federal agencies for the period that was coincident with the One-Unit Survey, and the measured dye concentrations from the Two-Unit Survey. The details and results of the One-Unit Survey are presented in (Exhibit E-1-2). The details and results of the dye-tracer study, which included a background fluorescence survey, are presented in Exhibit E-1-3.

Consistent with the calibration process, the verification included an "estuary-wide" component and a "plume" component. The "estuary-wide" verification establishes RMA-10's ability to simulate the tidal hydrodynamics and transport processes of the Estuary. The "plume" verification establishes RMA-10's ability to simulate the transport and mixing of the Salem thermal discharge in the Estuary.

The "estuary-wide" verification was based on comparisons of observed and simulated tidal elevations, currents, salinity concentrations, and water temperatures for the period of the One-Unit Survey (namely, from 21 October 1997 through 1 November 1997). The "plume" verification is based on comparisons of observed and simulated distributions of surface water temperatures from the One-Unit Survey, and dye concentrations at the times of the shipboard surveys measurements from the Two-Unit Survey, which lasted from 21 May 1998 through 4 June 1998. Although the dye measurements were taken concurrently with the temperature measurements used for the "plume" calibration, the measured dye concentrations from the shipboard surveys were considered to be an independent data set because they were not relied upon explicitly for the calibration. Furthermore, the water temperatures used for calibration reflected a thermal plume that likely was fully developed after several weeks of a constant discharge of heat from Salem. In contrast, the dye measurements were made after only two days of dye injection, when the dye plume was still developing, and therefore more difficult to detect.

Section III.C.6.a. summarizes the data that were input to RMA-10 to perform the "estuary-wide" and "plume" verification for the One-Unit Survey. The input to RMA-10 for the "plume" verification needed to simulate the transport and mixing of dye for the May 21, 1998 through 4 June 1998 period was presented earlier in Section III.C.5.a. Section III.C.6.b summarizes the data that were used to evaluate the performance of

RMA-10. The results of the "estuary-wide" verification are presented in Section III.C.6.c. The results of the "plume" verification are presented in Section III.C.6.d.

III.C.6.a. Input Data Sets for RMA-10 Verification for the One-Unit Survey

The "estuary" and "plume" verification for the 21 October 1997 through 1 November 1997 period followed the general approach used for the calibration. Coincident time-series of data sets were assembled and provided as input to RMA-10. These data include boundary and initial conditions, tributary flow rates and water temperatures, discharge flows and $\Delta T_{\text{condenser}}$ for the Salem thermal discharge, and point source discharges. The data were assembled and provided as input to RMA-10 using the same methodology employed for the calibration. The following section summarizes each type of input.

III.C.6.a.i. Boundary Conditions

Table III-10 summarizes the data and data sources for each open boundary of the model domain. The following paragraphs briefly explain the boundary conditions and the procedures that were used to develop the specific model input from the observed data.

The boundary conditions for the verification were specified to the model using similar data collection methods and correlations that were used for the calibration.

- Tidal Boundaries

Tide level was specified to the Delaware Bay boundary based on a linear interpolation between corrected tide data recorded by NOAA at Cape May, NJ and Lewes, DE between 21 October and 1 November 1997. The same method was used for verification as was used for calibration (Section III.C.5.a.i. (a))

The temperature and salinity of the water flowing into the Estuary across the Bay boundary were derived from measurements during the One-Unit Survey period. The vertical distribution of water temperature and salinity at three locations across the mouth of Delaware Bay during the flood showed no significant lateral or vertical variability (Exhibit E-1-2). Therefore, the constant values of salinity and temperature prescribed at the Bay boundary on the flood tide are averages of the measured water temperatures (60°F) and salinity concentrations (22 parts per thousand (ppt)) collected on 27 October 1997. RMA-10 computes water temperature and salinity across the Bay boundary during ebb tides; therefore, these input data are only required on the flood tide.

A tidal boundary condition also was prescribed at the Chesapeake and Delaware Canal (C&D Canal). Time-series of tidal elevations were recorded at Courthouse Point, Delaware along with the water temperature and salinity that were recorded as part of the One-Unit Survey. Similar to the Bay boundary, temperature and salinity were specified on the flood tide, and RMA-10 computes the water temperature and salinity on the ebb tide.

- **Freshwater Inflow**

The methods and data sources used to specify freshwater inflows for the verification run were the same as those for the calibration run. Freshwater inflow and water temperature were specified at the Delaware River in Trenton, New Jersey, the Schuylkill River in Philadelphia, Pennsylvania, and other tributaries. Daily-averaged time-series of freshwater inflow from the Delaware and Schuylkill Rivers were obtained from the United States Geological Survey (USGS). Time-series of the hourly water temperature and conductivity (which were used to compute equivalent salinity concentrations) for the inflow at Trenton, NJ also were obtained from the USGS. The water temperature and salinity concentration of the Schuylkill River inflow were assumed to be the same as the Delaware River in Trenton, NJ. This was justified based on recorded water temperatures at Trenton, NJ and Fort Mifflin on the Schuylkill River south of Philadelphia, which were compared and found to be similar.

Daily-averaged freshwater flows from the ungauged tributaries were estimated based on the ratios of the tributaries' and the Schuylkill River's drainage areas. Each tributary's daily average inflow rate was calculated by multiplying the daily average flow from the Schuylkill River by this ratio. The water temperature and salinity concentration of the flows from the ungauged tributaries and the Schuylkill River were assumed equal. Table III-5 lists the names and drainage areas of the ungauged tributaries for which flows were provided to RMA-10.

- **Surface Heat Exchange**

The meteorological inputs to RMA-10 are expressed as time-series of short-wave solar radiation, long-wave solar radiation, dew point, and wind speed. The data to construct these time-series, except dew point, were recorded at the Station. Although dew point is measured at the Station also, the availability of the data is sporadic. Therefore, the dew points were obtained from the National Weather Service (NWS) for Wilmington, Delaware.

The wind speeds for the verification were reduced to 68% of their measured value. An initial attempt to verify water temperatures in the Estuary showed that RMA-10 underestimated water temperatures by approximately 1.0°C (1.8°F). The steady decline in observed and calculated water temperatures indicated that the Estuary in late October 1997 was cooling more rapidly in the model than in nature. An analysis of the components of the RMA-10 heat budget indicated that the losses due to evaporation and conduction were overestimated in the model. The reasons for this behavior were investigated further.

The empirical equations that RMA-10 uses for the surface heat exchange due to evaporation and conduction are published by EPA (1985) and have been applied successfully elsewhere (LMS 1995 and LMS 1996b). These equations include a wind function that is based on wind speeds that are measured two meters above the water surface. The wind speed at the Station is measured at 10 meters above local grade. For certain meteorological conditions, the use of the measured wind speed, uncorrected for

the elevation difference, results in an over-prediction of heat loss to the atmosphere due to evaporation and conduction. An independent analysis of measured wind profiles at the Station for the calibration and verification periods confirmed that the 68 percent adjustment adequately accounted for the difference in the wind speeds at two and ten meters. When this correction was applied to the model input, the observed and predicted water temperatures compared very well. The computed water temperatures that are used for the "plume" verification are based on the adjusted wind speeds.

The evaporative and conductive terms for the calibration period, when the Estuary was warming, were not major components of the total heat budget. The effect of using a lower wind speed on the calibration was determined by reapplying RMA-10 with the adjusted wind speed. The effect on water temperature was less than 0.2°C (0.4°F). This small change cannot be detected from the field measurements because it is masked in the vicinity of Artificial Island by the sharp spatial temperature gradients in the thermal plume, and at the edges of the thermal plume by the background variability which can exceed 4°F. The effect on the characterization of the thermal plume was also found to be small for the calibration period. The average change in ΔT along the centerline of the thermal plume for the four tidal cycles varied between -0.2°C (-0.4°F) to 0.1°C (0.2°F). Thus, the correction to the wind speed did not significantly affect the calibration of RMA-10, or the characterizations of the thermal plume that were derived using simulations for the period from 21 May 1998 through 4 June 1998.

- Initial Conditions

Initial estimates of the spatial distributions of water temperature and salinity concentration throughout the Estuary were derived using data collected during the One-Unit Survey initial condition survey component, and a RMA-10 hot-start simulation (explained in Section III.C.5.a.ii). The initial conditions survey measured vertical profiles of water temperature and conductivity (salinity) at discrete points in or near the shipping channel from the mouth of the Delaware Bay to Trenton, New Jersey. Values for salinity and temperature based on these data were prescribed to each model node at the beginning of the verification period.

- Point Source Discharges of Heat

The model requires an intake/discharge flow rate and the increase in water temperature caused by the Station ($\Delta T_{\text{condensers}}$). The discharge flow rate of once-through cooling water, and hourly measurements of intake and discharge temperatures of once-through cooling water were obtained from Salem. Time series of the discharge flow rate and ΔT were provided as input to RMA-10.

Similar information for other major point source discharges of heat to the Estuary was obtained from state and federal agencies including the New Jersey Department of Environmental Protection (NJDEP), Pennsylvania Department of Environmental Protection (PADEP), and Delaware Department of Natural Resources and Environmental Conservation (DEDNREC). Table III-11 lists the names and discharge characteristics of

these major point sources of heat. These other point sources of heat were input to RMA-10 as element inflows with an elevated water temperature.

III.C.6.b. Data Available to Evaluate the Performance of RMA-10

The data used to evaluate the performance of RMA-10 for "estuary-wide" and "plume" verification were collected during the One-Unit and Two-Unit Surveys. The data from the One-Unit Survey are summarized in Section III.C.6.b.i. The data from the Two-Unit Survey are summarized in Section III.C.6.b.ii.

III.C.6.b.i. One-Unit Survey

The One-Unit Survey produced most of the data that were needed to verify RMA-10. Additional data were tidal elevations at the City of Burlington, NJ; and Philadelphia, PA that were obtained from USGS and NOAA, respectively. Table III-12 lists an inventory of the types and sources of data. The table summarizes how the data were used to verify RMA-10, the periods for which data were available, and the frequencies of data collection.

The One-Unit Survey consisted of four components (namely, a network of instrumented moorings, a shipboard survey, a hydrodynamic survey of tidal elevations and currents, and a marsh survey). Although this survey was less extensive than the Two-Unit survey, it still produced a high-quality and comprehensive data sets for verifying RMA-10. Exhibit E-1-2 presents the One-Unit Survey methods and data.

The remainder of this section briefly summarizes how the available data were used to verify RMA-10.

The moorings and shipboard surveys were intended to complement each other. The moorings provided data that primarily captured temporal variability, whereas the shipboard surveys provided data that captured spatial variability. The moorings measured time-series of water temperatures, conductivity (salinity) and dissolved oxygen concentrations within the near- and far-fields of the Salem plume and where ΔT is less than 1.5°F. The shipboard surveys measured the surface distribution of water temperatures. Vertical profiles of temperature and conductivity (salinity) also were collected as part of the shipboard survey. The shipboard measurements were taken at four phases of a tidal cycle (approximately at maximum flood, end-of-flood, maximum ebb and end-of-ebb). For the RMA-10 verification, the data from the moorings and shipboard surveys were primarily used to verify the shape of the thermal plume. Data from the shipboard surveys in the near-field were also used to verify the configuration of computational elements that were specified as part of the calibration process to approximate the near-field and intermediate field.

A mobile Acoustic Doppler Current Profiler ("ADCP") measured vertical profiles of the current speed across several transects of the Estuary at the four phases of a tidal cycle during the shipboard surveys. The current measurements, plus the observations of tidal elevations, were used to verify that RMA-10 accurately simulates the tidal hydrodynamics

of the Estuary, and correctly calculates the flux of water over cross sections of the Estuary.

The results of the marsh survey were not used directly for verification, because the simplified marshes were not designed to simulate natural heating that occurs in the marshes. Instead the simplified marshes were intended to simulate cooling of the thermal plume that occurs in the marshes. A better understanding of the natural heating and cooling processes that occur in tidal marshes was obtained from an analysis of the data (Exhibit E-1-5). The analysis showed that marshes can contribute significant heat to the Estuary naturally in excess of the heat load from the Station.

III.C.6.b.ii. Dye Measurements from the Two-Unit Survey

The dye-tracer study provided measurements of dye concentrations at the water surface along tracks for the shipboard surveys at four phases of a tide (ebb, end of ebb, flood, and end of flood) on 29 May 1998. Typically, the measurements for each phase were completed within approximately two-hours. The surface dye concentrations were used to construct plots showing the surface distribution of dye concentrations using lines of constant dye concentration.

III.C.6.c. Estuary-Wide Verification Results

The purpose of the Estuary-wide verification is to provide assurance that RMA-10 can predict large-scale processes that may affect transport and mixing of the thermal plume. As for the Estuary-wide calibration, the focus of the Estuary-wide verification was on tides, currents, salinity, and water temperature.

- Tides

Modeled tides were compared to measurements at five locations within the Estuary (see Figure III-43): Woodland Beach (RM 42), Salem Barge (RM 50), Reedy Point (RM 59), Marcus Hook (RM 82) Philadelphia (RM 99) and Burlington (RM125).

Figures III-79a and III-79b compare modeled (thin line) and measured (thick line) tides for the eleven day period. Figures III-80a and III-80b provide a close-up of one day's tide measurements on 28 October 1998. Additionally, Figure III-81 illustrates the variation in tide range and tidal time delay as a function of distance (in River Miles) along the axis of the Estuary. Average modeled tide height and tidal time delay over the eleven day period is illustrated by the solid lines, which are bracketed by thin lines that represent the maximum and minimum modeled tide height during that time. Model results were extracted from nodes nearest the tide gage. Average observed tide heights from the gages are represented by the squares, and are bracketed by the maximum and minimum tide height observed during the verification period.

The graphical comparisons verify that the tides predicted by RMA-10 compare reasonably well with observations. As discussed in the calibration section (Section III.C.5.e.i), the model reproduces observed features of the tide related to tidal range, tidal

amplification, tidal asymmetry, and tidal phases. Section IV provides an assessment of RMA-10's ability to simulate tidal processes.

- **Currents**

Current data were verified using the Acoustic Doppler Current Profiler (ADCP) data. Vessel-mounted, mobile ADCPs were used to measure currents along three cross-sections of the Estuary for various tidal phases. One cross-section is located at the Station. The other two cross-sections are location six miles up- and down-estuary, respectively (Figure III-43). A description of the ADCP survey methods and observations is provided in Exhibit E-1-2.

The mobile ADCP cross-section data were post-processed to estimate total flow through the measured cross-section of the Estuary. Figure III-82 compares the total observed flow (dots) through each of the three transects with the modeled flow (line). The observed data are available for the four phases of the tide during which the vessels traversed each Estuary transect, and the model reproduces this measured flow.

A more detailed comparison measured of modeled currents based on the mobile ADCP cross-sections is provided by Figures III-83 and III-84. Positive values are typical of flood tides and represent currents oriented up-estuary (vice-versa for negative values). The New Jersey (east) side of the Estuary is on the right-hand side of the page; therefore, positive currents are directed into the page. Inspection of these figures shows that as with the calibration, the modeled currents agree with the observed currents best on the east side of the Estuary. This region is generally characterized by currents that are uniform over depth. The detailed observed cross-Estuary and depth-varying current patterns that are not reproduced by the model though. The model smoothes the distribution of velocity significantly, but maintains concentrated flow in the channel as observed in the field.

- **Salinity**

As discussed on the calibration section (III.C.5.e.iii), the ability of RMA-10 to simulate the salinity mixing processes on an Estuary-wide basis is a measure of the model's general ability to transport constituents that travel with water, such as the Salem plume. Consequently, it is important to verify the model's performance with regard to Estuary-wide salinity distributions.

Salinity data available for comparison to the model simulations include vertical profiles and mooring time series. The vertical profiles provide the basis for evaluating RMA-10's ability to simulate the spatial distribution of salinity at discrete times in the tide. The time-series of salinity provide the basis for evaluating RMA-10's ability to simulate the temporal variability at fixed points. Vertical salinity profiles were collected at various points during the shipboard surveys on 28 October 1997. The moorings recorded salinity at near-surface, near-middle, and near-bottom depths in October 1997. Exhibit E-1-2 describes the methods and results of the salinity data collection program in detail.

Figure III-85 shows the location where the vertical salinity profiles were measured during the flood tide on 20 October 1997. Figure III-86 and III-87 compare the computed and observed profiles. The data indicate that the vertical stratification was weak or non-existent with the possible exception of the southern most profile in the shipping channel (VERT-DEL-35). The observed salinity ranged from a minimum of 5 ppt at the northern-most profiles (VERT-DEL-24 and VERT-DEL-23) to a maximum of 14 ppt at the southern-most profiles (e.g. VERT-DEL-26). The simulated vertical profiles are reasonably reproduced by RMA-10; thus, demonstrating that the longitudinal gradient in salinity and, hence, transport is being simulated. The computed vertical profiles at other points for the end-of-flood, ebb, and end-of-ebb tides (which are not shown graphically) showed less consistent agreement with the observed vertical profiles. Vertical stratification was not reproduced where it was measured. At some locations, the computed salinity underpredicted the measured salinity (which typically was 7 ppt to 10 ppt) by 2 to 3 ppt. But as discussed in Sections IV.B.3, these differences do not significantly affect the transport and mixing of the thermal plume because the Estuary is sufficiently turbulent to cause the thermal plume to mix over the water volume. The salinities are much higher in the vicinity of the Station than during the calibration scenario.

E-2 Figure III-57 shows the mooring locations. Generally, the model simulates the range and tidal fluctuation of salinity reasonable well. Figure III-88a compares observed with modeled salinities at Mooring 5, which is located offshore of the station near the shipping channel. This figure shows a similar diurnal variability in salinity, but modeled salinity is generally low by about 2 ppt. Figure III-88b shows Mooring 9, which is near the channel and just upstream model's southern 2-D boundary. At this location, the observed data demonstrate higher salinity water at the bottom than at the surface. The model does not reproduce this vertical distribution, but it is not expected to influence simulations of the thermal plume.

RMA-10's ability to simulate the Estuary-wide distribution of salinity was verified for the One-Unit survey period in October 1997. This time period was characterized by much higher salinity than the calibration period. The model simulated salinity gradients under these diverse conditions. The differences between modeled and measured salinity are on the order of a few ppt, and are not expected to have a significant influence on the transport and mixing of the thermal plume.

- Water Temperature

As with salinity, the ability of the RMA-10 to reproduce observed water temperature gradients is a measure of the model's ability to simulate large-scale transport and mixing processes.

For the RMA-10 Estuary-wide verification, modeled time-series of water temperatures were compared to the time-series of water temperature at moorings outside the thermal plume. Comparison of time-series at moorings within the thermal plume, and of vertical profiles at locations in the shipboard surveys are presented in Section III.C.6.d.i.

Example time-series of water temperature are shown in Figure III-88c (for Mooring 2), Figure III-88d (for Mooring 9), Figure III-88e (for Hope Creek), Figure III-88f (for Mooring 5), and Figure III-88g (for Mooring 6). The locations of the moorings are shown in Figure III-57. Moorings 2 and 9 are located six miles north and south of the Station, respectively. The Hope Creek mooring is at the mouth of Hope Creek. Mooring 5 is located directly offshore of the Salem discharge, close to the shipping channel. Mooring 6 is located on the western side of the shipping channel. The time-series of temperatures predicted by RMA-10 throughout the mooring array compared well against data, with few exceptions that are generally far from the Station. The semi-diurnal (twice daily) fluctuation of water temperature exhibited by the data is reproduced by the model. Also, the model simulates the general trend of cooling that occurred in this October period. The effect of the tidal marshes on water temperatures is clearly evident from the observed data in Figure III-88c. The range of temperature variations is significantly greater at Hope Creek than the range of variations at moorings away from the marshes.

The ability of RMA-10 to simulate water temperatures in the Estuary has been verified. The model simulates the general distribution of temperatures throughout the Estuary where measurements were taken, simulates the effects of tide on water temperature, and simulates the general trend of cooling during the October verification period. A detailed assessment of the model's ability to simulate Estuary-wide temperature is discussed in the plume verification section that follows.

III.C.6.d. RMA-10 Plume Verification Results

This section presents the verification of RMA-10's ability to simulate the transport and mixing of heat in the Salem discharge using direct comparisons of observed and modeled water temperatures for the One-Unit Survey, and using dye-concentrations from the Two-Unit Survey. A separate assessment of RMA-10's ability to simulate plume dynamics are discussed in Section IV.

The temporal and spatial variability of water temperature and dye concentration reflect (in varying degrees) the dilution of Salem's discharge in the Estuary. Because dilution is caused by the transport and mixing processes, favorable comparisons between modeled and observed temperatures and dye concentrations are evidence that RMA-10 correctly simulates the transport and mixing of the Salem discharge in the Estuary.

Comparisons using water temperature were limited primarily to the immediate vicinity of Artificial Island with a sharp focus on the region between the northern tip of Artificial Island and Hope Creek Jetty. At further distances, water temperature may not be a reliable reference for measuring the dilution of Salem's heat, because the spatial and temporal variations in water temperature are due more to natural processes (such as heat loads from the tidal marshes) and less to Salem.

The components of the assessment of plume verification are comparisons of surface water temperatures from the shipboard surveys, comparisons of water temperature at the

moorings, and comparisons of vertical profile at discrete locations established for the shipboard surveys. Additional comparisons were made to verify the distribution of ΔT fields according to the methods established for the calibration (Section III.C.5.f.v).

III.C.6.d.i. Observed Versus Simulated Water Temperature

The transport and mixing of Salem's heat causes a non-uniform and unsteady increase in water temperature in the Estuary. Although the temperature increases can not be measured directly, the general spatial distribution of Salem's heat at most times is readily apparent from spatial gradients in water temperature as shown in Figure III-89a through III-96b. Figures III-89a through III-92b show the isotherms of surface water temperature for ebb, end-of-ebb, flood, and end-of-flood tides on 28 October 1997. The boat location for each surface water temperature is shown by a "+". The corresponding results from the simulations are provided in Figures III-93a through III-96b. The sets of figures include the observed and modeled surface isotherms for the surveyed region and a "close-up" view for each of the four tidal phases. These tracklines combined with the presentation of contours assist in interpretation of the observed data. These data were collected on 21 October 1997, and are summarized in Exhibit E-1-2.

Comparison of the spatial distribution of higher surface temperature isotherms using data from the shipboard surveys and the simulations provide a measure of the transport and mixing of the Salem thermal discharge in the Estuary. Consistent agreement in the shape and dimensions of these isotherms over a tidal cycle, after several days of continuous heat, is evidence that RMA-10 is properly reproducing the dilution of the Salem thermal plume due principally to ambient currents. The spatial distributions of lower temperature isotherms may not be a reliable measurement of dilution since uneven natural heating/cooling and tidal marshes may have a strong affect on the locations of these isotherms. Comparisons of the surface distributions in Figure III-89a through III-92b with the corresponding surface distributions in Figures III-93a through III-96b show that RMA-10 not only reproduces the shape and dimensions of the isotherms over a range of temperatures but also reproduces (on balance) the magnitudes of the temperatures.

The orientation of the highest temperature isotherms for the One-Unit Survey and the simulations are similar, which suggests that RMA-10 is transporting the thermal plume correctly. When the heated water moves upstream, it moves along Artificial Island, sometimes attached and sometimes detached (see Figures III-91b through III-95b). When the heated water moves downstream, it heads off shore, just outside Hope Creek Jetty (see Figures III-89a through III-93a).

For example, Figures III-92 (a and b) and III-96 (a and b) show a 14°C isotherm extending along Artificial Island at the end-of-flood. The observed and simulated length and width of this isotherm compare well. In addition, the spatial distributions of higher temperature isotherms within the computed and simulated 14°C isotherms are fairly consistent. The field data show some small pools of warm water to the south of the Salem discharge, but these may be artifacts of sampling over two-hours (Section III.C.5.f.ii), and the approximation of the near-field as a volume source of Salem's

thermal discharge (Section III.C.5.d). Both the field data and simulations indicate the presence of residual heat that has been transported north by the ambient currents. For the end-of-ebb, Figures III-90 (a and b) and Figures III-94 (a and b) show similar sized pools of heated water in the vicinity of the thermal discharge. In both figures, isotherms of 13°C water remain along the shore of Artificial Island. The somewhat disordered patterns of the lower temperature isotherms that are based on the field data are likely due to rapid change in tidal currents about the time of the measurements. The simulated water temperatures show slightly cooler water along the northern half of Artificial Island.

The data from the shipboard survey and the simulation exhibit consistent temporal patterns in the manner in which Salem's heat is dispersed in the Estuary. Generally, heated water accumulates in the vicinity of the discharge for brief periods of time near end-of-ebb and end-of-flood. The heated water then is dispersed over a much larger region during flood (Figure III-91 and Figure III-95) and during ebb (Figure III-89 and Figure III-93). The shapes, orientation, and distributions of the higher temperature isotherms, for the flood and ebb tide based on the One-Unit Survey compare well. This favorable comparison indicates that RMA-10 properly simulates the transport of the thermal discharge in the Estuary.

The time-series of observed and modeled temperatures at moorings within the influence of Salem's heat also are similar. The mooring locations were presented in Figure III-57. Temperatures at moorings downstream of the thermal plume, such as at Moorings H and N (Figures III-97a and III-97b), show excellent agreement. Some short-duration, small-scale observed temperature fluctuations are not reproduced by the model (nor would one expect them to be), and are not critical for the application. The temperatures at the upstream mooring seem to be obscured by the simulation of temperatures in the model-schematized marsh which includes Alloway Creek (Figure III-97c). Although the time-series are similar with respect to the ranges of water temperatures over successive tidal cycles, the simulated water temperatures are low. Given the good agreement at moorings in the main water body, these differences may be due to the approximation used for the tidal marshes. Comparisons of the vertical profiles of measured and computed water temperatures provide additional evidence that RMA-10 correctly simulates the spatial distribution of water temperature over the region of the Estuary that is potentially affected by the thermal plume. Examples of these comparisons are provided in Figure III-48 through III-101.

The field observations and the simulations show that there was almost no vertical temperature stratification during the One-Unit Survey in the 6-mile segment of the Estuary that is centered on Salem. Inspection of all the simulated and measured vertical profiles for the One-Unit shipboard surveys showed almost no difference between simulated and measured water temperatures at the vast majority of the shipboard survey locations. At the remaining locations, differences were typically much less than 0.5°C (0.9°F).

The greatest differences between model results and observed temperature profiles tended to include some vertical stratification. For reasons discussed in Section IV.B.3., RMA-10 does not reproduce local vertical stratification well, but RMA-10's inability to do so does not affect significantly the transport and mixing of the Salem thermal discharge.

In summary, the modeled and observed temperatures agree well. RMA-10's ability to simulate the variation of water temperature in the vicinity of the discharge and Artificial Island has been verified for the prevailing conditions that were different from the calibration period. Thus, RMA-10 simulates the accumulation of heat in the vicinity of the discharge, and the distribution of this heat by the tidal currents.

III.C.6.d.ii. Comparisons of ΔT for the Verification Period

This section provides further verification that RMA-10 can be used to provide a reasonable representation of the spatial distribution of ΔT at various phases of a tidal cycle. The excess temperature is the difference between the water temperature that includes heat from Salem and the ambient water temperature. Since ΔT can not be measured directly, it must be computed. The application of RMA-10 to compute ΔT requires two simulations. One simulation includes the Salem discharge. The other simulation does not, and thus provides an estimate of the ambient temperature, T_{ambient} . To obtain ΔT at any point and time, the results for the ambient simulation are subtracted from the results for the simulation that includes the Salem discharge.

The calculation of ΔT from the One-Unit field data requires an estimate of T_{ambient} . Any error in T_{ambient} will affect ΔT . These errors may be due to temporal and spatial variations in the actual ambient temperatures that are not represented by a single estimate of T_{ambient} . The effect of any error will be most apparent where Salem's thermal discharge is significantly diluted since the actual ΔT will be small. Nevertheless, a reasonable estimate of T_{ambient} can be used to calculate apparent spatial distributions of ΔT that indicate the transport and mixing of the Salem thermal discharge. Mooring data recorded on the day of the shipboard survey (28 October 1997) were used as an estimate of T_{ambient} . E-2 Figures III-103a through III-103d show the spatial distributions of ΔT based on the simulations. The corresponding results based on the 28 October 1998 shipboard surveys are provided in Figures III-103a through III-103d. Each set of figures includes the spatial distributions of ΔT for the four tidal phases during the shipboard surveys.

A direct comparison of the two sets show remarkably similar features. The location and characteristics of the thermal plume compare well. Some general observations about the tidal behavior of the plume were extracted from these figures. On the ebb tide (Figure III-102a and Figure III-103a), the plume is transported southeast, generally separated from the shoreline with some high temperatures behind Hope Creek Jetty. As the tide changes to end-of-ebb (Figure III-102b and Figure III-103b), the plume is carried north along the Artificial Island shoreline with some pooling in Sunken Ships Cove. The flood tide plume is relatively narrow, and reaches the northern tip of Artificial Island. On the end-of-flood tide (Figure III-102c and Figure III-103c), heat again begins to pool in the

vicinity of the discharge because the tidal currents are near-slack. Some heat remains along Artificial Island on the end-of-flood tide (Figure 102d and Figure 103d).

The gradients in ΔT isopleth provide additional information about the shape of the plume. Generally, gradients are sharpest near the discharge, which is expected since temperature decreases most rapidly near the discharge point. The sharpest gradients exist in the vicinity of the discharge during near-slack tides. Farther from the discharge, gradients are relatively mild along the trajectory of the thermal plume. Cross-plume gradients are relatively sharp, though, which shows the thermal plume is generally narrow compared to its length. These characteristics of the One-Unit plume are similar to the Two-Unit plume.

Visual comparisons between Figures III-102a through III-102d (modeled ΔT from the shipboard surveys) and Figures III-103a through III-103d suggest the modeled ΔT is reasonable. Although the actual values of ΔT do not compare exactly (they are not expected to), the general shape and gradients of the thermal plume are similar.

RMA-10 was calibrated and verified so that it could be used to calculate the far-field ΔT fields. The ΔT fields are required to characterize biological thermal exposure. The spatial distribution of ΔT at any time shows the influence of the Salem thermal discharge. Although the estimates of ΔT computed from the field data are not intended to be precise, they further confirm that RMA-10 simulates the transport and mixing of the Salem thermal discharge.

III.C.6.d.iii. Observed versus Simulated Water Temperature at the Salem Intake

The final component of the One-Unit verification was a check on intake temperature. The water that is withdrawn from the Estuary includes residual heat that remains in the vicinity of Salem. Heat from the discharge is recirculated due to tidal mixing, plus some additional heat is circulated back into the intake during slack water or when the ebbing currents direct the Salem plume past the intake. The recirculation of heat is important because it potentially adds to the increase in water temperature in the immediate vicinity of Salem (i.e., the ΔT across the Station's condensers is added to the intake temperature before it is discharged back to the Estuary).

Figure III-104 compares observed and modeled water temperatures at the Station's intake and discharge, starting at the end of the hydrodynamic spin-up time and ending on 1 November 1999. The observed water temperature is plotted as a daily average of the intake and discharge temperatures, which is consistent with the daily average heat loads and flows input to RMA-10. The modeled water temperature is plotted as a time series of the intake temperature. The upper panel of Figure III-104 compares the observed and modeled intake temperatures. The time-series of modeled intake temperature is consistent with the daily averages of measured intake water temperature. Although Unit I was not operating during the verification period, intake temperatures continued to be measured since some of its circulating pumps were operated to support other Station

operations. The agreement between the observed and computed intake temperatures indicated that local recirculation is being modeled correctly. The lower panel of Figure III-104 plots the daily average observed temperature at Unit 1 and Unit 2, and the time-series of calculated discharge temperatures for Unit 2. Unit 1 was not operating at this time, and the observed discharge temperatures reflect the operation of service water pumps and circulating water pumps. The observed average discharge water temperature from Unit 2 is approximately 1°C greater than the calculated discharge temperature. Since the intake temperatures are in good agreement, this difference is likely due to the actual heat rejection rate and the assumed discharge flow that was used to represent Station operations.

III.C.6.d.iv. Two-Unit Dye Verification

RMA-10 was used to simulate the dye-tracer study that was performed in the Estuary. Since dye is not present naturally in the Estuary, the detection of dye above the background fluorescence is a direct measurement of the dilution of the Salem discharge.

The surface dye concentrations discussed in Section III.C.6.b.ii were useful to construct contour plots showing the surface distribution of dye concentrations.

Plots over the twelve-mile reach centered on Salem and in the immediate vicinity of the Salem discharge for each phase of the tide were constructed using a commercial software program (SURFER). Figures III-105, III-106, III-107, and III-108 show the results over the twelve-mile reach centered on Salem. Figures III-105, III-106, III-107, and III-108 are enlargements of these plots for the immediate area surrounding the Salem discharge. The boat tracks and the points where the dye was measured at the surface are indicated by the line of "+"s.

In the simulation, dye was injected into the Salem thermal discharge commencing at the time of the actual injection and at the same mass loading rate. The dye concentrations at nodes on the water for the simulation times that were approximately mid-way between the start and end times of each boat-survey surface were considered to be representative of the actual dye concentrations. Plots showing lines of equal dye concentrations were constructed using SURFER for the four tidal phases on 29 May 1998. The results are shown in Figures III-109 through III-112. The corresponding results based on the measured dye concentrations are shown in Figures III-105 through III-108.

The spatial distributions of dye concentration show the net dilution due to the transport and mixing of the Salem discharge from the commencement of dye injection until the time of the dye measurement. Consistent agreement between the distributions of observed and modeled dye concentration at various phases of a tide is compelling evidence that RMA-10 correctly calculates the transport and mixing of Salem' heat which further verifies that the transport and mixing processes are simulated properly.

On the ebb tide, the general extent and shapes of the observed and simulated dye distributions are comparable for a distances approximately 3,000 ft from the discharge.

The maximum observed and simulated dye concentrations are at the discharge, but the observed dye concentration is 1.0 to 1.5 parts per billion greater than the simulated dye concentration. RMA-10 also appears to simulate a more continuous region of higher dye concentrations, but this is largely due to the spacing and location of the boat track and the interpolation of the field data. As shown in Figure III-105b, the separated pools of higher observed dye concentration occur where the boat track did not cross the centerline of the dye plume. Because the near-field is approximated as a volume heat (and dye) source having dimensions greater than the actual ZIM, the maximum concentrations at the discharge are not expected to agree. Between 3,000 ft and 15,000 ft south from the discharge, no comparison can be made because there are no observations. Beyond 15,000 ft, the observed and simulated southernmost extents of the 0.5 ppb line are almost identical. This indicates that the net advective and dispersion processes that control the development and growth of the Salem thermal discharge in the Estuary are being simulated to a reasonable extent. The trajectory of the simulated thermal plume based on dye concentrations is directed slightly away from the shore, while the trajectory of the thermal plume based on dye concentration parallels the shore. The difference in the trajectories was also evident from the comparison of observed and simulated trajectories thermal plume based on water temperatures for the "plume" calibration. Finally, observed and simulated dye plume have the same general features of the thermal plume as depicted by distributions of the isotherms. The surface distributions of dye concentration show that the regions of highest dye concentration are elongated in the direction of flow, and that lateral gradients of dye across the plume diminish rapidly with increasing distance with the Station.

The end of ebb (EOE) tide shows the dye plume as it redevelops to the north of the Salem discharge along the shore of Artificial Island about the time that the tidal currents change direction. RMA-10 simulates dye concentrations that are higher than observed. The simulated distributions of dye concentrations greater than 1.5 ppb are less dispersed than what is shown by the observations. The observation distribution shows the orientation of the more diluted region of the dye plume (where the dye concentration is between 0.5 and 1.0 ppb) as being perpendicular to Artificial Island. The southern extent of dye concentrations equaling 0.5 ppb is similar, although the observations suggest that the dye may be dispersed slightly farther south. The simulation at the EOE is in good agreement with the observations, considering the issue of data synopticity discussed previously (Section III.C.5.f.ii). The distributions of computed dye concentrations are for a specific time in the tidal cycle, whereas the data were collected over a two hour period when the direction and magnitude of the tidal currents in the Estuary were changing rapidly. The effect of rapid changes in the tidal currents on the distribution of observed dye concentrations is more likely to be evident in regions where dye remains concentrated.

The modeled and observed distributions of surface dye concentration on the flood tide compare well. To the north of the Salem discharge, the distributions of surface dye concentration show an elongated dye plume that is attached to Artificial Island. Thus, tidal trapping of dye (and hence heat) behind Artificial Island is over-estimated by RMA-10. The dye plume wraps around the northern tip of Artificial Island, but the simulation

results in a slightly greater dispersion of dye into the shallow area behind Artificial Island. To the north of Artificial Island, the simulated region of the dye plume where the dye concentration is greater than 0.5 ppb extends approximately 2 miles north of Artificial Island whereas the data indicate that this region may extend a little farther north. The actual lateral spreading of dye plume, referenced to 0.5 ppb, is slightly greater than the simulated lateral spreading. The dye plume extends to the south of the Salem as well. The data indicate that the region where the dye concentration is greater than 0.5 ppb is slightly larger and extends approximately 5,000 ft further south than the region computed by RMA-10. The simulations and the data indicate that the distribution of dye within the down-current region of the dye plume is more uniform than in the up-current region. The comparisons of the surface distributions of dye concentrations are consistent with the surface distributions of water temperature for the same period. The apparent differences in these comparisons indicate that RMA-10 may disperse the thermal effluent to the same extent as what occurs naturally. To some extent, the apparent differences between the observations and simulations are attributable to the comparison of synoptic simulation with non-synoptic measurements. Since dye is a tracer for Salem's heat, RMA-10 will tend to overestimate ΔT in the warmest areas of the thermal plume to the extent they are not. These areas would include the region along and behind Artificial Island.

At the end of flood (EOF), the observed and simulated distributions of dye to the north of the Salem discharge also compare well. In the up-estuary direction, the observed and simulated location in the dye plume where the concentration equals 0.5 ppb is 25,000 ft north of the Salem discharge. At the tip of Artificial Island, the simulated distributions show a region of more concentrated dye that is not manifested by the observations. This difference is attributed to the simulation's exaggeration of tidal trapping behind Artificial Island that also was evident for the time of flood. Along the length of Artificial Island, the observed and simulated width of the dye plume and the lateral distribution of dye concentration across the plume are in very good agreement. In the immediate vicinity of the Salem discharge, the only notable difference is the location of the 0.5 ppb line of dye concentration. Based on the observed data, the dye plume extends a few thousand feet further out in the Estuary than what is predicted by RMA-10. This difference is likely due to changes in the tidal current about the time of slack water and RMA-10's inability to account for the momentum of the Salem discharge. Since this difference only lasts for a brief period, it is not considered significant. The observations and simulations that the dye plume to the south of the Salem discharge began to redevelop with regions of relatively high dye concentrations extending southward. The magnitudes and gradients in the immediate area to the south of the Salem discharge are in good agreement considering the dynamic nature of the tidal currents about the time of the observations.

In addition to the distribution of dye in the Estuary, model dye concentrations were compared to observations at the Salem intake and discharge. Figure III-113 show the comparison of dye concentrations starting on 27 May 1998 when the dye injection commenced and ending on 29 May 1998 when the dye-tracer study was completed. The observed and computed time-series of dye concentrations at the Salem intake and discharge are in excellent agreement which further corroborates that RMA-10 is properly

accounting for the recirculation of heat. The apparent differences are well within acceptable bounds considering the accuracy of the measurements and the ability of RMA-10 to simulate all the temporal and spatial variability of the dye-tracer plume.

The "plume" verification using dye measurements from the Two-Unit Survey further demonstrates the ability of RMA-10 to simulate the transport and mixing of the Salem thermal discharge since dye is a conservative tracer of Salem's heat. The model versus data comparisons indicate RMA-10 simulates the measured distributions of surface dye concentration well, in terms of the shape and extent of isopleths of dye concentration. Although there are small-scale details in the data that are not reproduced by RMA-10, the differences are not of a magnitude or duration that negatively impacts the reliability of the simulations. The favorable comparison of modeled and observed dye concentrations at the intake also demonstrated that RMA-10 simulates the recirculation of Salem's heat accurately.

Tidal and meteorological conditions during the Two-Unit Survey, which included the dye-tracer study, were applied as the boundary conditions used to characterize the Salem thermal plume for the biothermal assessment. Therefore, the verification using the dye measurements from the Two-Unit Survey provides further assurance that the RMA-10 representation of the Salem thermal plume for the biothermal assessment is accurate.

III.D. Linkage of CORMIX and RMA-10

This section describes how the results from CORMIX (Section III.B) and RMA-10 (Section III.C) were integrated to produce a continuous field of ΔT .

The near-field is a highly turbulent region that is embedded within the Salem thermal plume. The hydrodynamic characteristics of the near-field are distinctly different from those of the far-field, and are too complex to be modeled using the fundamental hydrodynamic and transport equations that are used by the far-field model. Currently, no single numerical or physical model exists that efficiently simulates and integrates all the mixing processes that occur throughout all parts of the Salem thermal plume.

The near-field, where CORMIX is used, consists of a region where the momentum of the discharge dominates the mixing process. The far-field, where RMA-10 is used, is a less turbulent region where the plume transport and mixing is dominated by the receiving water processes (e.g., tidal action). Between these two regions, a method has been implemented to integrate the CORMIX and RMA-10 outputs in a region termed the "transition region." The transition region is an area where neither CORMIX nor RMA-10 demonstrate a clear advantage in matching observed data. Most importantly this model integration, via the application of the transition region, provides for a continuous ΔT field. The transition region is required to produce a continuous field of ΔT , because it is not possible to calibrate CORMIX and RMA-10 in such a way as to produce identical results at a particular location.

Additionally, it is relevant to note that the term "transition region" (lower case) presented in this section is not related to the larger "Estuary Transition Zone" (upper case) presented in Appendix C.

III.D.1. Methodology

CORMIX employs a dilution equation that calculates ΔT up to the beginning of the transition region (the near-field), and RMA-10 calculates ΔT beyond the transition region (the far-field). The procedure used to calculate ΔT at a point, "x" (ΔT_x), in the transition region uses a linear interpolation from the point where CORMIX results are no longer used (i.e., where the mixing process is no longer dominated by discharge momentum) to a point where RMA-10 begins to produce results that are used. The actual location of the transition region, which is different for running and slack tides, is presented in Section III.D.2.

An interpolation scheme also is used to compute cross-sectional thermal plume dimensions (width and depth) in the transition region. For the times of ebb and flood, the cross-section dimensions were approximated based on the linear variation in ΔT_x between the two points. This approximation assumes the transition region is laterally well mixed and similar in shape to the CORMIX zone, Salem's heat into and from the transition region is constant, and the velocity within the transition region is approximately equal to the ambient velocity, u_{ambient} . Based on these assumptions, the width of the transition region as it joins the far-field, " $W_{\text{far-field}}$ ", is given by the following equation:

$$W_{\text{far-field}} = \frac{Q_{\text{near-field}}}{U_{\text{ambient}} \times d_{\text{far-field}}} \times \left(\frac{[\Delta T_{\text{near-field}} - \Delta T_{\text{approach}}]}{[\Delta T_{\text{far-field}} - \Delta T_{\text{approach}}]} \right)$$

where $d_{\text{far-field}}$ is the local water depth, $\Delta T_{\text{far-field}}$ is the temperature above ambient at the end of the transition region, and where $Q_{\text{near-field}}$ and $\Delta T_{\text{near-field}}$ are the flow rate and the temperature above ambient at the end of the near-field. The field data support that the width of the plume increases linearly with distance over the transition field. Thus, the width of the transition region at a distance "x" from the near-field is given by:

$$W_x = W_{\text{near-field}} + \left(\frac{x}{\text{Distance}_{\text{transition zone}}} \right) \times (W_{\text{far-field}} - W_{\text{near-field}})$$

where "x" is given in feet and $\text{Distance}_{\text{transition region}}$ is the estimated length in feet of the transition region (as detailed in Section III.D.2). The corresponding depth at this location is equal to:

$$d_{\text{far-field}} = \frac{Q_{\text{near-field}}}{U_{\text{ambient}} \times W_x} \times \left(\frac{[\Delta T_{\text{near-field}} - \Delta T_{\text{approach}}]}{[\Delta T_x - \Delta T_{\text{approach}}]} \right)$$

The subsequent cross-sectional plume dimensions were applied to estimate the plume surface area and volumes within the transition region, which were incorporated into the summary tables (Appendix E Tables V-2, and V-3, respectively). These summary tables are conservative in that they include a "double counting" of the Station's thermal load, as the heat discharged during the CORMIX simulation is also included in the RMA-10 application. Furthermore, the extrapolated transition region volumes and areas (as noted above) are also appended to the CORMIX and RMA-10 results.

For the brief slack tides, the supplemental calculation of the transition region volumes and areas was not necessary. During the slack tides, the RMA-10 model simulates the discharge of heat in a way that mimics the observed plume behavior, as heat is discharged into model elements that extend from the discharge to approximately 2,000 feet across the Estuary (Section III.C.5.d). Given that the application of CORMIX ends at 1,000 feet, and the slack tide transition region extends to 1,700 feet (Section III.D.2), implicit in the RMA-10 simulation is an approximation of the transition region dimensions during the brief slack tides.

In addition to the linear interpolation methodology required to compute plume temperature, width, and depth in the transition region, a methodology is required to compute ΔT using CORMIX. CORMIX requires information from RMA-10 in order to produce accurate estimates of ΔT . In the regions where CORMIX results are used, dilution is expressed as the ΔT that results after two streams, each with a known (or calculable) flow rate and ΔT , have mixed completely. In this case, one stream represents the thermal discharge having a flow rate equal to the cooling water discharge (Q_{Salem}), and an excess temperature that is dependent on Station operations and the far-field plume. The ΔT of the discharge equals the sum of the excess temperature of the once-through cooling water at the Station's intake (ΔT_{intake}), and the temperature increase across the Station's condensers ($\Delta T_{condensers}$). The other stream is the portion of the receiving water that is drawn into, and dilutes, the near-field. CORMIX computes the average dilution flow rate ($Q_{dilution}$) which increases with distance from the Salem Station discharge point. Output from RMA-10 is used to compute the ΔT of the dilution water ($\Delta T_{approach}$) and ΔT_{intake} . Using these variables, the fully mixed excess temperature at a point in the near-field ($\Delta T_{near-field}$) is:

$$\Delta T_{near - field} = \Delta T_{approach} + \frac{\Delta T_{intake} + \Delta T_{condensers} - \Delta T_{approach}}{S}$$

The first term on the right hand side of the equation, $\Delta T_{approach}$, or the ΔT of the dilution water, is derived from RMA-10 output for points outside and up-current of the near-field. The second term on the right hand side of the equation is calculated by CORMIX, and is equivalent to the incremental increase in ΔT above $\Delta T_{approach}$. CORMIX computes the dilution (S) and the ratio of:

$$\Delta T_{intake} + \Delta T_{condensers} - \Delta T_{approach}$$

to S, for points along the plume centerline. S is equivalent to:

$$S = \frac{Q_{approach} + Q_{Salem}}{Q_{Salem}}$$

The equation for $\Delta T_{near-field}$ is solved only for discrete times in the tidal cycle since CORMIX calculates dilution and mixing for constant hydrodynamic and discharge conditions (CORMIX is a steady-state model). Each solution is based on the values of ΔT_{intake} , $\Delta T_{condensers}$, $\Delta T_{approach}$ and S, that are calculated by, or derived using output from, CORMIX and RMA-10 for those times.

III.D.2. Application

The method described in the previous section was applied to produce a set of ΔT from CORMIX. ΔT fields were also generated from RMA-10 by subtracting a without-Station simulation from a with-Station simulation (Section III.C). The goal of the integration is to connect the CORMIX and RMA-10 ΔT fields at a desired time or tidal phase to produce one continuous ΔT field. As also described in the previous sections, there is an area termed the transition region, where ΔT fields were interpolated between CORMIX and RMA-10. The location of the transition region, which varies between running and slack tides, is described below. The development of the transition region location was based on the Two-Unit Survey temperature data and the respective near-field and far-field model predictions. The resultant transition region was then applied to the model projection run output presented in Appendix E Section V.F.

The modified CORMIX model employs a theoretical dilution equation that accounts for momentum-induced mixing (Adams 1982) where discharge momentum induces an "ambient mixing flow" from behind the front of the discharge. Within the area affected by this induced flow (e.g., the near-field), the discharge momentum dominates the mixing process. As such, the applied dilution equation does not account for less significant far-field mixing processes, such as lateral entrainment. In CORMIX, the momentum-induced dilution equation is applied to the point where the momentum of the discharge is fully dissipated (i.e., where the plume velocity is equal to the ambient current).

For the running tide simulations, the discharge momentum (i.e., velocity) decays rapidly, as the predicted trajectory end-point of the discharge momentum ranges from approximately 250 to 300 feet from the discharge (as simulated for the CORMIX Two-Unit Calibration runs, Section III.B.9). Thus, the assumption of negligible lateral entrainment is reasonable in light of the short distance of the predicted plume path.

For the slack tides, the predicted discharge momentum decreases rapidly up to the point of surfacing (approximately 45 feet from the discharge), and then decays slowly over the remaining 3,300 feet (approximate) of the full CORMIX predicted near-field plume path. The assumption of negligible lateral entrainment, therefore, is less appropriate given the

extended distance over which the "momentum only" dilution equation is applied. Therefore, the CORMIX predicted mixing is only accurate over a portion of the 3,300 feet simulated by CORMIX. The portion for which CORMIX is valid was specified based on field observations from the 29 May Two-Unit Survey. As shown in Figure III-17, the model-predicted dilution (e.g., temperature) agrees with the observed data up to approximately 1,000 feet. Afterwards, the observed data is much lower than CORMIX predictions. The reason for this departure between the simulated and observed temperatures is that the CORMIX model-predicted dilution does not account for such far-field mixing processes as lateral entrainment, which as shown in Figure III-17, begin to become significant after approximately 1,000 feet. Therefore, CORMIX results for slack tide are used to a distance 1,000 feet from the discharge.

Thus, having defined the end-points of the CORMIX model application for both the running (end of discharge momentum) and slack tides (1,000 ft from the discharge), the RMA-10 results were reviewed to determine the appropriate starting point for its application (with the transition region defined as the distance in between the above end and starting points). For both the running and slack tides, an RMA-10 "starting point" distance of approximately 1,000 and 1,700 feet, respectively, was determined to provide a reasonable integration of the above-noted models. Thus, the applied transition region distance ranged from 650 to 750 feet for the Two-Unit model calibration period. This integration of the CORMIX and RMA-10 model results for running tides during the May 1998 calibration simulation is illustrated by E 2 III-114, 115, 116 and 117. The end-of-ebb slack condition was treated as a running tide since the survey was performed just after slack, during the early flood tide. For the end-of-flood slack tide, Figure E-2 III-117 shows the linkage results for applying CORMIX up to 1,000 feet, a linear interpolation of ΔT over the 700 foot transition region, and the application of RMA-10 thereafter (i.e., 1,700 feet).

With respect to the subsequent projection runs, it is important to note that the CORMIX-predicted "end of discharge momentum" is largely a function of such input parameters as discharge flow and ambient current speed. For example, for the CORMIX projection runs (Appendix E Section V.F) which used the reasonable worst case Station conditions (i.e., low discharge, high ΔT), the predicted discharge momentum endpoint during running tides is somewhat less (approximately 150 feet) than for the calibration simulation (250 to 350 feet). Thus, for the projection run results presented in Appendix E Section V.F, the transition region is slightly longer (i.e., 850 feet = 1,000 feet [start of RMA-10 application] - 150 feet [end of CORMIX application]).

In this context, it is relevant to note that the model-predicted plume velocity at 1,000 feet from the discharge for the slack tide model projection runs and subsequent biological work products (Appendix E Section V.F) is approximately 1.85 feet per second (fps). Compared to observed data, the overall depth-averaged ambient velocity measured by the bottom ADCP from 11 May 1998 to 3 June 1998 is equal to 1.81 feet per second. Thus, truncating the slack CORMIX model prediction at 1,000 feet is equivalent to using CORMIX to describe the slack tide region where the discharge induced velocities are

greater than the typical ambient current speed. This is an exception to the method applied for the running tides, where CORMIX projection results are used to a distance of 150 feet, and where the momentum of the discharge is fully dissipated.

Overall, the approximate 650 to 850 foot transition region length is a small fraction of the overall length of the plume (Appendix E Section V.F), and the approximations for ΔT within this area have a negligible effect on the overall characterization of the Salem thermal plume. Furthermore, the approximations for the transition region temperatures are also supported by observed temperatures, as shown by Figures E-2 III-114, 115, 116 and 117.

III.E. Total Temperature Model

III.E.1. Description of the Total Temperature Model (TTM)

The purpose of the TTM is to provide estimates of water temperatures expected to occur when Salem is operating. The estimates are used to evaluate potential effects on aquatic biota. Available water temperature observations, such as those from the USGS Reedy Island (Appendix L) gauging station, are not sufficient to support a biothermal assessment (Section III).

As discussed in the opening paragraphs to Section III, the "total water temperature" is composed of three elements: the ambient temperature, the far-field ΔT associated with the long-term discharge of heat from the Station, and the near-field ΔT associated with the presence of the Salem thermal plume in the immediate vicinity of the discharge. The water temperature at any point in Salem's thermal plume varies with time. Short-term variations primarily reflect the effects of tidal action, which causes the Salem thermal plume to be transported up-estuary and down-estuary at tidal periods. Long-term variations are primarily due to daily, seasonal, and annual variations in the ambient water temperature.

The TTM can be used to estimate water temperatures in the immediate vicinity of Salem's thermal discharge for times of maximum flood and ebb, and of slack water. It can also be used to estimate far-field temperatures during any moment of a tidal cycle, and to estimate the seasonal and annual variations in water temperature.

For the near-field region or ZIM, TTM adds the output from ATM, CORMIX and RMA-10, as shown in Figure-III-1. The estimated water temperature is the sum of the daily average T_{ambient} , the near-field component of ΔT , and the "approach ΔT " ($\Delta T_{\text{approach}}$), which takes into account the continuous presence of the thermal discharge (temperature build-up). The near-field component of ΔT and the $\Delta T_{\text{approach}}$ fluctuate with the short-term variations of the tidal cycle. Although T_{ambient} does exhibit some diurnal variability, a daily average T_{ambient} is used in this calculation. As discussed in Section III.B.4., the near-field component of ΔT accounts for the incremental temperature increase that results from Salem's thermal discharge, which is calculated using CORMIX at four times in the tidal cycle. The $\Delta T_{\text{approach}}$ is calculated with RMA-10 for the same four tidal cycles, and

accounts for previously heated Estuary water that passes back over Salem's thermal discharge when the tidal current reverses and changes the orientation of the plume.

In the far-field region, TTM adds the output from ATM and RMA-10, because the near-field ΔT (modeled by CORMIX) is zero. TTM assumes a constant value for T_{ambient} throughout the Salem thermal plume. Time-varying spatial distributions of water temperatures in the far-field are obtained by superimposing the time-varying spatial distributions of ΔT , which are calculated by RMA-10, on a T_{ambient} , which is calculated by the ATM.

III.E.2. Methodology

The TTM takes into account the variations that occur during a single tidal cycle, as well as the daily, seasonal, and annual variations in solar inputs and meteorological conditions. The output from the TTM is then used to derive characteristics of the Salem thermal plume that are needed for the 316(a) Biothermal Assessment presented in Appendix E.

Before it was used to generate temperature predictions, TTM was validated using observed water temperatures. Once validated, TTM was applied using hypothetical combinations of natural conditions and Station operations selected to simulate reasonable worst case water temperatures in the Salem thermal plume. The selected combinations were based on an assessment of the sensitivities of key plume characteristics (such as magnitude and duration) to potential tidal range, surface heat exchange, freshwater inflows, discharge flow rate, and $\Delta T_{\text{condenser}}$.

Output from TTM is processed to predict regions of the Estuary in which the Balanced Indigenous Community (BIC) may be affected by the duration and magnitude of water temperatures. Predictions are obtained for various times during a tidal cycle (the intra-tidal predictions) and throughout the year. The intra-tidal predictions address the effect of the periodic up- and down-estuary plume movement on the extent and position of these regions. The inter-annual predictions estimate the effects of seasonal and annual variability, which are taken into account in the derivation of T_{ambient} . The T_{ambient} used in this Demonstration has recurrence intervals of 2 and 10 years (the recurrence interval is the average number of years between years in which T_{ambient} is equaled or exceeded).

III.E.3. Set-Up

TTM uses the direct output of CORMIX, RMA-10, and ATM. Since each of the three component models of TTM was independently calibrated and verified, no additional calibration or verification of TTM is required.

However, TTM output was validated by comparing its estimates of water temperature for several points in the Salem plume with measured water temperatures at the same points. The methodology and results of this validation are provided in Section III.E.4. below.

TTM was validated using: (1) coincident time-series of measured water temperatures, estimated T_{ambient} , and actual Station operations, and (2) specific estimates of the near-

field current speeds for times of maximum flood and ebb, and end-of-flood and end-of-ebb slack.

The time series of measured water temperatures were recorded at four near-field moorings (Moorings 21, 22, 23 and 24) and two far-field moorings (Moorings M9 and 9M) from 17 May 1998 through 05 November 1998, as part of the Modified TMP (Exhibit E-1-3 Figure 1). The time series of T_{ambient} was calculated by ATM based on the solar and meteorological conditions that existed during the same six-month period. Coincident time-series of discharge flow rates and temperature increases across Salem's once-through cooling water system ($\Delta T_{\text{condenser}}$) were used to identify those inputs to CORMIX that would result in estimates of the near-field component of ΔT consistent with actual measurements of near-field plume temperatures.

The calculation of short-term variations occurring in the immediate vicinity of the discharge required estimates of values for $\Delta T_{\text{approach}}$ and for current speeds in times of maximum flood and ebb, and of high and low water slack. The $\Delta T_{\text{approach}}$ represents the contribution of previously heated water entrained in the mixing zone to the total water temperatures in the near-field. The current speeds are used by CORMIX to calculate the dilution of the thermal discharge in the ambient current.

Because CORMIX does not provide continuous calculations of time-varying near-field mixing processes, representative values for $\Delta T_{\text{approach}}$ and current speed were established for the four predefined times in the tidal cycle and used in lieu of a complete time-series. Current speeds for the approximate times of maximum flood and ebb, and high and low water slack were obtained from the Acoustic Doppler Current Profiler (ADCP) deployed near Mooring V (Exhibit E-1-3 Figure 1) on 29 May 1998. The $\Delta T_{\text{approach}}$ were derived using coincident, far-field calculations of ΔT based on output from RMA-10. The selection of these representative values for current speed and $\Delta T_{\text{approach}}$, and their effects on the accuracy of the calculations is discussed in Section III.E.4.

Because it has been observed that tidally-averaged ΔT varies primarily in space and only secondarily in time, the sole consideration in studying the far-field is the long-term average ΔT resulting from the plume. Its value is derived by using RMA-10 to generate a time-series of ΔT in the vicinity of the far-field moorings, then computing the daily average ΔT from these time-series.

Once verified, TTM is used to estimate water temperatures in the Salem plume during the natural conditions and Station operations that would result in the hypothetical "reasonable worst-case" Salem's thermal plume. Natural conditions influencing a worst-case plume include the tide range, freshwater inflows, and surface heat exchange, which would produce an intense and prolonged elevated water temperature in the Estuary.

III.E.4. Validation

The TTM was validated based on the observation that the 6-month time series of measured water temperatures at the four near-field moorings fall within the range of

estimated daily maximum and minimum water temperatures for each day of the 6-month period.

The four near-field moorings were distributed around the immediate area where Salem's thermal discharge initially mixes with the Estuary water and rises to the surface. Moorings 21 and 22 were located in the typical trajectory of the plume during times of slack water in a southwesterly direction from Salem's thermal discharge. Mooring 23 was located up-estuary from Salem's thermal discharge in the path of the plume during times of flood. Mooring 24 was located down-estuary from Salem's thermal discharge in the path of the plume during times of ebb. Each mooring was equipped to measure water temperatures at three strata: near the water surface, at mid-depth, and near the bottom.

The relative positioning of the four moorings typically resulted in at least one mooring in the path of the plume at any given time. The TTM was considered validated if coincident time series of estimated daily maximum and minimum water temperatures spanned the range of measured water temperatures at the four moorings. The maximum estimated water temperature corresponded to periods when the tidal current caused the plume to flow toward the mooring, when its temperature equaled the sum of T_{ambient} , the near-field component of ΔT , and $\Delta T_{\text{approach}}$. The minimum estimated water temperature corresponded to periods when the plume was directed away from the mooring, and equaled the sum of T_{ambient} and $\Delta T_{\text{approach}}$.

The near-field component of ΔT was calculated by CORMIX based on: (1) pump flow rate and temperature increase across the once-through cooling water system during the times of the water temperature measurements, and (2) representative estimates of the corresponding current speed for these times. The representative current speeds were approximately 1.7 fps for maximum flood, 1.4 fps for maximum ebb, 0.4 fps for end-of-flood slack, and 1.7 fps for end-of-ebb slack. (Section III. B.9 and Table III-2).

Representative estimates of $\Delta T_{\text{approach}}$ were derived from RMA-10 outputs for two simulations using the hydrodynamic, meteorological and solar conditions that existed on 29 May 1998. The simulation parameters were identical except that one simulation included Salem's thermal discharge, and the other did not. Estimates of $\Delta T_{\text{approach}}$ for locations immediately up- and down-estuary of the four near-field moorings were obtained by subtracting the results of the simulation run without the Salem thermal discharge from the results of the simulation run with the Salem thermal discharge. The resulting differences at times of maximum flood and ebb, and at times of end-of-ebb and end-of-flood slack water were used as estimates of $\Delta T_{\text{approach}}$. At times of maximum flood and ebb, Moorings 21 and 22 are not within the near-field mixing zone and the estimated $\Delta T_{\text{approach}}$ is 2.0°F (1.1°C). At times of slack water, the plume intercepts Moorings 21 and 22, and the estimated $\Delta T_{\text{approach}}$ is 1.7°F (0.9°C). The estimated $\Delta T_{\text{approach}}$ for Mooring 23 is 0.9°F (0.5°C) when the mooring is not in the direct path of the plume, and 2.1°F (1.2°C) when it is. The corresponding $\Delta T_{\text{approach}}$ for Mooring 24 are 2.1°F (1.2°C) and 0.9°F (0.5°C), respectively.

The values selected to approximate the $\Delta T_{\text{approach}}$ are relatively small, 0.9°F (0.5°C) to 2.1°F (1.2°C), in comparison to the near-field component of ΔT , which can be as high as 9.0°F (5°C). The selected values of $\Delta T_{\text{approach}}$ for 29 May 1998 were found to be relatively insensitive to tidal range, which is the key parameter affecting the spatial distribution of ΔT in the immediate vicinity of the Salem discharge. Other factors affecting the $\Delta T_{\text{approach}}$ include the amount of waste heat expelled by Salem over time and heat dissipation of the thermal plume through losses to the atmosphere. The $\Delta T_{\text{approach}}$ in TTM were calculated for conditions of maximum heat rejection rates and relatively low atmospheric heat dissipation. Thus, the $\Delta T_{\text{approach}}$ would be lower when Salem was discharging below its maximum heat rejection rate, and when atmospheric heat dissipation was greater. This over-estimation is expected to have little impact on the validation because the $\Delta T_{\text{approach}}$ is so small in comparison to the near-field component of ΔT , roughly equivalent to the level of uncertainty in values for T_{ambient} .

The time series of measured water temperatures and of estimated maximum and minimum water temperatures were compared to determine if there was any tendency for TTM to over- or under-predict water temperatures. The comparisons were made graphically for the entire six-month duration (17 May 1998 through 05 November 1998) of the data at each of the three depths where water temperature was measured at each of the four moorings. Figures III-118 through III-121 are examples of the 156 individual graph pages, showing cases ranging from good to poor during the period 04 October 1998 through 17 October 1998. Each graph page includes two graphs.

The upper graph displays the measured water temperatures (plotted as a continuous curve), and the daily estimated maximum and minimum water temperatures (plotted as "stepped" curves). The time series of measured water temperature for each of a mooring's three strata (the surface, mid-depth, and bottom) are labeled as "Observed". The lower stepped curve is the estimated minimum water temperature that would occur when the plume does not intercept a mooring, which is identified "Estimated Minimum" and is the sum of T_{ambient} and $\Delta T_{\text{approach}}$. The upper stepped curve, identified as "Estimated Maximum", is the sum of T_{ambient} , the near-field component of ΔT , and the impinged $\Delta T_{\text{approach}}$. The values are shown in degrees Fahrenheit (°F) on the left axis.

The lower graph displays two curves. One curve is the daily average total reactor thermal power (Total RTP) as a percentage of rated power. The corresponding values are shown on the left vertical axis. The other curve is the daily average ΔT for the once-through cooling water, in °F ($\Delta T_{\text{condenser}}$). These values are on the right axis and are computed as the difference between the daily average observed intake temperature and the daily average observed discharge temperature.

Figure III-118 shows an example of a comparison for the mid-depth stratum at Mooring 24, which is down-estuary from the discharge. The time series of measured water temperature is closely bounded by the estimated maximum and minimum water temperatures from the TTM. The "square wave" variation of observed water temperature

is a result of the reversing tidal currents that alternately cause the plume to pass over the mooring (Section III.B.10.f).

Figure III-119 is an example of a comparison for the near-surface stratum at Mooring 23, which is up-estuary from the discharge. As discussed in Section III.B.10.f., mooring 23 is not directly down current from the discharge, so the plume sweeps across the instruments producing a temperature pattern that is less regular than the one seen at mooring 24. Nonetheless, the measured water temperatures are nearly as well bounded by the estimated maximum and minimum water temperatures from the TTM.

Figure III-120 shows an example of a comparison for the near-surface stratum at Mooring 22, which is directly in front of the discharge. Mooring 22 is impinged by the plume during slack water conditions, as the tidal currents reverse. These conditions occur for periods of 0.5 hour to 1 hour during each tidal reversal, and result in the "spiked" pattern of measured water temperature seen in Figure III-120. Once again, the measured water temperature is well bounded by the estimated maximum and minimum water temperatures from the TTM.

Figure III-121 is an atypical example of a comparison for the near-bottom stratum at Mooring 21, which is the closer of the two moorings directly in front of the discharge. The maximum observed water temperature often exceeds the maximum estimated water temperature by as much as 5°F (3° C), while the minimum estimated and observed water temperatures agree closely. In this case, the TTM correctly predicts the sum of T_{ambient} and the $\Delta T_{\text{approach}}$, but underestimates the near-field component of ΔT .

Inspection of the graphical comparisons at the three strata for all four moorings over the six-month period shows the overall performance of the TTM is good in the highly dynamic near-field. The TTM correctly tracks the daily range of observed water temperatures as they vary from a high of approximately 90°F (32° C) in August 1998 to a low of 55°F (13° C) in November 1998. With few exceptions, the TTM correctly estimates the near-field component of ΔT during changing Station operations and can, thus, be used to estimate water temperatures in the plume for a range of conditions and operations. The effect of annual variations in T_{ambient} on water temperatures in the plume are addressed by varying T_{ambient} as a function of return period.

The Root Mean Squared (RMS) differences between the six-month time series of observed daily average water temperatures at far-field Moorings M9 and 9M, and the results of the TTM were compared with the RMS differences computed in the ATM calibration and verification. Because the principal source of variability in the far-field TTM is T_{ambient} and the far-field daily average $\Delta T_{\text{approach}}$ is seasonally constant, comparison of the RMS differences provides a valid measure of the performance of the TTM in the far-field.

The RMA-10 model runs with and without Salem's thermal discharge were used to compute the estimated $\Delta T_{\text{approach}}$ at each far-field mooring on 29 May 1998. The RMA-10

values were averaged over 24 hours to create a daily averaged $\Delta T_{\text{approach}}$. These values (0.34°F (0.19° C) at Mooring M9 and 0.12°F (0.07° C) at Mooring 9M) were added to the ATM forecasts for each day of the six-month period to produce the TTM estimates of daily average water temperature at the two moorings.

The observed water temperatures for the three strata (depths in the water column) at each far-field mooring were first averaged together, then averaged over each day to create a time-series of daily water column-averaged temperatures. Next, the mean difference between the daily water column-averaged observed temperatures and the TTM temperatures for the six-month period was computed. Part of this mean difference can be attributed to spatial variations in the ambient temperature. The mean difference at Mooring 9M is 1.46°F (0.81° C) and at Mooring M9 it is 0.22°F (0.12° C).

Finally, the RMS differences between the adjusted TTM time-series and the time-series of daily water column-averaged observed temperatures was computed for the six-month period. The RMS difference at Mooring 9M is 1.46°F (0.81° C), and at Mooring M9 it is 1.53°F (0.85° C). These values are close to the RMS differences achieved in the ATM calibration and verification, indicating that the TTM predictions for the far-field are reliable.

The demonstrated ability of TTM to reliably estimate the actual daily minima and maxima of water temperature over a six-month period (during which Station operations varied, as did solar inputs and meteorological conditions) also confirms that the two-week intensive field survey, as provided by the Modified Thermal Monitoring Program, yielded an adequate data set for characterizing both near-field and far-field mixing processes. When the Total RTP and $\Delta T_{\text{condensers}}$ remain constant, the data show that the difference between successive maximum and minimum observed water temperatures for any single tidal period remains relatively constant, persisting even under varying tidal conditions (such as spring and neap tides). The maximum observed water temperature occurs when the plume directly intercepts a mooring, and the minimum observed water temperature occurs when the tidal currents direct the plume away from the mooring. The constant difference between successive observed maximum and minimum water temperatures is further evidence that the near-field mixing processes, and hence the near-field component of ΔT , are primarily dependent on Salem's discharge rate and $\Delta T_{\text{condensers}}$, and are nearly independent of the tidal currents and tidal elevations occurring near the Station. Thus, the ability of a calibrated and verified version of CORMIX to characterize the near-field mixing processes was established using a short-term, well-defined field study.

IV. CONCLUSIONS AND COMPARISONS TO FAR-FIELD MODEL

IV.A. Consistency with Historical Data and Observations

In Attachment E-1 Section III, recent measurements of the physical environment in the vicinity of the Station were described in the context of historical observations of the area. New data from the Ambient Survey, the One-Unit Survey, and the Two-Unit Survey (conducted in accordance with the Modified Thermal Monitoring Program, Exhibit E-1-3) have been shown to be consistent with previous data and with the historical

understanding of circulation processes in the Estuary. The new data, furthermore, provide considerably more detail in regions around the Station at certain times. Since the old and new data are basically consistent, the evaluation of physical processes in this Attachment focuses on comparison of the numerical predictive model RMA-10 (Section III.C) with the combined old and new data, taking advantage of the increased detail provided by the new data.

IV.B. Consistency of Data and Simulations

In Attachment E-1 Section III, the main physical processes governing the motion of the water and the thermal plume were described in terms of features in the observations. Here the model's representation of some of these physical processes is investigated.

The Model

The goal of the numerical modeling effort (ATM, CORMIX, Linkage, and RMA-10) supporting the 316(a) Demonstration is to simulate the shape, advection, mixing, and dissipation of the thermal plume's ΔT from the Station against the background of the naturally occurring current, sea level, and water properties of the Estuary near the Station. Modeling is necessary because observational data alone cannot be used to infer ΔT associated with the Station's thermal plume; the natural background temperature variability is too large. Therefore, RMA-10 is intended primarily to represent the field of ΔT and to characterize the far-field plume. RMA-10 can be run for an identical set of conditions with and without Station operations. By subtracting model output representing with-Station and without-Station conditions, the ΔT due to the Station can be estimated. Although RMA-10 can be used to estimate ambient temperatures in the short term, another model, the Ambient Temperature Model (ATM) has been developed specifically for long-term ambient temperature prediction, so RMA-10 is primarily intended to characterize the plume ΔT . For the purpose of characterizing the plume ΔT , the RMA-10 model must accurately represent those physical processes that govern the mixing, dissipation, and advection of the Station's thermal plume.

The modeling approach taken for this Demonstration has been improved over previous studies (TRA et al. 1993) through the use of:

- Better observations and modeling of actual plume shape and evolution.
- More and vastly improved data for calibration, verification, and validation.
- Improved computational capabilities of modern computers, permitting the use of better spatial resolution and more realistic (and complex) formulations.

Numerical circulation models, such as RMA-10, are mathematical representations of the fundamental time- and space-dependent equations of motion on a discrete spatial grid. The computer solves for the velocity and water property fields by approximating the equations of motion in discrete time steps at each grid point. The acceleration (rate of change in momentum) of any fluid element is assumed to result from the input of momentum from surrounding fluid elements, or from external influences (forcing conditions) such as the interaction of fluid parcels with the sea bottom, the wind at the sea

surface, and inflow at the boundaries. On the smallest scales, molecular effects (such as the friction between molecules) ultimately control fluid motions and dissipate energy. Since it is not feasible to model the motion of individual molecules, and forcing information is not available at the boundaries on such small scales, model formulations inevitably contain parameterizations and simplifications of the basic physics.

For example, the dissipation of kinetic energy (movement of water particles) into heat is ultimately due to internal molecular friction, but the process is complex and takes place through a continuous cascade of eddies on a wide range of space scales (river-wide to molecular) and time scales, (hours to seconds). In total, this quasi-random process is referred to as turbulence. The non-linear effects of turbulent momentum exchange and frictional dissipation are simplified mathematically into the concept of turbulent viscosity, which represents much higher mixing rates than molecular viscosity would imply. The model parameterizes turbulent viscosity as horizontal and vertical turbulent exchange coefficients, which represent the transfer of momentum as a function of current shear, in a highly simplified way.

The model coefficients, including these turbulent exchange coefficients (among others), are adjusted to match a specific set of observations during calibration of the model (Section III.C.5). The calibrated model also matches a different, independent set of observations reasonably well during the verification process (Section III.C.6), so it will presumably work well for other conditions. In this section, the calibrated model's underlying parameterizations and simplifications are assessed through comparison of the model with physical processes, to provide additional confidence that the model's predictions are appropriate over a wide range of forcing conditions (e.g., boundary conditions).

The model is not optimized or calibrated to achieve agreement with specific physical processes. No attempt has been made to revise or re-adjust the calibrated and verified model based on the process assessments described in this section. As will be shown, the model's agreement with observed processes is generally good, so that no significant improvement in its ability to predict the plume's time-temperature curves and spatial extent would result from any such adjustments.

Plume Definition

In this Section, reference is frequently made to "the plume." Unless otherwise stated, this means the immediate plume, that is, the excess temperature field that is directly traceable to the thermal discharge within one-half tidal cycle (i.e., within about 6.21 hrs). This immediate plume is the most distinguishable feature in the data. The immediate plume is not the same as the total plume, as it is referred to in the rest of the Demonstration, which can include the accumulated excess temperature contributions from previous tidal cycles. The total plume is relevant for regulatory purposes, but is too complicated for most of the process comparisons presented in this Section.

Sources of Observational Data and Model Results

The primary source of observational data for this assessment is moored instruments deployed as part of the Two-Unit Survey, May-June 1998 (Exhibit E-1-3). Figure IV-1 shows the mooring locations on a map of the Estuary. Vessel surveys conducted as part of the Two-Unit Survey are also used, together with data from the Station itself. Model results used for comparison are taken from the calibration run, which covered the same time period.

IV.B.1. Tidal Hydrodynamics

For the purpose of this Section, the term "tidal hydrodynamics" is taken to mean the motion of the water and corresponding changes in sea level at tidal frequencies, principally semidiurnal (12.42 hour period). Attention is further limited in this Section to the bulk flow properties of the Bay, which are measurable and represented by sea-level and current fluctuations.

IV.B.1.a. Tidal Hydrodynamics in RMA-10

Both in nature and in the model, tidal flow and tidal sea-level changes inside the Estuary are forced by changes in sea level and in flow along the boundaries of the region. The primary driving force is sea-level fluctuation at the mouth of the Estuary (the ocean tide). In RMA-10 this boundary is taken as a line between Cape Henlopen, Delaware and the tip of Cape May, New Jersey. Measured sea-level data from the National Ocean Service, NOAA, gauge at Lewes, Delaware, and from a PSE&G tide gauge at Cape May are used for model input. The sea level boundary condition for the model consists of a linear interpolation of measured sea surface height from these two measurement locations along the line connecting these points. The actual tidal amplitude (tide range) is slightly greater at Cape May than at Lewes, and high- and low-water timing is earlier at Cape May by about an hour (phase lag). By using the actual values at these two locations, a physically realistic forcing that has appropriate temporal and spatial variability is applied to the model.

A secondary driving force is sea-level change at the western end of the C&D Canal. The Canal joins the head of Chesapeake Bay to the Estuary about 6 miles north of the Station. As described in Section III.H., flow through the C&D Canal is governed by the sea-level difference (hydraulic gradient) between the east and west ends of the Canal. Tidal-frequency flow through the Canal can be significant because the tide range is lower in upper Chesapeake Bay than in the Estuary near the east end of the Canal, and the phase is also different (International Marine 1998). The tide range at Reedy Point, at the east end of the Canal, is typically 5.6 ft (1.7 m), whereas at the west end it is about 2.3 ft (0.7 m) (Wong, 1991). The phase in upper Chesapeake lags that in the Estuary by about 11 hours. The basic effect of the C&D Canal at tidal frequencies is that water flows toward the Estuary on the ebb flow phase, when the tide elevation in Delaware Bay is falling, and vice versa. This has the effect of reducing the tidal sea level variability that otherwise would occur in the Estuary near the Canal, while increasing the current speeds. It is also possible for the Canal to maintain unidirectional flow throughout the tidal cycle under some conditions. For example, high freshwater inflow from the Susquehanna River into

Chesapeake Bay can force a steady flow through the Canal into the Estuary. Such slowly varying flows of meteorological origin are superimposed on the higher-frequency oscillatory tidal flow.

To drive the model at the C&D Canal boundary, a time-series of sea level is required for Courthouse Point, Delaware, or some other point representing the west end of the Canal. For time periods when actual tide height data are not available at Courthouse Point, a time-series is constructed using a transfer function technique based on one or more NOAA tide gauging stations in upper Chesapeake Bay, depending on data availability.

The third major boundary condition for the model is applied at the head-of-navigation on the Estuary, at Trenton. There is no tidal sea level variability at this location, but freshwater inflow is specified as the boundary condition. The freshwater flow contributes to the variation of salinity in the Estuary (which is minimal since the Estuary is usually well mixed) and can also affect currents. Above a point representing Marcus Hook, New Jersey, (about 30 miles upstream of the Station) the model utilizes a one-dimensional (1-D) schematization of the Estuary, so there is neither vertical nor horizontal structure in the modeled Estuary from Marcus Hook to Trenton. River inflows are specified at several locations along this stretch, including the Delaware River at Trenton and the Schuylkill River at Philadelphia.

IV.B.1.b. Model versus Observed Tidal Variability

Given these forcing functions at the open boundaries, the RMA-10 model responds by simulating the tidal wave that propagates up the Estuary against the mean current due to freshwater flow, less the influence from the C&D Canal. The finite propagation speed of the wave causes an increase in tidal phase delay up the Estuary relative to the mouth. Narrowing of the Estuary from south to north is the principal cause of increasing tidal amplitude. Tidal flow in and out of the extensive marsh areas that lie along the edges of the Estuary tends to retard the propagation of the tide. Bottom friction affects the amplitude and speed of propagation of the wave as well. Internal mixing (diffusivity) is not dominant in terms of the bulk hydrodynamics. The depth of the Estuary is well represented in RMA-10, and assures that the model simulates the tidal prism (the net volume change from low water to high water). The model is optimized to agree with observed total tidal amplitude (all constituents taken together) in the region of the Station. Tidal phasing is not specifically optimized.

Tidal Constituent Amplitude and Phase Agreement

The model's agreement with observed amplitude (one-half the range) and phase for the principal tidal harmonic constituents is generally good (Figures IV-2a and 2b) over the entire longitudinal profile of the Estuary. Constituents shown in this figure are M_2 (12.42-hr periodicity), M_4 (6.21-hour periodicity), M_6 (4.14-hr periodicity), and K_1 (23.93-hr periodicity). Also shown on the amplitude plot (Figure IV-2a) is the ratio M_4/M_2 which is a measure of tidal non-linearity due to bottom friction; the corresponding phase plot on Figure IV-2b shows the difference between twice the M_2 phase and the M_4 phase. The tidal constituents were calculated from hourly data and model results over

identical 14.5-day intervals. The constituents are plotted as a function of River Mile (RM), with RM 50 representing the Station. Observed tidal constituents are plotted for Lewes, Cape May, Salem Barge Slip (at the Station), Reedy Point, Philadelphia, and Burlington (near Trenton, New Jersey). The Reedy Point NOS tide station, located at RM 58, is near the outlet of the C&D Canal. Tidal constituents such as N_2 , S_2 , O_1 , and S_1 , which are of smaller amplitude (less than 0.5 ft), compared to M_2 and K_1 are not shown on the plot.

The dominant semidiurnal constituent is M_2 , with an observed amplitude of almost 3 ft (slightly less than 1 m) at the Station. The observed M_2 amplitude increases slightly from Lewes to the Station, then decreases about 5 percent at Reedy Point. Wong (1991) asserts that this decline results from the influence of the C&D Canal. Beyond Reedy Point, the M_2 amplitude increases monotonically all the way up the River to Burlington. The M_4 and M_6 tidal overtones, which result from non-linear distortion of the M_2 wave as it propagates up the Estuary, each have an amplitude of a fraction of a foot. The largest observed diurnal constituent is the K_1 (23.93 hours), with an amplitude of about 0.4 ft. It also has a dip in amplitude around Reedy Island. The phase of the M_2 constituent (Figure IV-2b) increases linearly from the mouth of the Estuary to the upper end of the Estuary. The phase of the other plotted constituents show much more variability.

The model and the observations agree perfectly for the M_2 and K_1 constituents at RM 0 (Lewes) because that is where the boundary condition is applied. The non-linear constituents, M_4 and M_6 , are essentially zero at the mouth of the Estuary, because the tide in the open ocean does not contain these higher-order constituents.

In general, the model's M_2 constituent agrees well with the observations. Unlike the observed tide, the modeled M_2 amplitude is virtually constant from Cape May to the Station (RM 50) and then increases monotonically the rest of the way to the head of the River. At the Station, the model's M_2 amplitude is a few percent less than in the observations (3.0 ft vs. 2.9 ft). At Reedy Point (RM 58), the modeled and observed M_2 agree. Because the model underestimates the M_2 constituent at the Station, but is correct at Reedy Point, it does not reproduce the observed decline in M_2 amplitude from the Station to Reedy Point. At Philadelphia and Trenton, the model's M_2 constituent is about 10 percent higher than the observations, but this is in the 1-D model region, far from the Station, and does not affect RMA-10's prediction of plume lengths near the Station. M_2 tidal phase predicted by the model is in excellent agreement with the observations, but is slightly higher at the Station, indicating that the model's tidal timing (occurrences of slack water) slightly lags the observations. This is of no consequence in terms of modeled plume length.

The modeled K_1 constituent agrees with the observed K_1 amplitude and phase within about 10 percent from the mouth of the Estuary to Burlington. The observed K_1 amplitude exhibits a small decline (0.04 ft) at Reedy Point, similar to but smaller than the decline in the observed M_2 constituent. The model does not reproduce this decline. The modeled K_1 is lower than the observed constituent at the Station by 0.04 ft in amplitude.

In summary, RMA-10 slightly underpredicts the amplitude of both the dominant M_2 (3-ft amplitude) and K_1 (0.04-ft amplitude) tidal constituents at the Station by about 0.15 ft in total, although it agrees well with the observed phase. This small difference, about 5 percent of the combined amplitude of these constituents, may be a consequence of the model's bottom friction formulation, which may differ somewhat from nature. Alternatively, the difference may be a result of calibrating the model in terms of total tidal amplitude. The calibration process was not expected to produce perfect agreement at any point in the model domain; at the Station, the model was adjusted to agree with instantaneous tide height to within about 5 percent (Section III.C.5.f), as this produced the best overall agreement throughout the nearby model domain.

Nonlinear Effects

The ocean tide is a superposition of pure sinusoids having periodicities corresponding exactly to the astronomical gravitational forces. As the tide propagates from the open ocean up a shallow, narrowing estuary it becomes distorted due to hydrodynamic nonlinearities in the flow. The distortion can be represented by one or more shallow water harmonic overtones having frequencies that are multiples of the primary tidal constituents, and by compound frequencies that are sums and differences of the primary constituent frequencies (Friedrichs and Aubrey 1988). For example, bottom friction is dependent on the square of current speed, and this non-linearity applied to the dominant M_2 currents results in energy transfer to the first harmonic overtone (M_4) at a frequency of twice the M_2 , or a 6.21-hr periodicity. The amplitude and phase of the M_4 constituent relative to the M_2 helps determine the asymmetry of the tide. The measure of relevant phase difference is twice the M_2 phase minus the M_4 phase. If this sea-level phase difference is within 0 to 180 degrees with respect to the M_2 , then the flood tide current will have higher speed but shorter duration than the ebb. The system is then said to be flood-dominant (Friedrichs and Aubrey 1988). As shown in the discussion of currents below, the Estuary is a flood-dominant system.

Therefore, the ratio M_4/M_2 and its corresponding phase difference along the Estuary (Figure IV-2a and b) are sensitive measures of the model's performance from the perspective of bulk tidal hydrodynamics. For the principal non-linear overtone, M_4 , the observations and the model are in general agreement and show a pattern of steady increase from the mouth of the Bay up the River. The observations show a decline at Reedy Point, similar to the decline observed for the M_2 , which is not reproduced in the model. The observed amplitude of this constituent is about 0.2 ft at the Station and increases to about 0.5 ft at the head of the River. The model's M_4 amplitude at the Station is lower than observed by about 0.05 ft, and is higher than observed at Reedy Island by the same amount. The ratio of M_4 to M_2 amplitude matches closely between the model and the observations up to Reedy Island, which is an indication that the model has approximately the right amount of bottom friction in the lower Estuary. The modeled M_4/M_2 phase closely matches the observations at locations near the Station.

The M_6 constituent is also due to nonlinearities in the tidal flow, and it is usually taken to be a measure of the effect of freshwater flow opposing the upstream propagation of the tide (Friedrichs and Aubrey 1988). The observed M_6 rises from nearly zero at the mouth of the Estuary to 0.15 ft at the Station and 0.2 ft at Philadelphia, then declines farther upriver. The modeled M_6 amplitude is small (0.1 ft) at all locations. The modeled M_6 amplitude agrees well with the observations at the Station, although it diverges farther upstream. The modeled M_6 phase is in good agreement with the observations.

In summary, RMA-10 reproduces the observed non-linear constituents with some minor amplitude and phase differences, which are presumably due to the model's representation of bottom and internal friction.

Current Timing and Spatial Structure

Currents were observed during the Two-Unit Survey using an Acoustic Doppler Current Profiler (ADCP) deployed near mooring V, which was located about 1,000 ft (305 m) directly offshore from the discharge in water 25 ft (7.5 m) deep with respect to Mean Tide Level. Figures IV-3a and 3b show current speed and direction measured at three depths (5, 9, and 14 feet) together with the corresponding model output. Several features stand out from the observations:

- Tidal currents are essentially bidirectional. At all depths, the observed current direction alternates between 325 degrees (north-northwestward) on the flood and 145 degrees (south-southeastward) on the ebb. These directions are exactly 180 degrees apart. There is little variation in current direction during the ebb and flood. The constancy of direction during each phase indicates that the tidal flow is essentially reversing and bidirectional, not rotary.
- The 325-145 degree axis is not exactly parallel to the shorefront at the plant. The axis is rotated about 10 degrees counterclockwise, so that on the flood, the current is tending to move the plume slightly offshore. On the ebb, the plume moves into open water southeast of the Station.
- Current speed does not vary sinusoidally with time. Instead, both the ebb and flood phases are characterized by a rapid increase in current speed after slack water, followed by a more gradual decline during most of the phase, with a short period of rapid decrease in speed at the end of the phase.
- The duration of ebb phase current exceeds that of the flood phase by 2 to 3 hours (that is, the ebb current typically lasts 7.7 ± 0.5 hours and the flood lasts 4.7 ± 0.5 hours). Observed speeds during the ebb phase are generally lower than flood speeds, by about 20 percent, consistent with the longer duration of ebb flow.
- Current speed shows some vertical shear, with typical flood phase amplitudes increasing by about 20 percent from 14 ft (near-bottom) to 5 ft (near-surface) levels. Ebb phase speeds show similar vertical shear.
- The duration of the transition in direction varies from as little as 0.5 hours during the end-of-ebb (EOE) slack period, to 1.0 hours during end-of-flood (EOF) slack water. There is distinct asymmetry, with the EOE transition usually being shorter.

- Slack water, defined as the interval between stable directions, typically corresponds to current speeds less than 1 ft/sec (30 cm/sec), but the current approaches zero only for very brief periods.
- Slack water does not coincide with high or low tide, typically lagging by about 2 hours. The tide in Delaware Bay is neither a pure traveling wave (for which the sea level and currents would be in phase at each point), nor a pure standing wave (for which sea level and currents would be in quadrature, or 90° out of phase). Instead, the tide has some of the characteristics of both, as expected for a narrowing estuary. The fact that high and low tide events precede the corresponding slack water events suggests that the along-channel slope of sea surface (the pressure gradient) reverses sign before the current changes direction.
- Clearly visible during slack water periods is the Station's thermal discharge plume, in the form of a high-speed current pulse. This current jet ranges in speed from typically 2.0 to 2.5 ft/sec at 14 ft depth, to 2.5 to 3.0 ft/sec at 5 ft depth. For comparison, the velocity of the discharge at the outlet is about 10 ft/sec. It is reasonable to assume that the peak ADCP speed observed in each of these spikes represents the core velocity of the plume at this distance (1,000 ft from the outfall). In the absence of any other mechanism for dissipation of momentum over this distance, the approximately 4:1 reduction in core plume velocity would imply a dilution factor of 4 by the time the jet reaches the ADCP location. However, this is probably an upper bound because some of the jet's initial kinetic energy may be lost or deflected upward as the jet traverses the depression that lies in front of the Station's discharge outfall. For comparison, temperature measurements at mooring V, very close to the ADCP, show a reduction in temperature of about 5°C (9°F) relative to the discharge temperature. This is approximately 60 percent of the total ΔT , suggesting a dilution factor of about 1.7 at this distance, which is less than the factor of 4 implied by the ADCP measurements. This indicates that there is some reduction of plume velocity (but not temperature) due to bottom interaction.
- The plume signal is longest and strongest during the EOF slack, but is not symmetrical around the time of minimum ambient current. The peak discharge speed is associated with a flow direction of 220 to 230 degrees. The plume becomes visible when the flood current approaches zero speed, but the current direction is still 325 degrees. It persists as the ambient current speed increases to about 1 ft/sec (30 cm/sec) while the direction rotates counter clockwise from 325 to about 220 degrees (west southwestward). This is consistent with the fact that the ADCP is located on the south edge of the discharge jet flow (Figure IV-1 shows the general location of the ADCP, and Figure IV-14 shows its position relative to the outfall). Once the northward (flood) tidal current has stopped, the spreading jet flows over the current sensor due to its own momentum only; however, a significant southward (ebb) current is required to bend the jet, which is more than 100 feet wide, enough to avoid measurement by the ADCP.

The modeled currents show the same general patterns of current variability, with some differences:

- The model's slack water timing matches the observations within a fraction of an hour.
- The model's current magnitude agrees with or is lower than the observed flood tide current by a few percent, and is higher than observed on the ebb by 10 percent to 20 percent. This results in a reversal of the observed asymmetry in current speed. The modeling approach used to represent the marshes (see below) may account for the reversal of the asymmetry, or it may be a consequence of the model's parameterization of friction and mixing.
- The model shows the observed asymmetry of flow duration, as well as the rapid initial increase in speed.
- The RMA-10 model does not reproduce the jet itself, since the real discharge jet has momentum, whereas the plume is input to RMA-10 without momentum. CORMIX is the model used to represent the momentum-dominated near-field portion of the thermal discharge.

Conservation of Mass

To assess the model's stability and accuracy in computing tidal flows, a useful metric is the conservation of tidally averaged mass flux (volume transport) at various points along the Estuary. Limited observational data are available (Exhibit E-1-3) from vessel surveys using an ADCP for comparison with the model. Figure IV-4 shows a time history of modeled volume transport through cross-river sections near the Station, with the observed volume transport at several phases of the tide superimposed. This comparison shows excellent agreement between model and observations, with instantaneous differences of only a few percent of the peak flow.

To investigate mass conservation on larger scales within RMA-10, hourly cross-sectional river volume transports calculated by the model through exterior boundaries across the River were summed over 75 hours (which is an integral number of model timesteps), during 24-26 May 1998. This averaging interval is close to an integral number of tidal cycles (74.5 hrs). The sum is taken between slack water events at the Station. Table IV-1 shows the results expressed as tidal-cycle net flow, together with net half-cycle volume transports during the same tidal period. The transports given for the Delaware and Schuylkill Rivers are simply boundary inputs to the 3-D model domain. The model does an excellent job of balancing net inflow through the external boundaries (the rivers plus the C&D Canal and the Bay mouth). The net inflow per tidal cycle during this 75-hr period was 5.2 million ft³, which is negligible compared to the 126-billion ft³ inflow over a single tidal half-cycle at the Bay mouth. Thus, the model conserves mass within the external boundaries to the model domain.

IV.B.1.c. Conclusions from Tidal Hydrodynamics Comparison

A numerical model is an approximation to the complex physical reality of the Estuary. Although it cannot be expected to provide perfect simulations, RMA-10 is calibrated to

achieve good agreement with the amplitude of the total tide at the Station. Model results differ in detail from the observations when a specific tidal constituents, current patterns, and volume balances are considered. The following conclusions may be drawn from the tidal hydrodynamics comparisons:

- The model matches the observed amplitude of the major tidal harmonic constituents and non-linear constituents along the axis of the Estuary to within about ± 5 percent, and also reproduces the principal non-linear tidal harmonic constituents that represent the asymmetrical, flood-dominant character of the Estuary.
- The difference between modeled and observed tidal amplitude at the Station and at Reedy Point, where the model does not reproduce the observed amplitude decline, suggests that the model's parameterization leads to a greater degree of spatial smoothing than is observed in nature.
- The differences of 0 to 20 percent between modeled and observed current speeds may reflect localized differences in flow patterns due to bathymetry or the flow into marshes, which cannot be perfectly represented in the model.
- The model balances the volume flux across the external boundaries very well, suggesting that currents are correctly modeled in a spatially averaged sense, even though there may be localized differences.
- In view of the approximate 5 percent regional tidal amplitude differences between model and observations, it is reasonable to estimate that modeled particle displacements (maximum excursions upstream and downstream from the Station) are accurate to better than ± 5 percent.

IV.B.2. Ambient Temperature and Salinity

IV.B.2.a. Stratification in RMA-10

RMA-10 is a combined 1-, 2- and 3-dimensional numerical hydrodynamic and transport model. The RMA-10 numerical model of the Delaware Estuary is subdivided into 3 regions: (i) lower Delaware Bay, where a 2-dimensional grid is used, (ii) upper Delaware Bay (including the region around the Station) where a 3-dimensional grid is applied, and (iii) the Delaware River above Marcus Hook, NJ, where a 1-dimensional grid is employed.

The 2-D or southern region covers most of Delaware Bay, from the mouth of the Bay to a point about 15 miles south of the Station. In this region, the model computes depth-averaged velocity, temperature, salinity, and density at each grid point. Grid points are typically 2 miles apart, although the actual grid point separation is not uniform. A 2-D model schematization was chosen for this region because Delaware Bay is generally regarded as a well mixed or unstratified estuary (Appendix C). Resolution of vertical temperature and salinity stratification in the model is unnecessary in this region to achieve accurate representation of currents at the upper end of the Bay.

The 3-D region covers the entire vicinity of the Station, and the grid point spacing is much finer than in the lower region, with grid points spaced only a few hundred feet apart

in the vicinity of the Station and at other points where high spatial resolution is needed. In the 3-D region, the model has up to 5 computational nodes in the vertical, permitting good resolution of stratified flow. In this region, the ambient flow is generally unstratified, but a 3-D approach was chosen in order to provide the most accurate modeling of the Station's thermal plume, including buoyancy forces.

The 2-D model region forms the southern boundary of the 3-D region and vice versa. In essence, each region provides a time- and space-dependent boundary condition for the other, depending on the direction of flow. For example, when the motion of the water is northward, depth-averaged velocity, temperature, and salinity from the 2-D model are assigned uniformly to each of the 5 vertical nodes of the 3-D region at adjacent grid points. This has the effect of forcing the boundary of the 3-D transition region model with vertically uniform flow and no stratification whenever the current is northward (flooding). The opposite situation prevails during southward flow conditions, when the stratified flow approaching the southern boundary of the 3-D region is vertically averaged to provide a single boundary condition for the adjacent nodes of the 2-D region.

This internal boundary condition at the transition region imposes unsymmetrical dynamical constraints. During southward flow, the depth-averaged velocities and water properties from the vertical nodes of the 3-D region is an appropriate, non-limiting input condition for the 2-D region. During northward flow, the imposition of a vertically averaged boundary condition on the 3-D region from the 2-D region may reduce temperature and salinity stratification in the 3-D region, and may influence interior flows locally. This internal boundary condition is not expected to influence the modeled distribution of velocity, temperature, and salinity near the Station to such an extent as to affect the calculation of plume properties, because density plays only a minor dynamical role in the relatively unstratified region around the Station.

IV.B.2.b. Mean Longitudinal Temperature and Salinity Structure

Along-channel (longitudinal) temperature and salinity gradients are the largest gradients in the Estuary system. The model generally reproduces these gradients, with some differences in detail. Figure IV-5 shows observed and modeled mean salinity at surface, mid-depth, and bottom levels at mooring moorings M12, M9, 9, 5, 2, 9M, and 12M. As these moorings were located on the east edge of the main shipping channel in relatively deep water, the data are taken to be representative of the general longitudinal structure of the river. Mooring 5 is directly opposite the Station and is plotted at RM 0. Mooring M12 is located 12 miles south of the Station, mooring M9 is 9 miles south, and mooring 9 is about 6 miles south. Moorings 2, 9M, and 12M are located 6, 9, and 12 miles north of the Station, respectively. To provide an optimum comparison, a 75-hr period (an integral number of model timesteps) during 24-26 May 1998 was selected for computation of statistical properties of observed and modeled water properties at locations. This computational period is approximately equal to six full tidal cycles (74.52 hours). The observed data are from moored instruments at near-surface, mid-depth, and near-bottom levels, and the model results are taken from corresponding points in the model domain.

Patterns evident from this comparison are:

- Both the observations and the model show a pattern of steeply decreasing salinity from south to north. The mean salinity decreasing to nearly zero 12 miles north of the Station in both the observations and the model. Surface salinity in the model agrees well with the observations at most mooring locations. Also, observed and model salinities at mooring 5, opposite the Station, converge to the same value. The model's diffusivity parameters were adjusted during the calibration run to achieve this result.
- South of the Station, the longitudinal mean salinity gradient in the model is less than in the observations, especially at the bottom. The observations show significantly more salinity at the bottom at mooring M12, whereas the model is nearly homogeneous in the vertical. This difference may be a consequence of the vertically homogenous boundary condition imposed at the juncture of the 2-D and 3-D model regions. The model is not intended to represent vertical stratification in regions far south of the Station, as such stratification would have little effect on particle displacements and plume transport near the Station.

Modeled and observed mean longitudinal temperature gradients show similar features. Figure IV-6 compares observed mean and modeled temperatures at the same locations as the preceding salinity comparison. More temperature data points are plotted, because more of the moored instruments were equipped with temperature sensors than salinity sensors. This comparison shows that:

- Mean temperature increases from south to north, at least as far as the Station (at mooring 5). This is expected at this time of year, since the ocean is colder than both the River and the freshwater runoff, so the influx and mixing of ocean water will result in a positive south-to-north gradient.
- Temperature stratification is generally small in both the observations and the model (less than 1°F (1.8°C)) maximum difference from top to bottom. The difference between the observations and the model is most evident toward the south. The observations show relatively cold water near the bottom at mooring M12, corresponding to the higher salinity there; the model does not reproduce this observed vertical gradient, probably due to the imposition of vertical homogeneity at the 2-D/3-D boundary a few miles south of M12. From mooring 5 northward, temperature stratification is negligible (less than 1°F (1.8°C) over depth) in both observations and model, and accordingly will have no effect on modeled ΔT in the plume..
- Temperatures at all depths at mooring 5, opposite the Station, are higher in the observations than in the model by an average of about 0.5°C (0.9° F). This difference, although small, contrasts with the near-perfect agreement in salinity at this location, suggesting that in the vicinity of the discharge the model may tend to confine the ambient cross-river gradients or the thermal plume slightly more closely toward the east side of the river than in the observations, on average. This

is expected since the RMA-10 representation of the discharge does not include its momentum which can carry the heated plume farther offshore during slack current periods than the model can predict.

- The observations show a slight (0.2°F) mean stratification at the surface at mooring 5, about one mile offshore of the Station. Mooring 5 data at surface, mid-depth, and bottom levels (Figure IV-7) suggest that some of this temperature increment may be due to the presence of the thermal plume for brief periods of time, usually a few hours before slack water. At such times, the plume apparently reaches mooring 5 on most slack water occurrences, but only at the surface. It is not clear whether the observed temperature signal at mooring 5 is a direct result of impingement by the immediate plume, or the residual plume from farther upriver or downriver, which is being swept past the moored instrument after the change of tide. Whatever its origin, this plume impingement is purely a surface phenomenon, and is brief. This is consistent with previous studies of the Station's plume (e.g., Pritchard and Carpenter 1968), which concluded that the plume would reach the shipping channel only for brief periods of time.
- The model's temperature predictions for mid-channel mooring locations other than mooring 5 are slightly lower ($<0.5^{\circ}\text{F}$) than the observations, except at mooring M12 where the observed bottom temperature is lower than any model temperature.
- The model vs observed temperature differences noted above are small, in the narrow range of $\pm 1^{\circ}\text{C}$ (1.8°F) or less. They probably reflect: (1) small imperfections in the model's parameterization of mixing, transport, and exchange of heat with the air; (2) the effect of the 2-D/3-D transition south of the Station; and (3) the fact that the temperature in the natural environment varies on a wide variety of space and time scales that no model can fully mimic. For comparison, temperatures at the Station predicted by the Ambient Temperature Model (Section III.A) differ from observed temperatures by 0.6°C (1.15°F) rms, during a 26-month period, and by 0.75°C (1.35°F) rms, during the model verification run as measured against Reedy Island temperatures.

IV.B.2.c. Mean Cross-River Temperature and Salinity Structure

In upper Delaware Bay, both temperature and salinity vary in the cross-river direction (Appendix C), although the cross-river variability is smaller than the along-channel variability. As with the along-channel gradients, the observed cross-channel gradients show more stratification than the model's simulation. Sufficient data to show cross-river temperature structure are available at moorings G9, M9, and R9, located on a cross-river transect about 9 miles south of the Station. Figure IV-8 shows the mean temperature at surface, mid-depth, and bottom for both observations and model results at these moorings. On this figure, the bottom temperature for observed mooring M9 is extrapolated from the surface and mid-depth measurements, since the temperature recorder at the bottom at this location did not work. This extrapolation is valid since the vertical profile surveys (Exhibit E-1-3) clearly show that the water is isothermal from mid-depth to the bottom at all stages of the tide at this location.

The model shows a slight temperature rise, about 0.15°C (2.7°C), from west to east, and essentially no vertical temperature stratification at any cross-river location at this transect. In contrast, the observations show more cross-channel spatial structure, with low temperatures at the bottom in the middle of the channel and higher temperatures at all depths on both sides of the Estuary. The model's nearly uniform temperature is intermediate between the higher observed temperatures found at the surface near the edges of the River, and the lower temperatures found at the bottom of the deeper channel at mid-River. Since colder temperatures tend to be associated with higher salinities at the bottom, it is inferred that a core of slightly colder, saltier water is present in the deep channel. This stratified core of near-bottom water originates in lower Delaware Bay where stratification is much greater than in the well mixed upper Estuary. The depth-averaged 2-D model in that region cannot represent such features, and this follows through to the 3-D region as well.

IV.B.2.d. Spatial Salinity Patterns

As described in Section III, typical estuarine salinity distributions tend to show low salinities near the edges of the Estuary, whereas high salinities tend to be found toward the middle. This is partly a consequence of flow asymmetry in a flood-dominated estuary, such as Delaware Bay (Friedrichs and Aubrey 1988). In this type of estuary, the current tends to be concentrated in the middle of the channel during the flood flow phase, so the incoming salty water displaces fresher water toward the edges, and prevents it from flowing upstream. During the ebb current period, the flow is slower and spatially more uniform, allowing the pattern of low salinity at the edges to persist. Mean salinities predicted by the model, averaged over a full tidal cycle, (Figure IV-9) show this pattern, with low salinities along the New Jersey shore, extending from north of Artificial Island to about Mad Horse Creek (MHC on the figure). A pronounced tongue of lower salinity water extends southeast of the Station. Higher salinities are predicted by the model near the Delaware shore south of the Station, and at mid-channel near the Station. As a result, isopleths of salinity are not orthogonal to the channel. Observed salinities from moored instruments, averaged over the same tidal cycle, are also shown on Figure IV-9, and these show generally higher salinities than the model, especially southeast of Artificial Island. This is consistent with the model's lower-than-observed along-channel salinity gradient. The model's ability to simulate a high-salinity intrusion in the deeper parts of the channel provides confidence that the model is correctly representing these elements of estuarine physics.

IV.B.2.e. Temporal Variability of Temperature and Salinity South of the Station

Temperature and salinity fluctuations at any point are mainly the result of tidal advection of the mean longitudinal gradients. The difference between observations and modeled values as a function of time reflect these mean gradients. In Section IV.B.2.c above, it was noted that the model predicts lower longitudinal temperature and salinity gradients than observed, and that the model exhibits little vertical temperature or salinity structure at most locations and does not reproduce the bottom core of higher-salinity, lower-temperature water that is present in nature. The effect of these differences is clearly

visible in the time histories of temperature and salinity at mooring M9, located near the middle of the channel about 9 miles south of the Station. Figure IV-10 shows observed and modeled temperatures and time-series at surface, mid-depth, and bottom levels, together with tide height, solar insolation, and air temperature. Figure IV-11 shows the corresponding salinity plot.

This comparison shows that:

- The observed temperature fluctuations at all depths are entirely semidiurnal in character, and are unrelated to the solar heat input or the air temperature. These temperature fluctuations are evidently due to tidal advection of the longitudinal mean gradient.
- Observed temperatures are higher by about 0.5 °C (0.9°F) at the surface than at the bottom. The modeled temperature tracks both the mean and the tidal fluctuations of the observed surface temperature very well. At the bottom, the model is higher in the mean, although it tracks the tidal temperature fluctuations fairly well.
- Observed salinities are higher at the bottom than at the surface by about 2 ppt. The observed salinity fluctuations are semidiurnal and are closely synchronized with the temperature fluctuations, supporting the concept that they are caused by tidal advection. The modeled salinity fluctuations are relatively small in amplitude and the mean is lower, especially at the bottom. This reflects the model's underprediction of the mean bottom salinity and the longitudinal gradient in this model region.

IV.B.2.f. Conclusions Regarding Stratification and Mixing

The following conclusions about the model's performance may be drawn from the foregoing comparisons of modeled and observed stratification:

- The model reproduces the basic patterns of longitudinal temperature and salinity variability, and the surface salinity pattern of lower salinity at the edges of the River. The modeled gradients and fluctuations of both temperature and salinity are lower than observed, suggesting that the model is more smoothed than the observations. This may be a consequence of the model's high horizontal diffusivities, which cause more vigorous horizontal mixing than in nature. This will have little effect on the estimated maximum extent of the plume, although it may result in some smoothing of the edges of the plume where the horizontal gradients are steep.
- At slack water, the observations suggest that the thermal plume tends to spread at the surface, and sometimes extends as far offshore as mooring 5, at the eastern edge of the shipping channel. The signature of the warm surface water is seen only at the surface at this distance, about 4,500 feet offshore of the discharge. The model does not show this degree of plume surfacing and spreading. The model includes buoyancy forces, but the effect of these terms is small and does not result

in plume stratification at these distances, given the limitations of model grid resolution.

- The observations show that south of the Station, the water at the bottom near the center of the channel is significantly saltier and colder than at the surface. This is consistent with the classical concept of estuarine circulation, in which there is a net upstream flow of saltier bottom water and a net downstream flow of fresher water at the surface. This two-layer advection is the principal mechanism by which heat (or the absence of heat) and salt from the ocean are injected into an estuary and carried upstream. In the model, however, the colder and saltier water at the bottom is absent, due to the use of a 2-D model in the lower Bay and the vertically homogeneous internal boundary condition at the junction of the 2-D and 3-D model domains. As a result, the model cannot inject the same amount of salt and "cold" northward at the bottom, nor remove "freshness" and heat at the surface through advection. To achieve the correct mean longitudinal salinity and temperature gradient, the model relies on a high value of horizontal diffusivity in the 3-D region (Section III.C), which includes the Station. Although this results in some smoothing of velocity and water property fields, it will have little effect on plume extent.
- At mooring 5, modeled and observed salinities match closely while the observed mean temperatures are higher in nature than in the model, suggesting that the modeled thermal plume (and/or the actual ambient cross-river thermal gradients) may tend to be more confined somewhat more toward the east side of the River than is actually the case. The observations show that the plume reaches the shipping channel only for very brief periods and only at the surface.

IV.B.3. Thermal Discharge Plume Dynamics

IV.B.3.a. Thermal Plume Dynamics in RMA-10

RMA-10 was specifically formulated and implemented to represent the shape and extent of the Station's far-field thermal plume at various ΔT isopleths. The plume's shape and extent are controlled by physical processes such as buoyancy, advection and mixing (dilution) in the waters of the Estuary, and heat dissipation to the atmosphere. Although RMA-10 incorporates these physical processes in its parameterization and formulation in order to simulate the plume accurately, it is not intended to predict total temperatures or ambient temperatures over long periods of time. The Ambient Temperature Model (ATM) and the Total Temperature Model (TTM) (Section III) are used for these predictions. Differences between observed ambient currents, temperatures, and other water properties and those predicted by RMA-10 are not significant provided they do not affect the accuracy of the model's plume simulation.

A three-dimensional formulation is used in RMA-10 in the region near the Station specifically so that the model could simulate buoyant spreading of the plume. In this Section, attention is focused on the plume's tendency (if any) to separate from the bottom and spread at the surface under the influence of its own buoyancy, and the accuracy of the model's simulation of plume shape.

In the previous application of RMA-10 to estimate the impact of the Station thermal plume (TRA et al. 1993), it was assumed that the plume was primarily a surface phenomenon, consistent with observational evidence available at the time. The local models used for prediction of the plume's initial mixing and shape reflected this assumption, so that the plume was introduced into RMA-10 as a near-surface mass of heated water at the end of the ZIM. RMA-10's 3-dimensional formulation allowed this surface plume to be advected by ambient currents and dissipated by mixing and heat loss processes. The result was a modeled plume that persisted at the surface for significant distances, then became vertically homogenous at greater distances.

However, recent field observations (Exhibit E-1-3) suggest that the plume is, in fact, vertically well mixed at all times in the region close to the discharge and is also well mixed vertically at intermediate distances during the flood and ebb phases of the tide, when the strong current causes turbulent mixing of the water column. Based on this information, the present formulation of the combined near-field and far-field plume models (CORMIX and RMA-10) introduces a vertically homogenous plume into RMA-10 at the end of the ZIM. This adjustment to the previous formulation is intended to produce a more realistic plume shape and extent based on the more comprehensive data. As in the previous formulation, the plume is assumed to have no momentum at the location where it is inserted into RMA-10; CORMIX represents the momentum-dominant (near-field) region of the thermal discharge.

The behavior of the thermal plume depends on the stage of the tide. At slack water, the plume tends to spread locally and to move offshore under the influence of the initial momentum of the jet. During full flood or ebb flow, the plume is swept upstream or downstream by the current, and becomes elongated. The shape of the plume and its tendency to detach from the bottom (if any) are assessed separately for these different conditions.

IV.B.3.b. Slack Current Plume Shape

As the tidal current slows toward slack water, the plume abruptly appears in the observed temperature records at moorings directly offshore of the discharge. Figure IV-12 show surface temperature time-series at moorings 21, 22, V, and 5, which are located approximately on a line extending straight offshore from the discharge (Figure IV-1 shows mooring locations). Also shown on this figure are current speed and direction from the ADCP located near mooring V offshore of the discharge, and tide height at the Station. Slack water (defined as conditions of low current speed while direction is rapidly reversing) occurs about 2 hours after high or low tide. The presence of the plume for a short time around slack water is evident at moorings 21, 22, and V, which are within about 1,000 ft of the discharge, in the form of an abrupt temperature increase. Farther away, at mooring 5 (about 4,500 ft offshore), the plume is briefly present around slack water, but the timing of its appearance is different, suggesting that the plume does not extend directly to this location. Instead, the temperature signal appears briefly at this mooring only after the current has changed and swept the slack plume past the mooring.

The dilution and vertical structure of the plume at slack water are illustrated in Figure IV-13, which shows observed and modeled peak temperatures at all depths from mooring locations 21, 22, V, 5, and 6 during the EOF slack on 29 May 1998 (upper panel). Because these are peak temperatures, they represent the hottest part of the plume when it was present on this phase of the tide. Also shown on this figure is the surface temperature observed during the Two-Unit Survey (Exhibit E-1-3) by a vessel attempting to follow the peak temperatures from 1425 hrs to 1625 hrs. Model temperature predictions at points corresponding to the moored instrument data are shown on the lower panel, together with predicted temperature following the observed plume centerline. These predictions are based on CORMIX for the near-field region, Linkage for the transition region between the near-field and far-field models, and RMA-10 for the far-field predictions. There is a spatial discontinuity between the modeled and observed plume centerline, particularly at this nearly slack tide, because the RMA-10 model does not incorporate the discharge momentum.

Several facts emerge from this slack-current comparison:

- The plume reaches the surface close to the discharge, as shown by the presence of heated water at the surface at mooring 21, which was located immediately in front of the discharge and less than 275 ft from the outfall. By the time the discharge reaches the surface, it has already entrained an additional volume of ambient water, and is cooler than the actual discharge by nearly 5°C (9°F). This is consistent with the CORMIX formulation.
- At moorings 21 and 22, which are within 275 and 500 ft of the discharge, respectively, observed temperatures are vertically homogeneous, consistent with the concept of a vertically well mixed plume core. Temperature at mooring 22 is lower than at mooring 21 by about 1°C (1.8°F), indicating some dilution between these closely spaced mooring locations.
- At mooring V, about 1,000 ft from the discharge, observed temperatures have not decreased much further at the surface, but a slight stratification has developed with the water being 0.5°C (0.9°F) higher at the surface than at the bottom.
- Temperatures at all depths are slightly elevated above background (ambient plus the residual from previous plumes) indicating that the plume is still present throughout the water column.
- At mooring 5, about 4,500 ft from the discharge, the average temperature is close to ambient although there is still some stratification that is probably associated in part with the occasional presence of the plume. Again there is a difference of about 0.5°C (0.9°F) from bottom to surface. This suggests that while the plume has been greatly diluted by mixing with ambient water at all depths, it still retains some vertical stratification.
- At mooring 6, on the west side of the River, there is no sign of the plume. Average temperatures are higher there, but this is a consequence of the cross-river temperature structure and the fact that mooring 6 is in shallower water than mooring 5 (Section IV.B.2.c.; Figure IV-8).
- The surface temperature observations taken by a vessel attempting to follow the plume centerline are erratic, showing reasonably good agreement with the moored

instrument temperatures when the surface temperature was sampled in the plume core, and much lower temperatures when it was not. This finding reflects the difficulties encountered in field surveys when trying to track the inhomogeneous plume in moving water.

- RMA-10's predicted temperatures at the mooring locations are lower at all depths than the observations, and the model shows vertically homogeneous conditions at this stage of the tide. The RMA-10 model was not intended to represent the near-field, so the absence of the heated near-field plume from this prediction is expected.
- The CORMIX/Linkage/RMA-10 combined model prediction following the plume represents a good fit to the moored instrument data.

In general, the slack water period is difficult to observe or to model accurately, because in the absence of strong currents, the plume will move erratically; its surface expression may not follow its subsurface core exactly (due to wind and current effects); it may tend to spread at the surface due to buoyancy; and its momentum may still be relatively significant even at considerable distance from the discharge. Figure IV-14 shows the surface temperature observed during the Two-Unit Survey (Exhibit E-1-3), overplotted with the centerline and lateral extent of the CORMIX-predicted plume. While some of the variability of observed surface temperature may be an artifice of the limited sampling grid, it is nevertheless clear that the actual plume is erratic and complicated at slack water. The fact that the model does reasonably well even under these difficult conditions is evidence that the CORMIX/Linkage/RMA-10 approach is fundamentally sound.

IV.B.3.c. Flood and Ebb Current Plume Shape

The core of the plume remains well mixed out to much greater distances under high-current conditions. Figure IV-15 shows time-series of observed and modeled surface temperatures measured at moorings situated along a shore-parallel line passing through the discharge point. From south to north, the moorings plotted are H, 24, 23, and E. Also shown are current speed and direction from the ADCP offshore of the discharge, and tide height at the Station. At moorings 24 and 23, which are a short distance downstream and upstream from the discharge, respectively, the surface temperature exhibits a "square wave" character, indicating the presence of the plume core regardless of current speed. For example, the temperature at mooring 24 is high when the current is ebbing, but is approximately ambient (actually $T_{\text{ambient}} + T_{\text{approach}}$) when the current is slack or flooding. The pattern is similar at mooring 23, but on the opposite phase of the tide. At mooring H, about 2,700 ft downstream of the discharge, a clear temperature signal is present, corresponding to the presence or absence of the plume over the moored instrument. However, at mooring E, located a comparable distance upstream from the discharge, a more confused signal is seen, with only momentary presence of the plume at the beginning of the flood phase; this suggests that the core of the plume misses mooring E once the large slack-water "puddle" of warm water has been swept past by the increasing current.

Figure IV-16 shows peak observed (upper panel) and modeled (lower panel) temperatures on an along-shore line through the discharge using the same moorings (H, 24, 23, and E) as in the previous figure. This composite figure shows both flood and ebb peak conditions. Points plotted to the left of the discharge point on this figure represent peak temperatures observed during the ebb phase, 0640 to 0840 hrs on 29 May 1998. Points plotted to the right represent the flood phase, 1140 to 1340 hrs on 29 May 1998. This running tide comparison shows that:

- At mooring 24, located about 275 ft (84 m) offshore and slightly downstream (southward) from the discharge, peak temperatures are elevated at all sensor levels during the ebb flow phase, and a slight vertical stratification $\sim 0.5^{\circ}\text{C}$ (0.9°F) warmer at the surface than at mid-depth is evident. Observed surface plume temperatures collected during the vessel survey are lower than the moored temperatures, suggesting that the survey vessel did not actually follow the hottest part of the plume, or that the plume had cooled somewhat at the surface.
- At mooring H, located about 2,300 ft (700 m) downstream of the discharge, the peak temperature is slightly elevated above ambient, and vertical stratification is minimal. Since mooring H is believed to be directly in line with the plume at all times during the ebb phase, this implies that the central core of the plume is well-mixed out to considerable distances when the current is strongly ebbing.
- At mooring 23, about 250 ft (76 m) upstream and offshore from the discharge, strong stratification exists on the flood phase even though this mooring is close to the discharge, and temperatures are elevated at all depths. This implies that the plume is wider at the surface than at the bottom, and the center of the plume did not pass directly over this mooring during this particular flood current episode.
- At mooring E, about 2600 ft (790 m) upstream, peak temperatures during this particular flood were relatively low at all depths and were slightly stratified, with the mid-depth temperature being about 0.3°C (0.5°F) warmer than the bottom. (There is no surface temperature observation at this location for 29 May, but when the surface moored temperature sensor was present (prior to 26 May) the surface temperature at this location was typically more than 1°C (1.8°F) higher than at mid-depth or bottom.) The bottom temperature at mooring E during flood is close to ambient (21.25°C (38.25°F)). It is inferred that the plume is wider at the top than the bottom at this distance, and that the plume's narrower bottom width does not intersect this moored location.
- The RMA-10 model shows no vertical plume stratification, and it reproduces the plume temperature at the far-field moorings E and H, suggesting that it correctly predicts plume centerline location and temperature in both flood and ebb.
- The CORMIX/Linkage/RMA-10 combined model performs well at predicting temperatures in the near-field along the plume centerline.

The slight asymmetry between the observed temperatures at moorings E and H during flood and ebb is also evident in the surface temperature maps produced as part of the Two-Unit Survey (Exhibit-1-3). Figures IV-17 and IV-18 show the flood and ebb phases, respectively. On this particular flood phase (Figure IV-17), the plume centerline is

slightly shoreward of mooring E; the fact that the mooring is at the edge of the plume accounts for the vertical stratification observed there. In contrast, mooring H is in the center of the plume during ebb phase (Figure IV-18), consistent with the nearly homogeneous conditions observed there.

The width of the stratified region at the edge of the plume can be estimated from these observations. At the location of mooring E, about 2,600 feet (790 m) from the discharge, the cross-stream width of the surface plume during the flood current phase is estimated (Figure IV-18) to be 1,000 ft, or ± 500 ft on each side of the centerline. Mooring E's location is about 250 ft from the centerline of the plume, so the region of vertical stratification at the plume's edge must extend from less than 250 ft from the centerline out to more than 500 ft. Therefore, it is reasonable to infer that the stratified region must be approximately 300 ft wide on each side of the plume at this distance from the discharge. This further suggests that the width of the region where the plume remains fully in contact with the bottom is only about 400 ft wide at this distance. The plume evidently has a trapezoidal shape in cross-section, reflecting some tendency to lift off the bottom and spread at the surface due to its buoyancy.

RMA-10's grid point spacing in the vicinity of the discharge is typically a few hundred feet, and no finer than about 200 ft (Section III). With this resolution, it is unrealistic to expect RMA-10 to predict or resolve fine-scale vertical stratification at the edge of the plume.

IV.B.3.d. Conclusions Regarding RMA-10's Thermal Plume Structure

The foregoing analysis suggests that:

- In the near-field of the thermal discharge, the plume structure is always vertically homogeneous in its central core, consistent with the present CORMIX formulation.
- Under slack conditions, the plume tends to spread at the surface and become somewhat stratified in the far-field, at distances of up to one mile.
- Under high current conditions, the plume is wider at the top than at the bottom (trapezoidal shape), and consequently is partially stratified at the edges. At distances of about 2,500 ft from the Station's thermal discharge, the plume is neither a true 2-layer structure, with all the heat concentrated in a surface layer, nor is it a vertically homogeneous structure with its heat distributed uniformly through the water column. Except in the center, the plume appears to be spreading at the surface as it is advected and mixed horizontally and vertically. The result is that the plume develops a distinctly stratified character at its edges.
- The region of stratification at the edges of the plume is too narrow for the RMA-10 model to resolve, given its grid spacing.

The observations are not sufficient to show whether the plume remains stratified at greater distances. Dynamical considerations suggest that plume buoyancy becomes unimportant in relation to mixing forces at large distances, where the plume's ΔT is

small. For running tide conditions with current speeds of 2.0 ft/sec (0.6 m/s) and an assumed temperature difference of 1°C (1.8°F) from top to bottom of the plume, the bulk Richardson number is estimated to be 0.05. This ΔT corresponds to the outer extent of the plume, beyond the distance where moored instruments can reliably detect it. The bulk Richardson number is a dimensionless ratio of buoyancy forces (which promote stratification) to ambient current shear forces (which promote mixing). Richardson numbers in the range of 0.08 to 0.8 represent a transition from a strongly stratified flow to a highly turbulent, well mixed flow (Fisher 1979), with the low end of this range representing the most turbulent conditions. Therefore, the plume will be well mixed in the vertical during running tide conditions at distances where its ΔT is small.

IV.B.4. Tidal Marsh Exchange Processes

The importance of tidal marsh heat and mass exchange is discussed in Attachment E-1 Section III and Exhibit E-1-5. Recent measurements and a previous study (Weston Environmental Consultants, Inc. 1978) have shown a consistent picture of significant heat outflow from the marshes particularly when high tide occurs in the afternoon on days when solar radiation (insolation) is strong. In this Section, the evidence for high-temperature marsh outflow is reviewed, and the model's skill at predicting these outflows is assessed.

IV.B.4.a. Tidal Marsh Heat Exchange in RMA-10

The exchange of large amounts of heat between the River and the marshes can cause large temperature fluctuations in the River around the Station, complicating the task of assessing the impact of the Station's thermal plume. A marsh component was therefore added to the 1998 Modified Thermal Monitoring Program (Modified TMP). This marsh component was designed to account for the heat exchange with several marshes close to the Station, including the Alloway Creek, Hope Creek, and Mad Horse Creek marsh complexes. In the final RMA-10 simulations, each marsh module consists of a simple embayment having the same surface area as the actual marsh; the complex structure of the marsh flats and creeks was not represented in detail. The water depth in each embayment was taken to be constant at 5.3 ft below Mean Tide Level; this depth was chosen to be slightly greater than Mean Lower Low Water, so the modeled "marsh" never goes dry. These simplifications were necessary to ensure computational stability and flow continuity in the marsh areas. This relatively deep uniform depth results in the modeled marshes having more than 5 times as much volume as the actual marshes at high tide. The model marshes have only a single computational node at each grid point, so the heat exchanged at the surface is assumed to be depth-averaged over the entire marsh water column. The marsh model accounts for short- and long-wave solar and reflected atmospheric radiation, back radiation from the water column, and conductive heat exchange between the water and the air. Inputs to drive the marsh model include insolation measured at the Station (scaled with a "shading factor"), air temperature, relative humidity, and wind speed.

This marsh formulation differs from nature in several ways:

- Water can readily flow into and out of the modeled "marsh" embayments because there is no narrow inlet constricting the flow. This results in a broad, low-friction flow of water in and out of the open side of the embayment in the modeled marshes, in contrast to the concentrated high-friction flow at the creeks nature. This probably causes a localized effect in the River, but may influence the movement of the Station's thermal plume in the nearshore zone, and may affect the modeled propagation of the tide up and down the Estuary to a slight extent. There is no evidence to suggest that either of these effects is significant, or would have any effect on the calculated plume extent.
- The modeled marshes do not become dry at low tide, as the real marsh flats do. This means that the modeled outflow is more gradual and follows the tide height more closely than do actual marshes, whose outflow decreases quickly after mid-tide.
- The effective water volume into which the modeled solar and atmospheric heat is transferred is greater than in nature, due to the use of uniform-depth idealized embayments in the model.

The implications of these assumptions on marsh heat budget are difficult to assess. Neither RMA-10 nor any other model completely describes these physics. Therefore, these assumptions on marsh geometry represent an uncertainty in the model, much as other parameterizations of sub-grid scale or complex physical processes do.

Previous formulations of RMA-10 (PSE&G 1995) did not include any marsh treatment, thereby ignoring the heating and cooling effects of these large areas adjacent to the River. The incorporation of a marsh module into RMA-10 in the present study, represents a state-of-the-art attempt to represent the full surface area of a complex estuarine system. Modeling of heat exchange between estuaries and marshes is a developing science, not an established capability so there are differences when the modeled marsh outflow is compared to observations. This should not obscure the fact that by incorporating the marsh modules, the RMA-10 model now accounts for heat dissipation through the marsh surface area, which influences the plume extent.

IV.B.4.b. Heat Exchange with Nearby Marshes

The 1998 Modified TMP studies contained an observational marsh component, designed to measure the volume and temperature of the flow into and out of several marshes around the Station. During the Two-Unit Survey, May-June 1998, temperatures and salinities were measured in the mouths of Alloway, Hope, and Mad Horse creeks using moored instruments (Exhibit E-1-3). The cross-sectional area of the creek mouths were measured using a depth sounder, and tide heights were estimated from nearby fixed tide gauges. Intensive survey measurements of flow through the creek mouths were made on the four stages of the tide using a vessel-mounted ADCP.

Figures IV-19, 20, and 21 show the time history of temperatures at Alloway, Hope, and Mad Horse creek mouths, respectively. Also shown on these figures is tide height at each creek mouth and current direction measured at the bottom-mounted ADCP near mooring

V offshore of the Station, together with insolation and air temperature. Model-predicted temperatures are shown for comparison. At all three creeks, the water temperature time-series show a strongly diurnal pattern (one high temperature per day) when the insolation is strong and the ebb tide occurs in the afternoon or evening. This pattern is seen during half of each lunar month. However, on cloudy days (low insolation) or days when the ebb tide occurred during the morning, the temperature fluctuations become smaller, more erratic, and more semidiurnal in character, corresponding to weaker heat exchange with the atmosphere and a more clearly defined tidal advective transport.

The model's temperature predictions are moderately well correlated with observed temperatures for Hope Creek (Figure IV-20), but have less agreement with Alloway Creek (Figure IV-19) and Mad Horse Creek (Figure IV-21). Hope Creek is the smallest of the three modeled marshes, and the closest to the Station's discharge. The good agreement between model and observations obtained for Hope Creek suggests that the model's heat flow parameterization achieves the correct balance for this small marsh, whereas for the other, larger marshes, a different parameterization might have been more effective. However, the model's good performance for Hope Creek marsh may also be due, in part, to the entry of slightly heated residual plume water into this marsh following the end of the ebb flow phase. The model correctly predicts the plume in the region offshore of Hope Creek during the ebb flow phase, and predicts that some of this water (about 30 percent in terms of surface area) enters the marsh (Exhibit E-1-5) as the water level rises. The presence of this plume-related temperature variation at Hope Creek thus improves the correlation between model and observation there. The approximations in regard to marsh depth and surface heat exchange incorporated into the model may account for the lower correlation between model and observations at Mad Horse Creek and Alloway Creek.

IV.B.4.c. Heat Transfer From Marshes North of the Station

Temperature fluctuations of marsh origin in the River itself are also observed at moored instrument moorings located 9 and 12 miles north of the Station. At these distances, there is no discernable temperature increment due to the Station's thermal plume. Figure IV-22 shows temperature time-series at moorings 9G and 9R, located 9 miles upstream near the west and east sides of the River, respectively. Also shown on this figure are tide height, current direction at the ADCP near the Station, insolation, and air temperature. Marsh outflow is not evident at mooring 9G on the west side of the River, where a pattern of regular semidiurnal temperature fluctuations is observed, with an amplitude of up to about 1°C (1.8°F) peak-to-peak; these fluctuations are due to tidal advection of the mean longitudinal temperature gradient.

In contrast, mooring 9R on the east side of the River shows large temperature fluctuations of diurnal periodicity superimposed on top of smaller semidiurnal variability. Mooring 9R is located about 3,000 ft (1,000 m) offshore in a shallow, broad embayment (Salem Cove), which is directly offshore of a major marsh area and slightly upstream of the Salem River mouth. The diurnal signal occurs at all depths and is strongest when the ebb flow occurs in late afternoon or early evening on days when insolation is strong and air

temperature is high. For example, during the period 25-30 May 1998 temperature pulses of about 4.5° to 6.3°F (2.5° to 3.5°C) are evident late in the day (around 1800 hrs), with maxima occurring shortly after the end of ebb flow in the River. This warm water originated from sources nearby, or a short distance upstream, because there are no marshes or other thermal discharges on the west side of the River at this location, and no evidence of diurnal temperature fluctuations at the western moorings (9G and 12G). The Station cannot be the source of the temperature fluctuations, because peak temperatures are observed exclusively on the ebb flow phase, and the Station is located far downstream.

While there are no temperature observations at the Salem River mouth during this modeled time period, moored instrument measurements were made over a six-month period from late June to November, 1998 (Exhibit E-1-3). These measurements, shown in Exhibit E-1-5, demonstrate clearly that the Salem River marsh is the origin of significant temperature fluctuations on a diurnal basis. In addition to the Salem River itself, which drains most of this marsh region, there are several other creeks, such as Mill Creek, that drain into the River at Salem Cove; some of these outlets are north of the 9R mooring location.

The marsh-generated plume of elevated temperature water at mooring 9R is observed at all depths (as expected because the mooring is in shallow water) and at a distance of 3,000 ft (1000 m) offshore. This suggests that the volume of this marsh outflow is substantial, covering at least the entire area of Salem Cove (approximately 1400 acres) and probably much more.

In early June, when the tide phase has shifted relative to the solar day so that ebb tide is no longer in the afternoon, there is practically no diurnal temperature signal at mooring 9R. Insolation and the other heat exchange processes are presumably still active, but the change of tide phase results in the solar and atmospheric heating being more evenly distributed in the marsh water over the course of the day. With outflow occurring in the morning and inflow in the evening, outflow temperature variability is moderated, and no longer shows the strongly diurnal character that it does in late May.

The observations at moorings 12G and 12R (Figure IV-22), 12 miles north of the Station, show that a local source of solar-heated water must also be present on the east shore slightly upstream of this moored instrument line. Mooring 12R is located within a few hundred feet of the east shore of the River, just north of a major bend above Penns Neck. Temperature fluctuations at mooring 12 R at all depths show diurnal peaks that correlate well in time with the ebb tide, although the amplitude of the fluctuations is lower at 12R, typically only about 1.0° to 1.5°C (1.8° to 2.7°F), and the pulses are broader. It is unlikely that these temperature fluctuations at mooring 12R are due to outflow from the Salem River, because that outflow is located more than three miles south of mooring 12R, and the signal is observed at the end of the ebb phase. However, there is another outlet from the same marsh, through the Salem Canal, about three miles upstream from mooring 12R; the warm water could originate from there.

The model's predicted temperature for the 9R and 12R mooring locations, also shown on Figures IV-22 and 23, exhibits a small semidiurnal advective signal but does not show the marsh outflow signal. This is consistent with the marsh formulation incorporated in the RMA-10 model, which does not include any representation of the Salem River marsh.

IV.B.4.d. Conclusions Regarding Tidal Marsh Processes

It is shown elsewhere (Exhibit E-1-5) that the marshes adjacent to the River can absorb large amounts of heat (comparable to or greater than the heat rejected to the River by the Station) and transfer this heat to the River. Here the focus is on how well RMA-10 handles the marsh thermal input, and what the effect of these additional heat sources might be on the predicted Station plume length. The following conclusions are drawn:

- The marshes on the east shore of the River can contribute significantly to temperature fluctuations in the nearshore environment where the Station's plume is found. At some locations, such as those north of the Salem River, marsh-related excess temperatures can exceeded 3°C (5.4°F) over distances of up to a few thousand feet offshore.
 - The marshes contribute maximum heat to the river when the ebb phase occurs in late afternoon or evening following a day of strong sunshine and warm air temperatures.
 - Alloway, Hope, and Mad Horse creeks also provide significant heat contributions to the River, although the excess temperatures were not as high as those north of the Station at mooring 9R during the observation period. Temperature increases of 1° to 2°C (1.8° to 3.6°F) were observed at the mouths of these creeks.
 - The model accounts for marsh-related heat flux to and from the environment through the use of simplified, constant-depth embayments to represent each marsh. These embayments have the same surface area as the marshes and larger volume. This produces a correct heat balance, although the predicted temperature changes are a factor of two to four smaller than observed, due to mixing the surface heat flux into a volume of water that is larger than in the actual marshes. This formulation is an improvement over the prior model, which included no marsh representation.

The differences between modeled and observed marsh temperature variations are of little importance in determining the extent of the Station's plume, because such differences do not affect the calculation of ΔT , which is done by subtracting the modeled temperature fields with and without the Station's discharge. The modeling approach allows the extensive marsh surface area to contribute to the overall heat budget of the modeled Estuary, and to dissipating the heat from the Station's discharge.

IV.B.5. Exchange with Chesapeake Bay via the C&D Canal

The Chesapeake and Delaware (C&D) Canal is an important source and sink for water in upper Delaware Bay (Wong 1991). Due to the Canal's proximity to the Station, flows through the Canal could potentially affect the length of the thermal plume, therefore it is important to ensure that the model correctly represents the flow in the Canal. In this

Section, attention is focused on how well the model represents the flow in the Canal as a function of the driving force.

The Canal is a straight, open channel approximately 35 ft deep by 450 ft wide and 14 miles long. Flow in the Canal is driven by the sea-level difference from one end to the other (hydraulic gradient), and is regulated by bottom friction and internal viscosity. This implies a monotonic, nearly linear relationship between hydraulic gradient and flow. In actuality, the inertia of the fluid is not negligible, and its acceleration complicates the instantaneous head-vs-flow relationship. Various values of flow coefficient (volume flow per unit of height difference along the Canal) have been reported. Wong (1991) stated that the Canal's tidally averaged flow coefficient is 35 m³/sec per cm (37,670 cfs per foot) of hydraulic head difference between Reedy Point on the Delaware River and Old Town Point in upper Chesapeake Bay, which represent the eastern and western ends of the Canal, respectively. Boyd et al. (1973), in a report by the U.S. Army Corps of Engineers (USACE), estimated the flow coefficient to be 30,725 cfs per foot. Pritchard and Gardner (1974), in another study for USACE, gave a similar value of 30,500 cfs per foot.

In this assessment, the USACE (Pritchard and Gardner 1974) value of about 30,500 cfs per foot for the flow coefficient is taken as the standard, against which the model is compared. In view of the range of reported values, however, a model flow coefficient between 30,000 and 40,000 cfs per foot is regarded as satisfactory.

IV.B.5.a. The C&D Canal in the RMA-10 Model

The RMA-10 model represents the C&D Canal as a one-dimensional channel, with three computational elements (grid points) along its length. Flow in the Canal is driven by the time-varying sea-level elevation difference at both ends, and is regulated by friction and acceleration in the Canal. Model outputs include flow (integrated across the channel) and along-channel sea surface slope (in units of inches per mile). The length of the Canal between model grid points 364 and 371, representing approximately the west and east ends of the Canal, is 13.34 miles in the model. Therefore, to convert slopes from RMA-10's units of "inches per mile" to "head in feet," used by previous authors, it is necessary to multiply by 13.34/12, (or a factor of 1.11).

The model results presented here are from five separate model test simulations, designated here as Simulations A-E, which utilized harmonically predicted tide heights at the western end of the C&D Canal as the boundary condition. Due to the particular sea level meteorological conditions prevailing in the Estuary for these model simulations, all but one (Simulation D) exhibited a strong westward mean slope and flow in the Canal. The following analysis focuses on the relation of slope to flow, and is independent of whether the slope is realistically specified in these simulations.

IV.B.5.b. Instantaneous Flow Response to Slope Forcing in the RMA-10 Model

Sea surface slope along the Canal and flow in the Canal both exhibit a strong tidal signal (Figure IV-24), modulated with subtidal variability. Flow and slope are obviously

correlated. Peak flow in each direction follows closely in time after the peak slope, with a typical time lag of about one hour. Due to the time lag, scatter plots of instantaneous flow versus slope (Figures IV-25a-e) show elliptical patterns. Simulation D (Figure IV-25d) exhibits a symmetrical ellipse, reflecting the near-zero mean slope and mean flow conditions that prevailed during this simulation. All the other simulations exhibit asymmetrical ellipses, with tails on the negative side (indicating westward flow); the asymmetry is due to the presence of a strong westward mean in these cases.

A least-squares linear regression through the slope/flow data is also shown on these figures. The trendlines are forced to pass through the origin (zero flow, zero slope) in each simulation. The flow sensitivity to slope forcing based on these least-square regression lines is summarized below.

Simulation	Sensitivity (cfs/in/mi)	Coefficient (cfs/ft of head)
E	38,253	34,462
D	32,978	29,710
C	38,295	34,500
B	38,882	35,029
A	38,565	34,743

The average value of the flow coefficient for these five simulations is about 33,700, which is approximately 10 percent higher than the USACE 30,500 cfs per ft. value, but 9 percent lower than the Wong (1991) value. All but the Simulation D flow coefficient are higher than the USACE value by about 13 percent, and all simulations are within the acceptable range of 30,000 to 40,000 cfs/foot.

IV.B.5.c. Mean Flow and Mean Slope

Regression lines fitted to the instantaneous data may not be an optimum measure of the flow-vs-slope relationship due to the ellipticity of the scatter plots associated with the time lag. To investigate the sensitivity of the model-predicted flow to mean slope, average slope and flow were calculated for the last two days of model output (50 hours, or 4 tidal cycles) for each simulation. The mean slope and flow for each model simulation are:

Simulation	Mean Slope (inches/mile)	Mean Flow (cfs)	Coefficient (cfs/ft of heat)
E	-0.391	-19,953	45,973
D	+0.239	+6,484	24,441
C	-0.359	-18,585	46,639
B	-0.412	-17,319	37,870
A	-0.553	-24,970	40,479

A regression of these means yields a flow sensitivity of 40,904 cfs per foot of head if the regression is forced to pass through the origin, which is a physically reasonable presumption (no slope equals no flow). This mean flow sensitivity is higher (more flow per unit forcing) than the USACE value by 34 percent, but it is close to the acceptable range.

IV.B.5.d. Peak Flow and Slope

To further investigate the model's predicted flow sensitivity, peak values of flow and slope within each tidal cycle were extracted from the model's output time series for Simulation E. These peak values generally did not coincide in time, due to the time lag in flow response. The peak flow and slope values exhibit a much more linear relationship, as expected since the time lag has been ignored. The peak flow coefficient is 39,619 cfs per foot for eastward peak flows, and 36,941 cfs per foot of height for westward peak flows. The average of these values is about 25 percent higher than the USACE value and is well within the acceptable range. Because the time lag is ignored, these coefficients probably represent an upper bound on instantaneous flow sensitivity.

IV.B.5.e. Conclusions Regarding the Model's Representation of Flow in the C&D Canal

The RMA-10 model predicts generally higher flow in the C&D Canal per unit of sea surface slope than the USACE value, but it is close to the Wong (1991) estimate. The difference in flow coefficient is about 10 percent based on instantaneous model outputs, and is somewhat higher when evaluated in terms of mean flow and mean slope, or peak flow versus peak slope. This suggests that the model's bottom friction coefficient in the Canal may be slightly low. However, this small difference will have little influence on the Station's thermal plume. The Canal flow is only a small fraction of the River flow; hence, any error in the flow in the River flow due to a small error in the modeled Canal flow will also be small.

Substantial flows result from relatively small changes in the along-Canal slope. Simulations B, C, and E all exhibited strong westward (negative) mean flows of about 17,000 to 20,000 cfs in the Canal, due to the choice of western boundary condition, corresponding to mean slopes of about -0.35 to -0.40 in/mi. Simulation D had a weak eastward flow of about 6,500 cfs, corresponding to a mean slope of about +0.24 in/mi. The difference between these eastward and westward flow simulations is about 25,000

cfs, corresponding to a change in the hydraulic gradient of 0.62 in/mi (0.67 ft head change).

Subtidal sea-level differences from one end of the Canal to the other can be larger than 1.3 ft (40 cm) (Wong, 1990). Because such sea-level differences can cause significant flows in the Canal, it is important that the western Canal boundary condition should be as accurate as possible. No observation of sea-level data at Courthouse Point or any other location near the Canal is available except during the Two-Unit Survey (Exhibit E-1-3); these data were used for model calibration. For this reason, all other model simulations used extrapolated western C&D boundary time-series that were created using a frequency-dependent transfer-function method. Data used for the extrapolated boundary condition were taken from NOAA measured tide observations at Baltimore, Havre de Grace, or Tolchester Beach, DE depending on data availability. As reported by Wong (1991), subtidal sea-level variability is essentially constant and in phase over the entire upper part of Chesapeake Bay. Amplitude and phase changes are significant at semidiurnal periods, and the transfer function analysis accounted for these differences.

IV.C. Adequacy of Data and Models Towards Understanding of River Processes at the Station

The modeling effort and the field studies that support it are focused on the thermal plume ΔT , not specifically on improving the understanding of estuarine dynamics. The RMA-10 model is calibrated to achieve good agreement with observed tide heights and plume characteristics near the Station, and is not formulated or tuned to represent Estuary-wide physical processes. Nevertheless, the calibrated model reproduces observable physical processes in the Delaware Estuary remarkably well within the limits of the model parameterization. The physical-process analysis of Section IV.B. has shown that the combined model performs well in terms of its basic function of predicting the advection and dispersion of the thermal plume from the Station. As with all numerical models, however, differences between modeled and real processes exist. These differences and their importance in terms of predicted plume extent are summarized below.

IV. C. 1. Tidal Hydrodynamics

The model reproduces the basic propagation of tide height up the Estuary quite well, not only in the vicinity of the Station where it is calibrated to agree with the total tidal amplitude, but at other locations more than 9 miles upstream and downstream from the Station as well. Modeled total tide height is accurate to within a few percent, and the accuracy of each tidal constituent is within about ± 5 percent.

Observational data on currents are available only near the Station. At this location, modeled currents agree with observed currents in terms of direction, timing, and the variation of speed over time within each half cycle. The model underestimates peak flood speeds at this location by about 10 percent, and overestimates peak ebb speed by the same amount. This suggests that modeled particle displacement over a tidal cycle, which is an important element for predicting the maximum extent of the Station's plume, might also be accurate to about ± 10 percent. However, due to the sparseness of velocity

observations, and the strong spatial gradients in velocity, the observation at this single point off the Station cannot be generalized to the entire River surrounding the Station.

The modeled tidal phase lags the current observations by a fraction of an hour at the Station. This is not important in terms of local water particle displacement, but may be related to small differences between the model and observations at other locations, such as Reedy Point near the C&D Canal. The model does not reproduce the observed slight decline (about 5 percent) in tidal amplitude near the C&D Canal. This suggests that tidal currents, which are closely related to tide height, may also have an uncertainty of about ± 5 percent north of the Station.

IV. C. 2. Ambient Temperature and Salinity

The model reproduces the general observed longitudinal (along-channel) temperature and salinity gradients. The modeled temperature and salinity patterns are smoother than the observations, and do not contain the vertical stratification that exists in the Estuary south of the Station. As a result, modeled temperature and salinity fluctuations due to tidal advection of these gradients tend to be underestimated. When averaged over multiple tidal cycles, the model reproduces the observed pattern of higher salinity at the center of the channel, with lower-salinity water tending to hug the shores. The modeled salinities are lower than tidally averaged observations at most instrument locations, and show a region of relatively fresh water extending south past the Station, a feature not observed to the same degree in nature.

In general, the three-dimensional RMA-10 model domain, which is the region around the Station, exhibits little vertical stratification of the ambient water. In the region south of the Station, where stratification is present in nature, the 3-D model's low stratification results from the use of a 2-D schematization for lower Delaware Bay, and the imposition of a vertically homogeneous internal boundary condition at the junction of the 2-D and 3-D model domains, about 15 miles south of the Station. North of the Station, the absence of stratification is real, and is due to the low salinity and the intense vertical mixing of the Estuary there. Salinity is low everywhere in the upper Estuary, and is typically near zero in the River north of the Station. Density effects due to stratification are, therefore, negligible in comparison to inertial and frictional effects, in both the model and the observations. This implies that the modeled displacement of heated water will be unaffected by the model's representation of the salinity and density structure in the region well south of the Station.

IV. C. 3. Thermal Discharge Plume Dynamics

The observations made using both moored instruments and vessel-mounted survey instruments during the Two-Unit Survey show that the thermal plume from the Station surfaces close to the discharge, and is vertically well mixed in a region extending at least 500 feet from the discharge. These observations strongly support the concept, embedded in the revised CORMIX formulation, of a vertically homogeneous thermal plume in the near- and intermediate-field regions, rather than a surface plume as previously used in the Station's thermal discharge modeling.

The observations also show that the real plume has some tendency to float, due to its buoyancy, as it spreads beyond the ZIM, becoming wider and warmer at the top than at the bottom. The plume cools as it entrains ambient water and becomes wider overall. During running flood and ebb phases of the tide, when the currents are strong and bottom friction and mixing are high, the plume does not appear to separate from the bottom, so its core remains vertically homogenous even out to distances of several thousand feet. Under these conditions, the plume develops stratification at its edges as the top widens more than the bottom, but the stratified region remains small compared to the width. Observations at mooring E under flood conditions show that the plume's stratified edge is only a few hundred feet wide. Although RMA-10 incorporates buoyancy effects, it cannot be expected to reproduce such fine-scale stratification due to its limited spatial grid resolution, therefore it can not show stratification of the plume edge at these intermediate distances. At greater distances, where RMA-10's horizontal resolution is adequate to resolve the horizontal thermal gradients, dynamical considerations suggest that the plume's buoyancy becomes negligible, thus RMA-10's vertically homogeneous prediction is correct at these greater distances as well.

During slack water, the plume's behavior is dominated by buoyancy and momentum effects as well as by the spatially erratic slack currents. The initial momentum of the outfall (which is not modeled in RMA-10), the plume's tendency to float, and the absence of strong current-generated mixing combine to create a highly inhomogeneous surface plume, which spreads across the river to distances of nearly a mile. RMA-10 is not optimized to predict the characteristics of the slack-current plume which exists only during brief periods and does not represent the limiting condition for the Station's operating permit. CORMIX and Linkage provide physically reasonable approximations to the behavior of the plume in the near-field, where buoyancy effects are not relevant.

In summary, the observations support the near- and intermediate-field formulations of the combined CORMIX, Linkage, and RMA-10 model. Although the exact plume trajectory predicted by RMA-10 differs in minor detail from the observations, the observations suggest that the modeled magnitude and extent of the excess temperature due to the Station are reasonable.

IV. C. 4. Tidal Marsh Heat Exchange

Observations show significant outflow of heated water from the marshes on the outgoing tide during sunny days when the ebb occurs in the afternoon or early evening. For example, temperature increments of up to 5°C (6.3°F), unrelated to the thermal discharge from the Plant, are observed north of the Station (near Salem River) and the warm water extends more than 1,000 ft offshore. Excess temperatures are also seen under similar conditions at marsh outlets (closer to the Station within the model domain), such as Alloway, Hope, and Mad Horse creeks, although the excess temperatures are not as high there. The RMA-10 model parameterizes heat transfer from the sun and the atmosphere in the simplified marsh, but the actual process is complex. The model gives accurate predictions for Hope Creek marsh, the smallest and closest of the modeled marshes. For

Alloway Creek and Mad Horse Creek marsh areas, the model's prediction is less accurate although the heat flux components are the same. This response difference may be a result of the approximations made to simulate some aspects of marsh processes, and also may result in part from entry of a low- ΔT portion of the Station's ebb plume into Hope Creek Marsh, which the model predicts accurately. The RMA-10 formulation includes only the marshes surrounding the Station on the east side of the River, and does not attempt to model temperature variability associated with marsh heat-exchange processes in other marshes at greater distances from the Station.

The model's inclusion of heat-exchange processes in the nearby marshes contributes to the overall Estuary heat balance, particularly at the eastern edge of the model domain where the thermal plume from the Station is located.

The model predicts that part of the thermal plume spreads into the marshes on the flood tide, particularly Hope Creek, where the excess heat becomes thinly spread due to the shallowness of the water. The marsh surface area contributes significantly to the exchange and dissipation of the plume's heat to the atmosphere.

IV. C. 5. Exchange with Chesapeake Bay via the C&D Canal

Historical studies have shown that flow through the C&D Canal can contribute to the variability of sea level, currents, and water properties in upper Delaware Bay. The flow in the Canal is sensitive to the sea-level difference (hydraulic gradient) between its eastern and western ends. The model's skill in reproducing the observed flow-versus-head relationship in the Canal has been assessed for instantaneous, mean, and peak flow conditions, and is found to be in general agreement with the range of historical evaluations, although it tends to exhibit more flow for a given pressure head than most historical estimates by about 10 percent.

Given that the model's response to pressurehead forcing of the Canal is reasonably correct, the effect of the Canal on modeled currents in Delaware Bay will depend mainly on correct specification of the boundary condition at the Canal's western end, combined with correct modeling of sea level at the eastern end. If sea level at both ends is correct, then the Canal's effect on particle displacement in the River near the Station must also be correct. Sea level at the eastern end of the Canal is not an imposed external boundary condition; it is predicted by the model. Accurate sea-level information at the Chesapeake Bay end, including both tides and subtidal variability, is therefore essential. Because sea-level measurements at the end of the Canal in Chesapeake Bay are not available for the time periods of the same model simulations, time-series of predicted sea level were created from available data at nearby locations using a transfer function approach to ensure adequate accuracy.

In summary, the physical process analysis of this Section has shown that the modeling approach adopted for thermal plume prediction correctly represents most of the basic physical processes in the Estuary. Confidence can, therefore, be placed in the model's prediction of plume characteristics and ΔT fields.

V CHARACTERIZATION OF THE THERMAL PLUME AND BIOLOGICAL THERMAL EXPOSURE

Hydrothermal modeling was performed to achieve multiple objectives. The first was to provide thermal exposure information (i.e., temperature experienced by organisms over a period of time to support the biothermal assessment for the 316(a) Demonstration. The second was to provide a reliable means of characterizing the dimensions, behavior, and features of the thermal plume from the Salem Station's thermal discharge.

To assess the potential plume impact on the BIP (BIC) of the Estuary, the effect of plume temperatures on critical life history functions (survival, growth, migration, and reproduction) must be evaluated. Methods and criteria for biothermal assessments were initially formalized in USEPA's Draft §316(a) Guidance in 1974 (USEPA 1974), later updated in 1977.

The biological thermal exposure characterization supports the predictive section of the biothermal assessment. These thermal exposures for biota are developed upon a basic premise of the hydrothermal assessment (Appendix E Section V.E), that the spatial- and time-varying water temperature distributions can be differentiated into two components: (1) the ambient temperature in the Estuary, which varies strongly with time and somewhat less strongly with space; and (2) the thermal plume-induced ΔT (increase in temperature above the ambient temperature), which varies strongly with space, but less strongly with time.

Based on this differentiation of water temperatures in the Estuary, the hydrothermal modeling conducted for this Demonstration (CORMIX and RMA-10) has focused on mapping ΔT distribution accurately within the near-field Zone of Initial Mixing (ZIM), transition zone, and far-field. Separate modeling based on thermal heat transfer equations (the Absolute Temperature Model or ATM) has been developed to estimate ambient temperatures throughout the remainder of Estuary. Integration of these three models provides an estimate of temperature at any point and time within the Estuary; this integrated model is the Total-Temperature Model (TTM). The ATM estimates long-term ambient temperatures near the Station making projections of temperatures over the next (a fifty year period which is much longer than pre-operational historical records for this area). The CORMIX and RMA-10 combination provides ΔT maps for various configurations of Station operation and representative forcing (or boundary) conditions such as river inflow, C&D Canal flow, tidal range, and surface heat exchange.

Various biological thermal exposures rely on different combinations of these model outputs as described in Section V.F.1. Section V.F.2 describes the models and methodology used to produce the thermal exposures. Section V.F.3 describes the approach used to define the hypothetical biological worst-case scenario. Section V.F.4 describes the biological thermal exposures themselves, and explains their results.

The major classes of hydrothermal information prepared for this Demonstration are characterization of thermal and velocity exposure within the ZIM; characterization of

thermal exposure due to plume entrainment; characterization of thermal exposure outside the ZIM; and seasonal temperature distribution. The characterization of the biological exposure within the ZIM focuses on the volumes and areas associated with different isopleths of ΔT (lines joining equal values of ΔT) and isovels of velocity (lines joining equal values of velocity). These products provide methods for evaluating the exposure of organisms to high temperatures and velocities within the ZIM, where the flow is turbulent and temperature is high relative to ambient.

The ZIM is defined in Section III.B as "that area of the receiving waterbody in which discharge-induced momentum produced by Salem's thermal discharge creates water currents exceeding ambient values, resulting in rapid mixing and dilution.

The characterization of thermal exposure due to plume entrainment organisms that are passively entrained along the plume centerline. It provides time-exposure plots identifying the ΔT within the plume centerline for both a biological worst case condition and a less conservative (lower ΔT) case.

Certain aspects of the biothermal assessment require characterization of the plume outside the ZIM. Maps of river temperature at the surface, along the bottom, and across the channel are used to evaluate impact on the BIC. Potential temperature effects in marsh creeks and on shore habitats are estimated by calculating plume temperatures of the plume where it meets the shoreline and marsh creek mouths.

The biothermal assessment also requires knowledge of the total temperature. Total temperature at any time is a function of seasonally-dependent temperatures plus the mapped ΔT of the plume. Temperature statistics, including seasonal temperature distribution, were compiled for seasonal and long-term (decadal) variability to support this biothermal assessment.

Rationales for developing biological thermal exposure products are described further in Section V.F.1.

E-2 REFERENCES

- Abraham, D.D. 1991. Analysis and Verification of a Three-Dimensional Hydrodynamic Numerical Model. MS Thesis. Texas A&M University, 93pp.
- Adams, E. Eric. 1982. Dilution Analysis for Unidirectional Diffusers. *Journal of the Hydraulics Division Proceedings of the ASCE*, 108(HY3). March.
- Akar, P.J. and G.H. Jirka. 1990. CORMIX2: An Expert System for Hydrodynamic Mixing Zone Analysis of Conventional and Toxic Multiport Diffuser Discharges (July Draft). Environmental Research Laboratory, U.S. Environmental Protection Agency. Athens, Georgia.
- Boyle, G.V., I.A. Valioulis, and L. Meiorin. 1993. Estimation of far-field dilution in ocean waste discharges. *ASCE, J. Watrwy., Port. Cstle. And Oc. Engrny.*, 199:15-29.
- Boyd, M.B., W.H. Bobb, C.J. Huval, and T.C. Hill. 1973. Enlargement of the Chesapeake and Delaware Canal-hydraulic and mathematical model investigation. Technical Report H-73-16, U.S. Army Waterways Experiment Station.
- DiLorenzo, J.L., P. Huang, M.L. Thatcher, M. ASCE, and T.O. Najarian. 1993. Dredging impacts on Delaware Estuary tides. In *Estuary and Coastal Modeling III. Proceedings of the 3rd International conference* (Spaulding, M.L., K. Bedford, A. Blumberg, R. Cheng, and C. Swanson, eds.), 86-104. Waterway, Port, Coast and Ocean Div./ASCE.
- Doneker, R.L. 1998. Personal Communication. Letter to Maureen Vaskis. Portland Oregon. 13 November.
- Doneker, R.L. 1999. Personal Communication. Letter to Maureen Vaskis. Portland, Oregon. 26 February.
- Fischer, H.B., E.J. List, R.C.Y. Koh, J. Imberger, N.H. Brooks. 1979. Mixing in Inland and Coastal Waters. Academic Press, New York.
- Friedrichs, C.T., and D.G. Aubrey. 1988. Non-linear tidal distortion in shallow well-mixed estuaries: a Synthesis. *Estuarine, Coastal, and Shelf Science* 27:521-545.
- King, I.P. 1985. Strategies for finite element modeling of three Dimensional Hydrodynamic systems. *Advances in Water Resources* 8:69-76.

- King, I.P. 1999. Users, Application and References for the RMA Suite of Finite Element Models. February.
- King, I.P., and J.F. DeGeorge. 1995. Multi-dimensional modeling of water quality using the finite difference method. In *Estuary and Coastal Modeling III. Proceedings of the 3rd International Conference* (Spaulding, M.L., K. Bedford, R. Cheng, and C. Swanson, eds.), 340-354. Waterway, Port, Coastal and Ocean Div./ASCE.
- King, I.P., and R.R. Rachiele. 1989. Simulation of impact of channel widening in San Francisco Bay using a three dimensional stratified flow model. Prepared for Waterways Experiment Station, U.S. Army Corps of Engineers.
- King, I.P., and L.C. Roig. 1988. Two-dimensional finite-element models for flood plains and tidal flats. Proceedings of Computational Methods in Flow Analysis (Niki, H., and M. Kawahara, eds.), Okayama University of Science, Japan.
- Lawler, Matusky & Skeller Engineers (LMS). 1990. Modeling and Data Assessment of Dilution of Chambers Works Discharge in the Delaware River. Task A III Report.
- LMS. 1995a. ConEd Power Plant Heat Load Effects on Dissolved Oxygen in the East River. Performed for Consolidated Edison. Pearl River, New York. April.
- LMS. 1995b. New York City Department of Environmental Protection Kensico Reservoir Water Pollution Control Study Contract CRO-233 Task 5.5 Summary Report Reservoir Water-Quality Modeling Kensico Reservoir Water Pollution Control Study Contract CRO-223. Prepared for: New York City Department of Environmental Protection. Pearl River, New York. 27 December.
- LMS. 1996. New York City Department of Environmental Protection Kensico Reservoir Water Pollution Control Study Contract CRO-233 Task 5.5 Reservoir Water-Quality Modeling Kensico Water Quality Model Users Manual. Prepared for: Bureau of Water Supply. Pearl River, New York. 29 February.
- Lee, J.H., G.H. Jirka, and D.R.F. Harleman. 1977. Modeling of Unidirectional Thermal Diffusers in Shallow Water. Ralph M. Parsons Laboratory For Water Resources and Hydrodynamics. Department of Civil Engineering, MIT. Report No. 228. Pp89-116 and 228-256.
- MacAthur, R.C., J.R. Dexter, D.J. Smith, and I.P. King. 1990. Two dimensional finite element simulation of the flooding characteristics in Kawainui Marsh, Hawaii. Proceedings of the 1990 ASCE Conference of Hydraulic Engineering, San Diego, California.

- McAnally, W.H., J.V. Letter, J.P. Stewart, W.A. Thomas, and N.J. Brogdon. 1994. Application of Columbia hybrid modeling system. *ASCE J. Hydr. Engrn.* 110:627-642.
- Norton, W.R., I.P. King, and G.T. Orlob. 1973. A finite element model for lower granite reservoir. Report to the U.S. Army Corps of Engineers, Walla Walla District.
- Pierson, W.L., and I.P. King. 1995. Coastal ocean model performance in eastern Australia. In *Estuary and Coastal Modeling Proceedings of the 4th International Conference* (Spaulding, M.L., and A. Cheng, eds.), 632-643. Waterway, Port, Coastal and Ocean Div./ASCE.
- Pritchard, D.W., and G.B. Gardner. 1974. Hydrography of the C&D Canal. Technical Report No. 85, Chesapeake Bay Institute, The Johns Hopkins University, Baltimore, MD. February.
- Ramsey, J.S., R.P. Hamilton, and D.G. Aubrey. 1995. Nested three-dimensional hydrodynamic modeling of the Delaware Estuary. In *Estuary and Coastal Modeling, Proceedings of the 4th International Conference* (Spaulding, M.L., and R.T. Cheng, eds.), 53-65. San Diego, California, 26-28 October 1995. Coastal Zone Management Committee, Waterways, Ports, Coastal and Ocean Division, and the Computational Hydraulics Committee of the Hydraulics Division, ASCE.
- Shrestha, P.L., and G.T. Orlob. 1996. Multiphase distribution of cohesive sediments and heavy metals in estuarine systems. *ASCE, J. Env. Engrn. Div.* 122:730-740.
- Thatcher Research Associates, Inc., LMS, and J.E. Edinger Associates, Inc. 1993. Appendix E Supplemental Information on Thermal Studies at Salem. 16 September.
- Thomas Reed Publications Inc. 1998. Reed's Nautical Almanac North American East Coast 1998. 25th Annual Edition. (Ellison, B., ed.). Boston.
- U.S. Environmental Protection Agency (USEPA). 1985. Rates, Constants, and Kinetics Formulations in Surface Water Quality Modeling (Second Editions). Athens, Georgia. June
- USEPA. 1990. Draft Technical Support Document for Water Quality-Based Toxics Control. Office of Water. Washington, D.C. pp121-182. April.
- Wong, K.C. 1990. The current and sea level variability in the Chesapeake and Delaware Cana. *Journal of Geophysical Research* 95(C10):18,343-18,352.

Wong, K.C. 1991. The Response of the Delaware Estuary to the Combined Forcing from Chesapeake Bay and the ocean. *Journal of Geophysical Research* 96(C5):8797-8809.

E-2 Table III-1. Synthesis of the basic Components of the Modified CORMIX Approach (in sequential order of application)

Item/Step Number	Parameter/Concept	Actual Discharge	Virtual Discharge ¹	Notes/Comments
1	Planar model coordinate system (x, y)	The CORMIX coordinate system's origin (x=0, y=0) is the center of the six outfall pipes, which are simulated as a line diffuser with six ports in CORMIX2. The x-axis is defined parallel to the direction of the ambient current (150° and 330° true north for the ebb and flood tides, respectively). The y-axis, by definition, is normal to the x-axis.		See Figure III-9
2	Predicted end-point along the y-axis	Termed Ys, which is equal to (Ld*sin(sigma))/2	Termed Yf, which is essentially where the ambient cross-flow momentum equals 2 times the discharge momentum. $Yf = (Qo * Uo * \sin(\sigma)) / (2 * Hd * Ua^2)$	The eqn. for Ys is from (E. Adam ref ¹) The Yf formulation is from the original CORMIX code
3	Y-component of plume velocity (Uy)	At end of pipe $Uy = Uo * \cos(\gamma)$ At Ys; $Uy = U2$ (plume velocity at the end of the acceleration region).	At end of pipe $Uy = Uo * \cos(\gamma) * \text{Calibration factor (0.8)}$. At Yf, $Uy = 0$ (by definition, plume momentum is fully dissipated).	An empirical quadratic interpolation is applied from the end-of pipe to the respective simulation end-point. Uy (average) equals the integral of Uy from Yo to Yf
4	Cumulative travel time (T)	$Ts = Ys / Uy$ (average from above)	$Tf = Yf / Uy$ (average from above)	Where time = distance / velocity
5	X-component of plume velocity (Ux)	Given that the x-axis is parallel to the ambient current direction (where Ua = current speed) and approximately normal to the discharge flow, Ux is approximated as the ambient current speed.		For simplicity, the lateral plume velocity is assumed to be instantaneously equal to Ua
6	Predicted end-point along the x-axis	$Xs = Ua * Ts$	$Xf = Ua * Tf$	Where X is equal to speed * travel time
7	Dilution (S)	St = dilution for a diffuser in a cross-flow. So = Dilution for a diffuser in stagnant water. $(St-1) = (So-1) / \text{dilution reduction factor due to the cross-flow effect (termed } Rs)$		The new $(St-1)/(So-1)$ ratio, to prohibit unrealistic dilutions (< 1), is a logical extension of the original St/So formulation
7a	Dilution [nominal]; for a diffuser in stagnant water	$So = (Hd * Uo * Ld / 2 * Qo)^{0.5}$	$So = (Hd * Uo * Ld / 2 * Qo)^{0.5}$	Hd = height of the water column Uo = discharge velocity Ld = length of the simulated diffuser Qo = discharge flow
7b	Cross flow effect [nominal]; (Rs)	$Rs = [1 + (5 * \cos(\text{alignment angle}) * Ua^2 * A) / (Qo * Uo)]^{0.5}$	$Rs = [1 + (5 * \cos(\text{alignment angle}) * Ua^2 * A) / (Qo * Uo)]^{0.5}$	Original CORMIX code with correction to cosine.

¹ For the virtual discharge simulation, the diffuser length (Ld) and initial discharge velocity (Uo) were adjusted by factors of 3.3 and 0.65, respectively. These adjustments account for the plume's bottom and surface deflections, which in turn, increase plume spreading (as simulated by increasing Ld) and reduce plume momentum (as simulated by decreasing Uo).

Item/Step Number	Parameter/Concept	Actual Discharge	Virtual Discharge ¹	Notes/Comments
7c	Small correction to St for low dilutions	The original derivation of St assumed that $S \approx S-1$ (i.e., the applied dilutions would be relatively large). Given that the dilutions for this application are on the order of 2:1, this assumption was re-evaluated. Based on a re-derivation without the above assumption (i.e., $S \neq S-1$), a dilution correction constant of +0.27 was determined and applied.		Re-derivation performed by paper's author.
8	Plume thickness at surfacing (BV)	BV = Hd (depth of the water column)		As per the original CORMIX code
9	Plume width at surfacing (BH)	BH = $(Q_0 * S) / (Hd * U_2)$ (plume velocity at X_s, Y_s)	BH = $(Q_0 * S) / (Hd * U_a)$; where plume velocity at X_f, Y_f is by definition the point when plume momentum is fully dissipated.	Via the conservation of flow/heat flux
10	Incremental Time from discharge to end-point (Ti)	Ti = Linear interpolation from To to Ts	Ti = Linear interpolation from To to Tf	Required input for subsequent vector component analysis
11	Incremental Xi	Ti * Ux (=Ua) for To to Ts	Ti * Ux (=Ua) for To to Tf	Vector component analysis provides for a non-linear plume trajectory.
12	Incremental Yi	Ti * Uy (above) for To to Ts	Ti * Uy (above) for To to Tf	
13	Incremental plume velocity (U _{pi})	$U_{pi} = (U_x^2 + U_y^2)^{0.5}$ for To to Ts	$U_{pi} = (U_x^2 + U_y^2)^{0.5}$ for To to Tf	
14	Plume travel distance along centerline (Di)	$D_i = (\Delta X^2 + \Delta Y^2)^{0.5}$ for To to Ts	$D_i = (\Delta X^2 + \Delta Y^2)^{0.5}$ for To to Tf	Pythagorean theorem
15	Incremental Si	Si = quadratic interpolation from To to Ts	Si = quadratic interpolation from To to Tf	As per the original CORMIX code
16	Incremental BHi	BHi = Linear interpolation from To to Ts	Via the conservation of flow/heat flux; $BH_i = (Q_0 * S_i) / (BV_i * U_{pi})$;	All incremental model predictions maintain the principle of heat and flow conservation.
17	Incremental BVi	Via the conservation of flow/heat flux; $BV_i = (Q_0 * S_i) / (BH_i * U_{pi})$ from To to Ts	Bvi = Linear interpolation from To to Tf	
18	Synthesis of results	The above actual and virtual discharge simulations yield two sets of predictions from the point of discharge to their respective end-points (X_s, Y_s or X_f, Y_f). While the maximum departure between the two predicted plume trajectories was approximately 1 meter, as a finishing step the two results are integrated into one continuous prediction. Thus, the real diffuser results are used up until the surfacing location. An interpolation was then performed from the surfacing location to the virtual diffuser endpoint of X_f, Y_f , with the plume fully mixed vertically in the water column.		Between the surfacing location and end of momentum, the resultant quadratic interpolation conserved both flow and heat flux.

E-2 Table III-2. Overview of CORMIX Inputs for the 2-Unit Survey Model Calibration (29 May 1998)

Input Requirement	Ebb	EOE	Flood	EOF	Source
Ambient velocity (m/sec)	0.441	0.508	0.509	0.113	1
Approach salinity (‰)	1.084	0.905	5.026	5.524	2
Approach temperature (°C)	21.72	22.13	22.50	22.53	2
Average or characteristic depth of the ambient water body (m)	7.48	8.41	9.20	8.74	3
Local depth near the discharge (m)	9.46	10.39	11.18	10.72	4
Angle sigma	276.5	96.5	96.5	276.5	5
Discharge temperature (°C)	30.37	30.23	31.13	31.00	6
Discharge salinity (= Approach salinity (‰))	1.084	0.905	5.026	5.524	2
Discharge ΔT (°C)	8.65	8.10	8.63	8.47	7
Discharge flow (m ³ /s)		136.4			8
Length of diffuser line (m); for the actual and virtual simulations		26.83 (88.54)			5
Average port diameter (m); for the actual and virtual simulations		3.05 (3.78)			5
Number of discharge openings		6			5
Discharge port orientation		Unidirectional			5
Diffuser array type		Same direction			5
Width of the channel in the vicinity of the discharge (m)		4600			9
Clockwise angle between the diffuser and the ambient current, gamma (°)		6.5			5
Relative orientation angle between the port centerline and the diffuser axis, beta (°)		90			5
Vertical angle of discharge above the horizontal plane, theta (°)		0			5

^a The values are provided in metric units, as this is the input format for the CORMIX Model

Source:

1. Bottom ADCP Data for Ebb, EOE and FLD tidal phase. For EOF, average velocity as defined by the intercept of Yf and Average ambient velocity
2. Upstream moorings; mooring E for Ebb/EOF, mooring H for FLD/EOE
3. NOAA chart of the Delaware River, Smyrna River to Wilmington (# 12311) and tidal stage observation
4. PSE&G Plant drawing and tidal stage observation
5. PSE&G Plant drawing
6. PSE&G Discharge Monitoring Report
7. Discharge Temp. - Approach Temp
8. LMS Dye Survey + 4% for service water flow
9. NOAA chart of the Delaware River, Smyrna River to Wilmington (# 12311)

E-2 Table III-3. Overview of CORMIX Inputs for the 1-Unit Survey Model Verification (28 October 1997)

Input Requirement	Flood	Ebb	Source
Ambient velocity (m/sec)	0.57	0.46	1
Approach salinity (‰)	10.9	10.1	2
Approach temperature (°C)	13.8	14.0	2
Average or characteristic depth of the ambient water body (m)	8.89	7.80	3
Local depth near the discharge (m)	10.87	9.78	4
Angle sigma	96.5	276.5	5
Discharge temperature (°C)	19.54	19.69	6
Discharge salinity (= Approach salinity (‰))	10.9	10.1	2
Discharge ΔT (°C)	5.74	5.69	7
Discharge flow (m ³ /s)	86.71		8
Length of diffuser line (m); for the actual and virtual simulations	17.89 (59.04)		5
Average port diameter (m); for the actual and virtual simulations	3.05 (3.78)		5
Number of discharge openings	6		5
Discharge port orientation	Unidirectional		5
Diffuser array type	Same direction		5
Width of the channel in the vicinity of the discharge (m)	4600		9
Clockwise angle between the diffuser and the ambient current, gamma (°)	6.5		5
Relative orientation angle between the port centerline and the diffuser axis, beta (°)	90		5
Vertical angle of discharge above the horizontal plane, theta (°)	0		5

^a The values are provided in metric units, as this is the input format for the CORMIX Model
 Source:

1. Bottom ADCP Data
2. Upstream moorings; mooring E for Ebb and mooring H for FLD
3. NOAA chart of the Delaware River, Smyrna River to Wilmington (# 12311) and tidal stage observation
4. PSE&G Plant drawing and tidal stage observation
5. PSE&G Plant drawing
6. PSE&G Discharge Monitoring Report
7. Discharge Temp. - Approach Temp
8. LMS Dye Survey + 4% for service water flow
9. NOAA chart of the Delaware River, Smyrna River to Wilmington (# 12311)

E-2 Table III-4. Boundary Conditions for the Calibration of RMA-10 (May 1998)

Boundary	Data	Source	Sampling Frequency
Mouth of Delaware Bay	Tidal Elevations	NOAA (Lewes, DE, and Cape May Canal, NJ) with calculated offsets	30 minutes
	Temperature Salinity Concentration	MTMP MTMP	Average over flood duration Average over flood duration
Chesapeake and Delaware Canal	Tidal Elevation	MTMP	6 minutes
	Temperature	MTMP	6 minutes
	Salinity Concentration	MTMP	6 minutes
Delaware River - Trenton, NJ	Freshwater Flow	USGS (Trenton, NJ)	Hourly
	Temperature	USGS (Trenton, NJ)	Hourly
	Salinity	USGS (Trenton, NJ)	Hourly
Schuylkill River - Philadelphia, PA	Freshwater Flow	USGS (Philadelphia, PA)	Hourly
	Temperature	USGS (Trenton, NJ)	Hourly
	Salinity	USGS (Trenton, NJ)	Assumed freshwater
Ungaged Tributaries	Freshwater Flow	USGS drainage area ratios	Hourly
	Temperature	USGS (Trenton, NJ)	Hourly
	Salinity	USGS (Trenton, NJ)	Hourly
Water Surface	Meteorological Conditions (except dew point and cloud cover)	Salem Generating Station Meteorological Station	Hourly
	Dew Point, Cloud Cover	National Weather Service, Wilmington, DE	Hourly

E-2 Table III-5. Names and Drainage Areas of Ungaged Tributaries Used in RMA-10

Tributary Name	Drainage Area (mi ²)	Surface area of Delaware and drainage area of lesser tributaries (mi ²)	Adjusted Drainage Area (mi ²)
Assunpink Cr	91.4	-1.4	90.0
Crosswicks Cr	144	149	293
Neshaming Cr	232	131.4	363.4
Rancocas Cr	340	192.6	532.6
Chritina R	563	107	670.0
Salem R	117	178	295.0
Cohansey R	107	208.1	315.1
Maurice R	382	742.9	1124.9

E-2 Table III-6. Major Point Source Discharges of Heat for Calibration (May 1998)

Point Source	Discharge Flows (cfs)	Heat Load (MBTU/hr)
Hope Creek GS	67.41	59.96
Motiva Enterprises	597.22	1085.54
Dupont Chambers Works	50.59	46.47
Deepwater GS	286.39	656.24
Bayway Refining	156.19	353.36
PECO Eddystone	1463.59	1231.08

E-2 Table III-7. Data for Evaluating the Performance of RMA-10 for Calibration (May 1998)

Data	Source	Application	Period	Sampling Frequency
Tidal Elevations - City of Burlington, NJ	USGS	Tidal Hydrodynamics	21 May - 4 June	15 minutes
Tidal Elevations - Philadelphia, PA	NOAA	Tidal Hydrodynamics	21 May - 4 June	6 minutes
Tidal Elevations - Reedy Point, DE	NOAA	Tidal Hydrodynamics	21 May - 4 June	6 minutes
Tidal Elevations - Salem Generating Station	MTMP	Tidal Hydrodynamics	21 May - 4 June	6 minutes
Tidal Elevations - Woodland Beach, DE	MTMP	Tidal Hydrodynamics	21 May - 4 June	6 minutes
Mooring Network - Salinity, Temperature, Dissolved Oxygen	MTMP	Tidal Hydrodynamics Thermal Plume Dynamics	Appendix E II.D	10 minutes, 5 minutes
ADCP Mooring - Currents	MTMP	Tidal Hydrodynamics Thermal Plume Dynamics	21 May - 2 June	2.5 minutes
Shipboard Surveys - Currents - Temperatures, Salinity	MTMP	Tidal Hydrodynamics Thermal Plume Dynamics	29 May	<1 second for sampling period
Dye Tracer Study	MTMP	Thermal Plume Dynamics	27 May - 29 May	<1 second
Infrared Surveys	MTMP	Thermal Plume Dynamics	29 May	1 per tidal phase
Marsh Surveys - Shipboard Surveys of Temperature and Flows - Moorings Temperature, Salinity, and Dissolved Oxygen	MTMP	Thermal Plume Dynamics	30 May 1998 2 June 1998	<1 second

E-2 Table III-8. Coefficients Used in the Calibration of RMA-10 Model (May 1998)

Element Type	Region of Model	Turbulent Exchange		Turbulent Diffusion		Manning Roughness Coefficients		Friction Factor (unitless)	Shortwave Radiation Coefficient (unitless)
		Horizontal (sq.ft/sec)	Vertical (lb-sec/sq.ft)	Horizontal (sq.ft/sec)	Vertical (sq.ft/sec)	Bottom (unitless)	Shoreline (unitless)		
1	Upper Bay and main river	7189 - 26.2	0.2	1078 - 1.31	36.0 - 0.13	0.02250	0.00	10	1.0
2	Northern 2D extent	12962 - 901	0.2	1296 - 27.0	2.59 - 0.18	0.02350	0.04	10	1.0
3	Delaware Bay	27993 - 4896	0.2	8398 - 1469	28.0 - 4.90	0.02250	0.00	10	1.0
4	Discharge	126 - 99.5	0.2	126 - 99.5	12.6 - 10.0	0.02250	0.00	10	1.0
5	Lower 1D region of river	46958 - 683	0.2	4696 - 20.5	9.39 - 0.14	0.04163	0.08	10	1.0
6	Northern 1D extent	43344 - 24033	0.2	4335 - 721	8.67 - 4.81	0.03330	0.08	10	1.0
7	Hope Creek Jetty	557 - 47.4	0.2	857 - 72.9	0.43 - 0.04	0.10000	0.10	10	1.0
8	Sunken Ships Cove	905 - 120	0.2	41.8 - 5.52	0.70 - 0.09	0.03000	0.10	10	1.0
9	Discharge to Hope Creek	1928 - 79.7	0.2	89.0 - 3.68	1.48 - 0.06	0.01750	0.06	10	1.0
11	Salem River	12854 - 1696	0.2	1285 - 50.9	2.57 - 0.34	0.02250	0.00	10	1.0
12	Marsh Embayments	11054 - 999	0.2	1105 - 30.0	2.21 - 0.20	0.02500	0.00	10	0.7
13	Northern end of Artificial Is.	2739 - 221	0.2	82.2 - 2.21	2.74 - 0.22	0.01500	0.00	10	1.0
14	Nearfield region	1393 - 100	0.2	418 - 30.1	13.93 - 1.00	0.02250	0.00	10	1.0
15	Nearfield region	409 - 126	0.2	40.9 - 12.6	1.23 - 0.38	0.02250	0.00	10	1.0

E-2 Table III-9. Figures for Comparing Observed and Modeled Distributions of Surface Water Temperature for Calibration (May 1998)

Phase Tide (Time Interval)	Coverage	Figure Showing Observations	Figure Showing Model Results
Ebb (06:40-08:40)	± 6 miles	E-2 Figure III-62a	E-2 Figure III-66a
	Local	E-2 Figure III-62b	E-2 Figure III-66b
EOE (09:10-11:10)	± 6 miles	E-2 Figure III-63a	E-2 Figure III-67a
	Local	E-2 Figure III-63b	E-2 Figure III-67b
Flood (11:40-13:40)	± 6 miles	E-2 Figure III-64a	E-2 Figure III-68a
	Local	E-2 Figure III-64b	E-2 Figure III-68b
EOF (14:25-16:25)	± 6 miles	E-2 Figure III-65a	E-2 Figure III-69a
	Local	E-2 Figure III-65b	E-2 Figure III-69b

E-2 Table III-10. Boundary Conditions for the Verification of RMA-10 (October 1997)

Boundary	Data	Source	Sampling Frequency
Mouth of Delaware Bay	Tidal Elevations	NOAA (Lewes, DE, and Cape May, NJ) with calculated offsets	30 minutes
	Temperature Salinity Concentration	MTMP MTMP	Average over flood duration Average over flood duration
Chesapeake and Delaware Canal	Tidal Elevation	MTMP	5 minutes
	Temperature	USGS (Elk River, MD)	Hourly
	Salinity Concentration	USGS (Elk River, MD)	Hourly
Delaware River - Trenton, NJ	Freshwater Flow	USGS (Trenton, NJ)	Hourly
	Temperature	USGS (Trenton, NJ)	Hourly
	Salinity	USGS (Trenton, NJ)	Hourly
Schuylkill River - Philadelphia, PA	Freshwater Flow	USGS (Philadelphia, PA)	Hourly
	Temperature	USGS (Trenton, NJ)	Hourly
	Salinity	USGS (Trenton, NJ)	Hourly
Ungaged Tributaries	Freshwater Flow	USGS drainage areas ratios	Hourly
	Temperature	USGS (Trenton, NJ)	Hourly
	Salinity	USGS (Trenton, NJ)	Hourly
Water Surface	Meteorological Conditions (except dew point and cloud cover)	Salem Generating Station Meteorological Station	Hourly
	Dew Point, Cloud Cover	National Weather Service, Wilmington, DE	Hourly

E-2 Table III-11.
Major Point Source Discharges of Heat for Verification (October 1997)

Point Source	Discharge Flows (cfs)	Heat Load (MBTU/hr)
Hope Creek GS	65.52	10.77
Motiva Enterprises	645.18	1104.10
Dupont Chambers Works	59.88	32.42
Deepwater GS	208.72	653.83
Bayway Refining	149.69	293.79
PECO Eddystone	1068.64	330.62

E-2 Table III-12. Data for Evaluating the Performance of RMA-10 for Verification (October 1997)

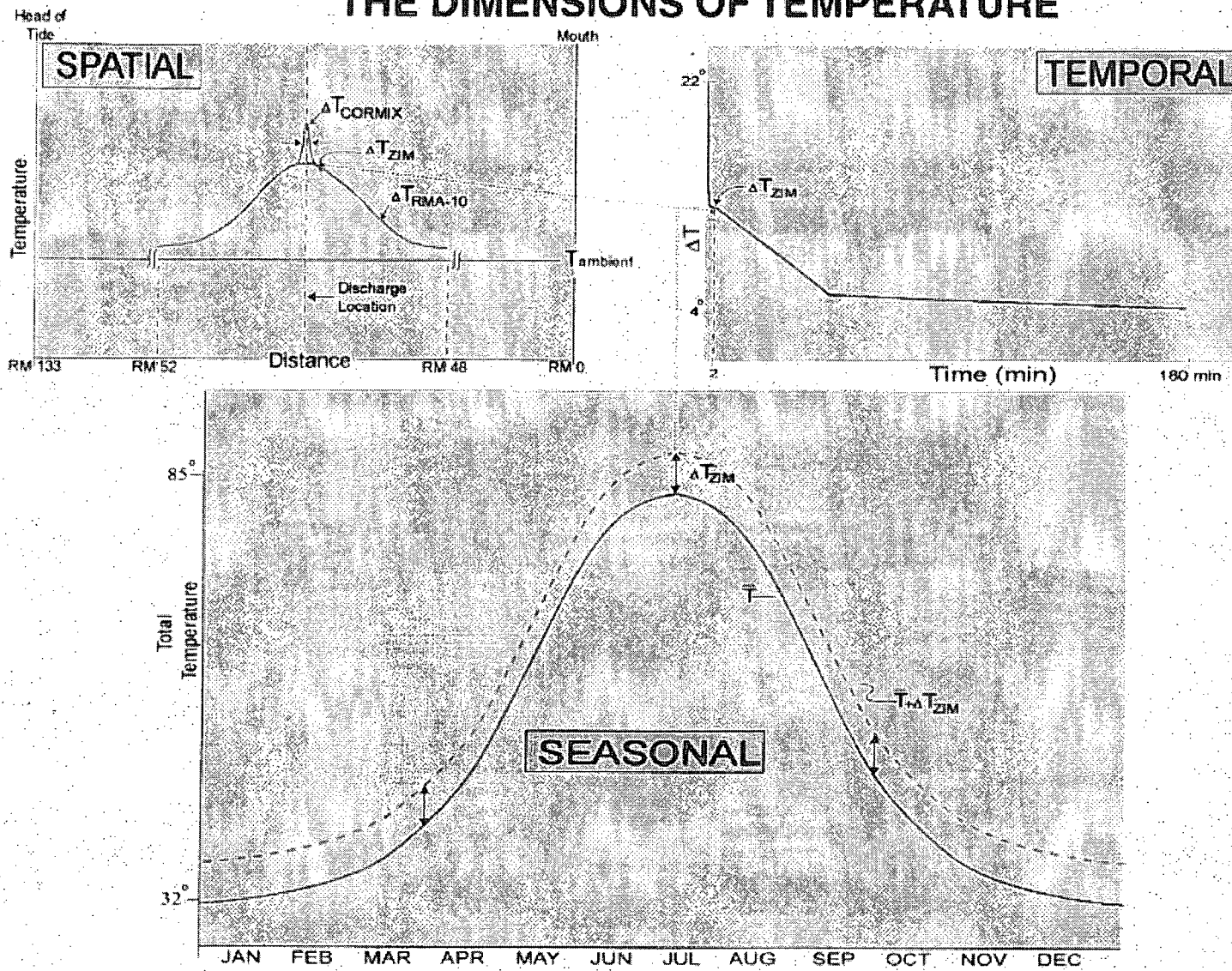
Data	Source	Application	Period	Sampling Frequency
Tidal Elevations - City of Burlington, NJ	USGS	Tidal Hydrodynamics	21 Oct - 1 Nov	
Tidal Elevations - Philadelphia, PA	NOAA	Tidal Hydrodynamics	21 Oct - 1 Nov	
Tidal Elevations - Marcus Hook, PA		Tidal Hydrodynamics	21 Oct - 1 Nov	
Tidal Elevations - Reedy Point, DE	NOAA	Tidal Hydrodynamics	21 Oct - 1 Nov	
Tidal Elevations - Salem Generating Station	MTMP	Tidal Hydrodynamics	21 Oct - 1 Nov	
Tidal Elevations - Woodland Beach, DE	MTMP	Tidal Hydrodynamics	21 Oct - 1 Nov	
Mooring Network - Salinity, Temperature, Dissolved Oxygen	MTMP	Tidal Hydrodynamics Thermal Plume Dynamics	Appendix E II.D	10 minutes, 5 minutes
ADCP Mooring - Currents	MTMP	Tidal Hydrodynamics Thermal Plume Dynamics	16 Oct - 18 Oct	2.5 minutes
Shipboard Surveys - Currents - Temperatures, Salinity	MTMP	Tidal Hydrodynamics Thermal Plume Dynamics	28 Oct	<1 second for sampling period
Marsh Surveys - Shipboard Surveys of - Temperature and Flows - Moorings - Temperature, Salinity, and - Dissolved Oxygen	MTMP	Thermal Plume Dynamics	29 Oct	<1 second

E-2 Table IV-1. Volume conservation in RMA-10 through exterior model boundaries over a 75-hour period (6 complete tidal cycles) during 24-26 May 1998.

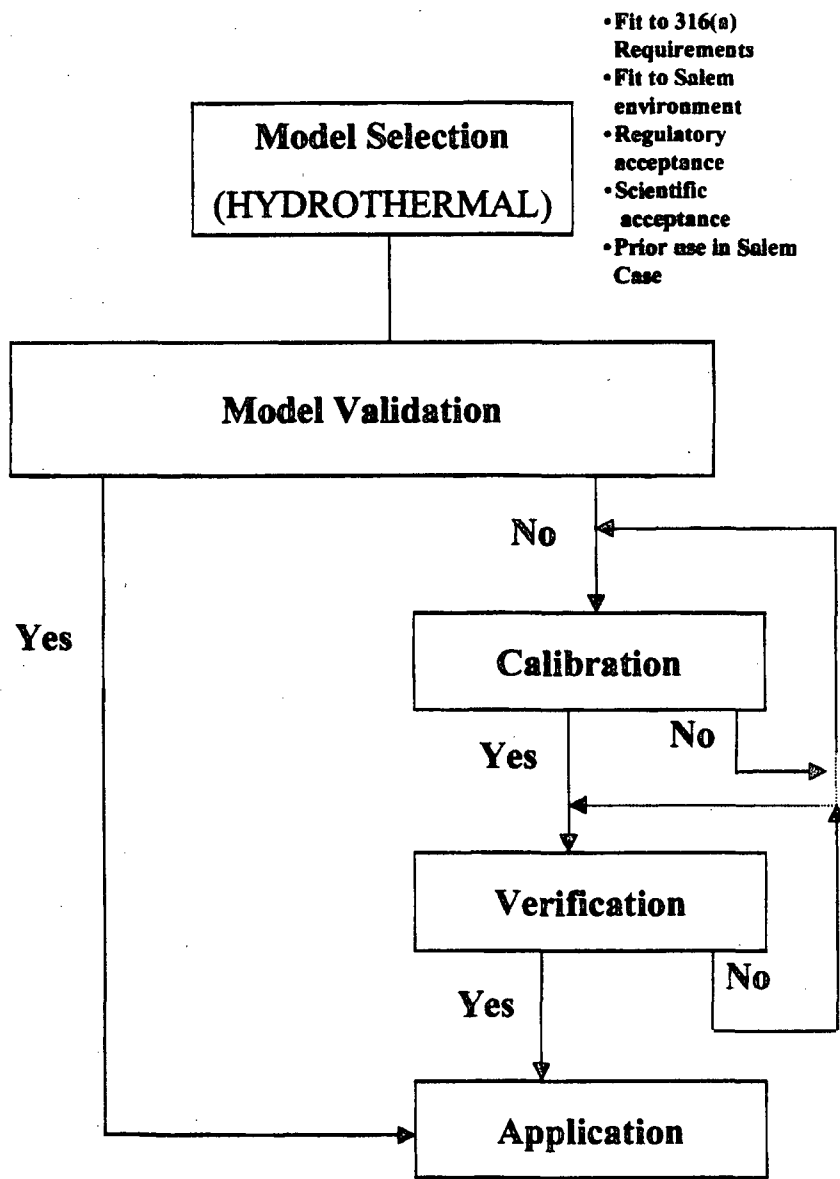
Positive values represent water flowing into the model

Continuity Line	TIDALLY AVERAGED VOLUME FLOW (6 cycle average) (millions of cu. ft.)		
	Total Volume per Tidal Half-Cycle Flood	Ebb	Net Volume per Tidal Cycle
Delaware River @ Trenton Boundary	0	416	413.54
Schuylkill River @ Philadelphia Boundary	0	112	111.28
C&D Canal Boundary (positive = eastward)	-1,309	1,334	24.52
Bay Boundary (Lewes/Cape May)	-126,429	125,881	-544.17
Net Inflow to Model Domain per Tidal Cycle = (Delaware River + Schuylkill River + C&D Canal + Bay Boundary)			5.17

THE DIMENSIONS OF TEMPERATURE

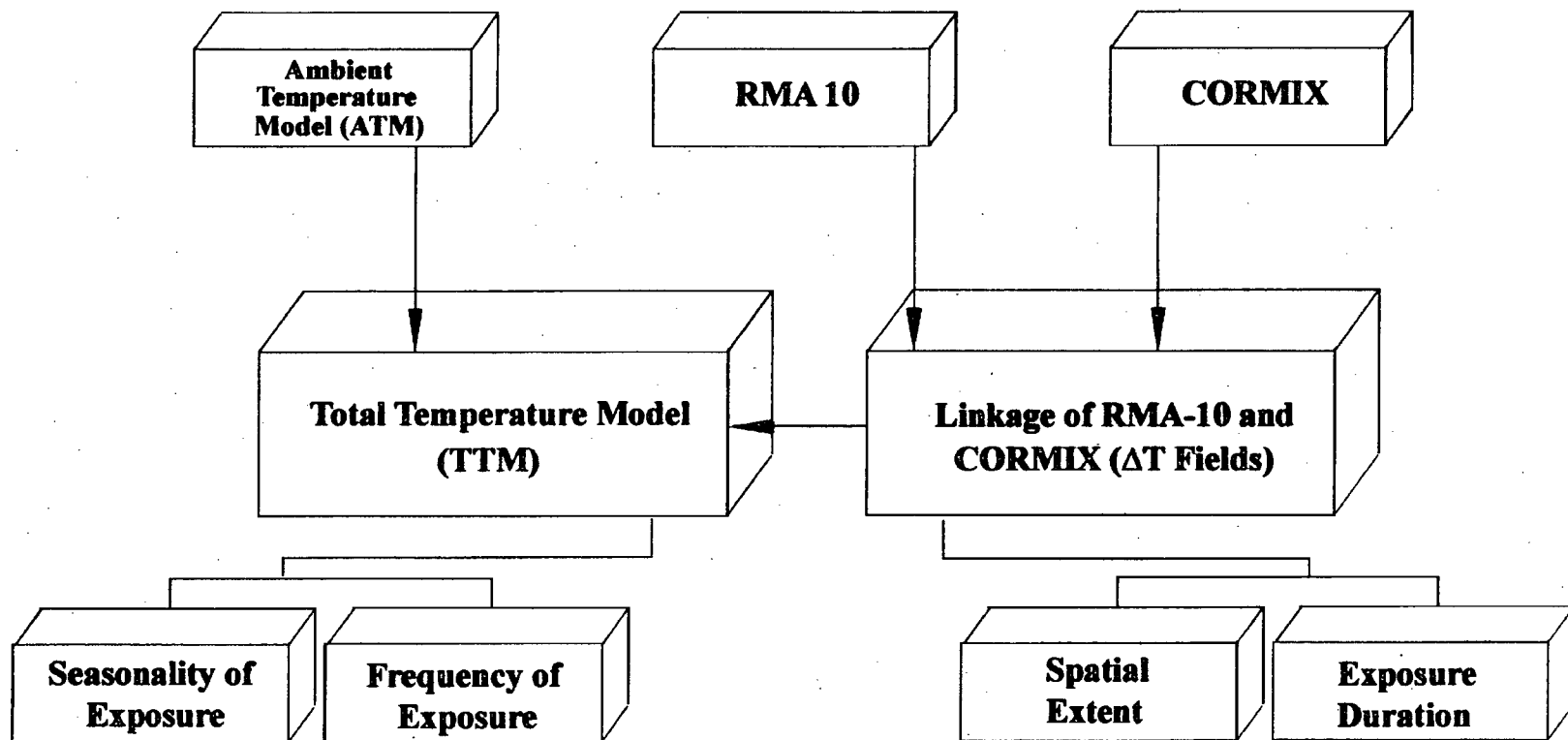


E-2 Figure III-1a. Components of the Total Temperature Model where \bar{T} represents $T_{ambient}$.

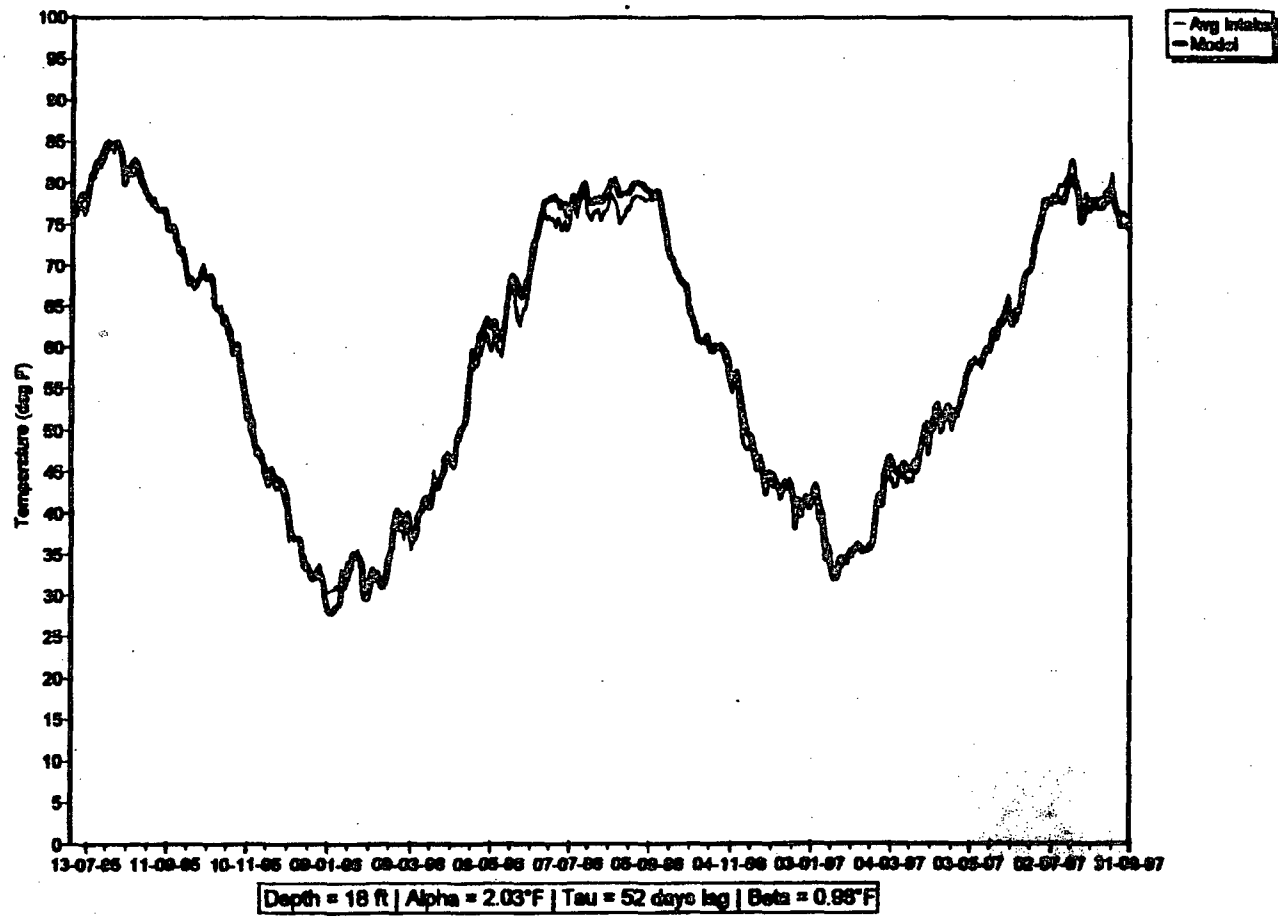


E-2 Figure III-1b. General numerical modeling procedure.

Hydrothermal Modeling of Thermal Exposures

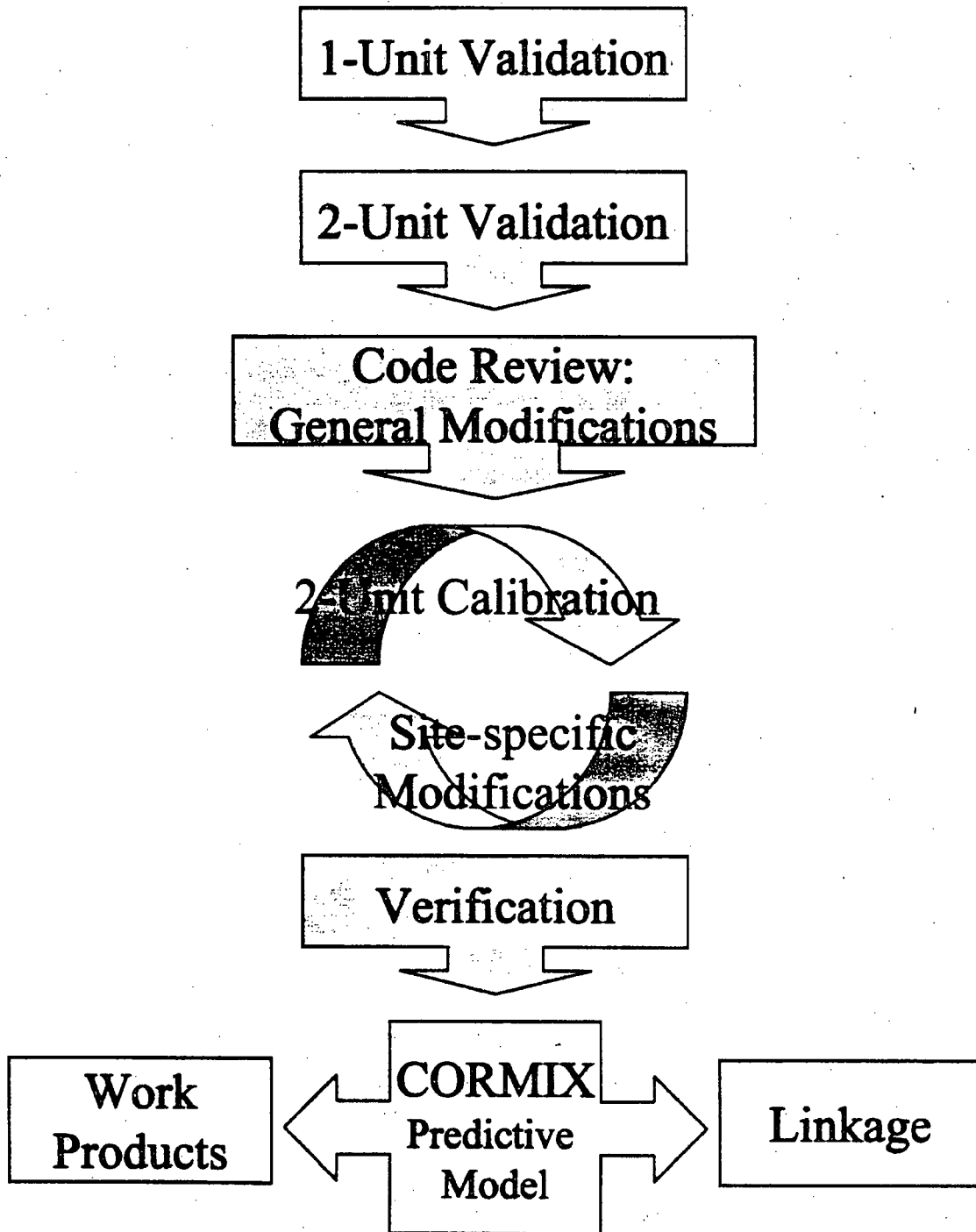


E-2 Figure III-1c. Schematic showing how the hydrothermal models are used to define the thermal exposure.

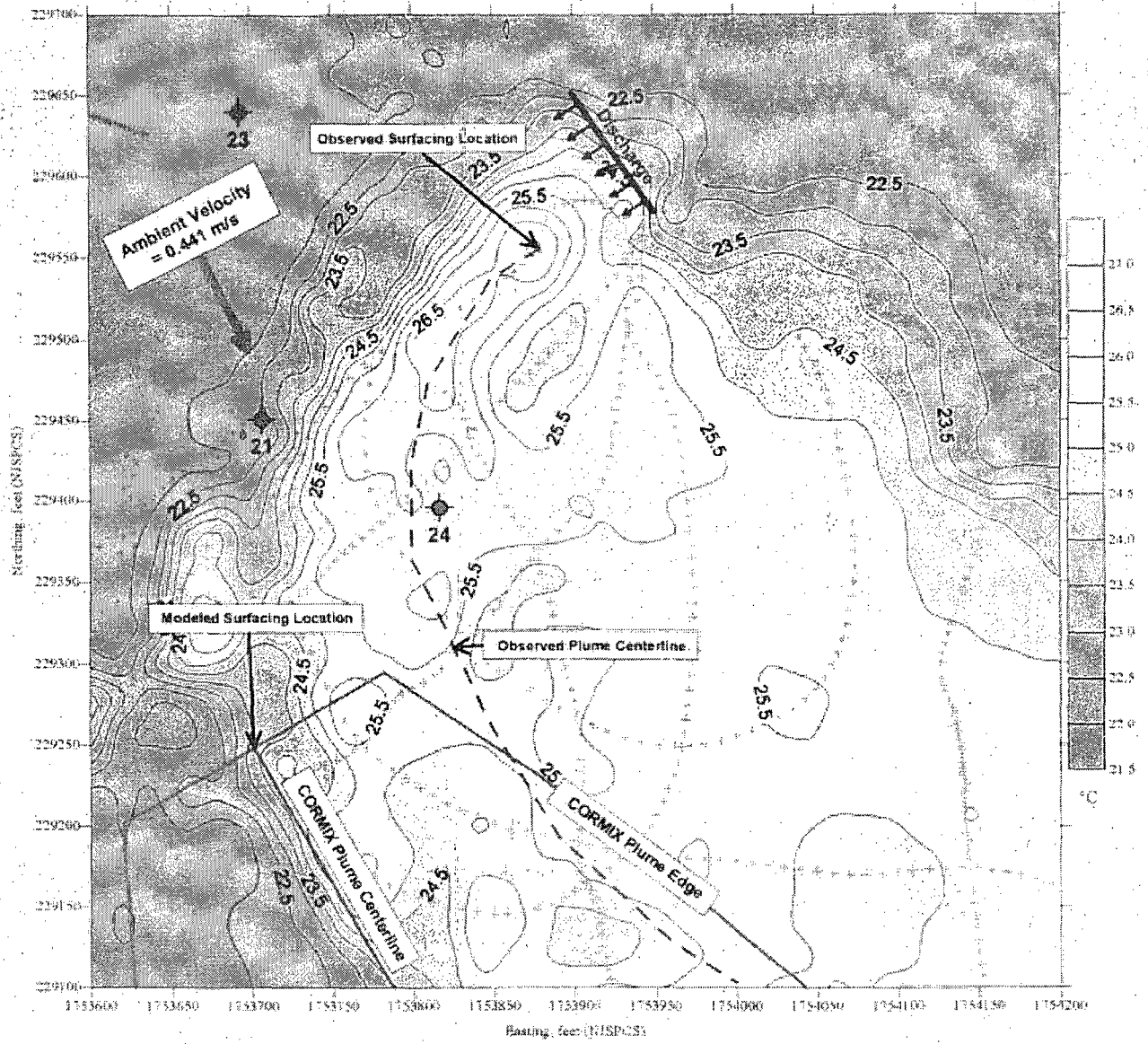


E-2 Figure III-2. Ambient temperature model calibration comparison.

CORMIX MODELING PROCEDURE



E-2 Figure III-3. CORMIX Modeling Procedure for the Salem Plume

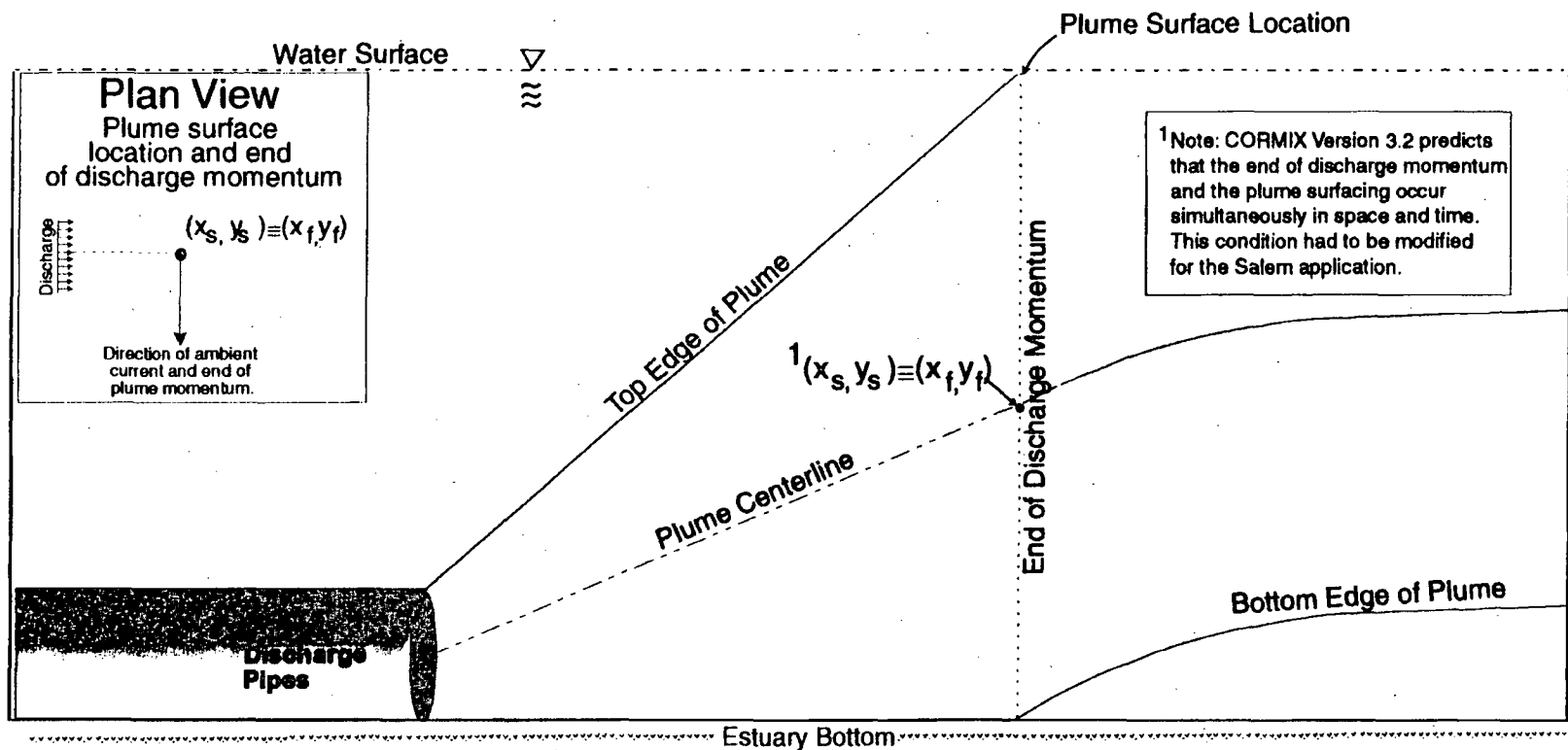


Note: The original CORMIX formulation used for this 2-Unit Validation was deemed unsuccessful.

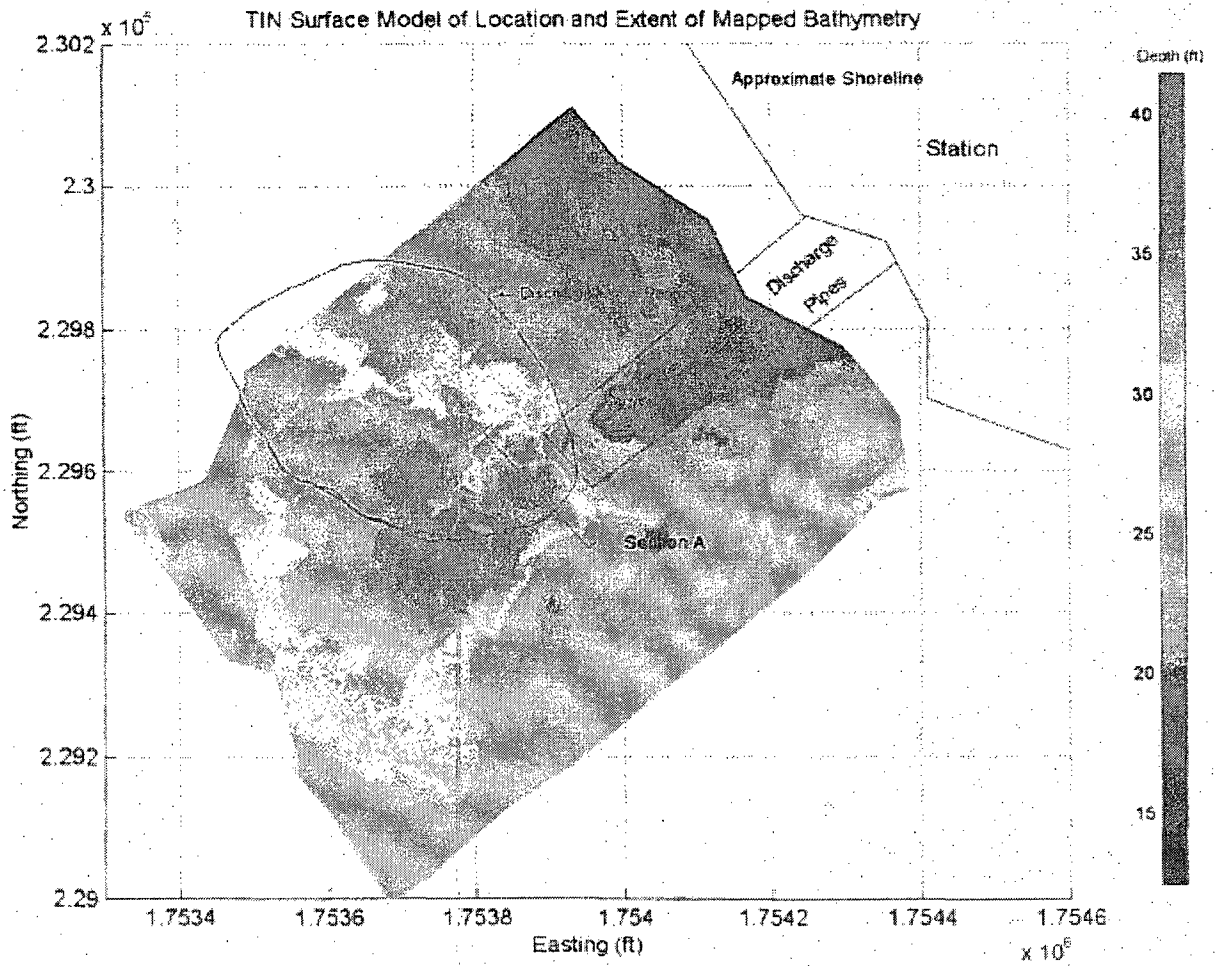
- ◆ = Mooring number & location
- = Boat track positions

**E-2 Figure III-4. Sample of CORMIX Two-Unit Validation; 29 May 1998
 Temperature Contours & CORMIX Predicted Plume Dimensions at the Surface
 Ebb Phase (06:40 - 08:40)**

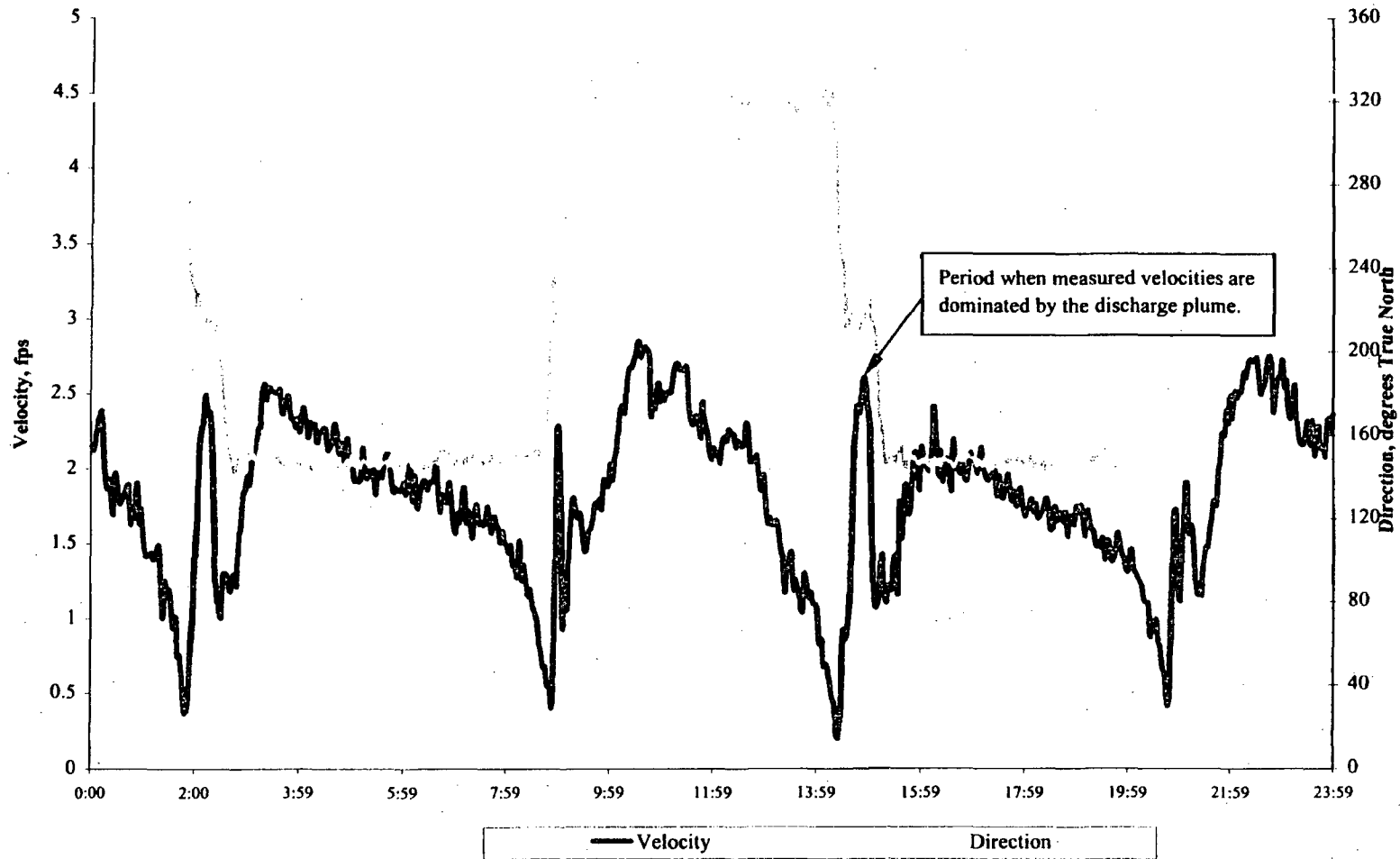
CORMIX Version 3.2 Schematic For the Salem Application



E-2 Figure III-5. Schematic of the CORMIX version 3.2 treatment of the Salem thermal plume (not to scale).

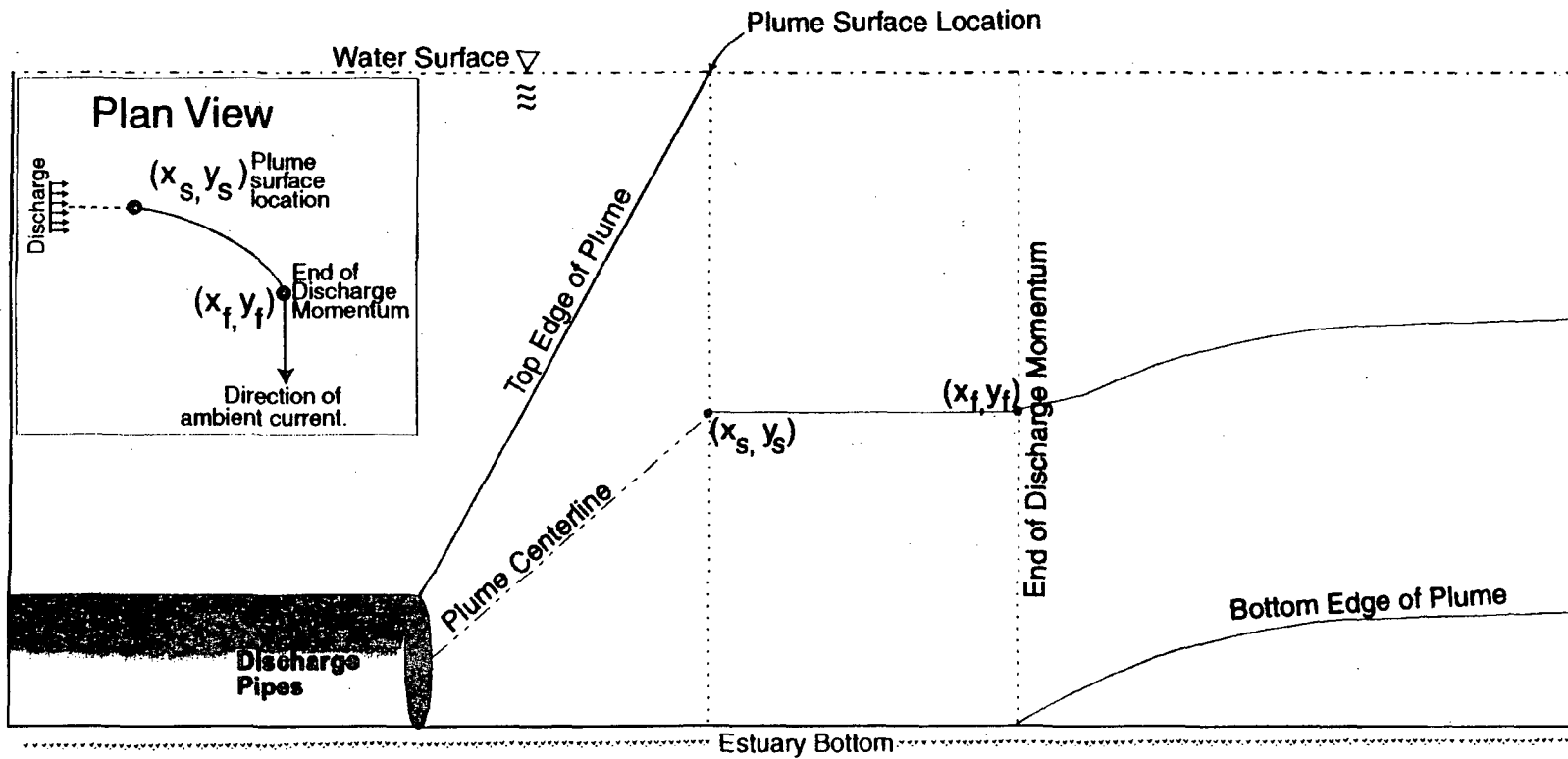


E-2 Figure III-6. Plan View: Triangular irregular network (TIN) of bathymetry at the Salem discharge. The approximate location of the discharge pipes and the surface upwelling measured on a flood tide are shown.

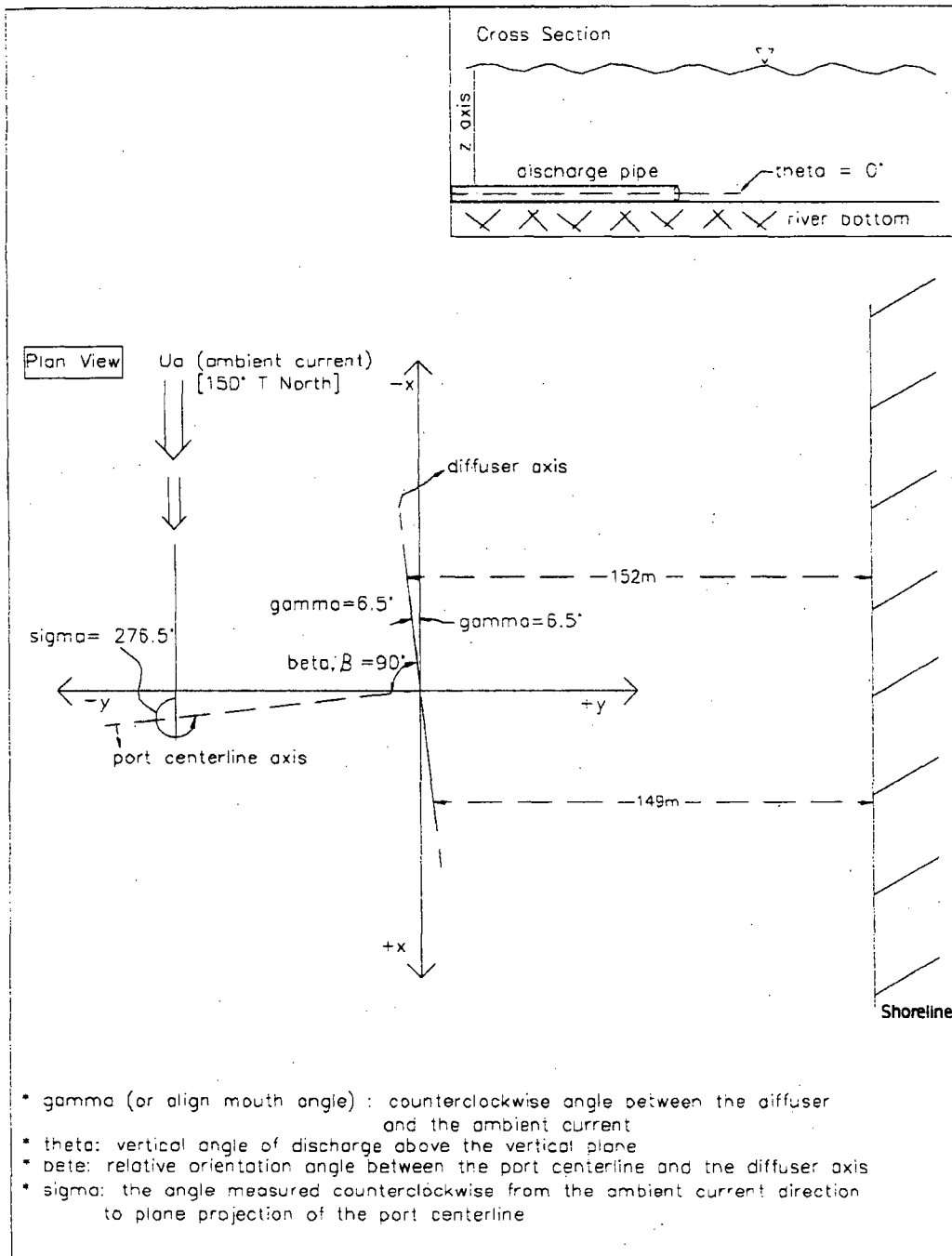


E 2 Figure III-7. CORMIX Two-Unit Calibration; 29 May 1998 Velocity and Direction of Ambient Flow at Bottom ADCP Depth = 9 to 10 feet (Mid-depth).

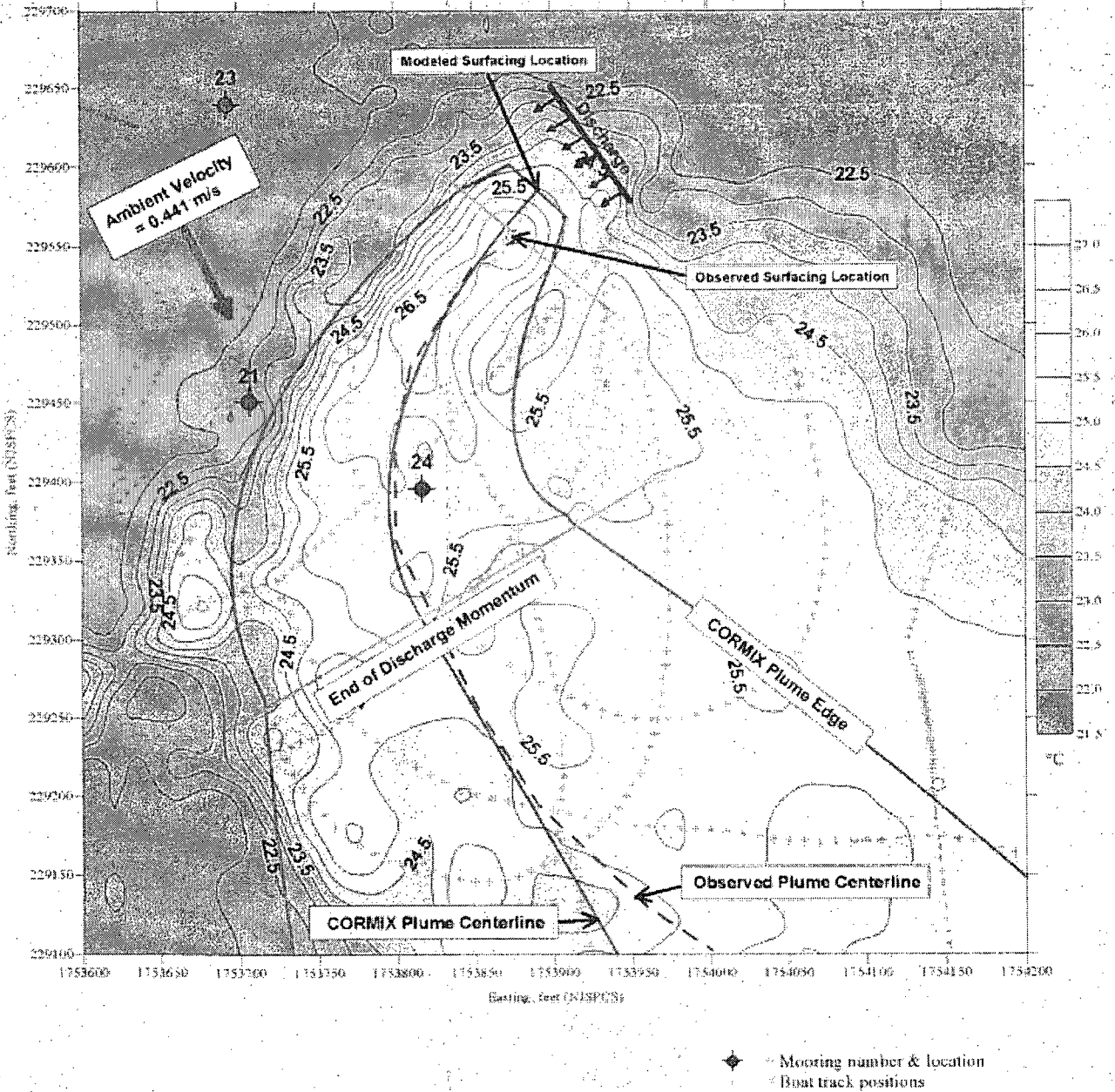
Improved CORMIX Schematic For the Salem Application



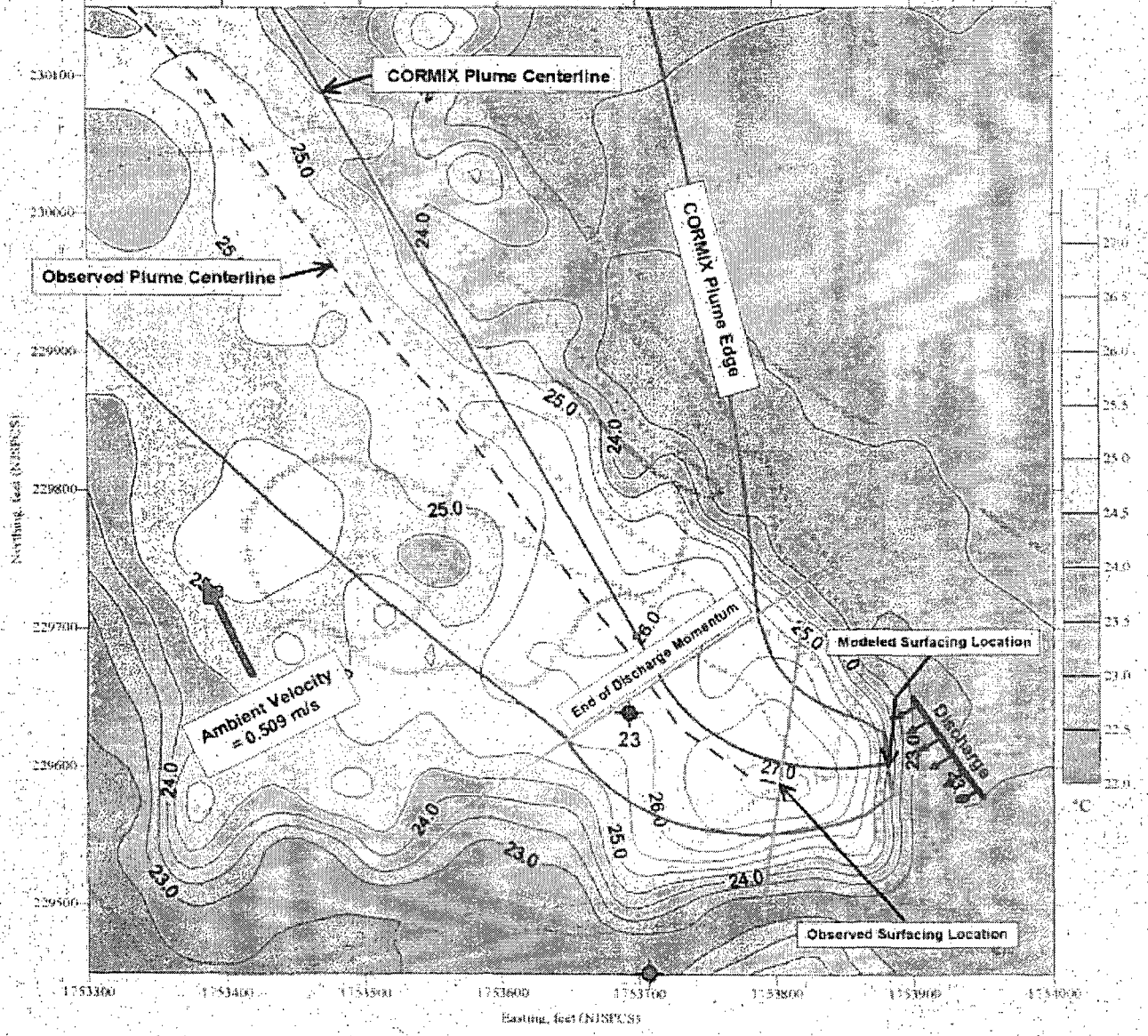
E-2 Figure III-8. Schematic of the improved CORMIX treatment of the Salem thermal plume (not to scale).



E-2 Figure III-9. CORMIX model coordinate system for a representative ebb tidal phase.

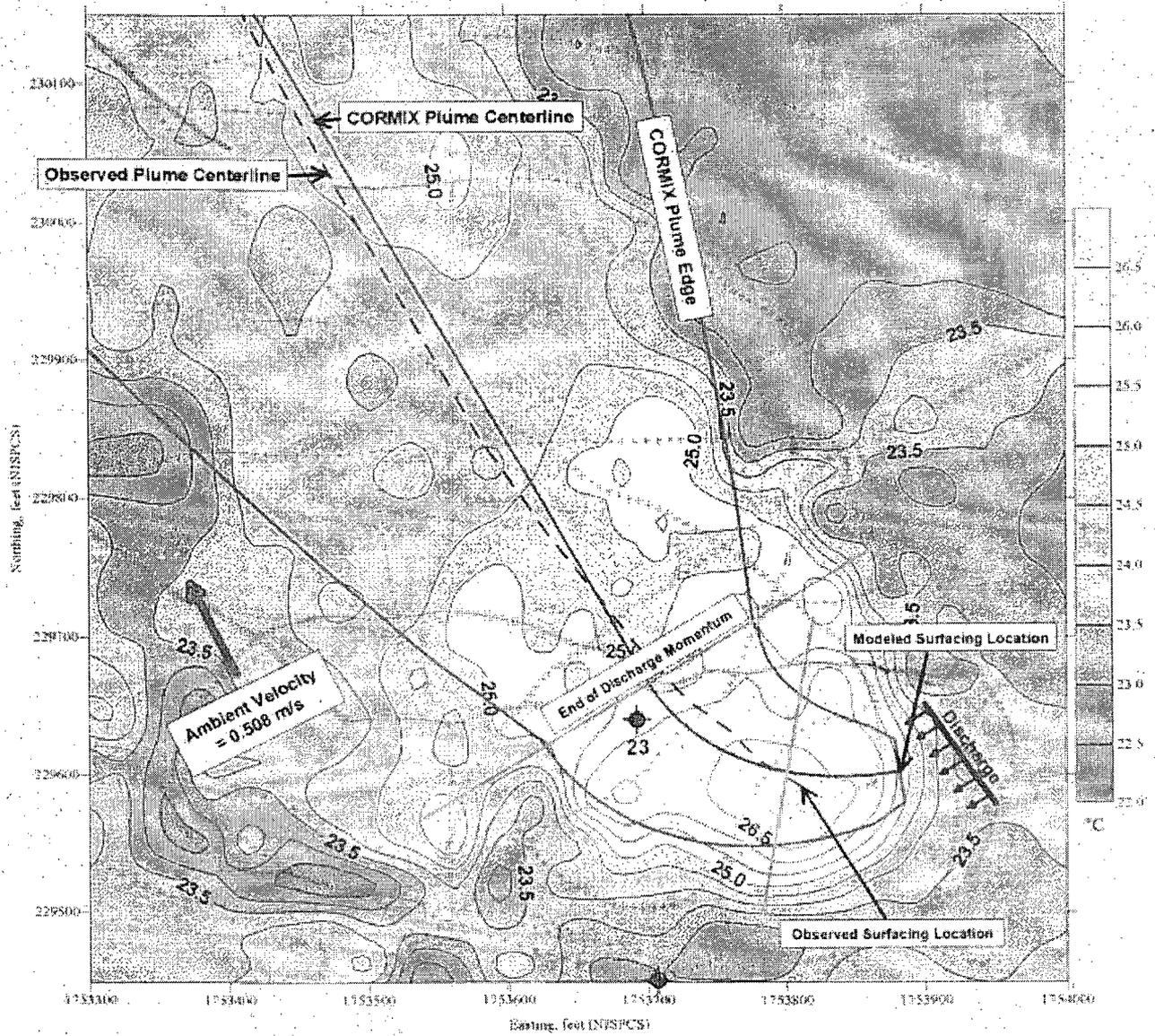


E-2 Figure III-10. CORMIX Two-Unit Calibration; 29 May 1998
 Temperature Contours & CORMIX Predicted Plume Dimensions at the Surface
 Ebb Phase (06:40 - 08:40)



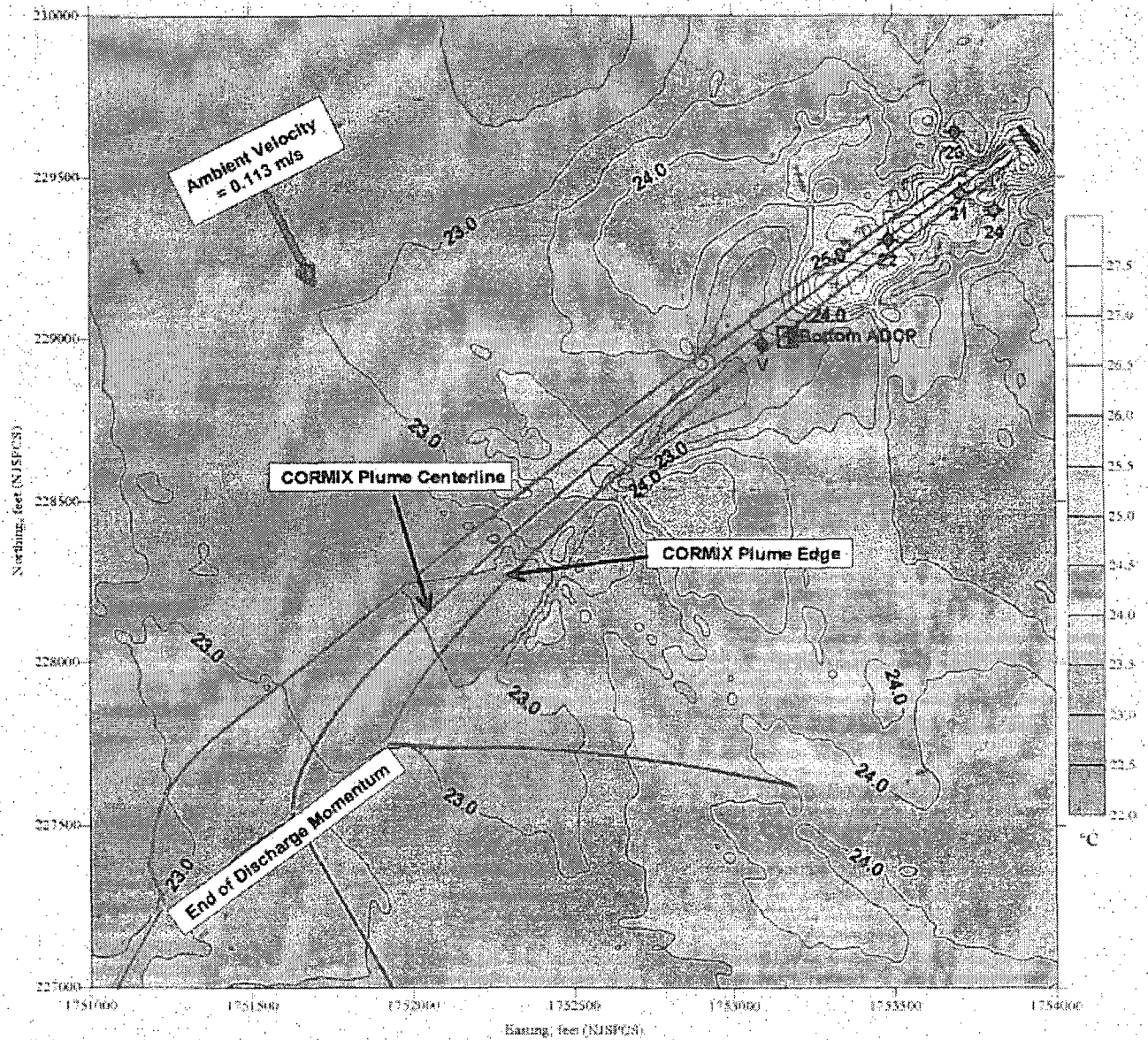
◆ = Mooring number & location
 = Boat track positions

E-2 Figure III-11. CORMIX Two-Unit Calibration; 29 May 1998
 Temperature Contours & CORMIX Predicted Plume Dimensions at the Surface
 Flood Phase (11:40 - 13:40)



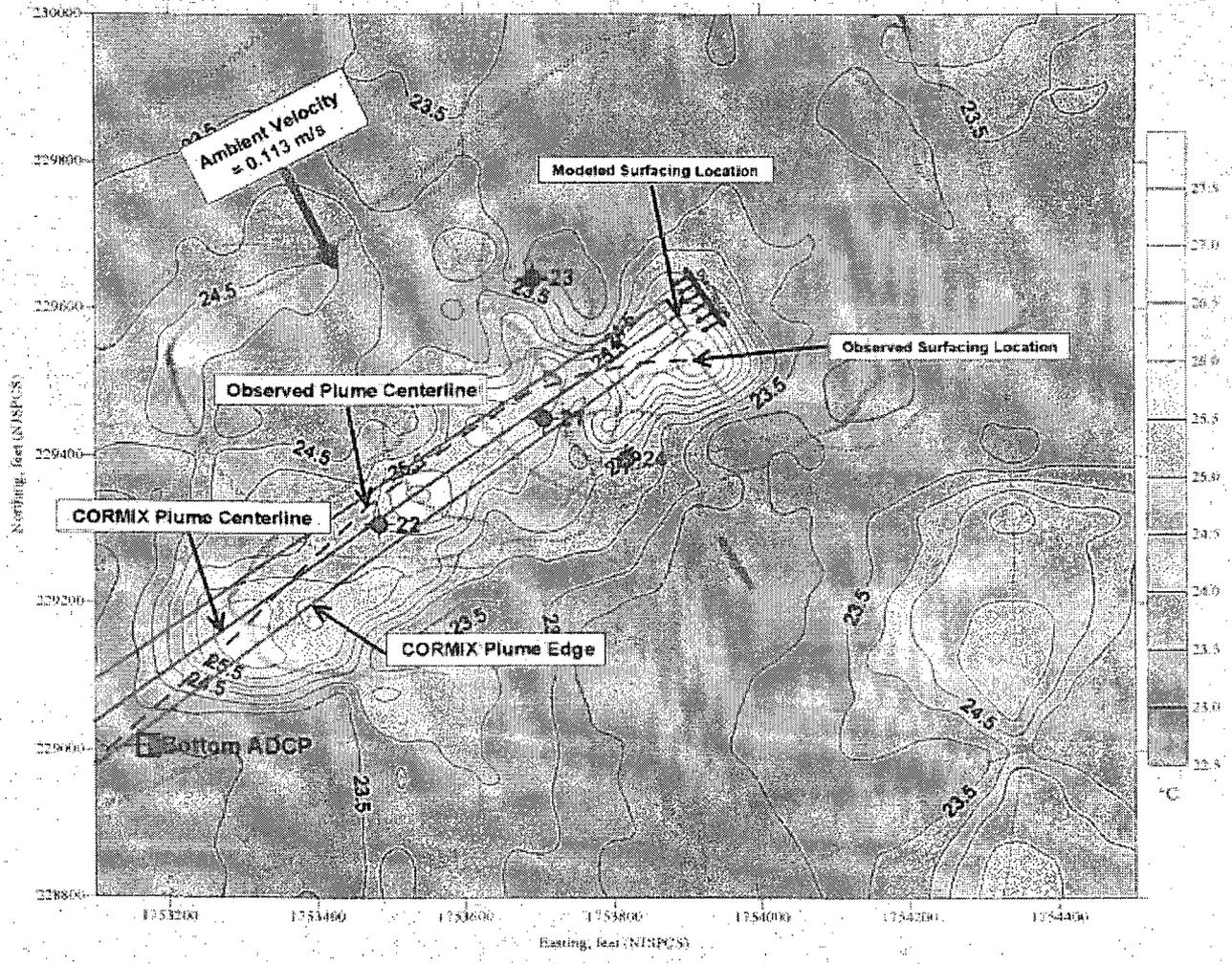
◆ Mooring number & location
 ○ Boat track position

**E-2 Figure III-12. CORMIX Two-Unit Calibration; 29 May 1998
 Temperature Contours & CORMIX Predicted Plume Dimensions at the Surface
 End-of-Ebb Phase (09:10 - 11:10)**

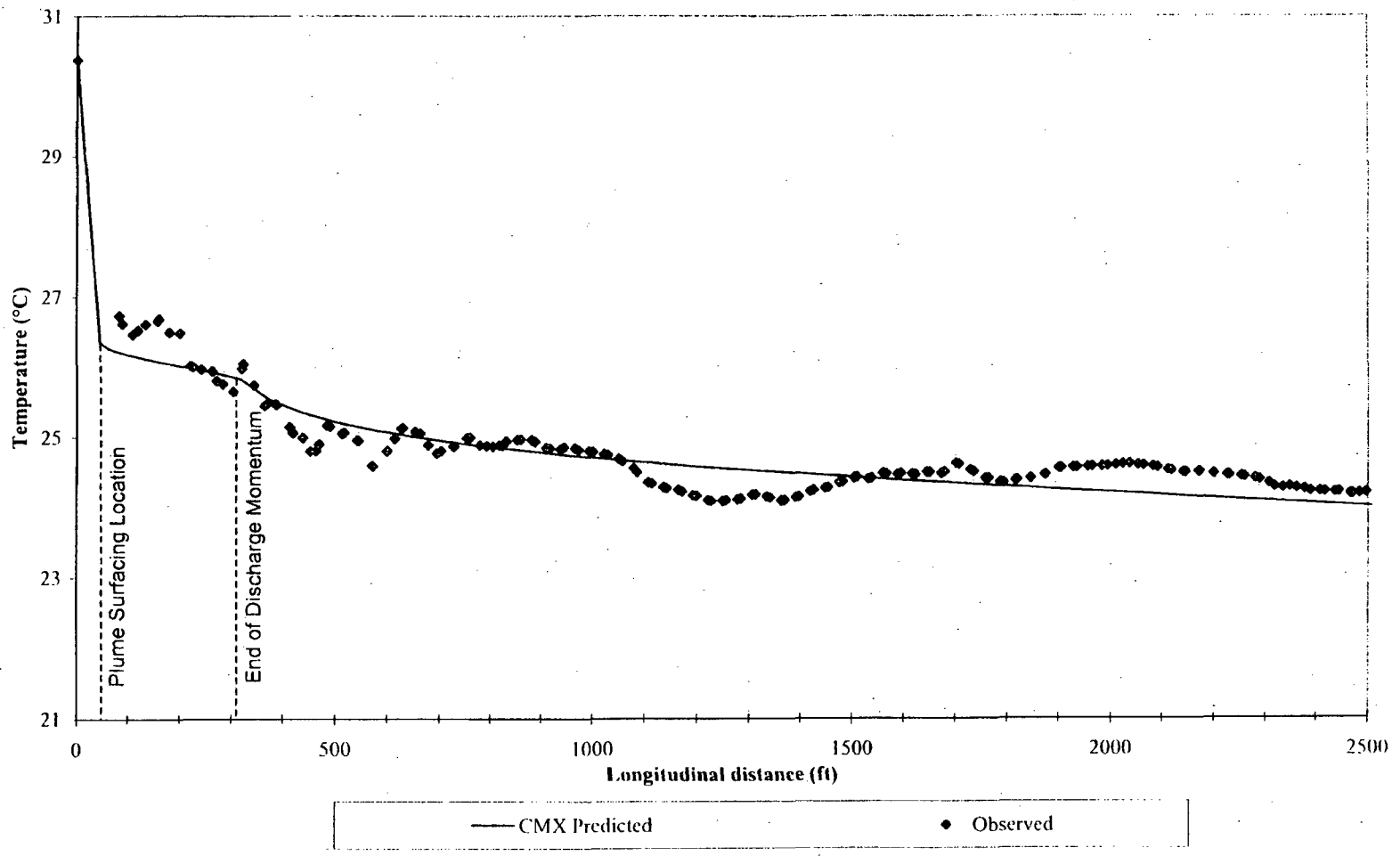


- ◆ = Mooring number & location
- = Bottom ADCP location
- = Boat track position

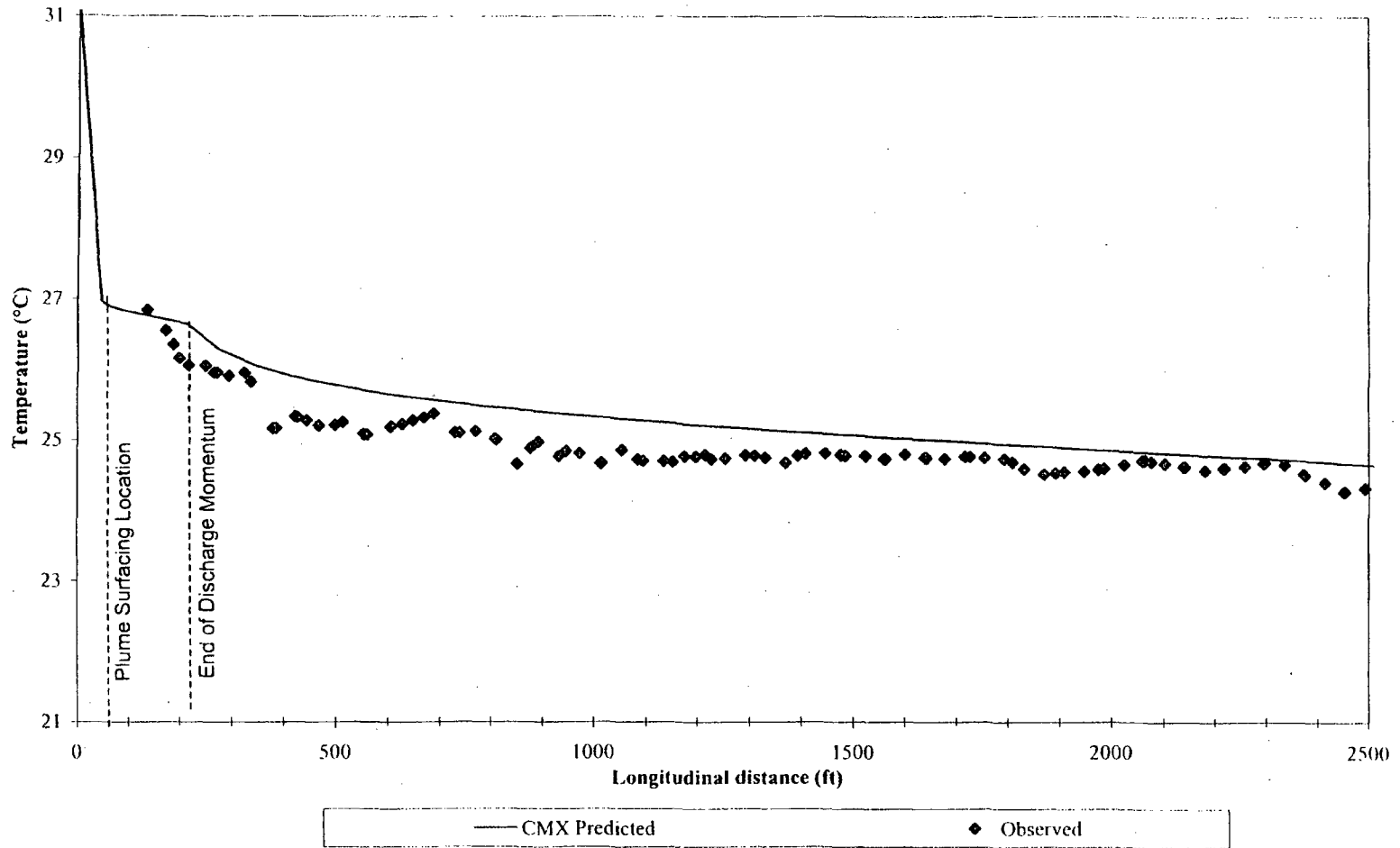
E-2 Figure III-13. CORMIX Two-Unit Calibration; 29 May 1998
Temperature Contours & CORMIX Predicted Plume Dimensions at the Surface
End-of-Flood Phase (14:25 - 16:25)
Expanded Area



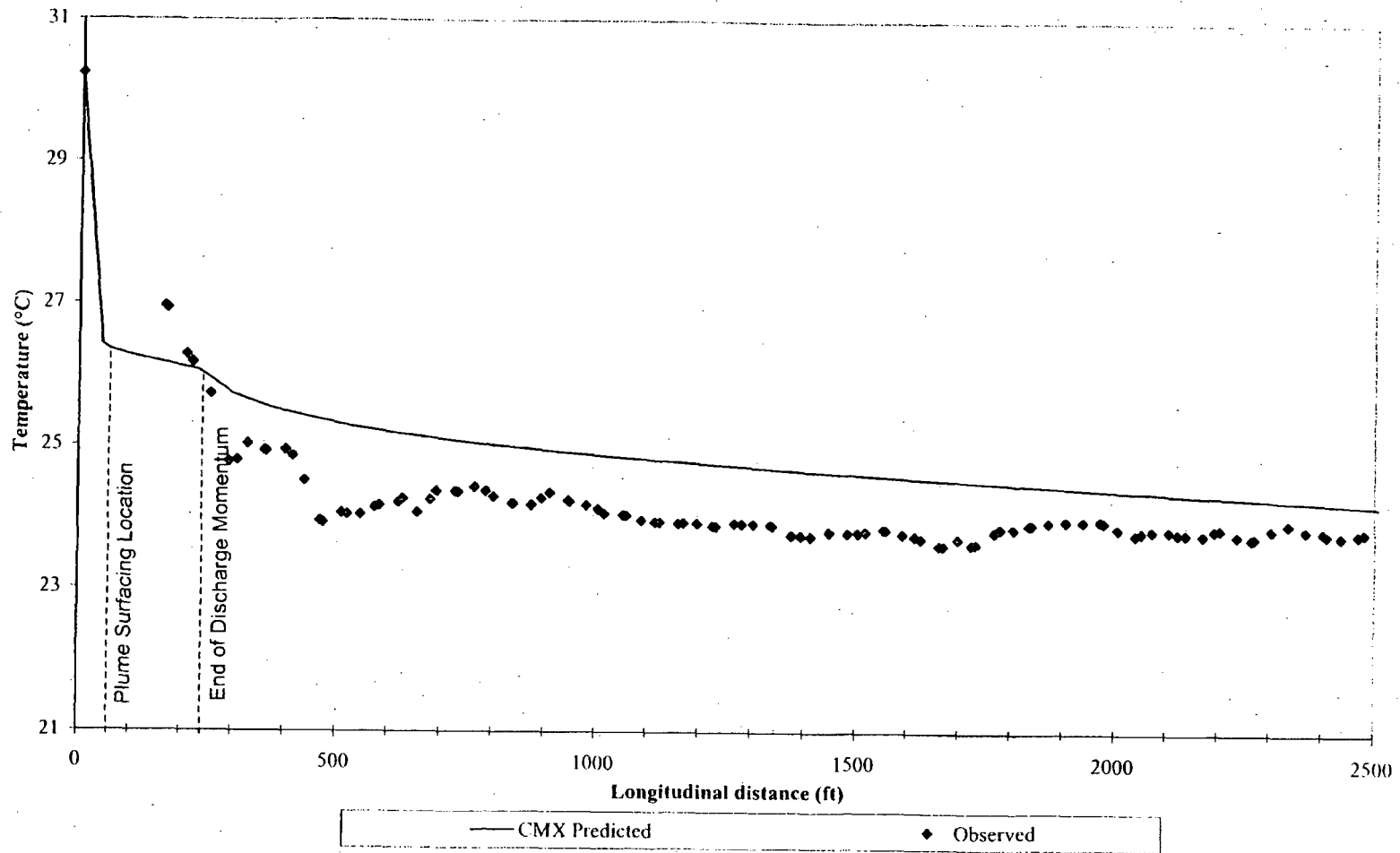
E-2 Figure III-13a. CORMIX Two-Unit Calibration; 29 May 1998
 Temperature Contours & CORMIX Predicted Plume Dimensions at the Surface
 End-of-Flood Phase (14:25 - 16:25)



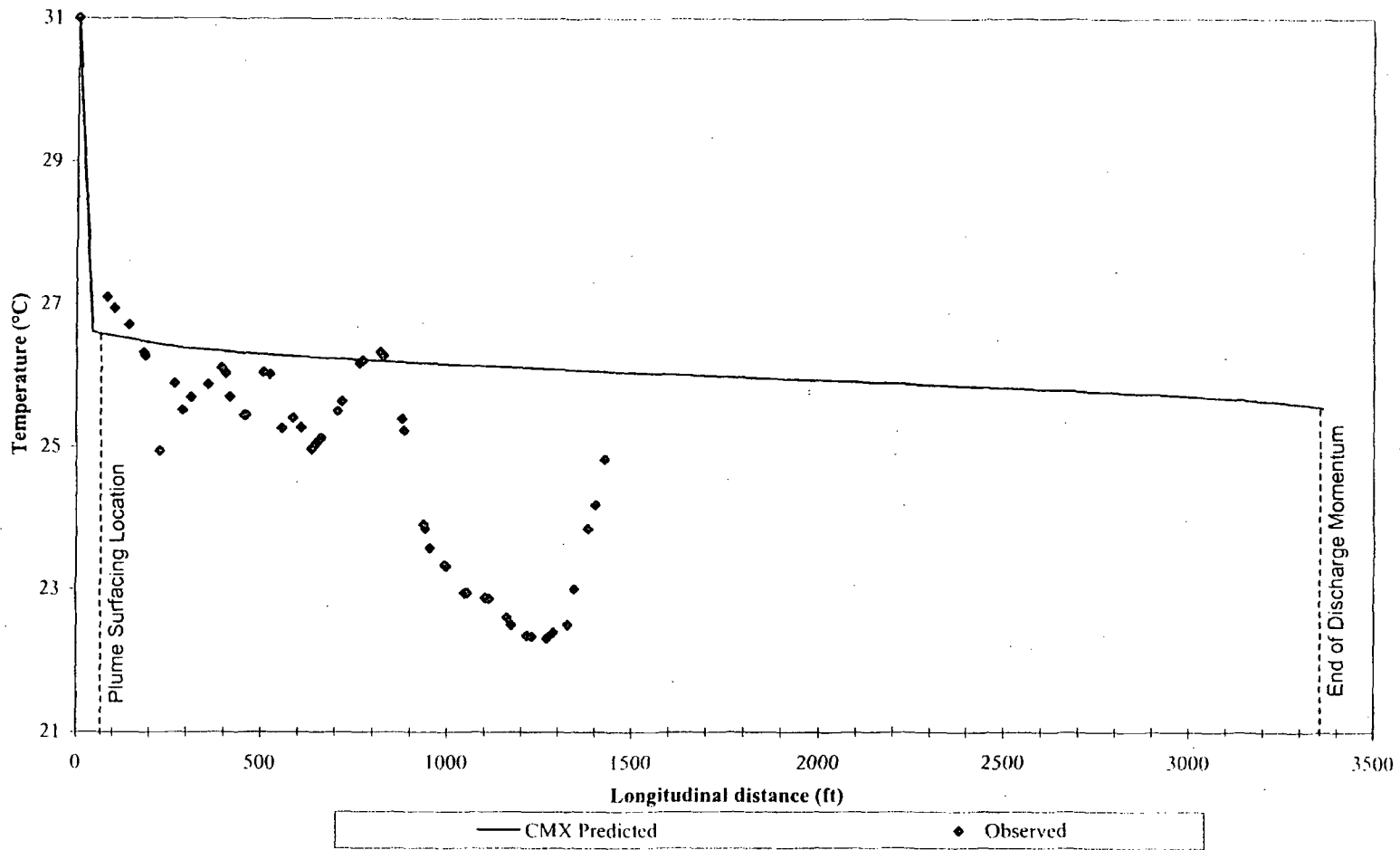
E-2 Figure III-14. CORMIX Two -Unit Calibration; 29 May 1998
Observed vs. CORMIX Predicted Surface Temperatures
Ebb Phase [Approach Temperature = 21.72 °C]



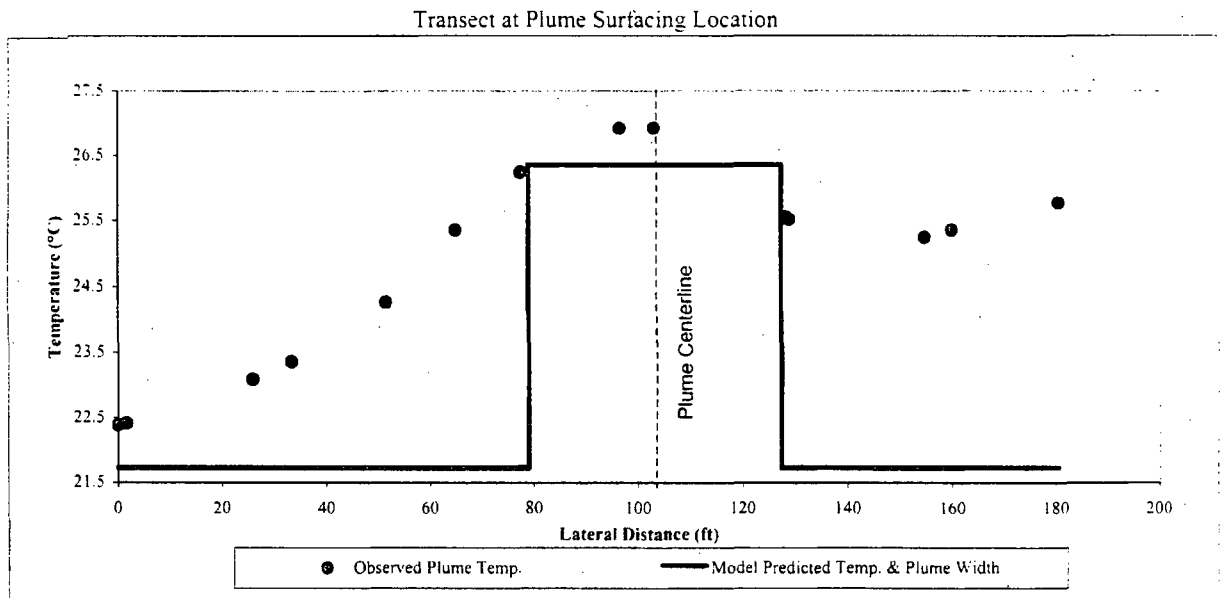
E-2 Figure III-15. CORMIX Two-Unit Calibration; 29 May 1998
Observed vs. CORMIX Predicted Surface Temperatures
Flood Phase [Approach Temperature = 22.50 °C]



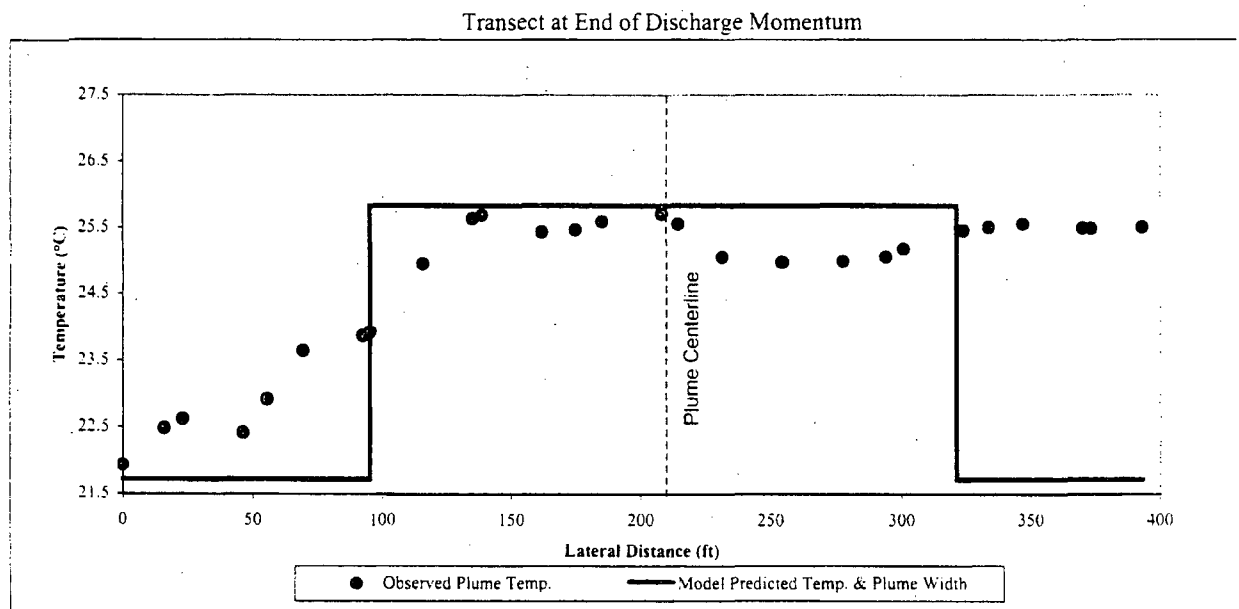
E-2 Figure III-16. CORMIX Two-Unit Calibration; 29 May 1998
Observed vs. CORMIX Predicted Surface Temperatures
End-of-Ebb Phase [Approach Temperature = 22.13 °C]



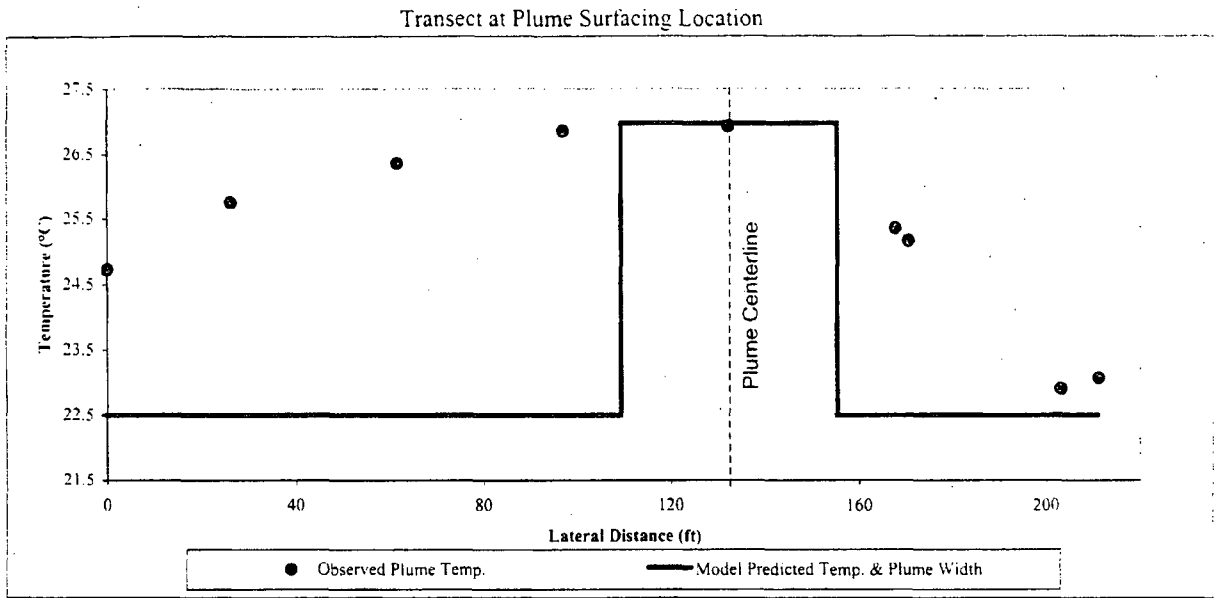
E-2 Figure III-17. CORMIX Two-Unit Calibration; 29 May 1998
Observed vs. CORMIX Predicted Surface Temperatures
End-of-Flood Phase [Approach Temperature = 22.53 °C]



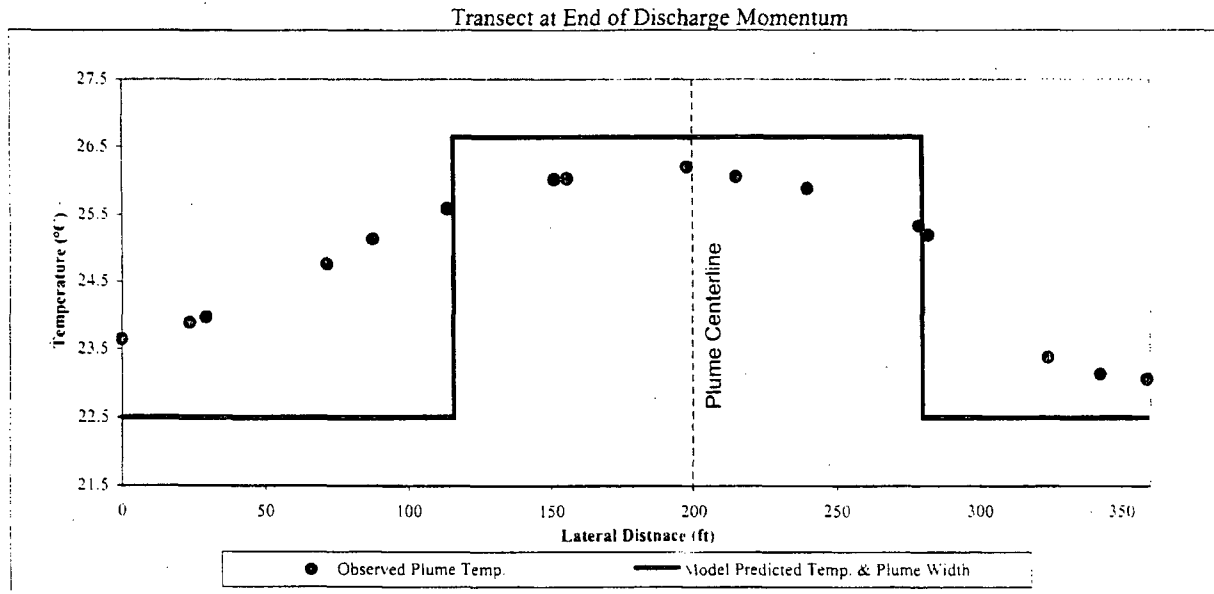
Note : Vantage point is facing the oncoming plume.



**E-2 Figure III-18. CORMIX Two-Unit Calibration; 29 May 1998
Comparison of Model Predicted vs. Observed Lateral Temperature Distributions
Ebb Phase**

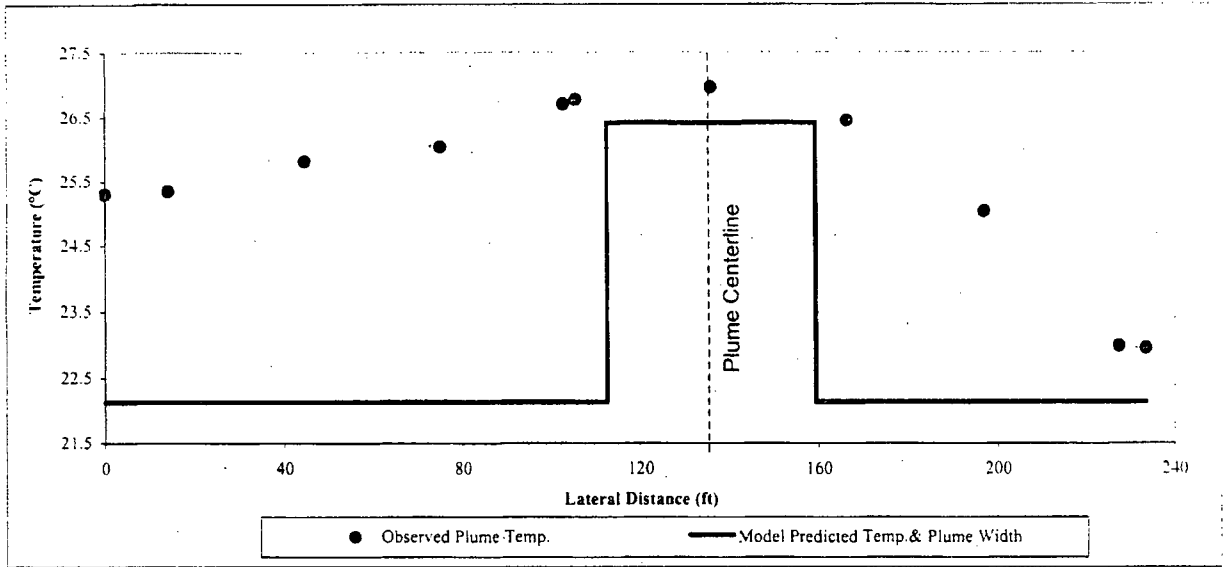


Note : Vantage point is facing the oncoming plume.



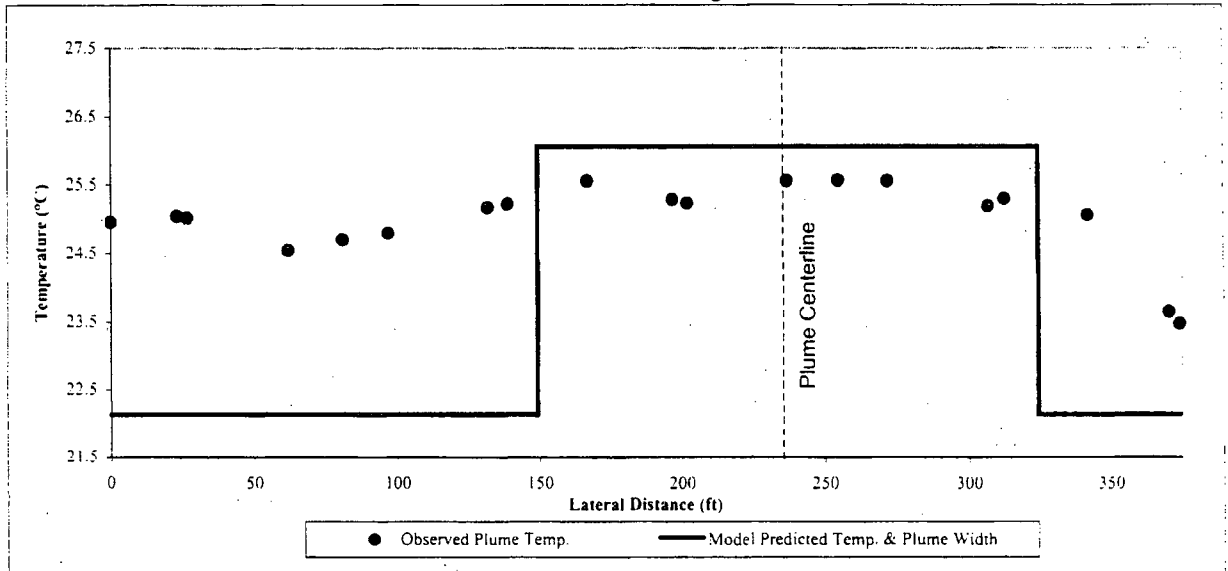
**E-2 Figure III-19. CORMIX Two-Unit Calibration; 29 May 1998
Comparison of Model Predicted vs. Observed Lateral Temperature Distributions
Flood Phase**

Transect at Plume Surfacing Location

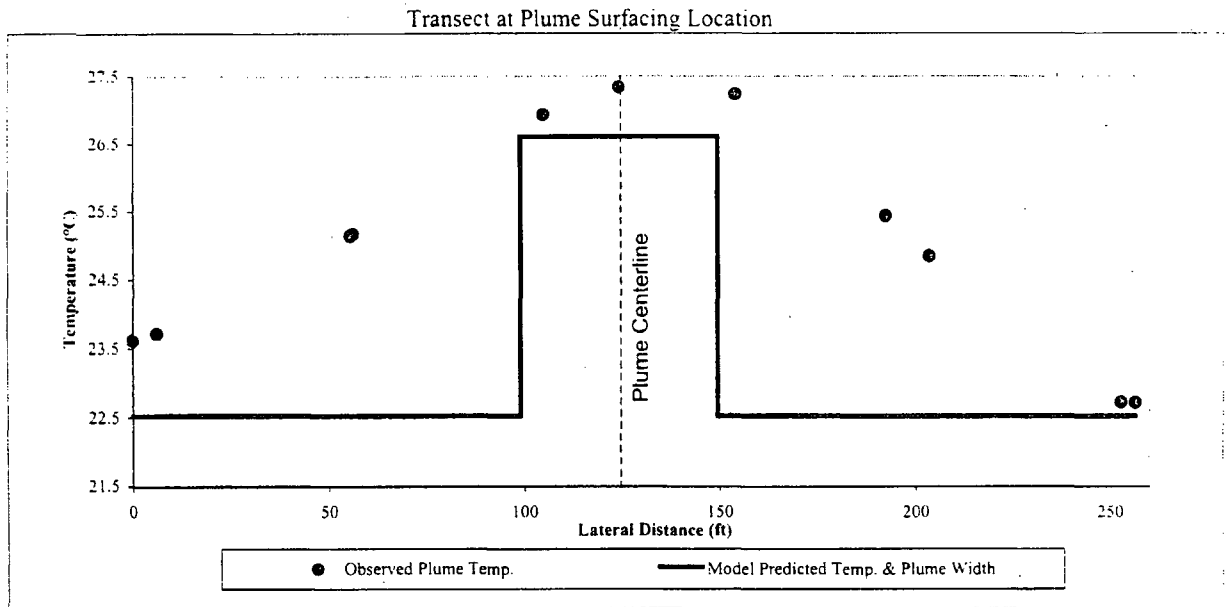


Note : Vantage point is facing the oncoming plume.

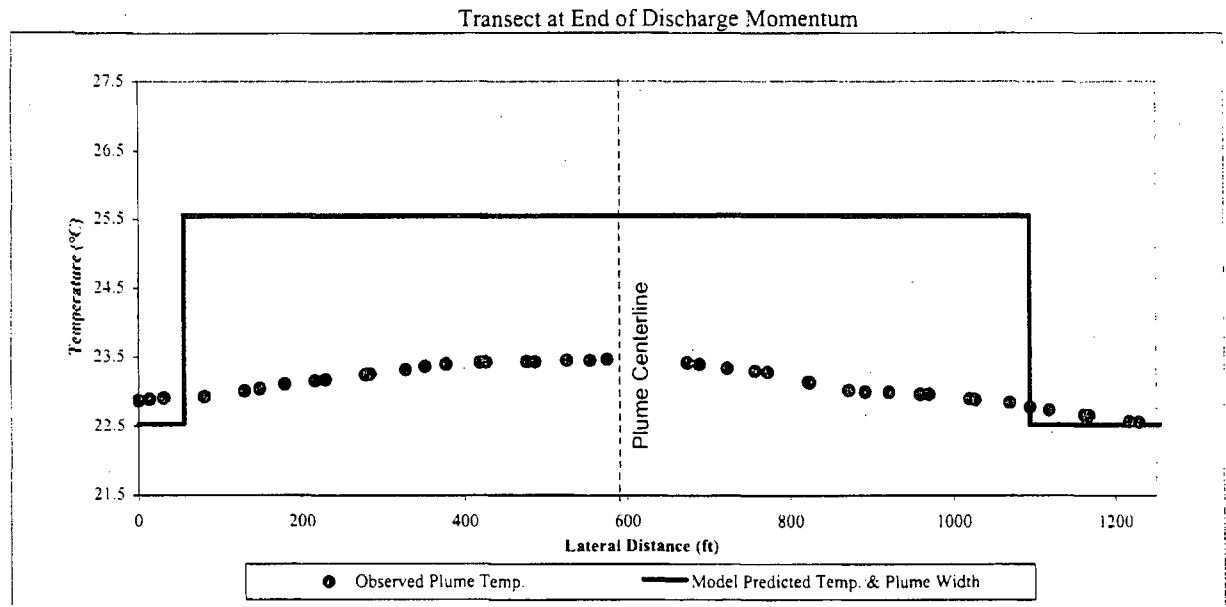
Transect at End of Discharge Momentum



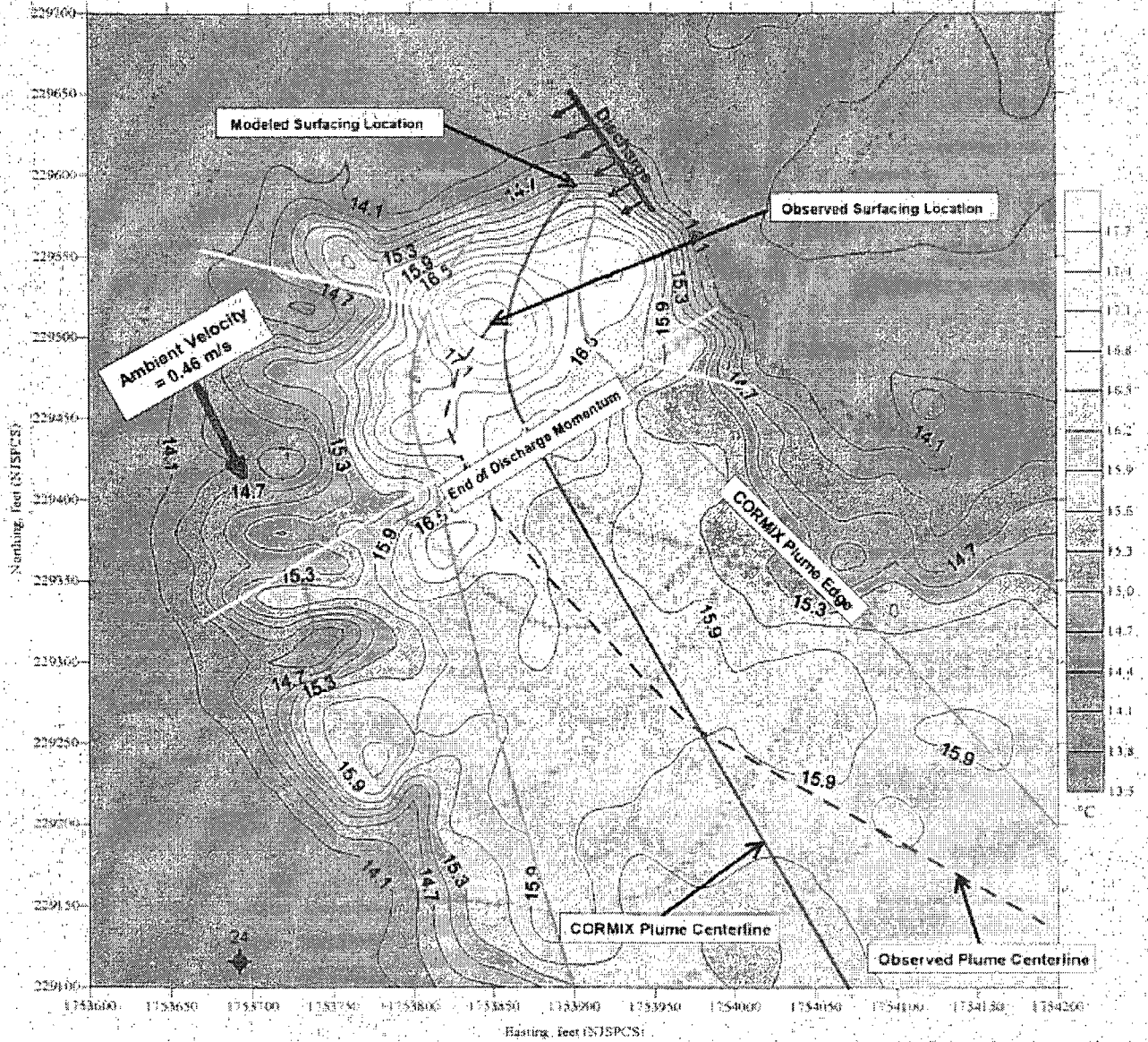
E-2 Figure III-20. CORMIX Two-Unit Calibration; 29 May 1998
 Comparison of Model Predicted vs. Observed Lateral Temperature Distributions
 End-of-Ebb Phase



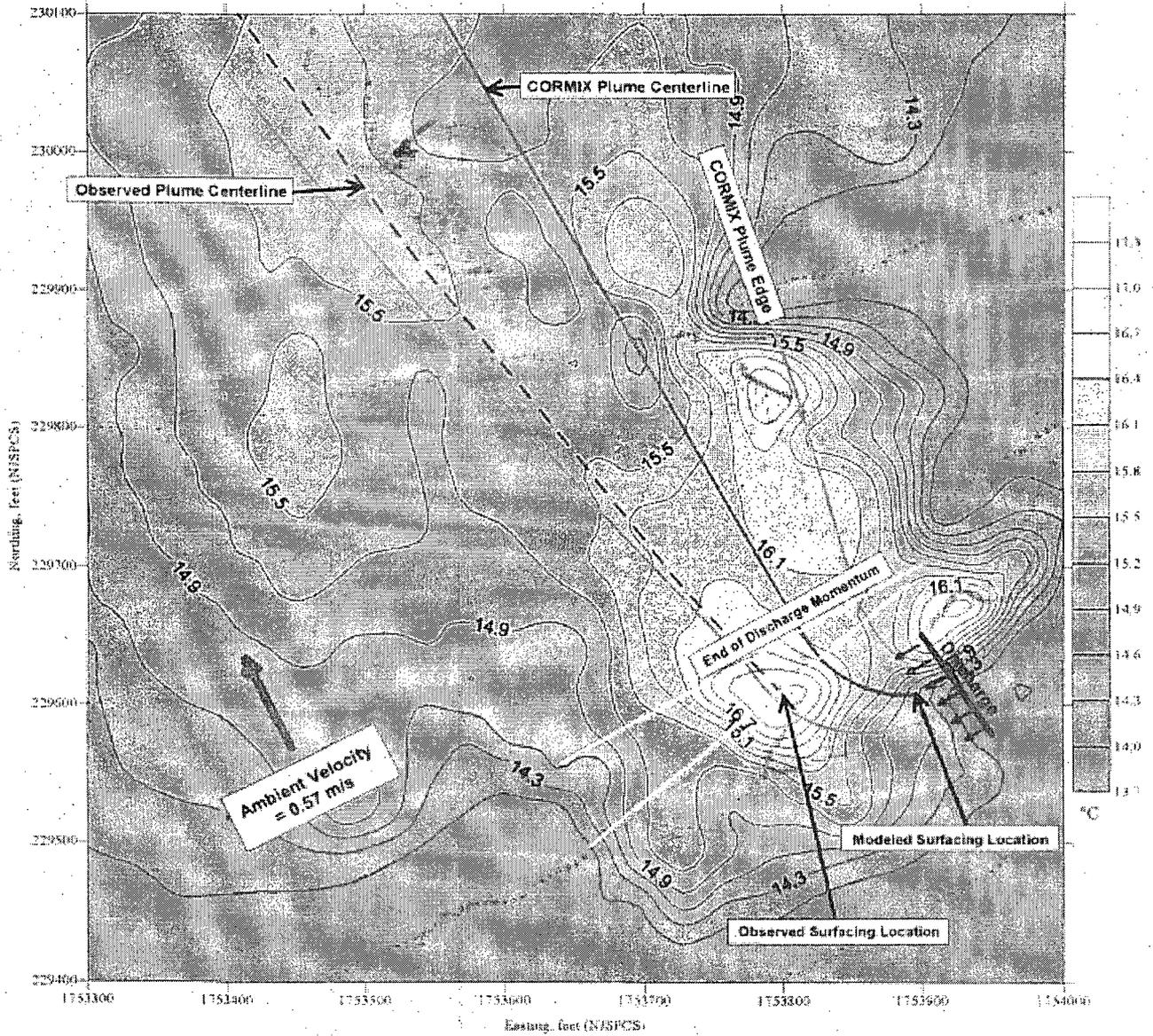
Note : Vantage point is facing the oncoming plume.



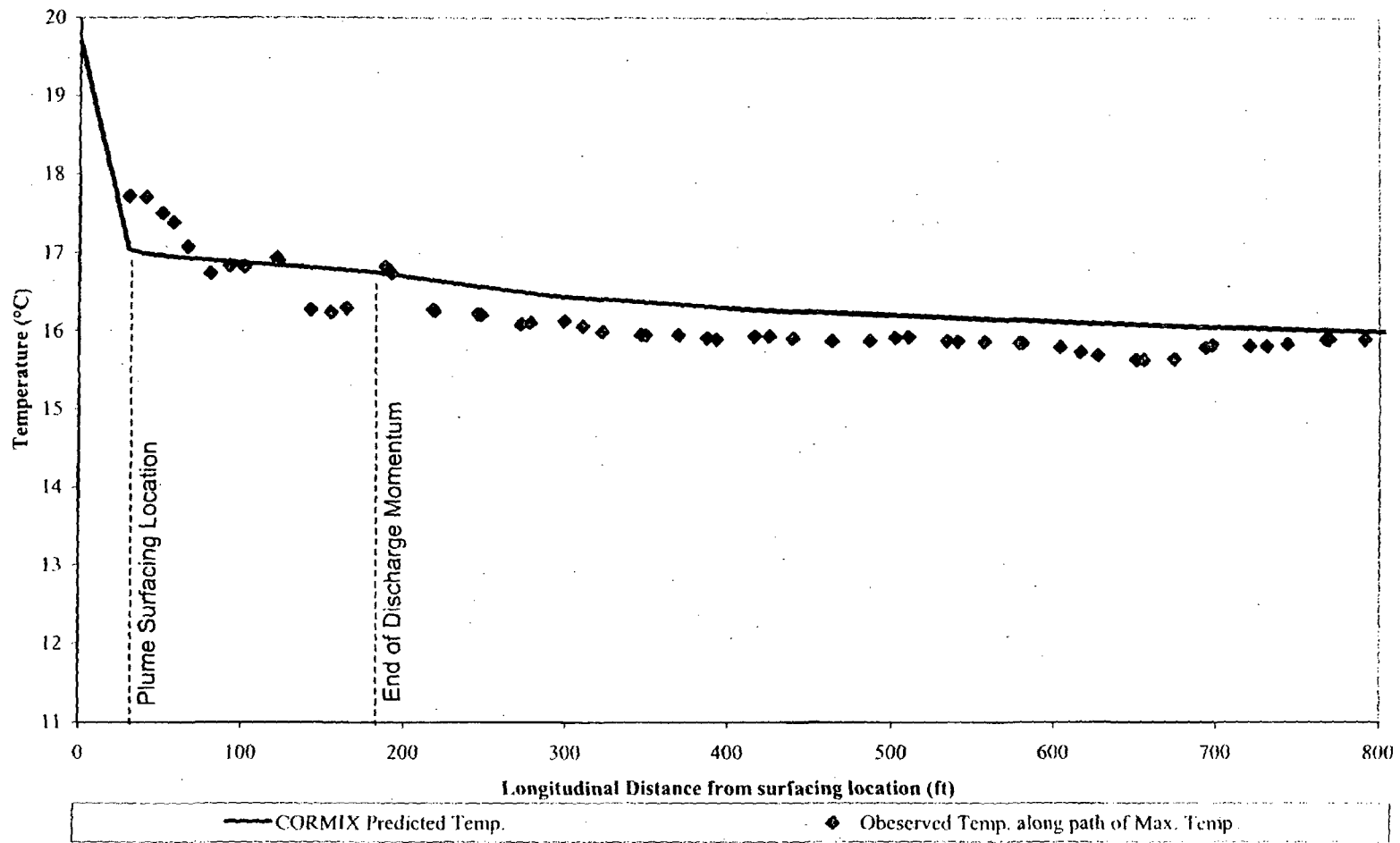
E-2 Figure III-21. CORMIX Two-Unit Calibration; 29 May 1998
Comparison of Model Predicted vs. Observed Lateral Temperature Distributions
End-of -Flood Phase



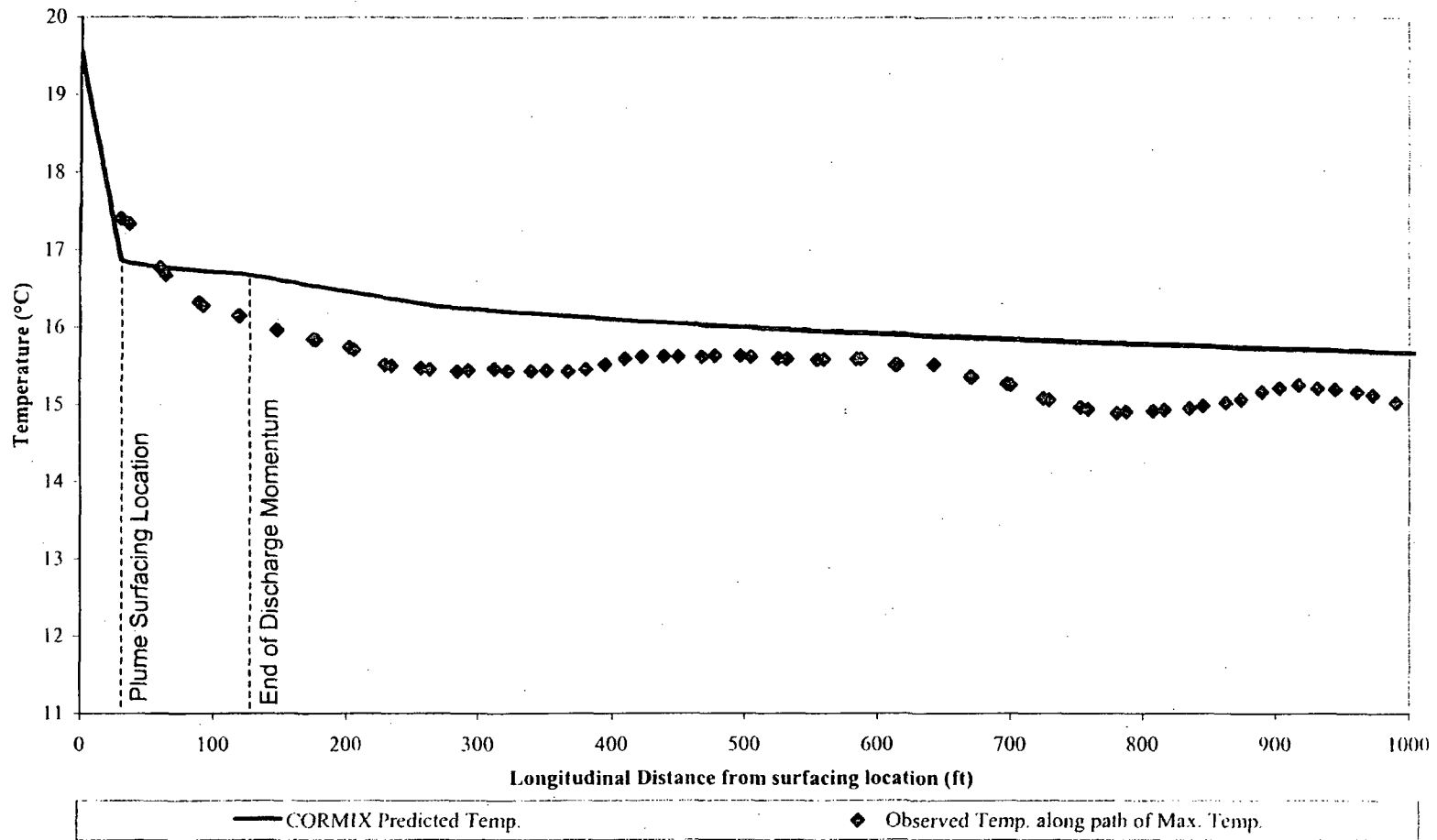
E-2 Figure III-22. CORMIX One-Unit Verification; 28 October 1997
 Temperature Contours & CORMIX Predicted Plume Dimensions at the Surface
 Ebb Phase (12:25 - 14:25)



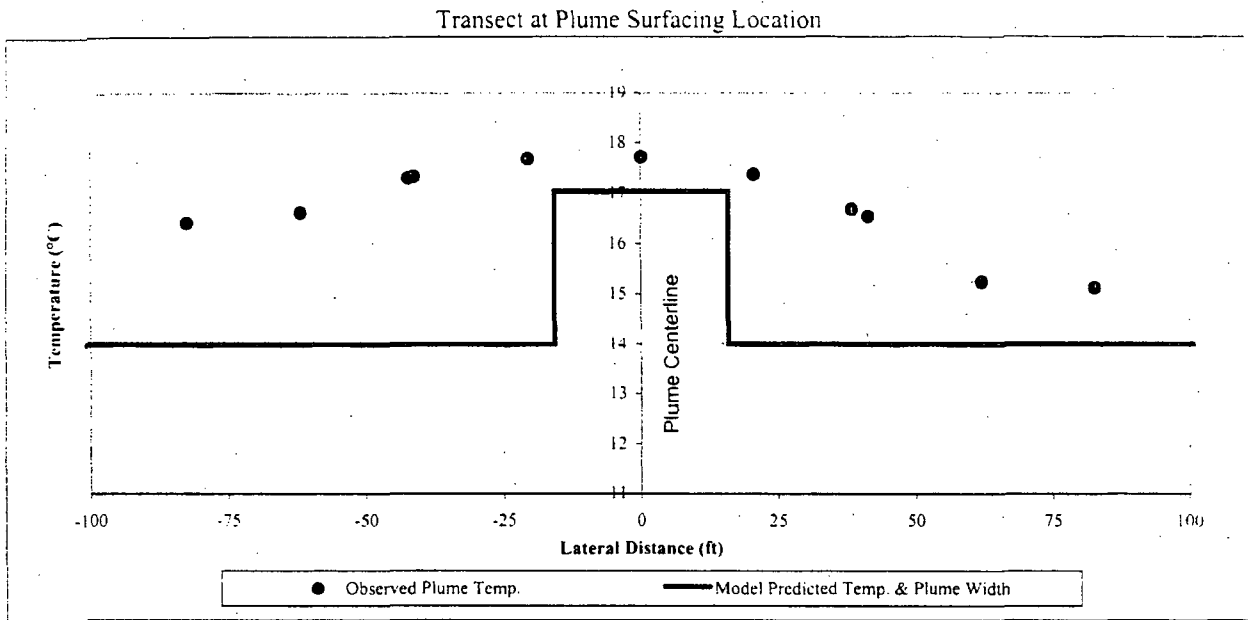
E-2 Figure III-23. CORMIX One-Unit Verification; 28 October 1997
 Temperature Contours & CORMIX Predicted Plume Dimensions at the Surface
 Flood Phase (06:30 - 08:30)



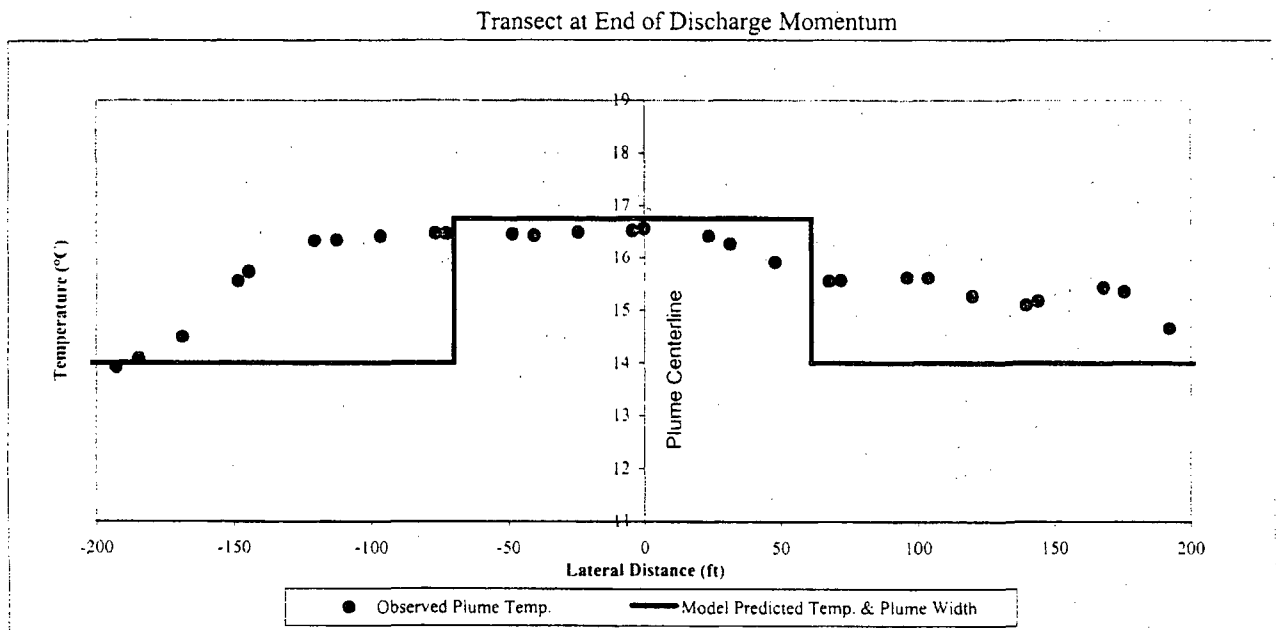
E-2 Figure III-24. CORMIX One-Unit Verification; 28 October 1997
 Observed vs. CORMIX Predicted Surface Temperatures
 Ebb [Approach Temperature = 14.0 °C]



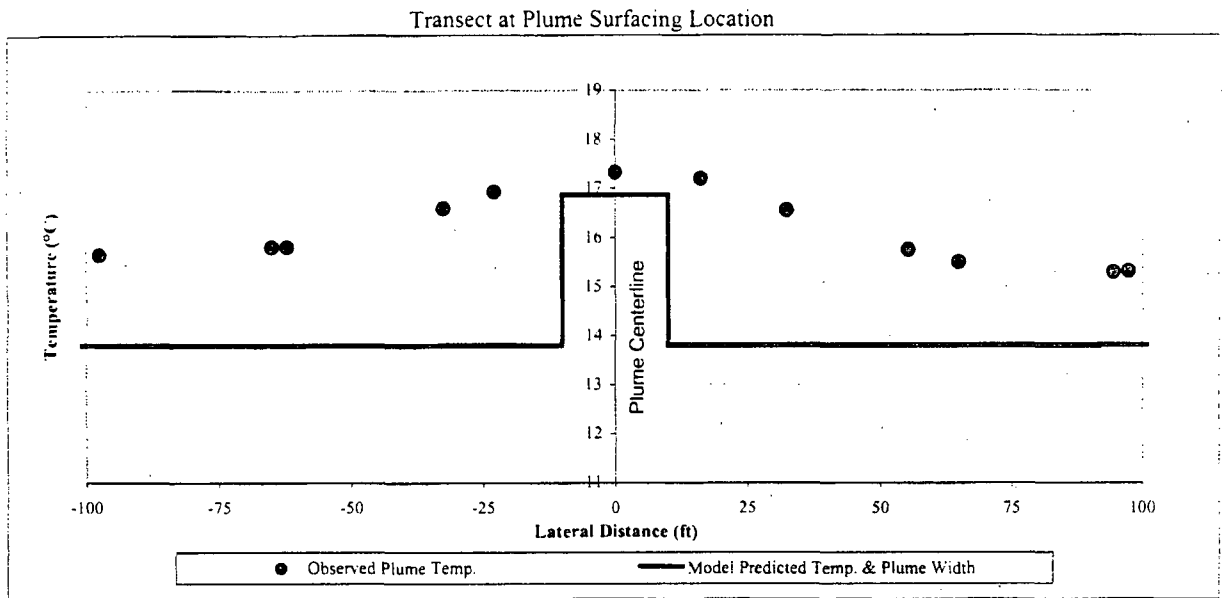
E-2 Figure III-25. CORMIX One-Unit Verification; 28 October 1997
 Observed vs. CORMIX Predicted Surface Temperatures
 Flood [Approach Temperature = 13.8 °C]



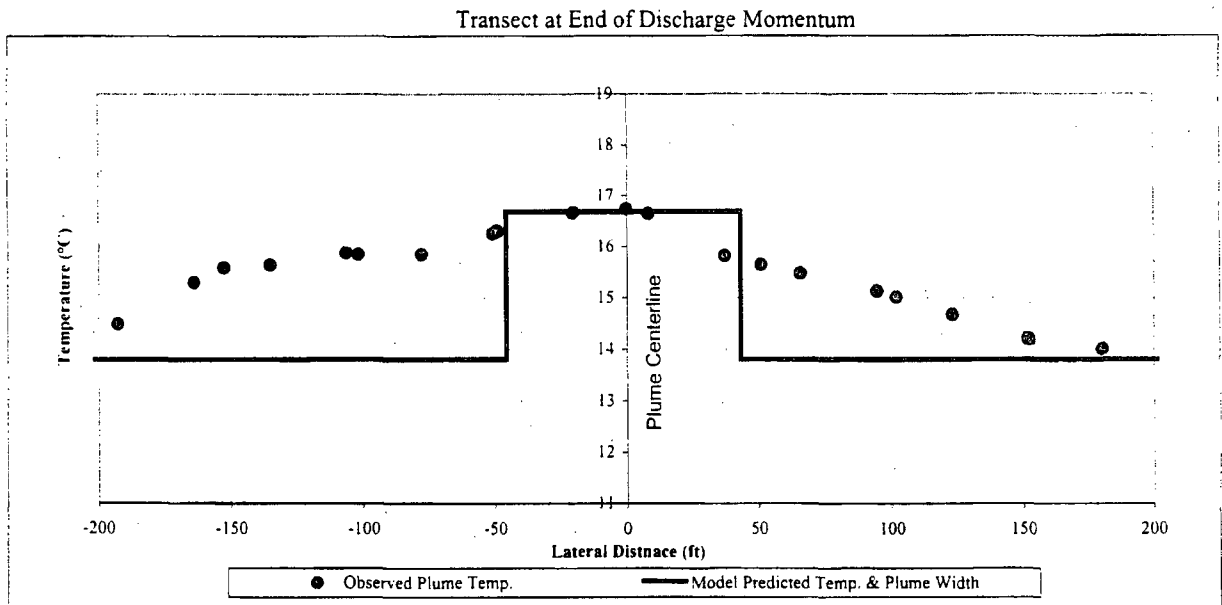
Note : Vantage point is facing the oncoming plume.



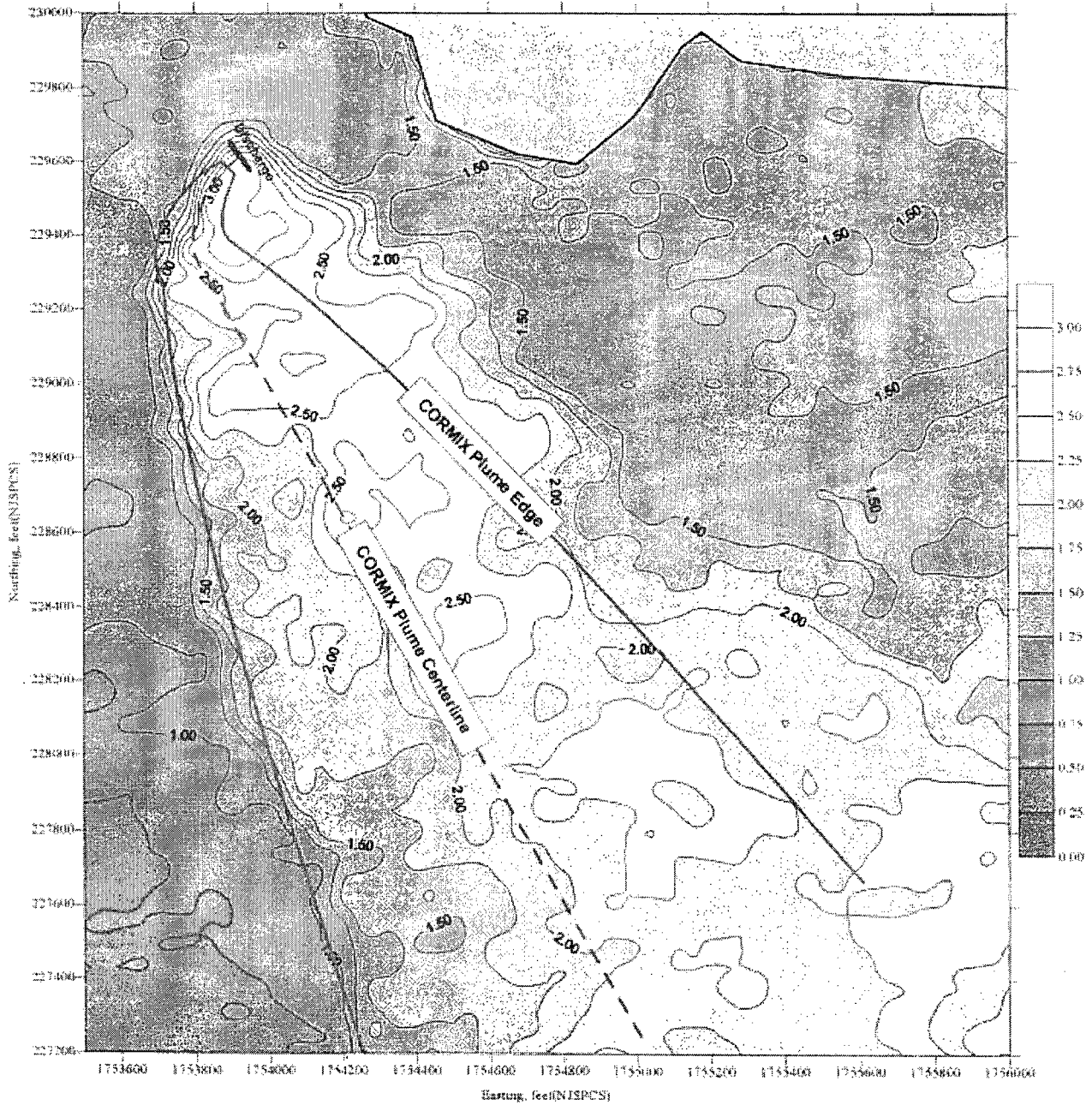
E-2 Figure III-26. CORMIX One-Unit Verification; 28 October 1997
Comparison of Model Predicted vs. Observed Lateral Temperature Distributions
Ebb Phase



Note : Vantage point is facing the oncoming plume.

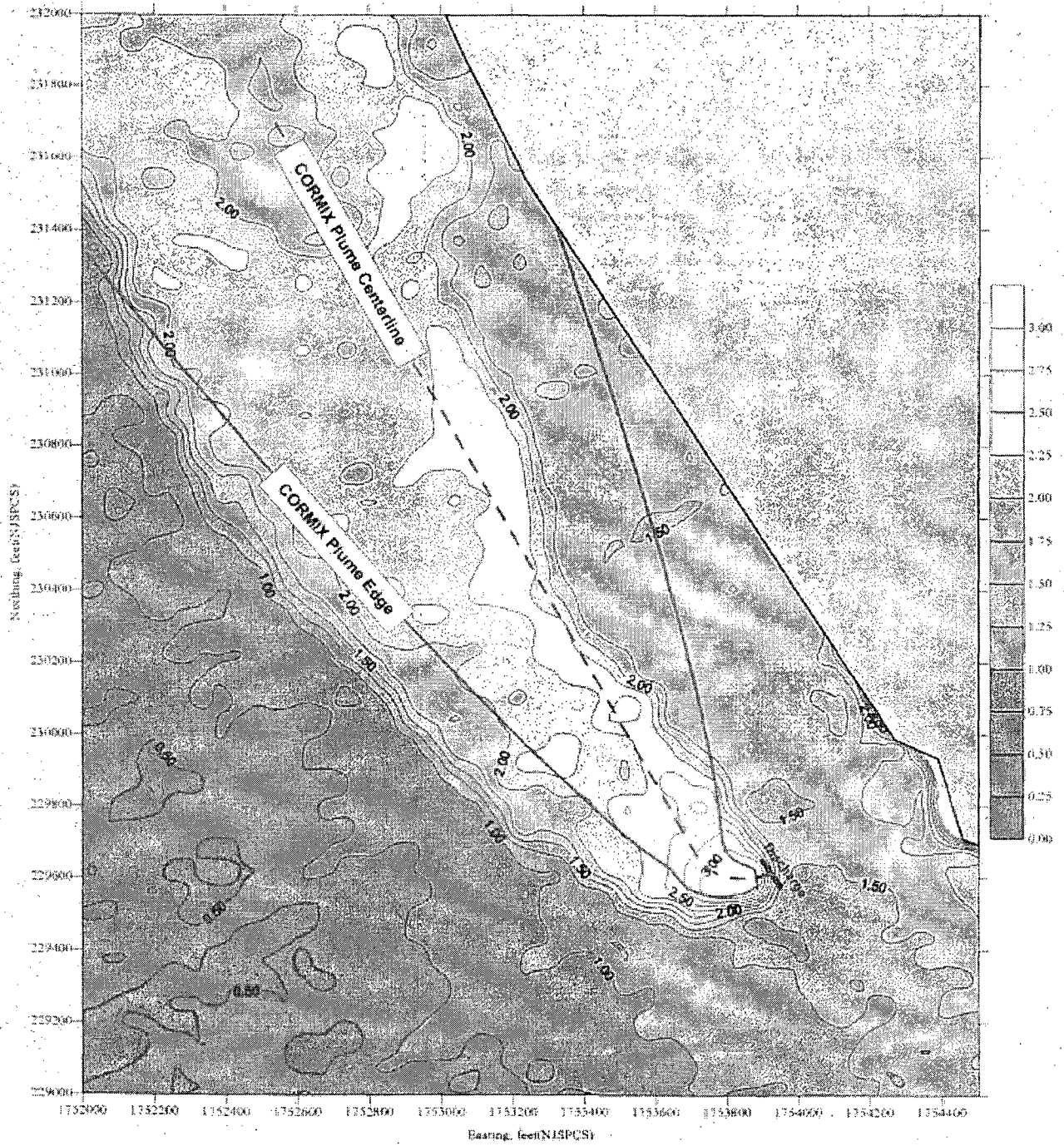


**E-2 Figure III-27. CORMIX One-Unit Verification; 28 October 1997
Comparison of Model Predicted vs. Observed Lateral Temperature Distributions
Flood Phase**



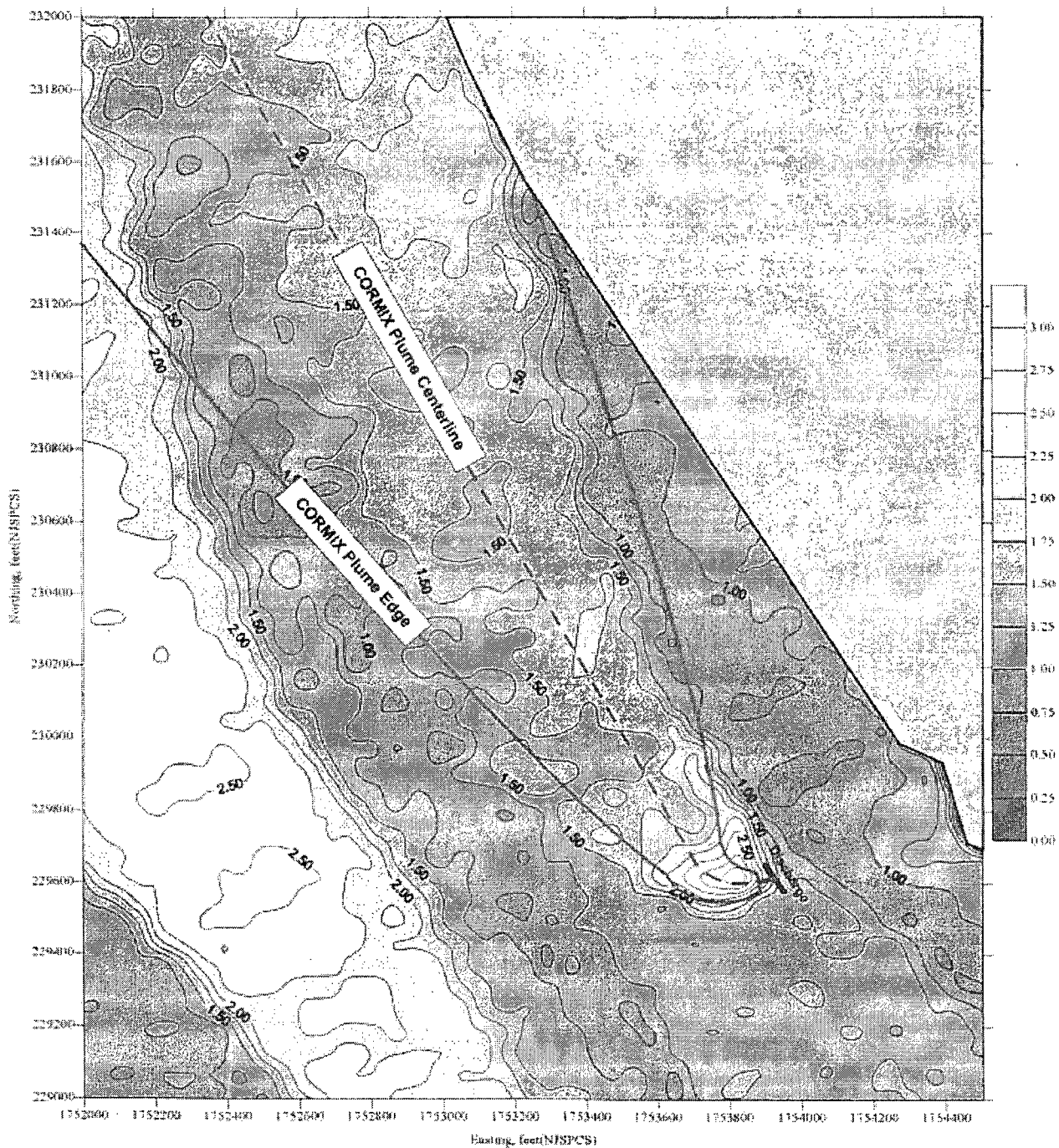
Note : Isotherms represent relative temperature gradients.
 The values do not represent actual delta-Ts.

E-2 Figure III-28. Infrared Imaging Contours, 29 May 1998
 Ebb Phase (18:07 - 18:10)



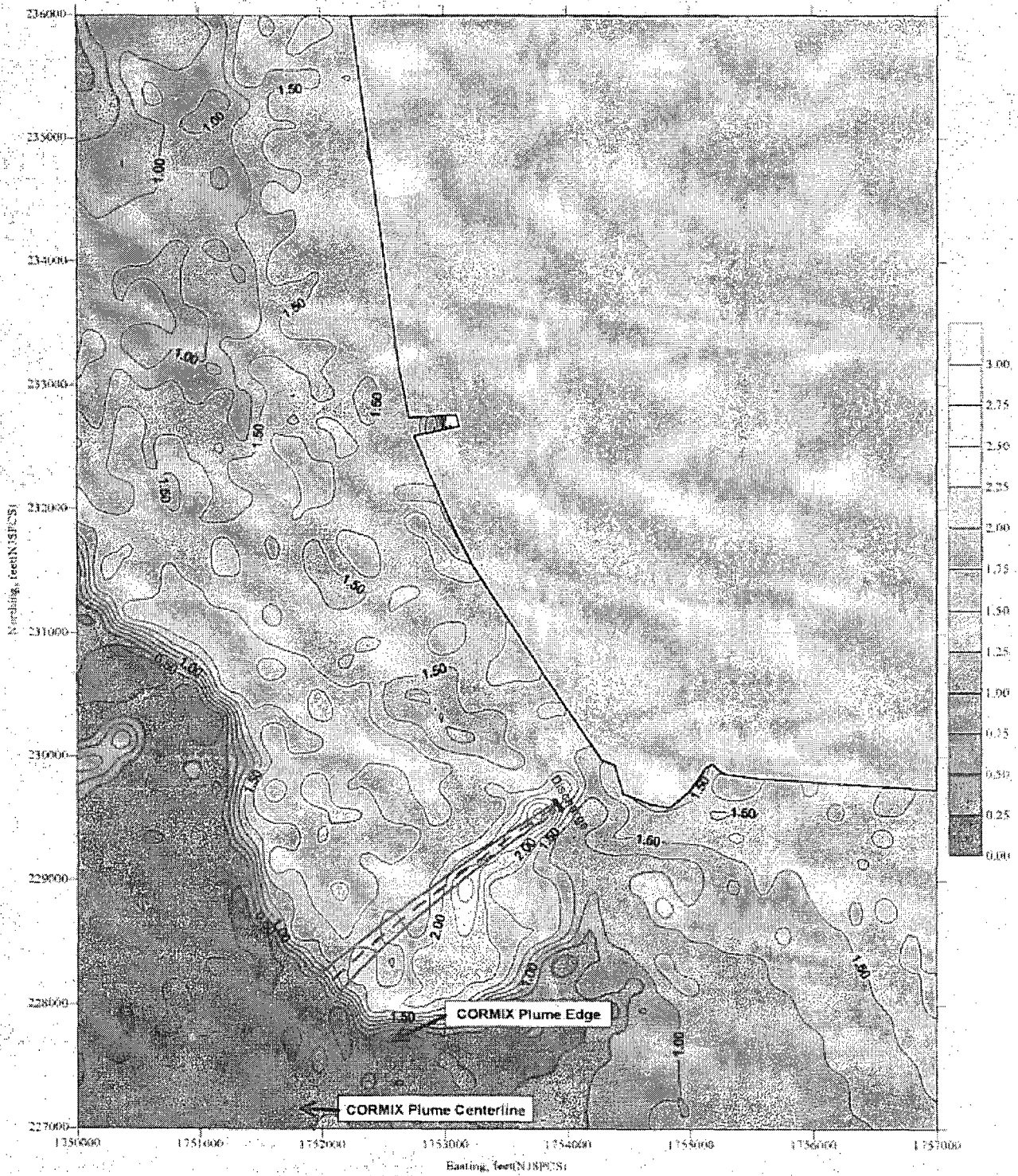
Note: Isotherms represent relative temperature gradients.
 The values do not represent actual delta-Ts

E-2 Figure III-29. Infrared Imaging Contours, 29 May 1998
 Flood Phase (12:39 - 12:41)



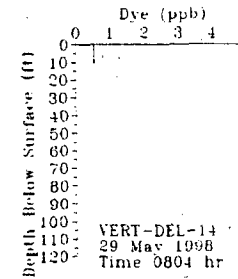
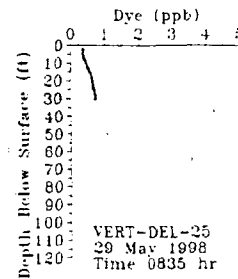
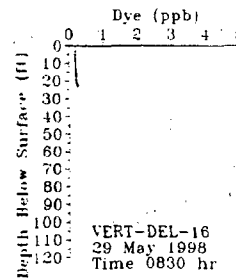
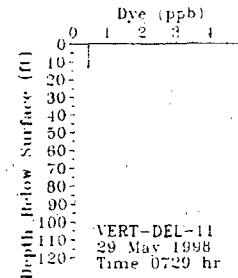
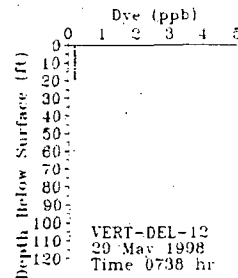
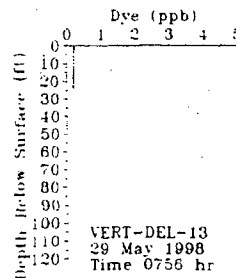
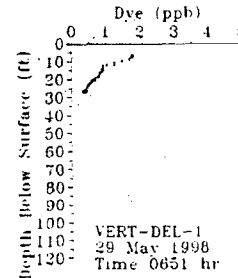
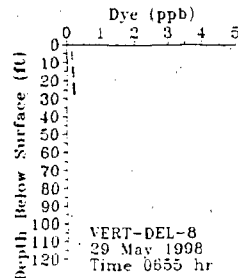
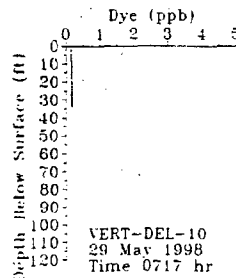
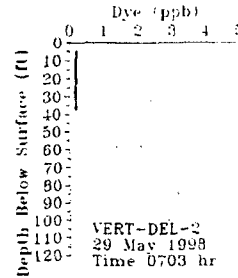
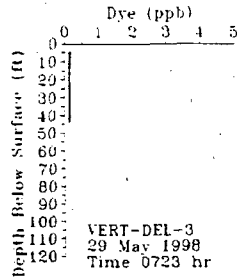
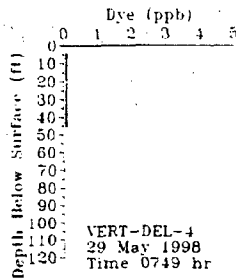
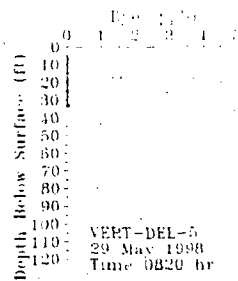
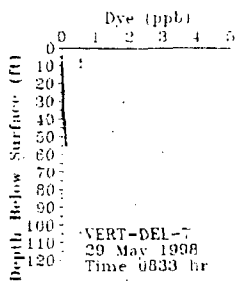
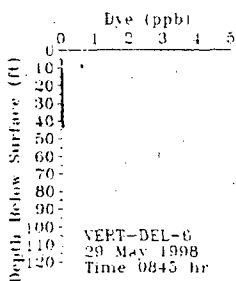
Note: Isotherms represent relative temperature gradients.
 The values do not represent actual delta-T's.

E-2 Figure III-30. Infrared Imaging Contours, 29 May 1998
 End-of-Ebb Phase (10:31 - 10:34)

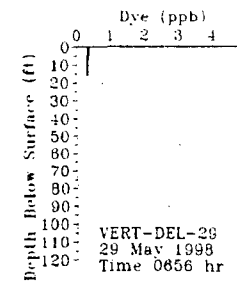
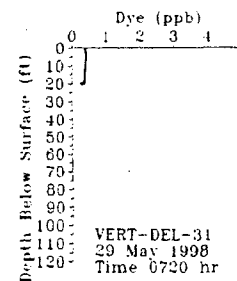
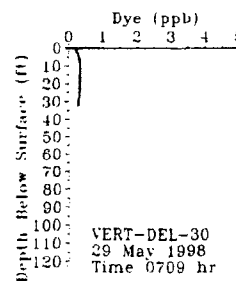
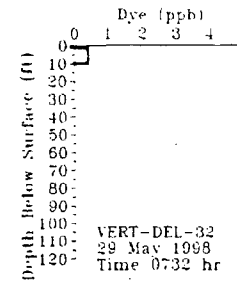
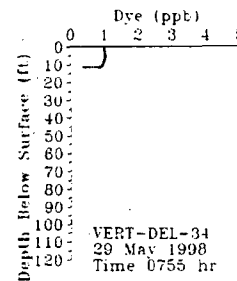
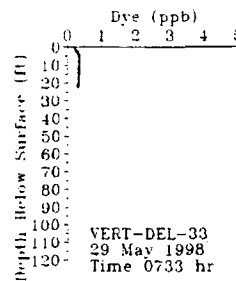
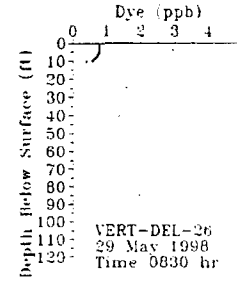
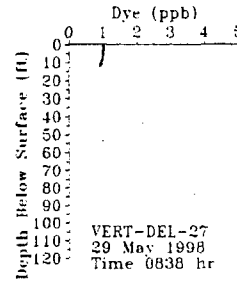
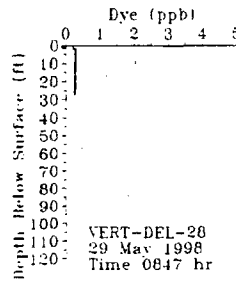
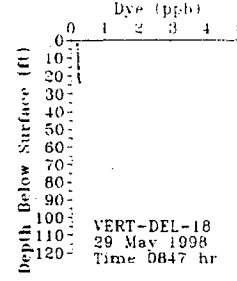
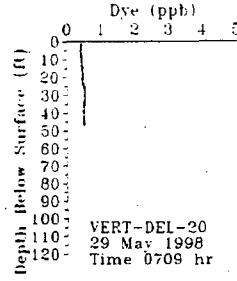
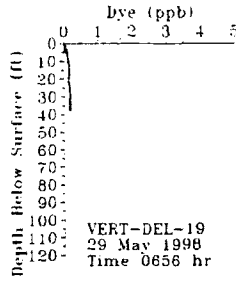
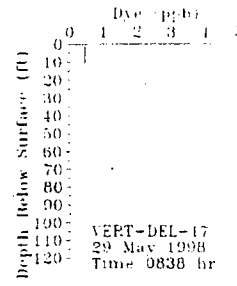
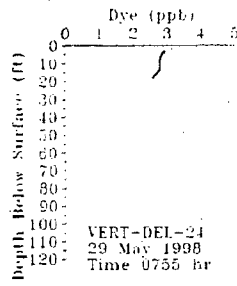
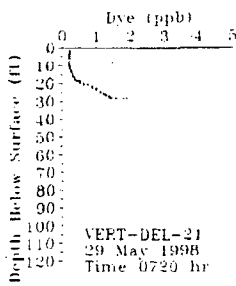


Note: Isotherms represent relative temperature gradients.
 The values do not represent actual delta-Ts.

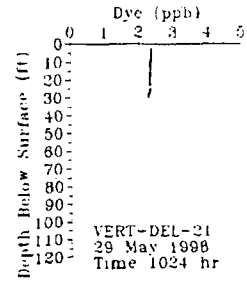
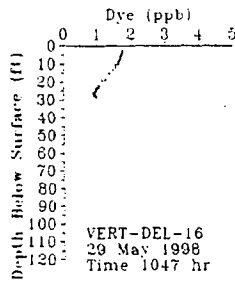
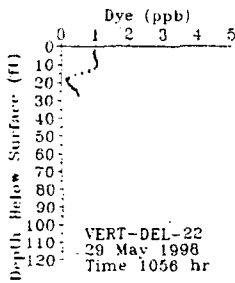
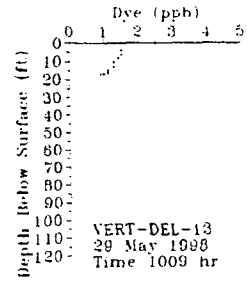
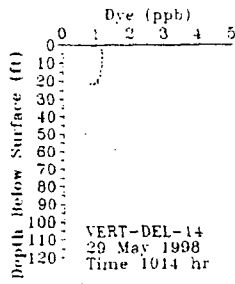
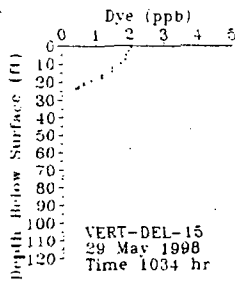
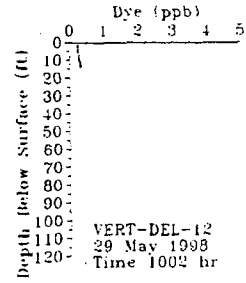
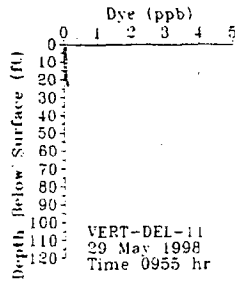
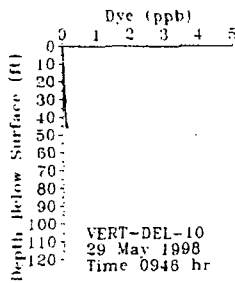
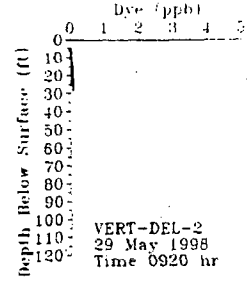
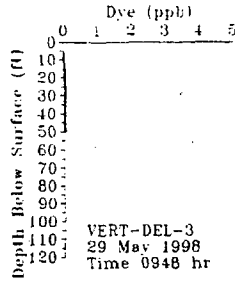
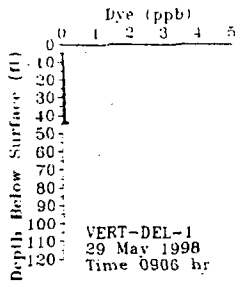
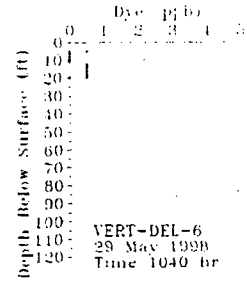
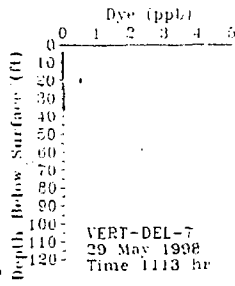
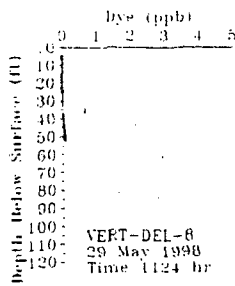
**E-2 Figure III-31. Infrared Imaging Contours, 29 May 1998
 End-of-Flood Phase (14:50 - 14:52)**



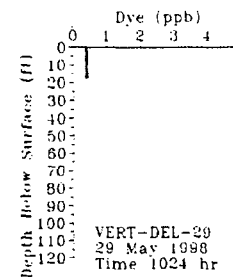
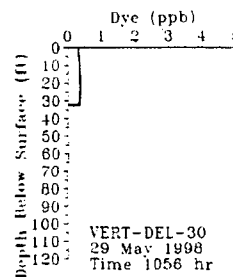
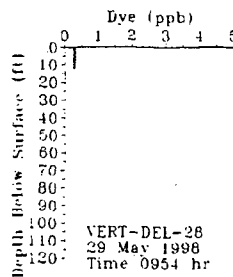
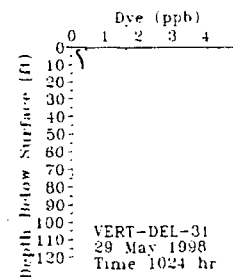
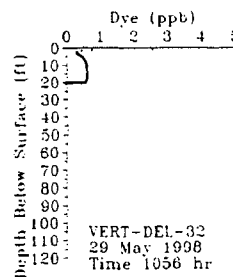
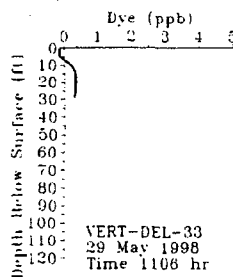
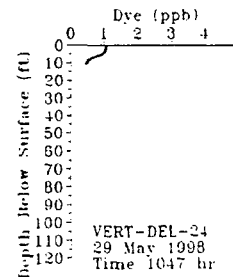
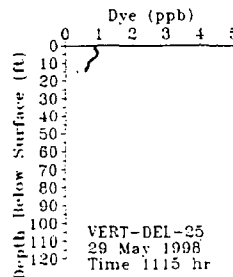
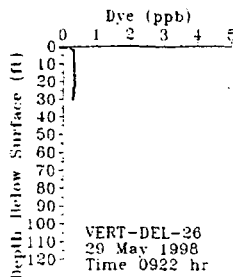
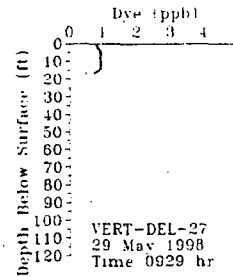
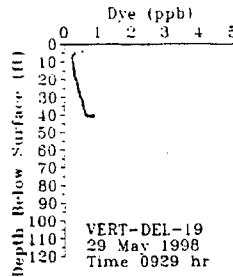
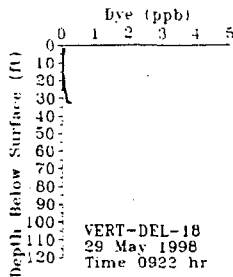
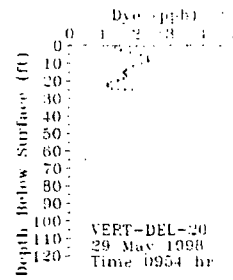
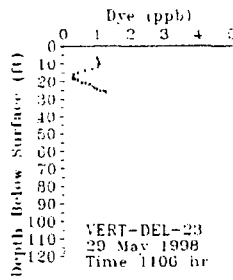
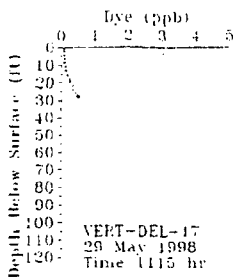
E-2 Figure III-32a. Measured dye at locations of shipboard verticals north of the Station during an ebb phase on May 29, 1998.



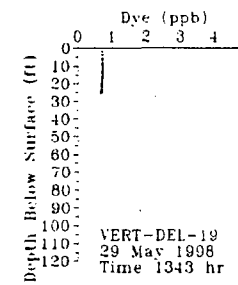
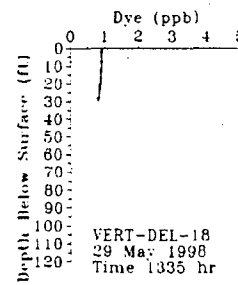
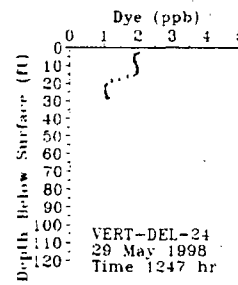
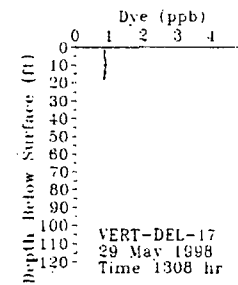
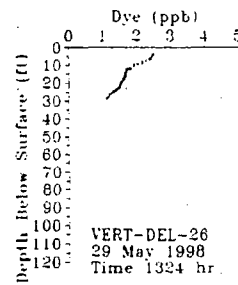
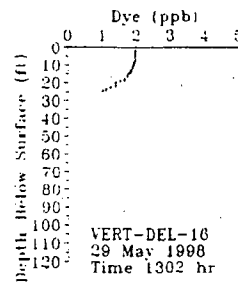
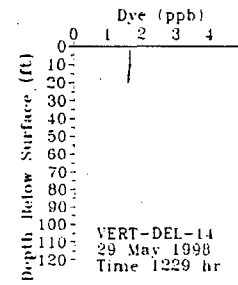
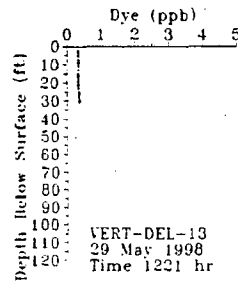
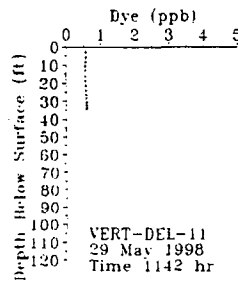
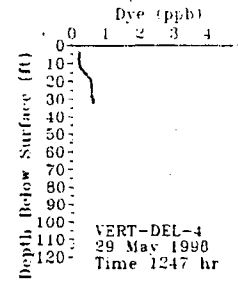
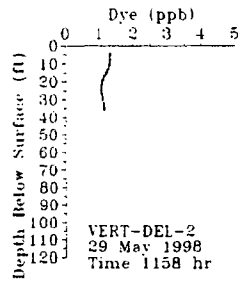
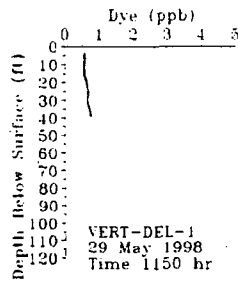
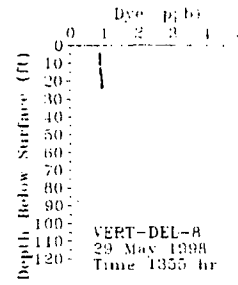
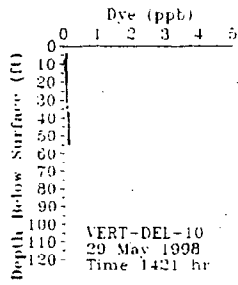
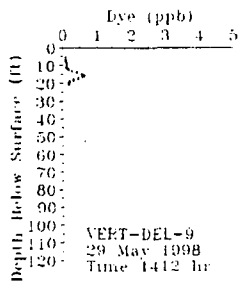
E-2 Figure III-32b. Measured dye at locations of shipboard shipboard verticals south of the Station during an ebb phase on May 29, 1998.



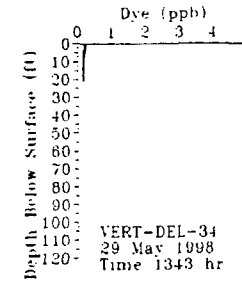
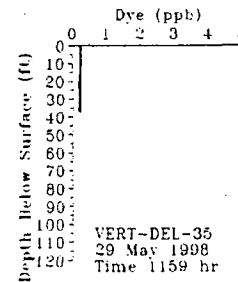
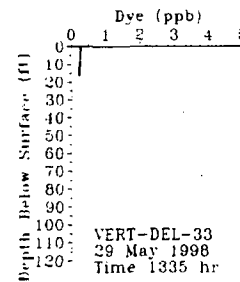
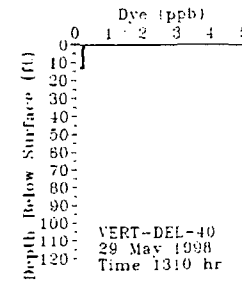
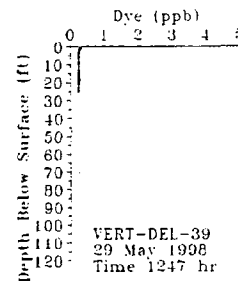
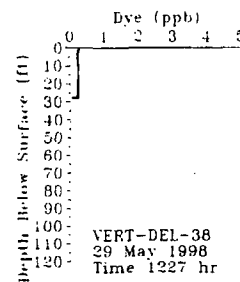
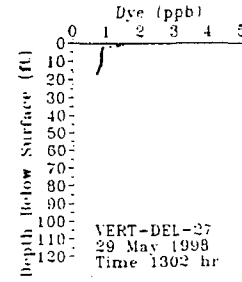
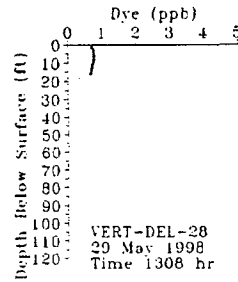
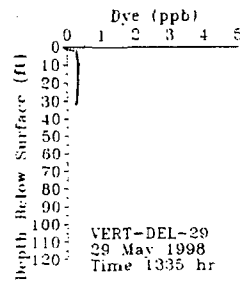
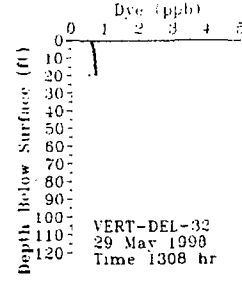
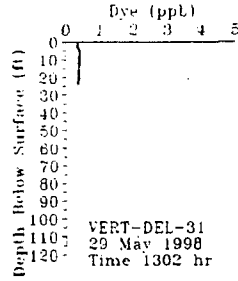
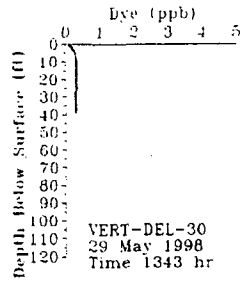
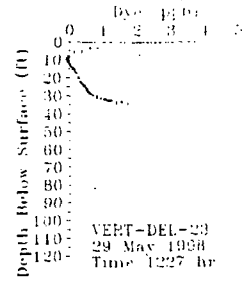
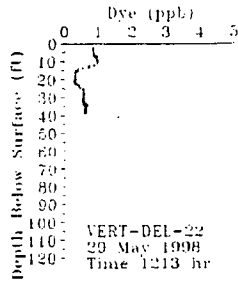
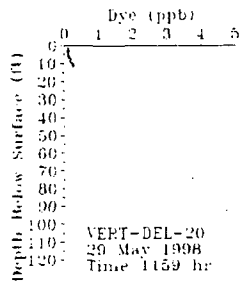
E-2 Figure III-33a. Measured dye at locations of shipboard shipboard verticals north of the Station during a slack phase (end-of-ebb) on May 29, 1998.



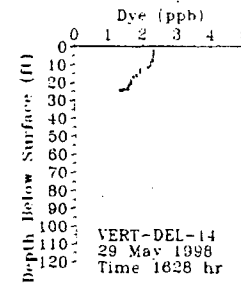
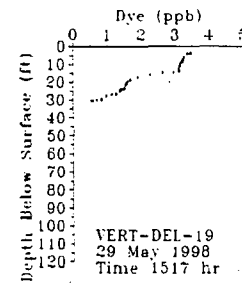
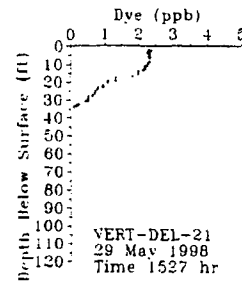
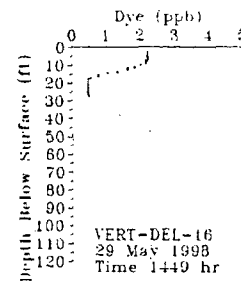
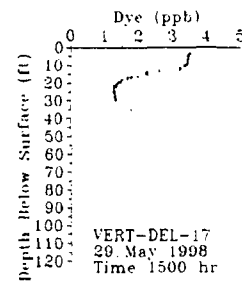
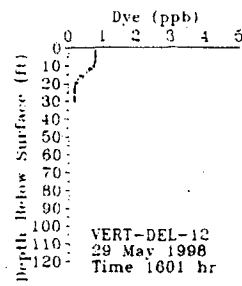
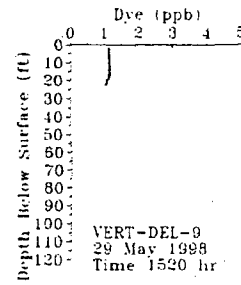
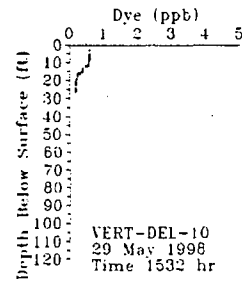
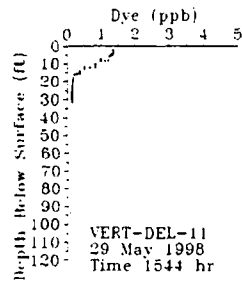
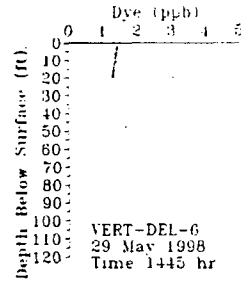
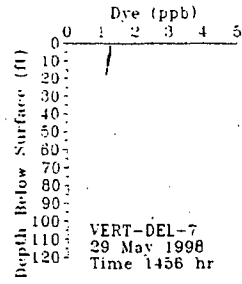
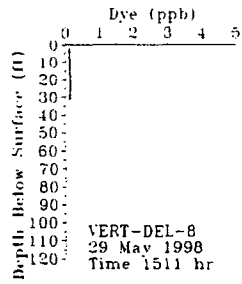
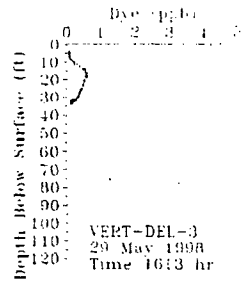
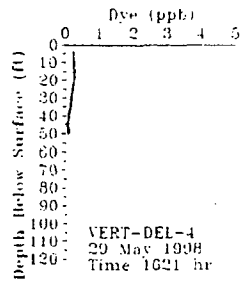
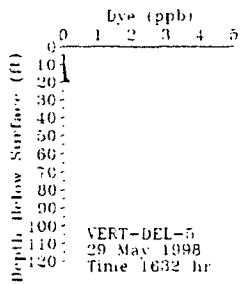
E-2 Figure III-33b. Measured dye at locations of shipboard shipboard verticals south of the Station during a slack phase (end-of-ebb) on May 29, 1998.



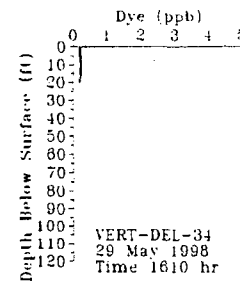
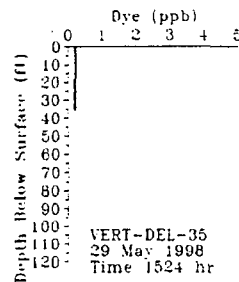
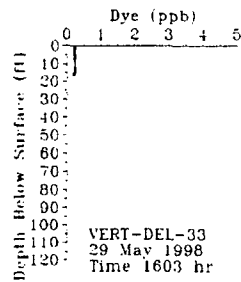
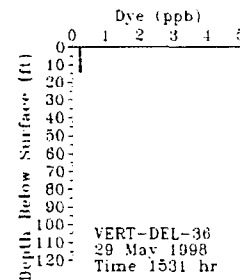
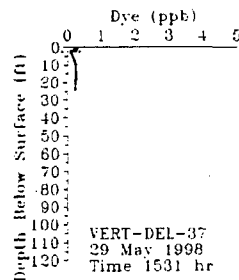
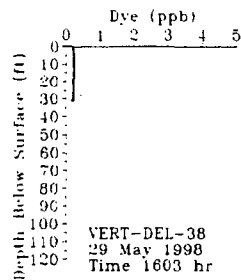
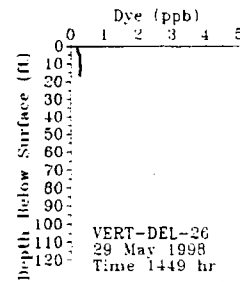
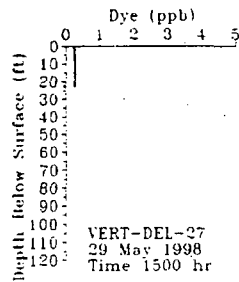
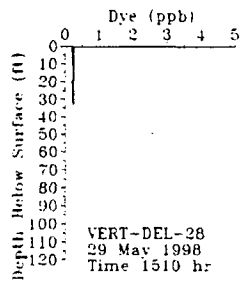
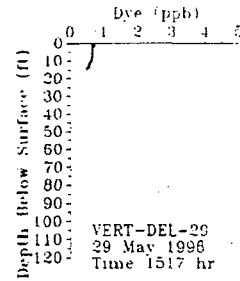
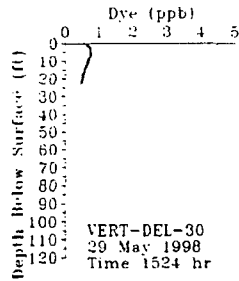
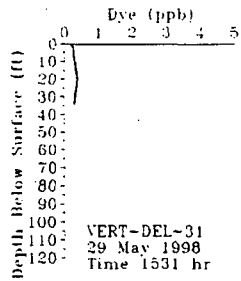
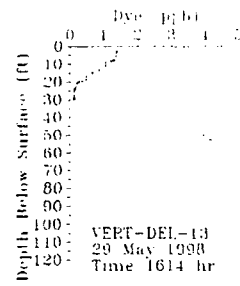
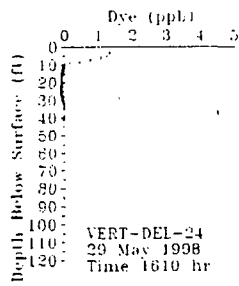
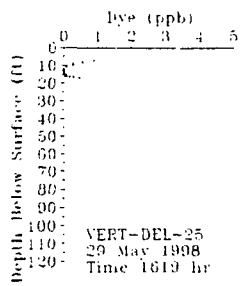
E-2 Figure III-34a. Measured dye at locations of shipboard shipboard verticals north of the Station during a flood phase on May 29, 1998.



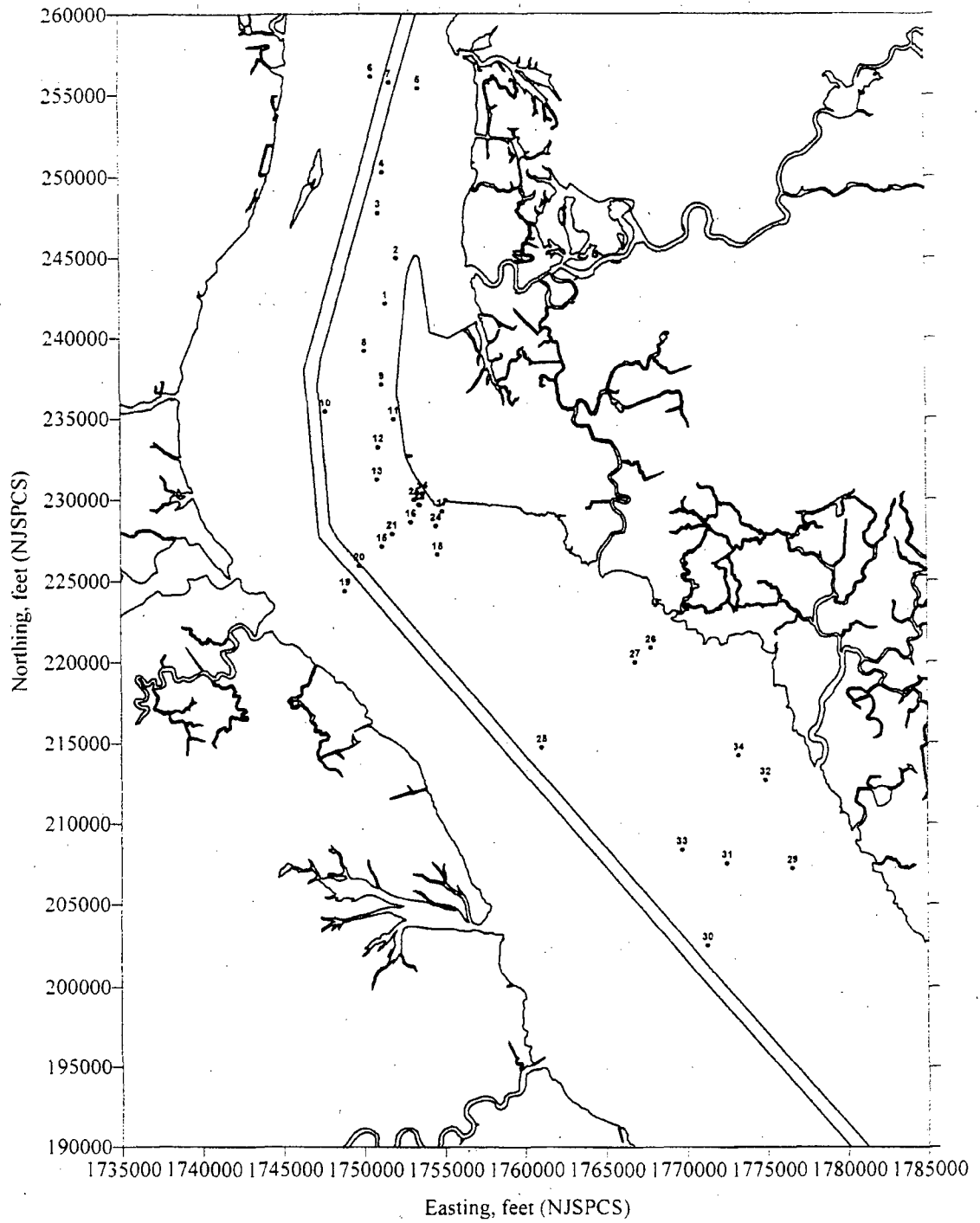
E-2 Figure III-34b. Measured dye at locations of shipboard shipboard verticals south of the Station during a flood phase on May 29, 1998.



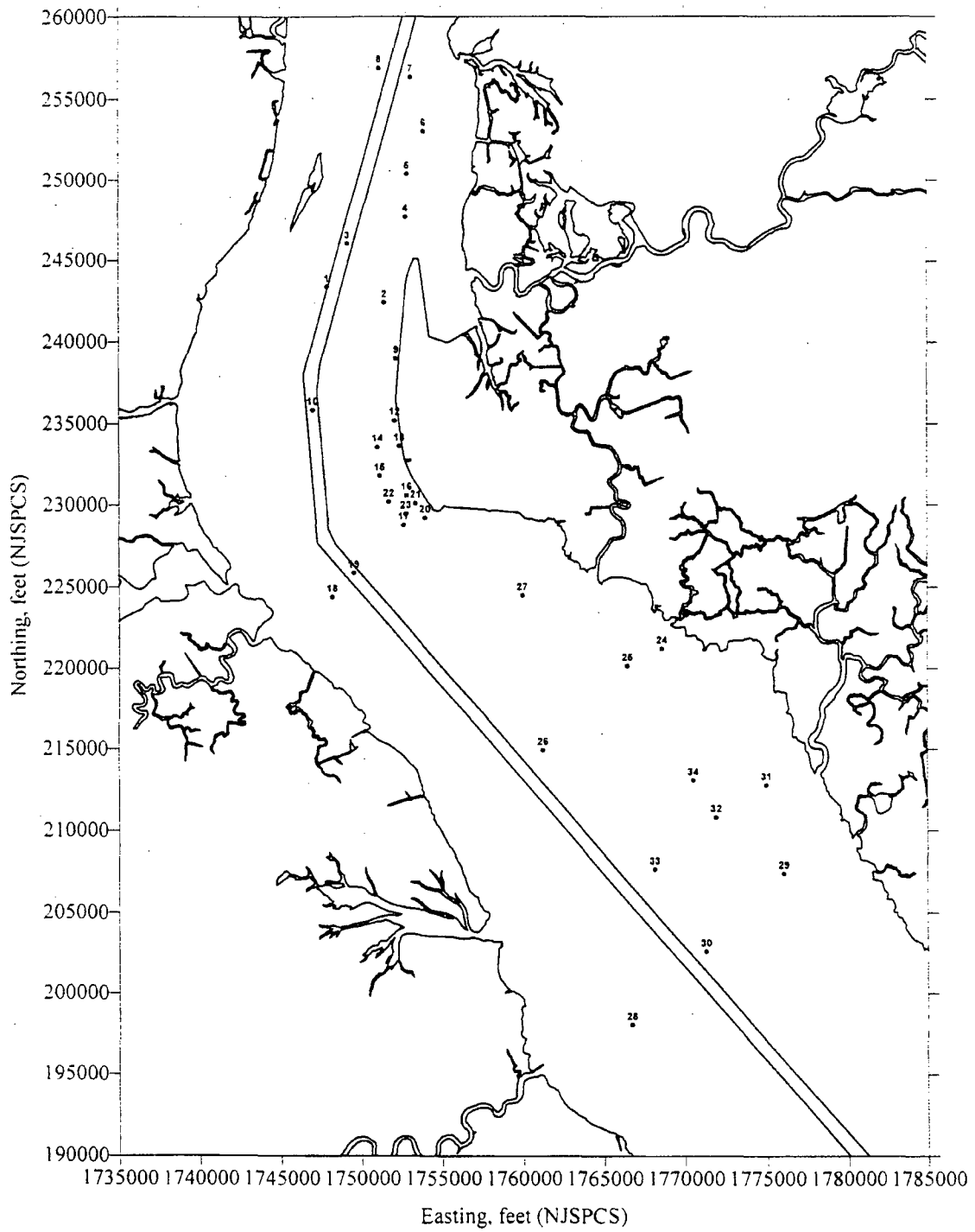
E-2 Figure III-35a. Measured dye at locations of shipboard verticals north of the Station during a slack phase (end-of-flood) on May 29, 1998.



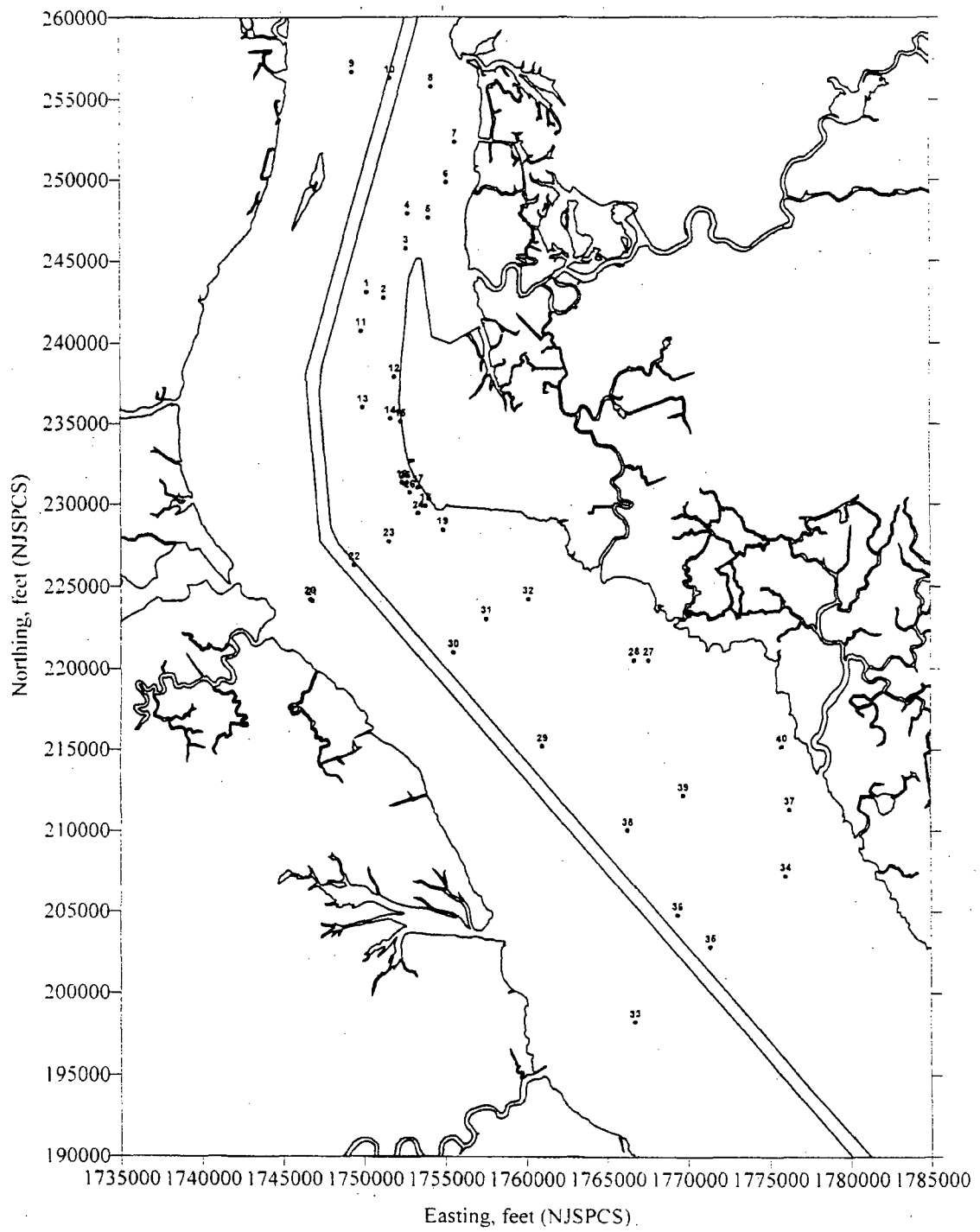
E-2 Figure III-35b. Measured dye at locations of shipboard verticals south of the Station during a slack phase (end-of-flood) on May 29, 1998.



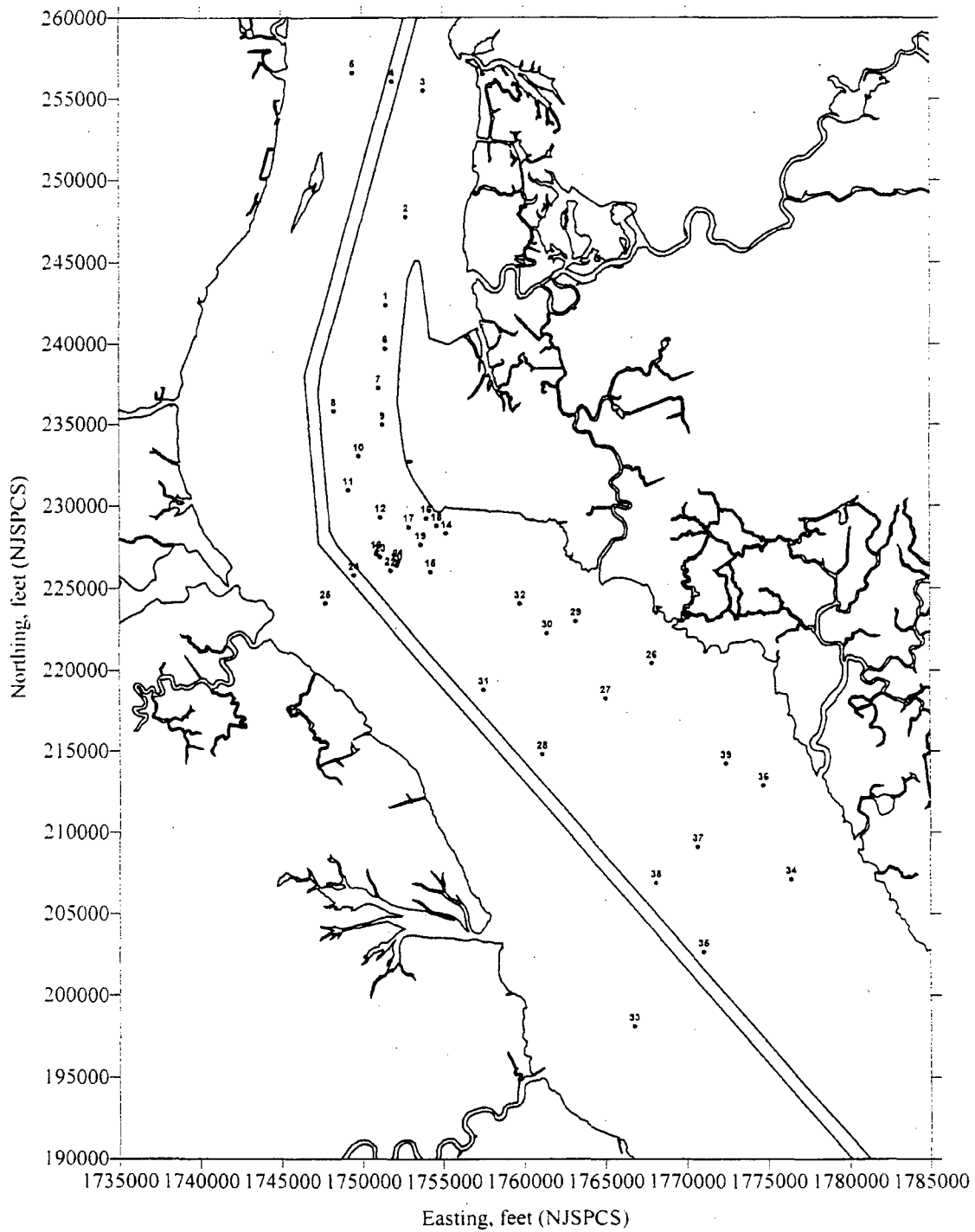
E-2 Figure III-36a. Locations of shipboard vertical profiles measured during an ebb phase on May 29, 1998.



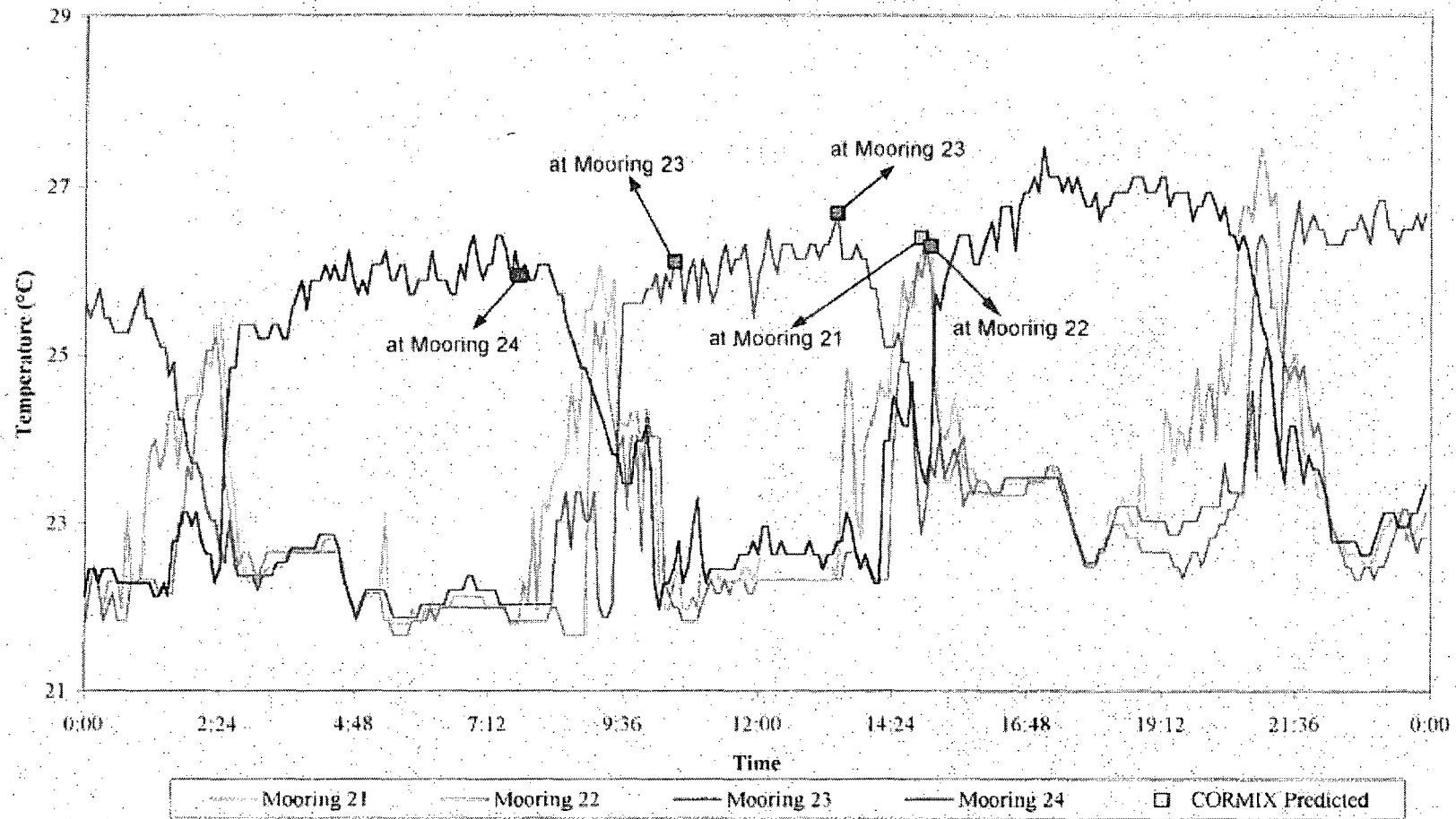
E-2 Figure III-36b. Locations of shipboard vertical profiles measured during a slack phase (end-of-ebb) on May 29, 1998.



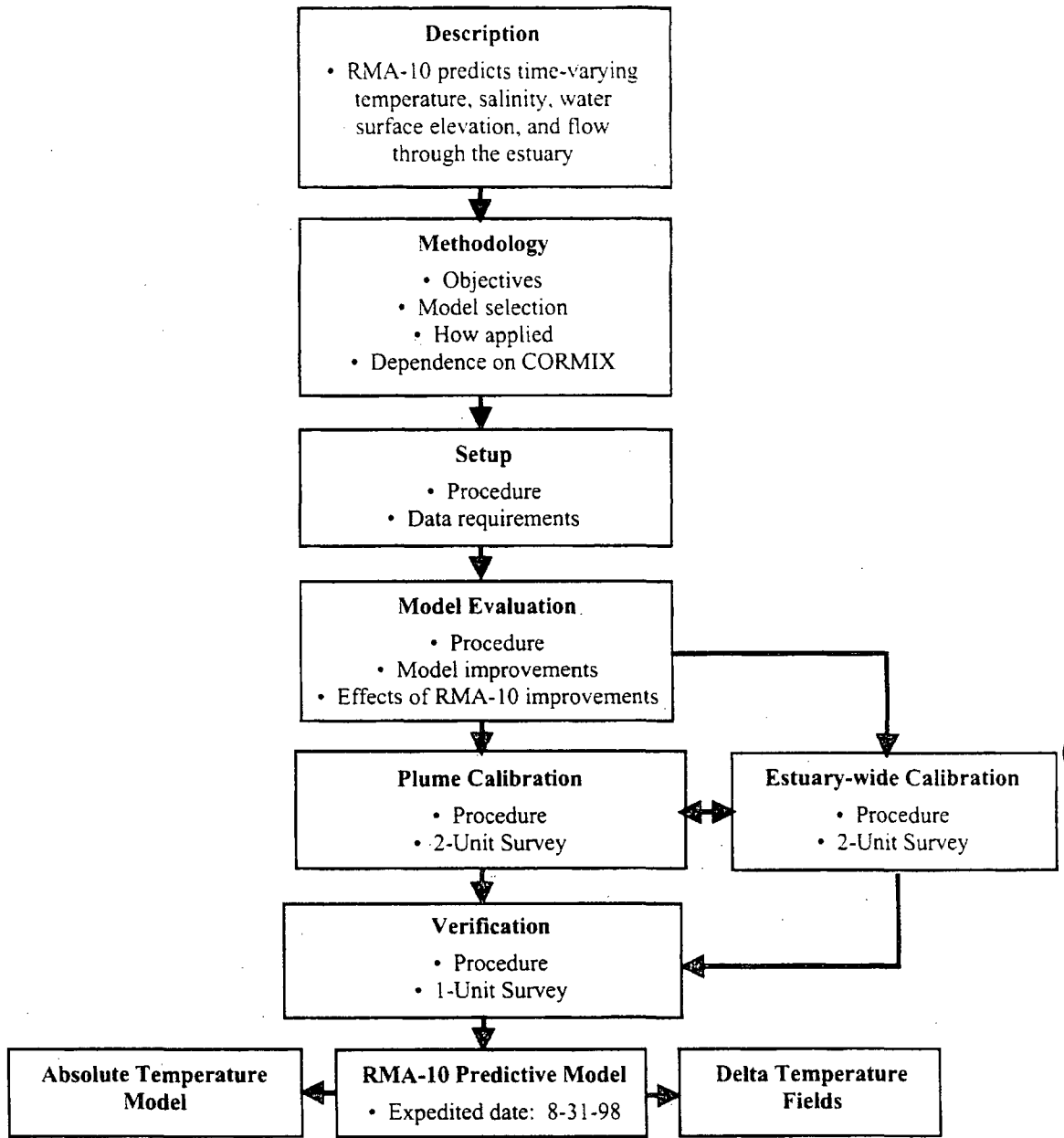
E-2 Figure III-36c. Locations of shipboard vertical profiles measured during a flood phase on May 29, 1998.



E-2 Figure III-36d. Locations of shipboard vertical profiles measured during a slack phase (end-of-flood) on May 29, 1998.



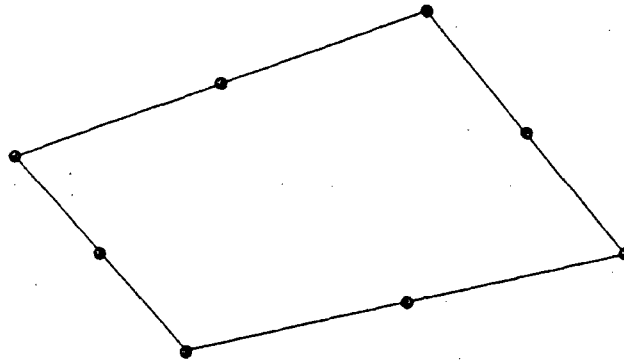
E-2 Figure III-37. Observed Near-field Surface Mooring Temperature vs. Model Predicted Plume Surface Temperature, 29 May 1998



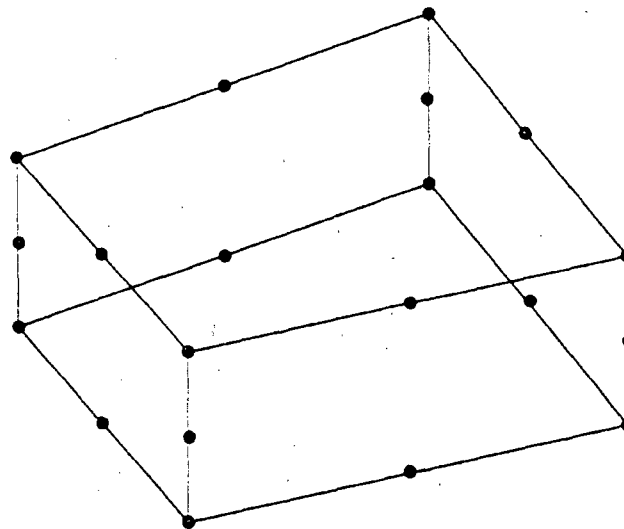
E-2 Figure III-38. Schematic of RMA-10 Work Plan.



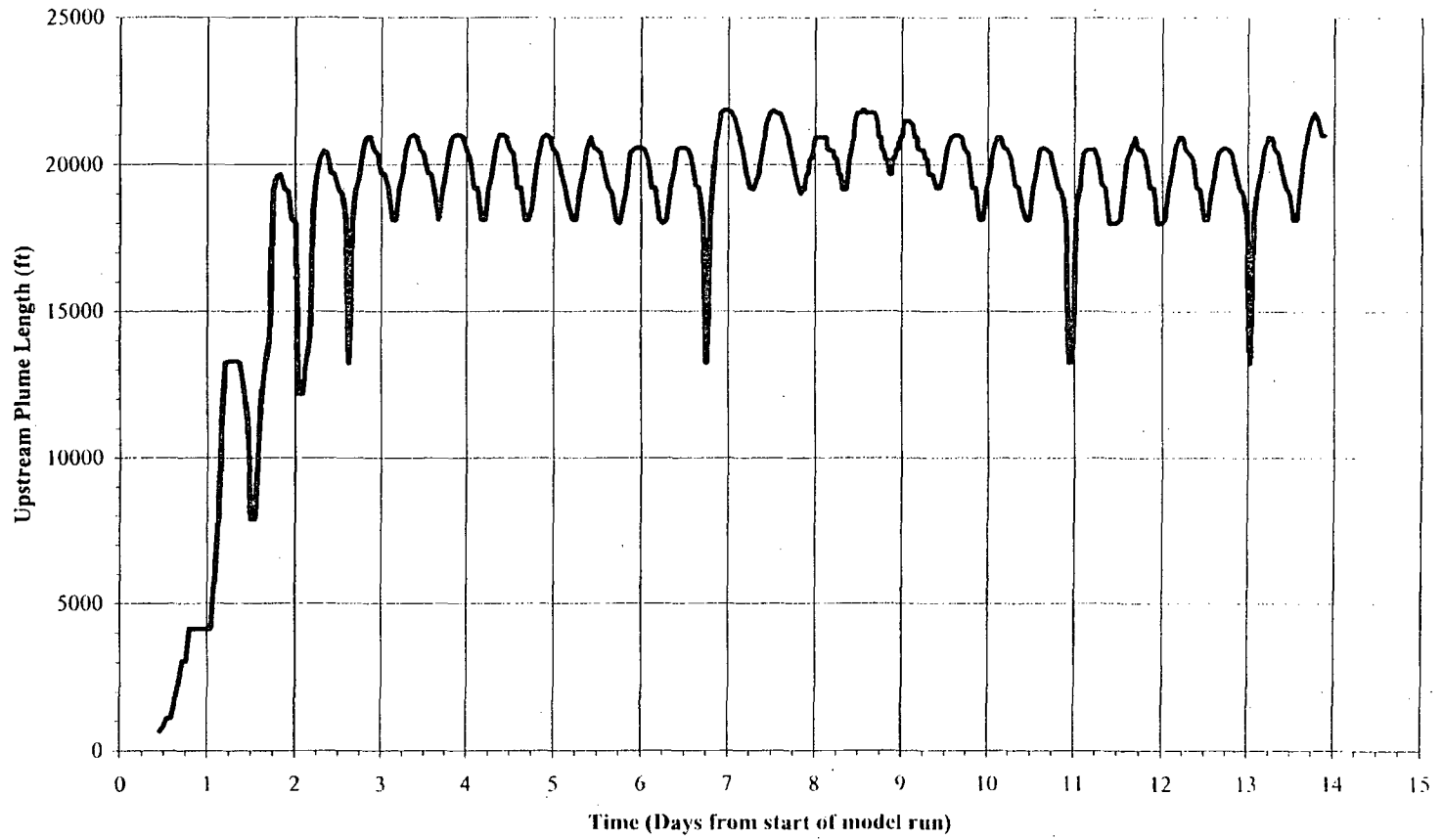
(a) One-dimensional element with three nodes



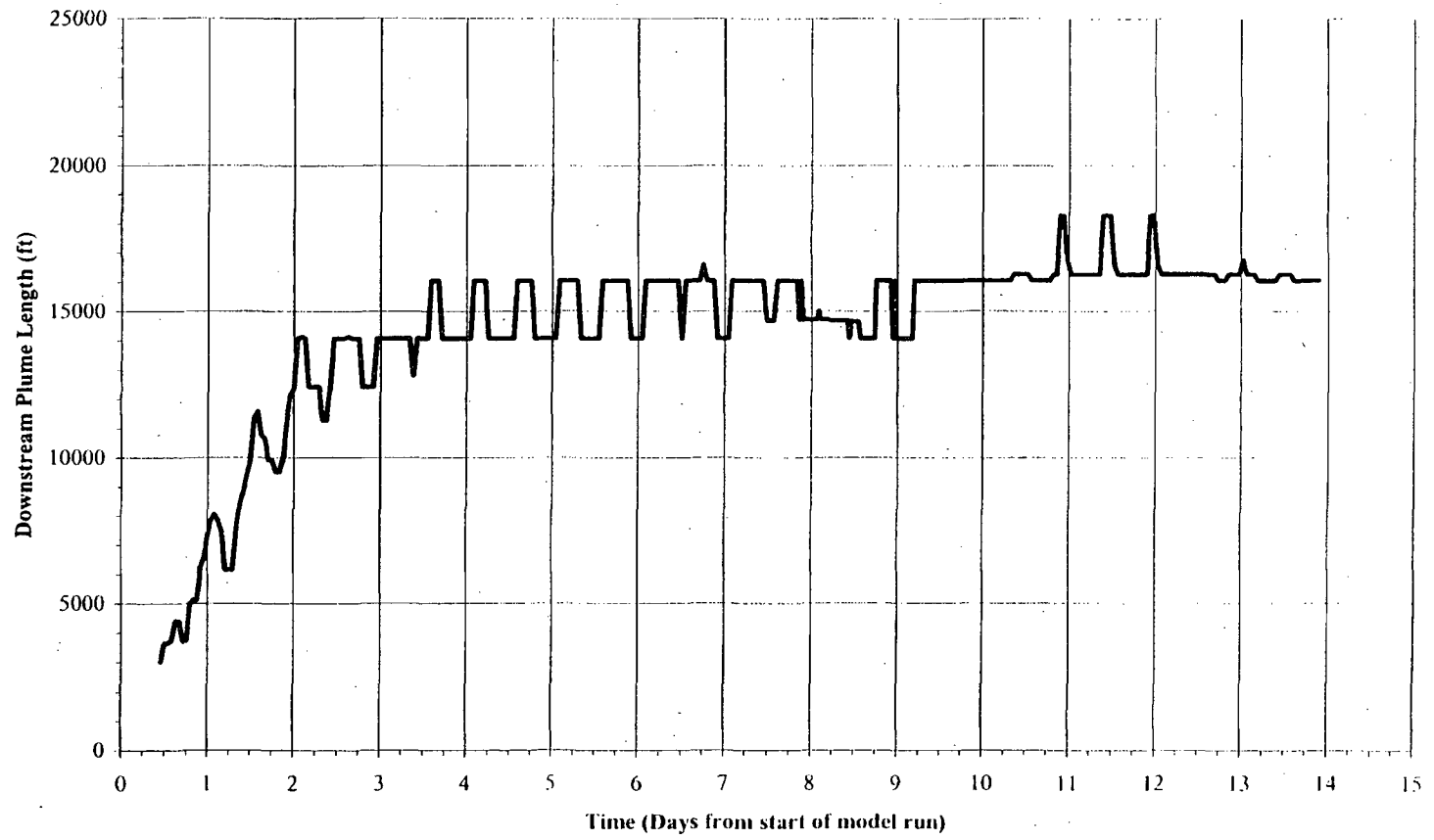
(b) Two-dimensional quadrilateral element with eight nodes



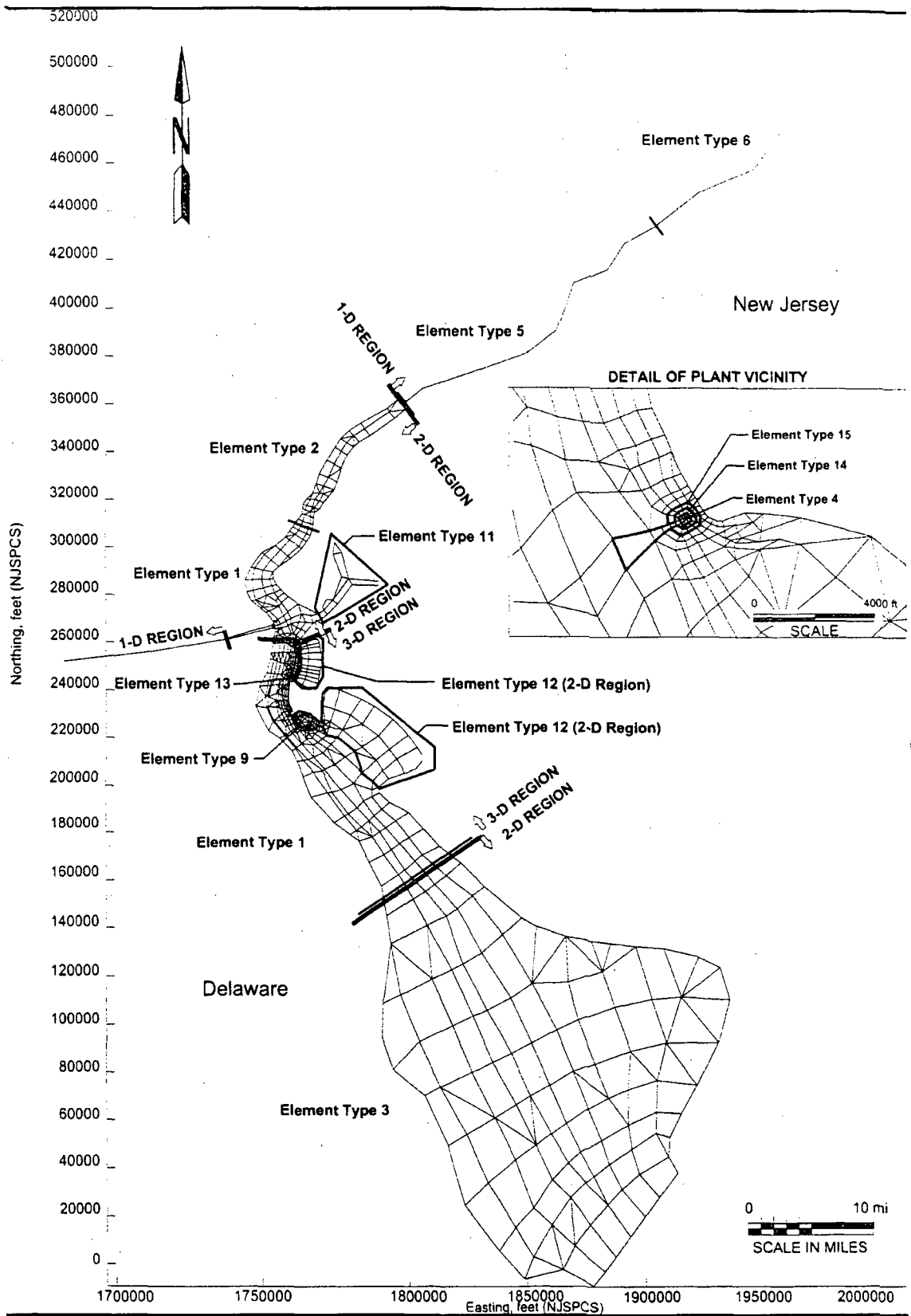
(c) Three-dimensional brick element with twenty nodes



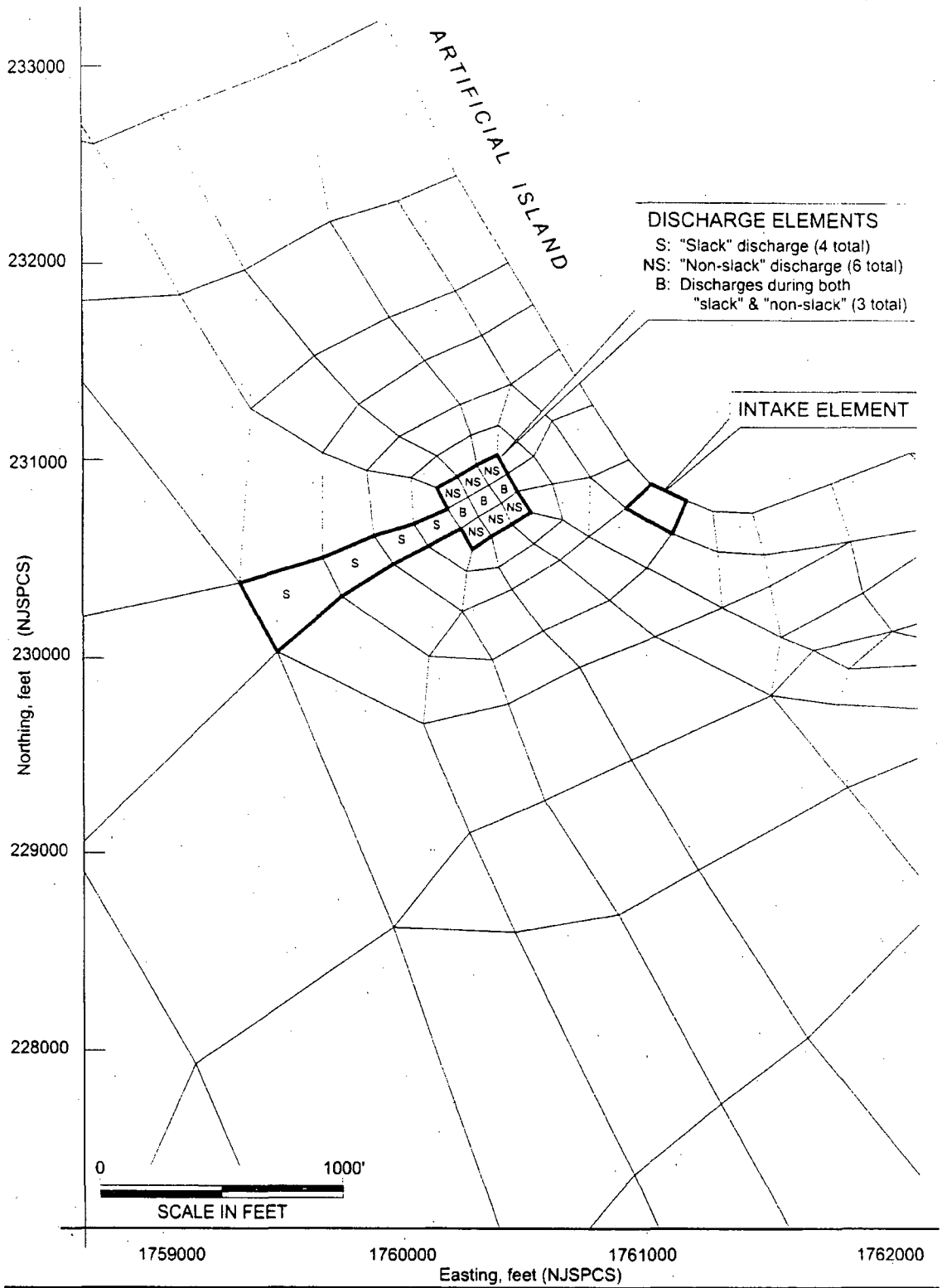
E-2 Figure III-40a. Model spinup based on upstream plume lengths.



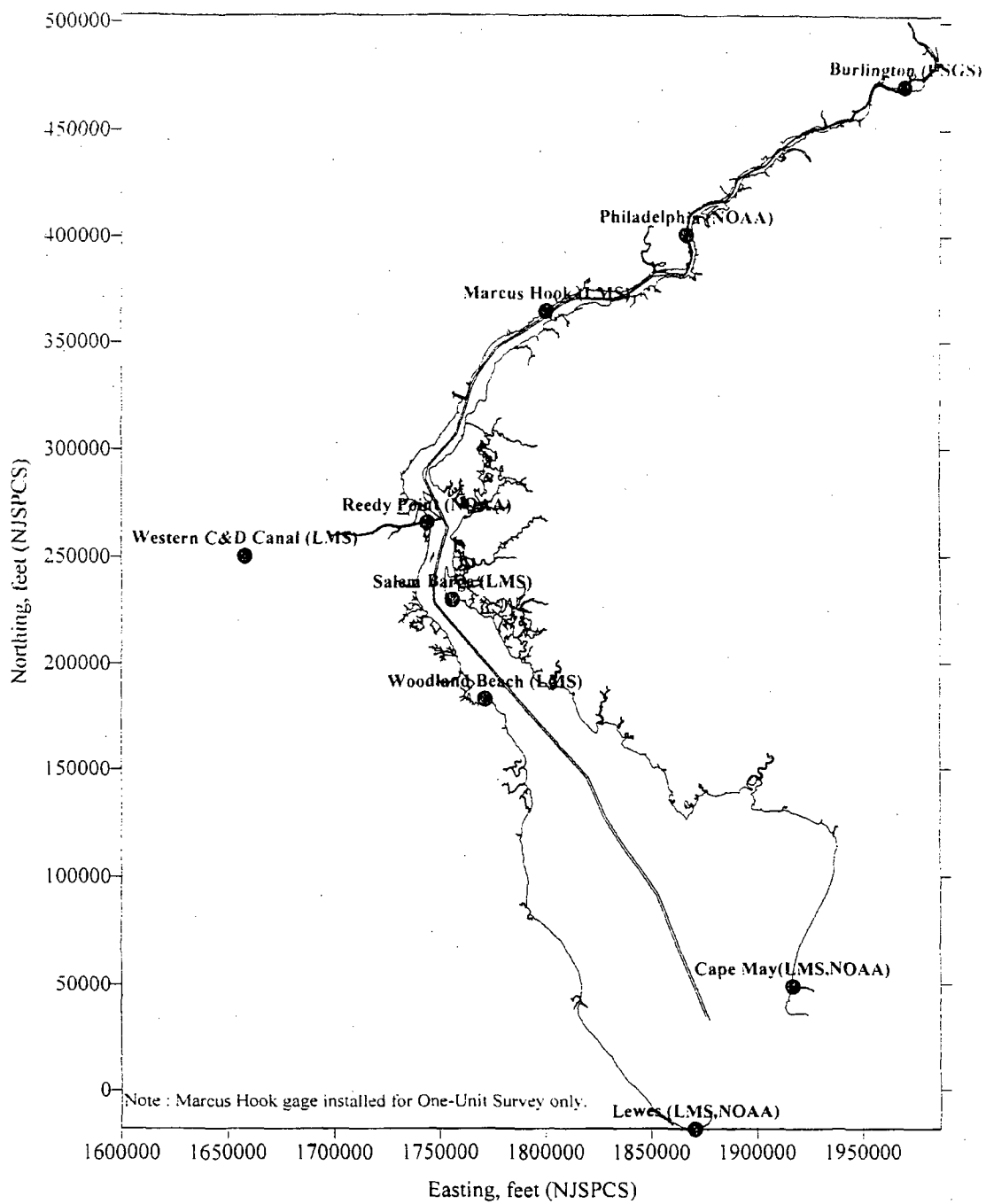
E-2 Figure III-40b. Model spinup based on downstream plume lengths.



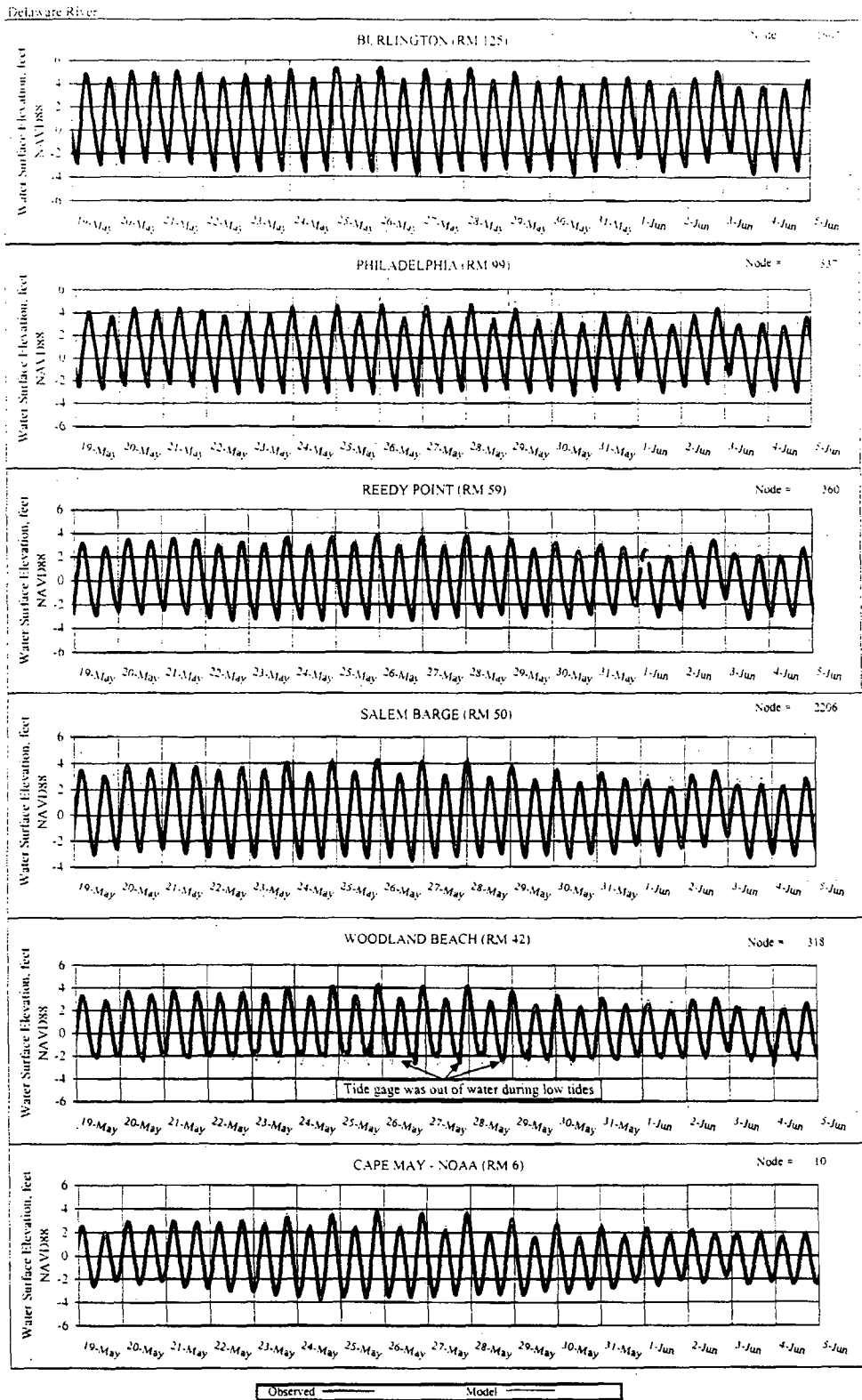
E-2 Figure III-41. Model grid showing element types and dimensional classifications (i.e., 1-D, 2-D, and 3-D regions).



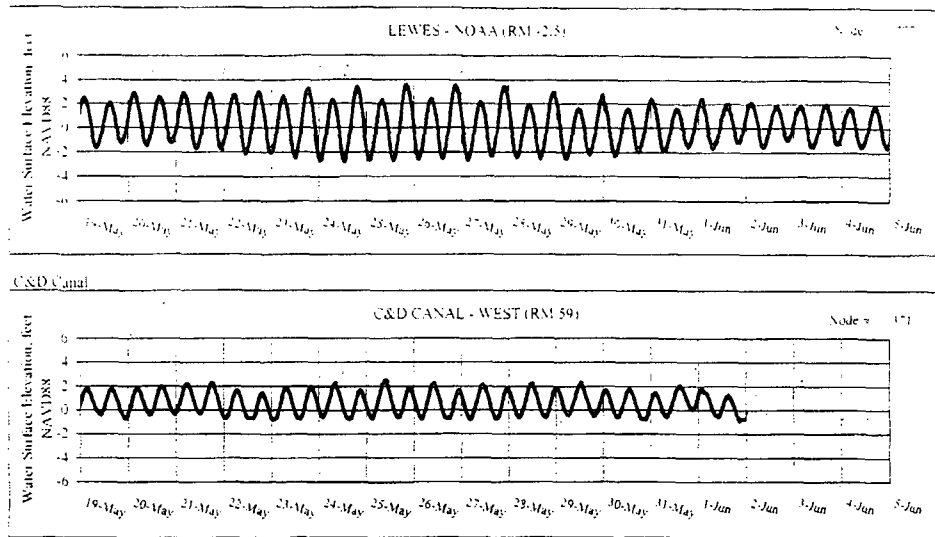
E-2 Figure III-42. Model grid in the vicinity of the Station showing intake and discharge elements.



E-2 Figure III-43. Locations of tide gages for One-Unit Survey (21-31 October 1997) and Two-Unit Survey (19 May-4 June 1998)

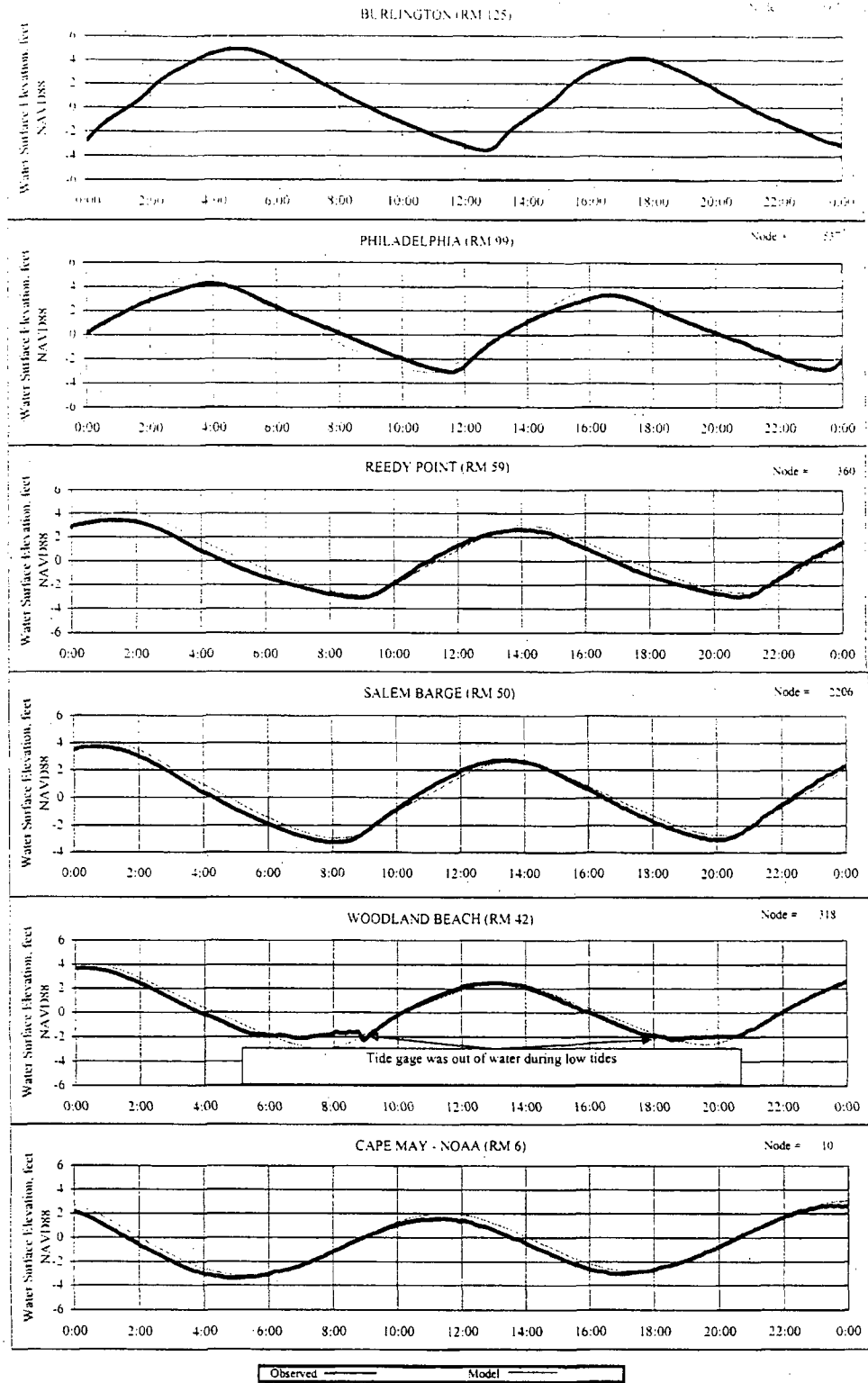


E-2 Figure III-44a. Comparison of modeled and measured tides in the Estuary for the calibration period (19 May - 4 June 1998).

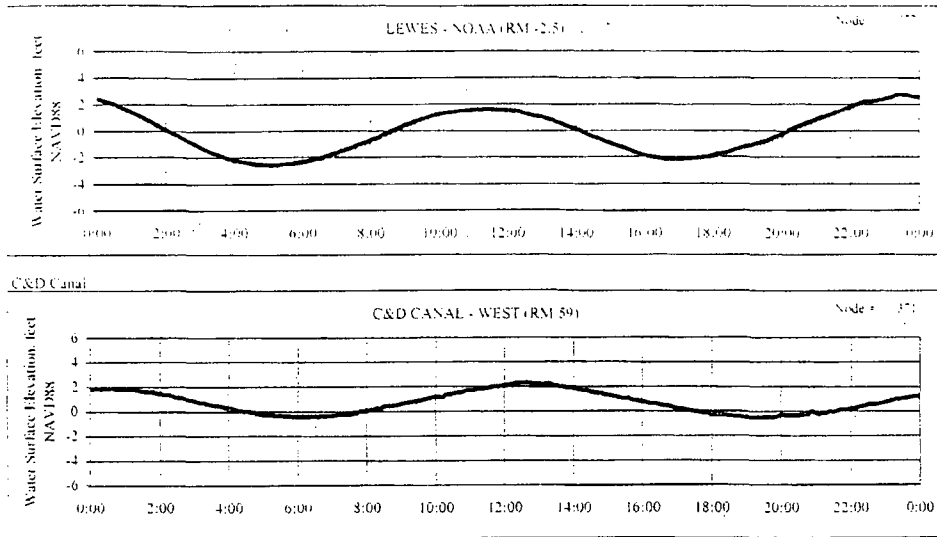


Observed ——— Model - - - -

E-2 Figure III-44b. Comparison of modeled and measured tides at the west side of the Bay mouth (Lewes, DE) and the western end of the C&D Canal for the calibration period (19 May - 4 June 1998).

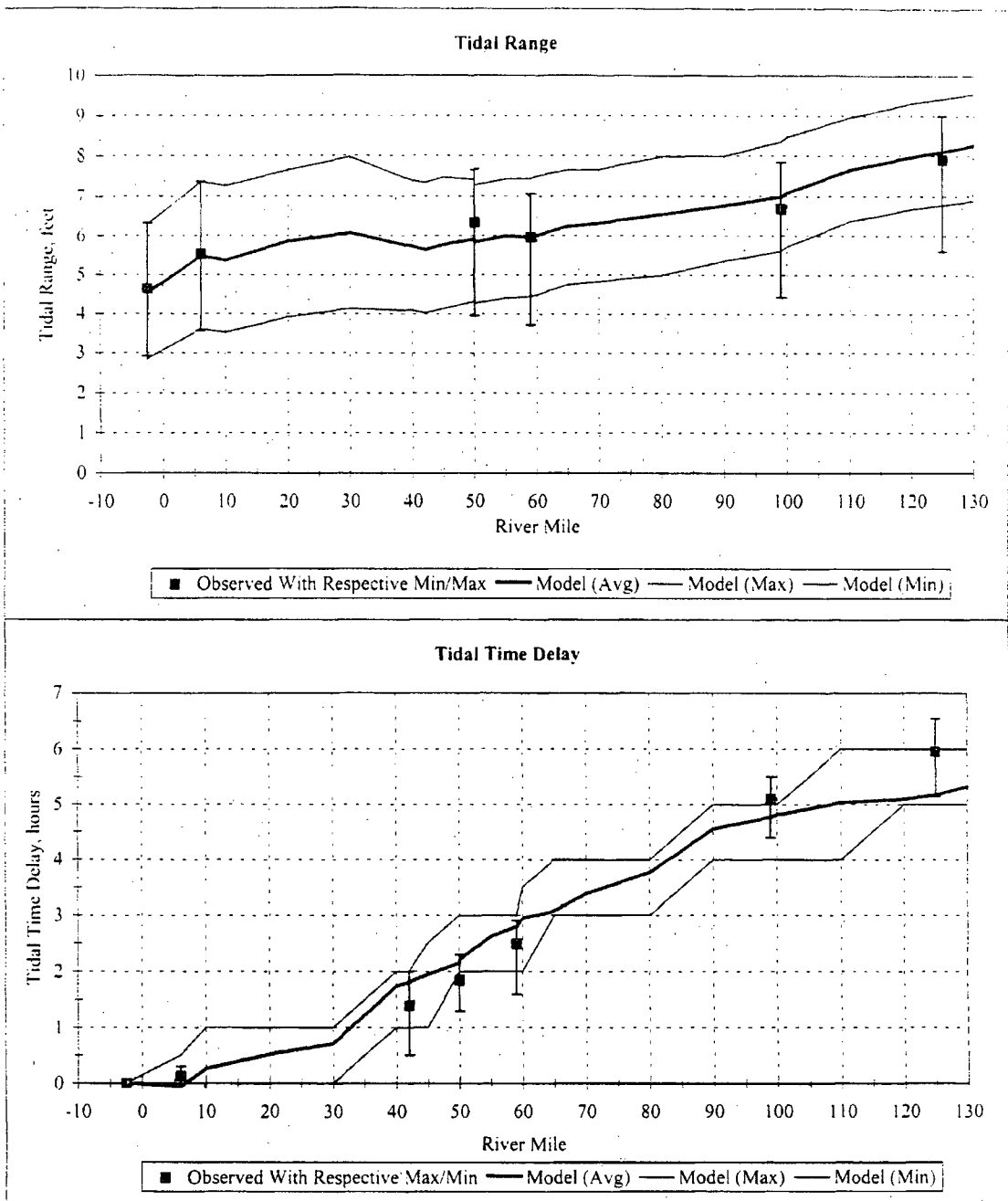


E-2 Figure III-45a. Comparison of modeled and measured tides in the Estuary for 29 May 1998.

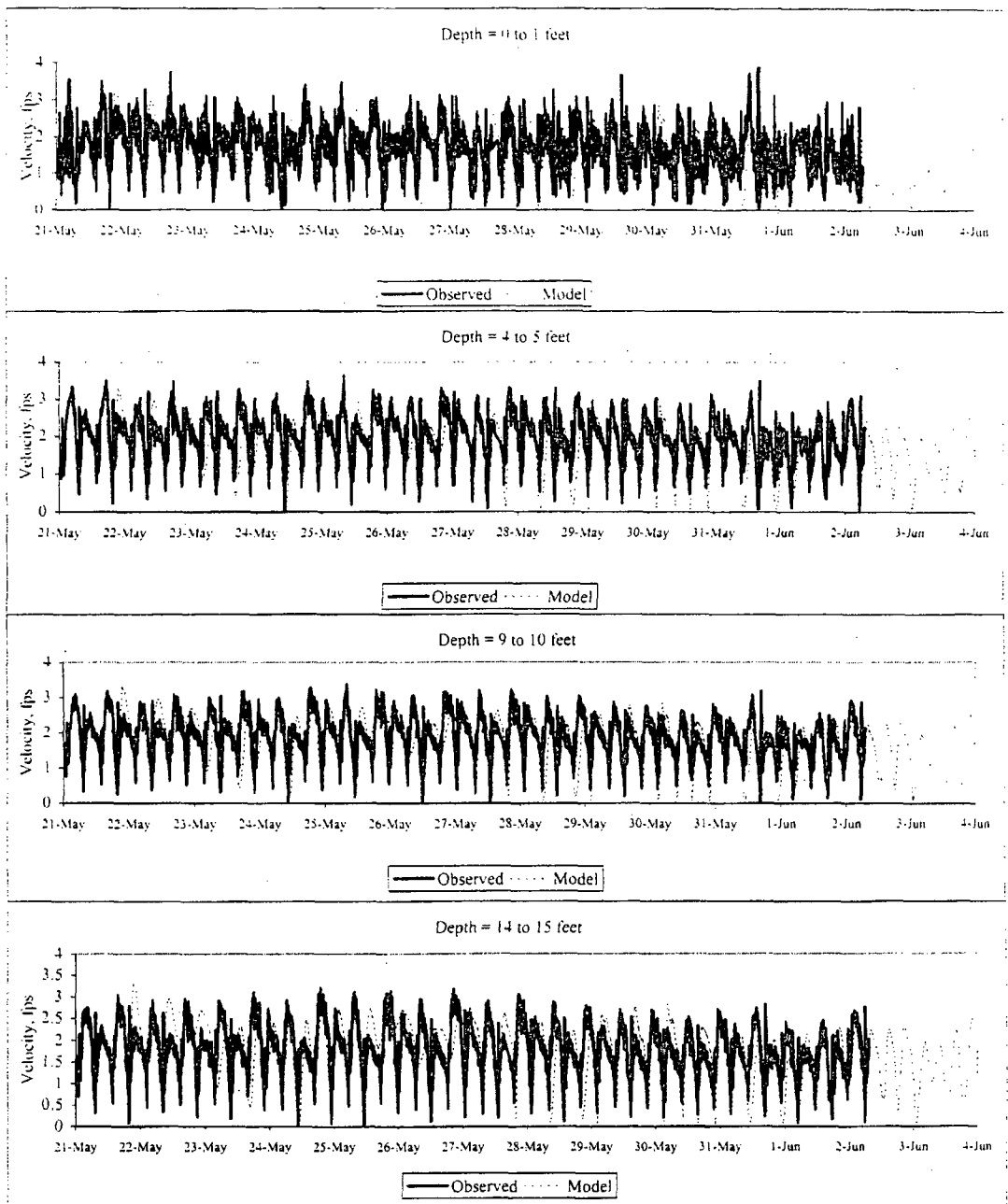


Observed ——— Model - - - -

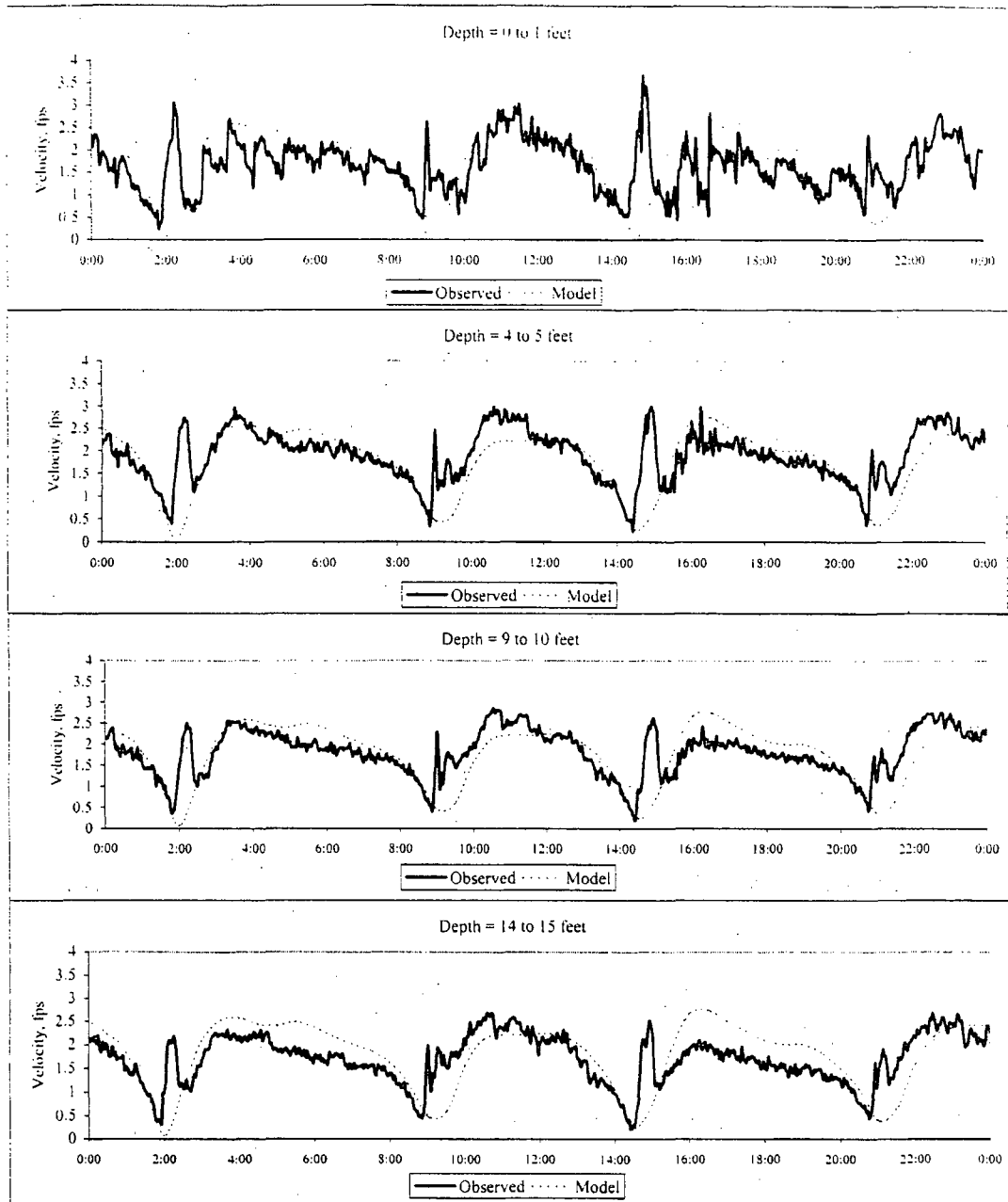
E-2 Figure III-45b. Comparison of modeled and measured tides at the west side of the Bay mouth (Lewes, DE) and the western end of the C&D Canal for 29 May 1998.



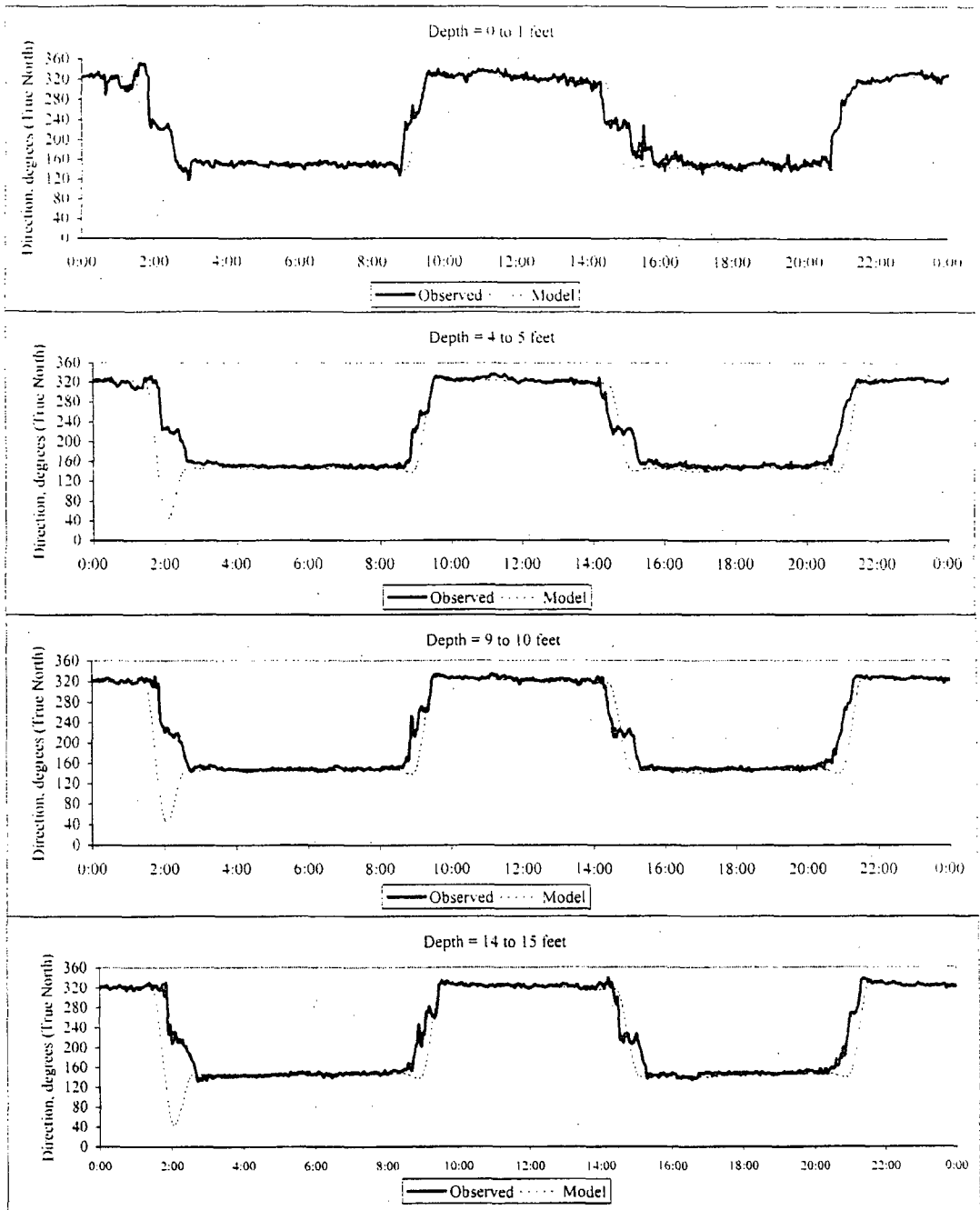
E-2 Figure III-46. Variation in tide range and tidal delay along the axis of the Estuary for the calibration period (22 May - 4 June 1998).



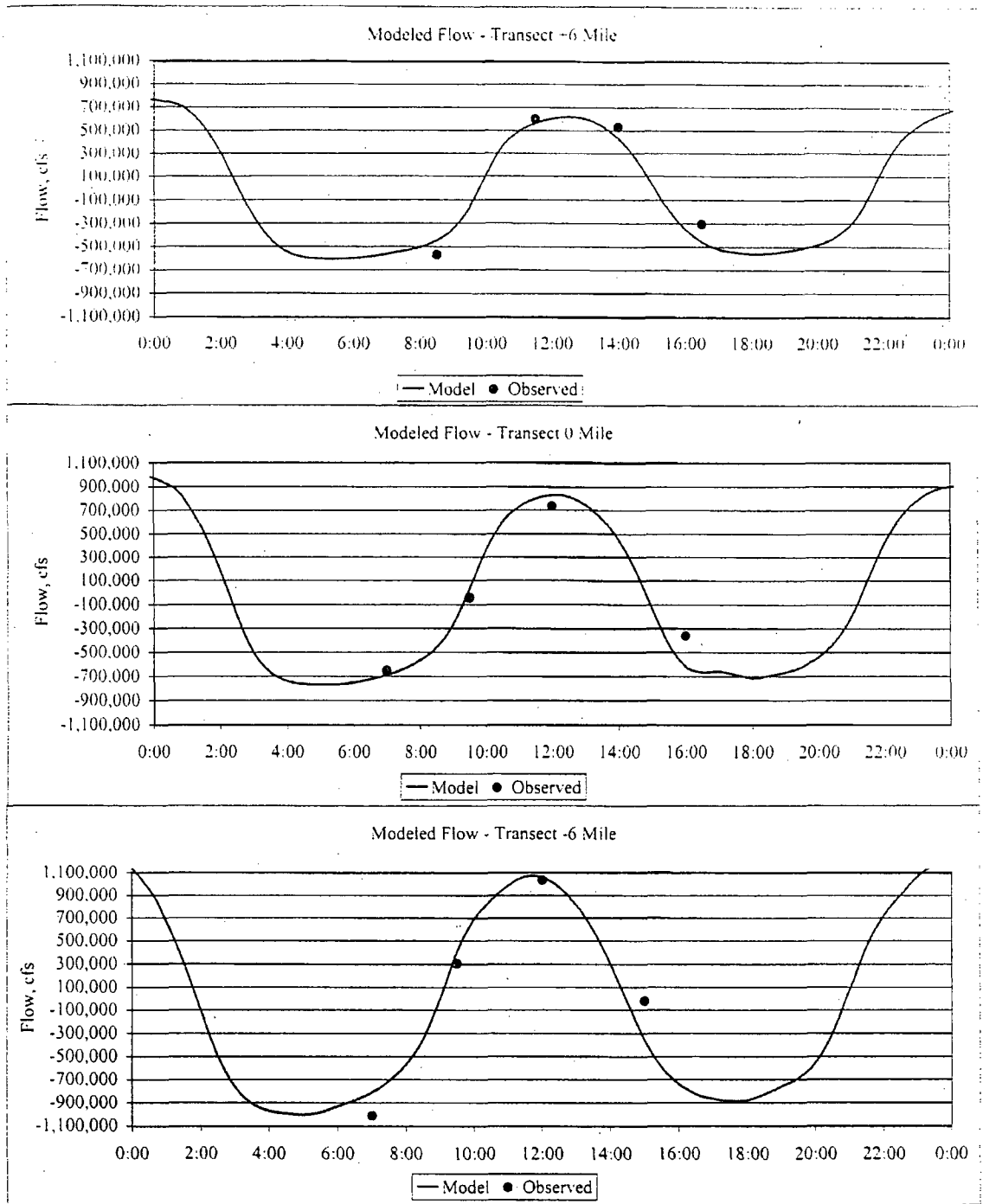
E-2 Figure III-47. Comparison of the magnitude of the modeled and measured current velocities at the fixed-station ADCP located offshore of the discharge for the calibration period (21 May - 4 June 1998).



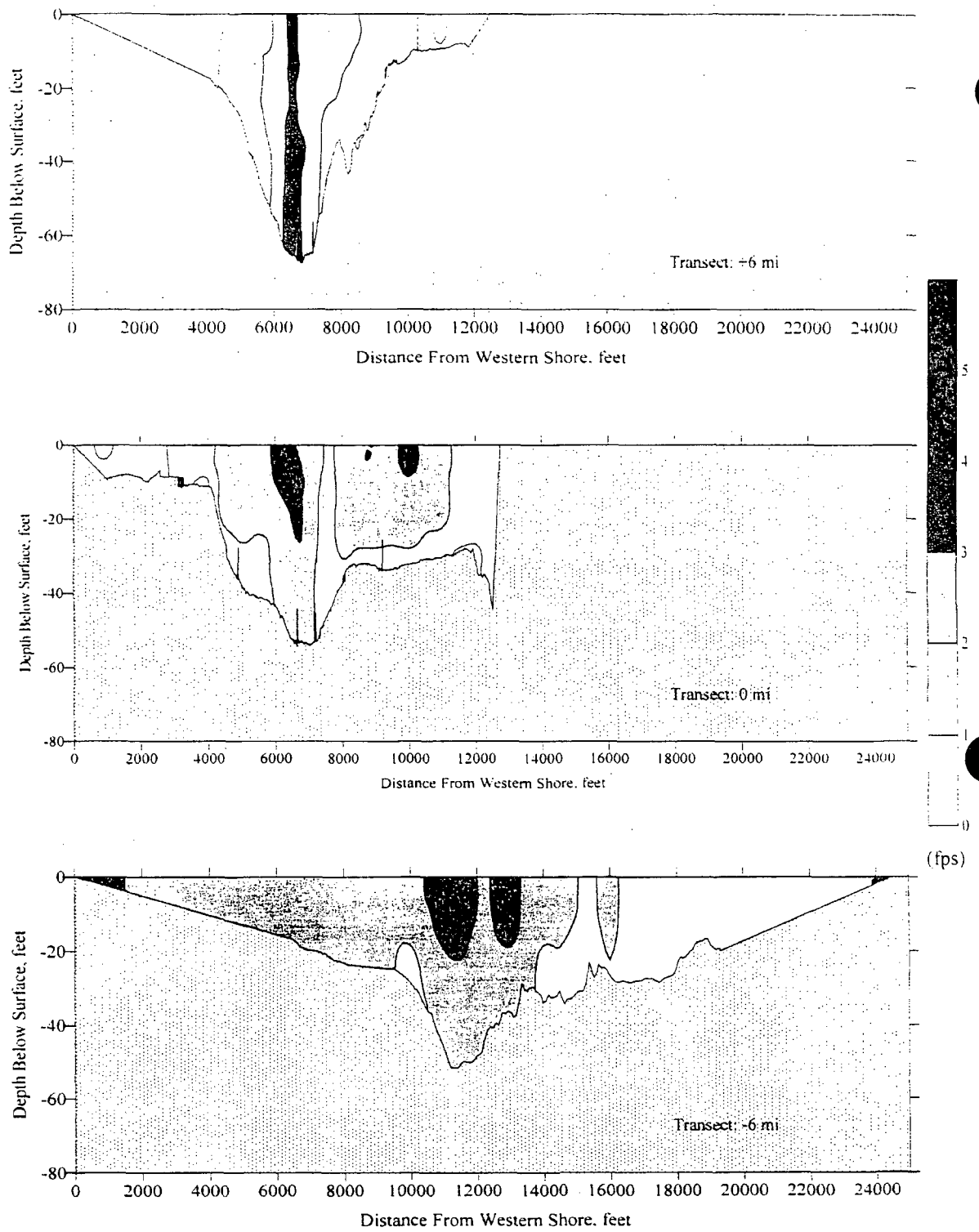
E-2 Figure III-48. Comparison of the magnitude of the modeled and measured current velocities at the fixed-station ADCP located offshore of the discharge for 29 May 1998.



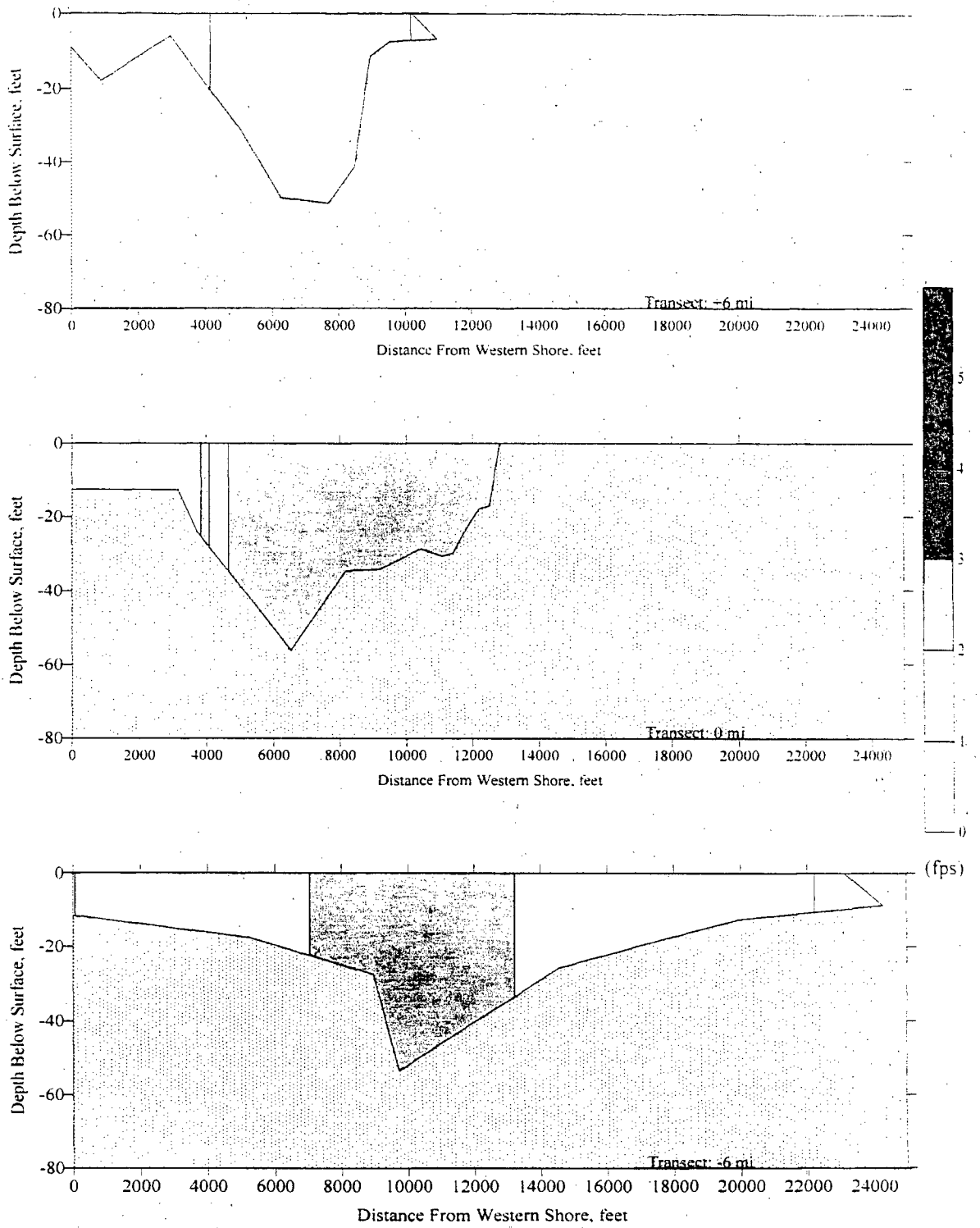
E-2 Figure III-49. Comparison of modeled and measured current directions at the fixed-station ADCP located offshore of the discharge for 29 May 29 1998.



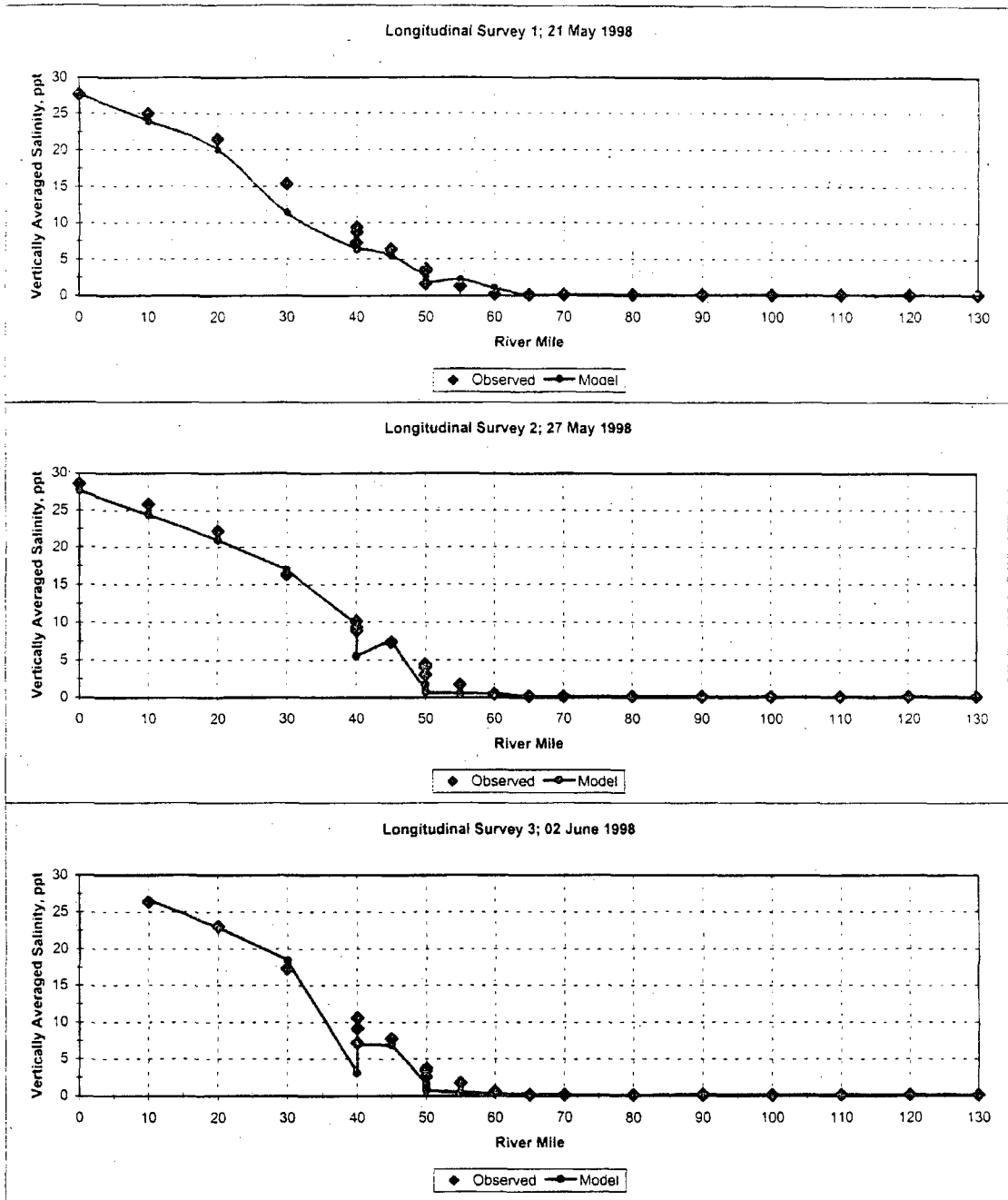
E-2 Figure III-50. Comparison of measured and modeled flow through three transects located 6 miles north of the Station, at the Station and 6 miles south of the Station for 29 May 1998.



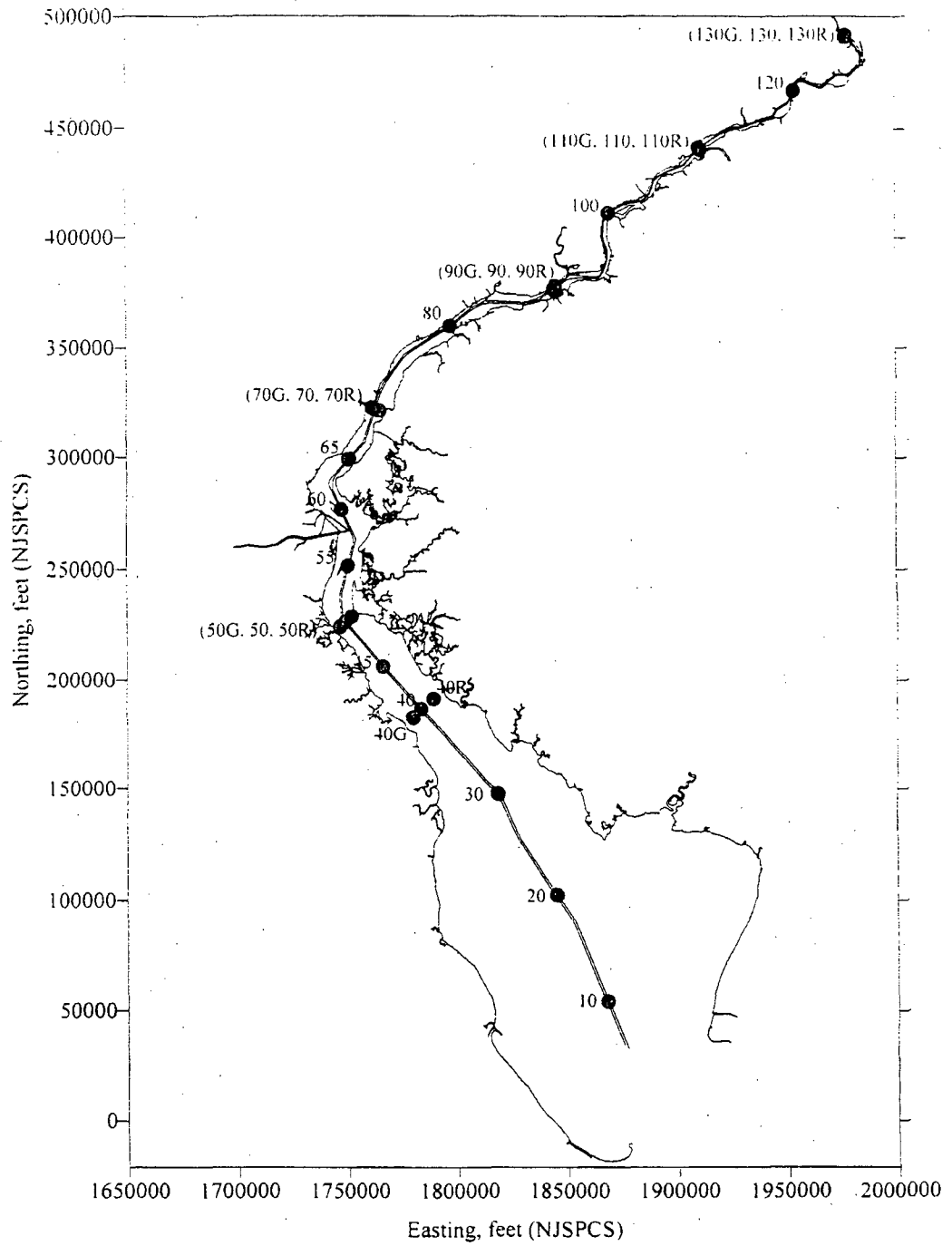
E-2 Figure III-51a. Measured current speeds along three transects located 6 miles north of the Station, at the Station and 6 miles south of the Station for a flood phase on 29 May 1998.



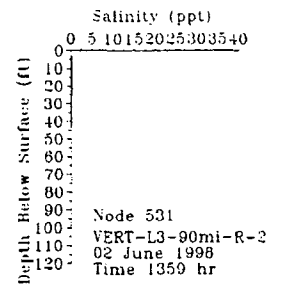
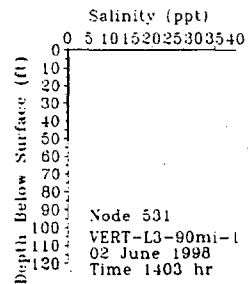
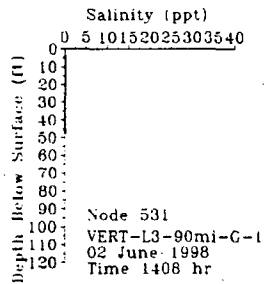
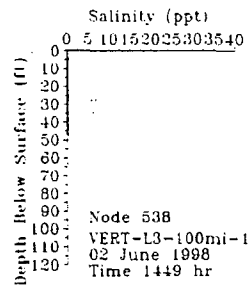
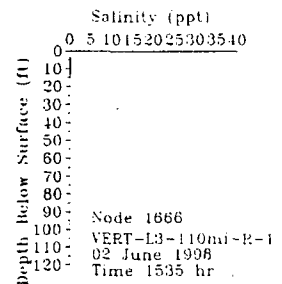
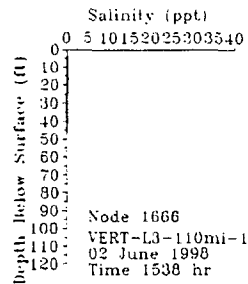
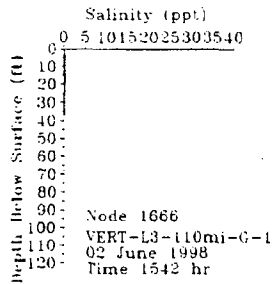
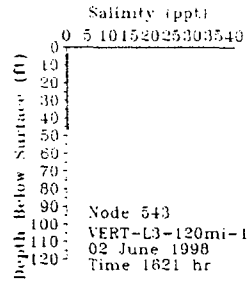
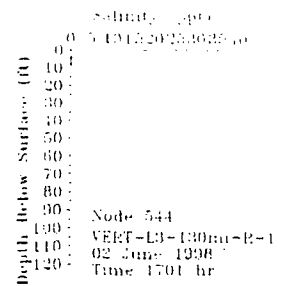
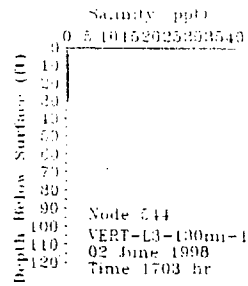
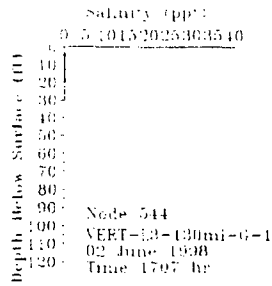
E-2 Figure III-51b. Modeled current speeds along three transects located 6 miles north of the Station, at the Station and 6 miles south of the Station for a flood phase on 29 May 1998.



E-2 Figure III-52. Comparison of measured and modeled depth-averaged salinity along the shipping channel for 21 May, 27 May, and 2 June 1998.

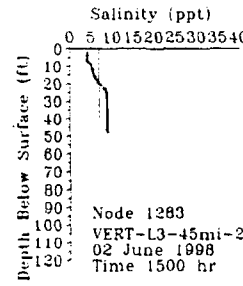
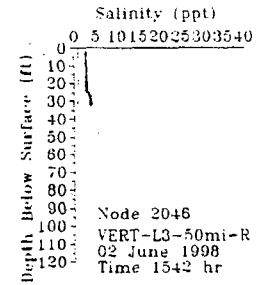
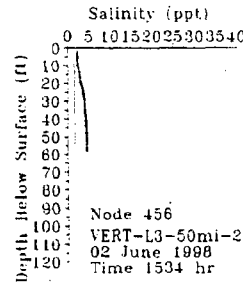
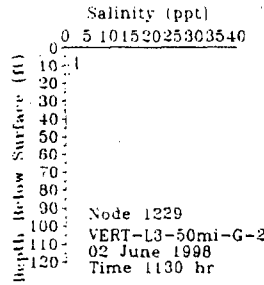
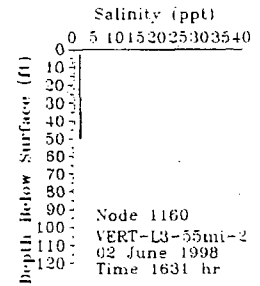
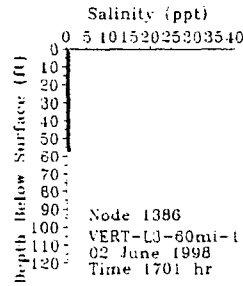
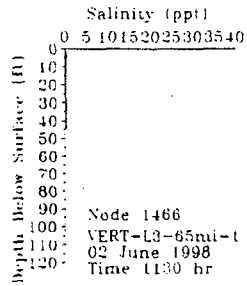
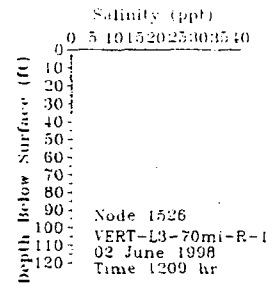
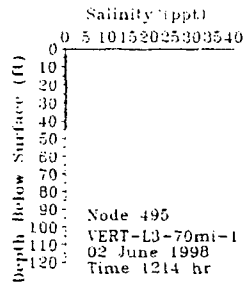
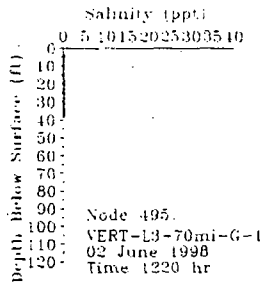
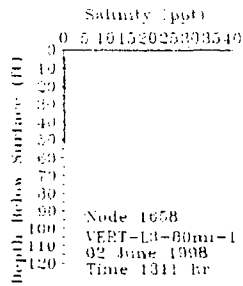


E-2 Figure III-53. Locations of shipboard vertical profiles collected along the axis of the Estuary on 2 June 1998.



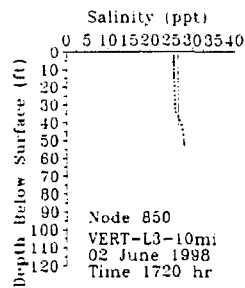
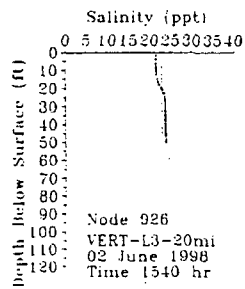
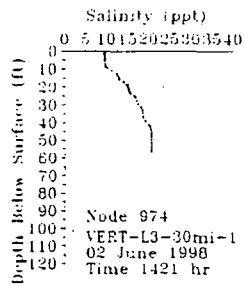
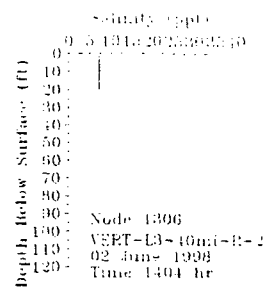
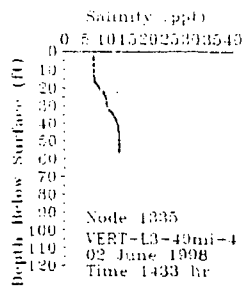
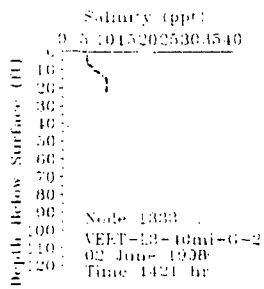
Observed=***** Model=_____

E-2 Figure III-54a. Comparison of modeled and measured salinities along the axis of the Estuary for 2 June 1998 (RM 130 to 90).



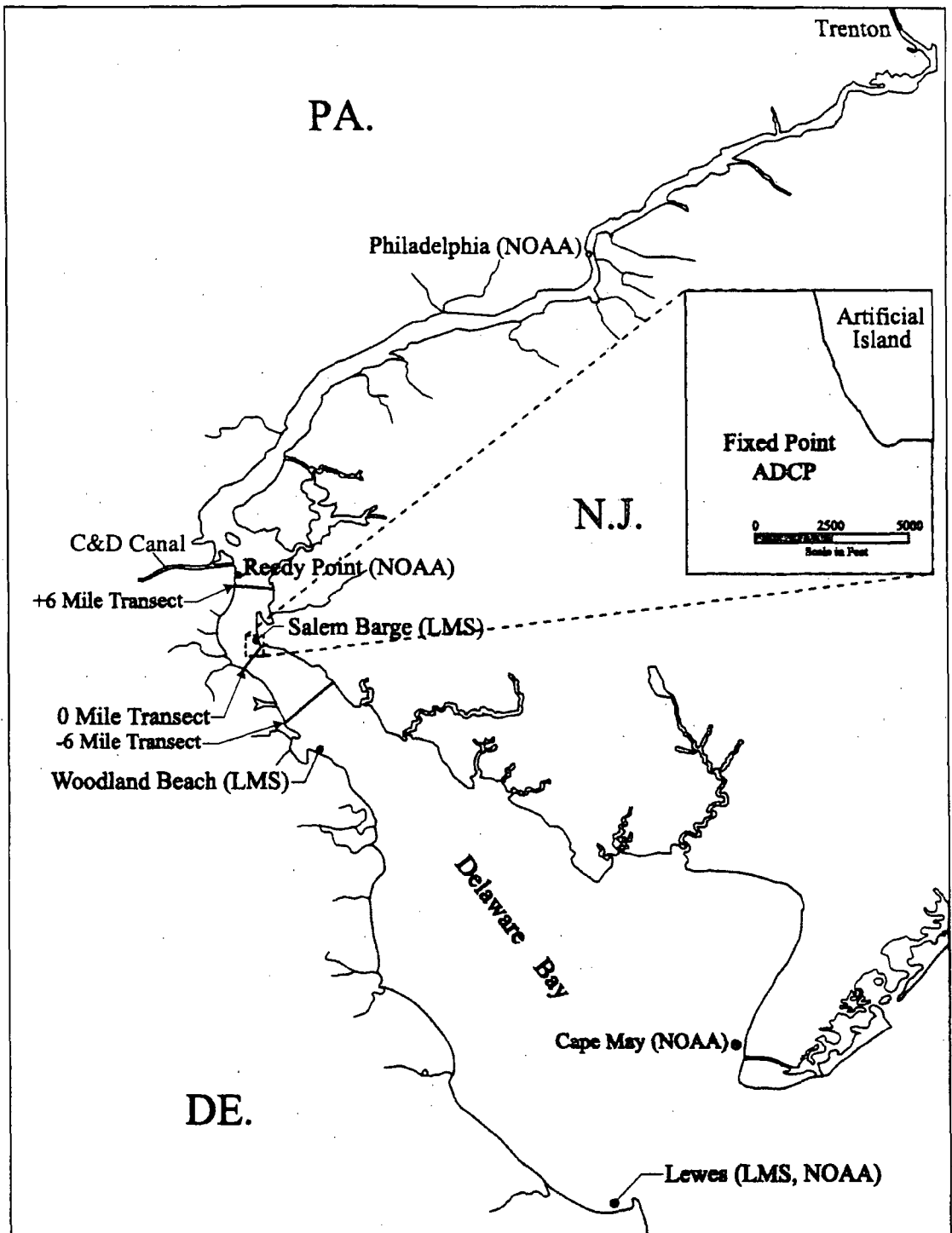
Observed=***** Model=_____

E-2 Figure III-54b. Comparison of modeled and measured salinities along the axis of the Estuary for 2 June 1998 (RM 80 to 45).

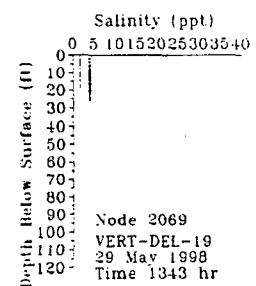
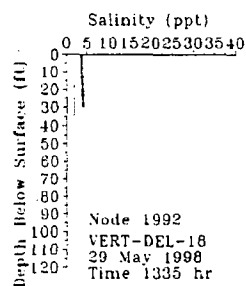
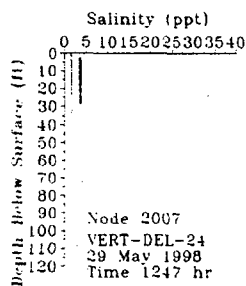
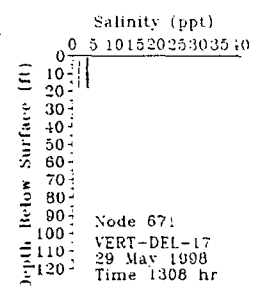
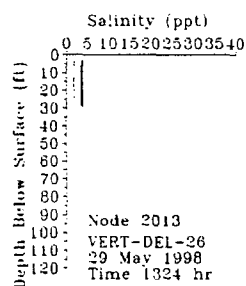
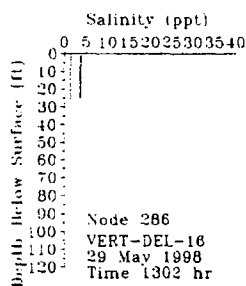
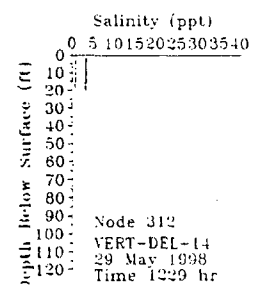
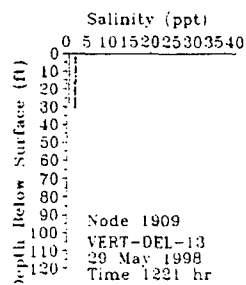
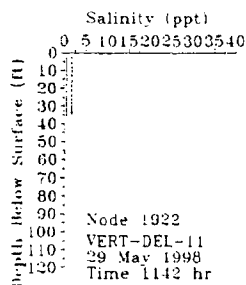
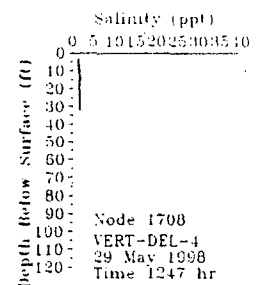
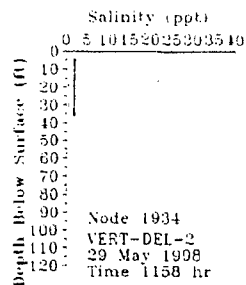
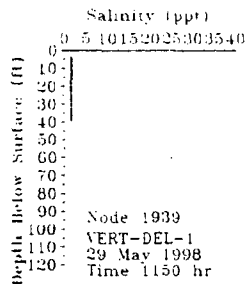
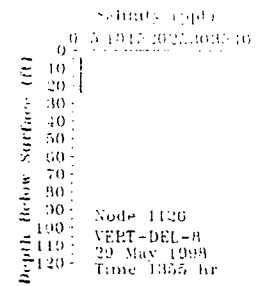
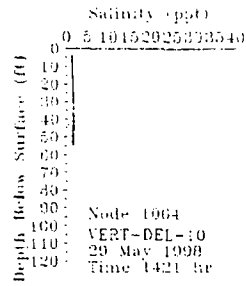
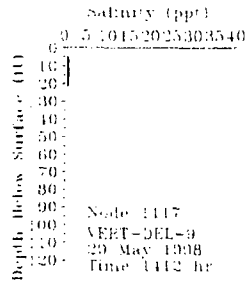


Observed=***** Model=_____

E-2 Figure III-54c. Comparison of modeled and measured salinities along the axis of the Estuary for 2 June 1998 (RM 40 to 10).

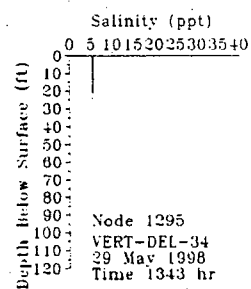
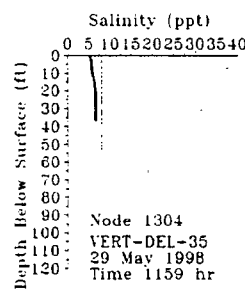
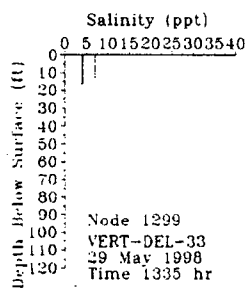
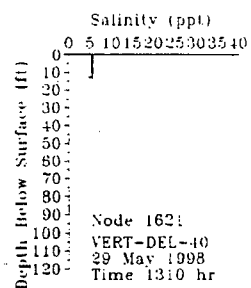
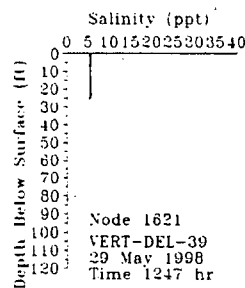
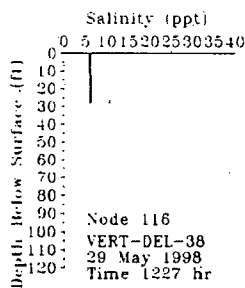
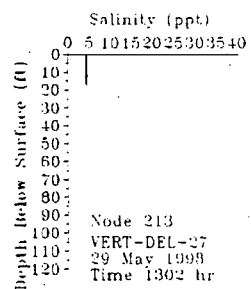
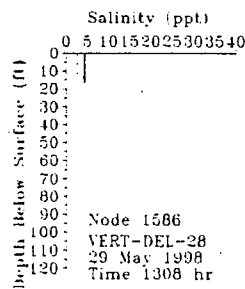
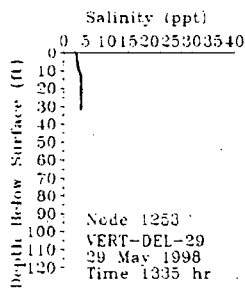
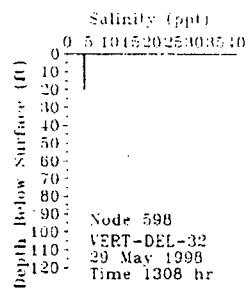
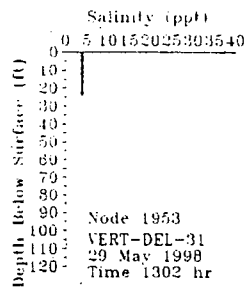
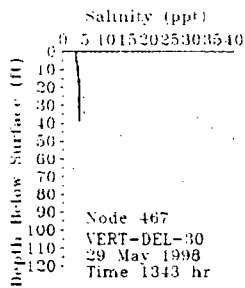
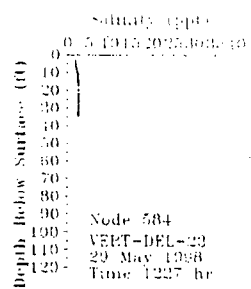
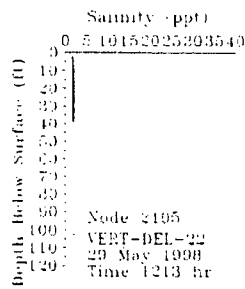
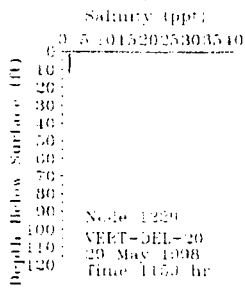


E-2 Figure III-55. Delaware Bay tide gauge locations, mobile ADCP transects, and the fixed-point ADCP.



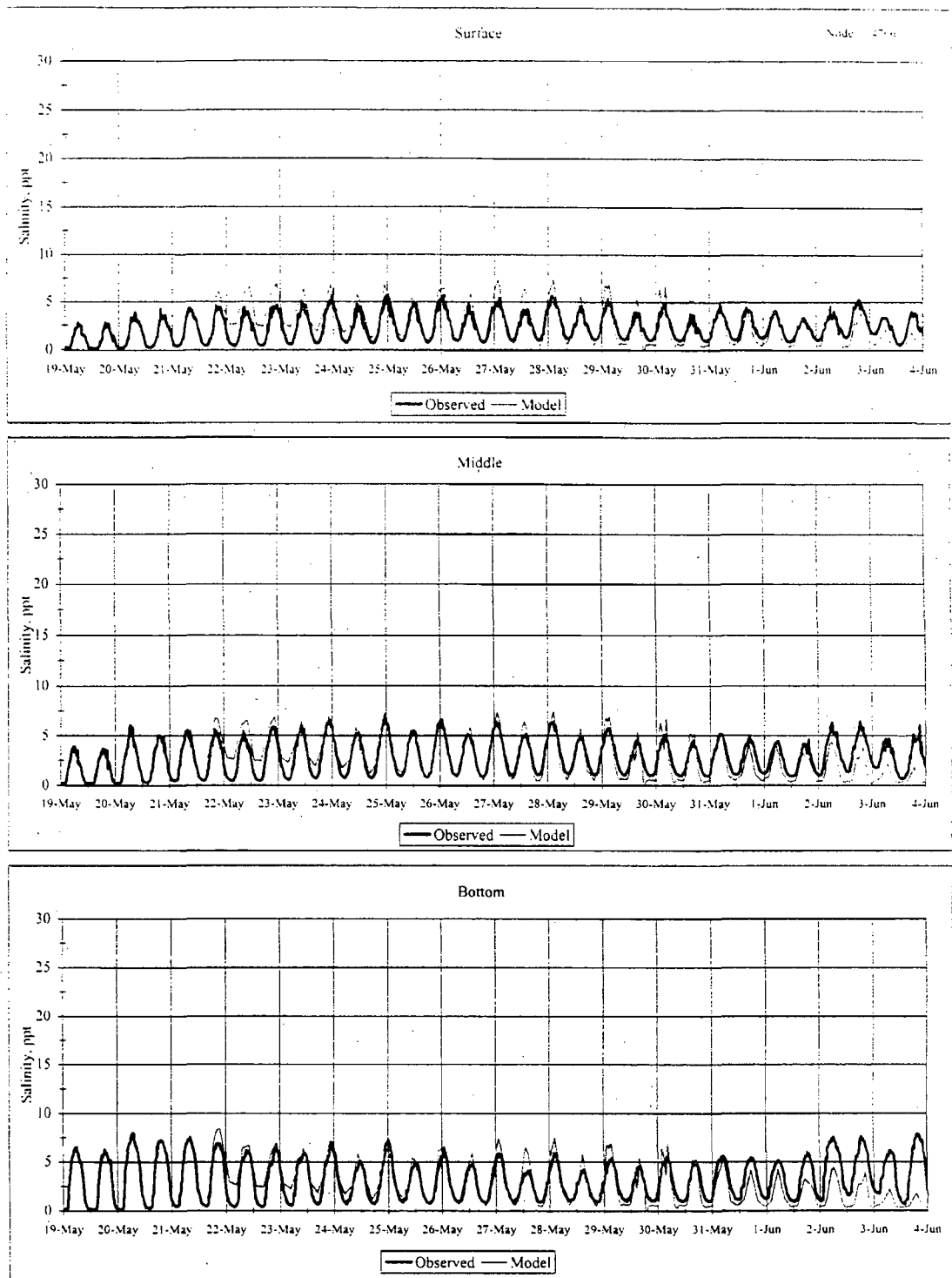
Observed=***** Model=_____

E-2 Figure III-56a. Comparison of modeled and measured salinities at locations of shipboard verticals north of the Station during a flood phase on 29 May 1998.

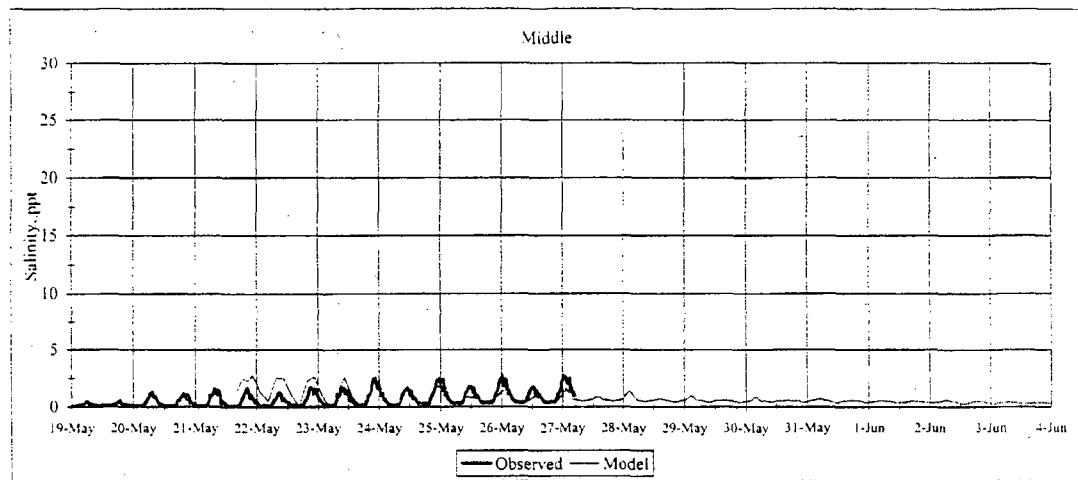


Observed=***** Model=_____

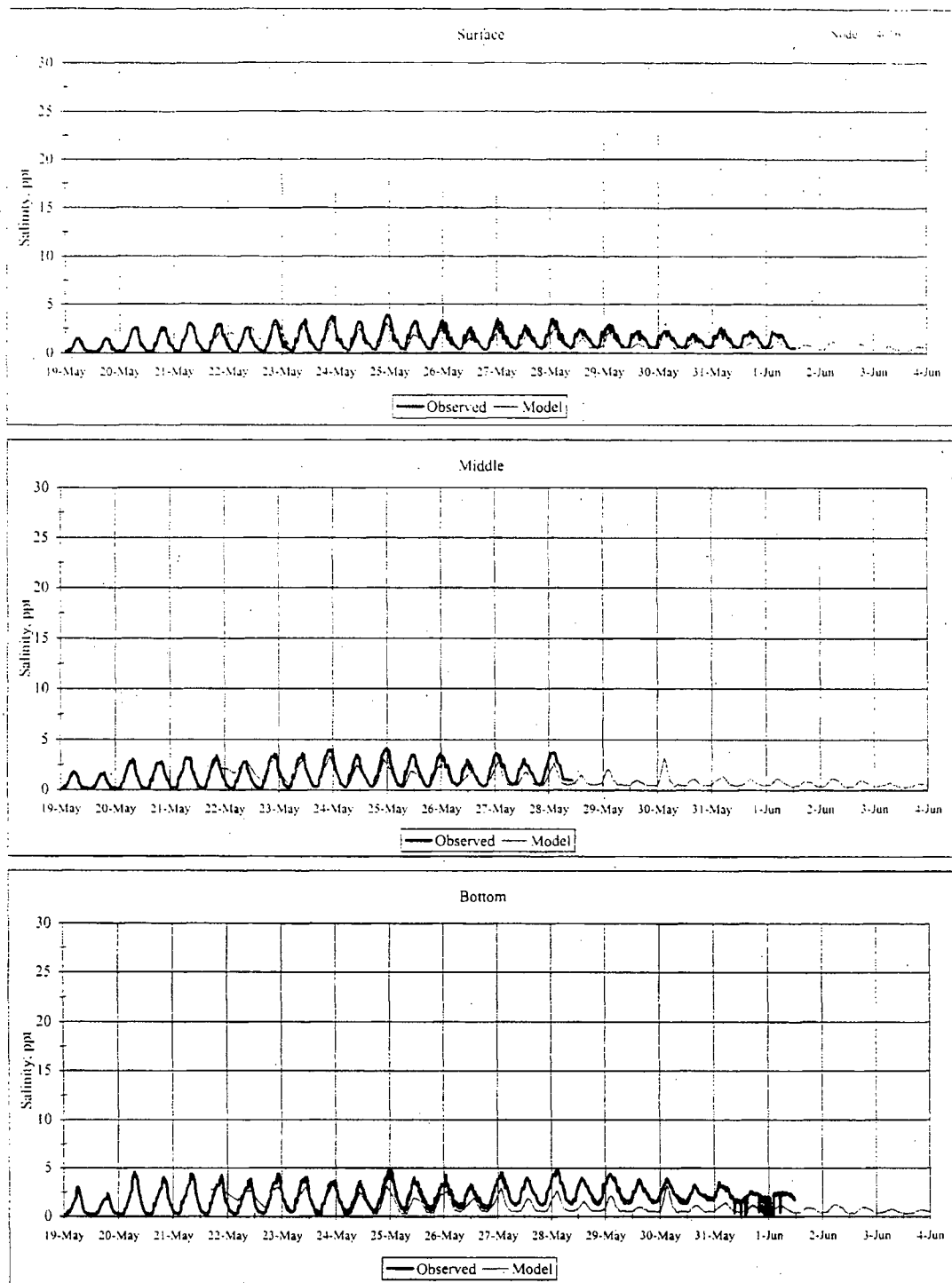
E-2 Figure III-56b. Comparison of modeled and measured salinities at locations of shipboard verticals south of the Station during a flood phase on 29 May 1998.



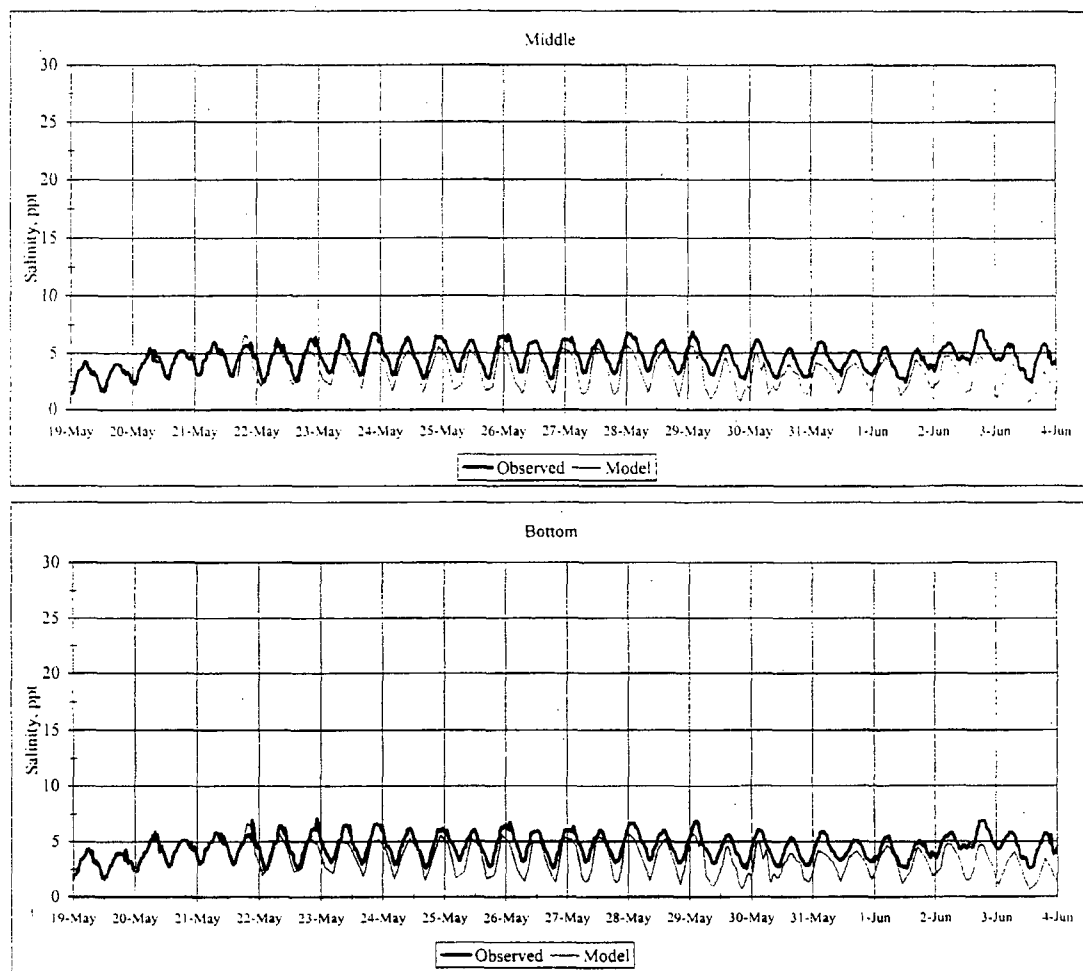
E-2 Figure III-58a. Comparison of modeled and measured salinity at Mooring 5, which is located offshore of the Station near the shipping channel, for the calibration period (19 May - 4 June 1998).



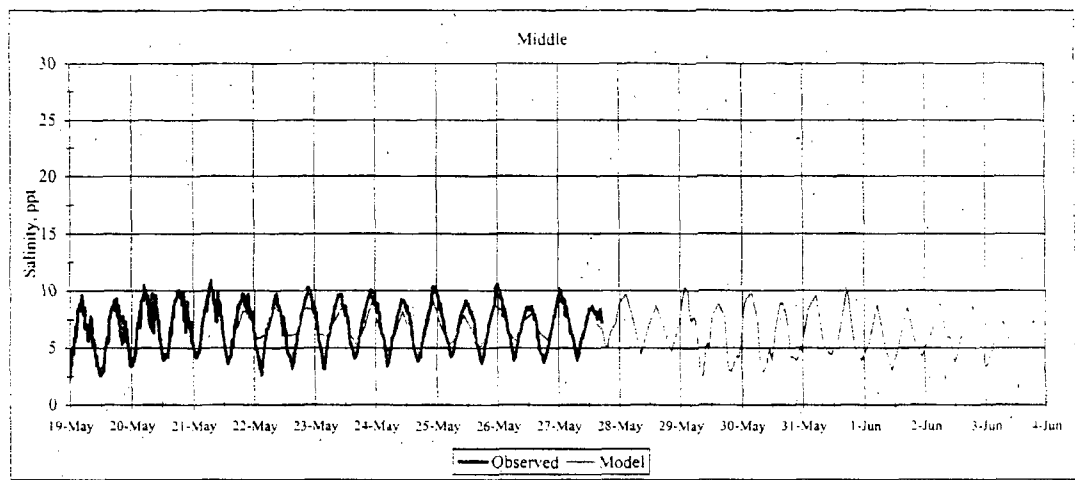
E-2 Figure III-58b. Comparison of modeled and measured salinity at Mooring 2, which is located 6 miles north of the Station near the shipping channel, for the calibration period (19 May - 4 June 1998).



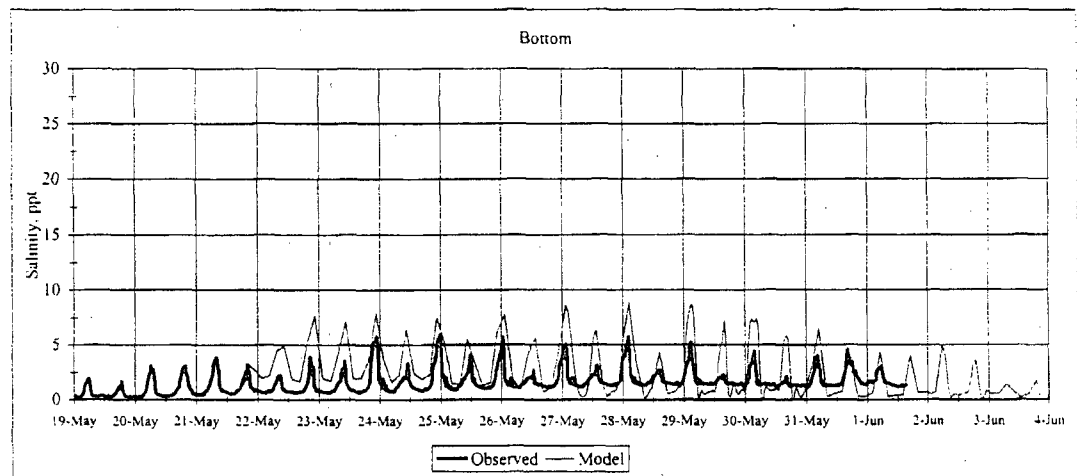
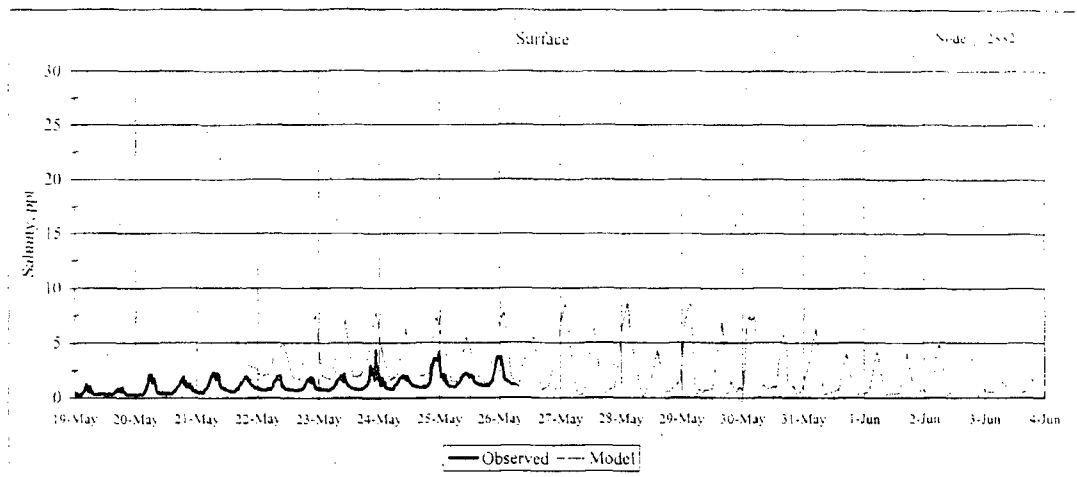
E-2 Figure III-58c. Comparison of modeled and measured salinity at Mooring 4, which is located towards the northern end of Artificial Island near the shipping channel, for the calibration period (19 May - 4 June 1998).



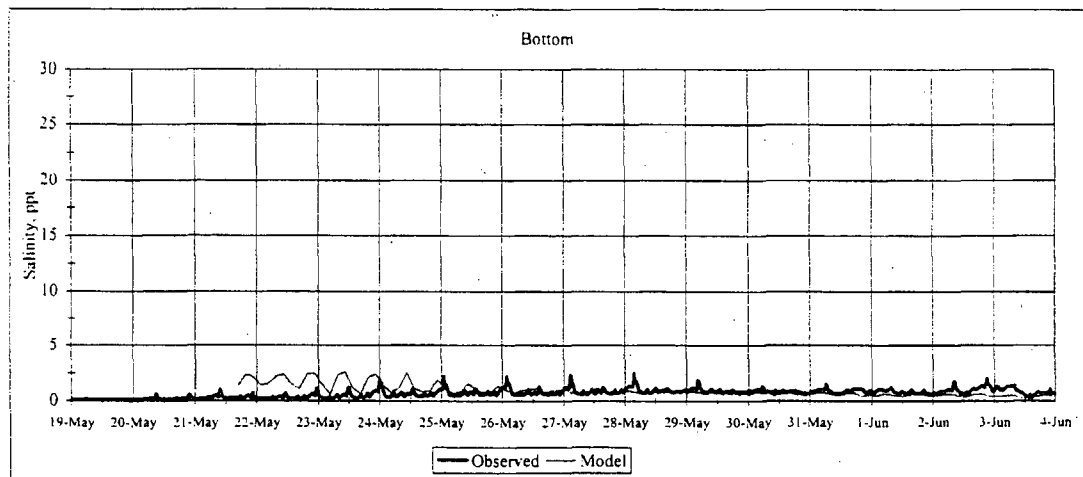
E-2 Figure III-58d. Comparison of modeled and measured salinity at Mooring 7, which is located 3 miles south of the Station, for the calibration period (19 May - 4 June 1998).



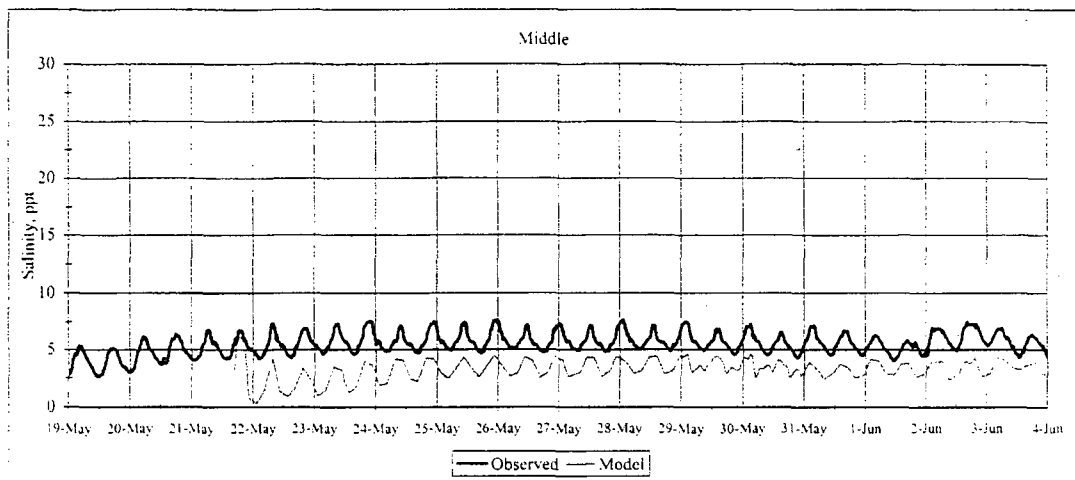
E-2 Figure III-58e. Comparison of modeled and measured salinity at Mooring 9, which is located 6 miles south of the Station near the shipping channel, for the calibration period (19 May - 4 June 1998).



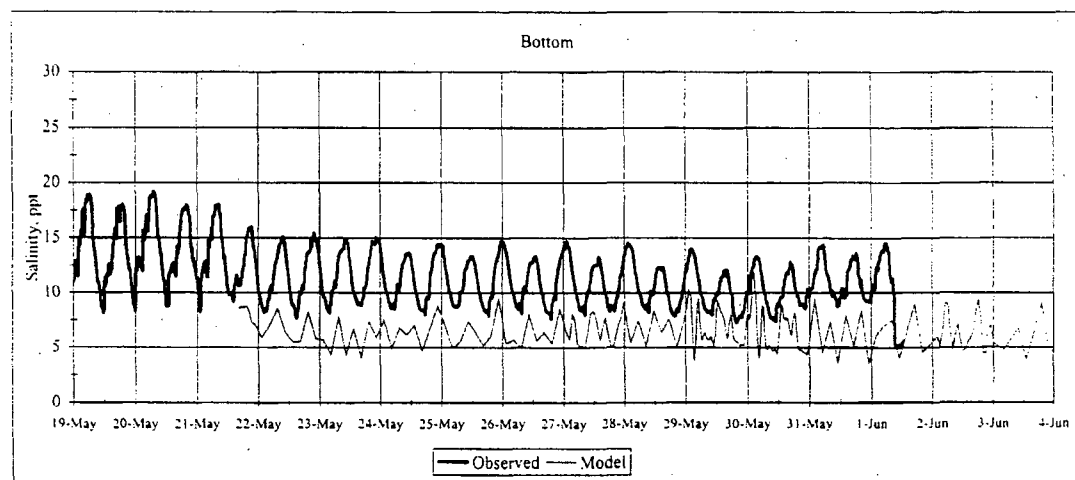
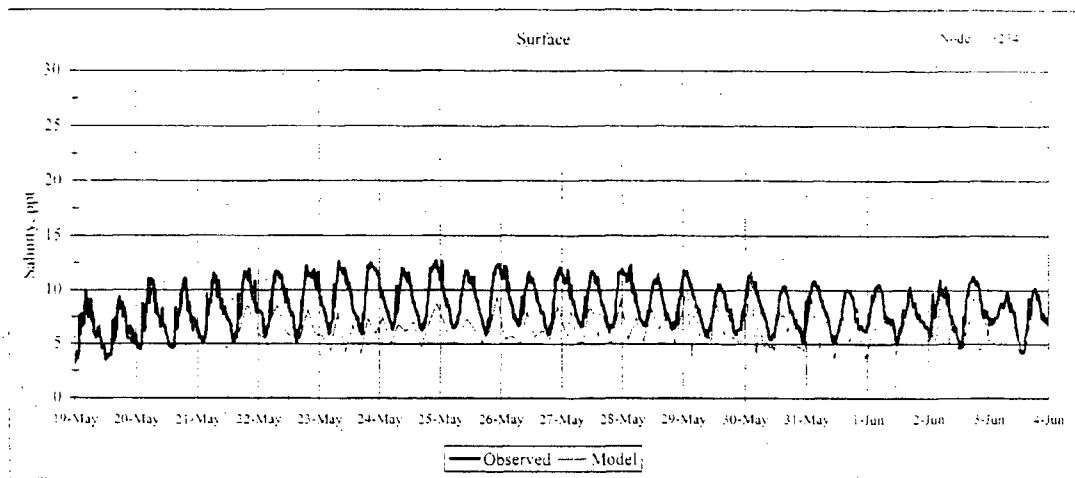
E-2 Figure III-58f. Comparison of modeled and measured salinity at Mooring 6, which is located near the Station on the western side of the shipping channel, for the calibration period (19 May - 4 June 1998).



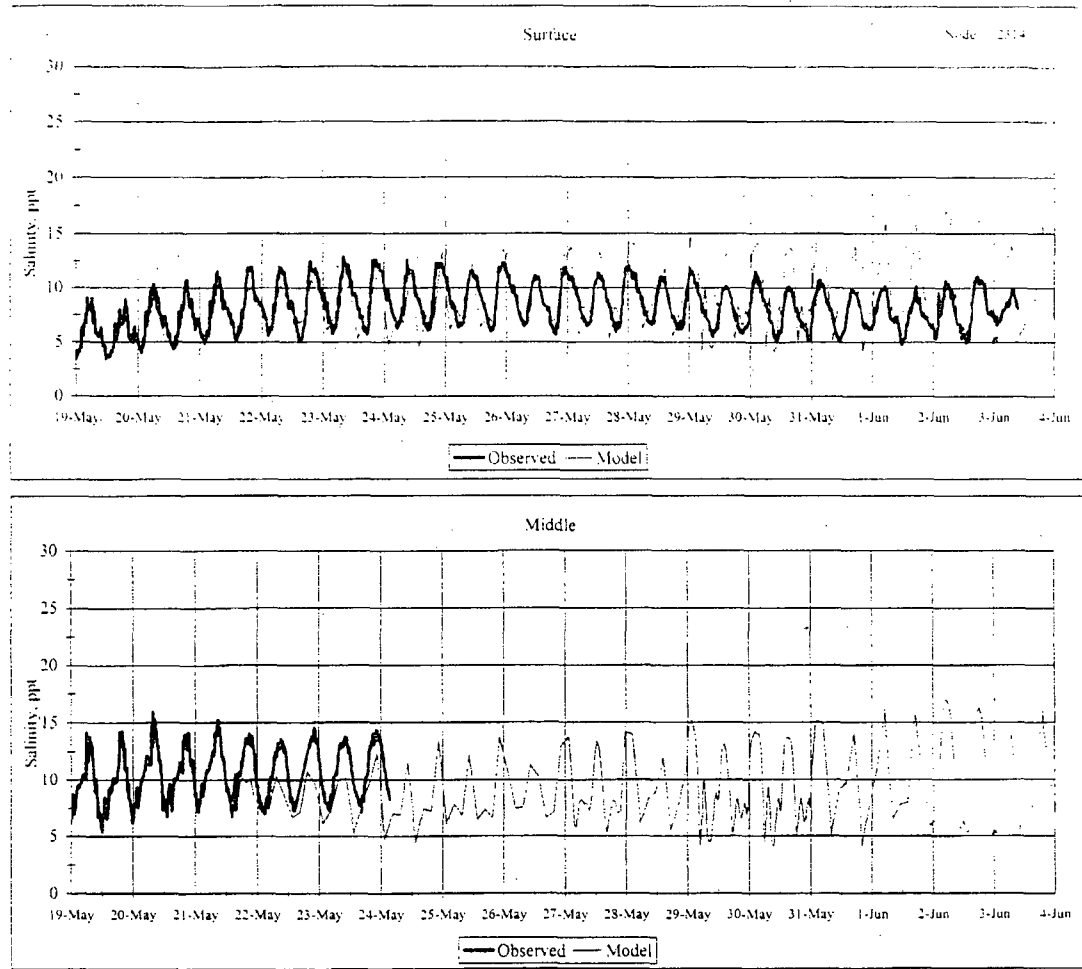
E-2 Figure III-58g. Comparison of modeled and measured salinity at Mooring 1, which is located 6 miles north of the Station on the western side of the shipping channel, for the calibration period (19 May - 4 June 1998).



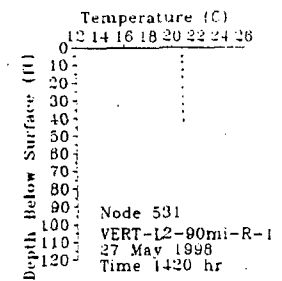
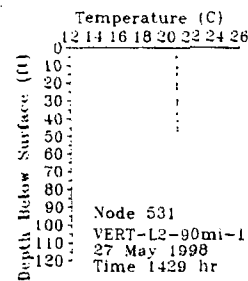
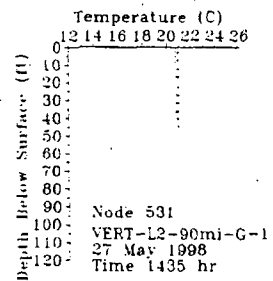
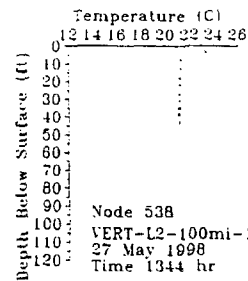
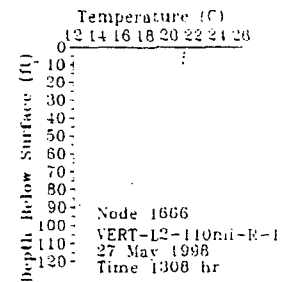
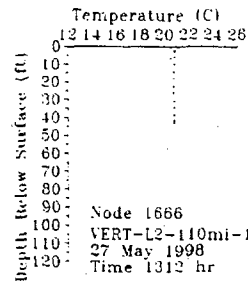
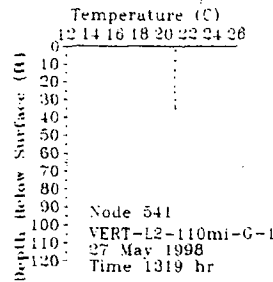
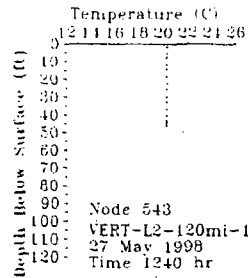
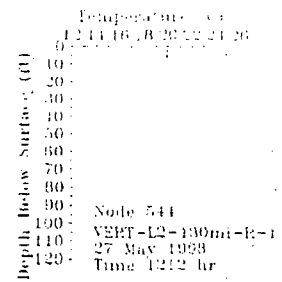
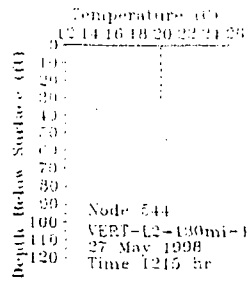
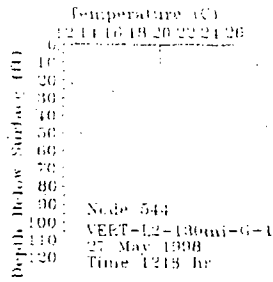
E-2 Figure III-58h. Comparison of modeled and measured salinity at Mooring 10, which is located 6 miles south of the Station on the eastern side of the shipping channel, for the calibration period (19 May - 4 June 1998).



E-2 Figure III-58i. Comparison of modeled and measured salinity at Mooring M9, which is located 9 miles south of the Station near the shipping channel, for the calibration period (19 May - 4 June 1998).

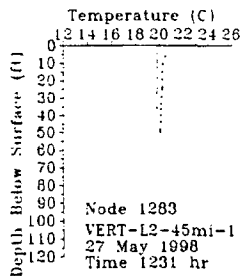
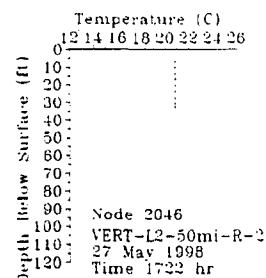
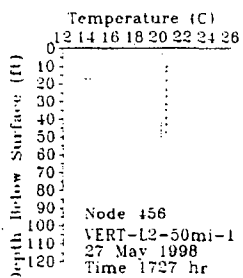
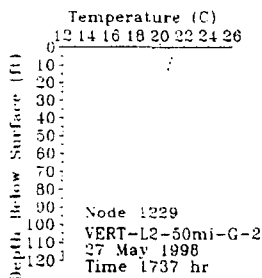
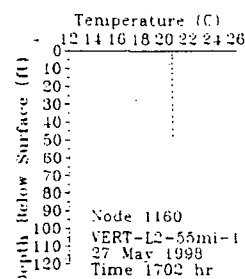
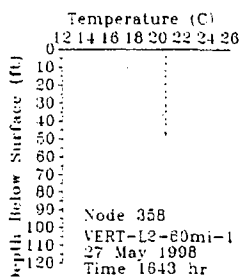
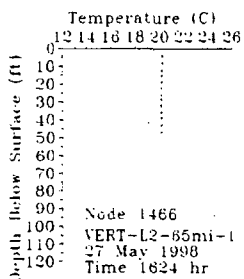
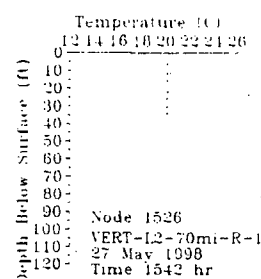
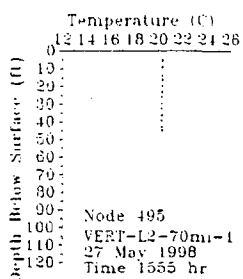
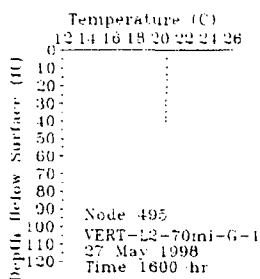
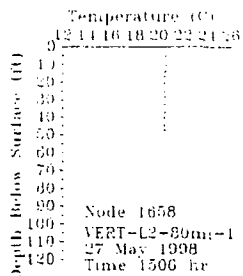


E-2 Figure III-58j. Comparison of modeled and measured salinity at Mooring M12, which is located 12 miles south of the Station near the shipping channel, for the calibration period (19 May - 4 June 1998).



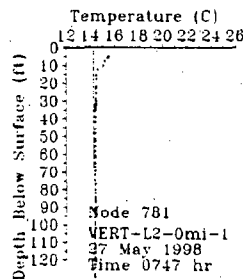
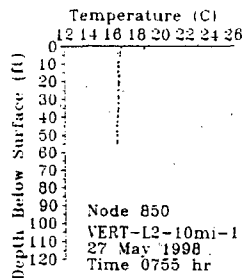
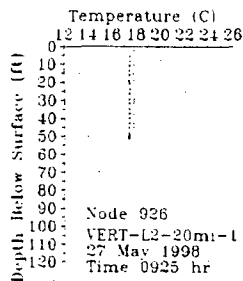
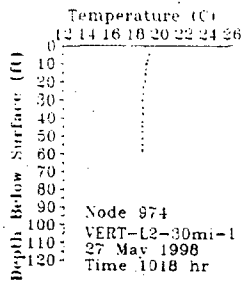
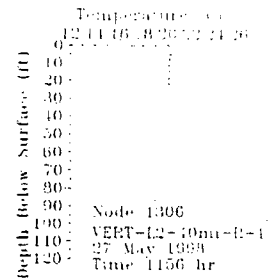
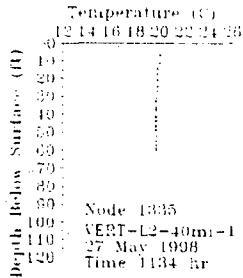
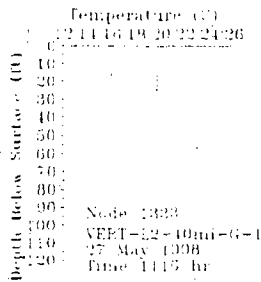
Observed=***** Model=_____

E-2 Figure III-59a. Comparison of modeled and measured temperatures along the axis of the Estuary for 27 May 1998 (RM 130 to 90).



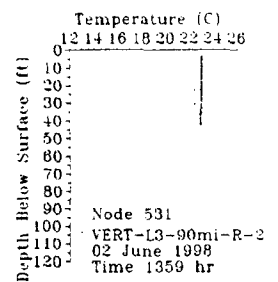
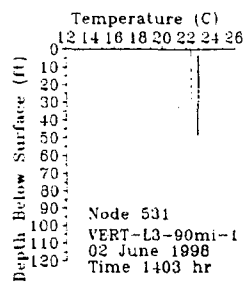
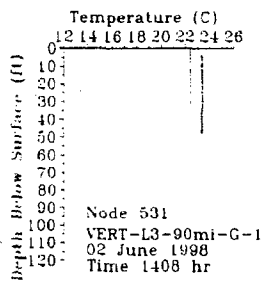
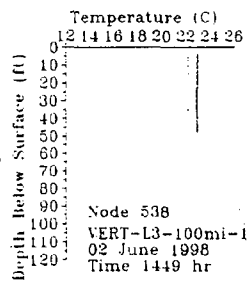
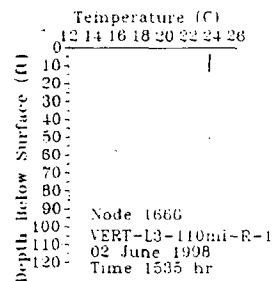
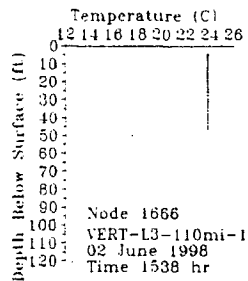
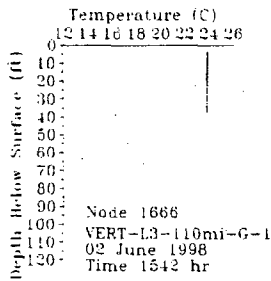
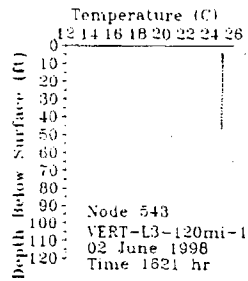
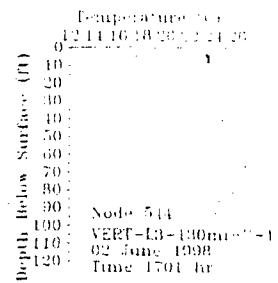
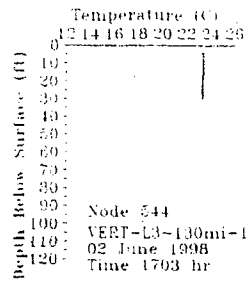
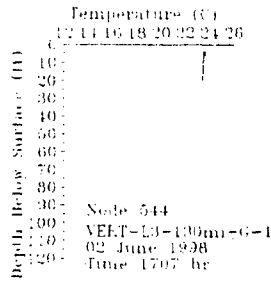
Observed=***** Model=_____

E-2 Figure III-59b. Comparison of modeled and measured temperatures along the axis of the Estuary for 27 May 1998 (RM 80 to 45).



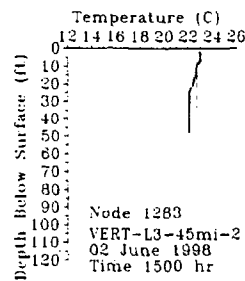
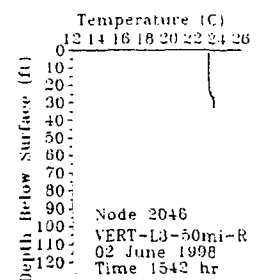
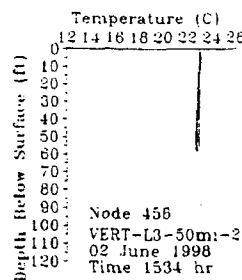
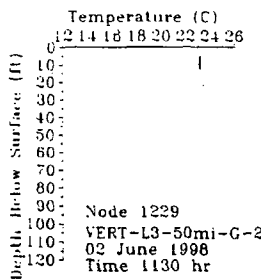
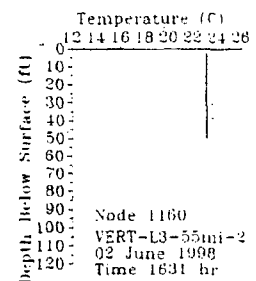
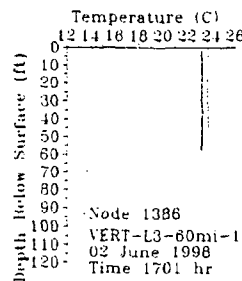
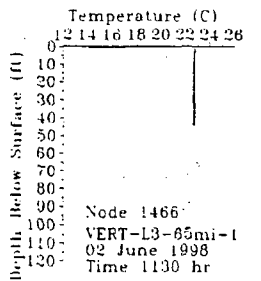
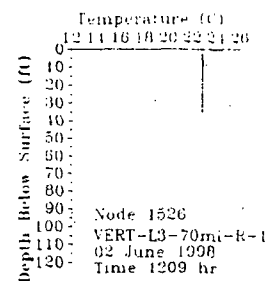
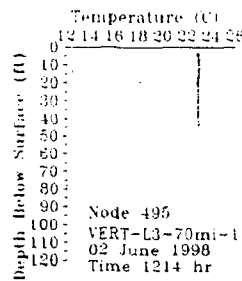
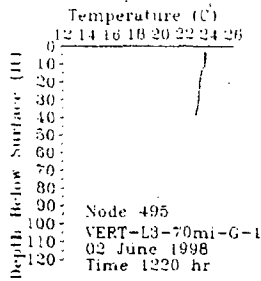
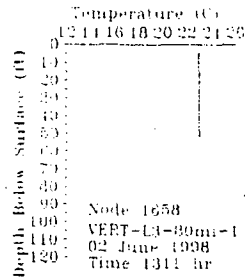
Observed=***** Model=_____

E-2 Figure III-59c. Comparison of modeled and measured temperatures along the axis of the Estuary for 27 May 1998 (RM 40 to 0).



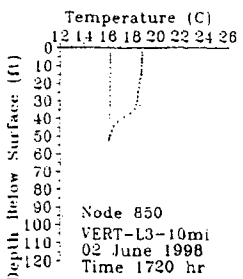
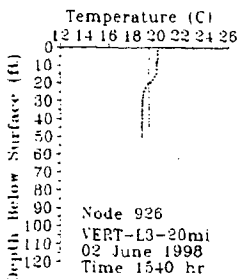
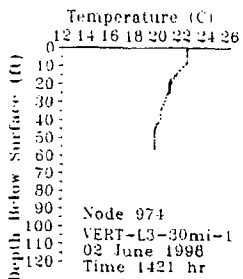
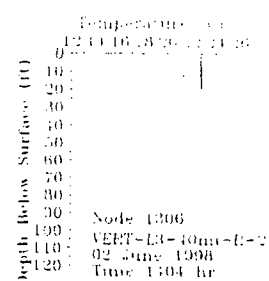
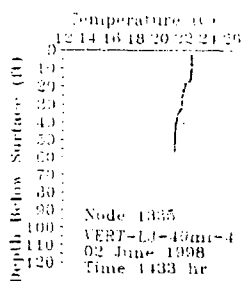
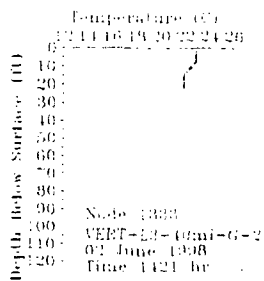
Observed=***** Model=_____

E-2 Figure III-60a. Comparison of modeled and measured temperatures along the axis of the Estuary for 2 June 1998 (RM 130 to 90).



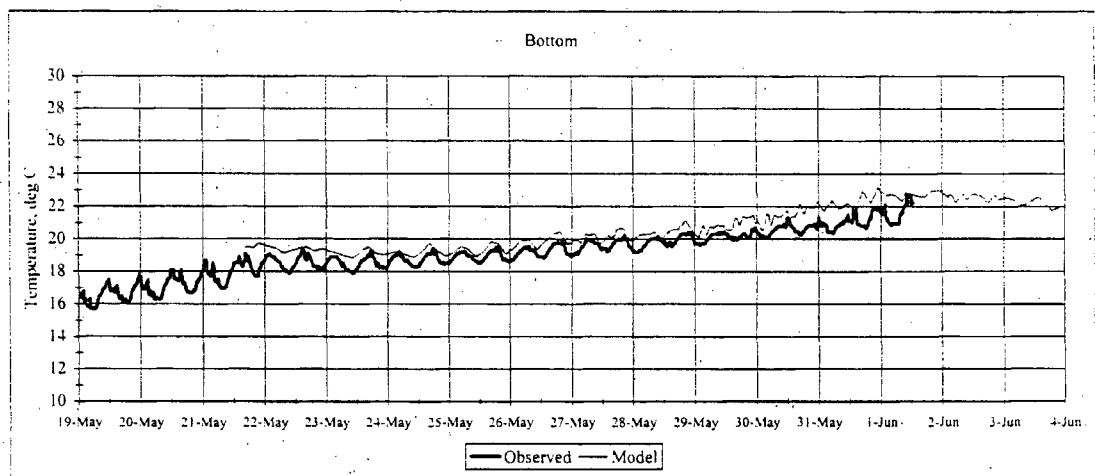
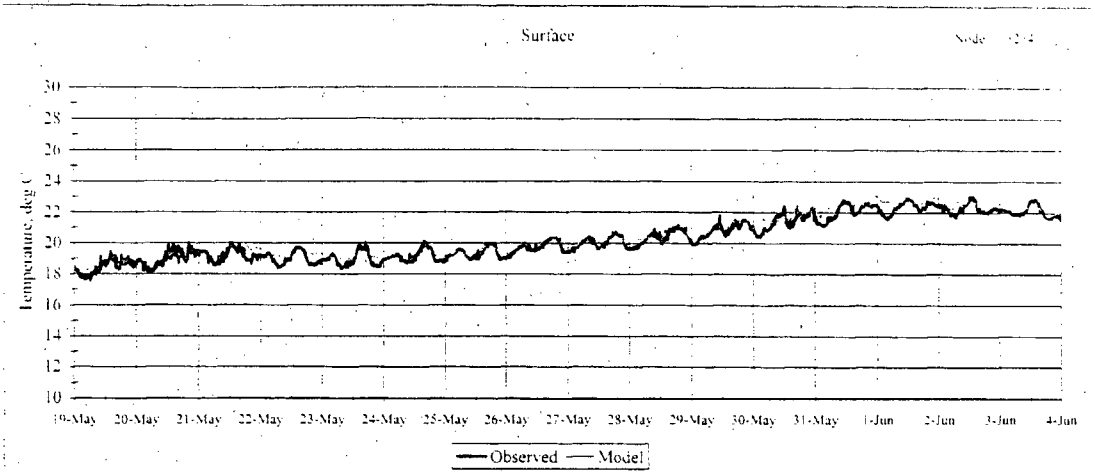
Observed=***** Model=_____

E-2 Figure III-60b. Comparison of modeled and measured temperatures along the axis of the Estuary for 2 June 1998 (RM 80 to 45).

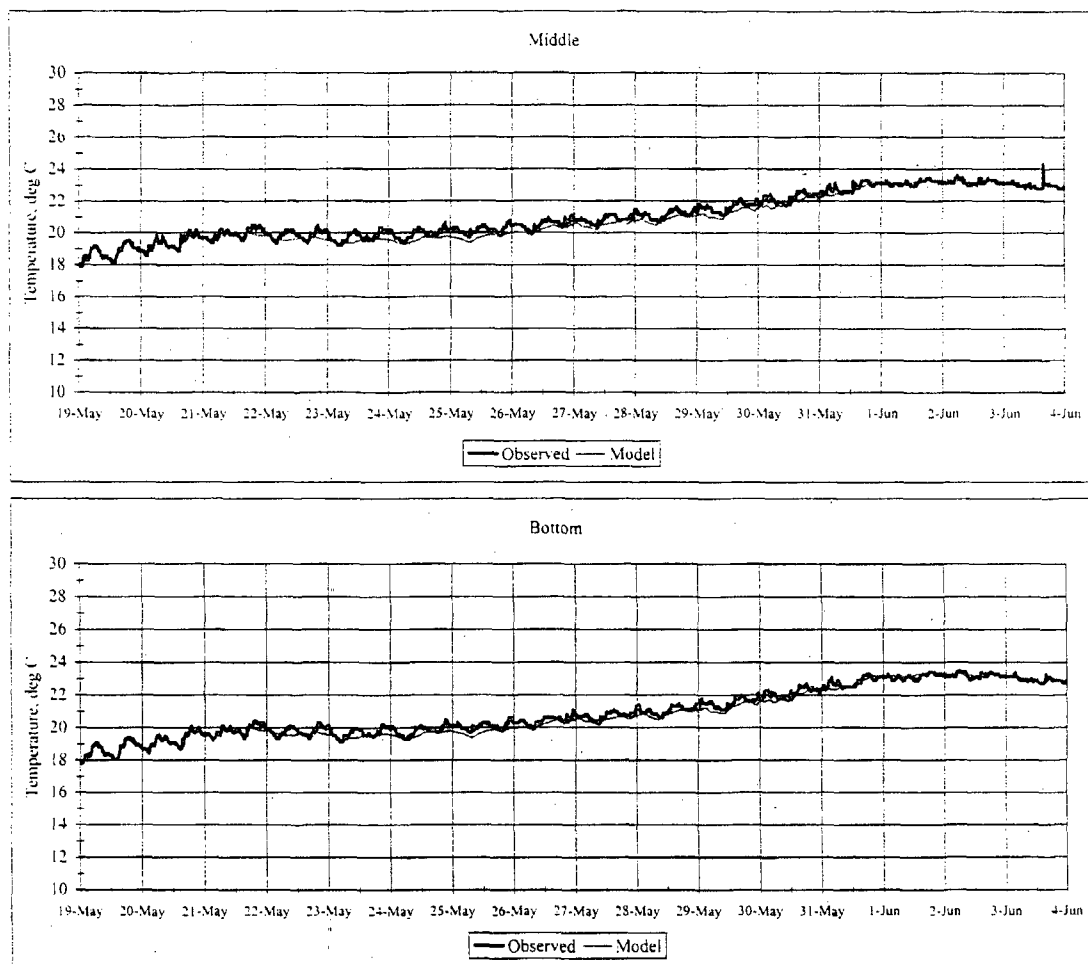


Observed=***** Model=_____

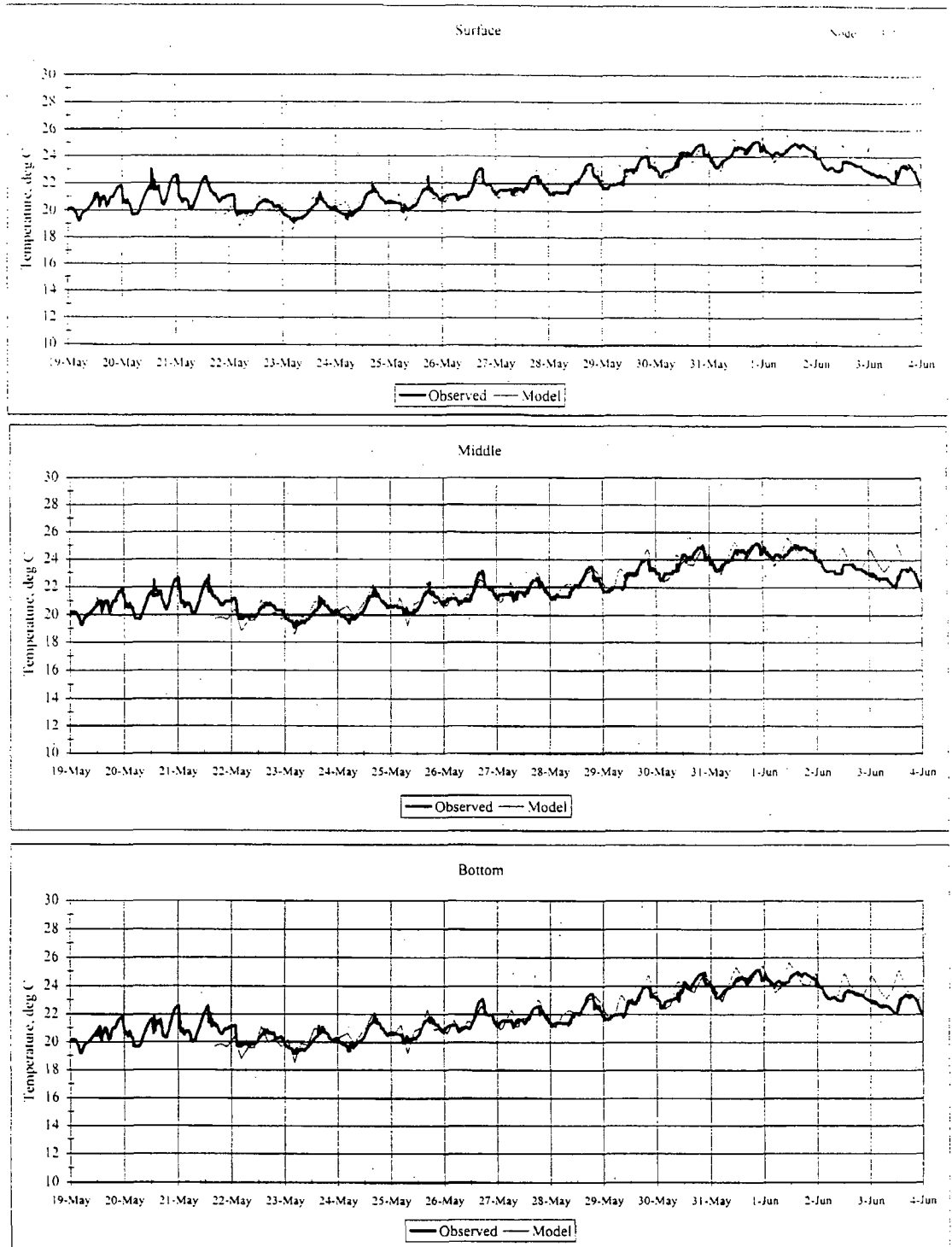
E-2 Figure III-60c. Comparison of modeled and measured temperatures along the axis of the Estuary for 2 June 1998 (RM 40 to 10).



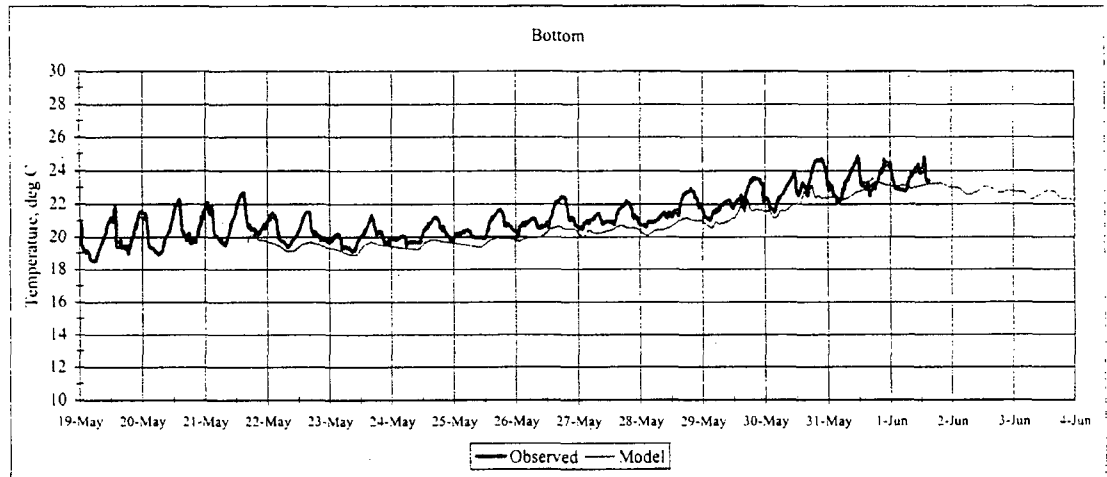
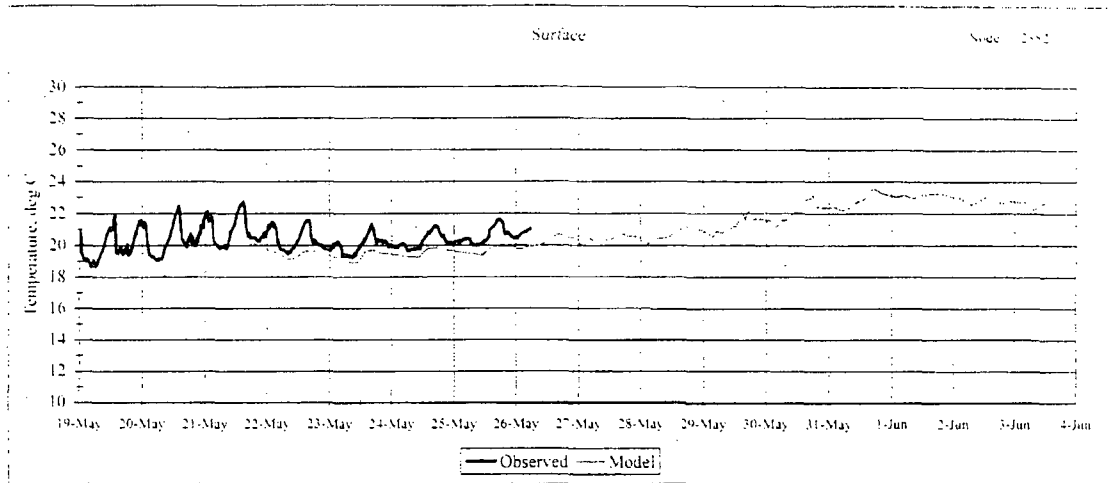
E-2 Figure III-61a. Comparison of modeled and measured temperature at Mooring M9, which is located 9 miles south of the Station near the shipping channel, for the calibration period (19 May - 4 June 1998).



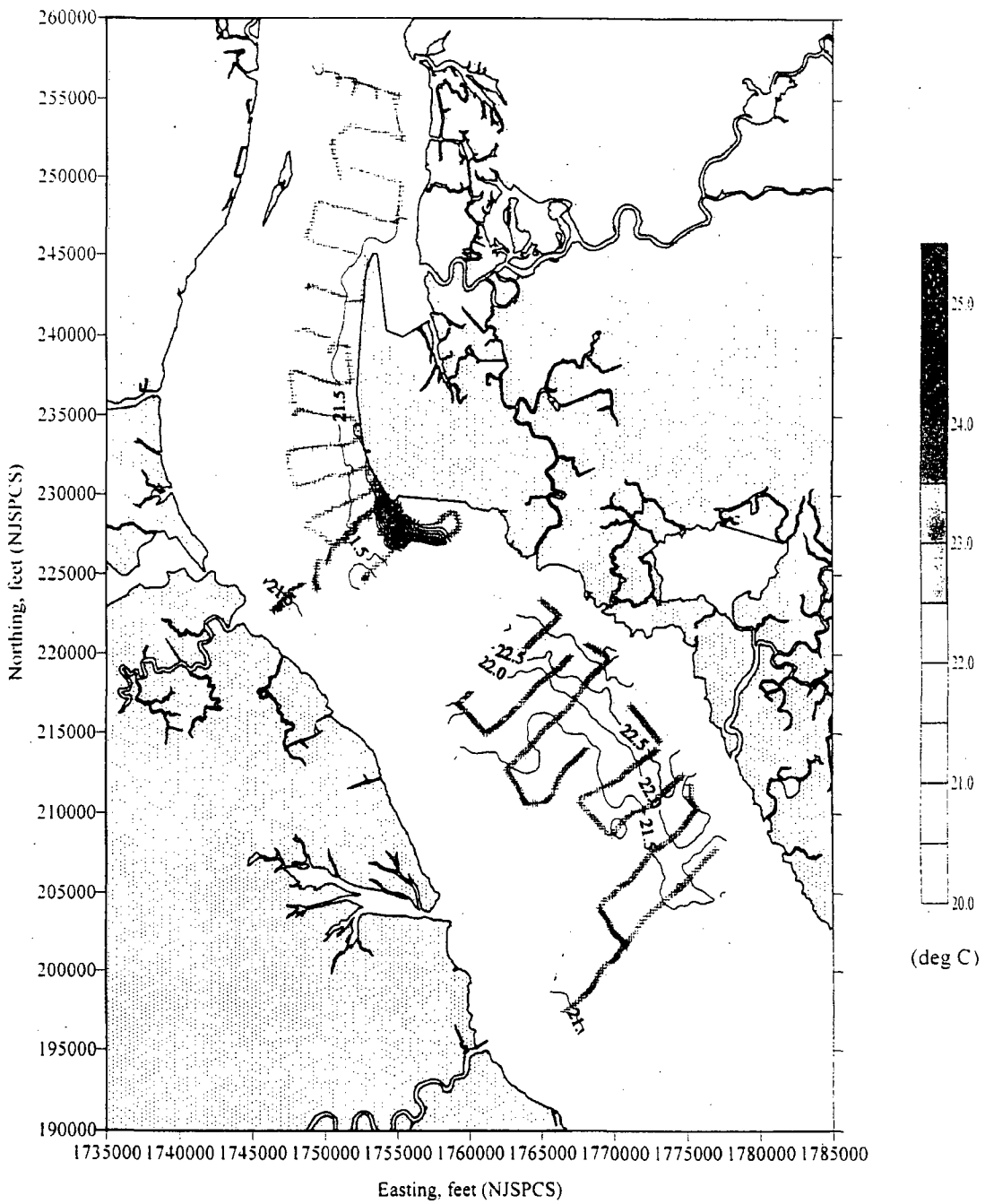
E-2 Figure III-61b. Comparison of modeled and measured temperature at Mooring 9M, which is located 9 miles north of the Station near the shipping channel, for the calibration period (19 May - 4 June 1998).



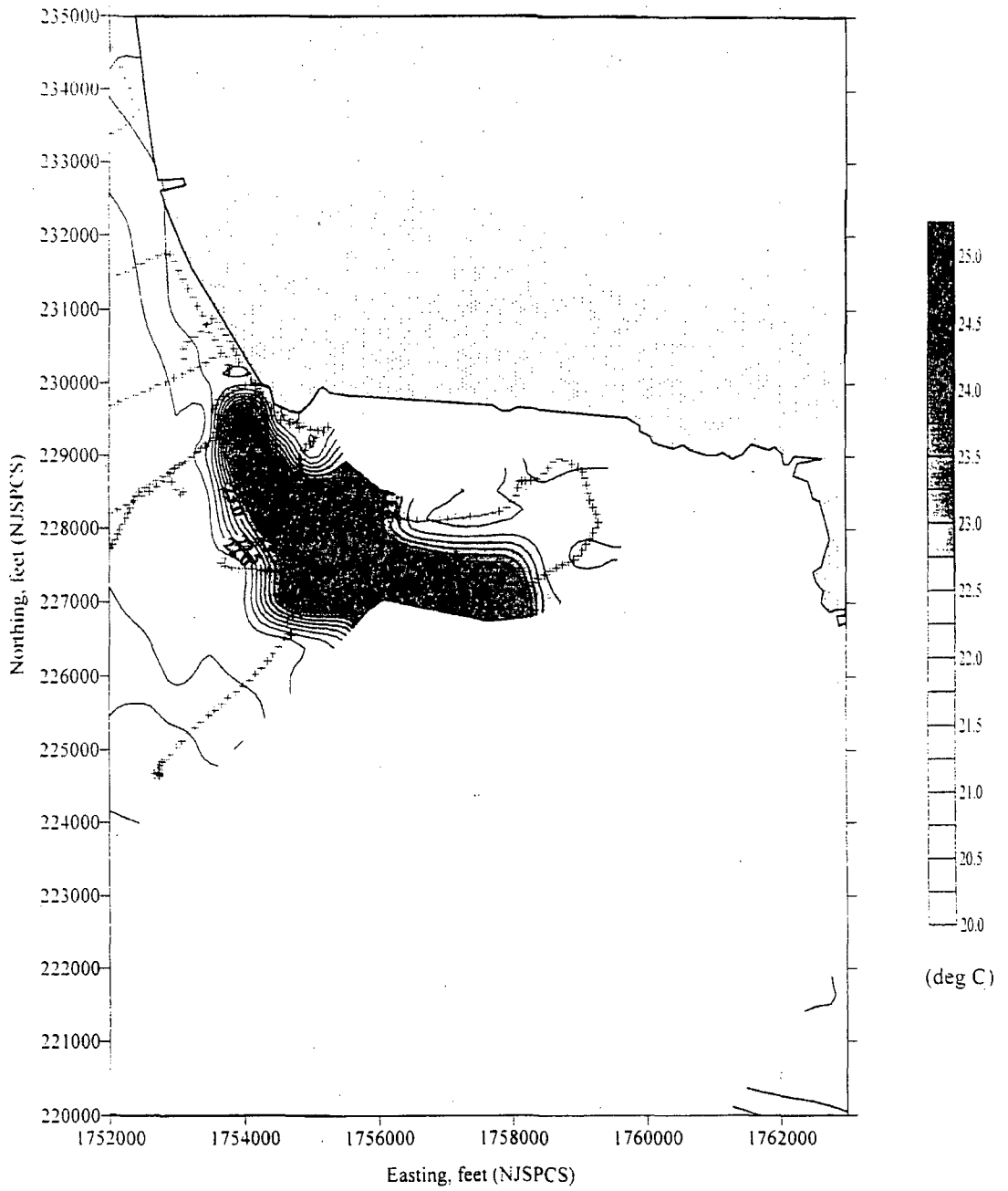
E-2 Figure III-61c. Comparison of modeled and measured temperature at the Hope Creek mooring for the calibration period (19 May - 4 June 1998).



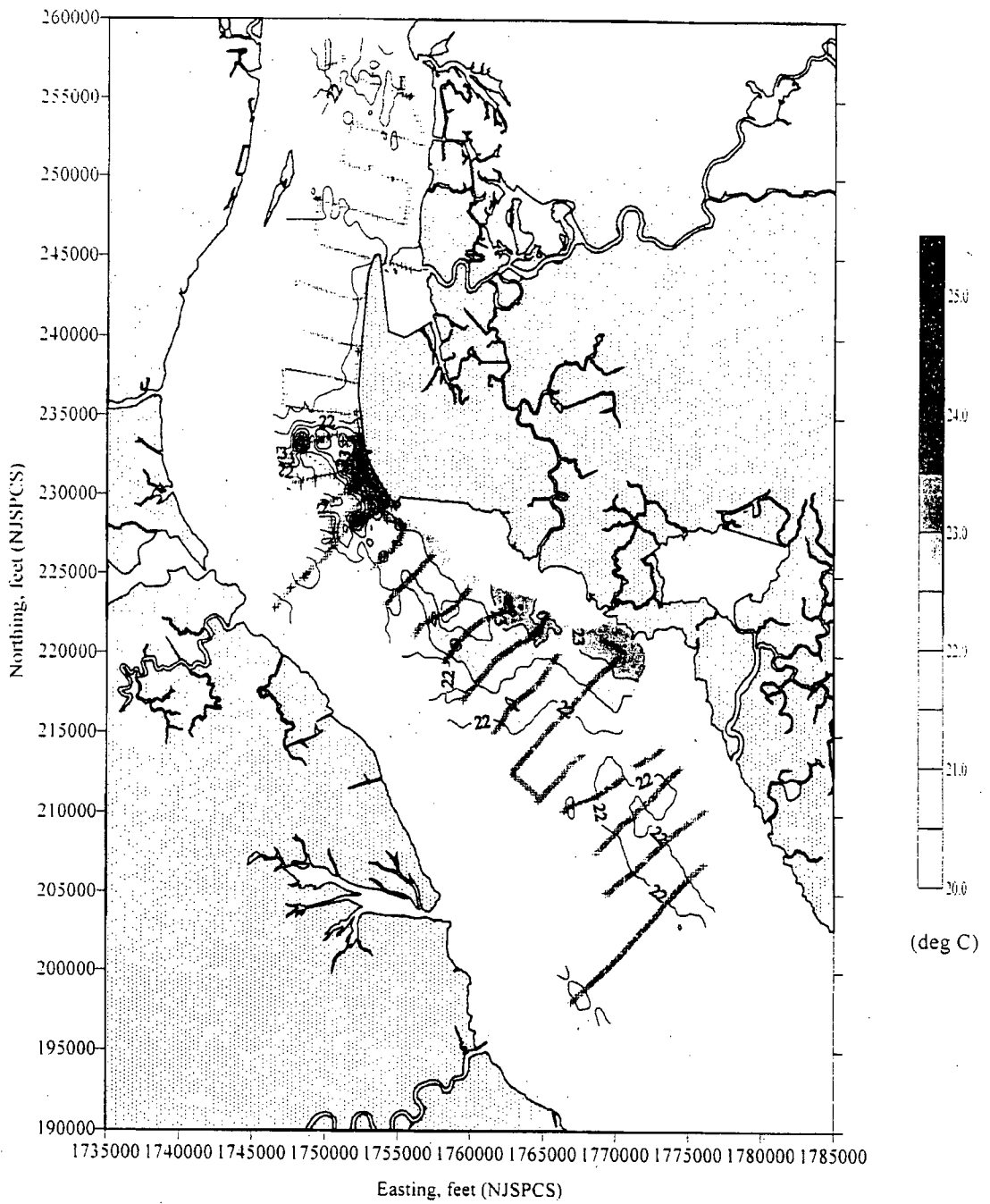
E-2 Figure III-61d. Comparison of modeled and measured temperature at Mooring 6, which is located near the Station on the western side of the shipping channel, for the calibration period (19 May - 4 June 1998).



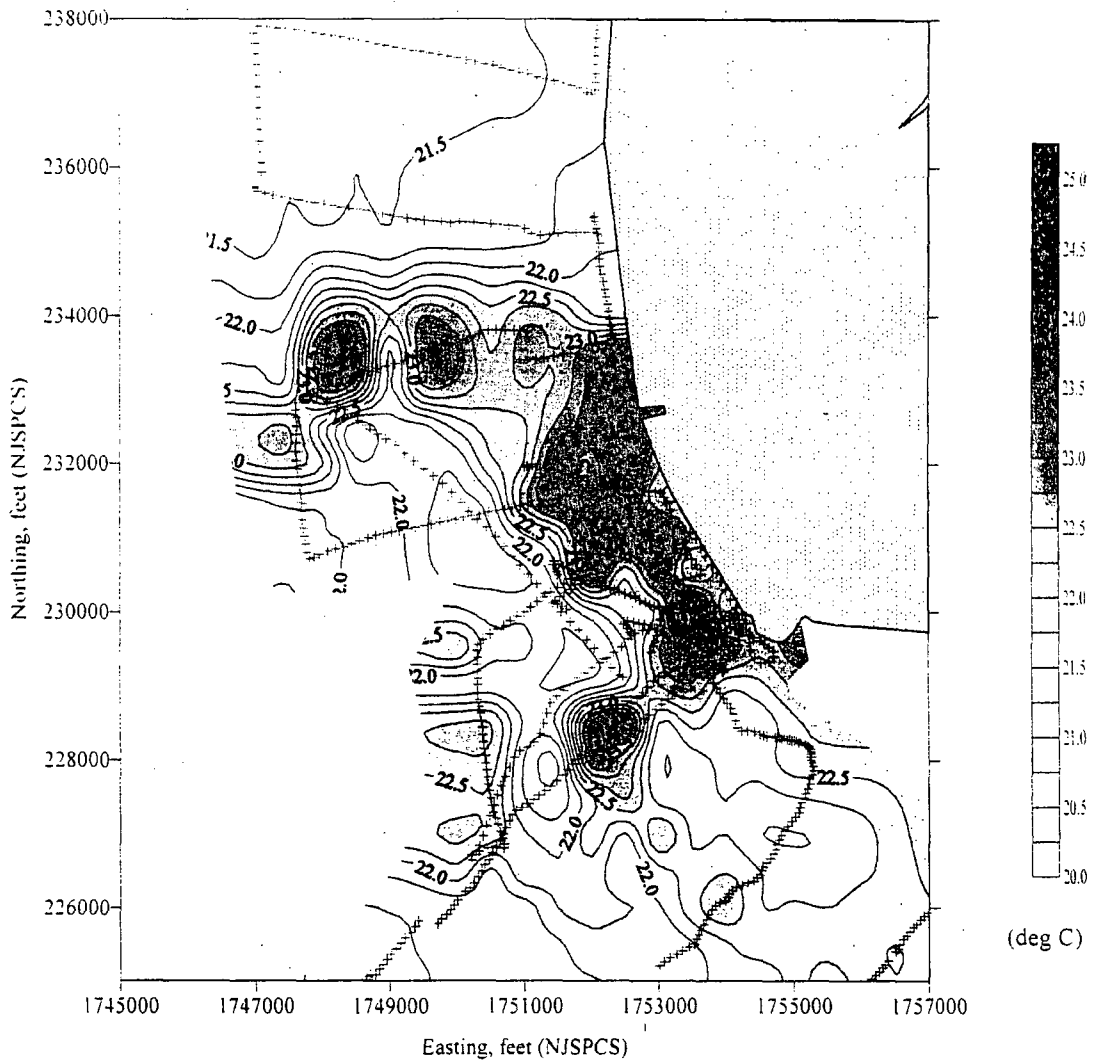
E-2 Figure III-62a. Contours of measured surface temperatures with boat trackings for an ebb phase on 29 May 1998.



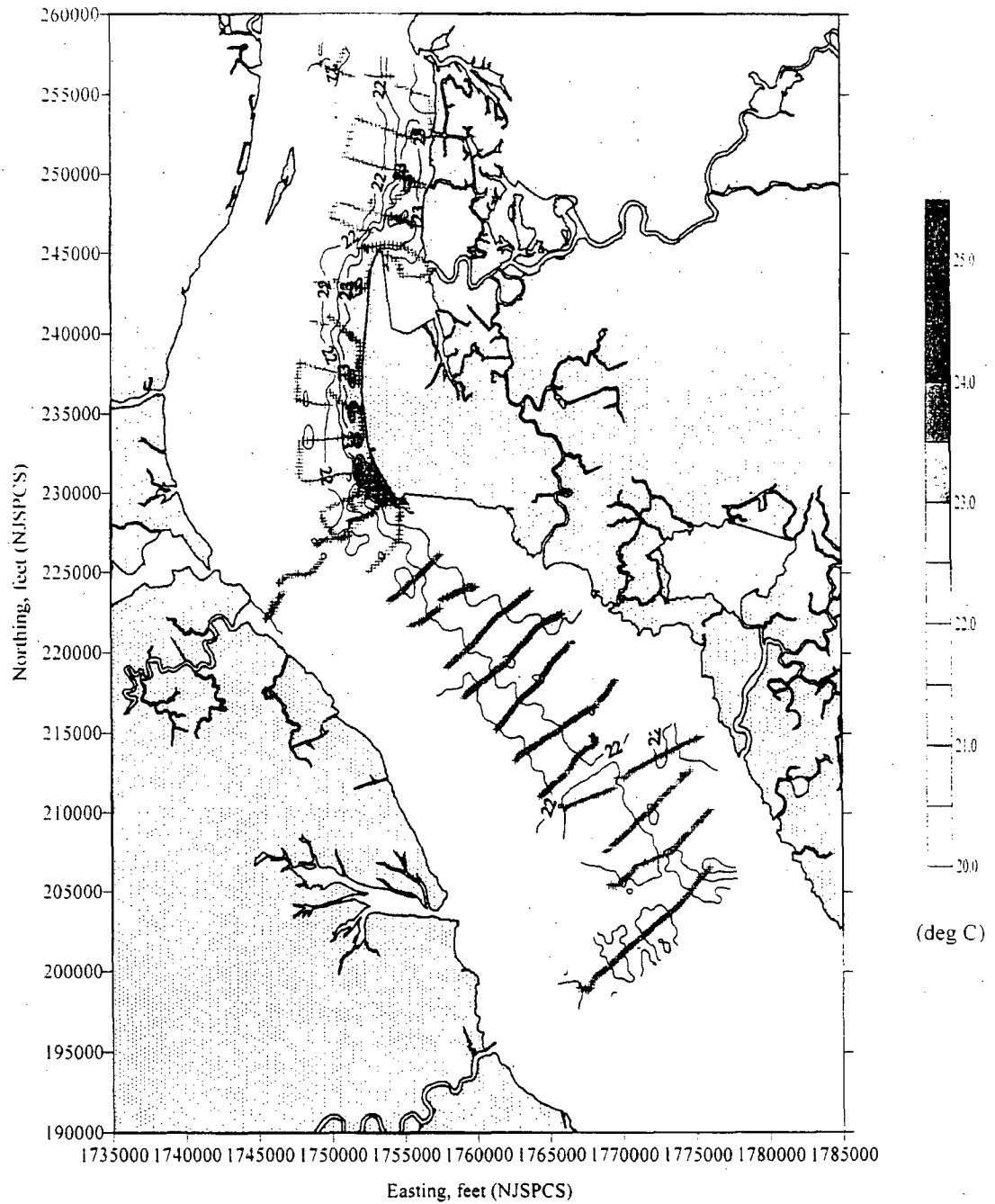
E-2 Figure III-62b. Contours of measured surface temperatures with boat trackings for an ebb phase on 29 May 1998 (close-up view).



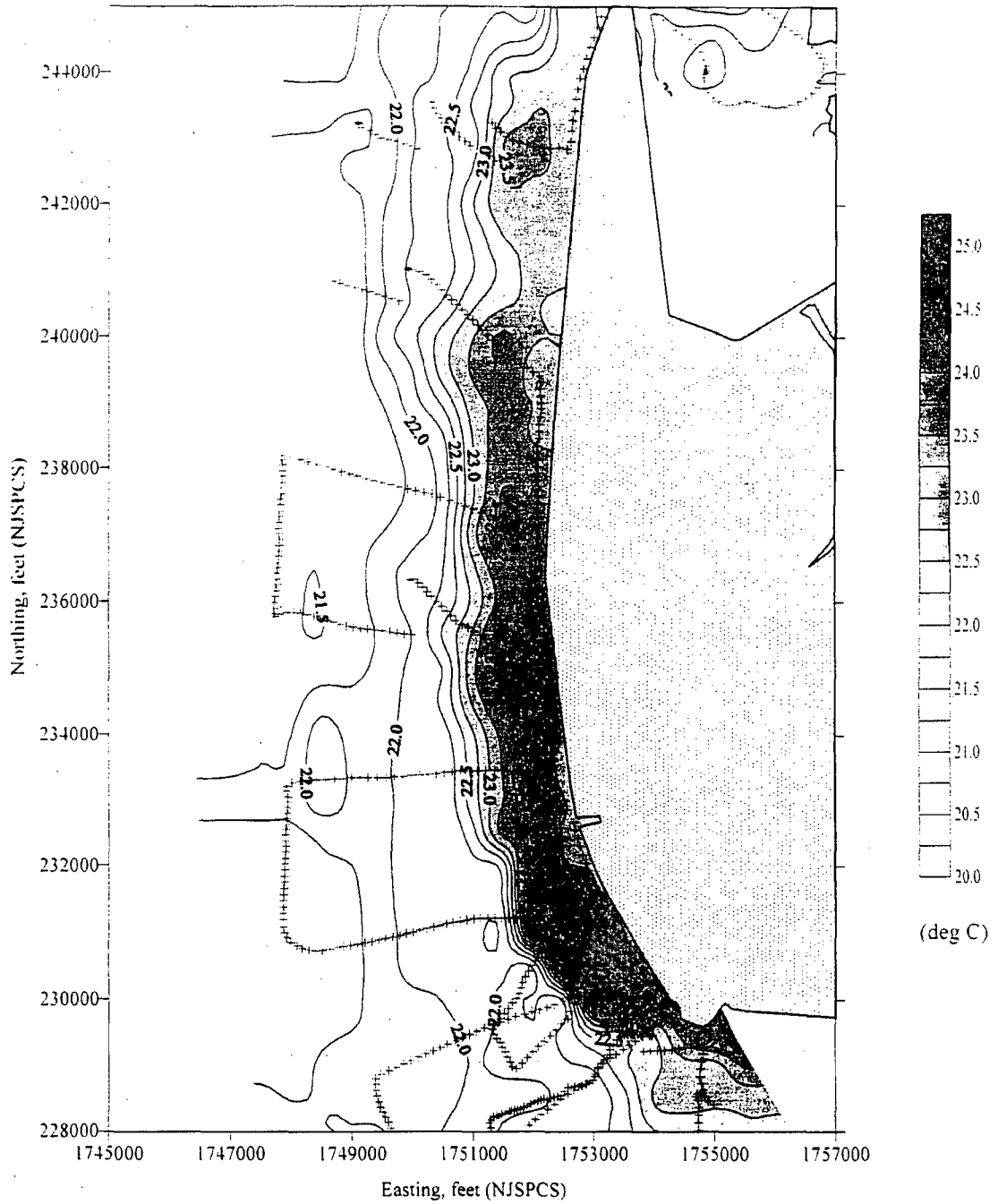
E-2 Figure III-63a. Contours of measured surface temperatures with boat trackings for a slack phase (end-of-ebb) on 29 May 1998.



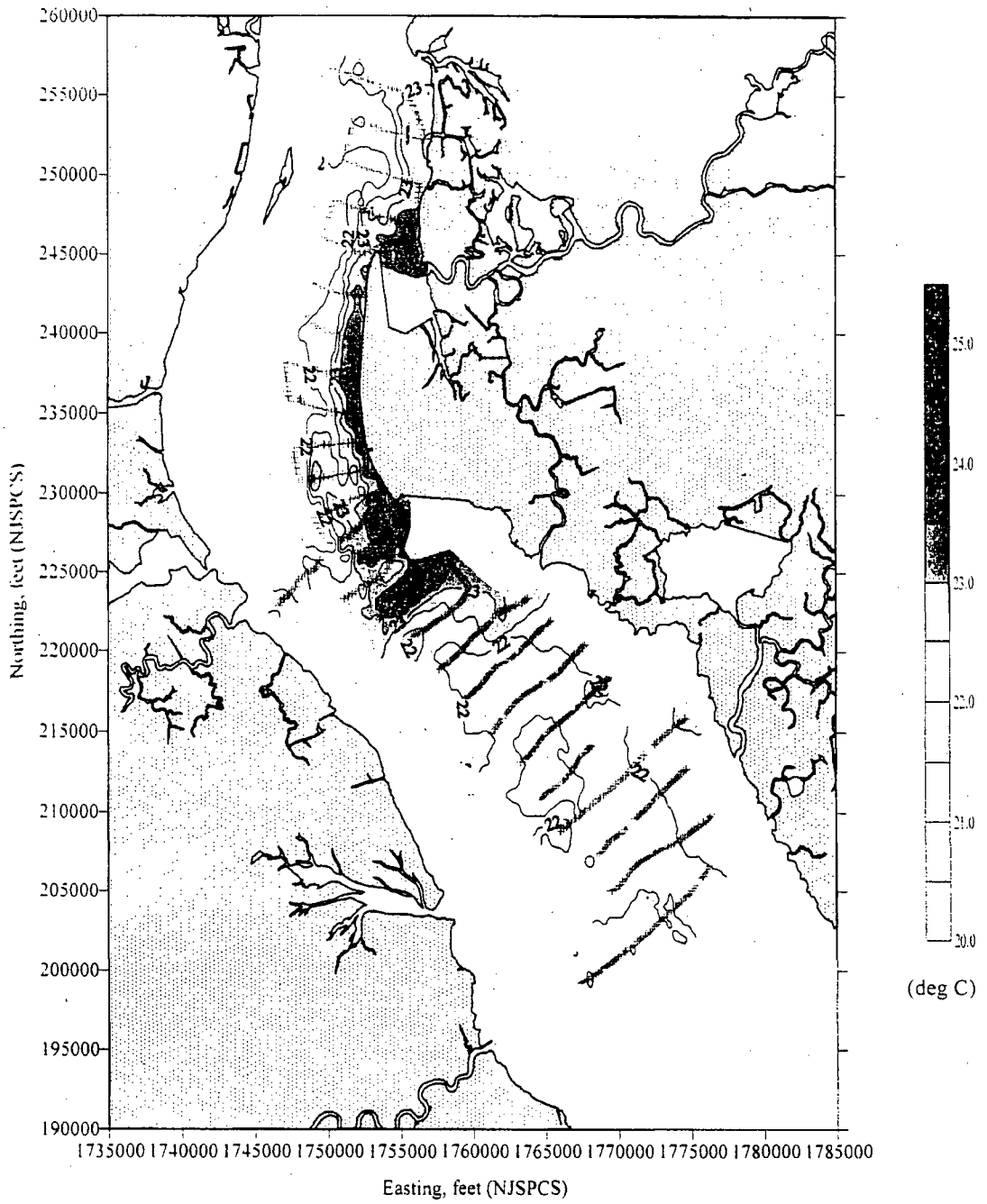
E-2 Figure III-63b. Contours of measured surface temperatures with boat trackings for a slack phase (end-of-ebb) on 29 May 1998 (close-up view).



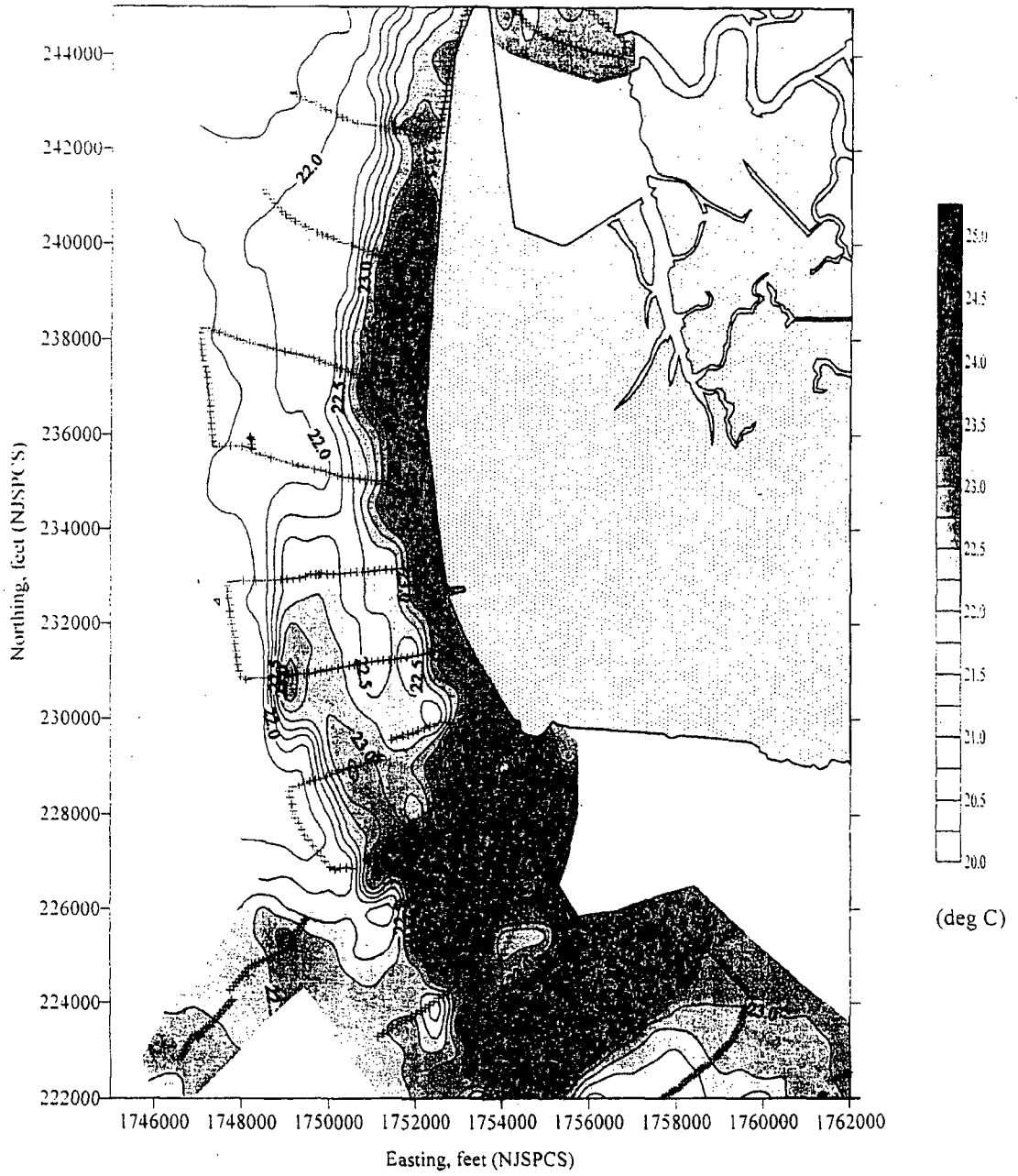
E-2 Figure III-64a. Contours of measured surface temperatures with boat trackings for a flood phase on 29 May 1998.



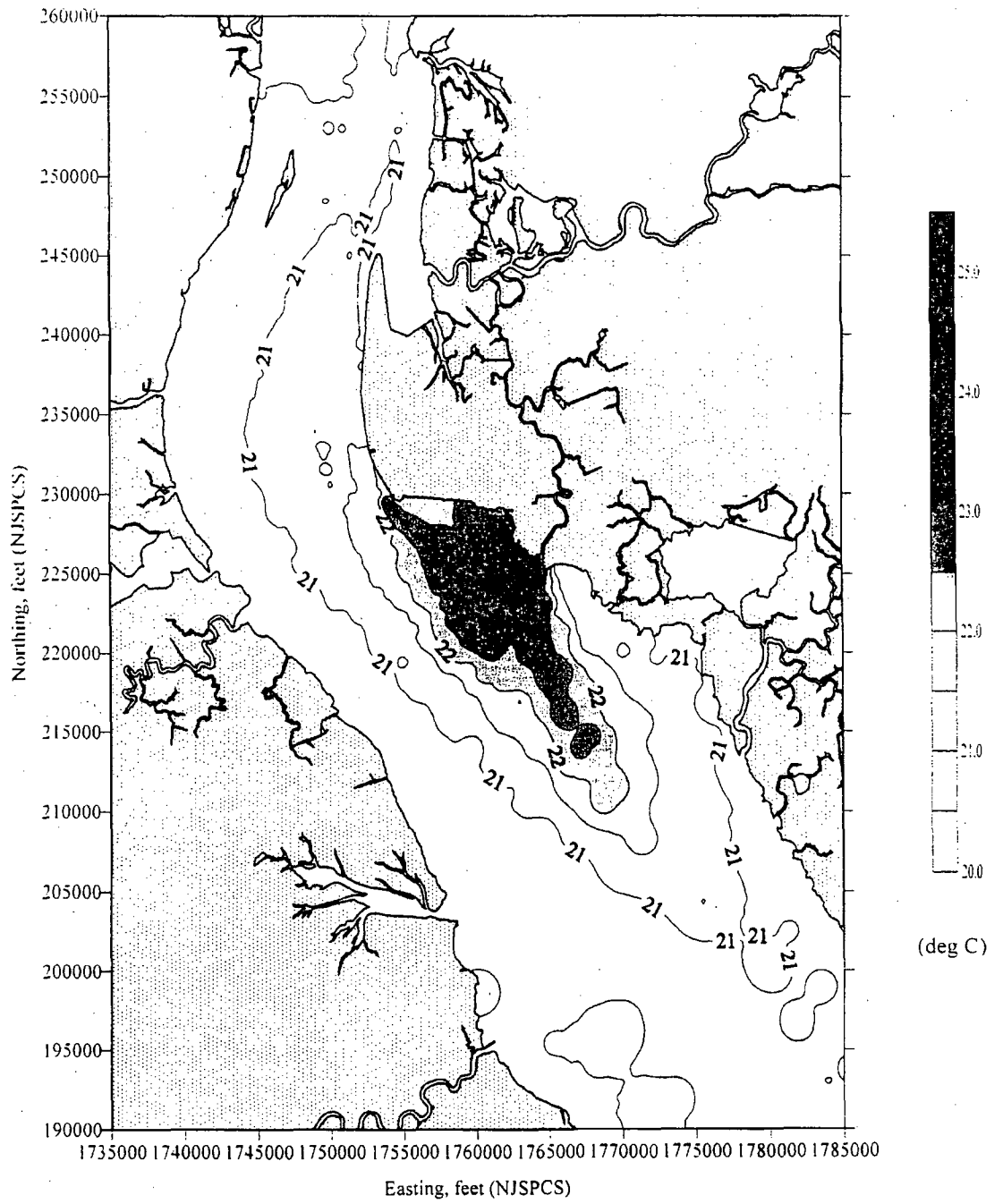
E-2 Figure III-64b. Contours of measured surface temperatures with boat trackings for a flood phase on 29 May 1998 (close-up view).



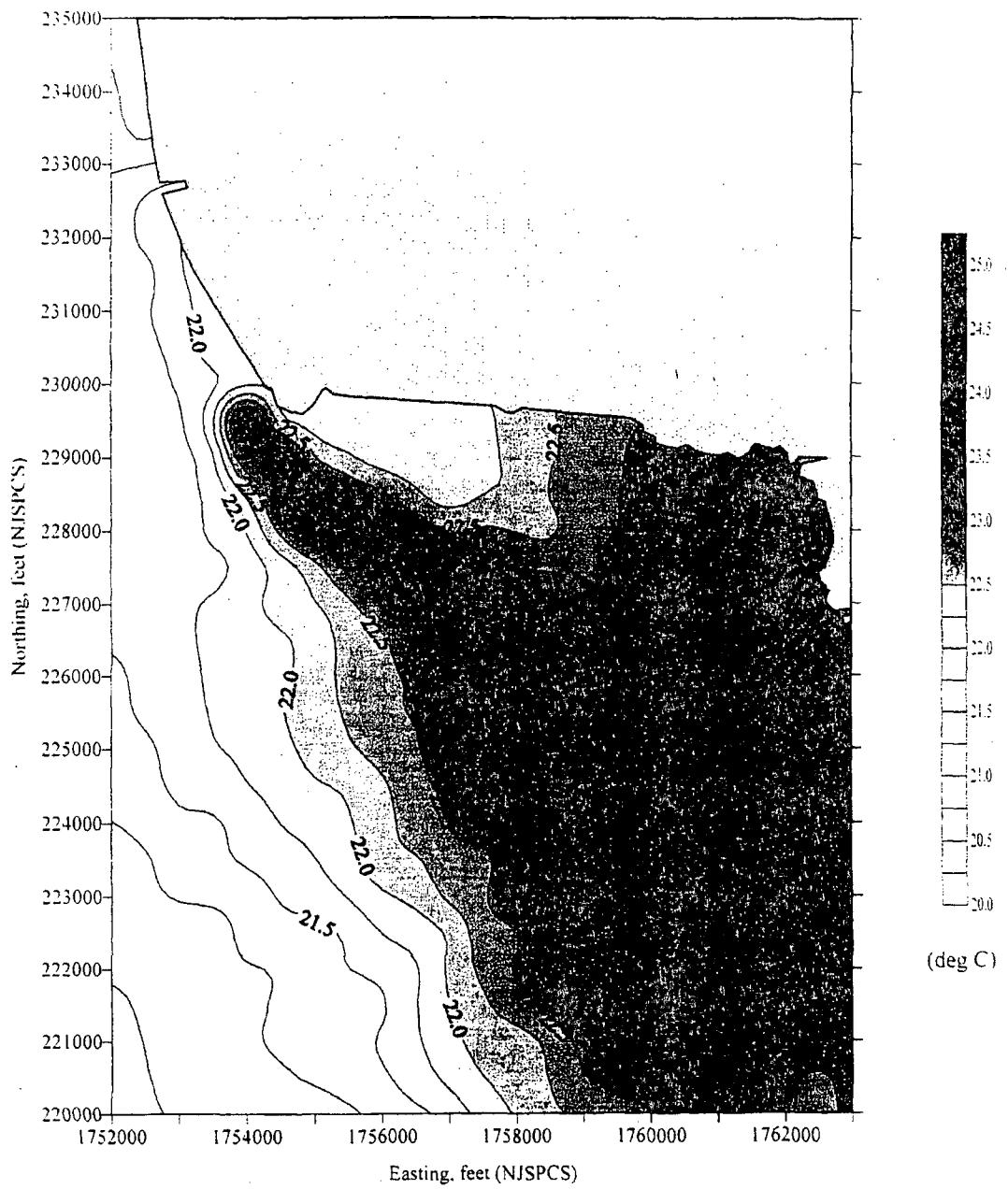
E-2 Figure III-65a. Contours of measured surface temperatures with boat trackings for a slack phase (end-of-flood) on 29 May 1998.



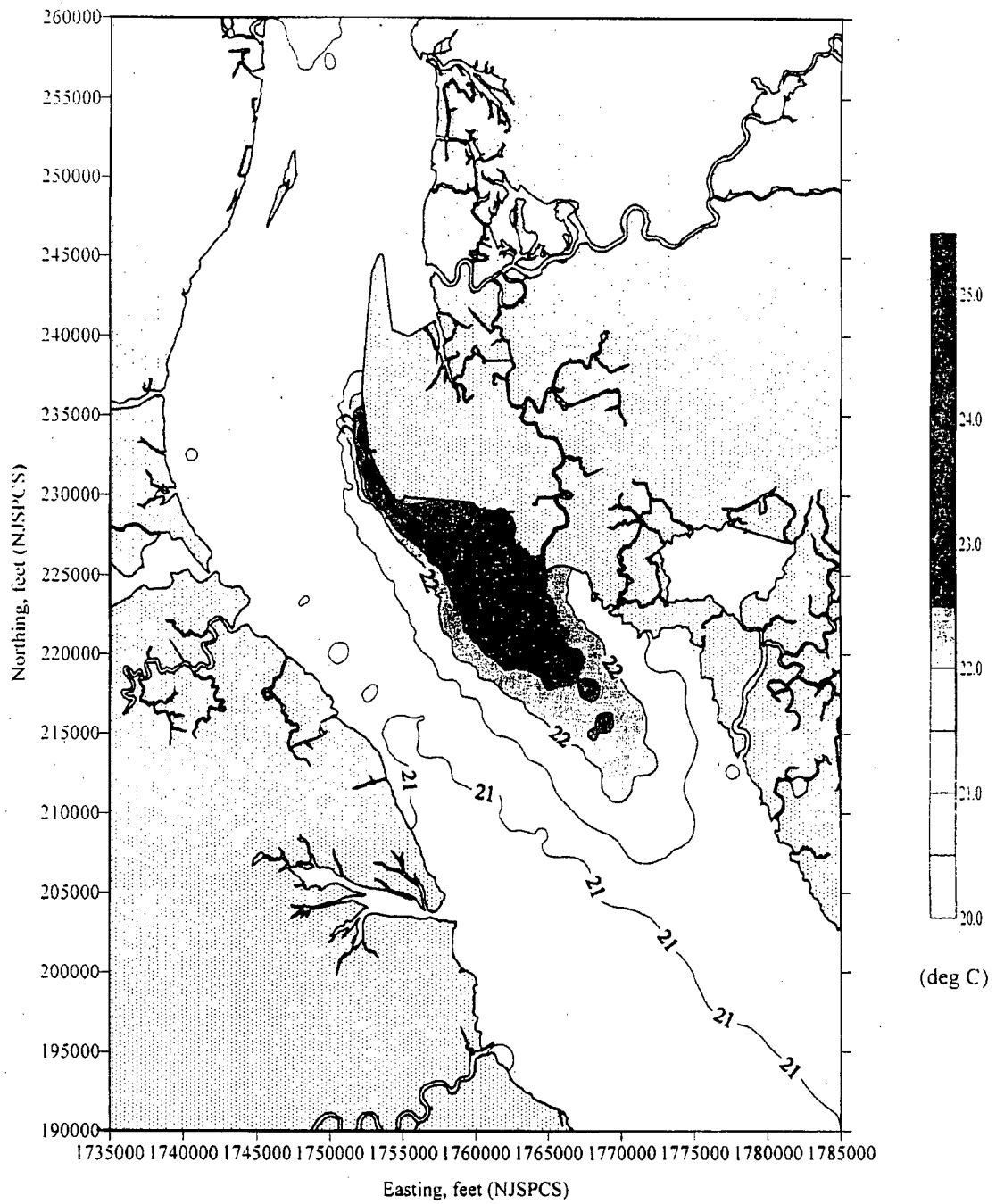
E-2 Figure III-65b. Contours of measured surface temperatures with boat trackings for a slack phase (end-of-flood) on 29 May 1998 (close-up view).



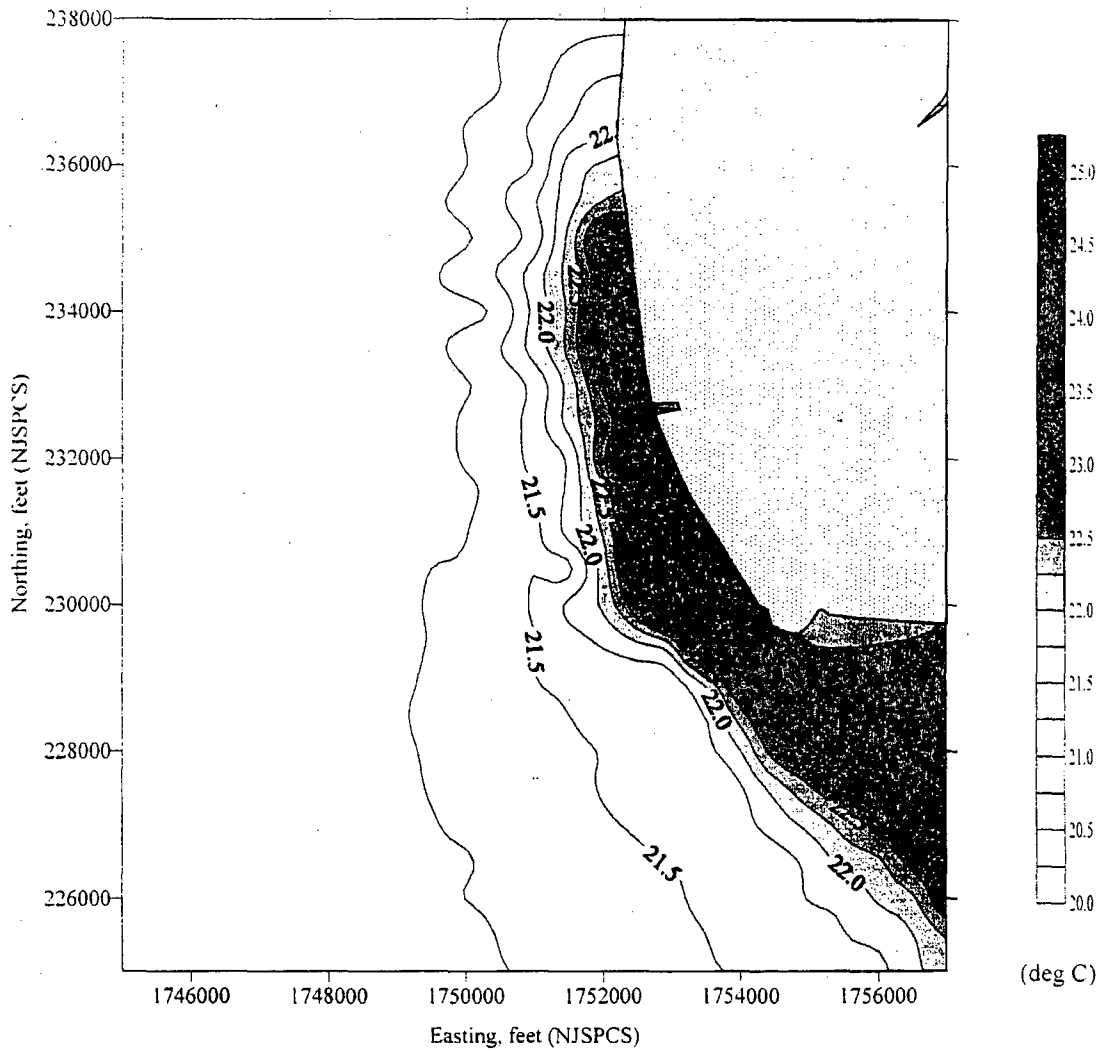
E-2 Figure III-66a. Contours of modeled surface temperatures for an ebb phase on 29 May 1998.



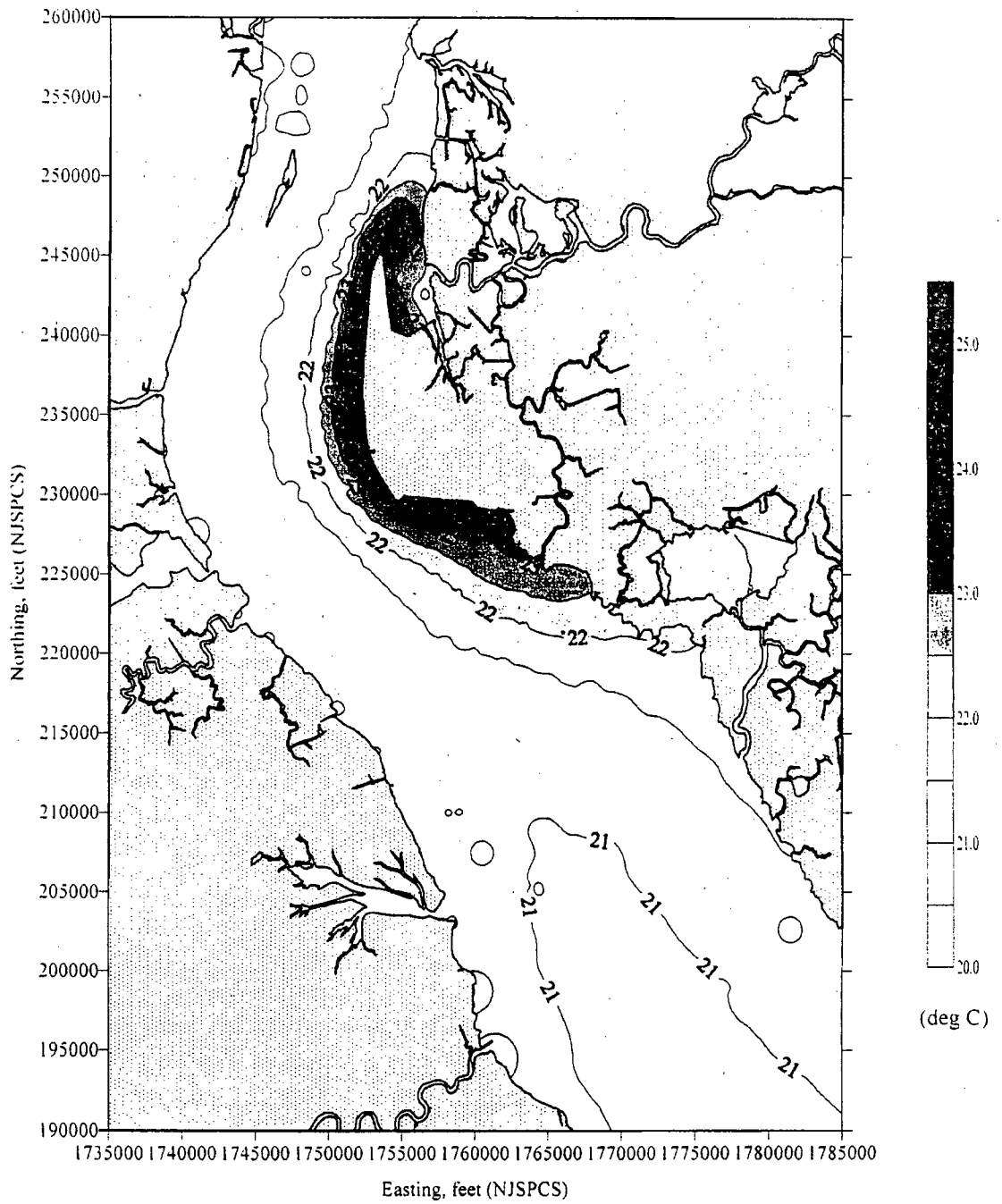
E-2 Figure III-66b. Contours of modeled surface temperatures for an ebb phase on 29 May 1998 (close-up view).



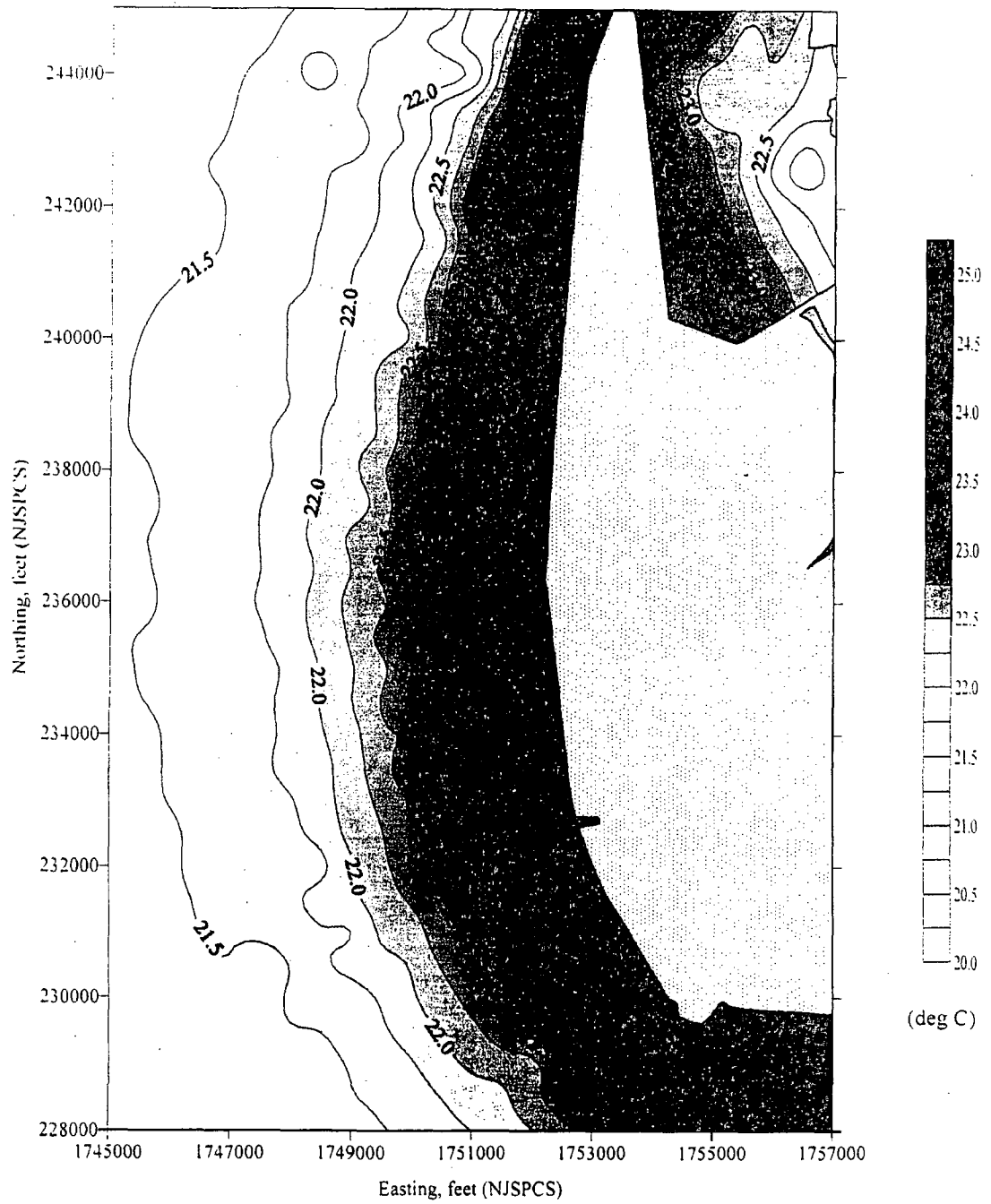
E-2 Figure III-67a. Contours of modeled surface temperatures for a slack phase (end-of-ebb) on 29 May 1998.



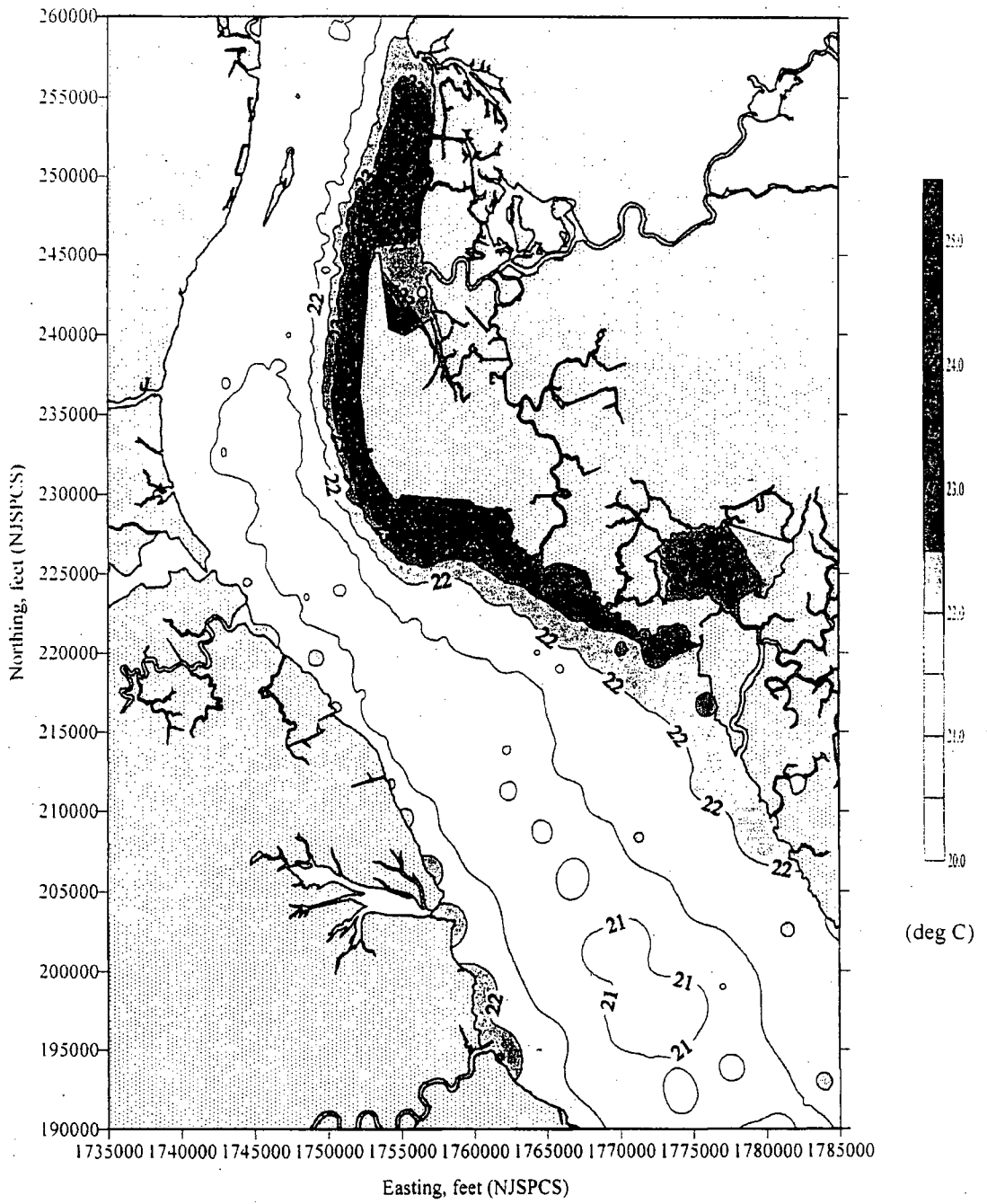
E-2 Figure III-67b. Contours of modeled surface temperatures for a slack phase (end-of-ebb) on 29 May 1998 (close-up view).



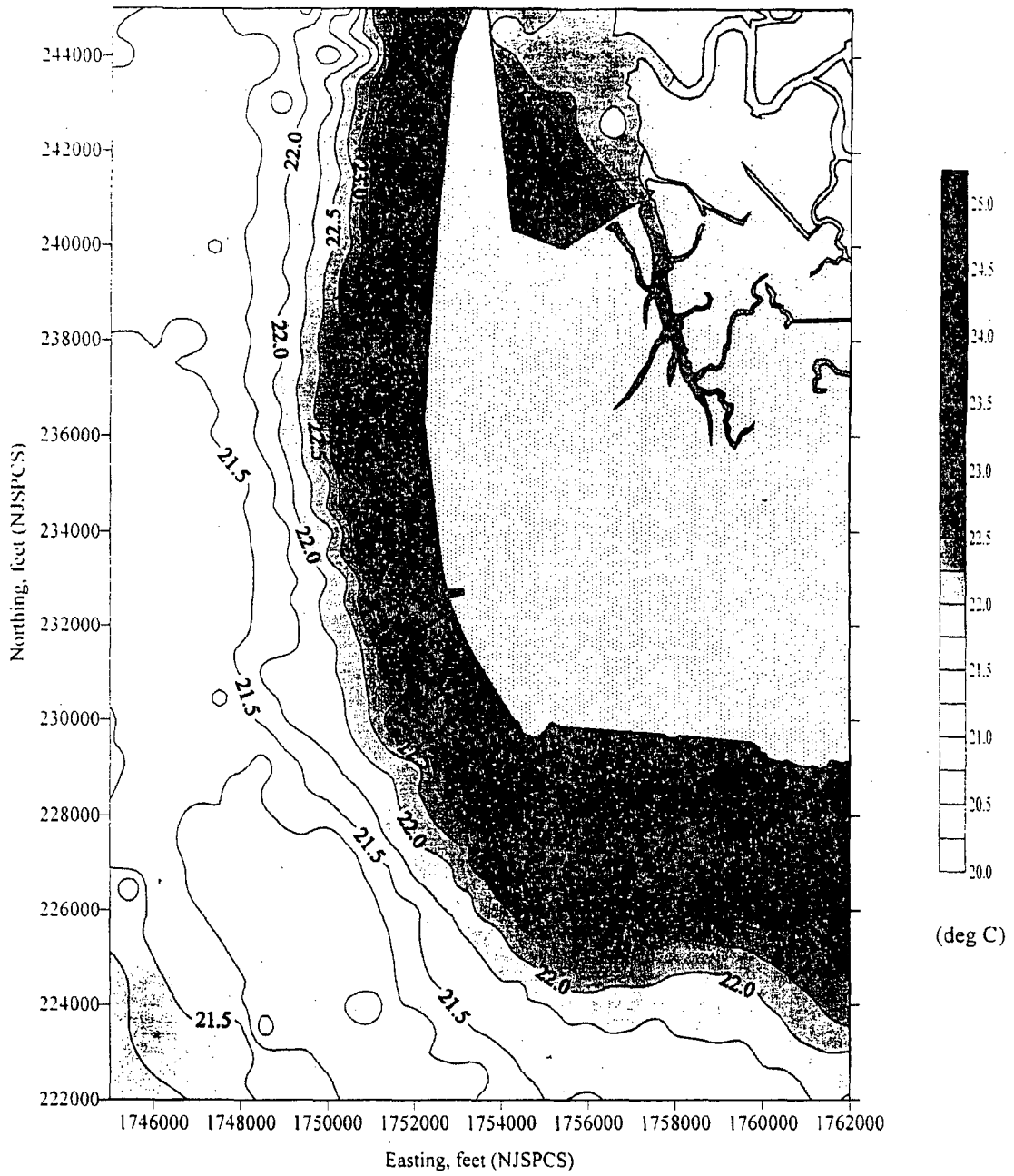
E-2 Figure III-68a. Contours of modeled surface temperatures for a flood phase on 29 May 1998.



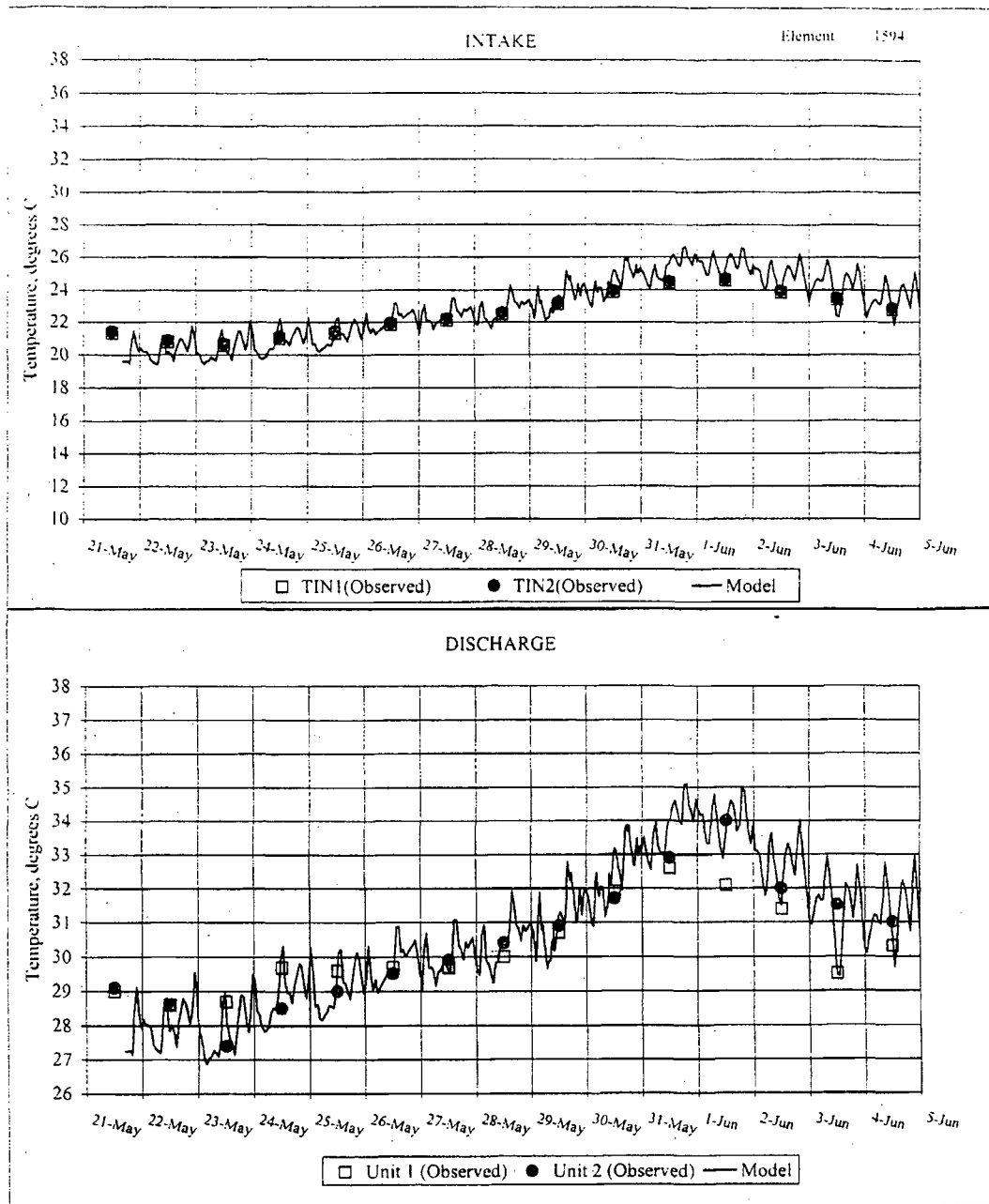
E-2 Figure III-68b. Contours of modeled surface temperatures for a flood phase on 29 May 1998 (close-up view).



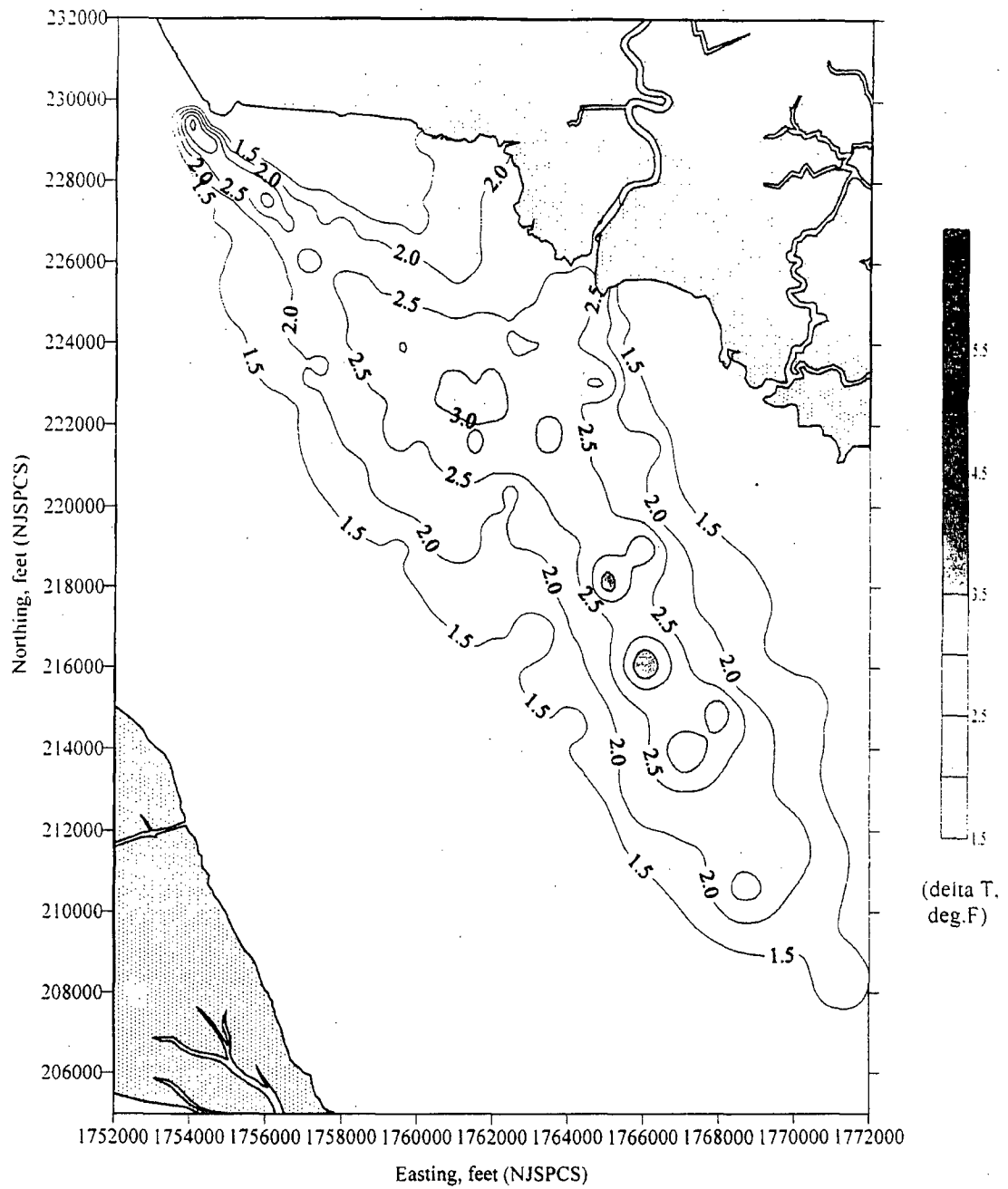
E-2 Figure III-69a. Contours of modeled surface temperatures for a slack phase (end-of-flood) on 29 May 1998.



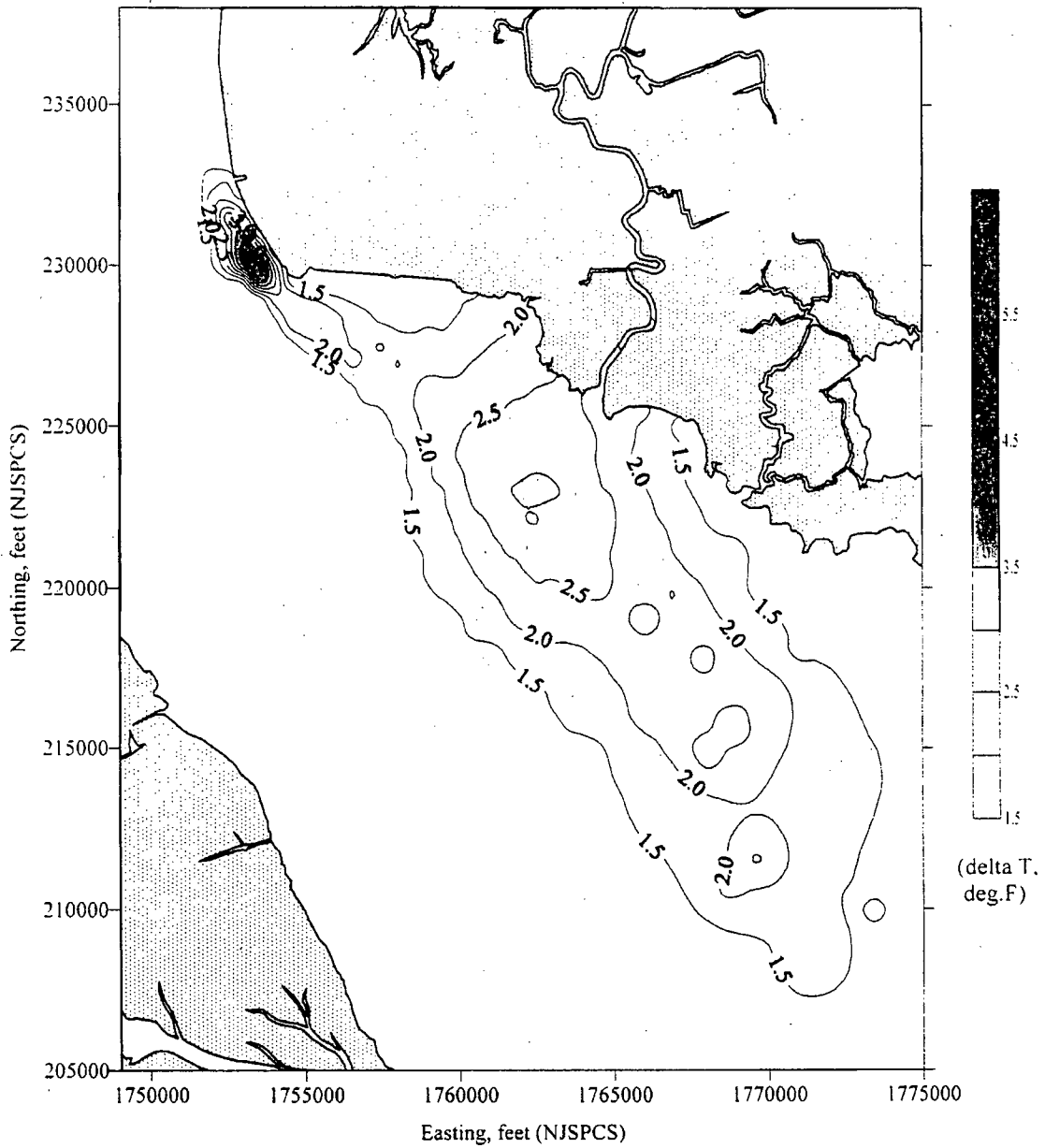
E-2 Figure III-69b. Contours of modeled surface temperatures for a slack phase (end-of-flood) on 29 May 1998 (close-up view).



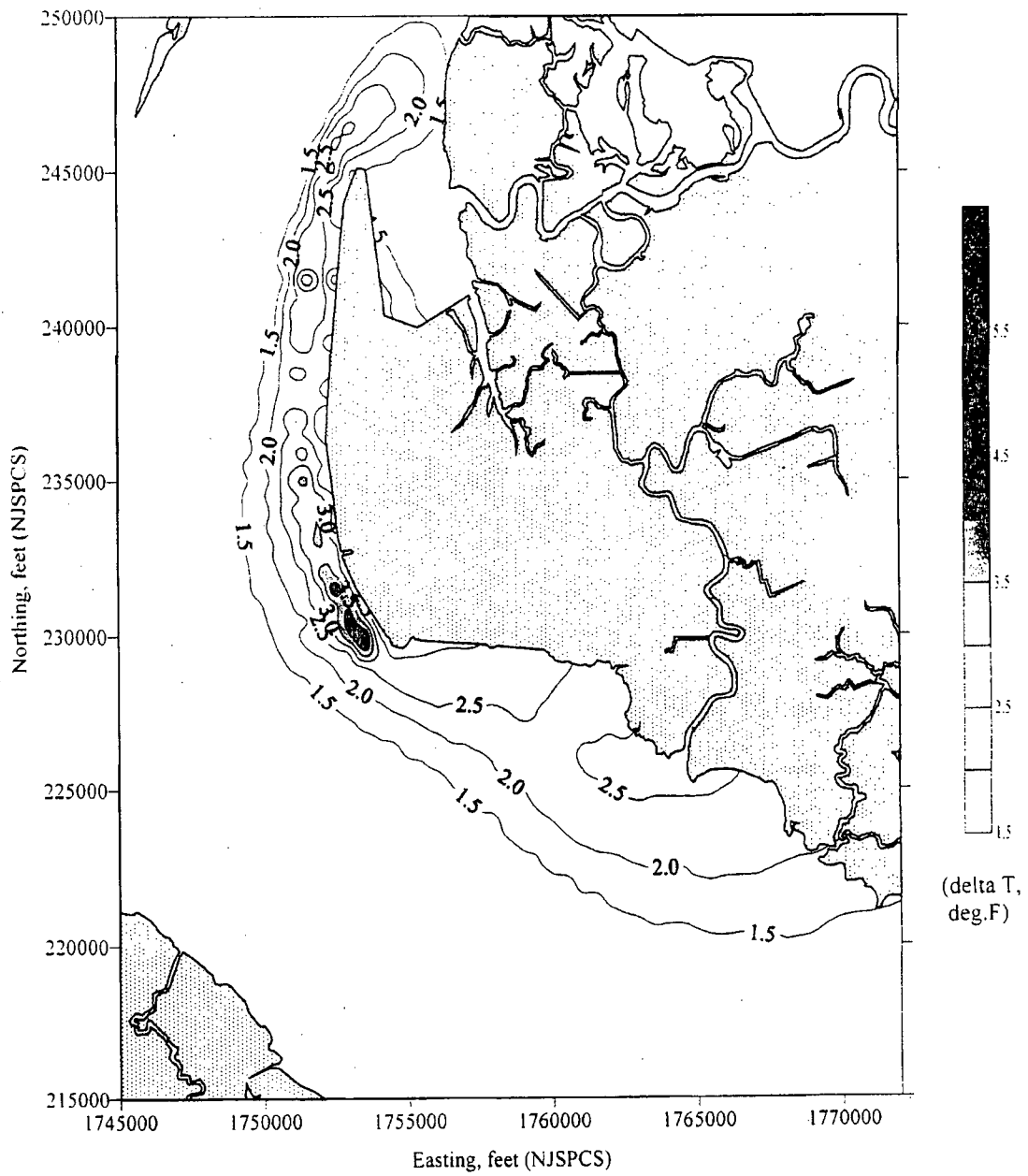
E-2 Figure III-70. Comparison of modeled Station intake and discharge temperatures to measured intake (TIN1 and TIN2) and discharge (Unit 1 and Unit 2) temperatures for the calibration period (21 May - 4 June 1998).



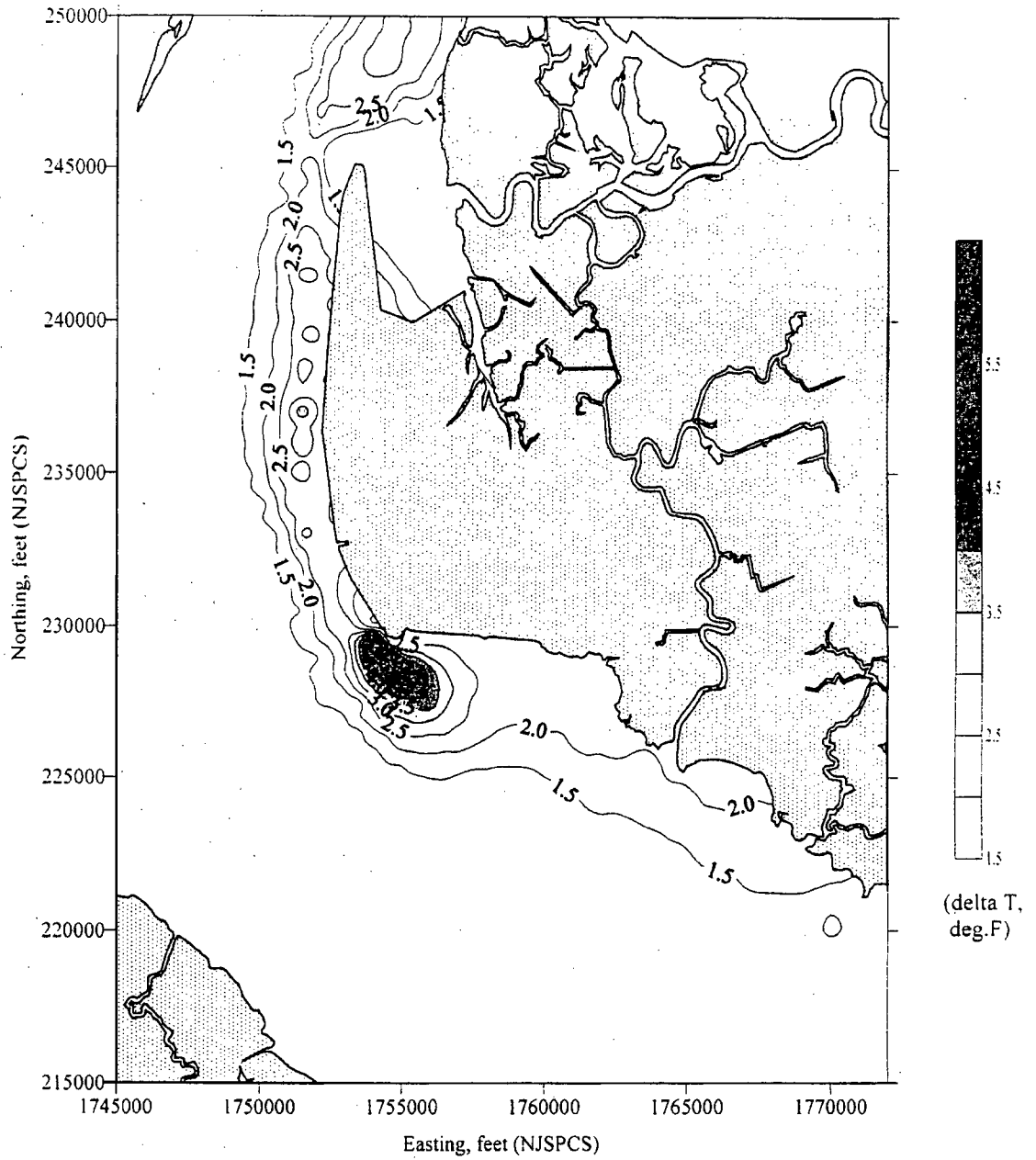
E-2 Figure III-71. Contours of modeled surface delta temperatures for an ebb phase on 29 May 1998.



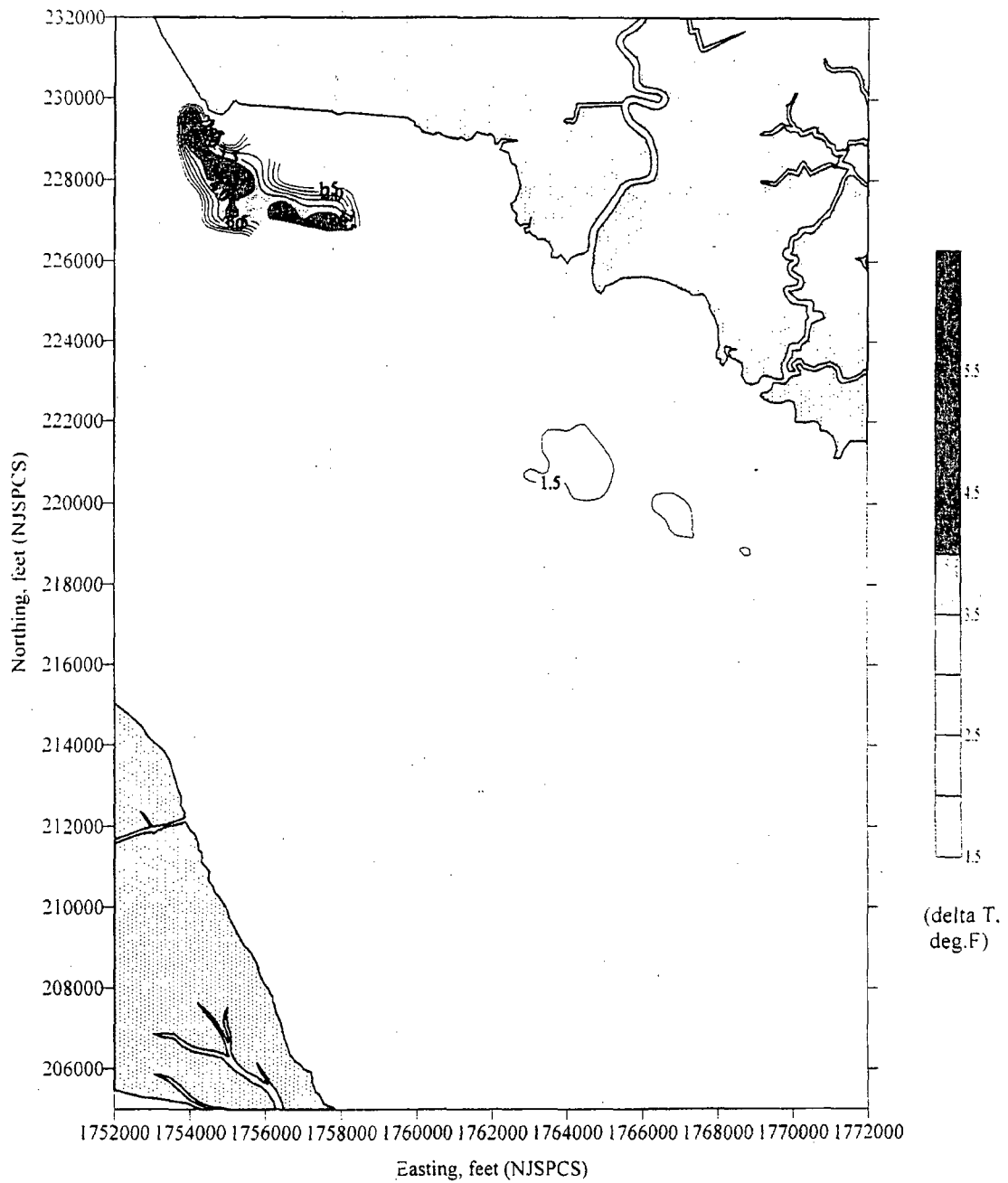
E-2 Figure III-72. Contours of modeled surface delta temperatures for a slack phase (end-of-ebb) on 29 May 1998.



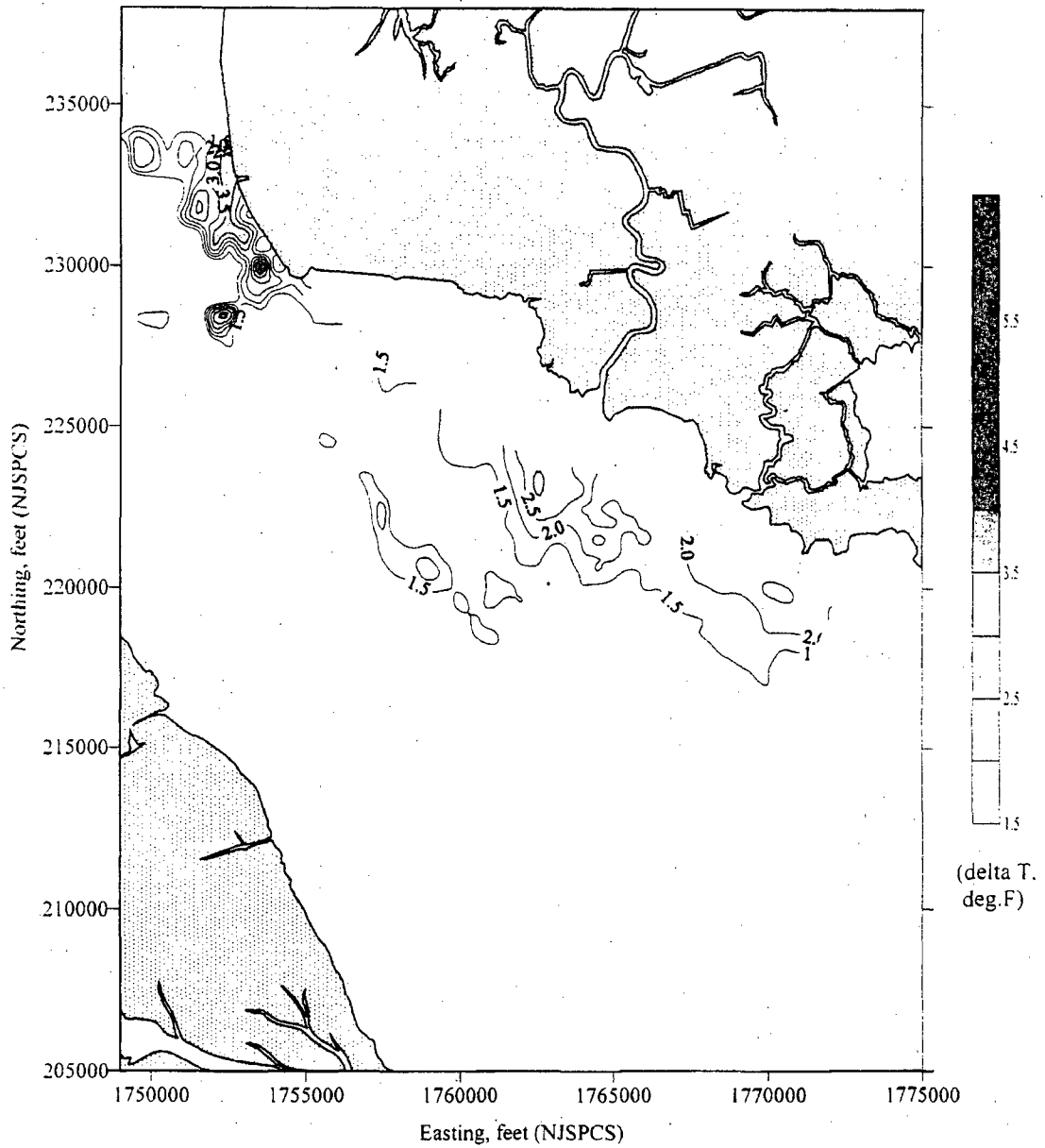
E-2 Figure III-73. Contours of modeled surface delta temperatures for a flood phase on 29 May 1998.



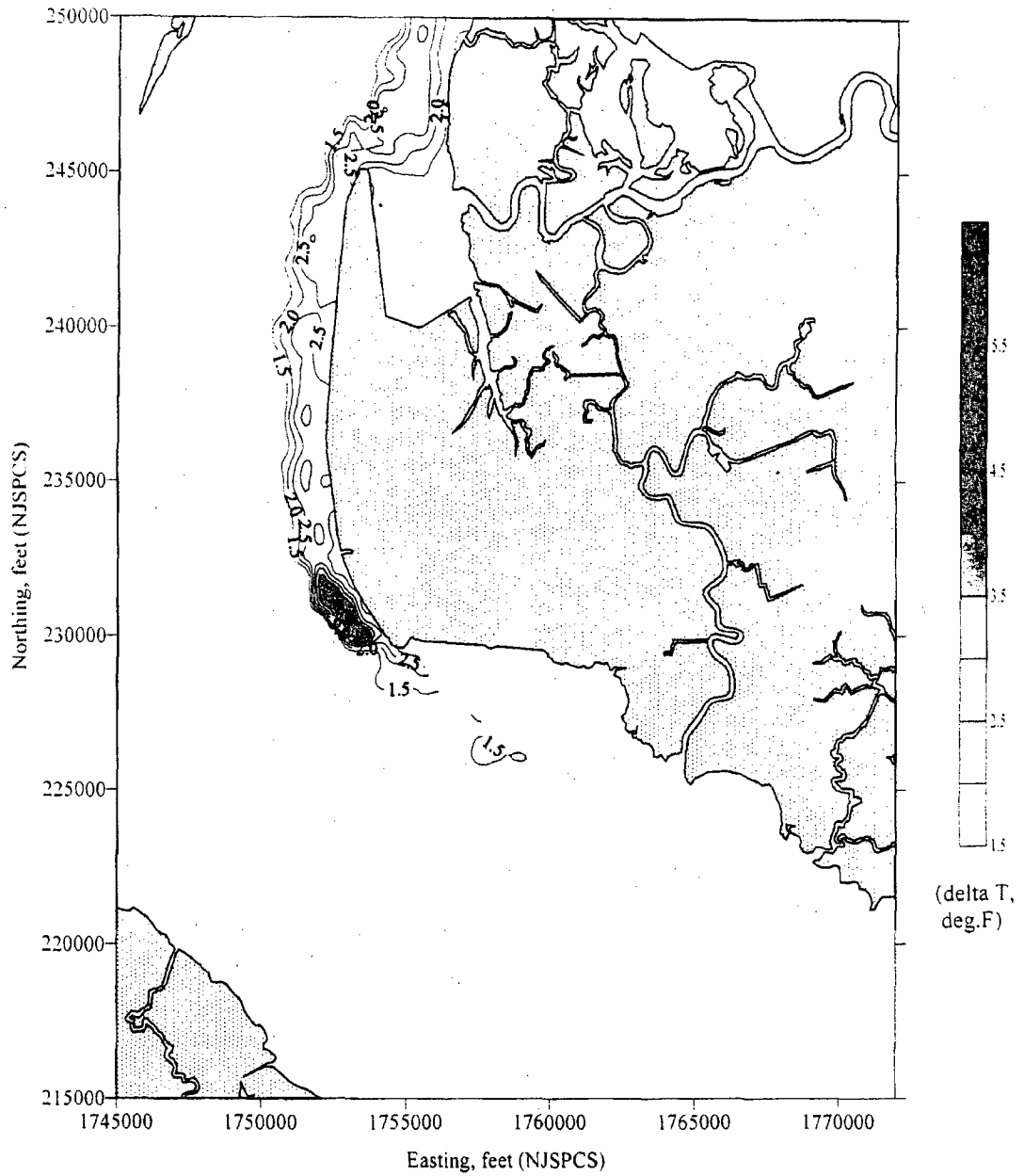
E-2 Figure III-74. Contours of modeled surface delta temperatures for a slack phase (end-of-flood) on 29 May 1998.



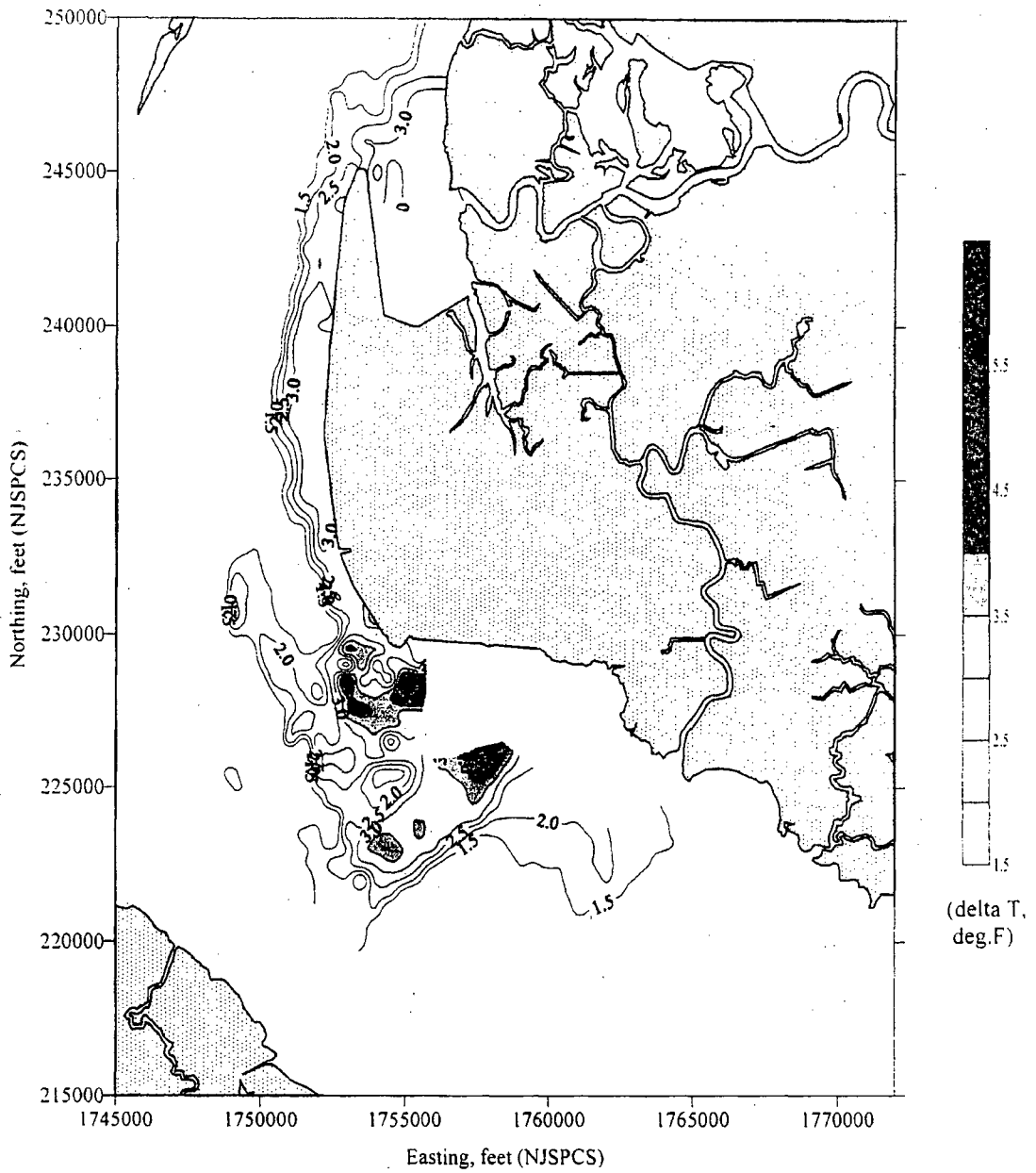
E-2 Figure III-75. Contours of measured surface delta temperatures for an ebb phase on 29 May 1998 (Based on an ambient temperature of 71.42 deg.F).



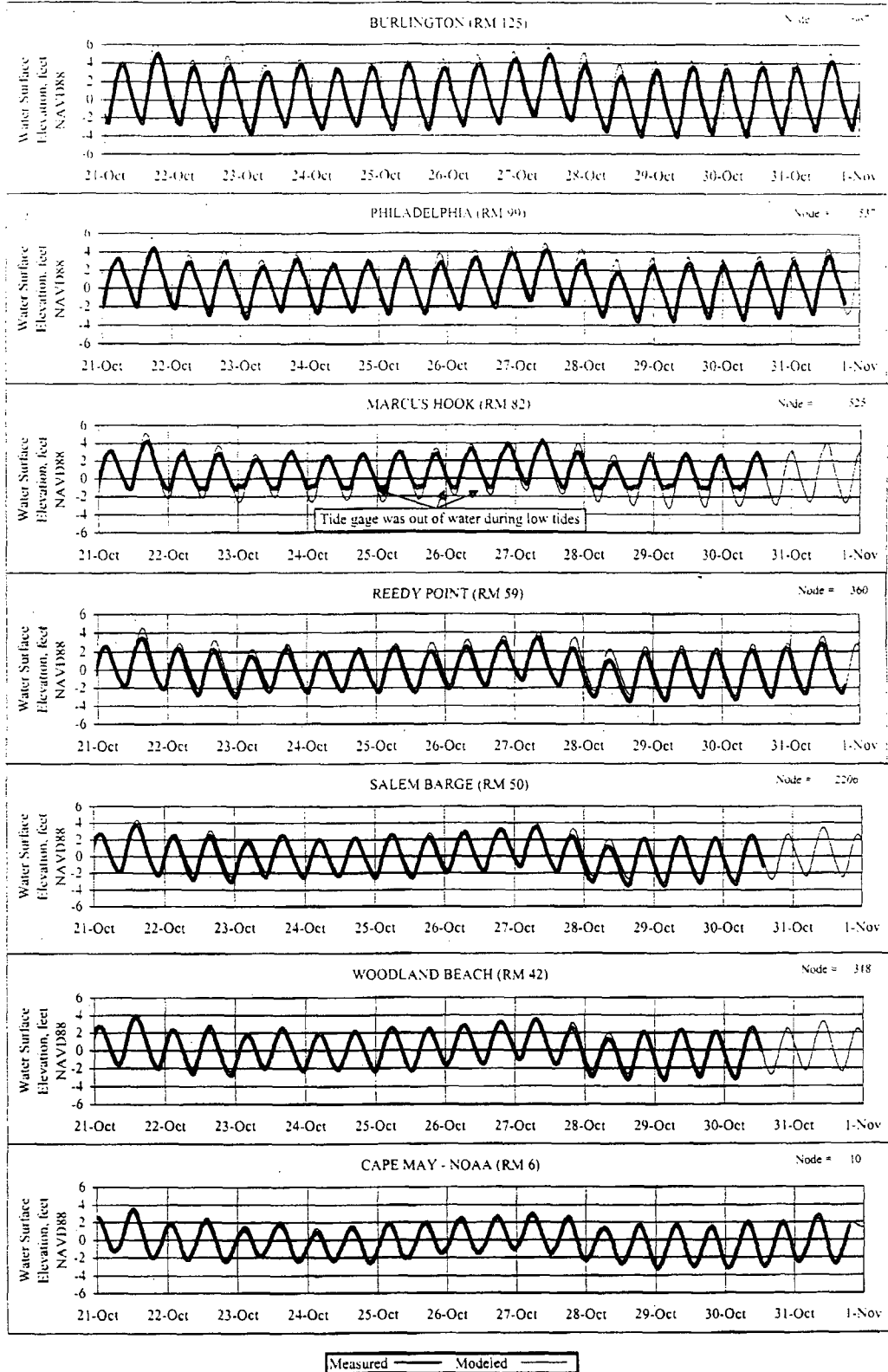
E-2 Figure III-76. Contours of measured surface delta temperatures for a slack phase (end-of-ebb) on 29 May 1998 (Based on an ambient temperature of 71.42 deg.F).



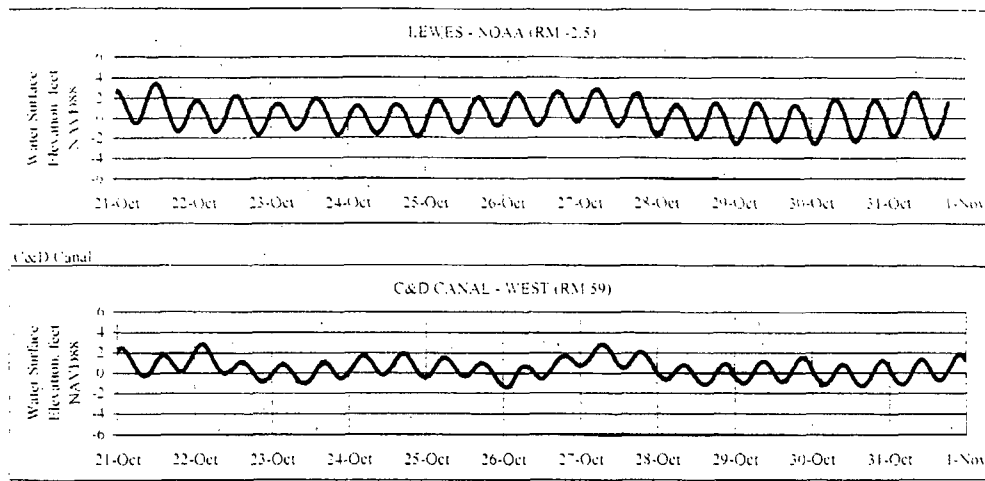
E-2 Figure III-77. Contours of measured surface delta temperatures for a flood phase on 29 May 1998 (Based on an ambient temperature of 71.42 deg.F).



E-2 Figure III-78. Contours of measured surface delta temperatures for a slack phase (end-of-flood) on 29 May 1998 (Based on an ambient temperature of 71.42 deg.F).



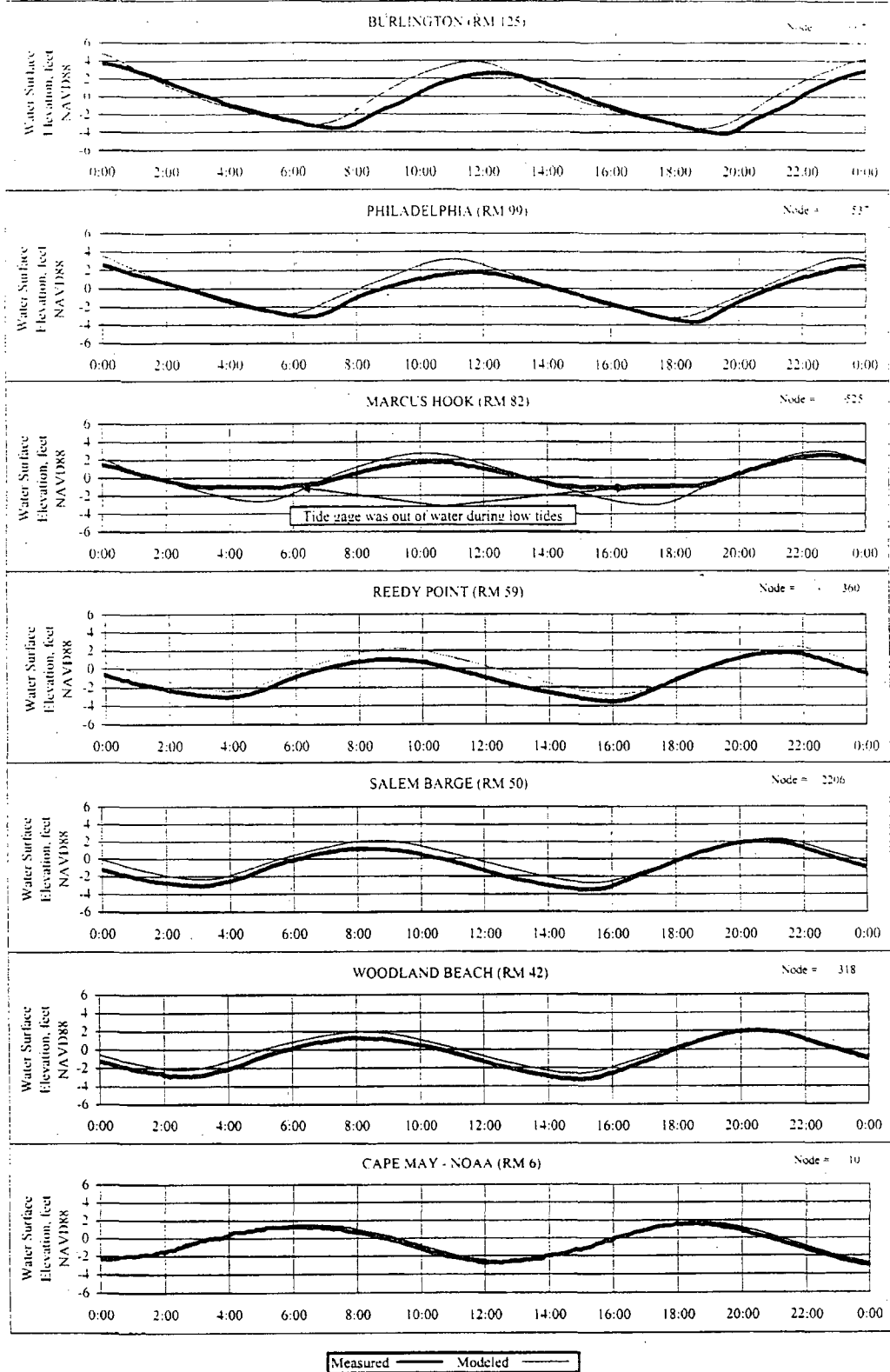
E-2 Figure III-79a. Comparison of modeled and measured tides in the Estuary for the verification period (21-31 October 1997).



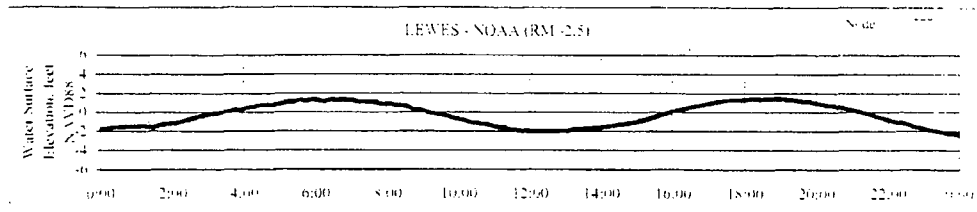
Measured — Modeled —

E-2 Figure III-79b. Comparison of modeled and measured tides at the west side of the Bay mouth (Lewes, DE) and the western end of the C&D Canal for the verification period (21-31 October 1997).

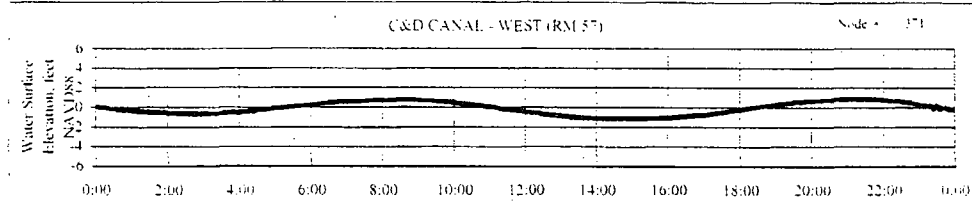
Data Gate River



E-2 Figure III-80a. Comparison of modeled and measured tides in the Estuary for 28 October 1997.

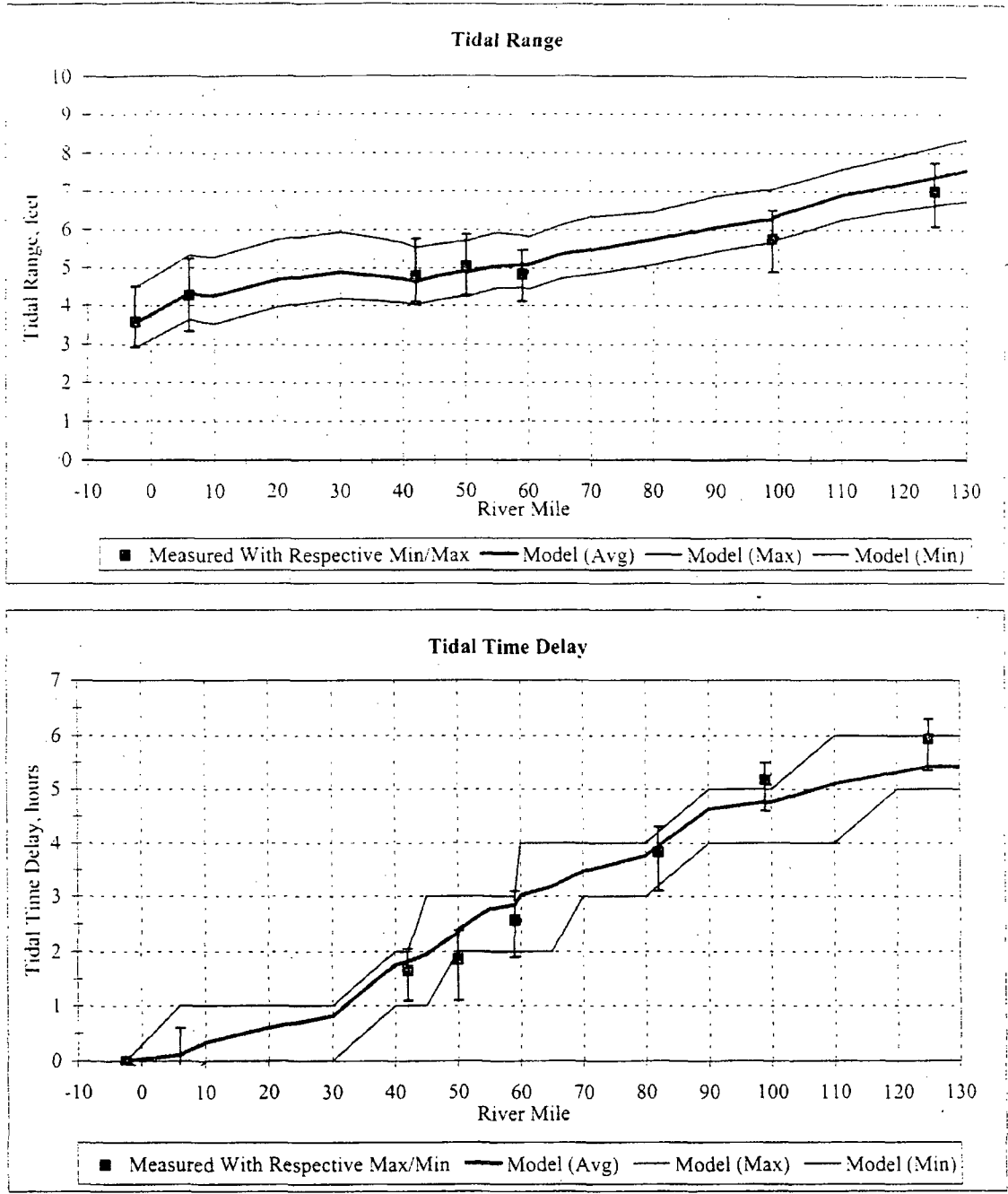


C&D Canal

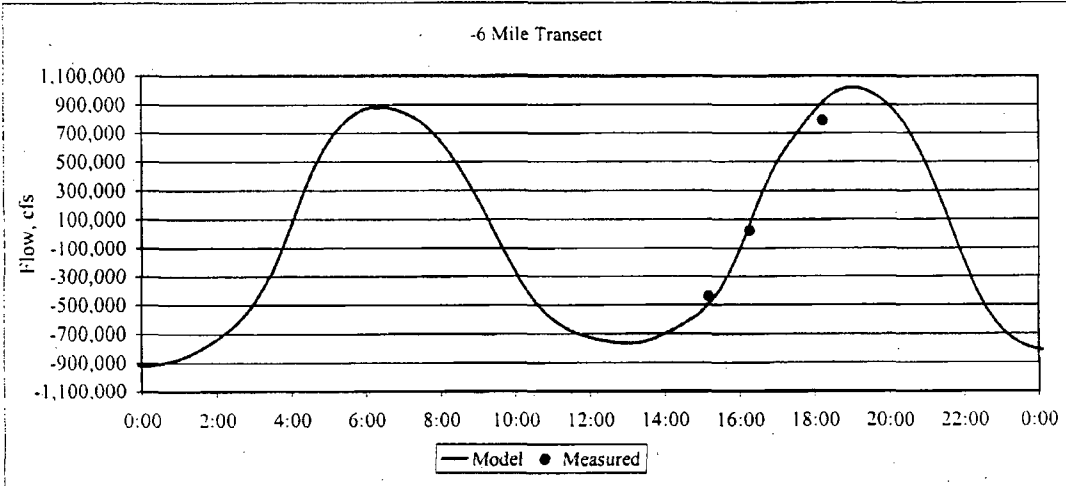
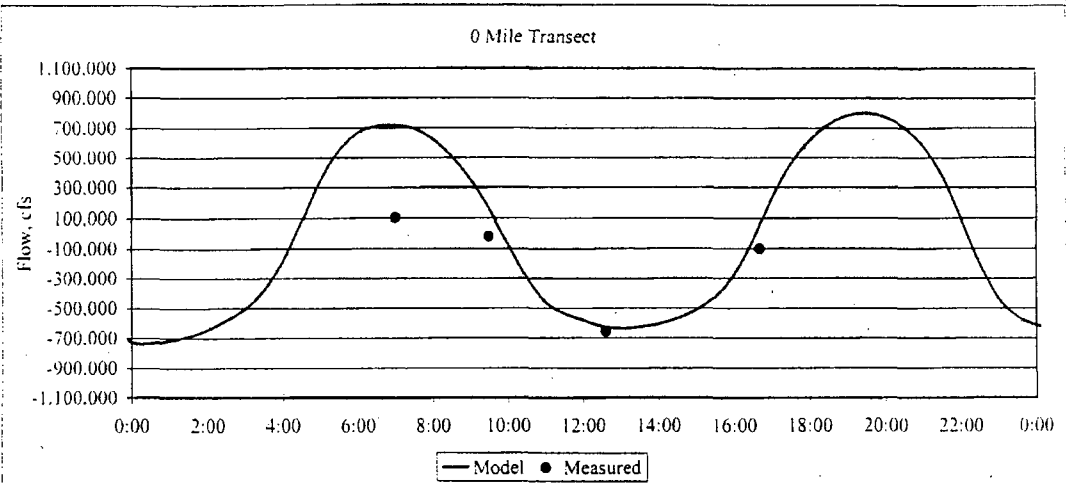
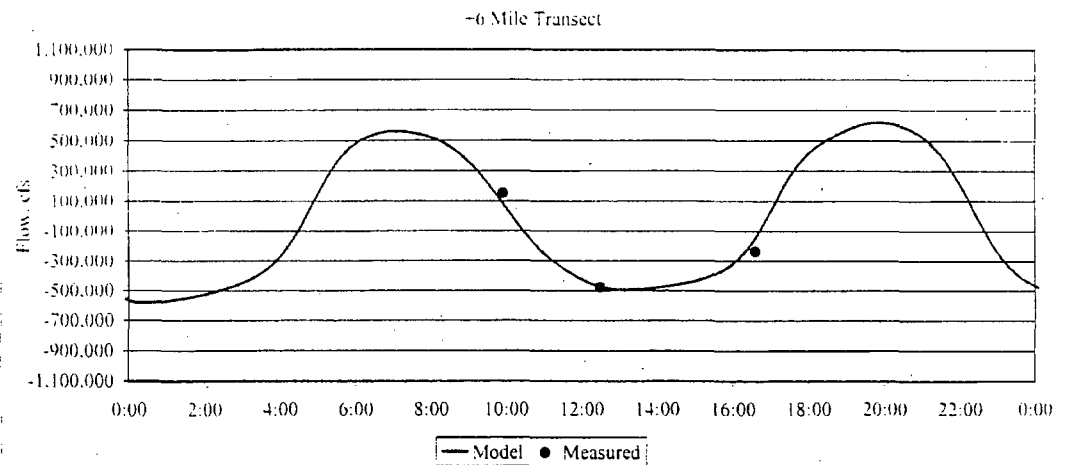


Measured — Modeled

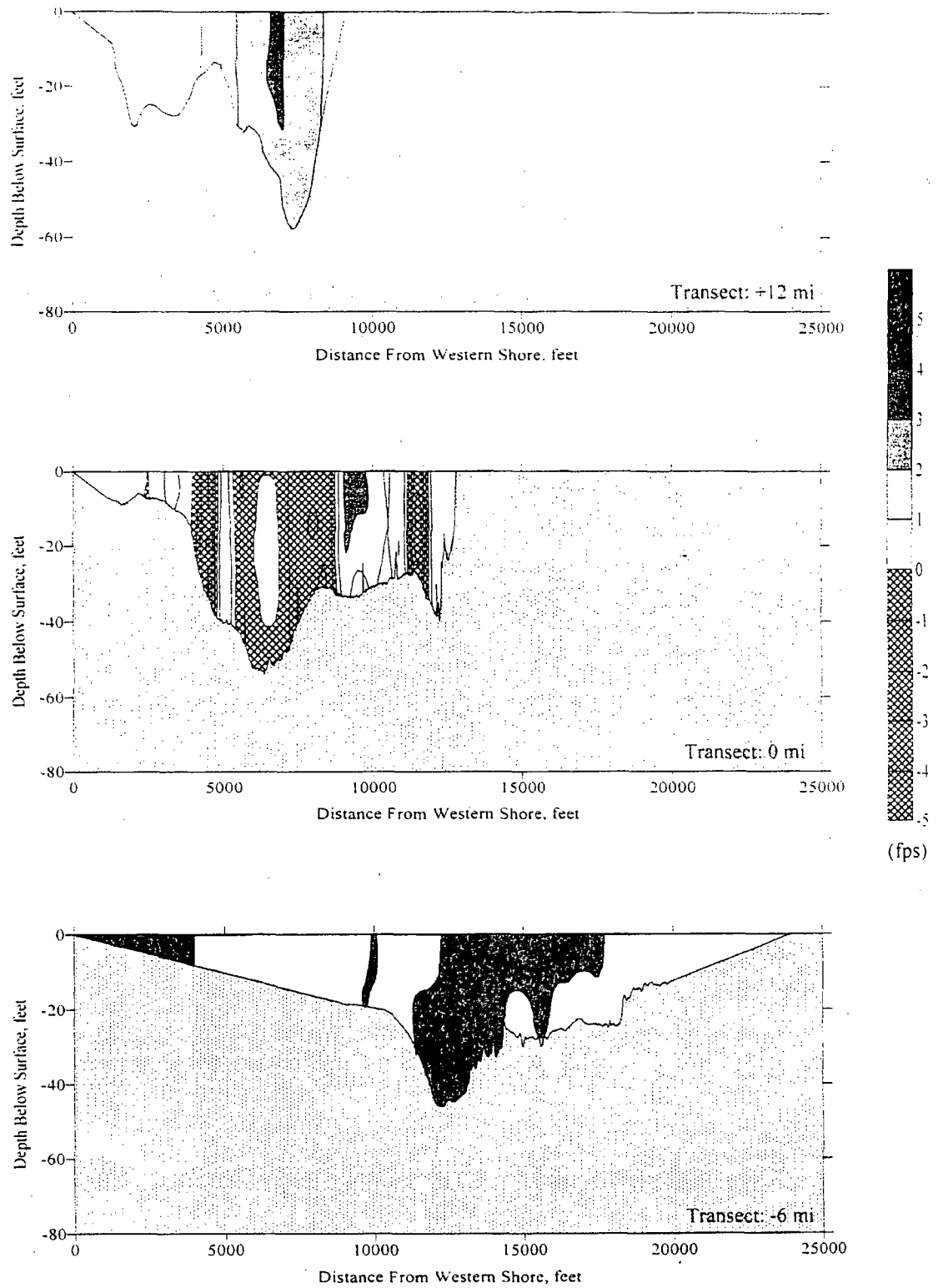
E-2 Figure III-80b. Comparison of measured and modeled tides at the west side of the Bay mouth (Lewes, DE) and the western end of the C&D Canal for 28 October 1997.



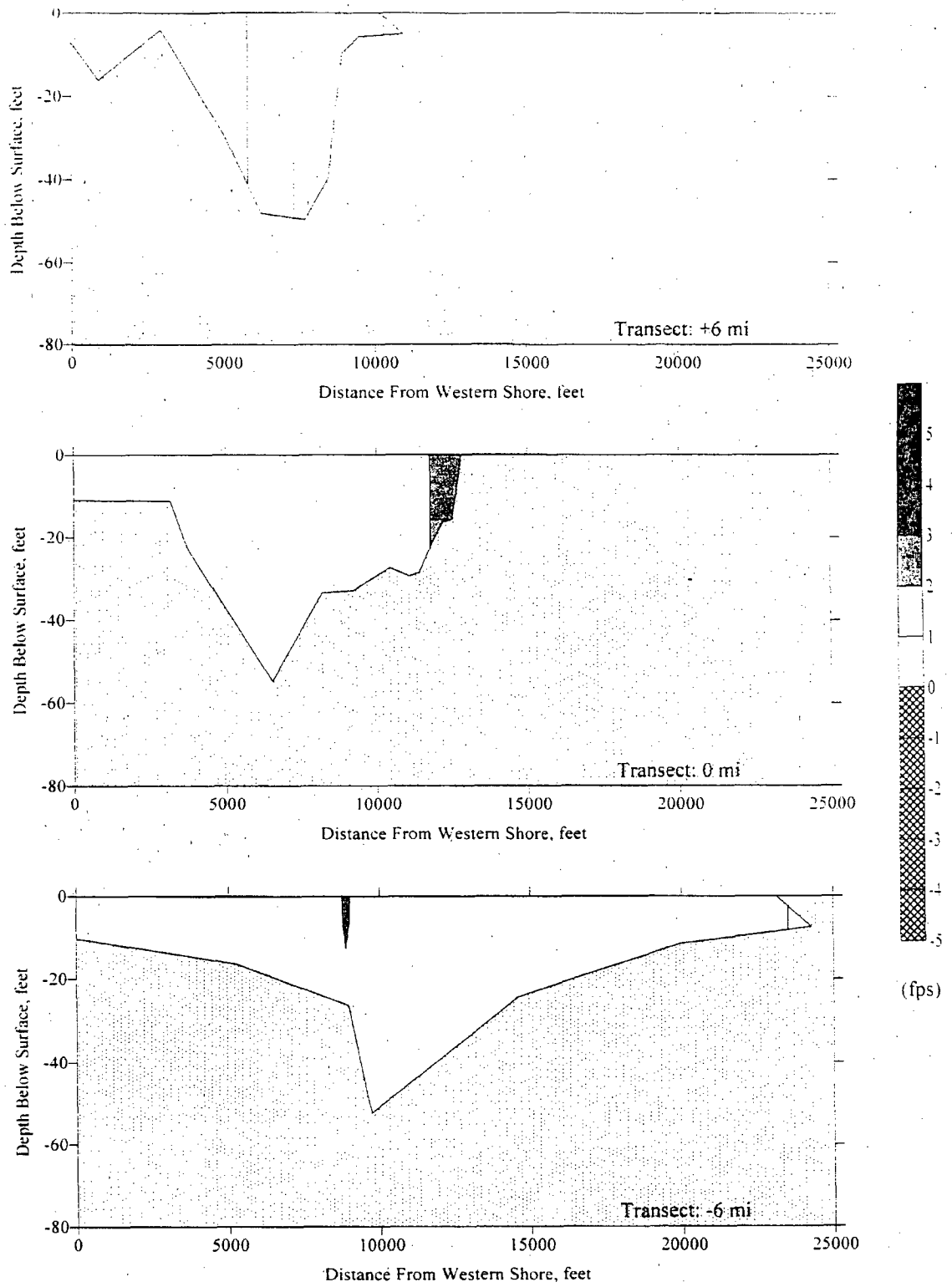
E-2 Figure III-81. Variation in tide range and tidal delay along the axis of the Estuary for the verification period (21-31 October 1997).



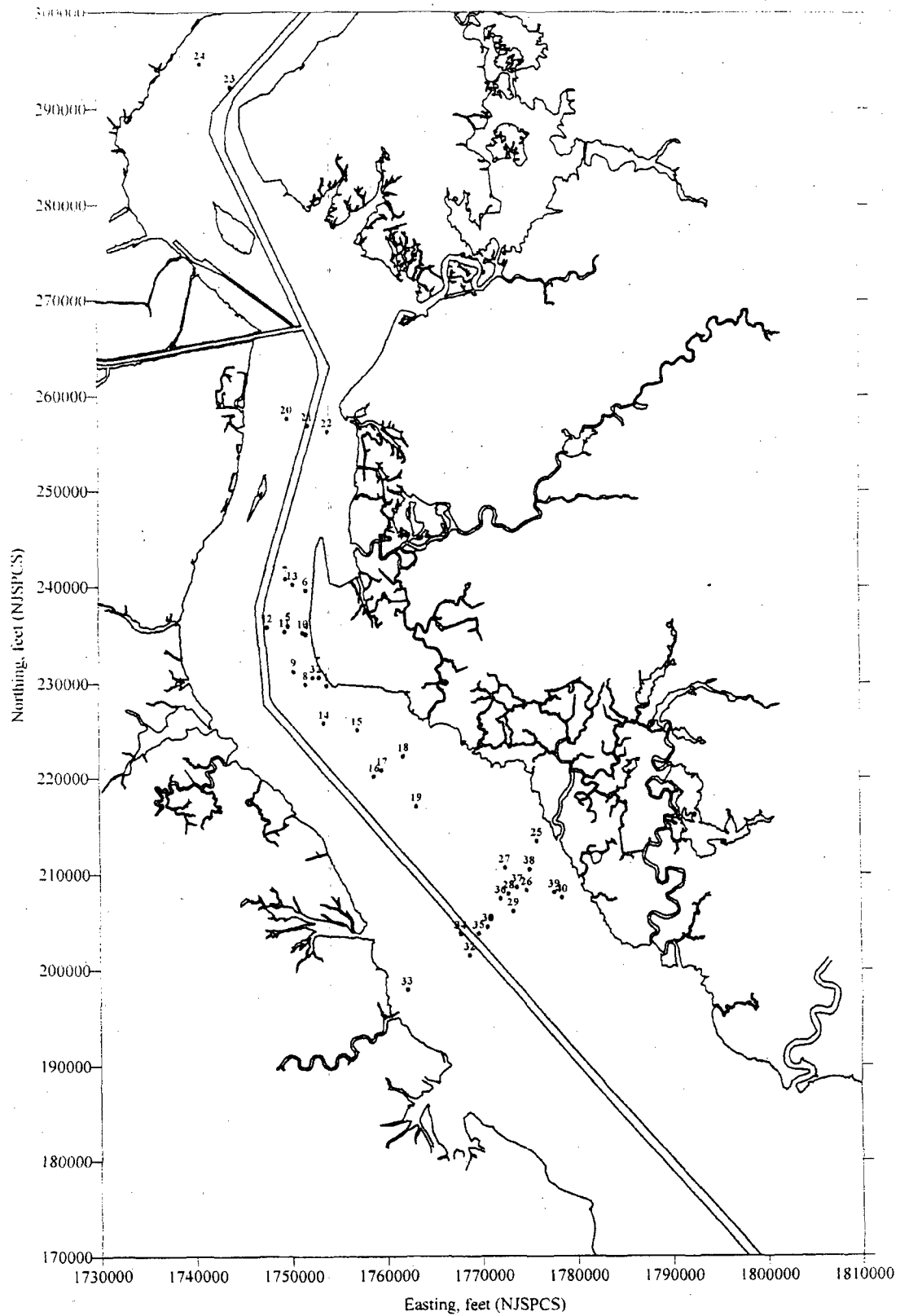
E-2 Figure III-82. Comparison of measured and modeled flow through three transects located 6 miles north of the Station, at the Station and 6 miles south of the Station for 28 October 1997.



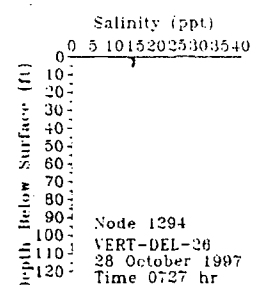
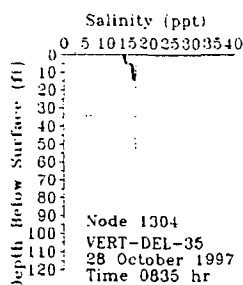
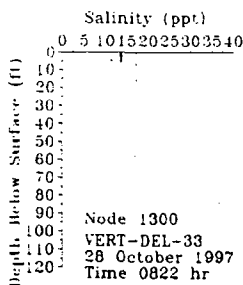
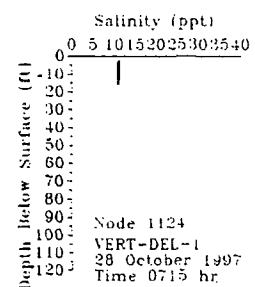
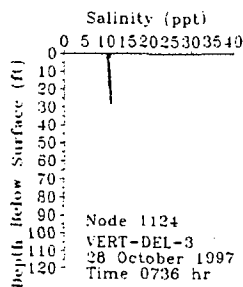
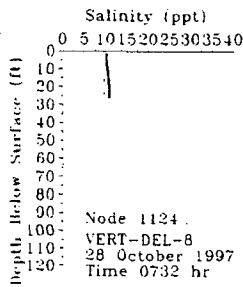
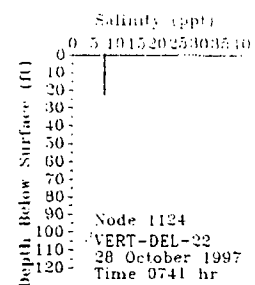
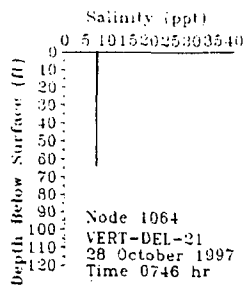
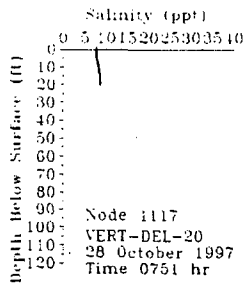
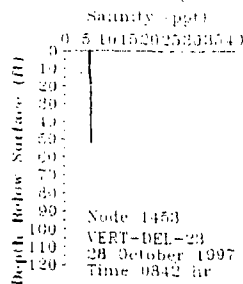
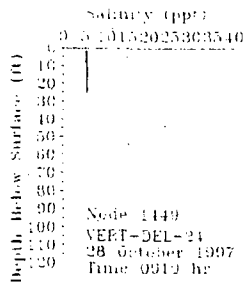
E-2 Figure III-83. Measured current speeds along three transects located 12 miles north of the Station, at the Station and 6 miles south of the Station for a flood phase on 28 October 1997.



E-2 Figure III-84. Modeled current speeds along three transects located 6 miles north of the Station, at the Station and 6 miles south of the Station for a flood phase on 28 October 1997.

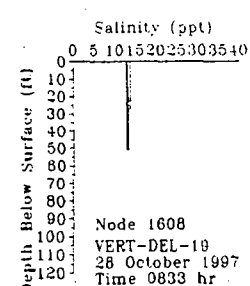
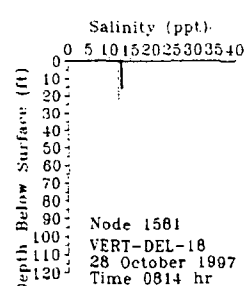
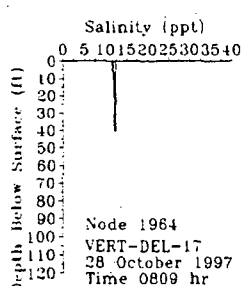
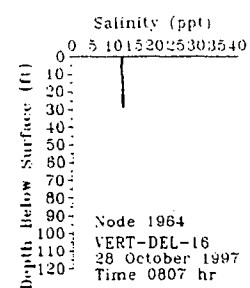
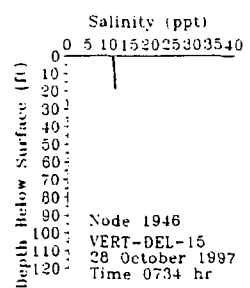
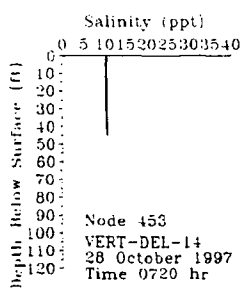
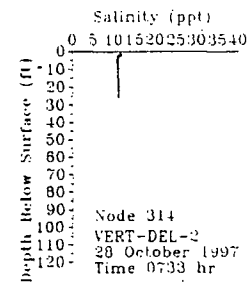
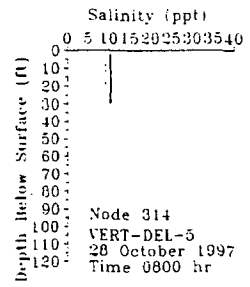
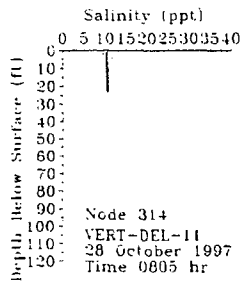
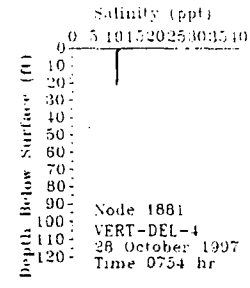
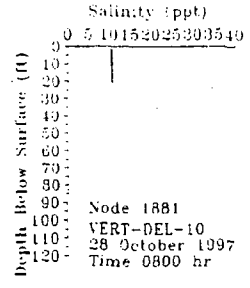
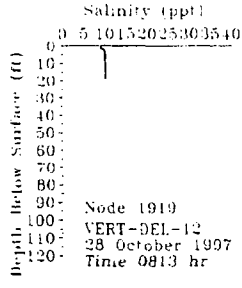
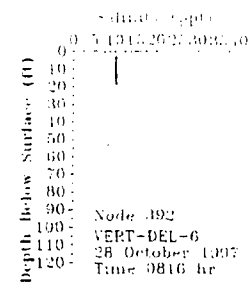
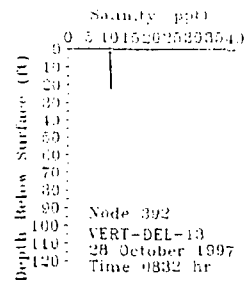
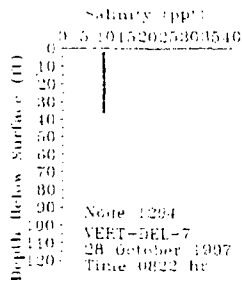


E-2 Figure III-85. Locations of shipboard vertical profiles measured during a flood phase on 28 October 1997.



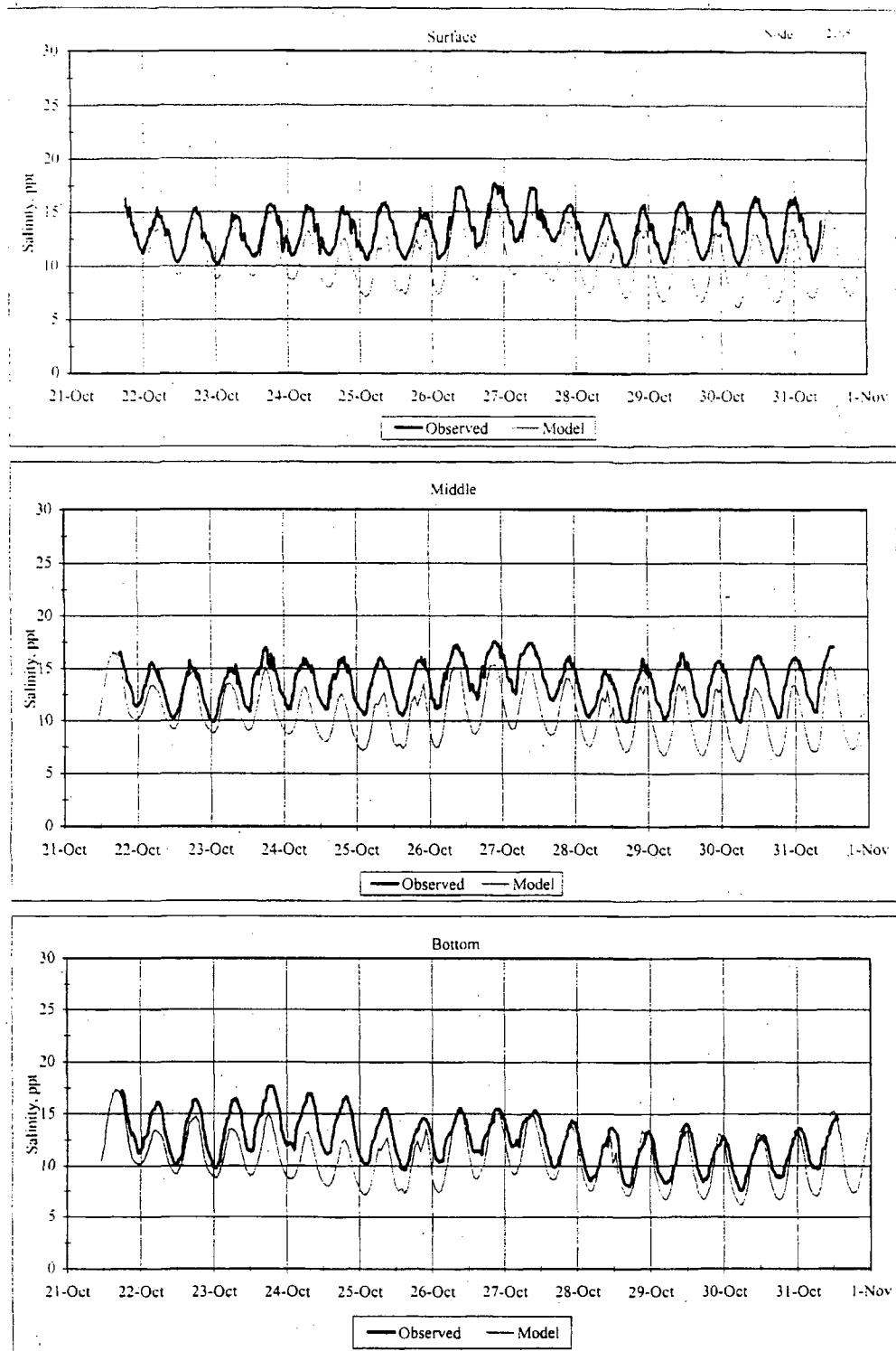
Observed=***** Model=_____

E-2 Figure III-86. Comparison of modeled and measured salinities at locations of shipboard verticals near the limits of the sampling region during a flood phase on 28 October 1997.

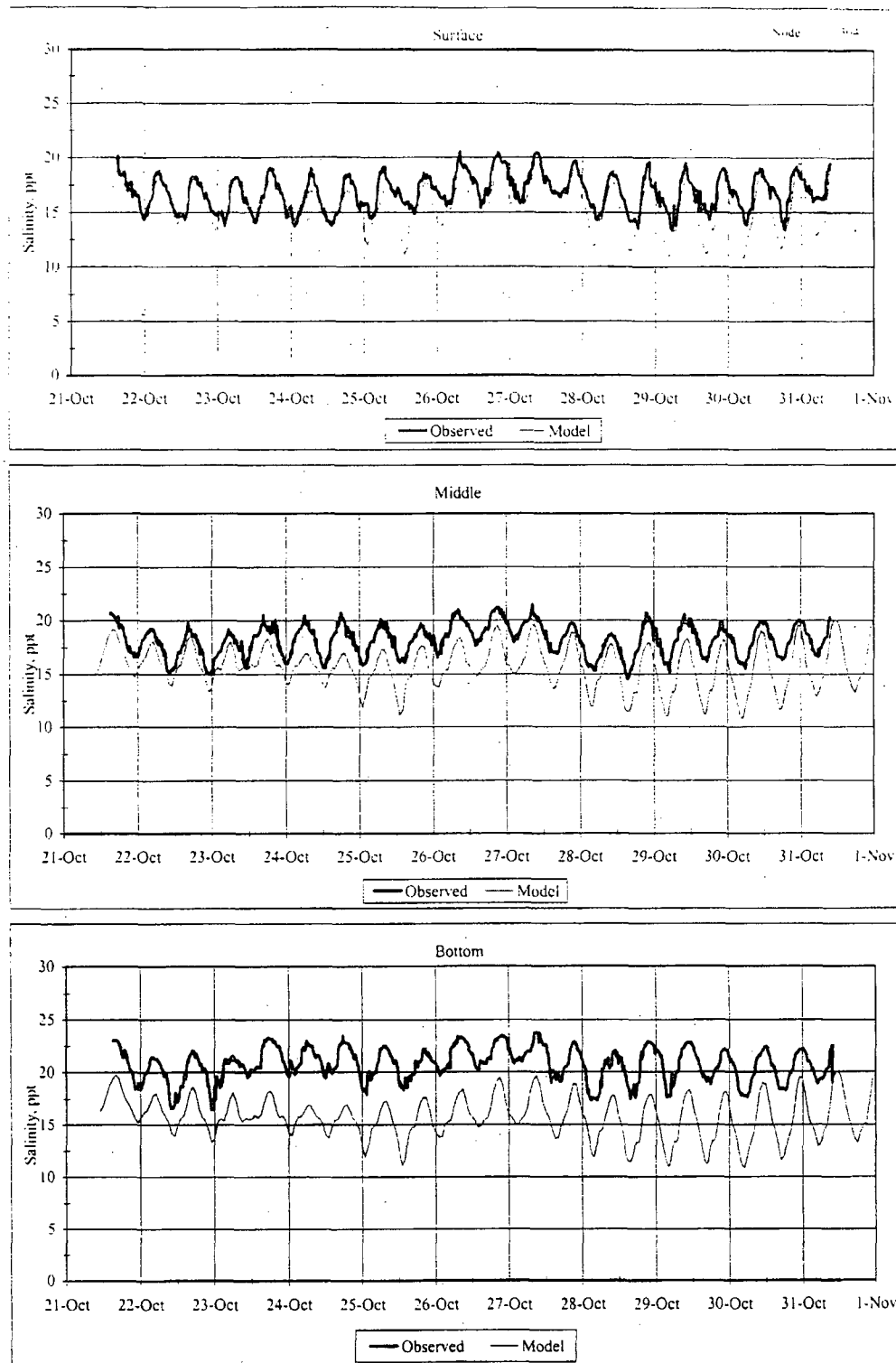


Observed=***** Model=_____

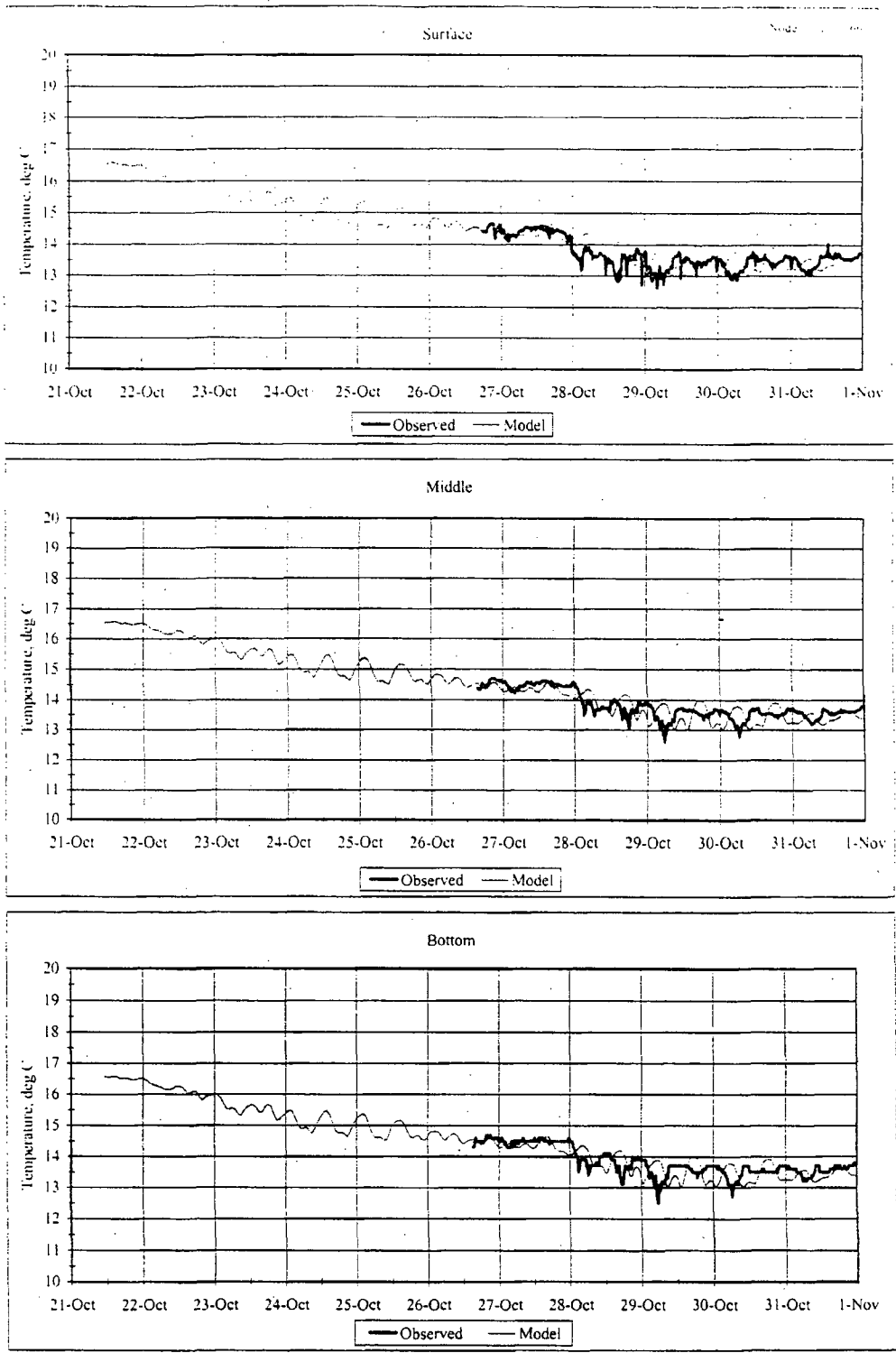
E-2 Figure III-87. Comparison of modeled and measured salinities at locations of shipboard verticals in the vicinity of the Station during a flood phase on 28 October 1997.



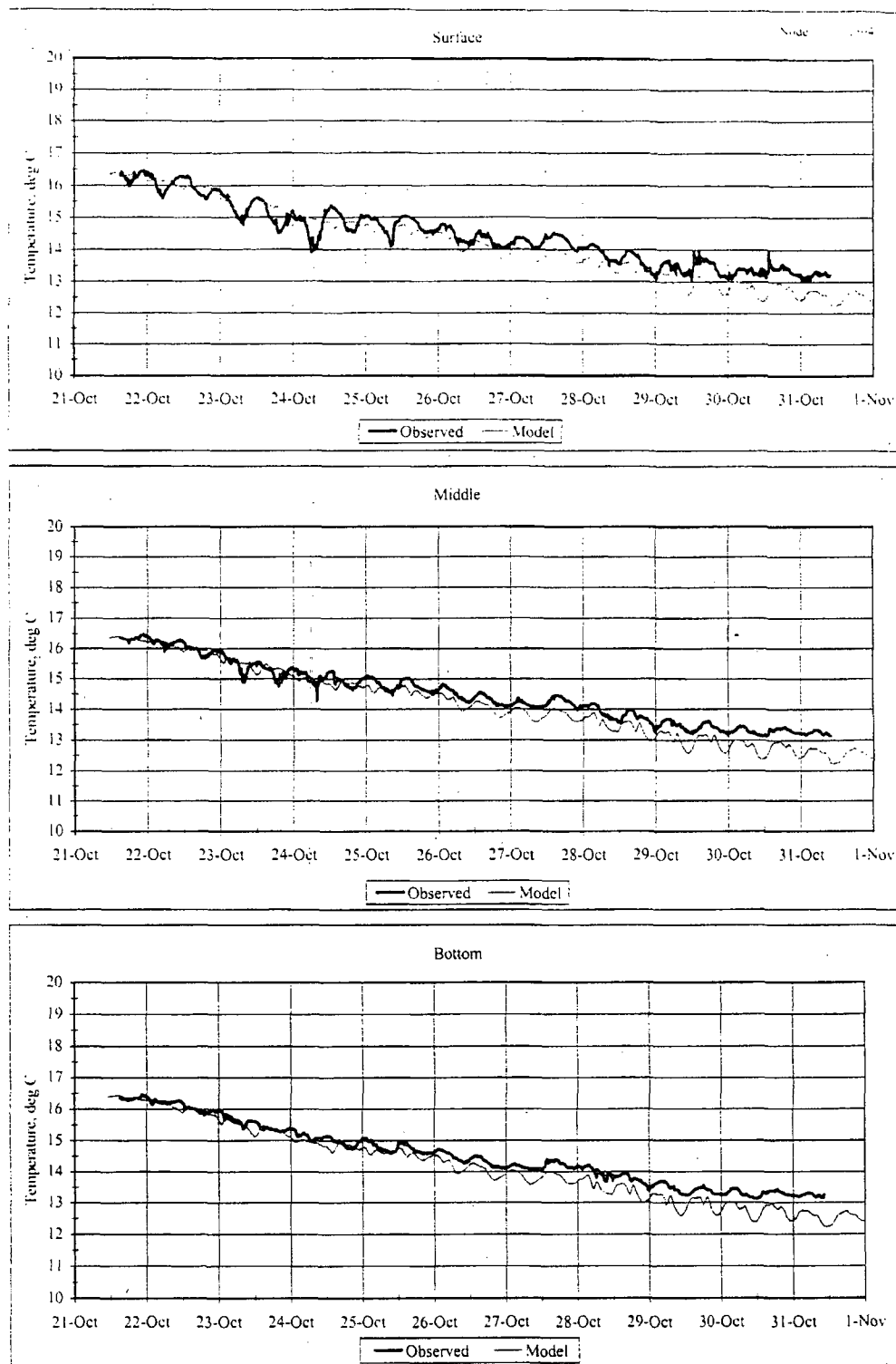
E-2 Figure III-88a. Comparison of modeled and measured salinity at Mooring 5, which is located offshore of the Station near the shipping channel, for the verification period (21-31 October 1997).



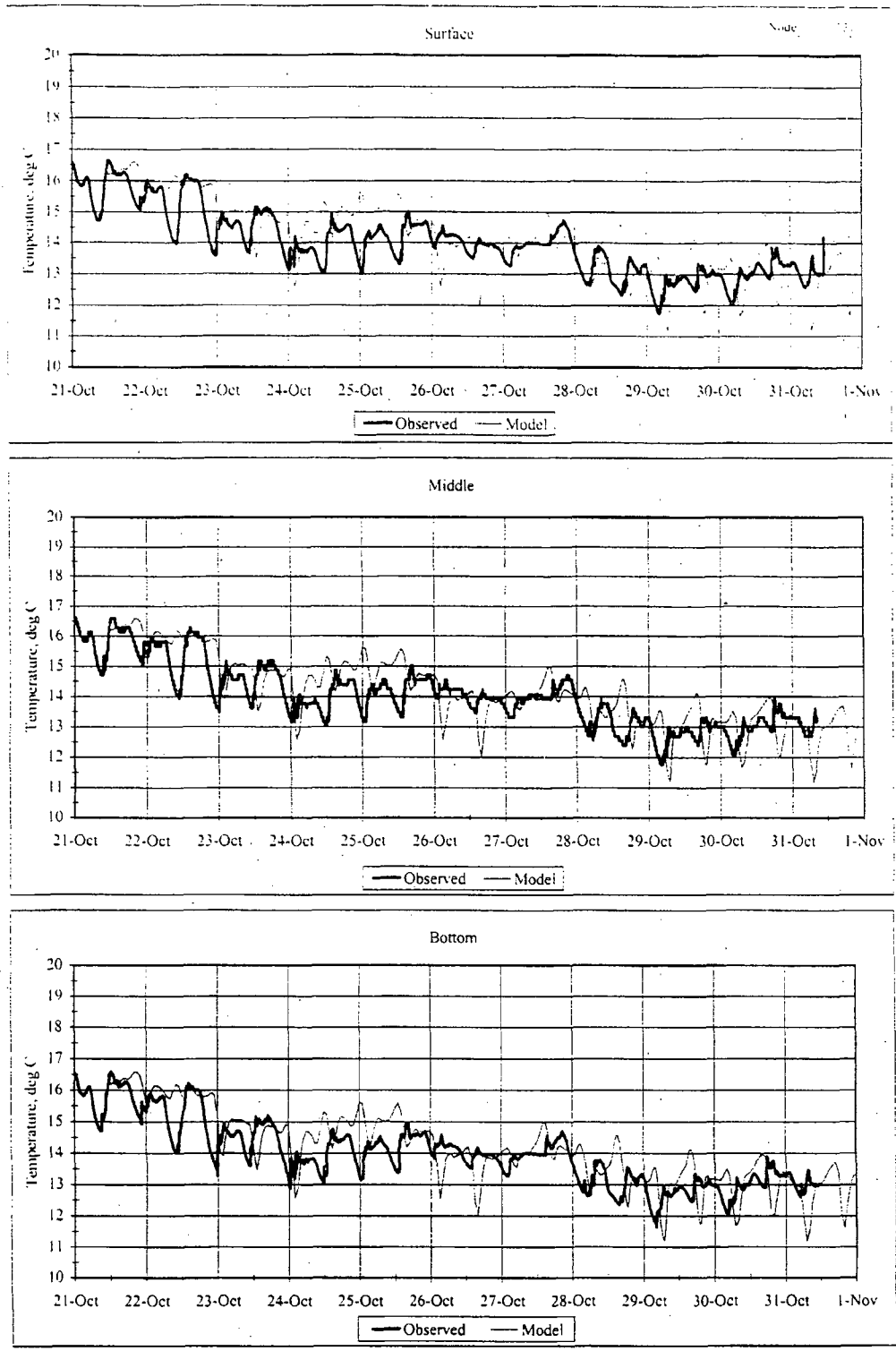
E-2 Figure III-88b. Comparison of modeled and measured salinity at Mooring 9, which is located 6 miles south of the Station near the shipping channel, for the verification period (21-31 October 1997).



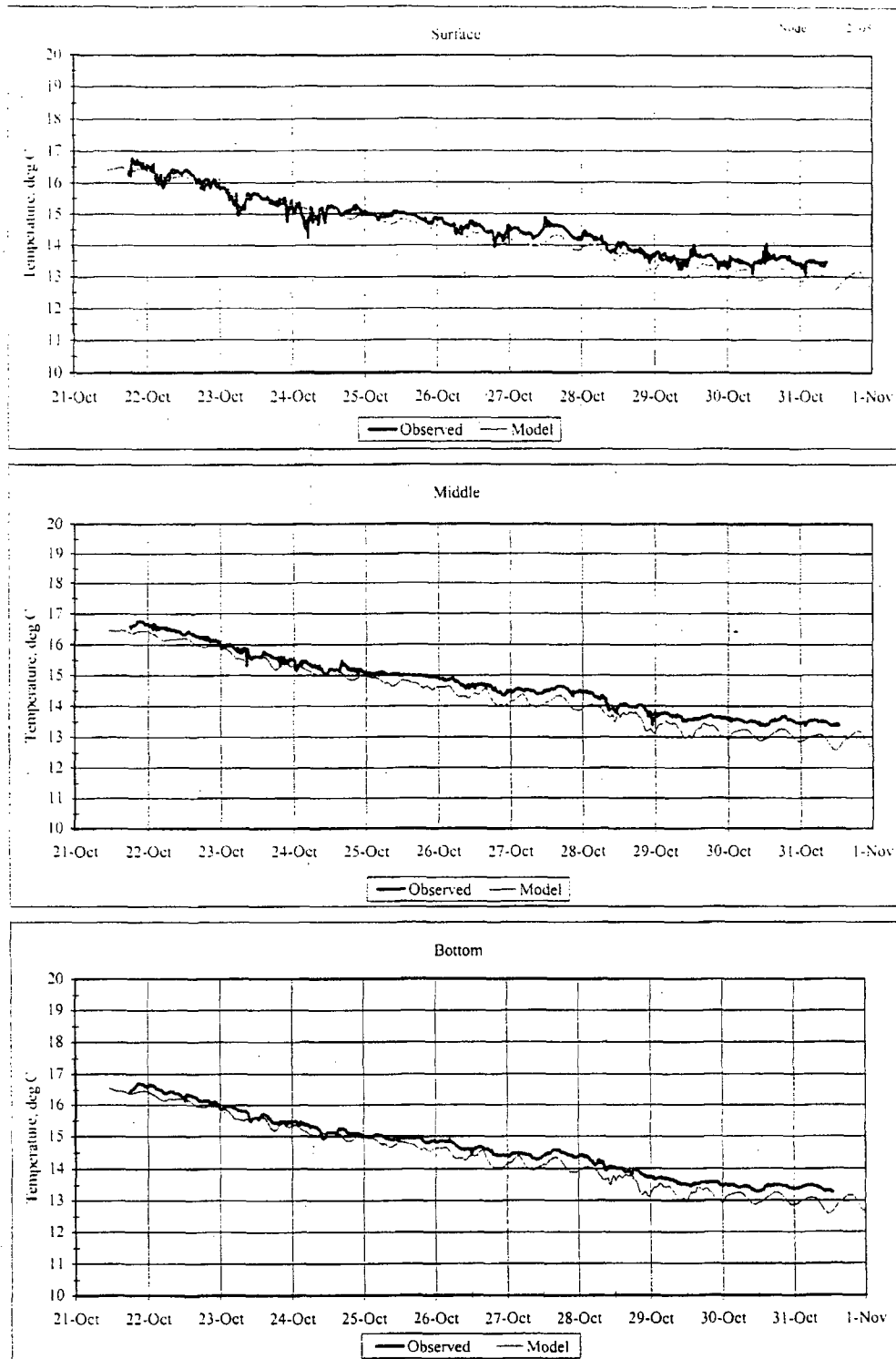
E-2 Figure III-88c. Comparison of modeled and measured temperature at Mooring 2, which is located 6 miles north of the Station near the shipping channel, for the verification period (21-31 October 1997).



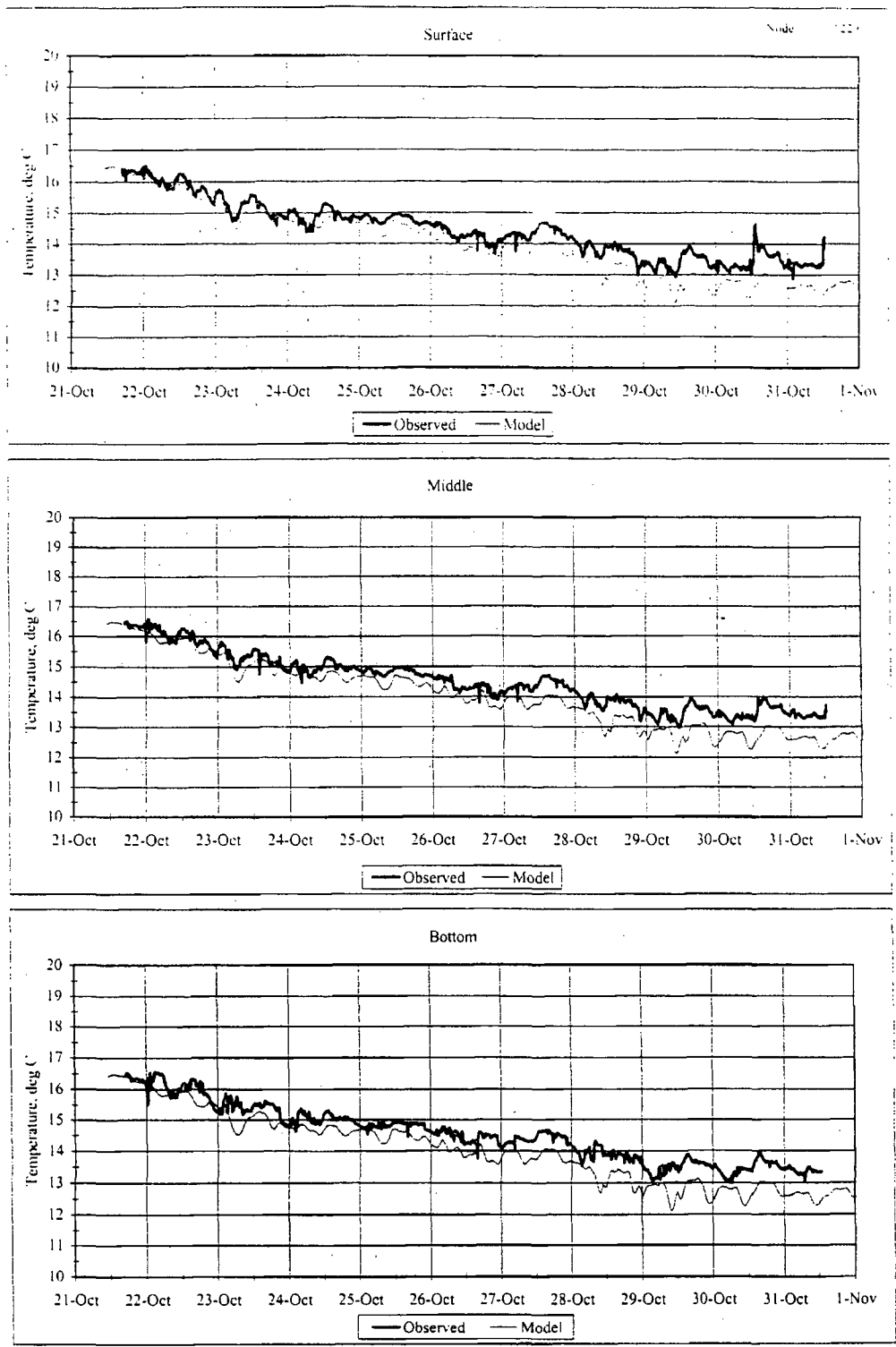
E-2 Figure III-88d. Comparison of modeled and measured temperature at Mooring 9, which is located 6 miles south of the Station near the shipping channel, for the verification period (21-31 October 1997).



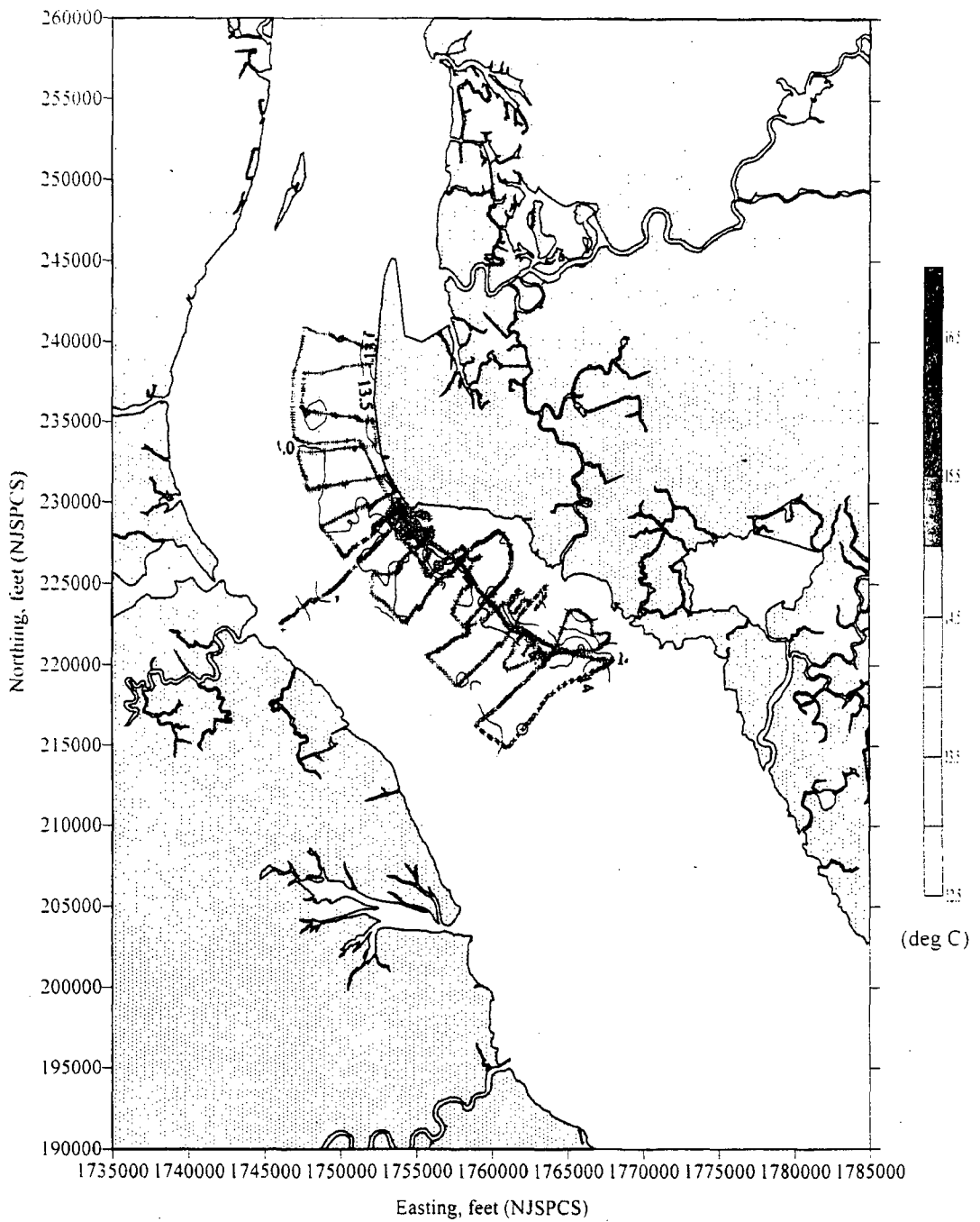
E-2 Figure III-88e. Comparison of modeled and measured temperature at the Hope Creek mooring for the verification period (21-31 October 1997).



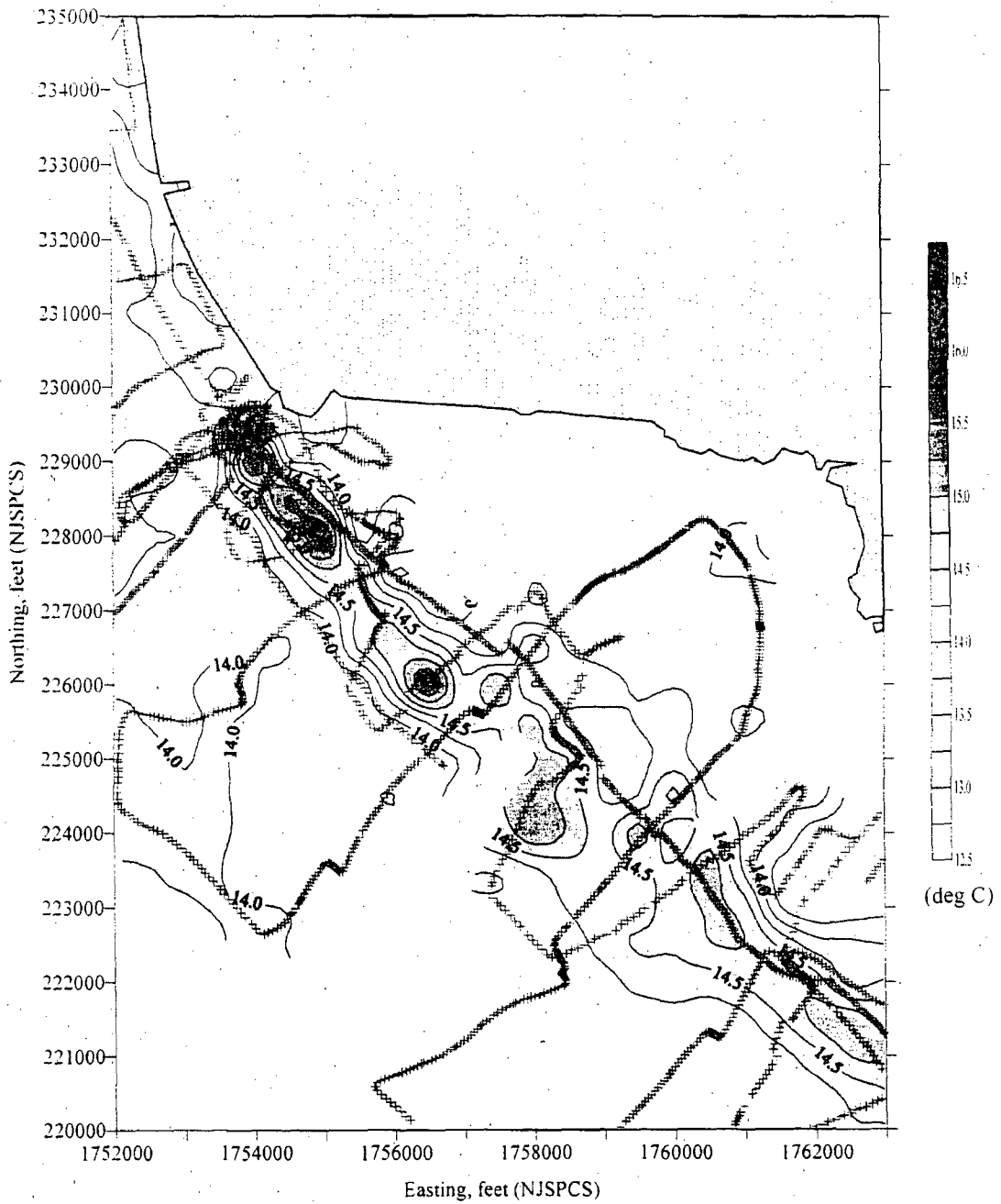
E-2 Figure III-88f. Comparison of modeled and measured temperature at Mooring 5, which is located offshore of the Station near the shipping channel, for the verification period (21-31 October 1997).



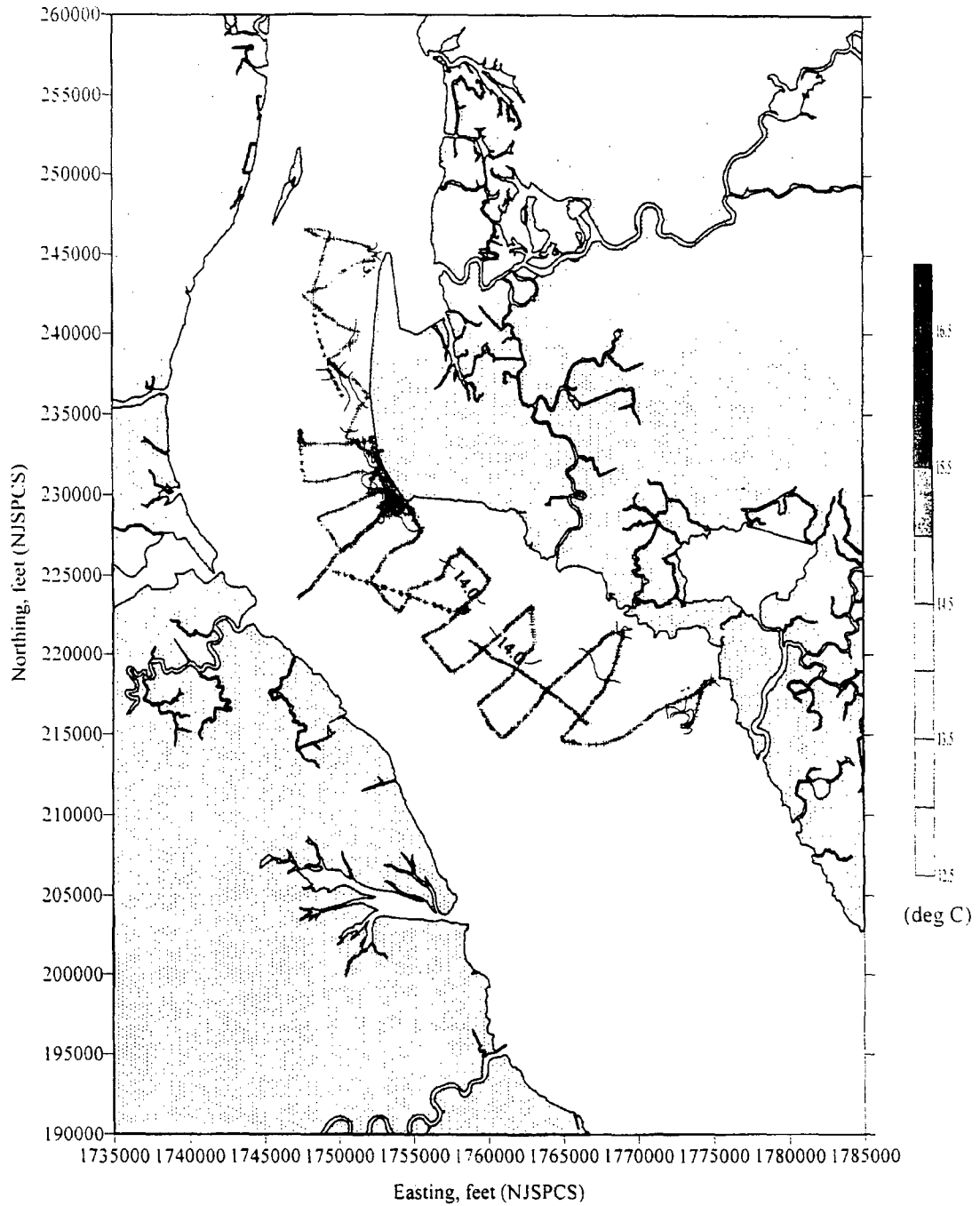
E-2 Figure III-88g. Comparison of modeled and measured temperature at Mooring 6, which is located near the Station on the western side of the shipping channel, for the verification period (21-31 October 1997).



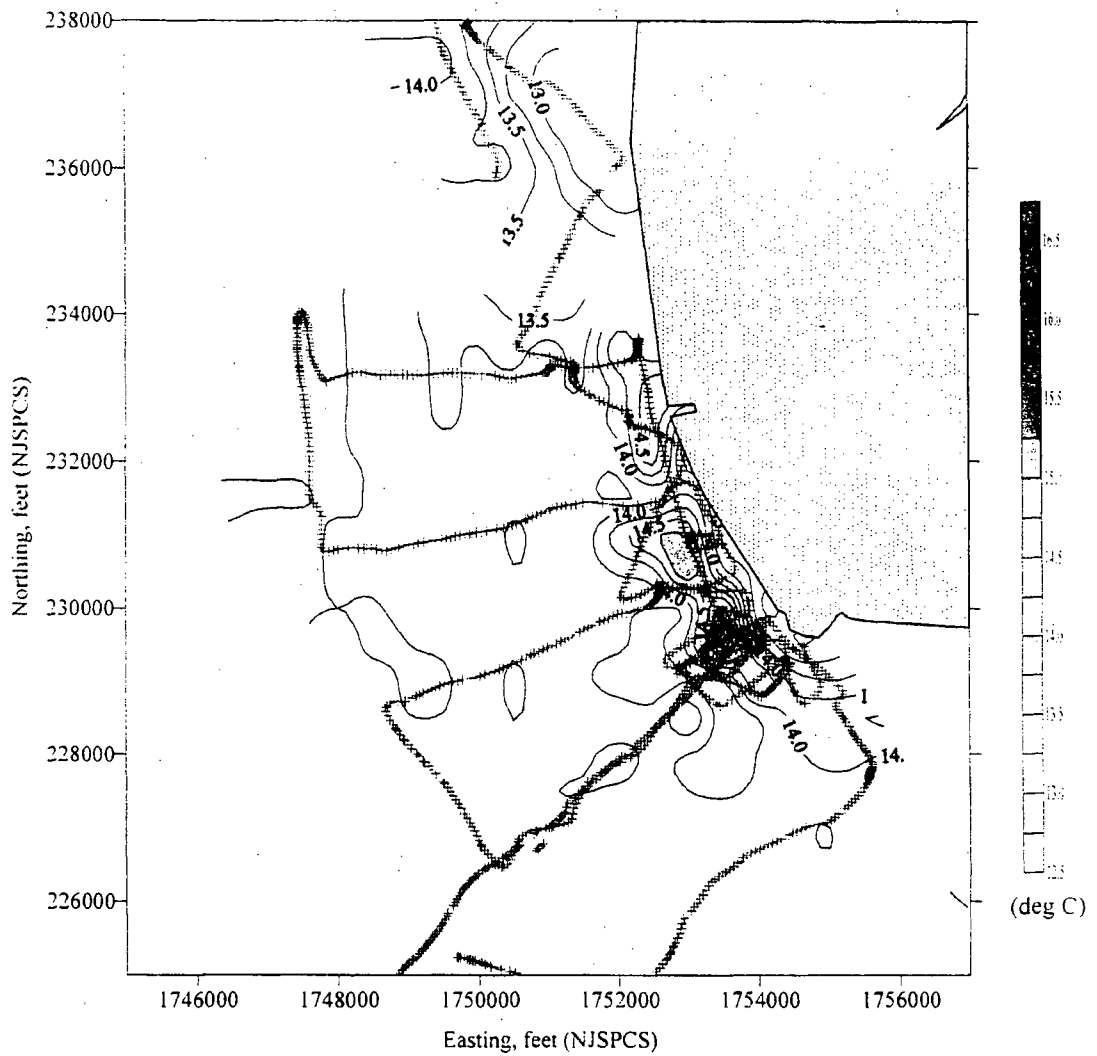
E-2 Figure III-89a. Contours of measured surface temperatures with boat trackings for an ebb phase on 28 October 1997.



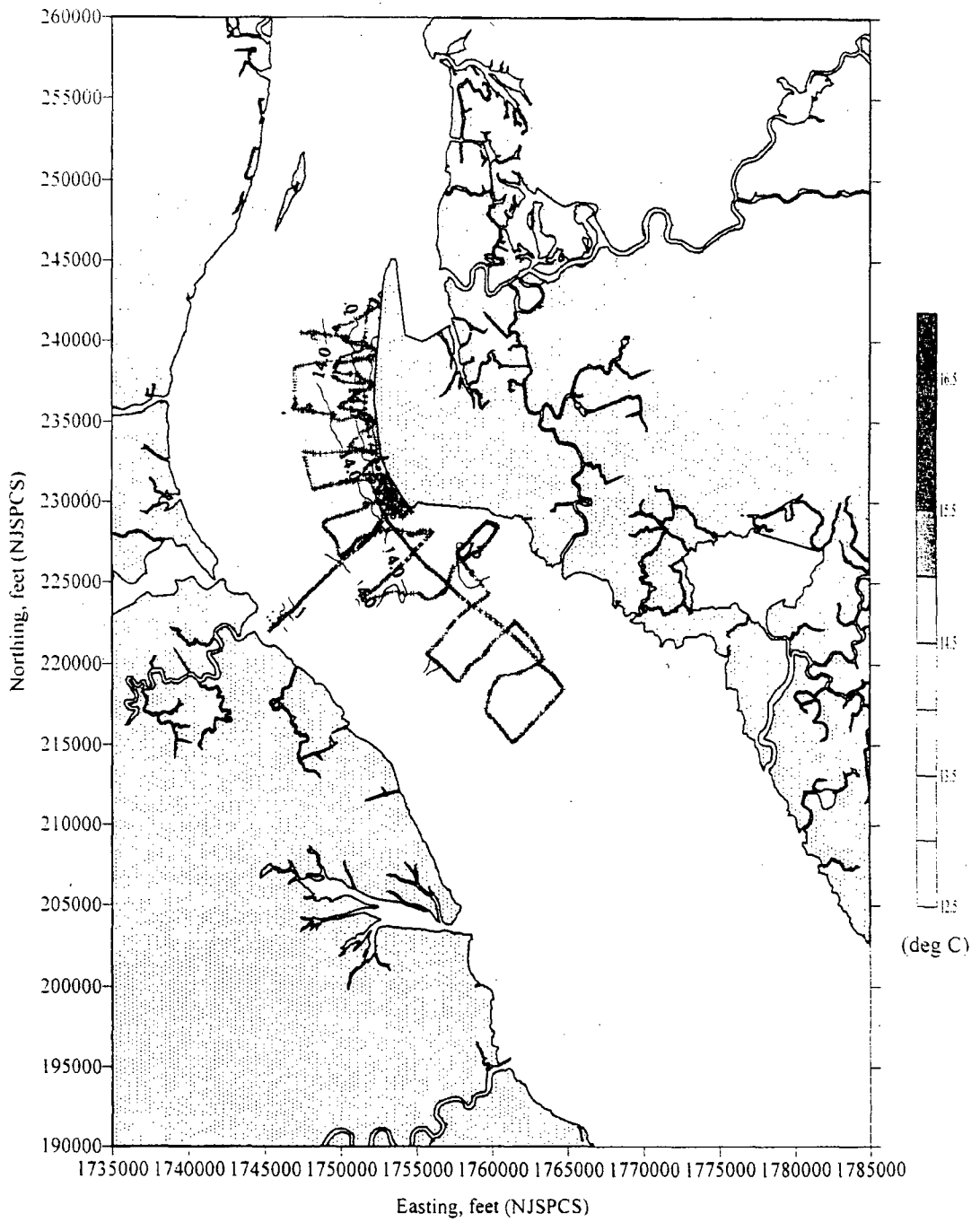
E-2 Figure III-89b. Contours of measured surface temperatures with boat trackings for an ebb phase on 28 October 1997 (close-up view).



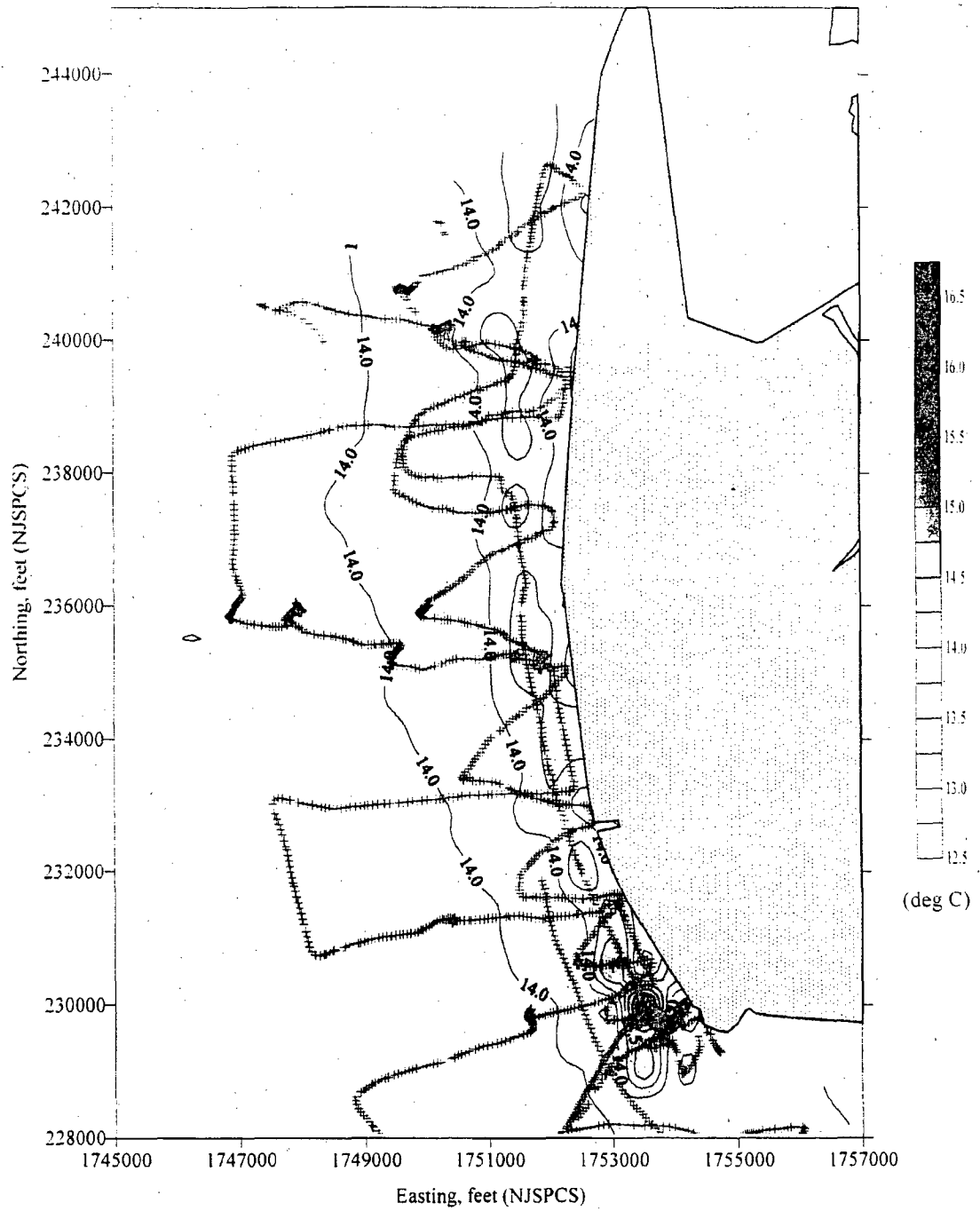
E-2 Figure III-90a. Contours of measured surface temperatures with boat trackings for a slack phase (end-of-ebb) on 28 October 1997.



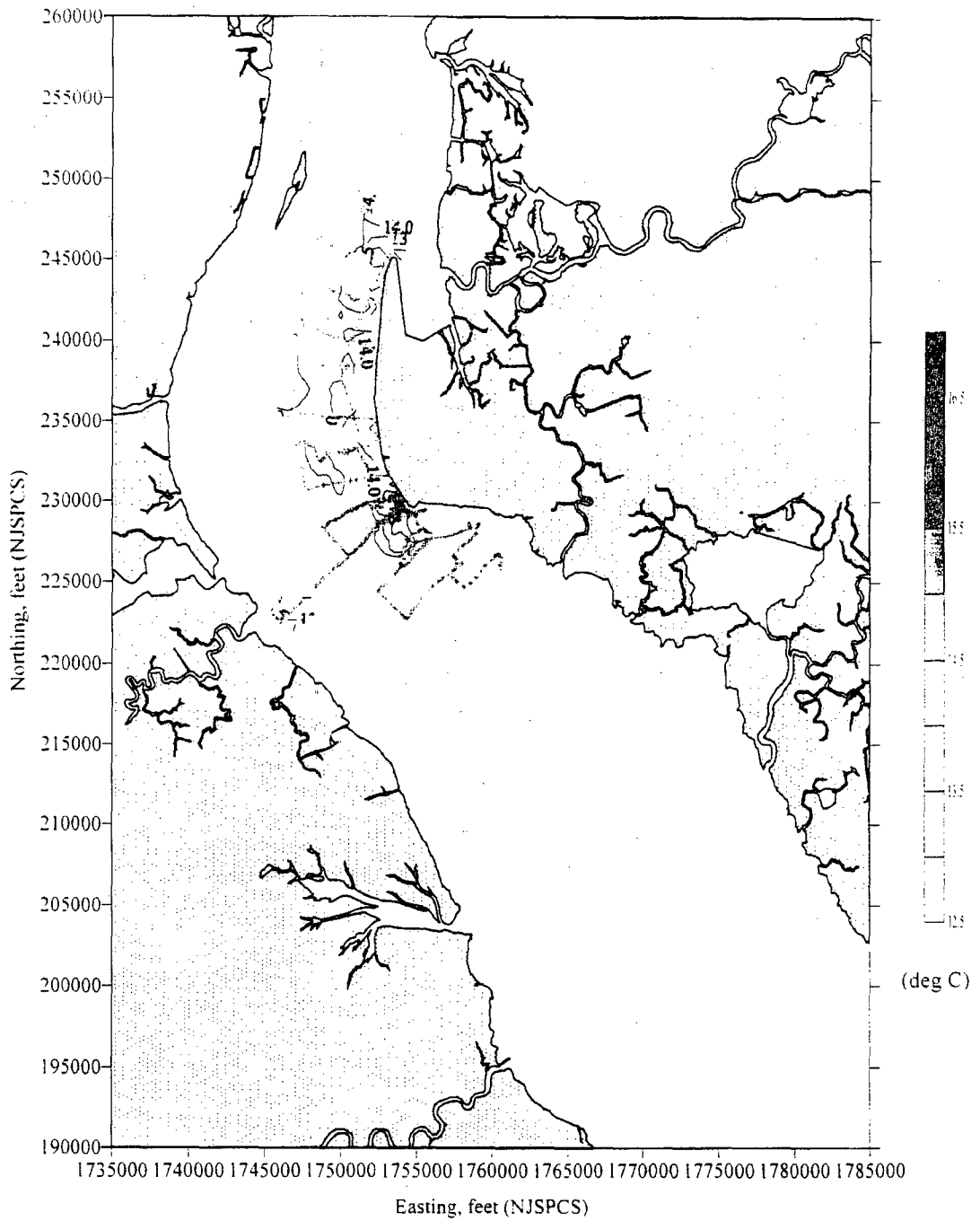
E-2 Figure III-90b. Contours of measured surface temperatures with boat trackings for a slack phase (end-of-ebb) on 28 October 1997 (close-up view).



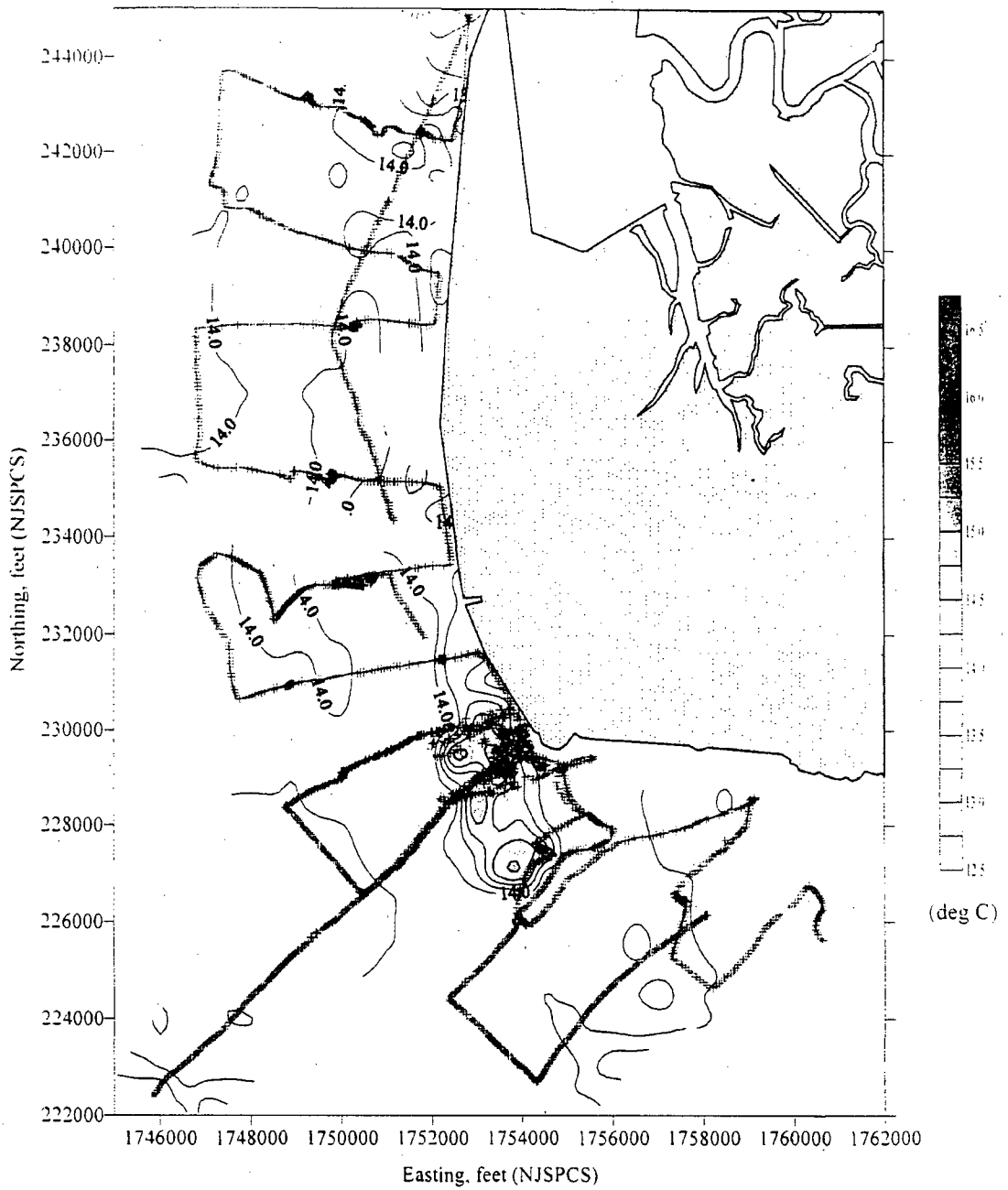
E-2 Figure III-91a. Contours of measured surface temperatures with boat trackings for a flood phase on 28 October 1997.



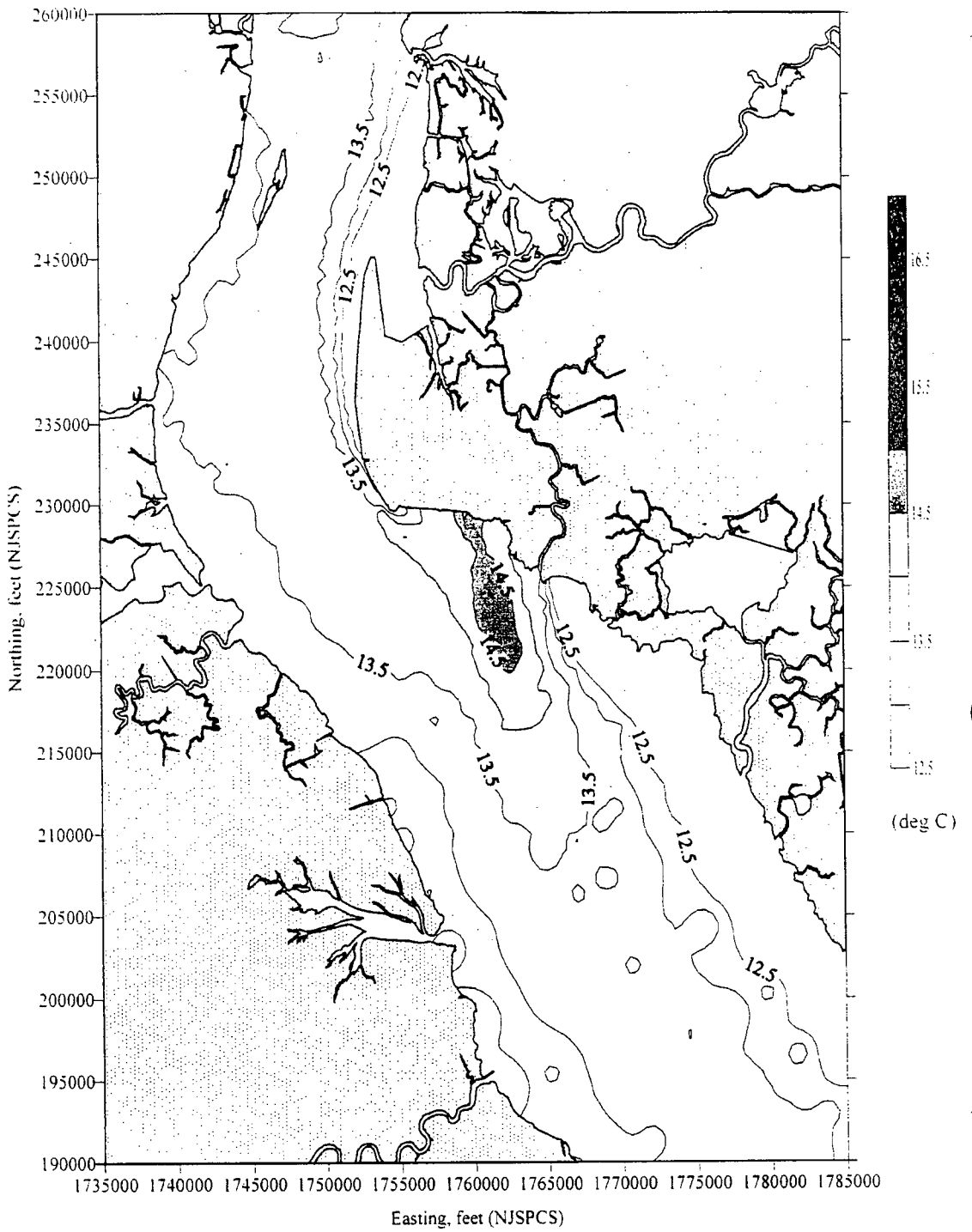
E-2 Figure III-91b. Contours of measured surface temperatures with boat trackings for a flood phase on 28 October 1997 (close-up view).



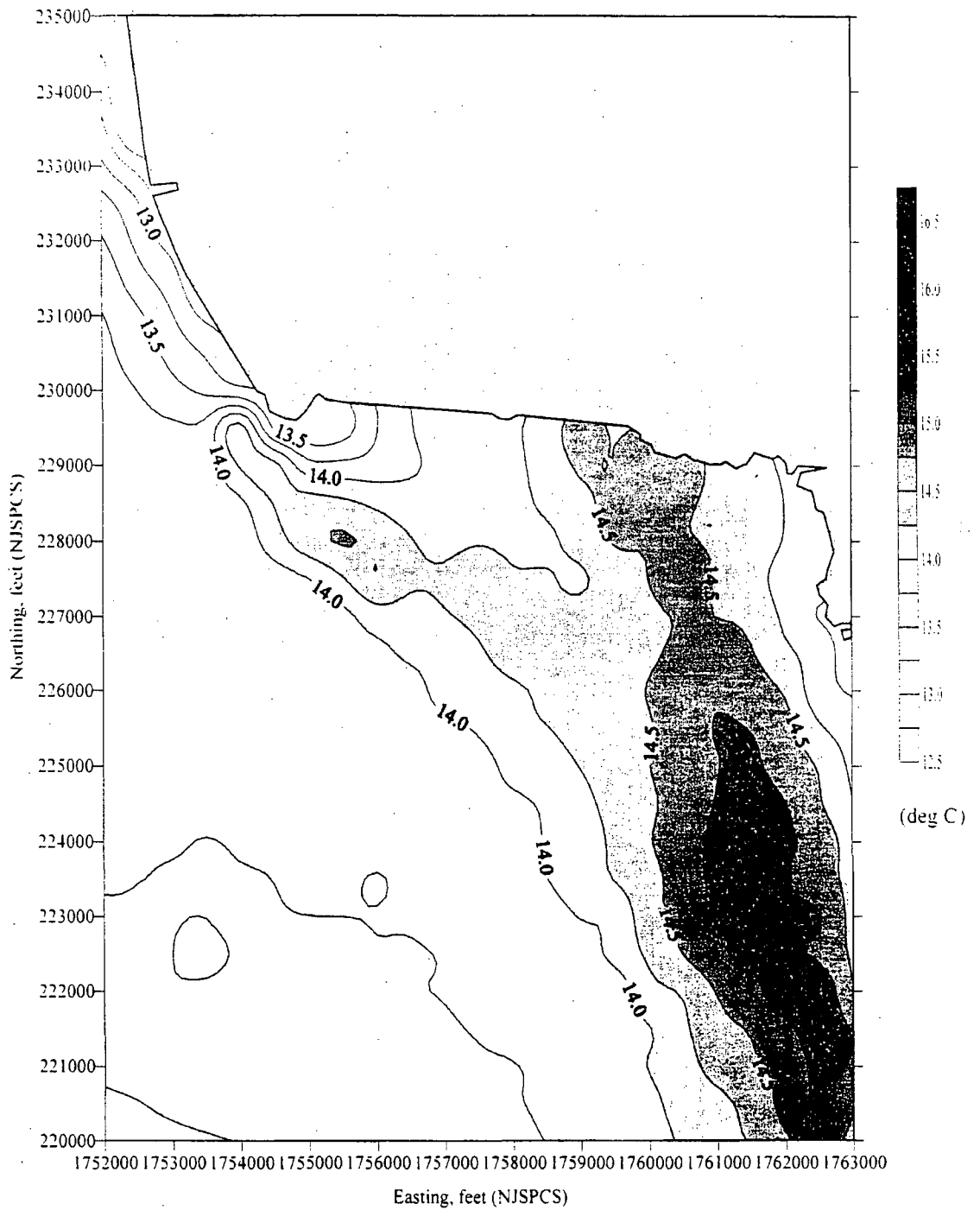
E-2 Figure III-92a. Contours of measured surface temperatures with boat trackings for a slack phase (end-of-flood) on 28 October 1997.



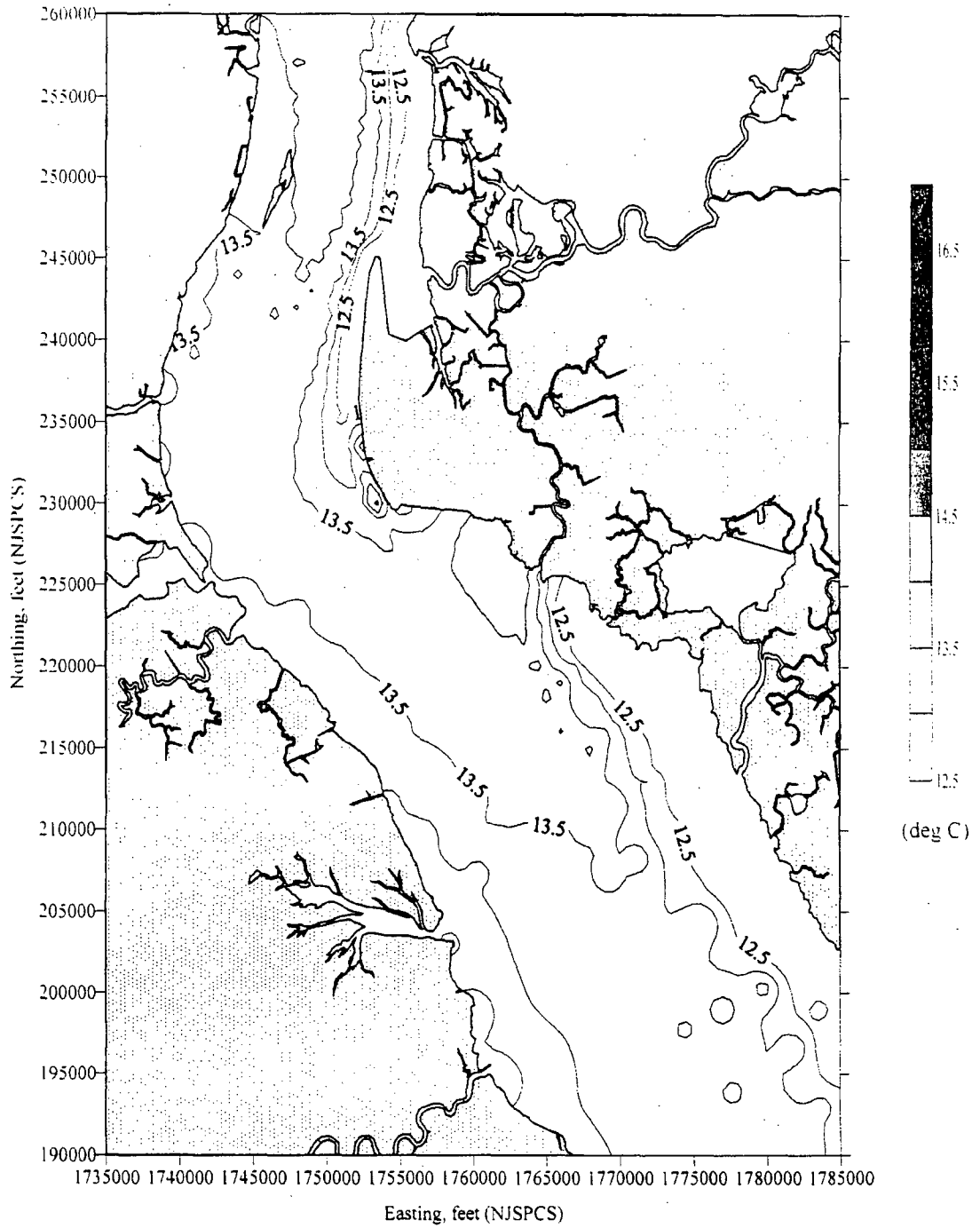
E-2 Figure III-92b. Contours of measured surface temperatures with boat trackings for a slack phase (end of flood) on 28 October 1997 (close-up view).



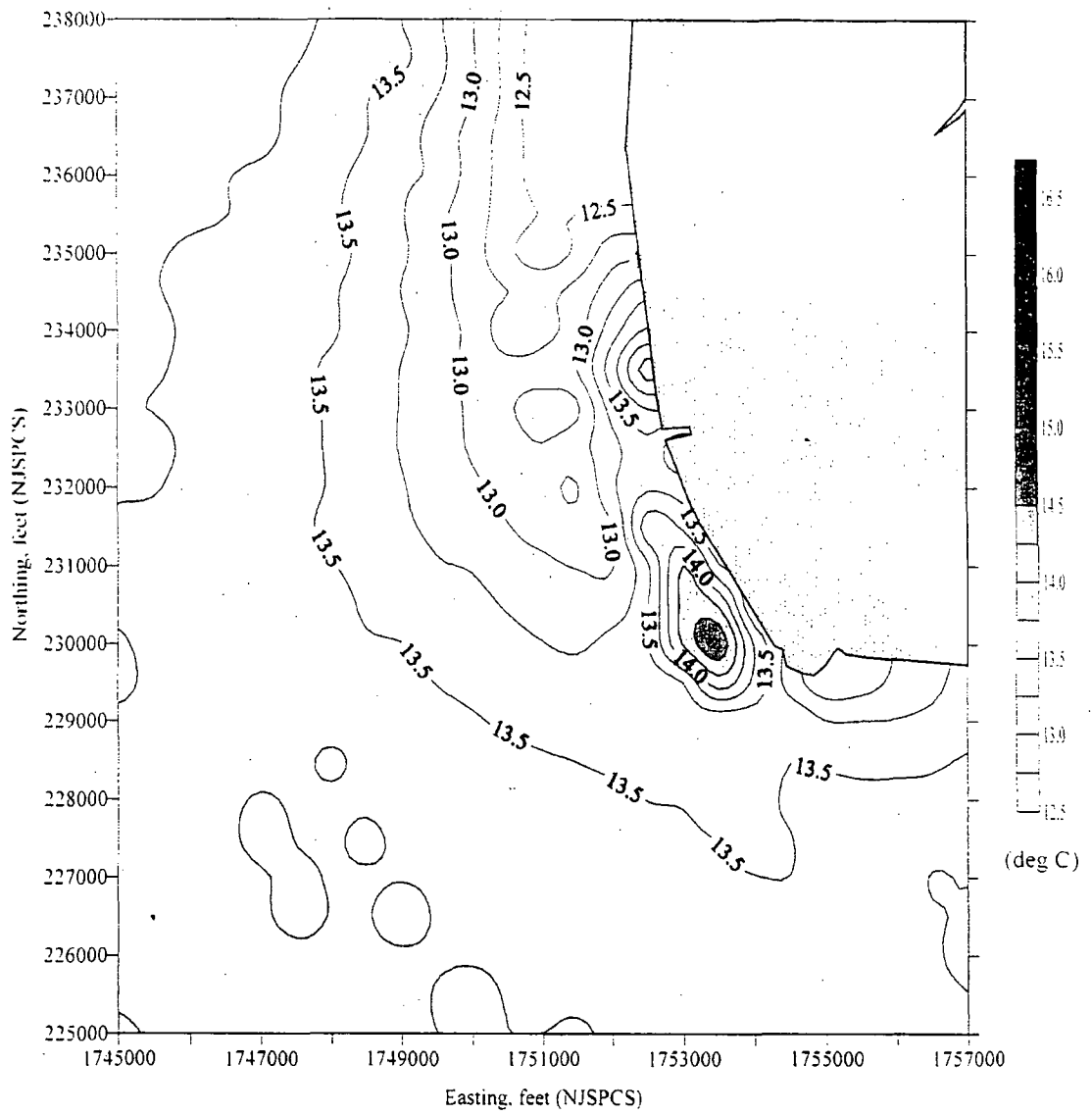
E-2 Figure III-93a. Contours of modeled surface temperatures for an ebb phase on 28 October 1997.



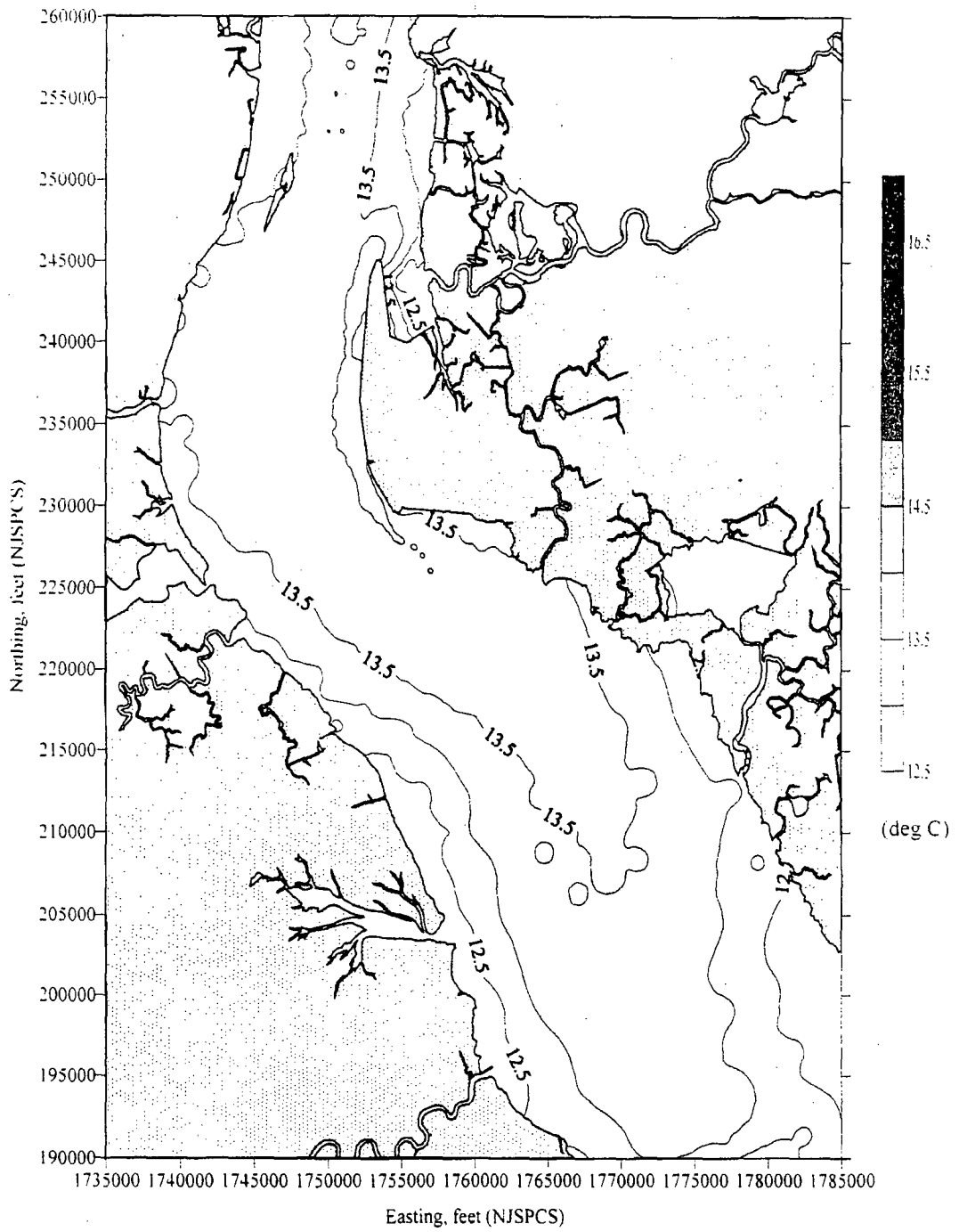
E-2 Figure III-93b. Contours of modeled surface temperatures for an ebb phase on 28 October 1997 (close-up view).



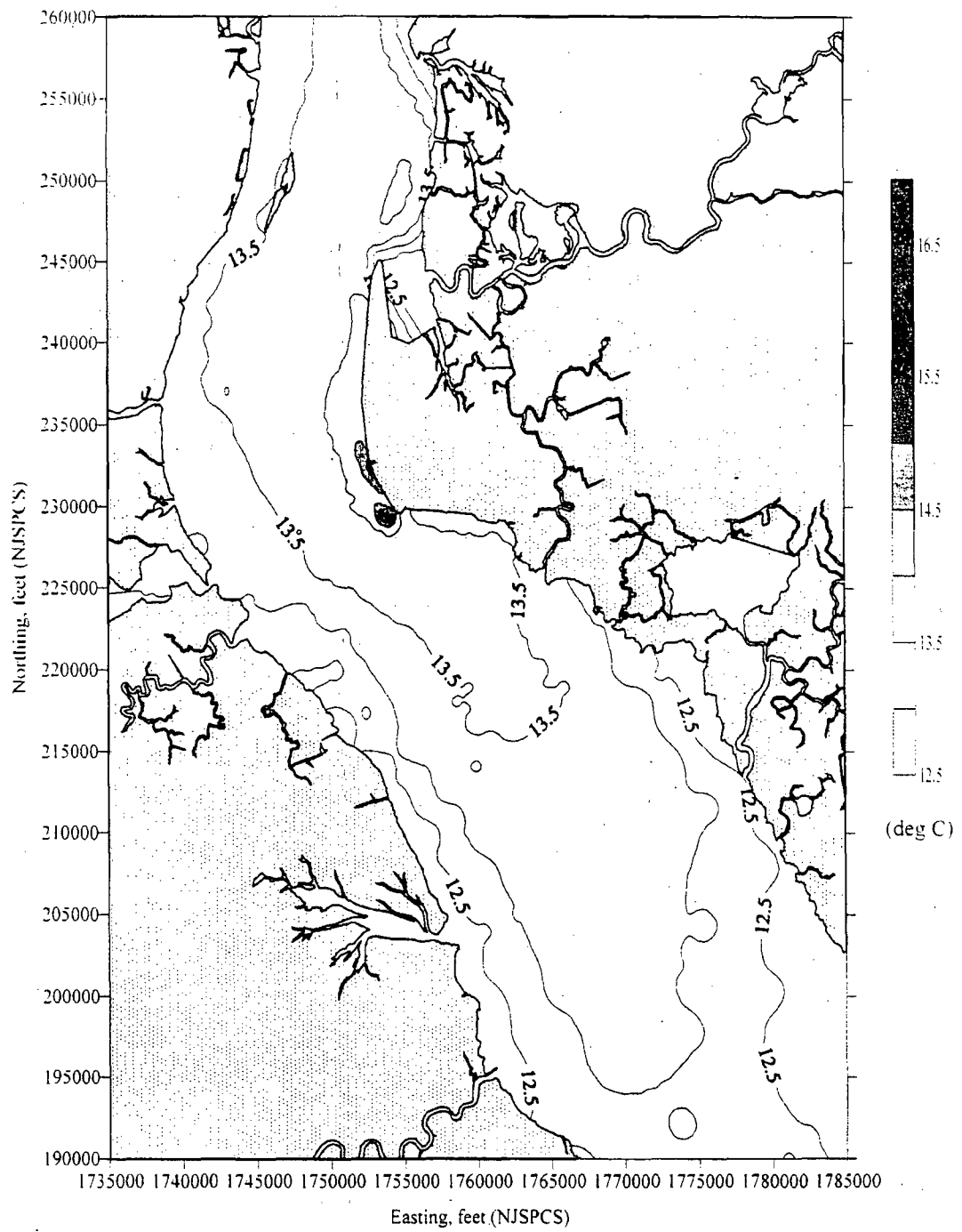
E-2 Figure III-94a. Contours of modeled surface temperatures for a slack phase (end-of-ebb) on 28 October 1997.



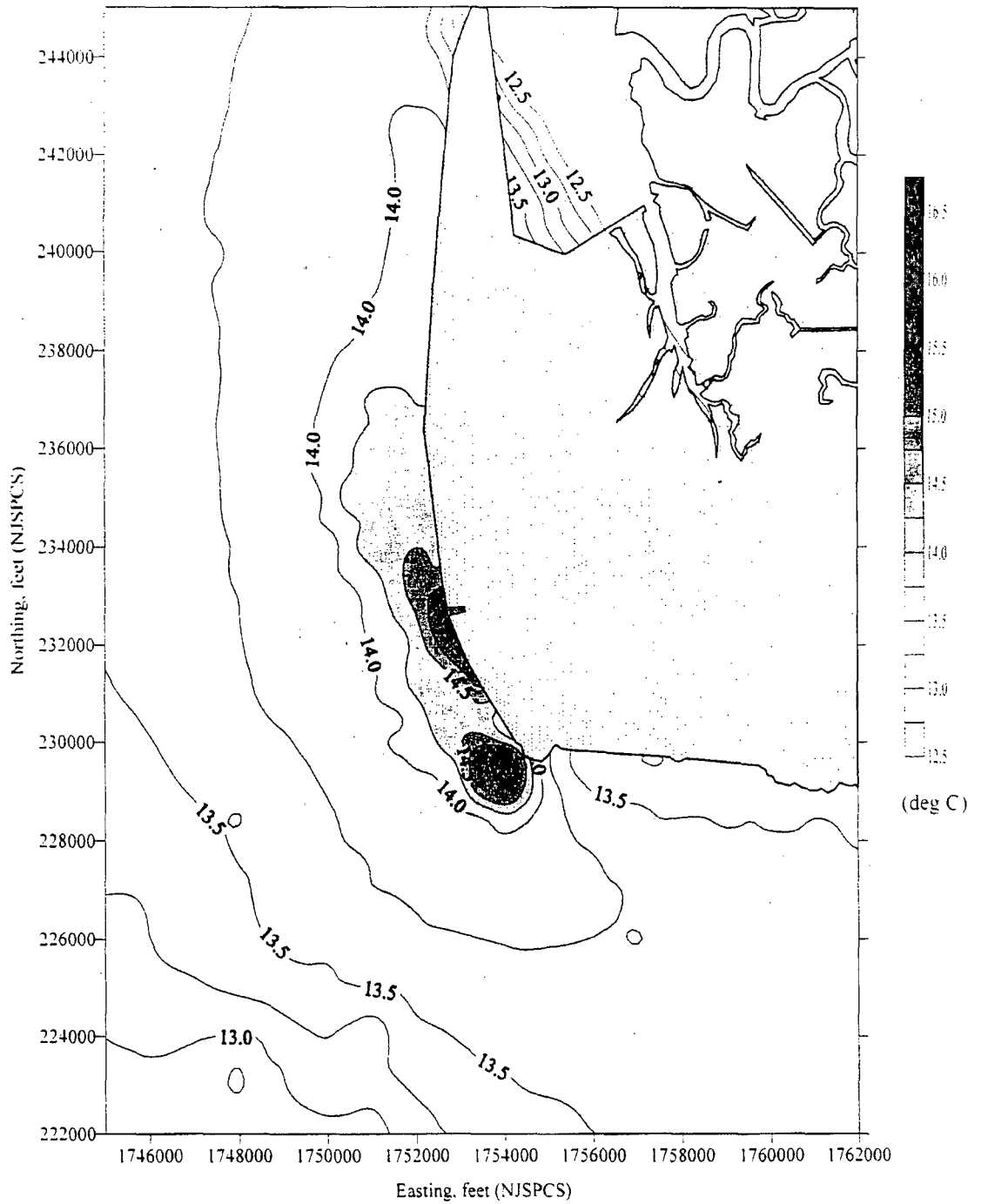
E-2 Figure III-94b. Contours of modeled surface temperatures for a slack phase (end-of-ebb) on 28 October 1997 (close-up view).



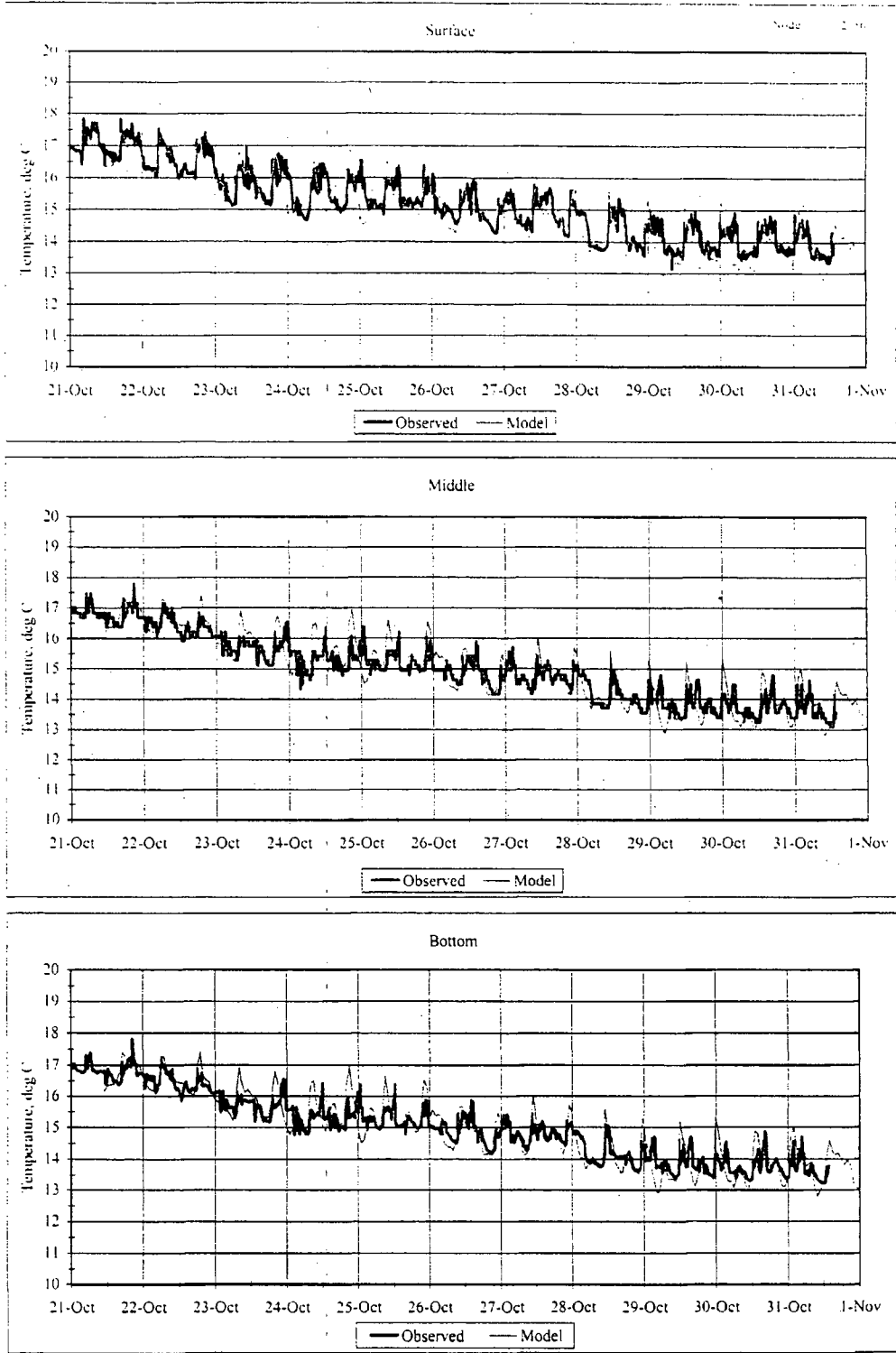
E-2 Figure III-95a. Contours of modeled surface temperatures for a flood phase on 28 October 1997.



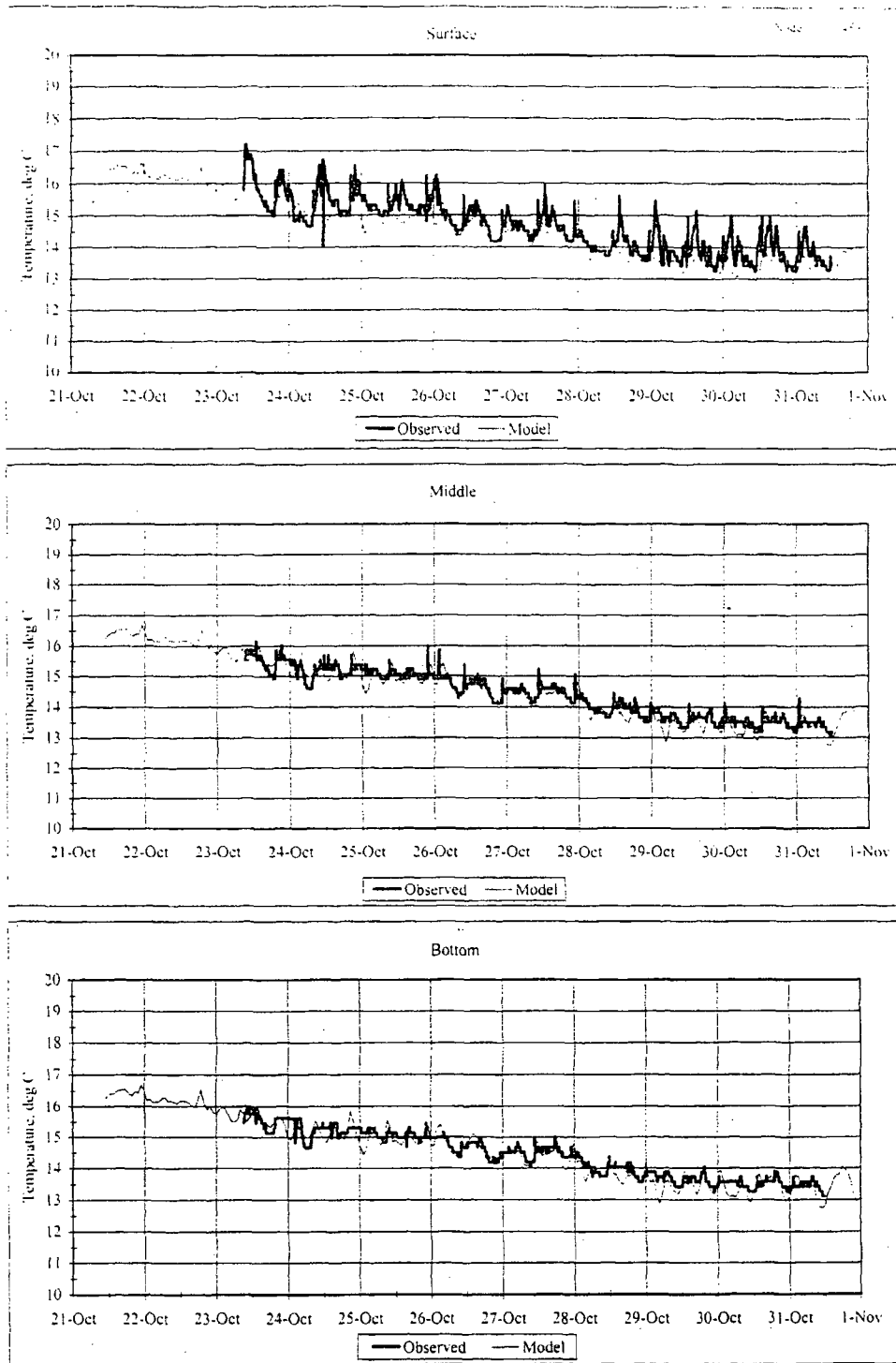
E-2 Figure III-96a. Contours of modeled surface temperatures for a slack phase (end-of-flood) on 28 October 1997.



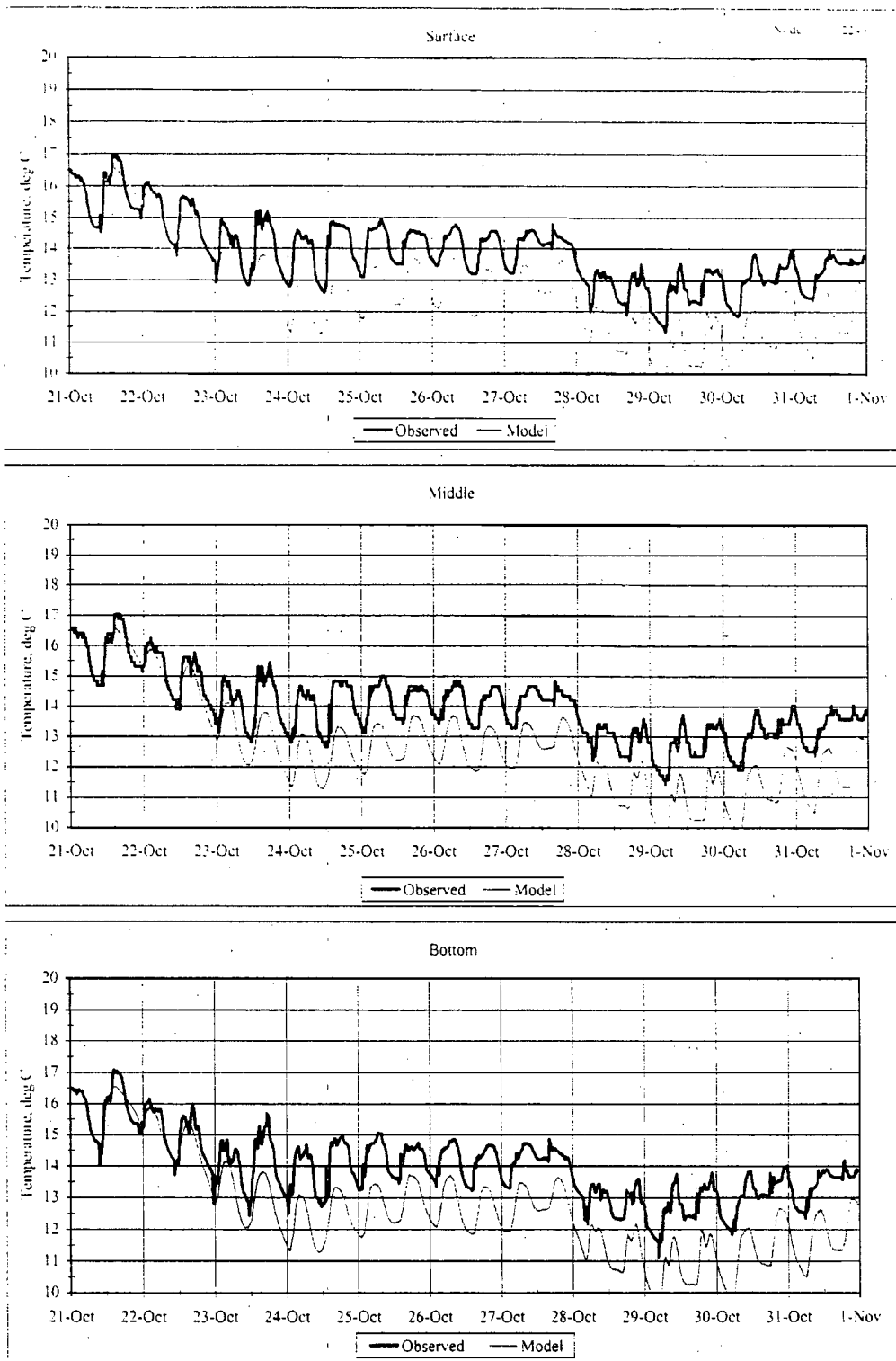
E-2 Figure III-96b. Contours of modeled surface temperatures for a slack phase (end-of-flood) on 28 October 1997 (close-up view).



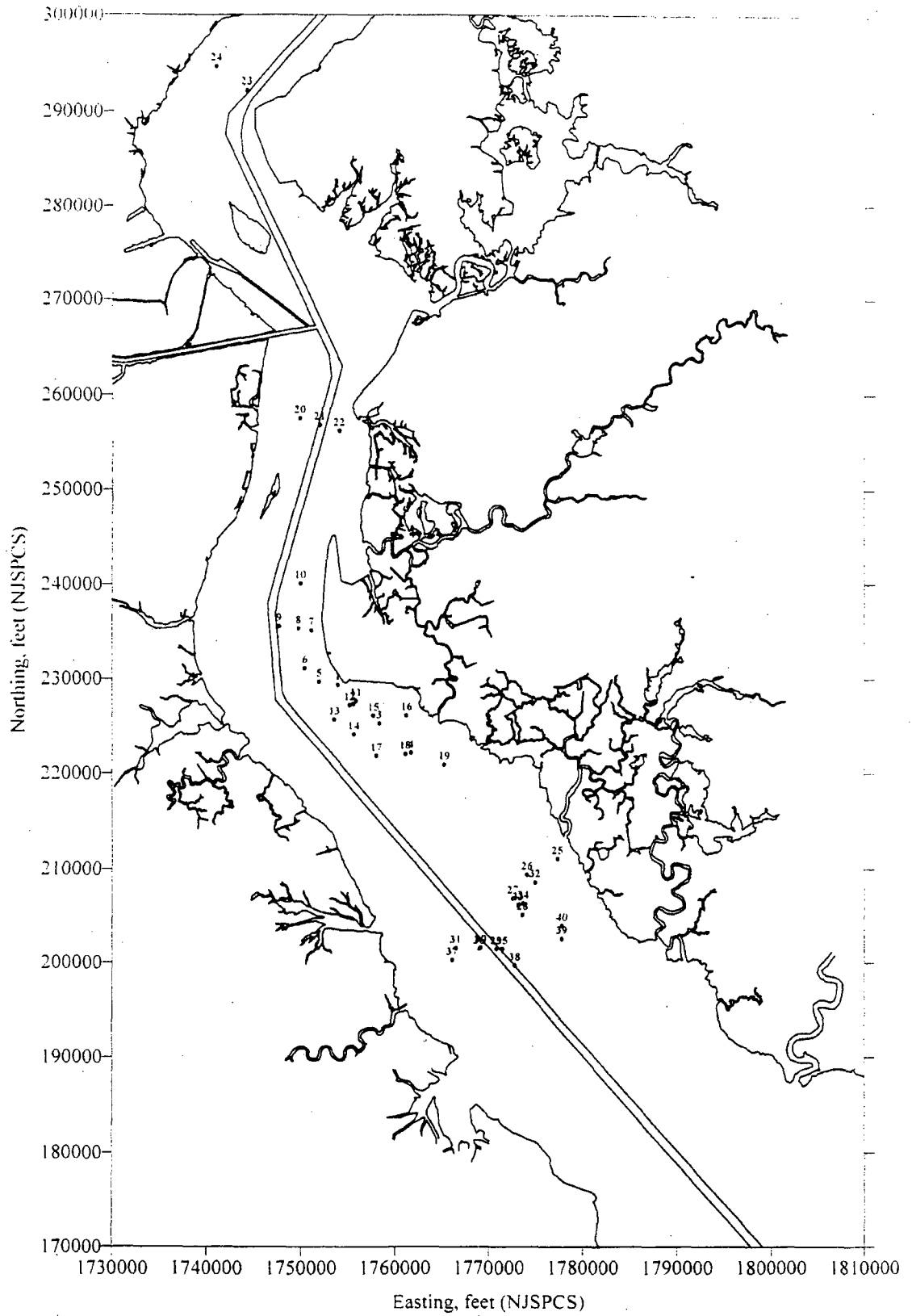
E-2 Figure III-97a. Comparison of modeled and measured temperature at Mooring H, which is located approximately 1/2 mile south-east of the Station, for the verification period (21-31 October 1997).



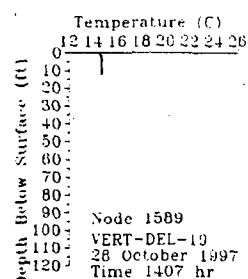
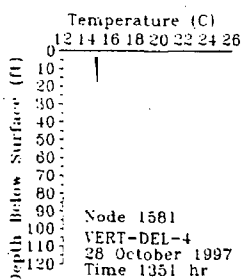
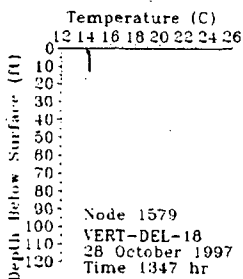
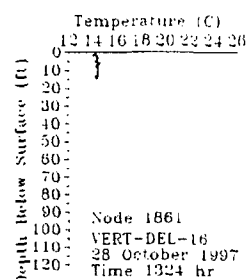
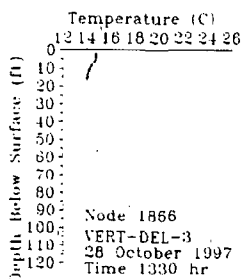
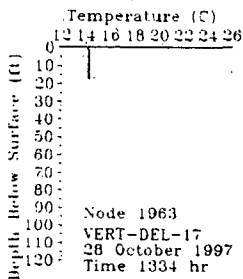
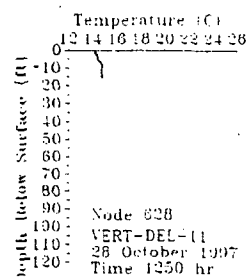
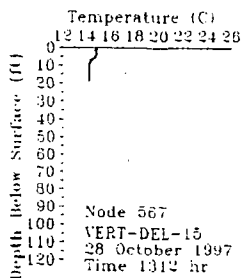
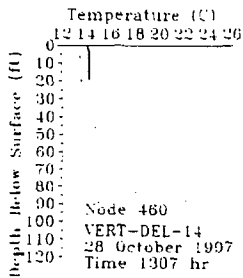
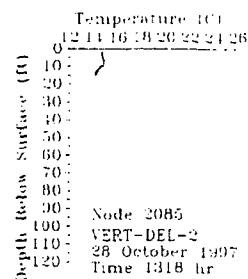
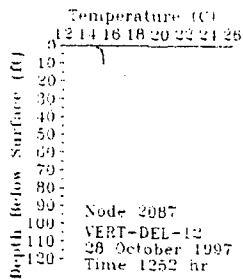
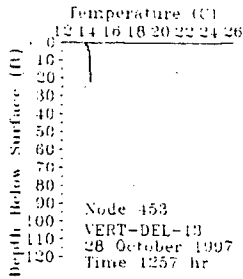
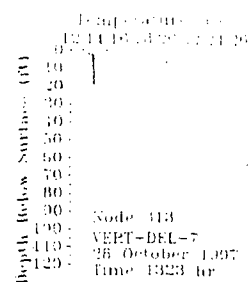
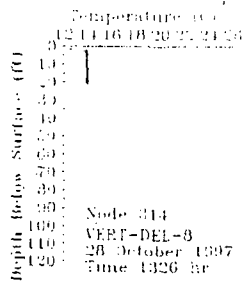
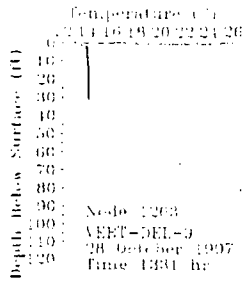
E-2 Figure III-97b. Comparison of modeled and measured temperature at Mooring N, which is located approximately 1 mile south-east of the Station, for the verification period (21-31 October 1997).



E-2 Figure III-97c. Comparison of modeled and measured temperature at the Alloway Creek mooring for the verification period (21-31 October 1997).

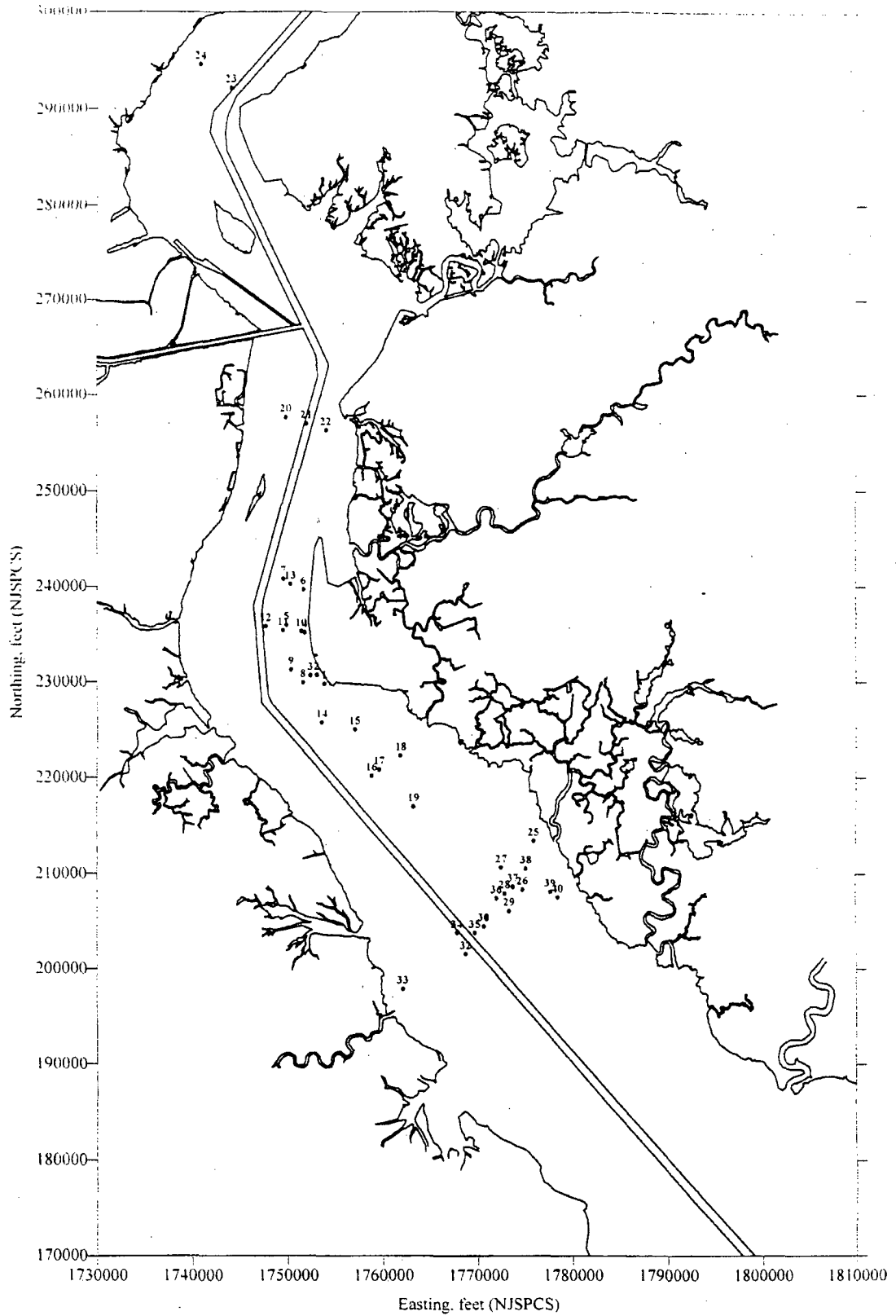


E-2 Figure III-98. Locations of shipboard vertical profiles measured during an ebb phase on 28 October 1997.

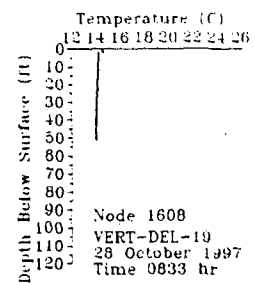
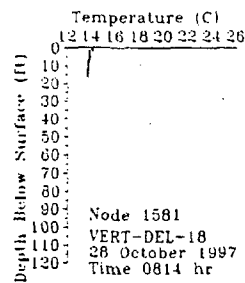
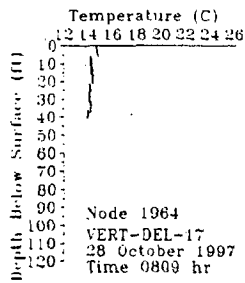
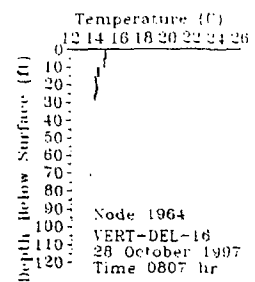
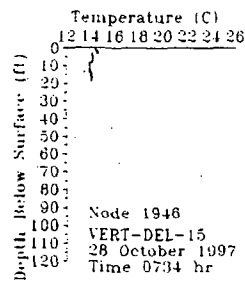
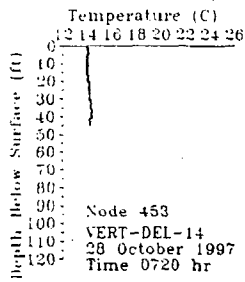
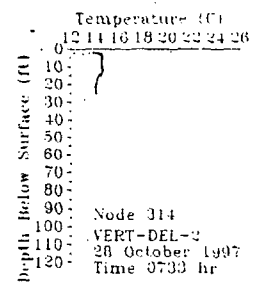
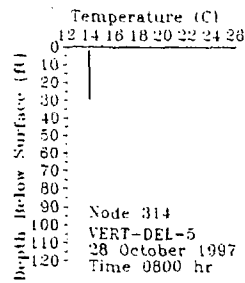
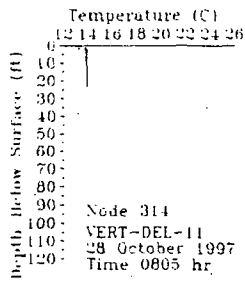
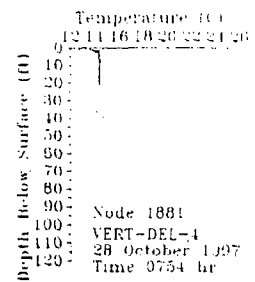
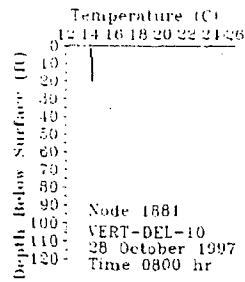
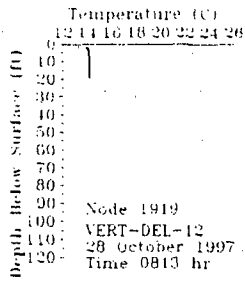
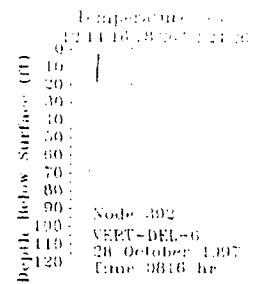
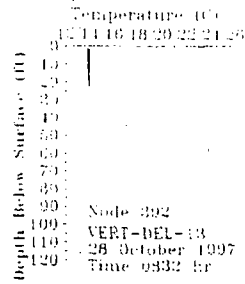
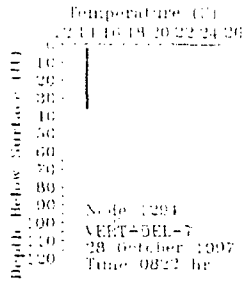


Observed=***** Model=_____

E-2 Figure III-99. Comparison of modeled and measured temperatures at locations of shipboard verticals in the vicinity of the Station during an ebb phase on 28 October 1997.

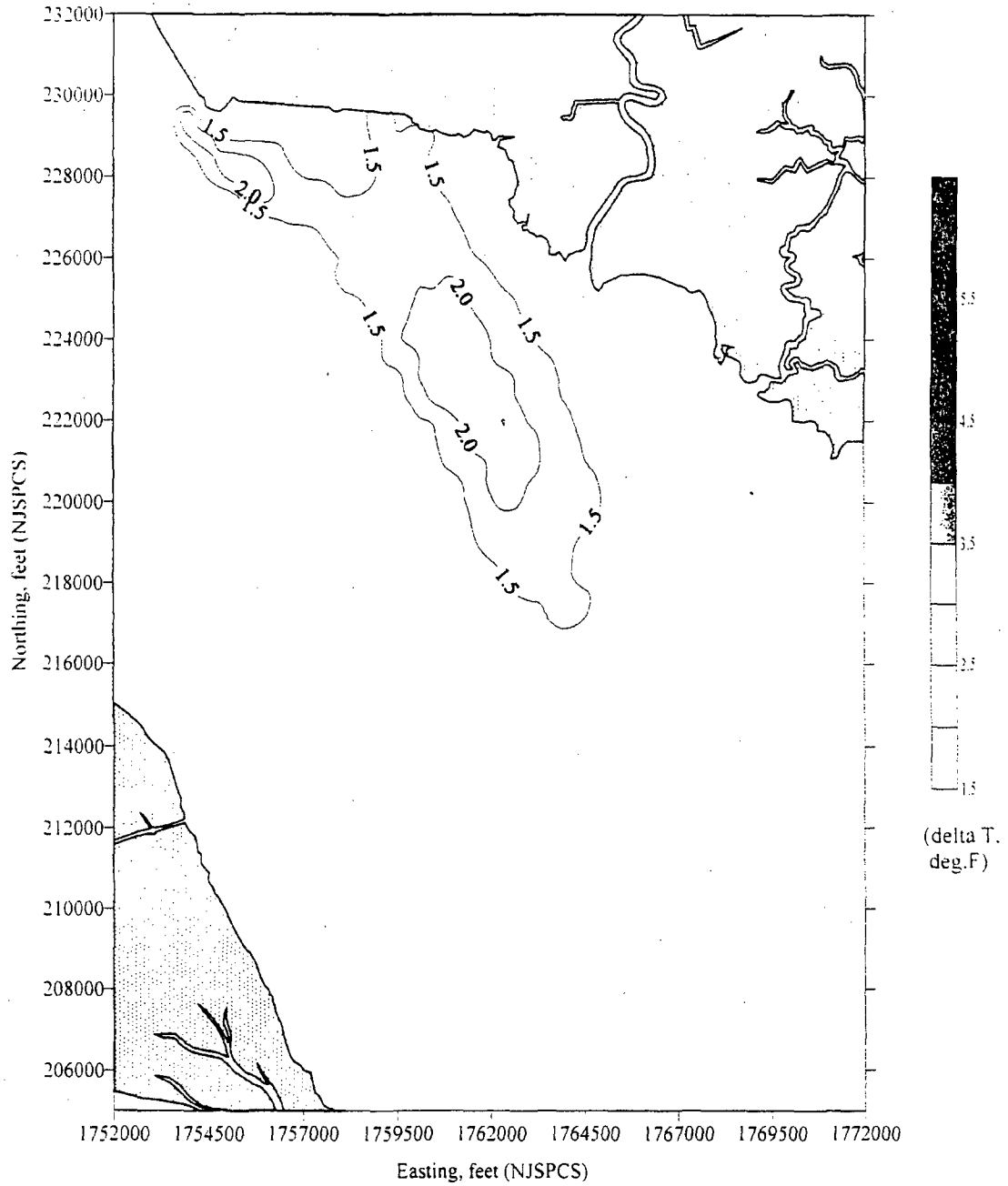


E-2 Figure III-100. Locations of shipboard vertical profiles measured during a flood phase on 28 October 1997.

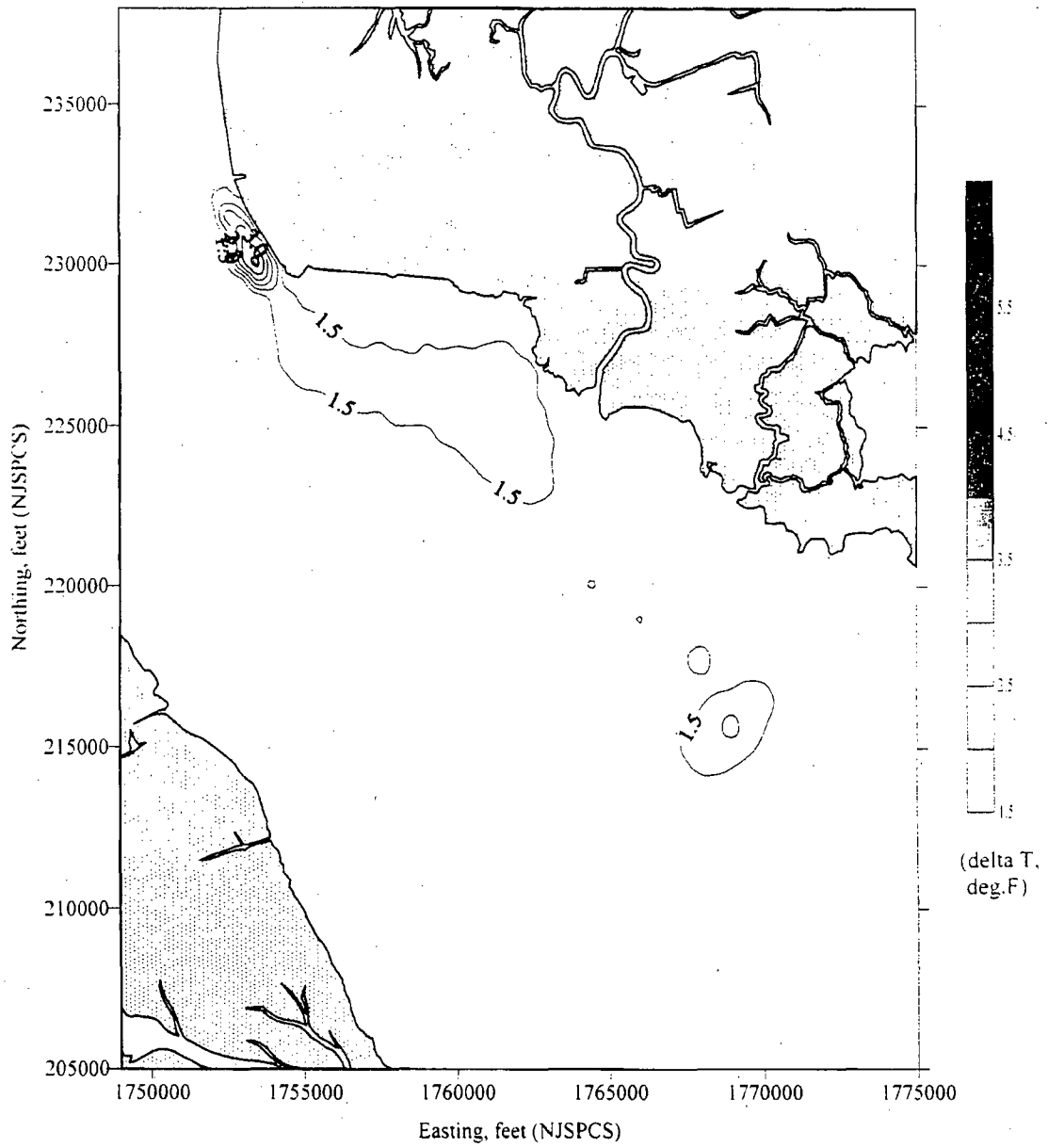


Observed=***** Model=_____

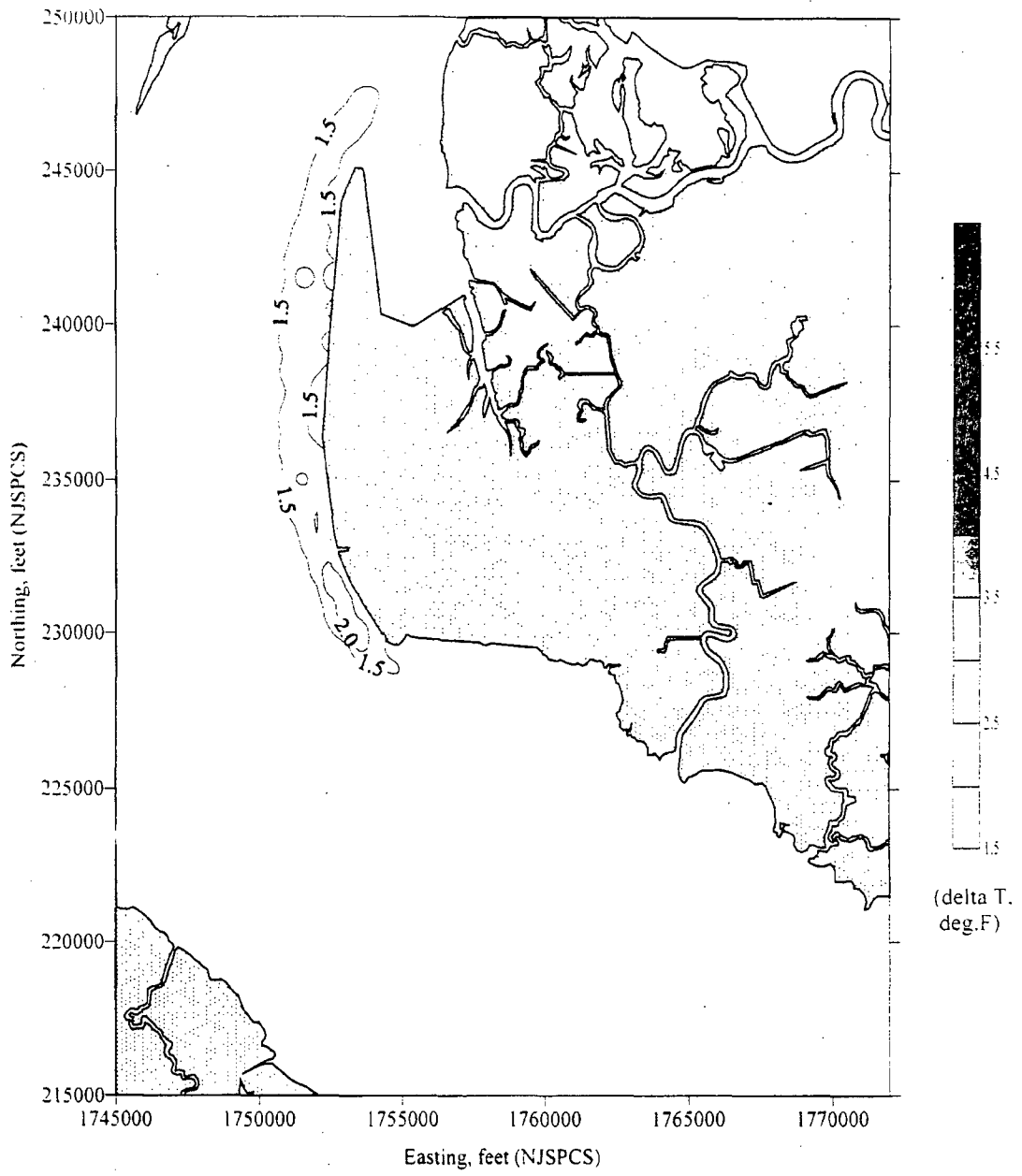
E-2 Figure III-101. Comparison of modeled and measured temperatures at locations of shipboard verticals in the vicinity of the Station during a flood phase on 28 October 1997.



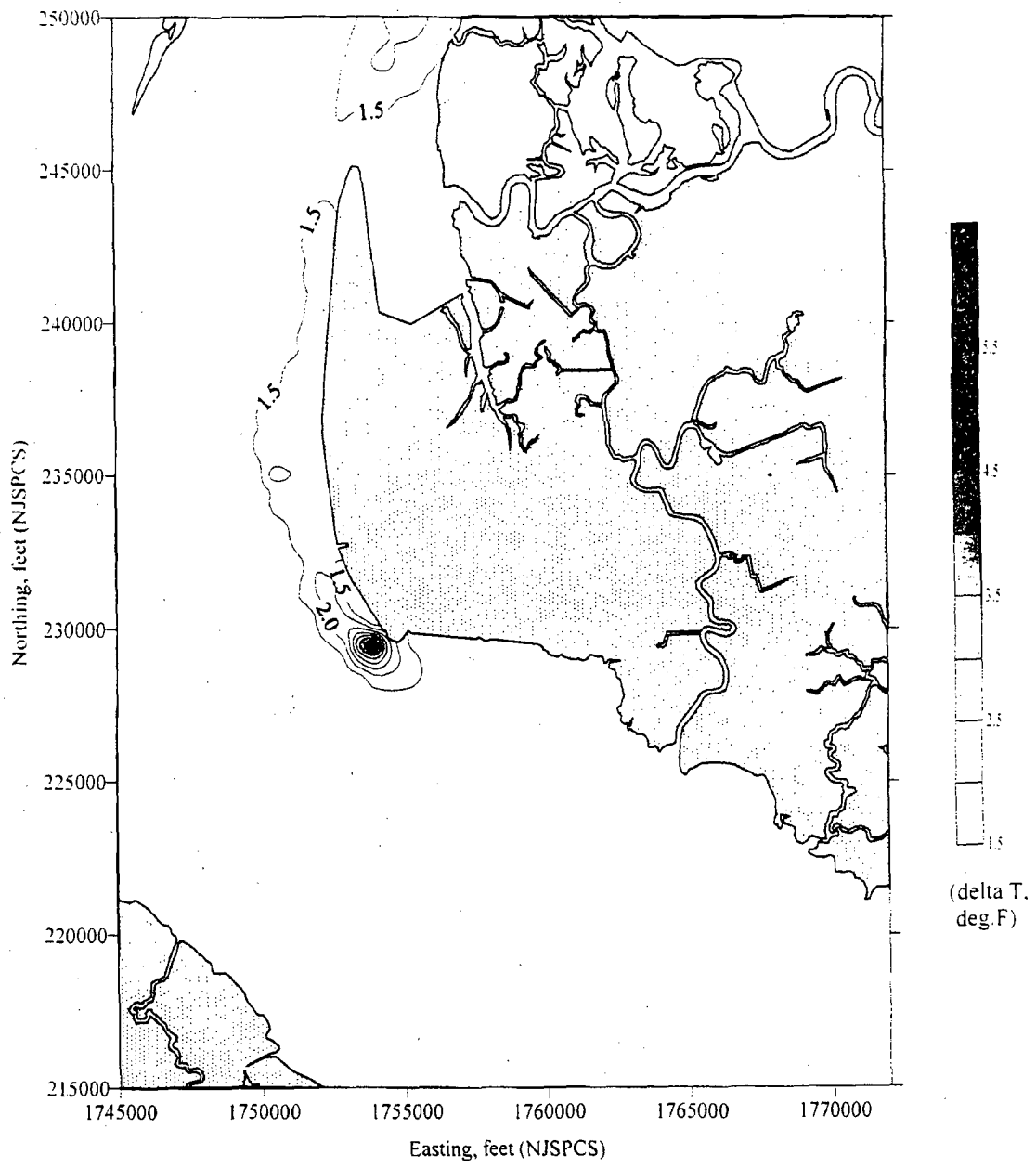
E-2 Figure III-102a. Contours of modeled surface delta temperatures for an ebb phase on 28 October 1997 (Based on an ambient run).



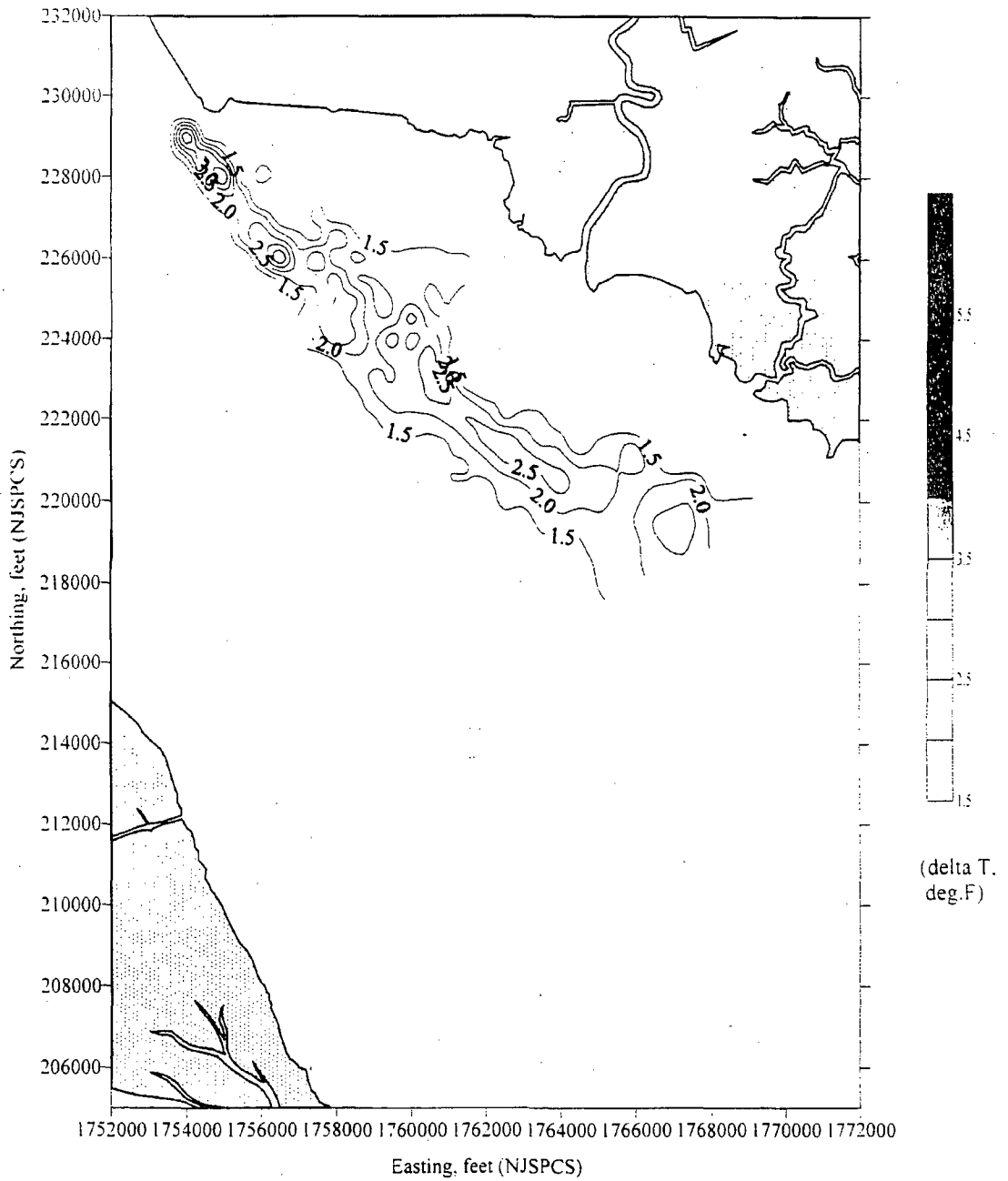
E-2 Figure III-102b. Contours of modeled surface delta temperatures for a slack phase (end-of-ebb) on 28 October 1997 (Based on an ambient run).



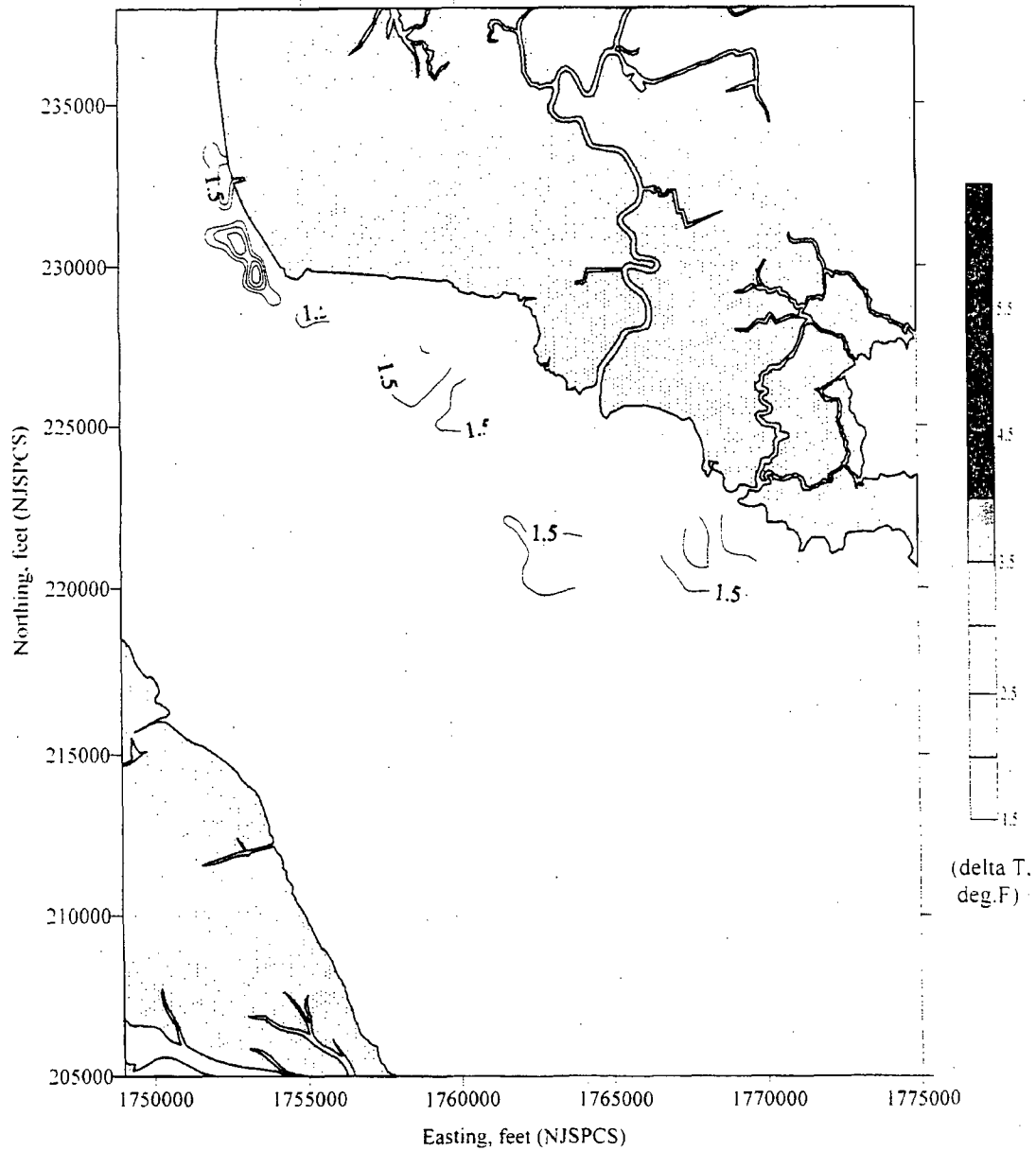
E-2 Figure III-102c. Contours of modeled surface delta temperatures for a flood phase on 28 October 1997 (Based on an ambient run).



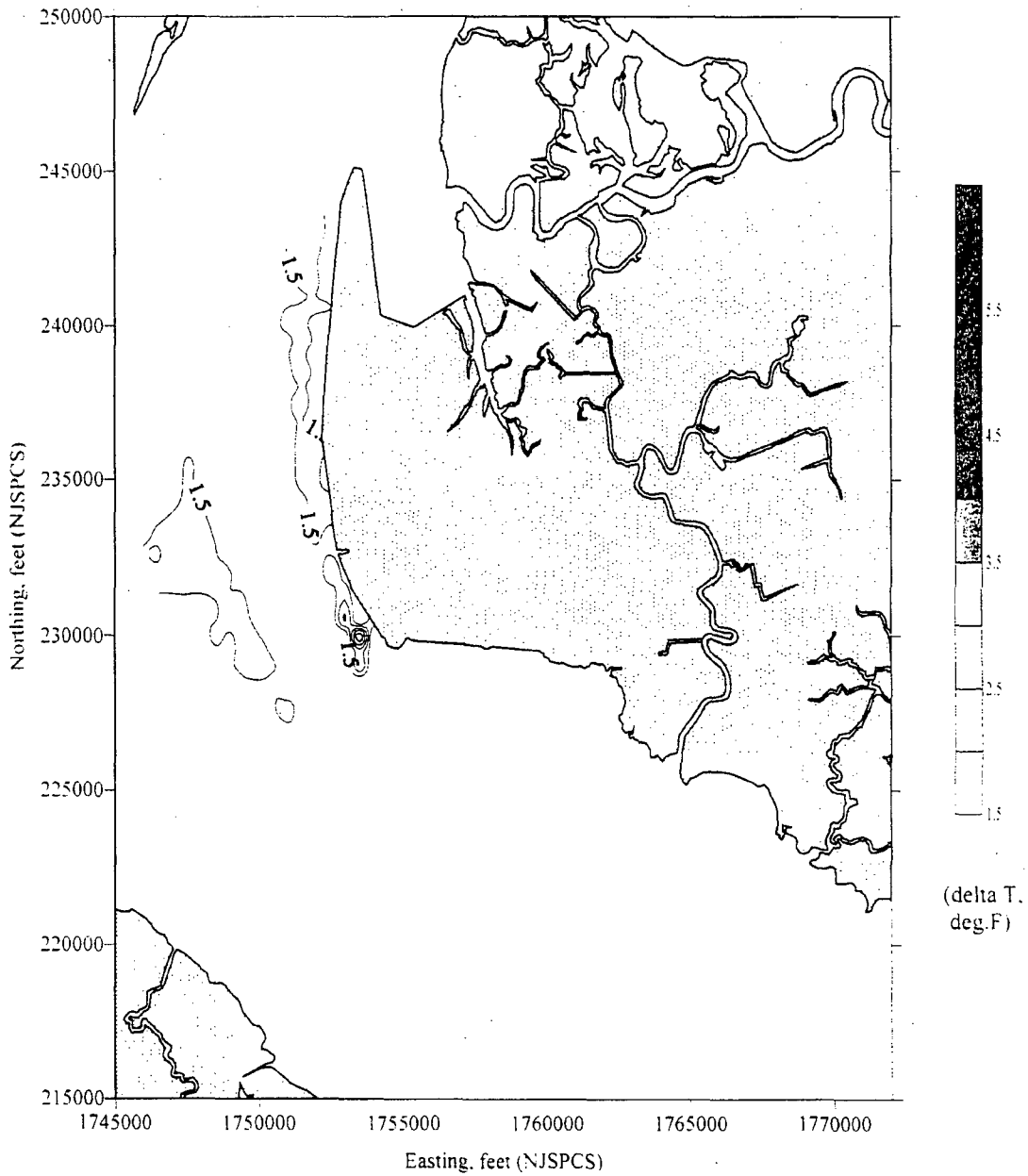
E-2 Figure III-102d. Contours of modeled surface delta temperatures for a slack phase (end-of-flood) on 28 October 1997 (Based on an ambient run).



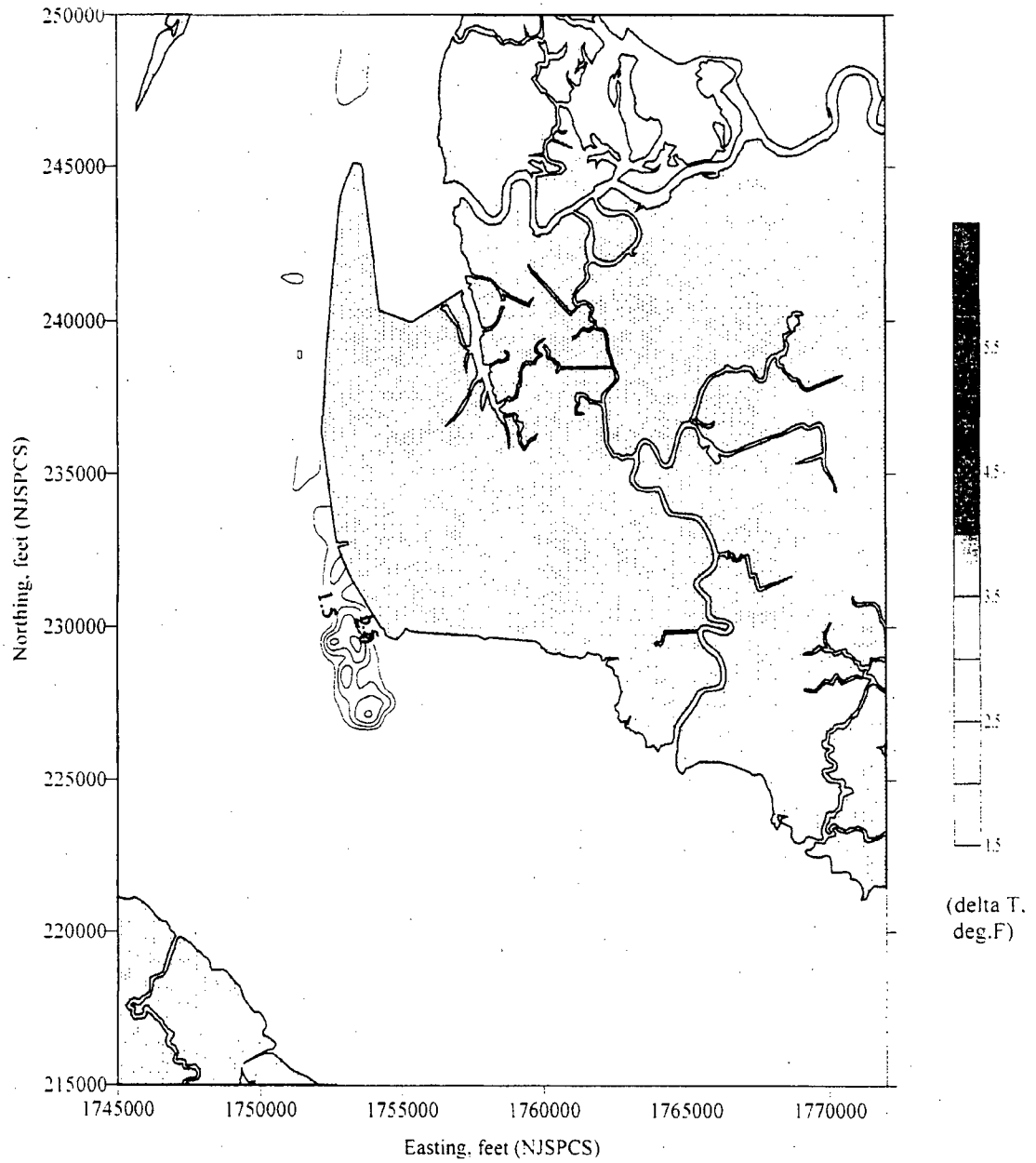
E-2 Figure III-103a. Contours of measured surface delta temperatures for an ebb phase on 28 October 1997 (Based on an ambient temperature of 56 deg.F).



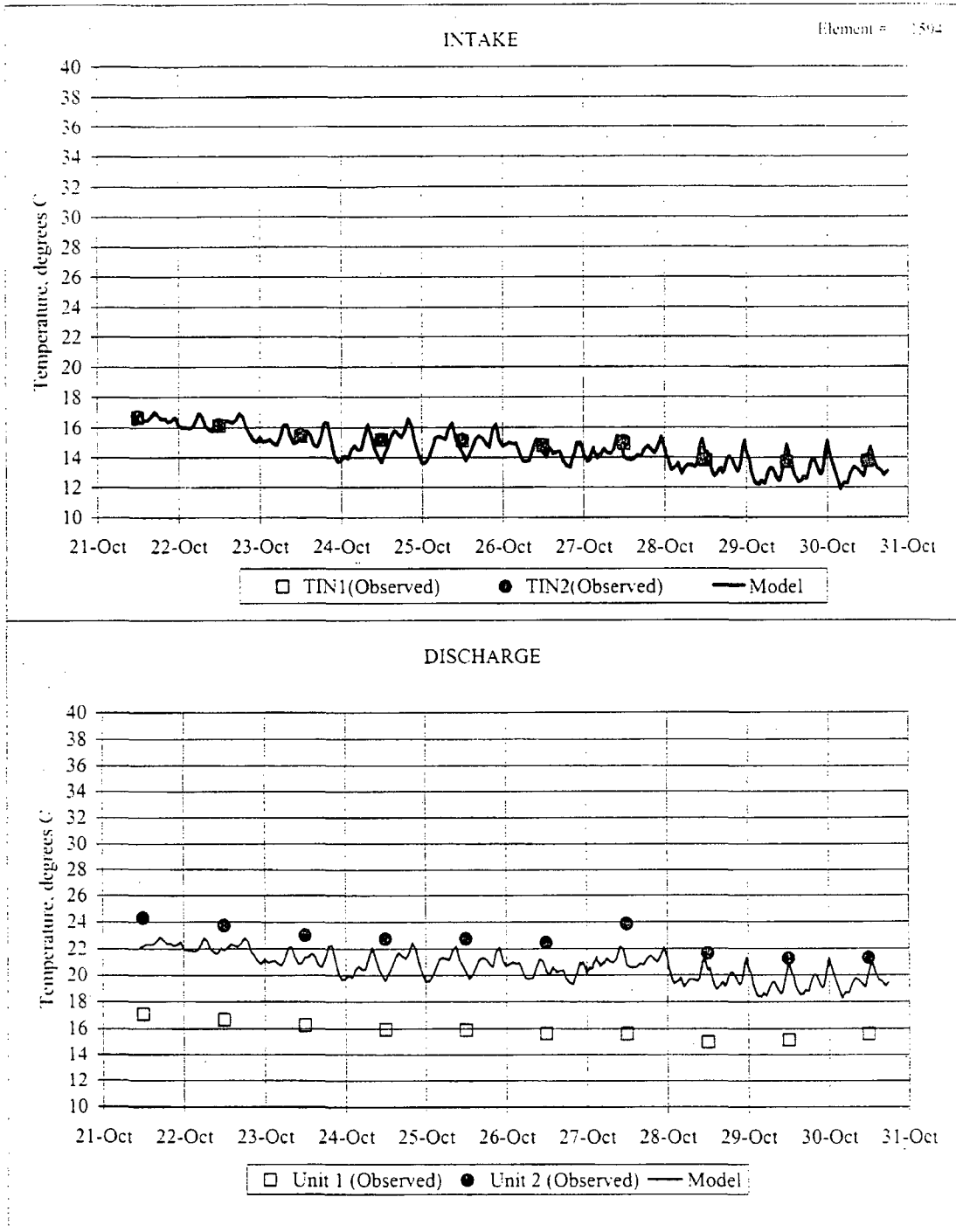
E-2 Figure III-103b. Contours of measured surface delta temperatures for a slack phase (end-of-ebb) on 28 October 1997 (Based on an ambient temperature of 56 deg.F).



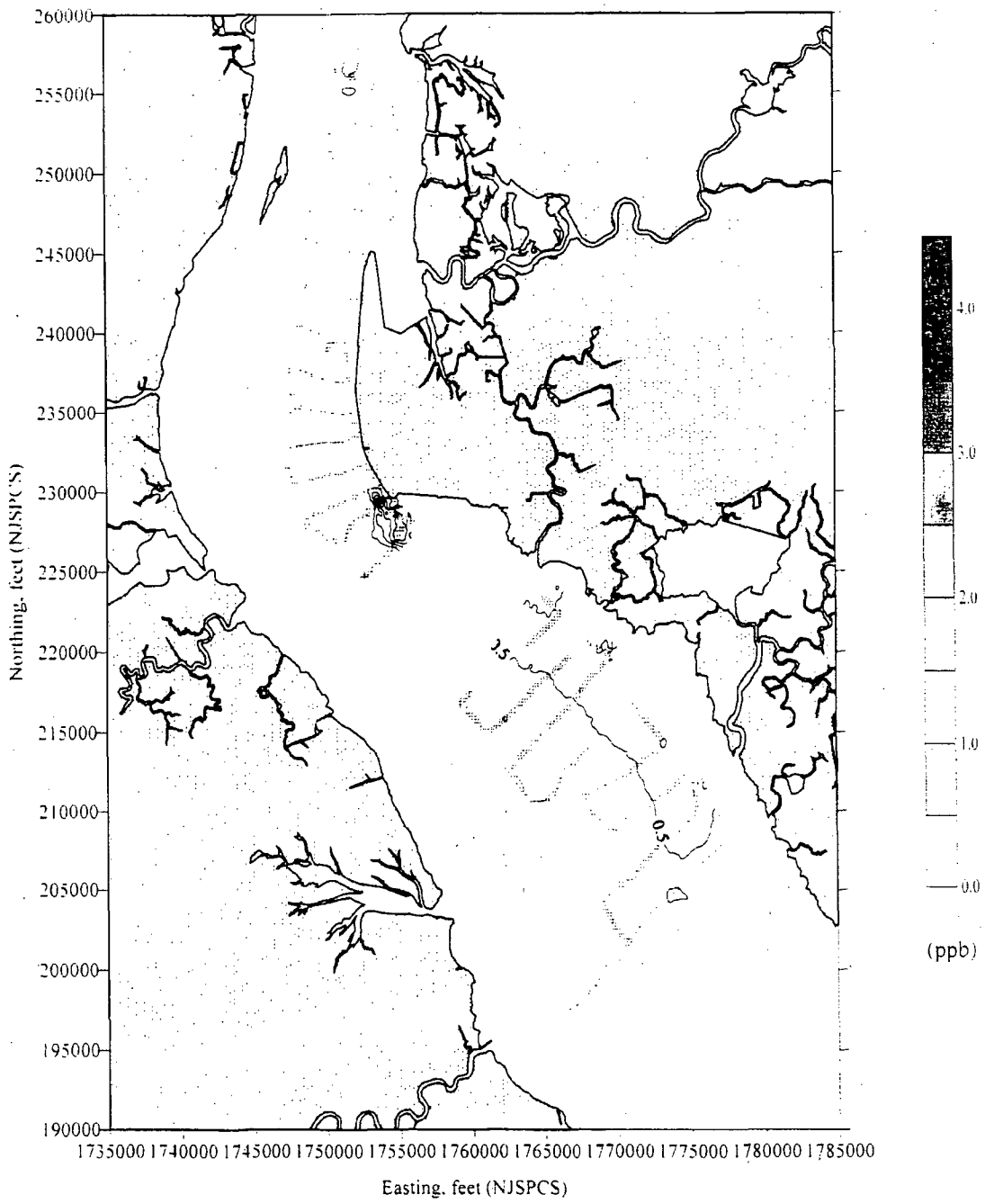
E-2 Figure III-103c. Contours of measured surface delta temperatures for a flood phase on 28 October 1997 (Based on an ambient temperature of 56 deg.F).



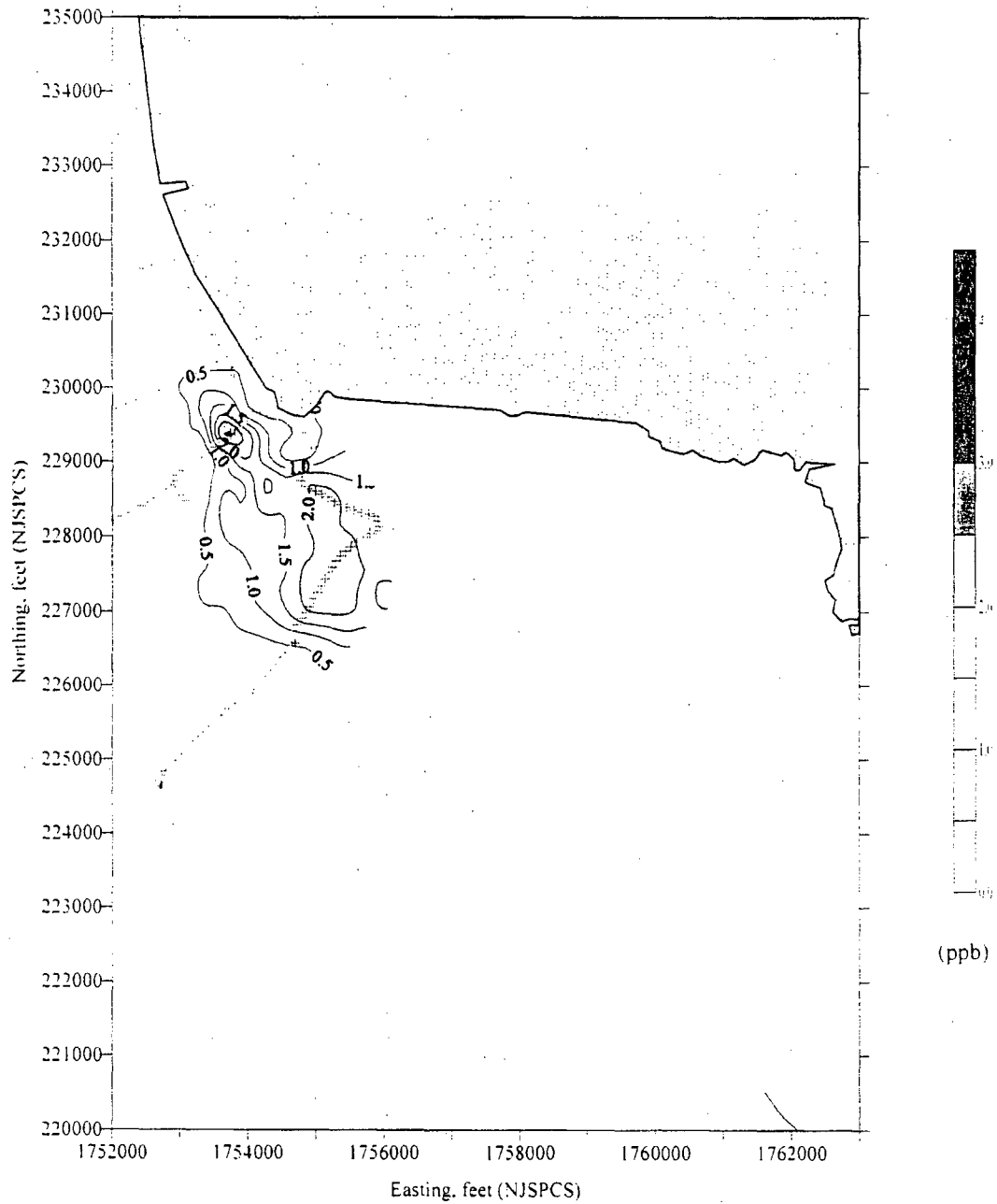
E-2 Figure III-103d. Contours of measured surface delta temperatures for a slack phase (end-of-flood) on 28 October 1997 (Based on an ambient temperature of 56 deg.F).



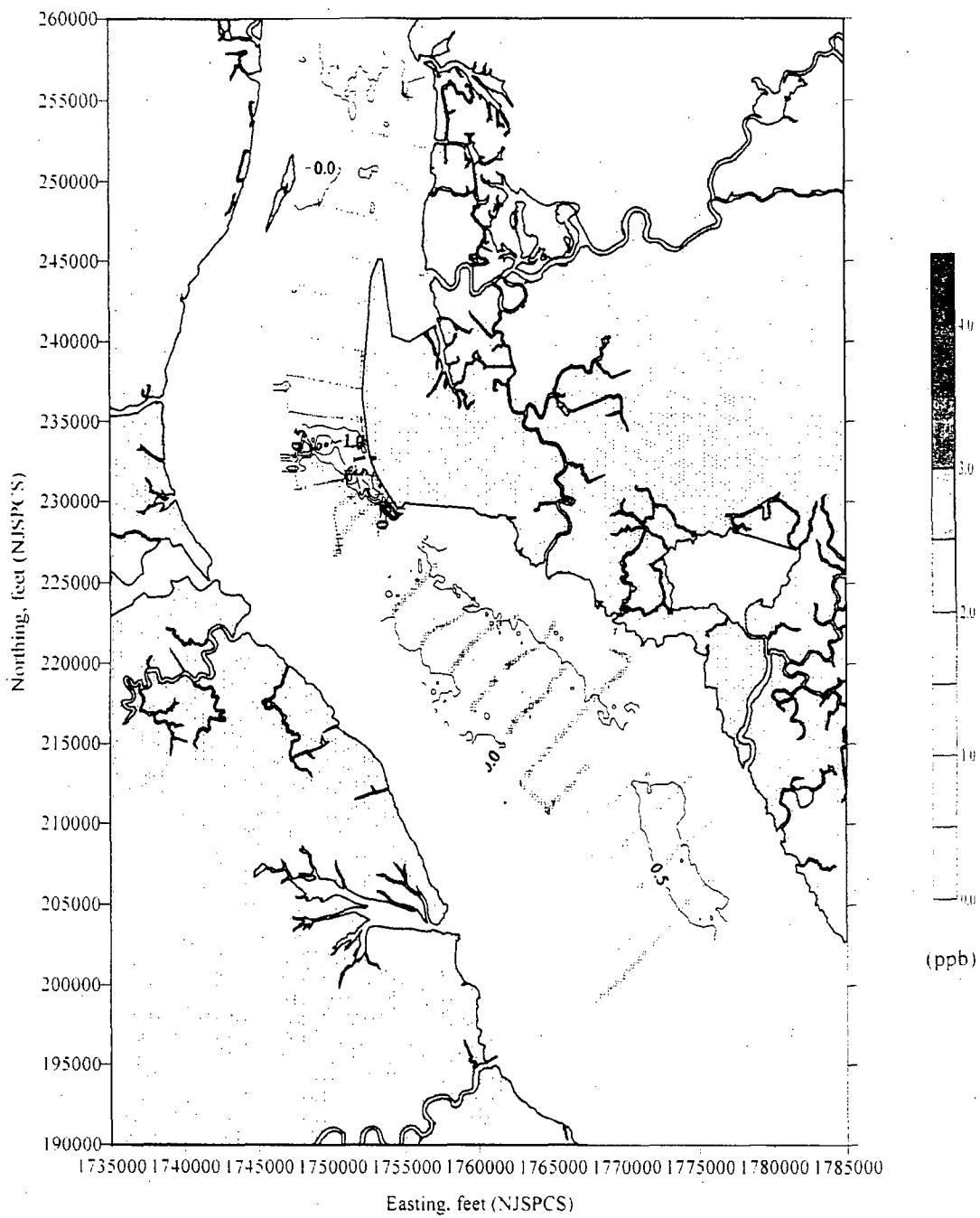
E-2 Figure III-104. Comparison of measured and modeled Station intake and discharge temperatures for the verification period (21-31 Oct 1997).



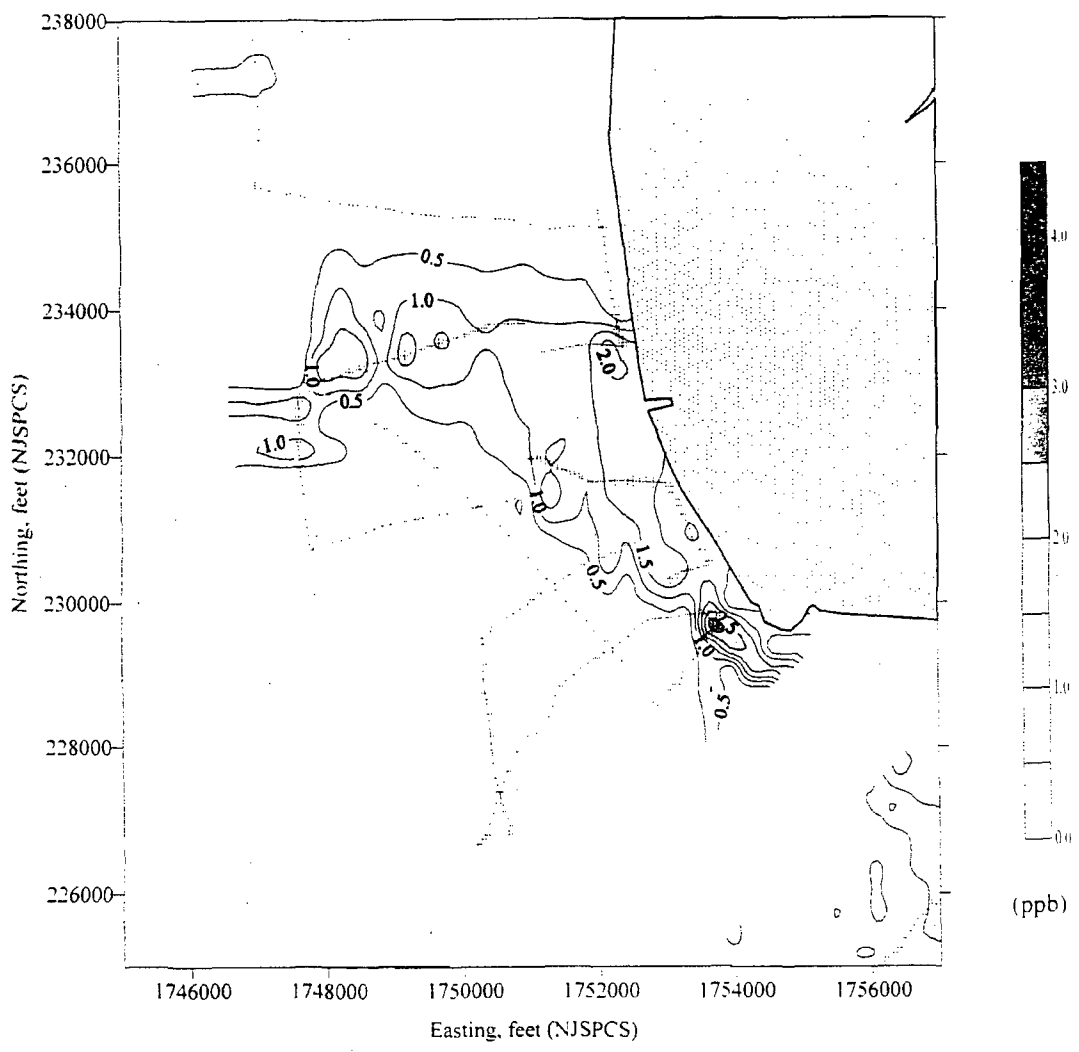
E-2 Figure III-105a. Contours of measured surface dye with boat trackings for an ebb phase on 29 May 1998.



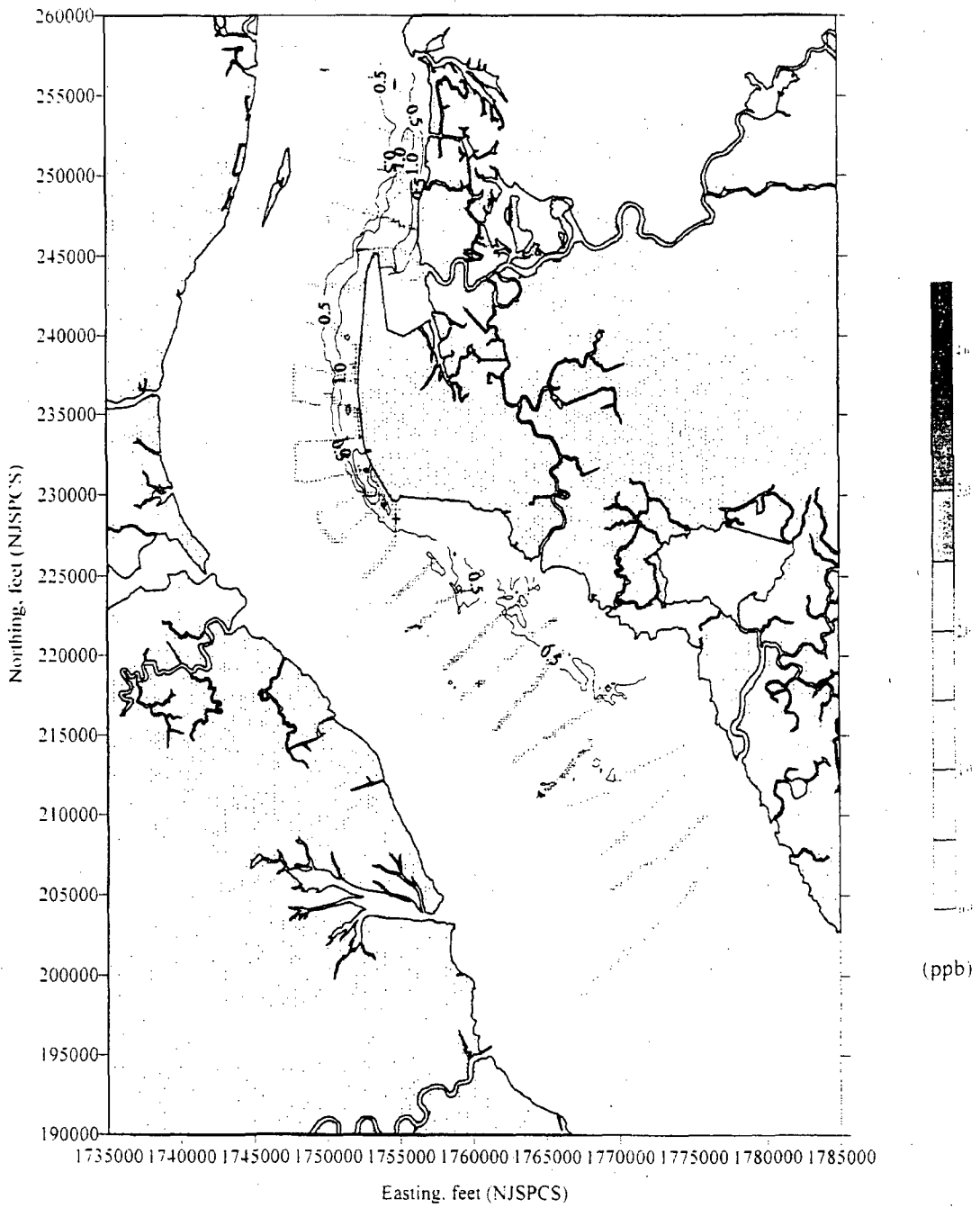
E-2 Figure III-105b. Contours of measured surface dye with boat trackings for an ebb phase on 29 May 1998 (close-up view).



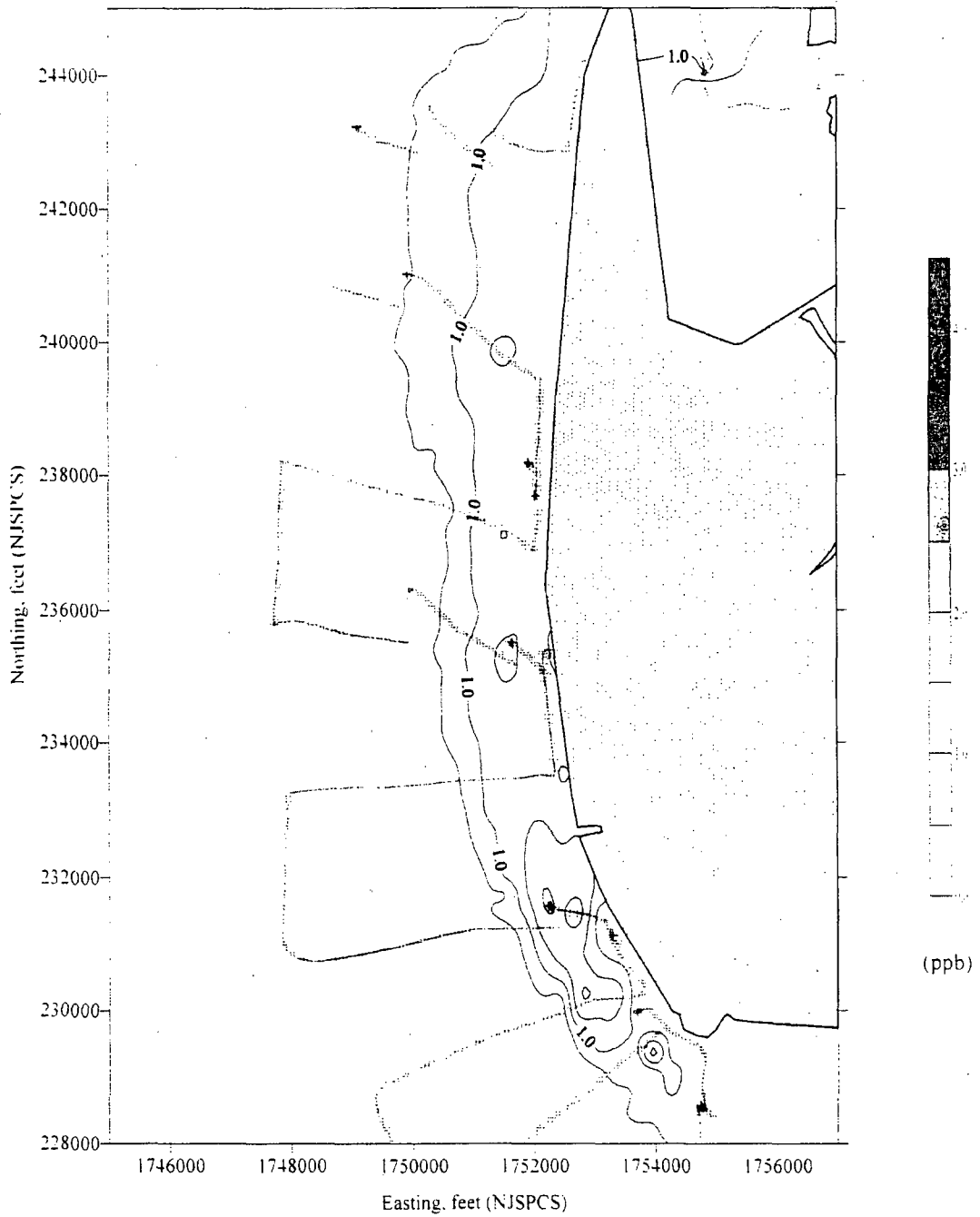
E-2 Figure III-106a. Contours of measured surface dye with boat trackings for a slack phase (end-of-ebb) on 29 May 1998.



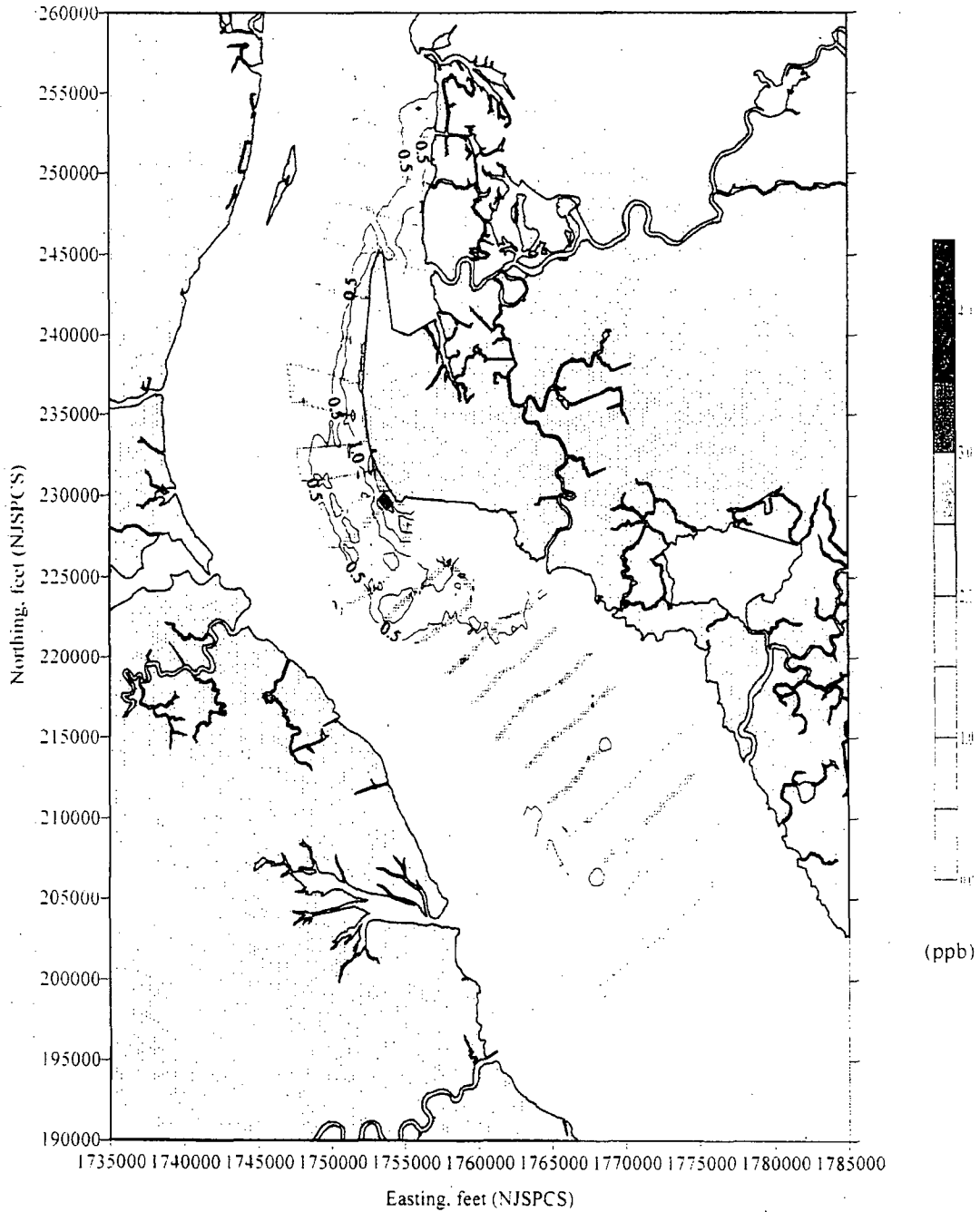
E-2 Figure III-106b. Contours of measured surface dye with boat trackings for a slack phase (end-of-ebb) on 29 May 1998 (close-up view).



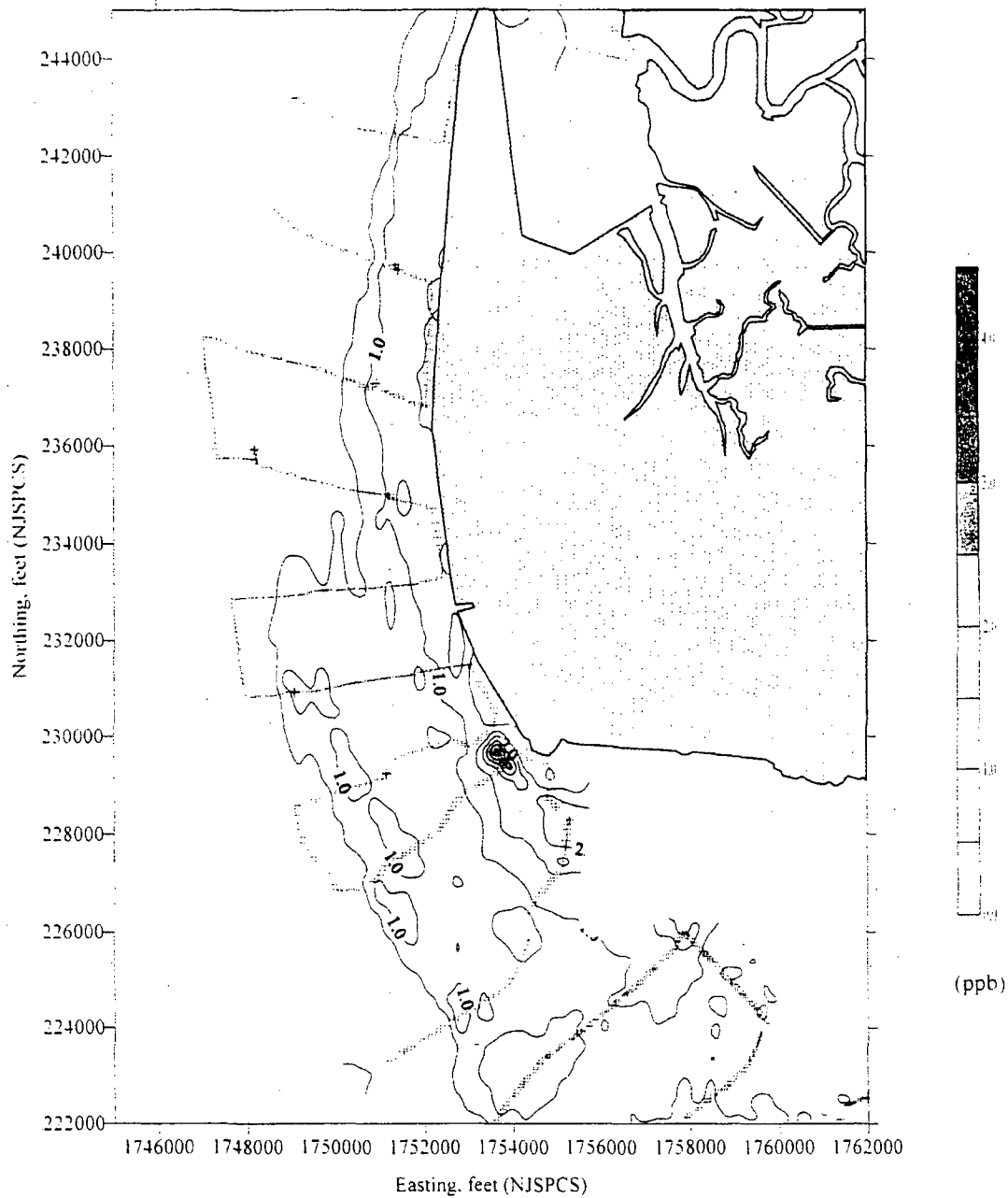
E-2 Figure III-107a. Contours of measured surface dye with boat trackings for a flood phase on 29 May 1998.



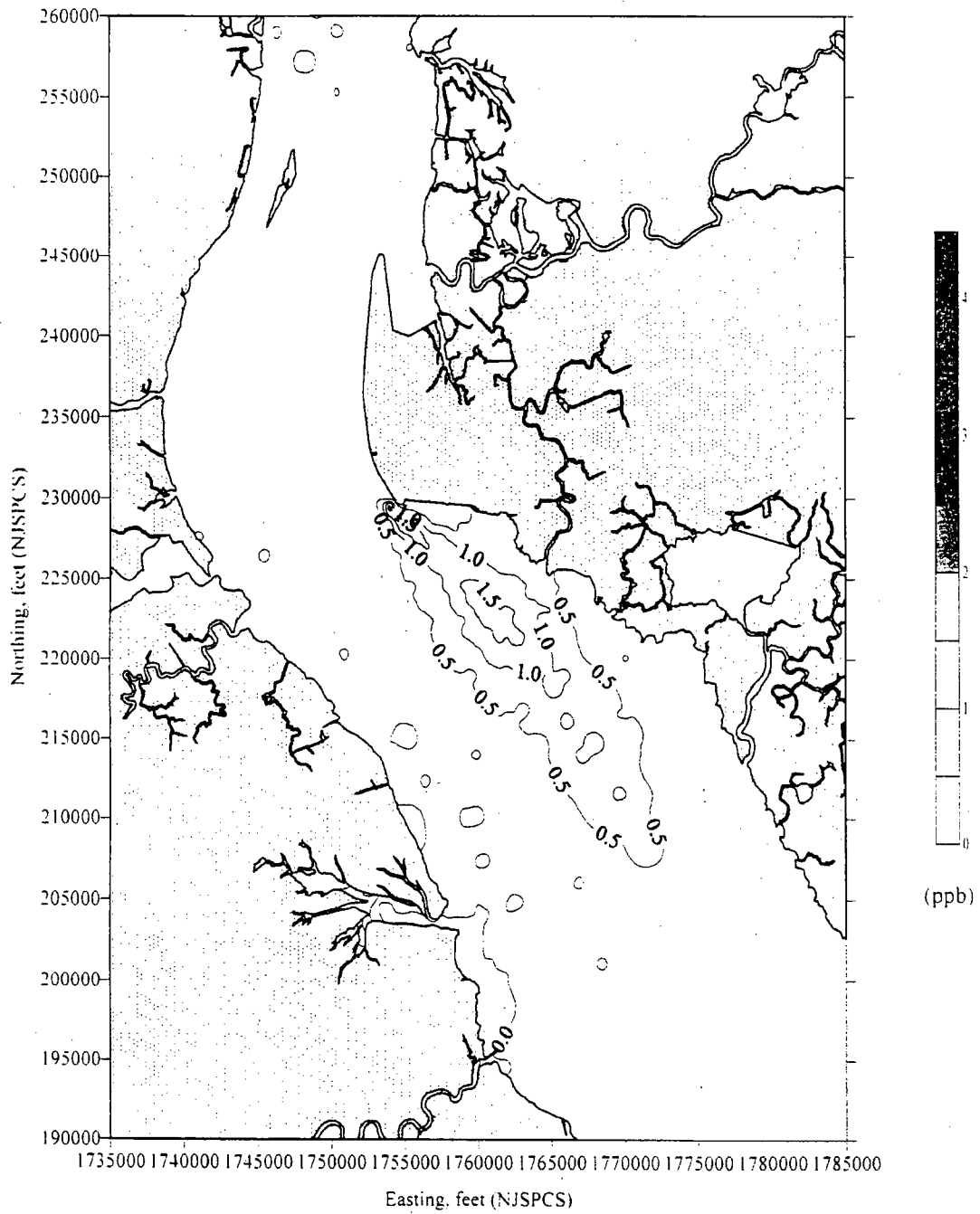
E-2 Figure III-107b. Contours of measured surface dye with boat trackings for a flood phase on 29 May 1998 (close-up view).



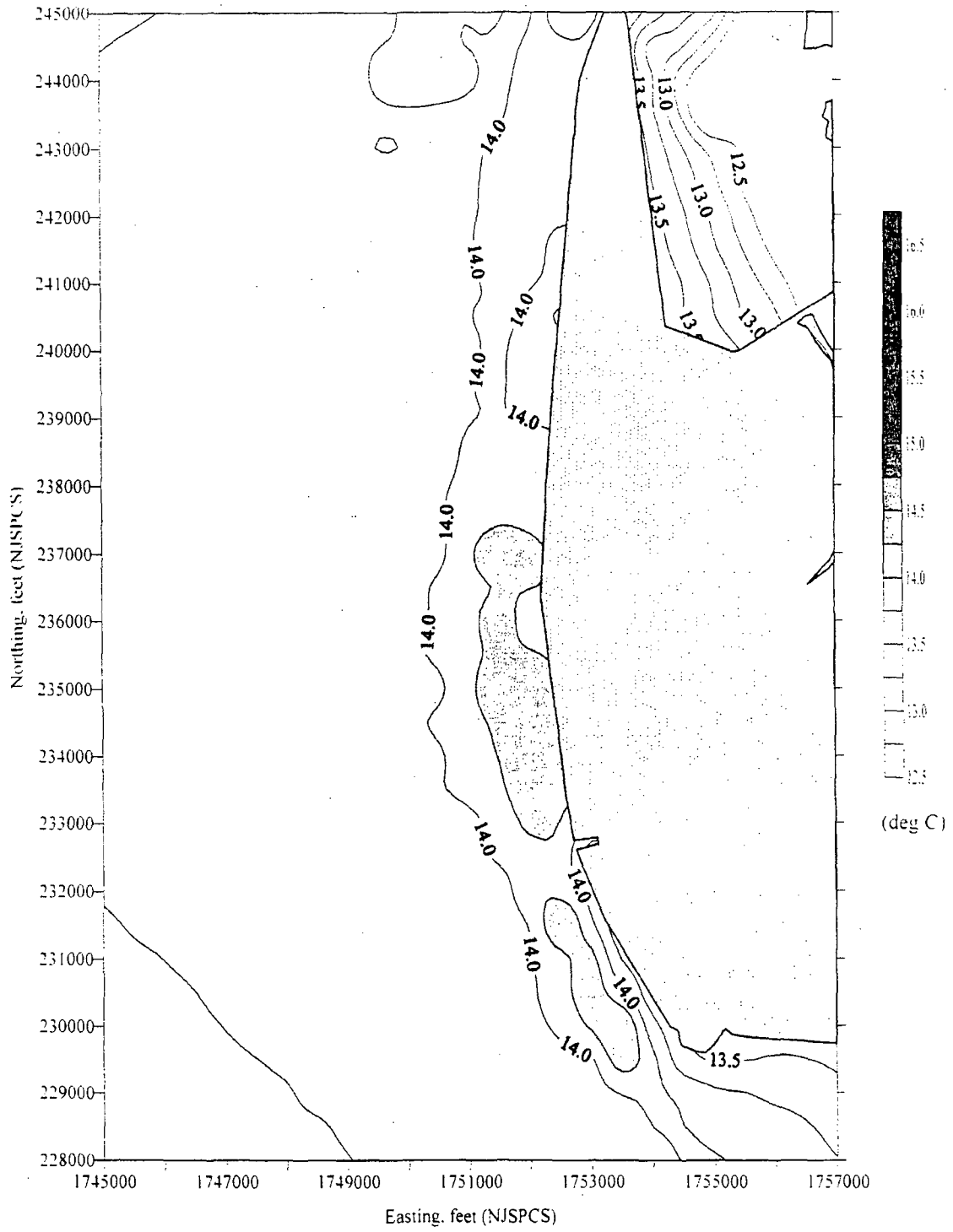
E-2 Figure III-108a. Contours of measured surface dye with boat trackings for a slack phase (end-of-flood) on 29 May 1998.



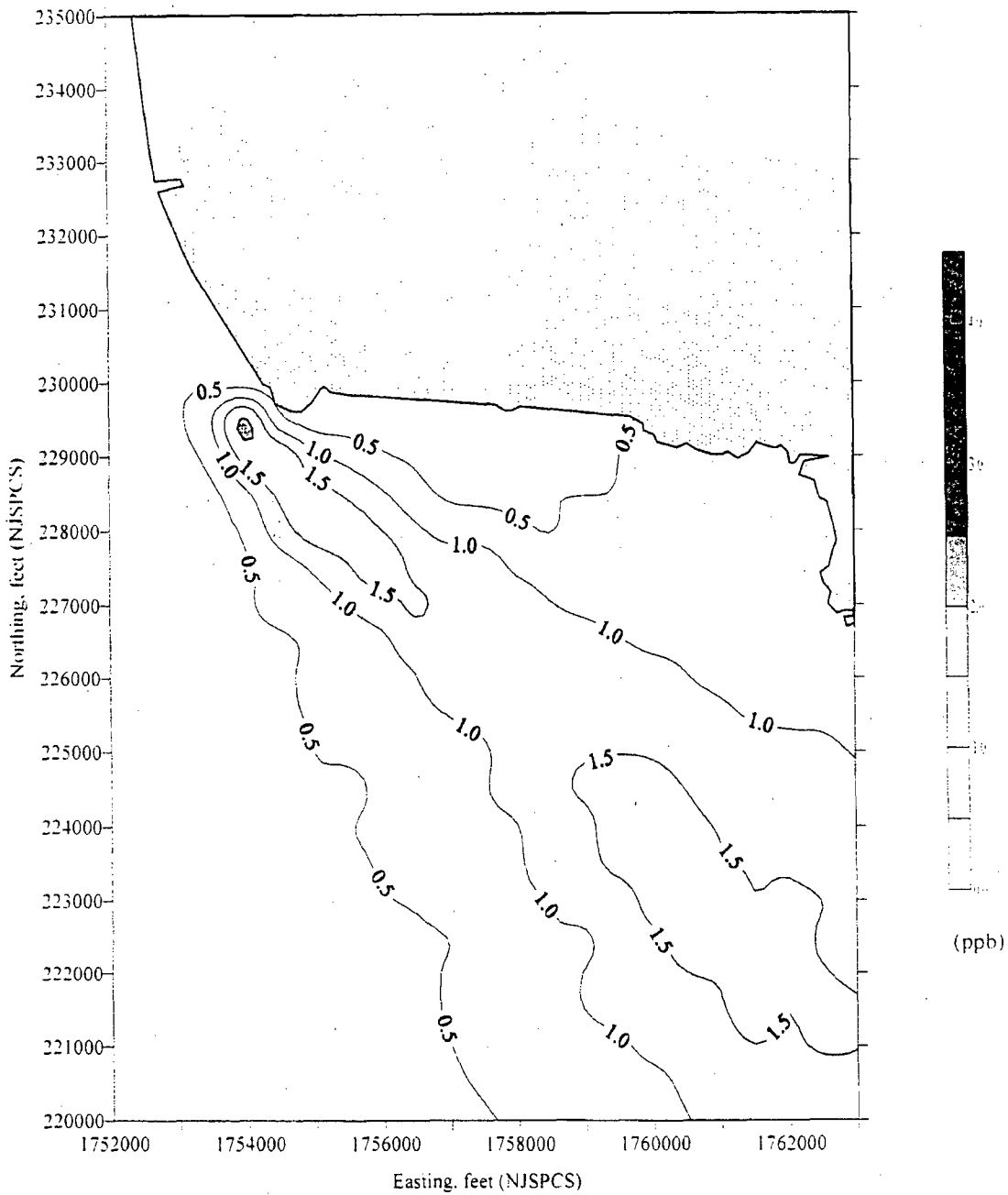
E-2 Figure III-108b. Contours of measured surface dye with boat trackings for a slack phase (end-of-flood) on 29 May 1998 (close-up view).



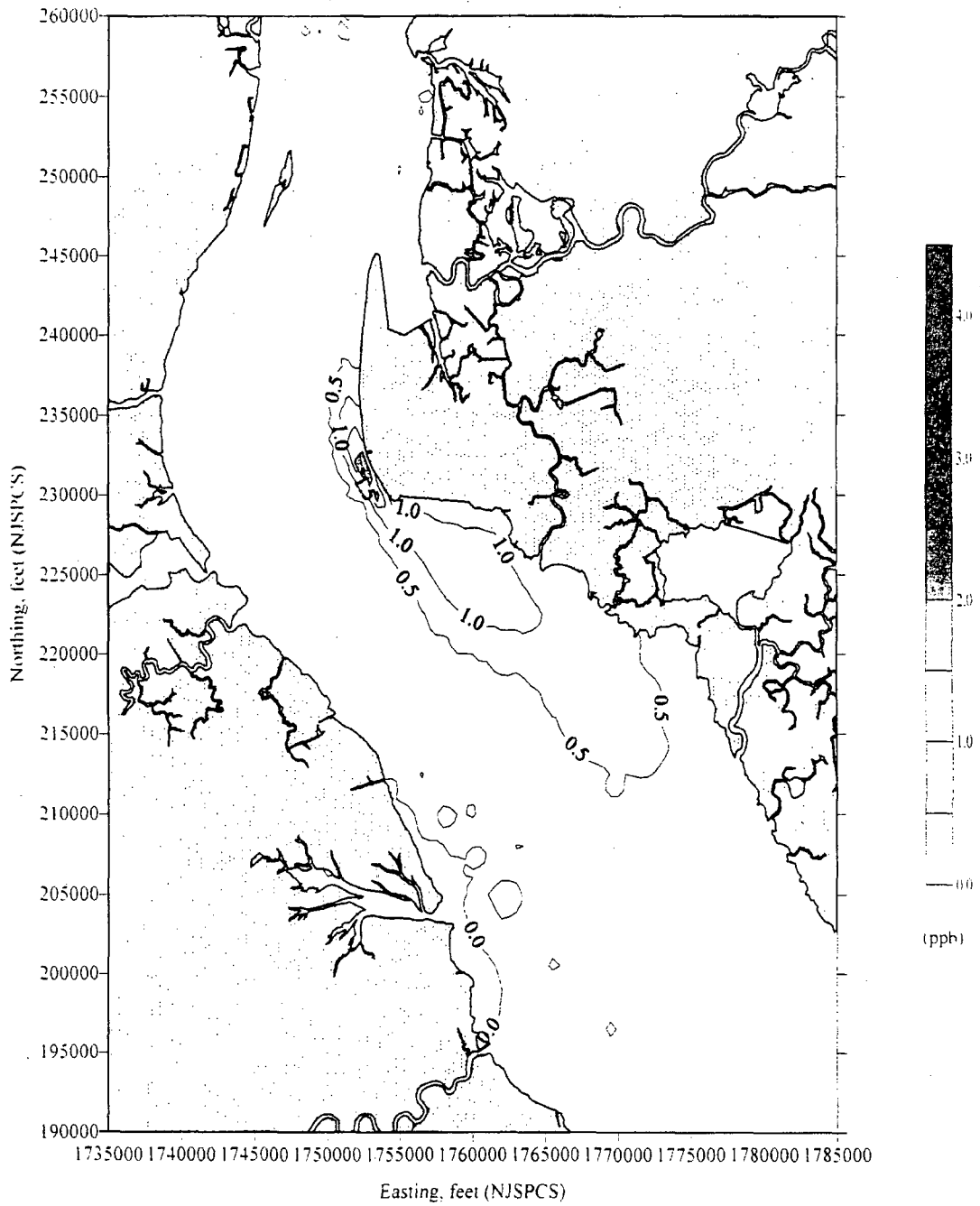
E-2 Figure III-109a. Contours of modeled surface dye for an ebb phase on 29 May 1998.



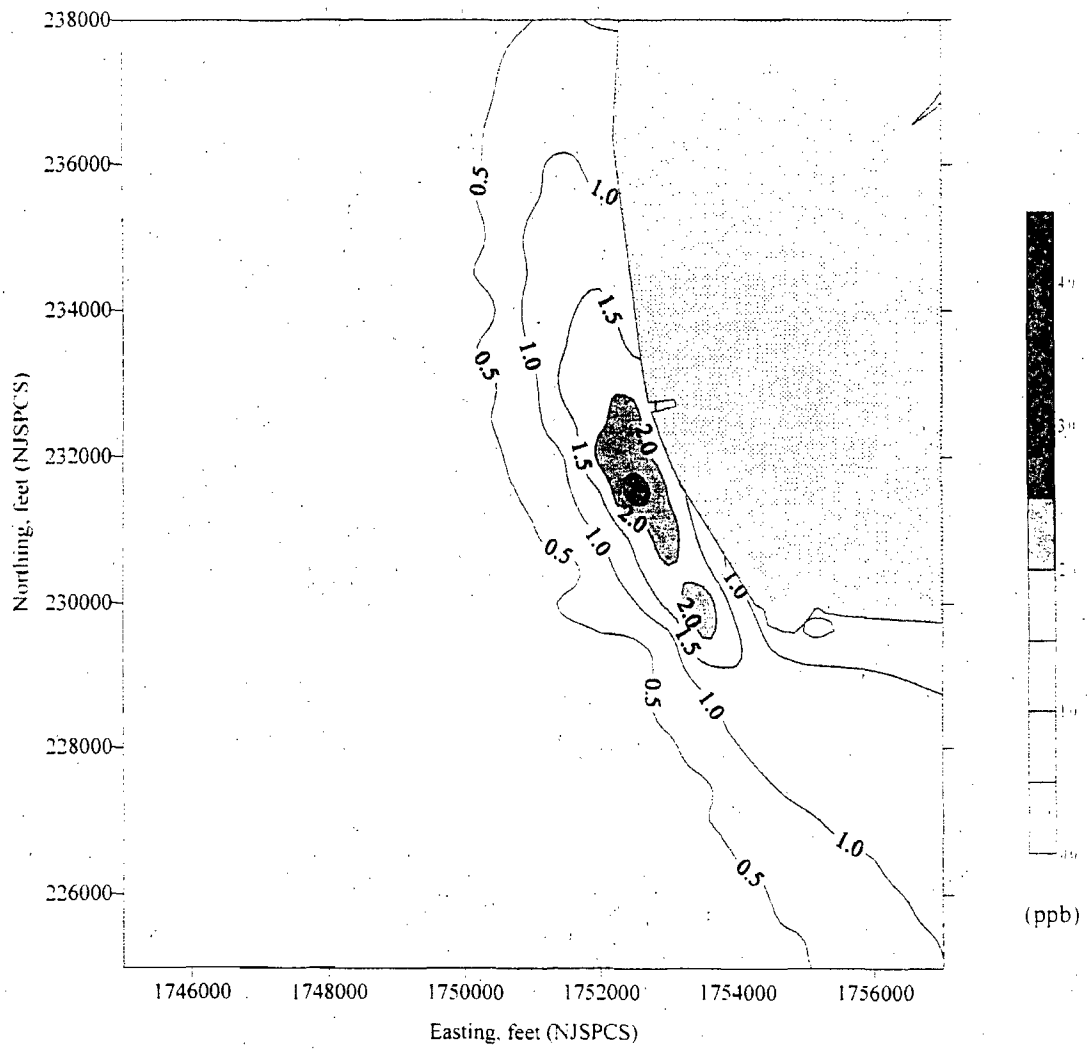
E-2 Figure III-95b. Contours of modeled surface temperatures for a flood phase on 28 October 1997 (close-up view).



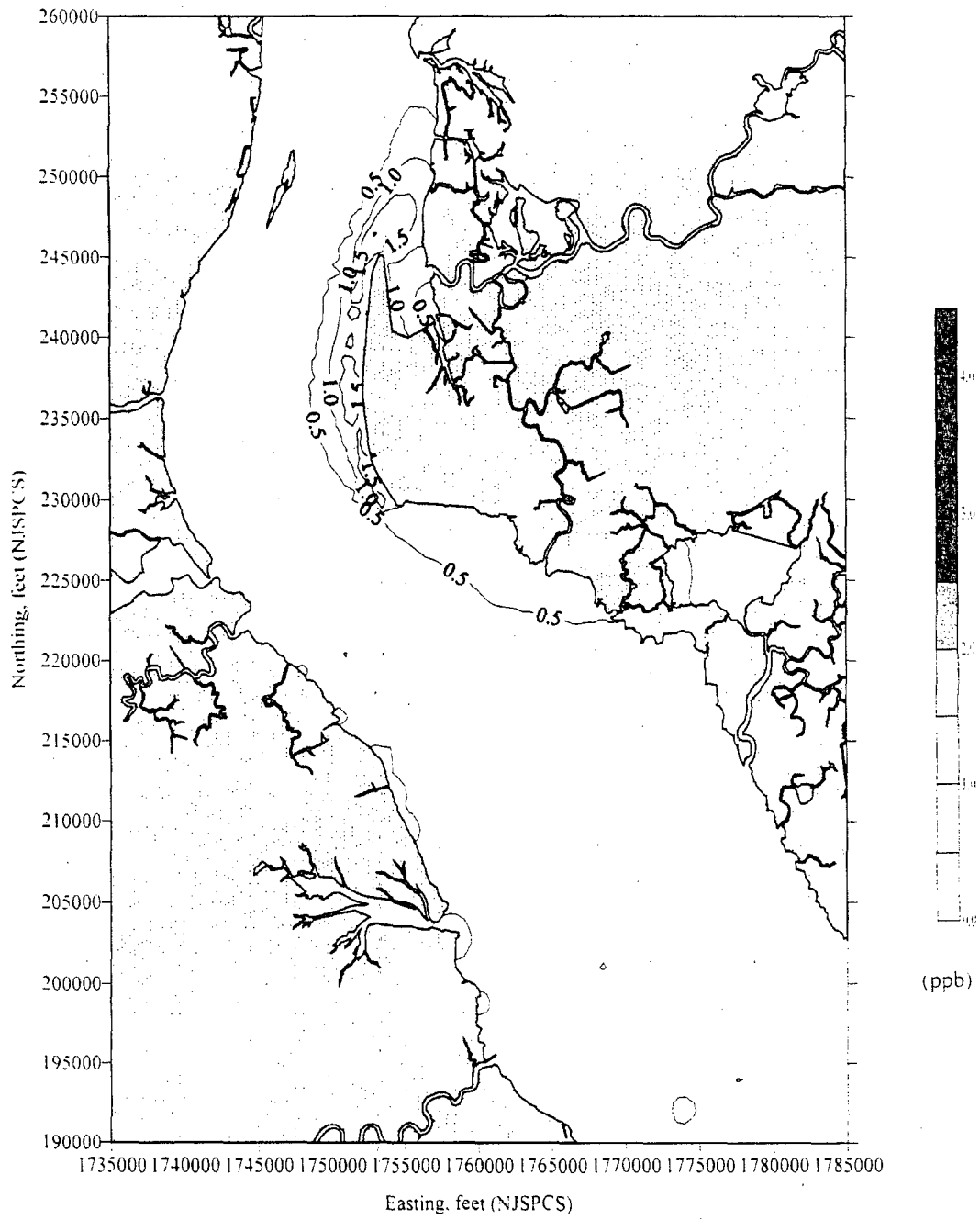
E-2 Figure III-109b. Contours of modeled surface dye for an ebb phase on 29 May 1998 (close-up view).



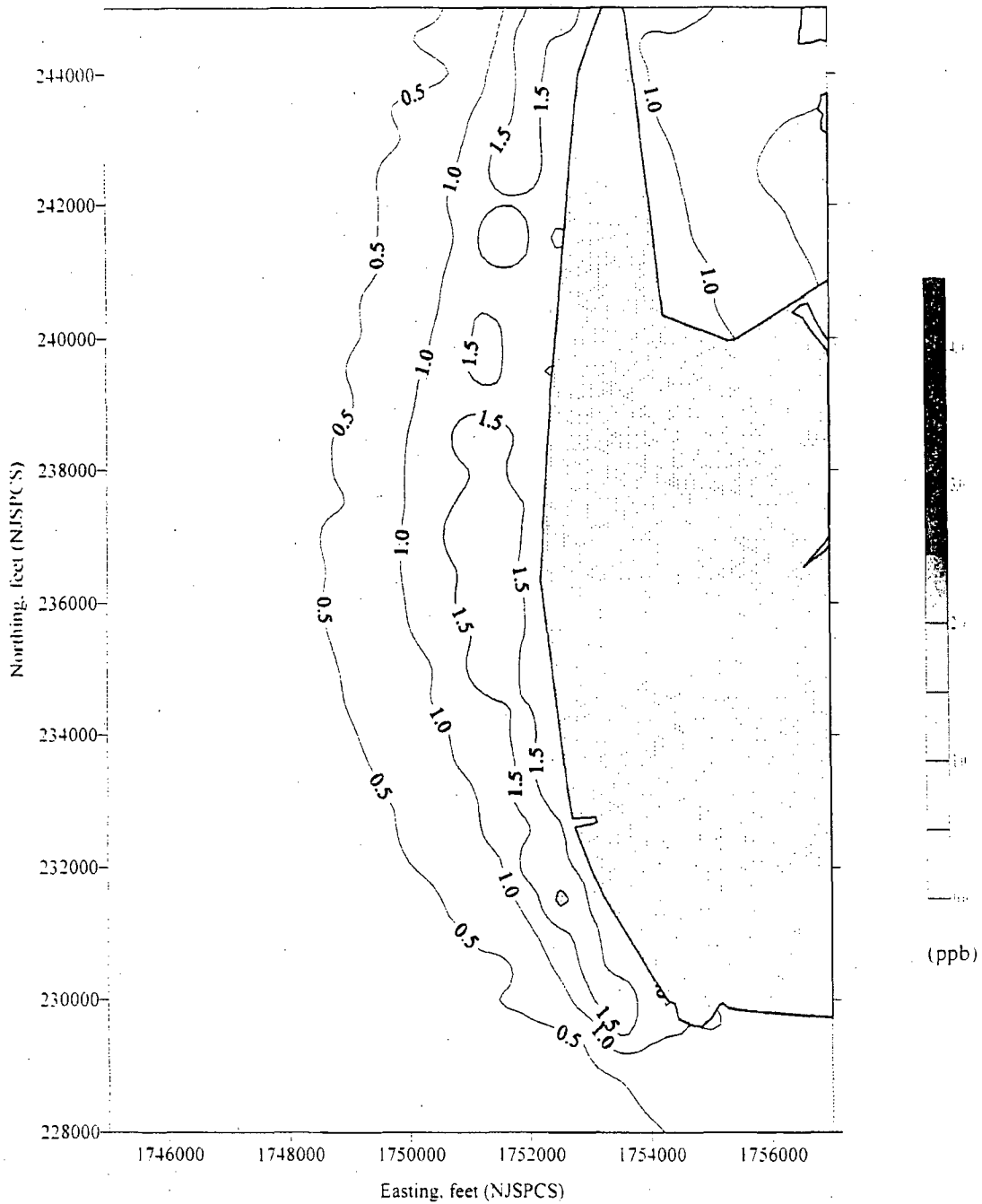
E-2 Figure III-110a. Contours of modeled surface dye for a slack phase (end-of-ebb) on 29 May 1998.



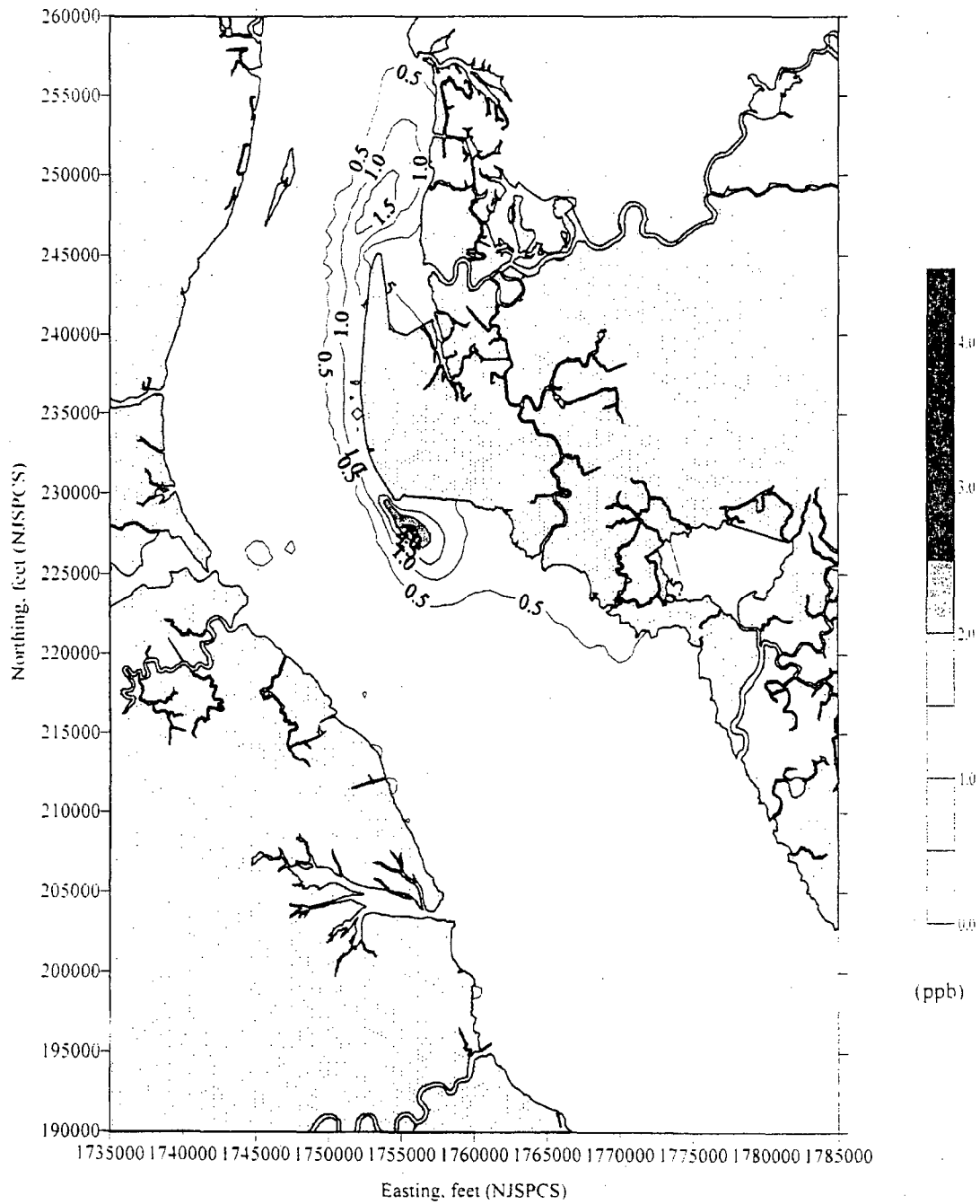
E-2 Figure III-110b. Contours of modeled surface dye for a slack phase (end-of-ebb) on 29 May 1998 (close-up view).



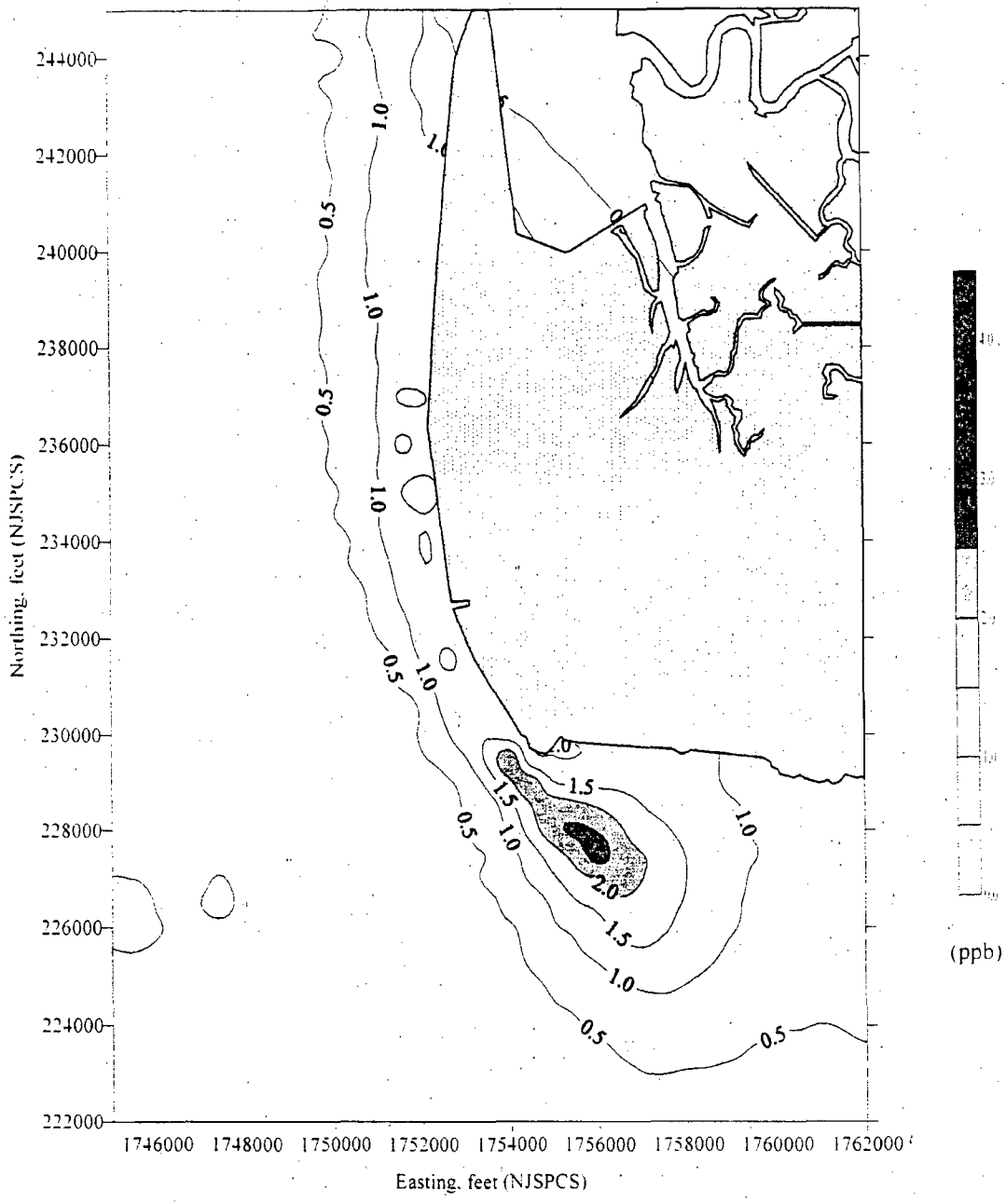
E-2 Figure III-111a. Contours of modeled surface dye for a flood phase on 29 May 1998.



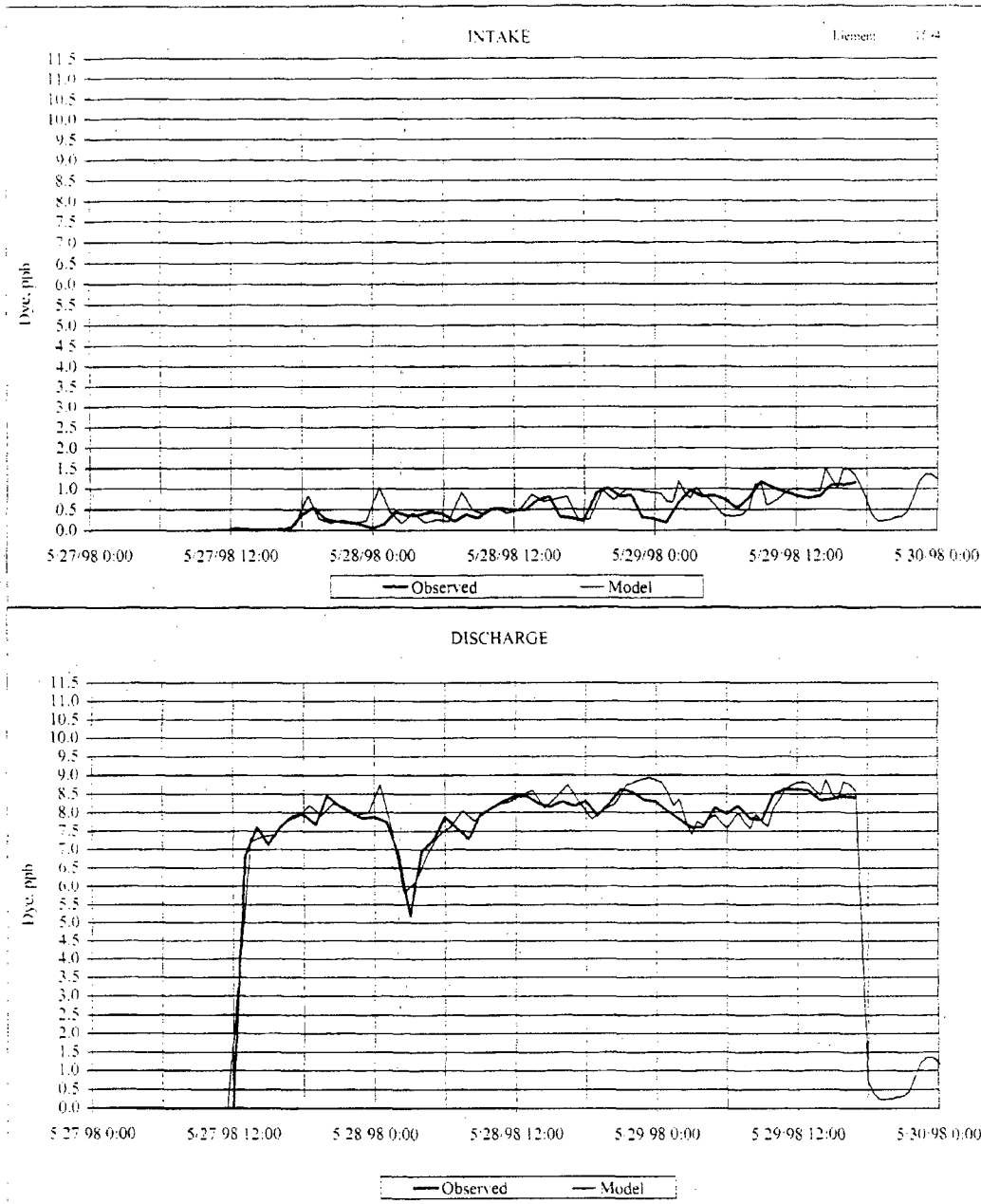
E-2 Figure III-111b. Contours of modeled surface dye for a flood phase on 29 May 1998 (close-up view).



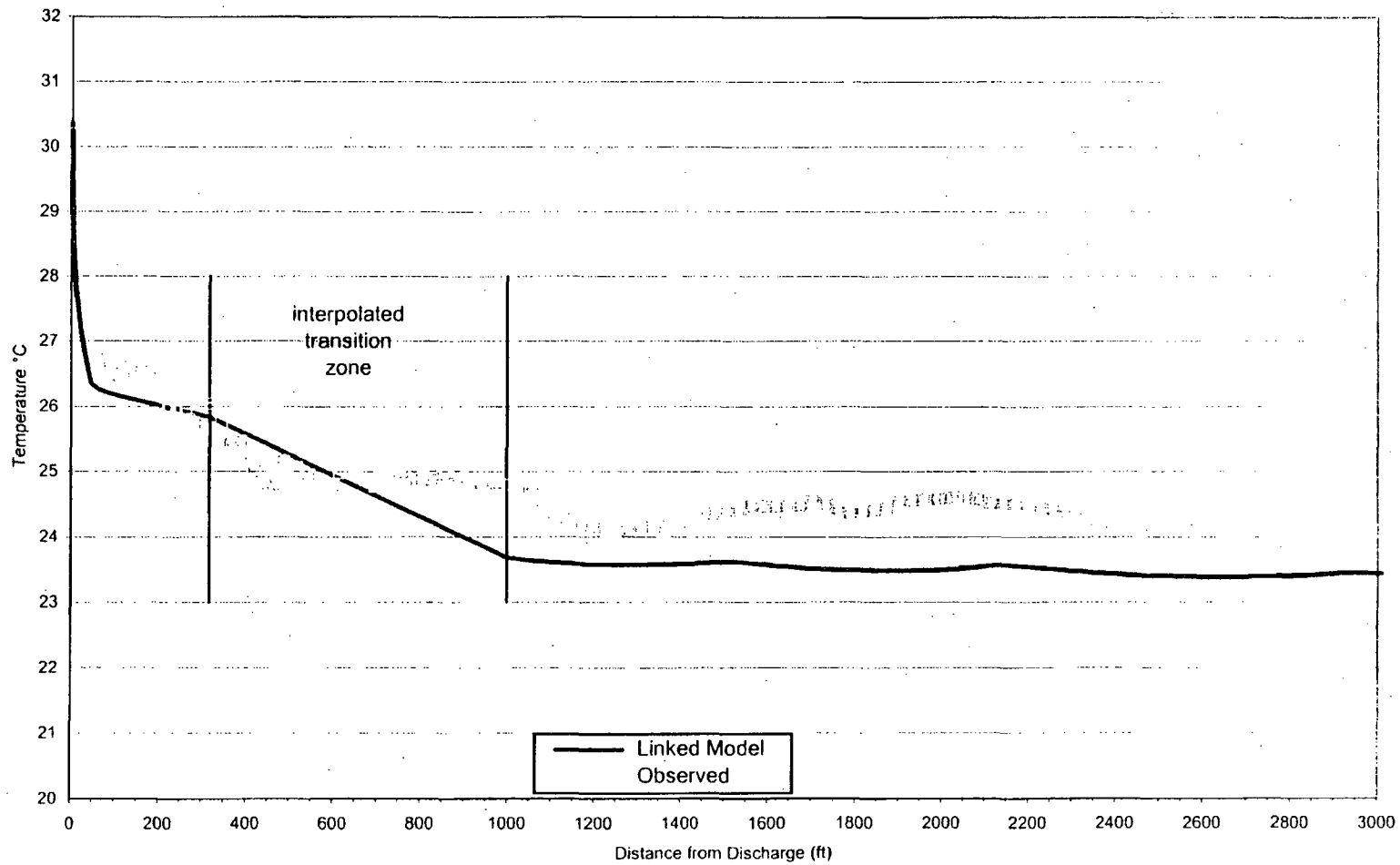
E-2 Figure III-112a. Contours of modeled surface dye for a slack phase (end-of-flood) on 29 May 1998.



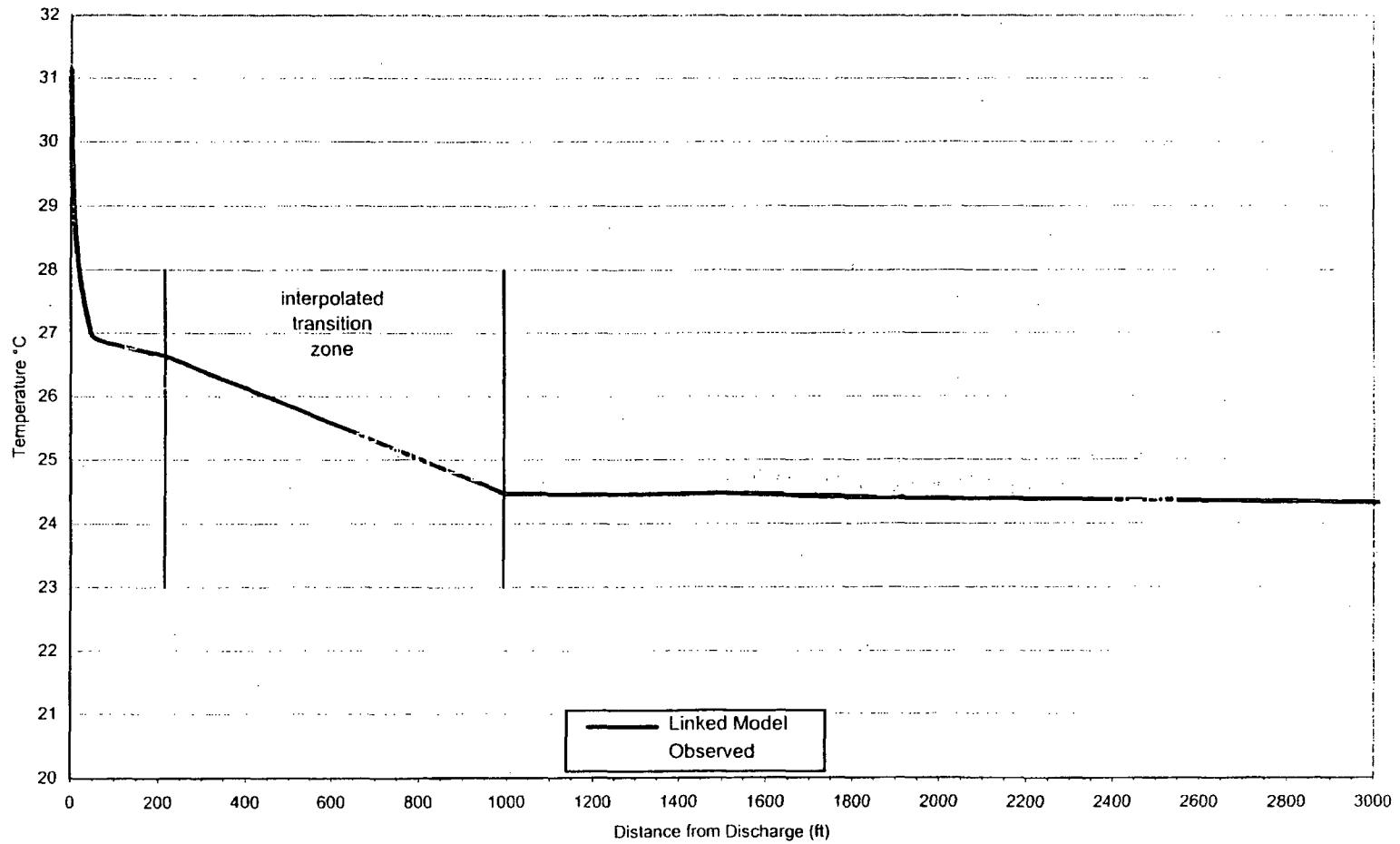
E-2 Figure III-112b. Contours of modeled surface dye for a slack phase (end-of-flood) on 29 May 1998 (close-up view).



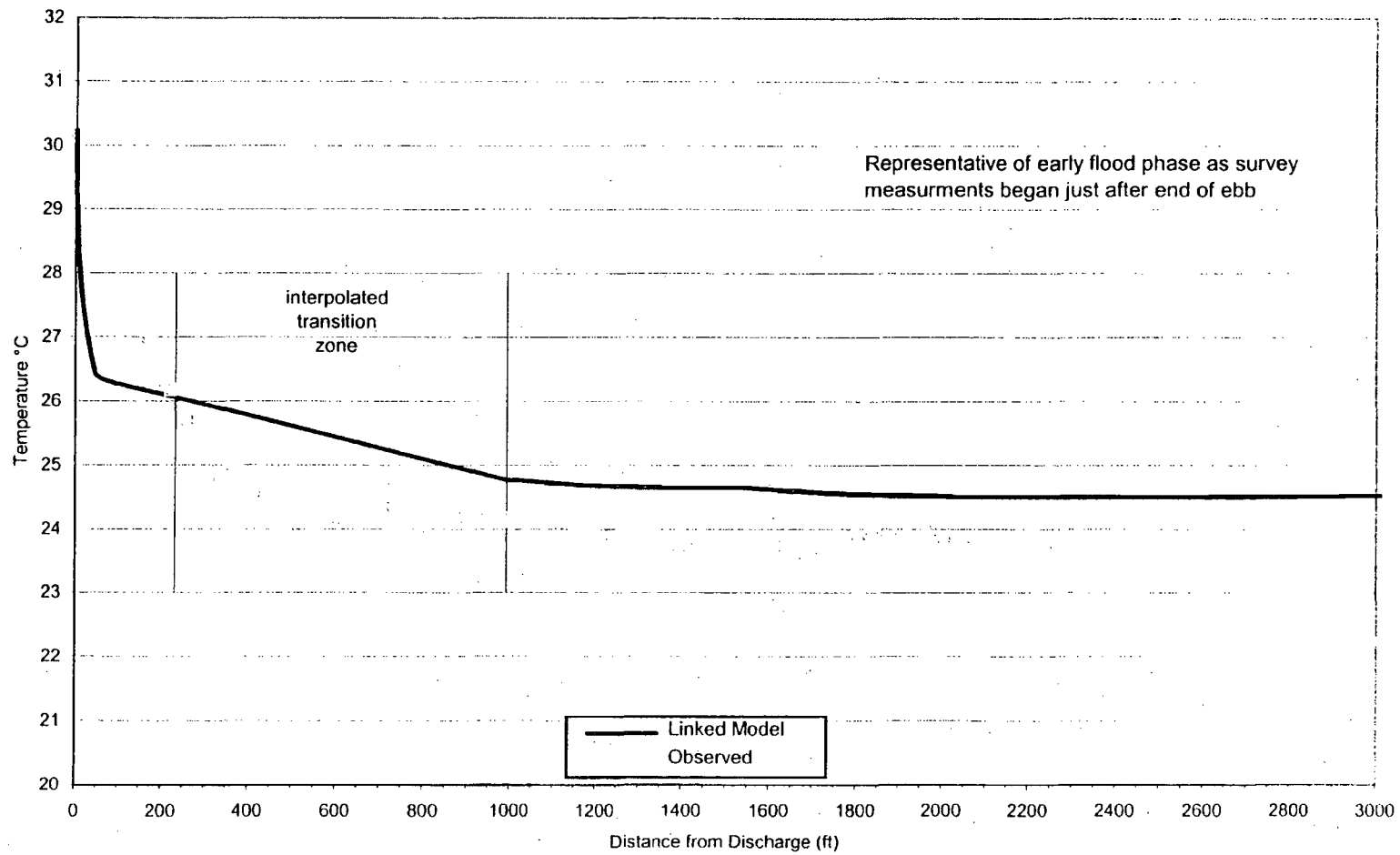
E-2 Figure III-113. Comparison of modeled and measured Station intake and discharge dye concentrations for the calibration period (27-30 May 1998).



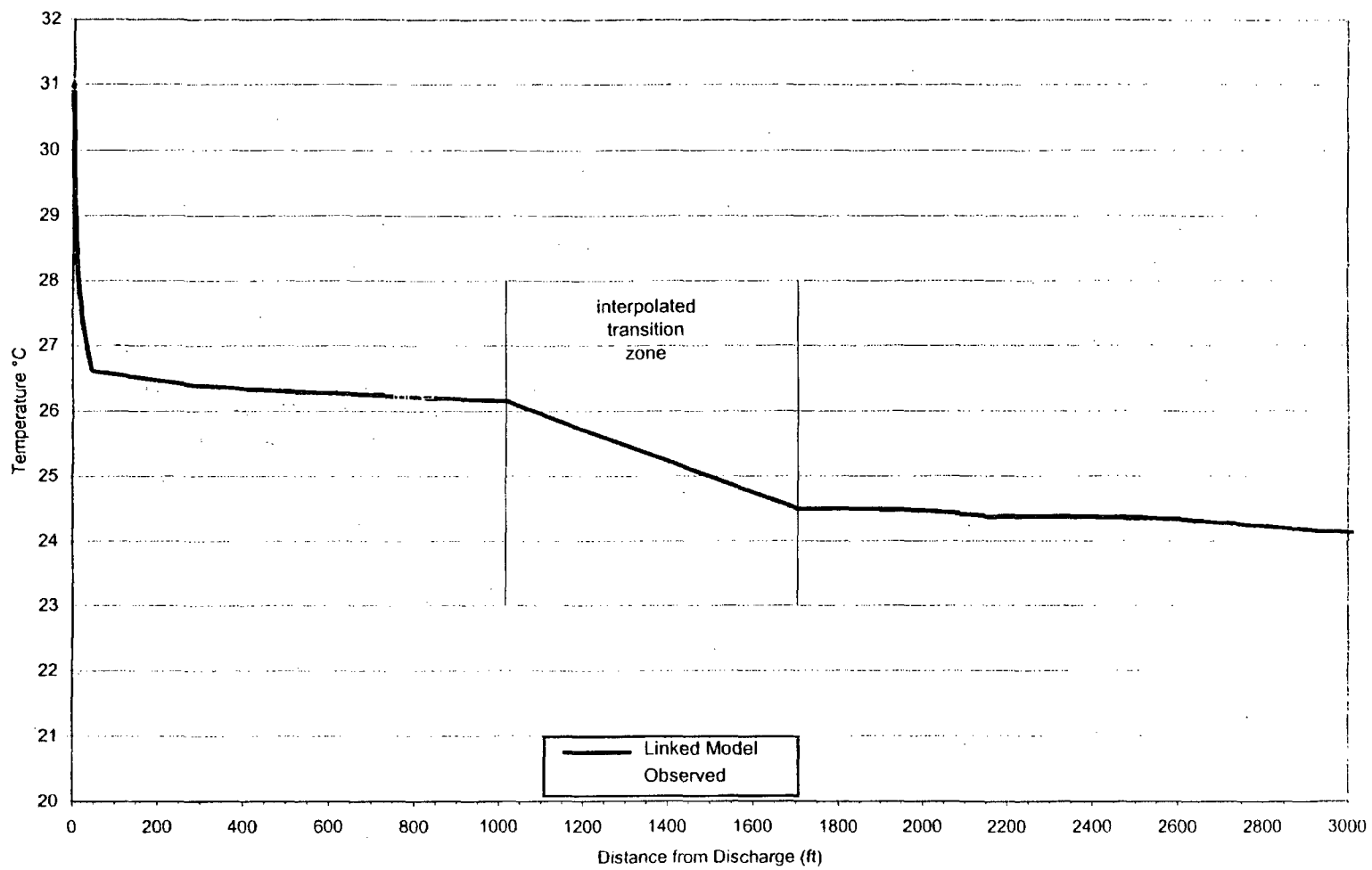
E-2 Figure III-114. Linkage results for the ebb tidal phase (29 May 1998 model calibration period).



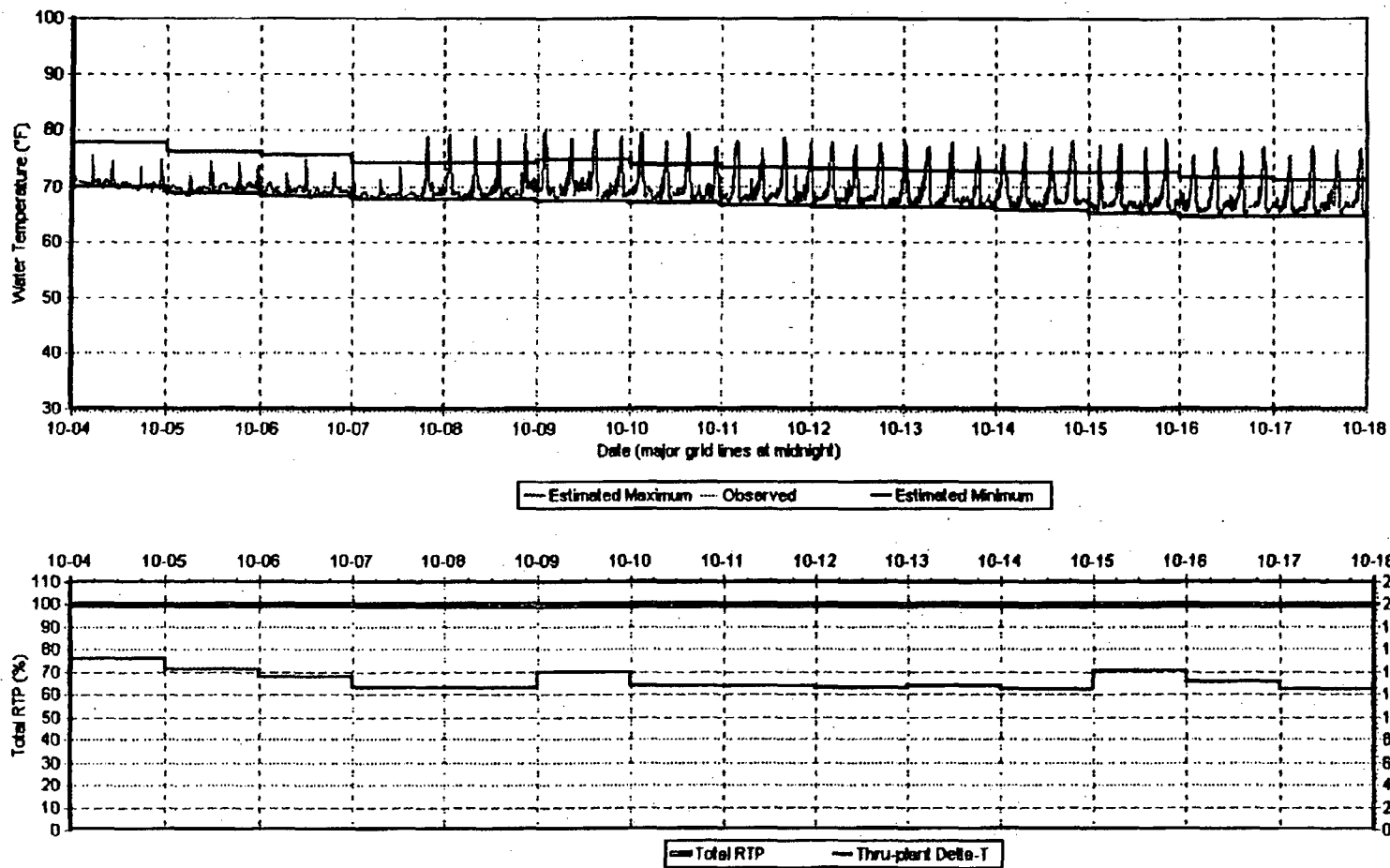
E-2 Figure III-115. Linkage results for the flood tidal phase (29 May 1998 model calibration period).



E-2 Figure III-116. Linkage results for the end of ebb tidal phase (29 May 1998 model calibration period).

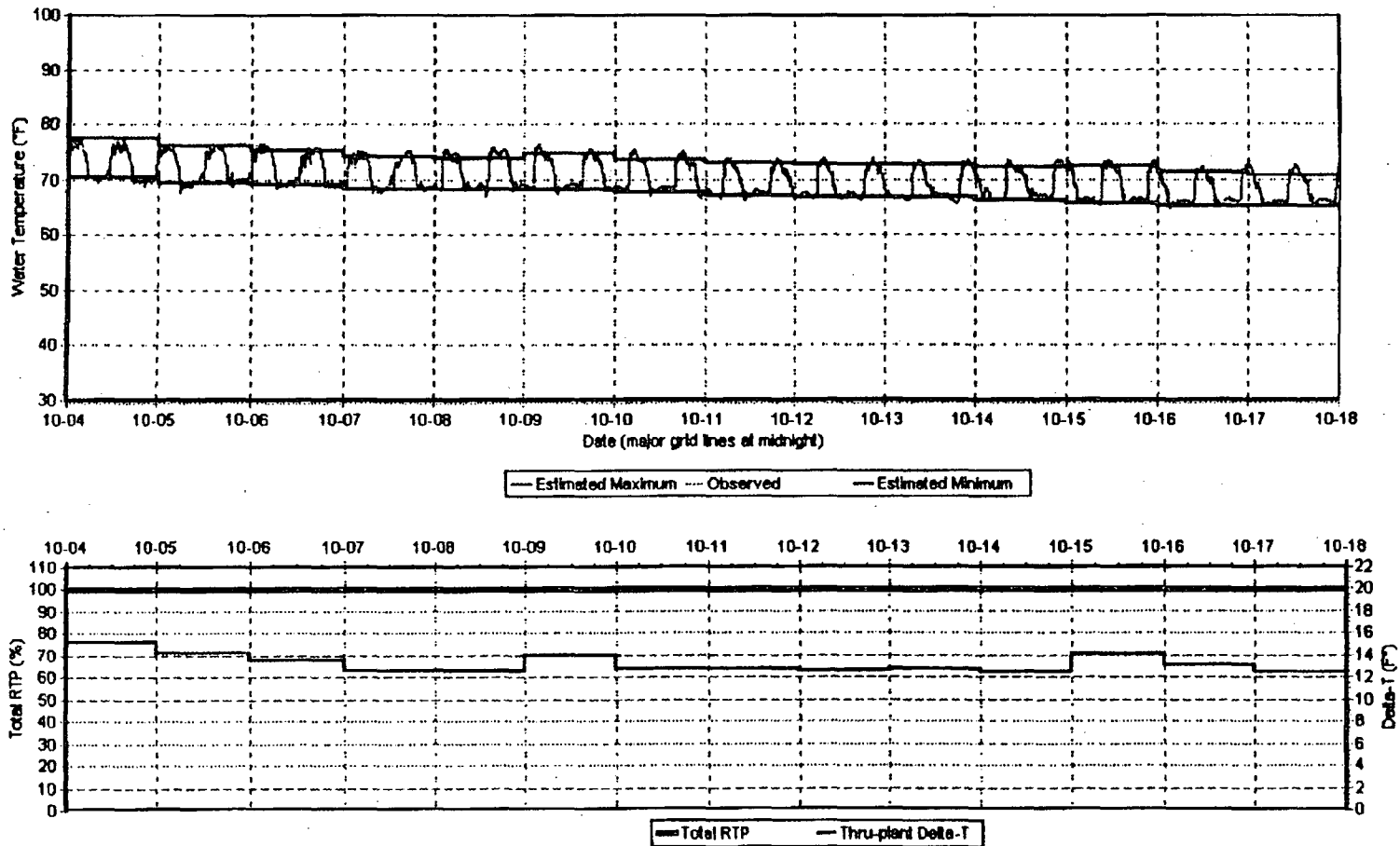


E-2 Figure III-117. Linkage results for the end of flood tidal phase (29 May 1998 model calibration period).

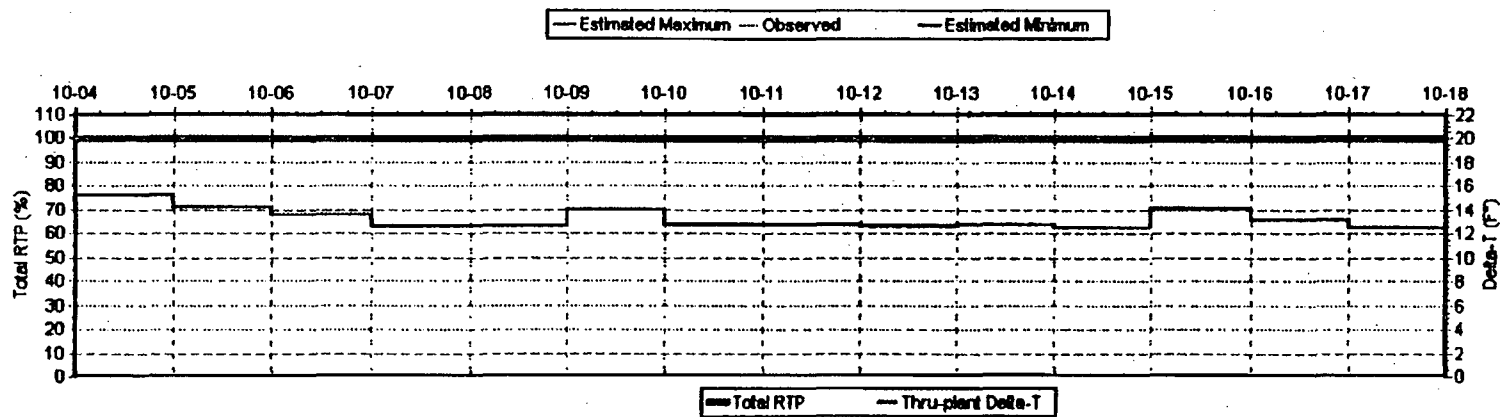
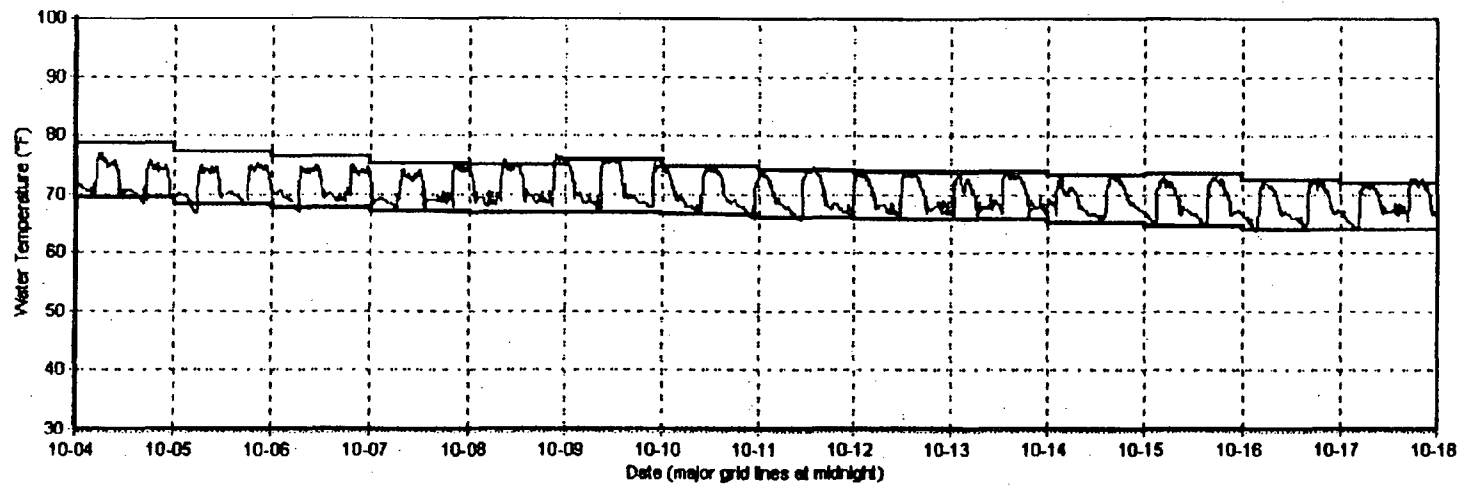


E-2 Figure III-118. Comparison of TTM results with observed mid-depth water temperatures at Mooring 24 (04 October 1998 through 17 October 1998).

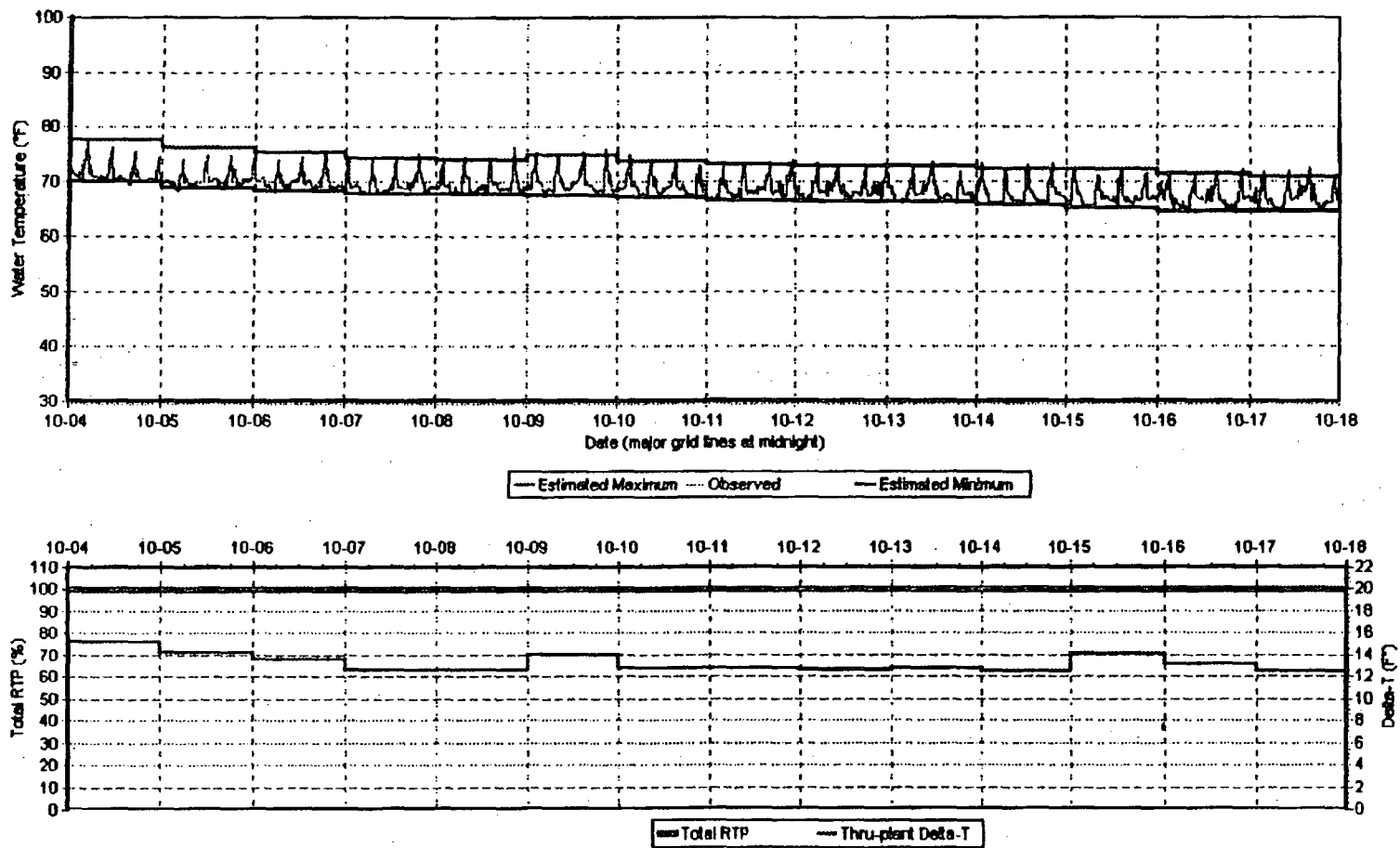
Mooring 24 Mid-Depth (down river from discharge)



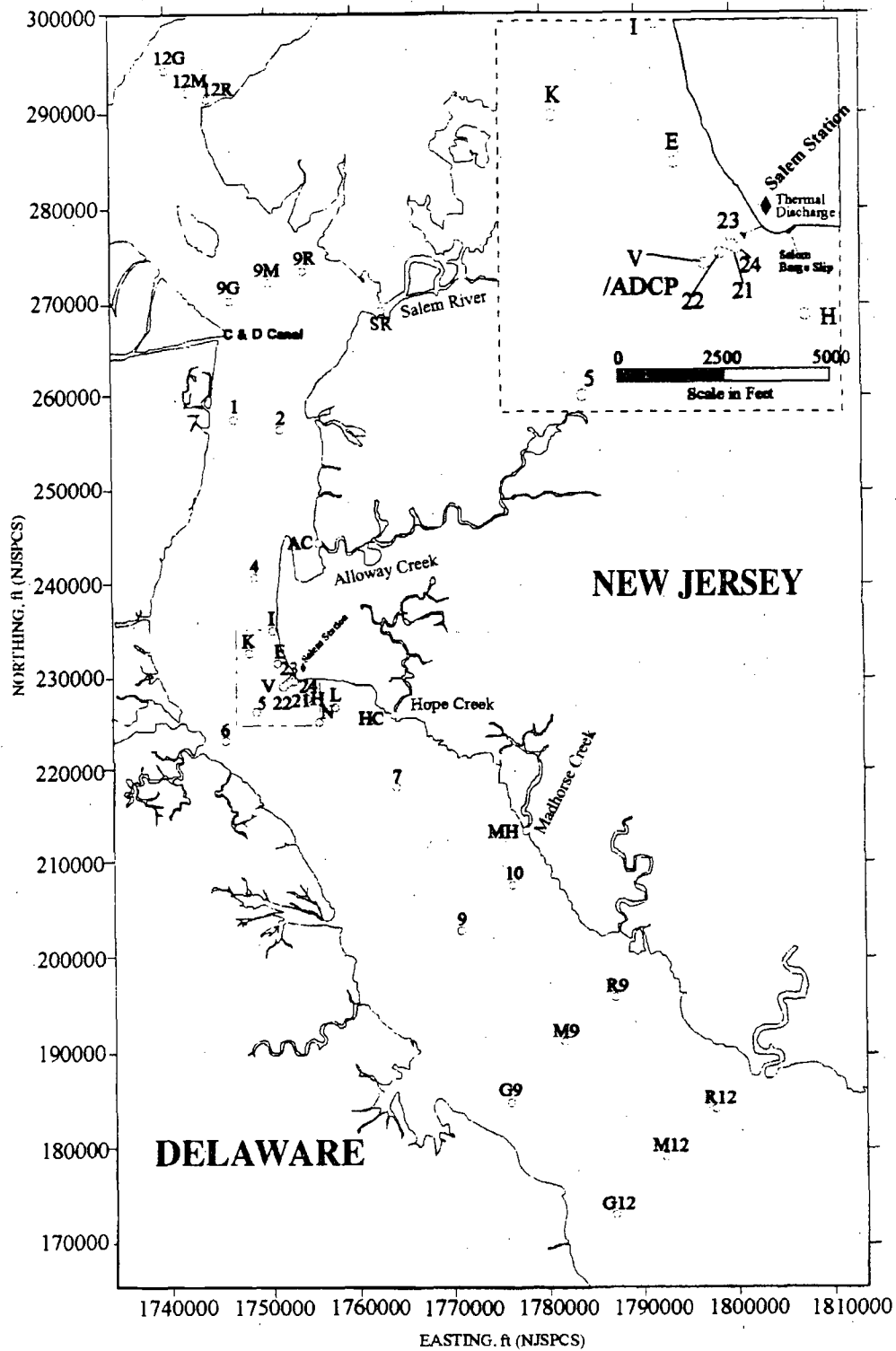
E-2 Figure III-119. Comparison of TTM results with observed surface water temperatures at Mooring 23 (04 October 1998 through 17 October 1998).



E-2 Figure III-120. Comparison of TTM results with observed surface water temperatures at Mooring 22 (04 October 1998 through 17 October 1998).

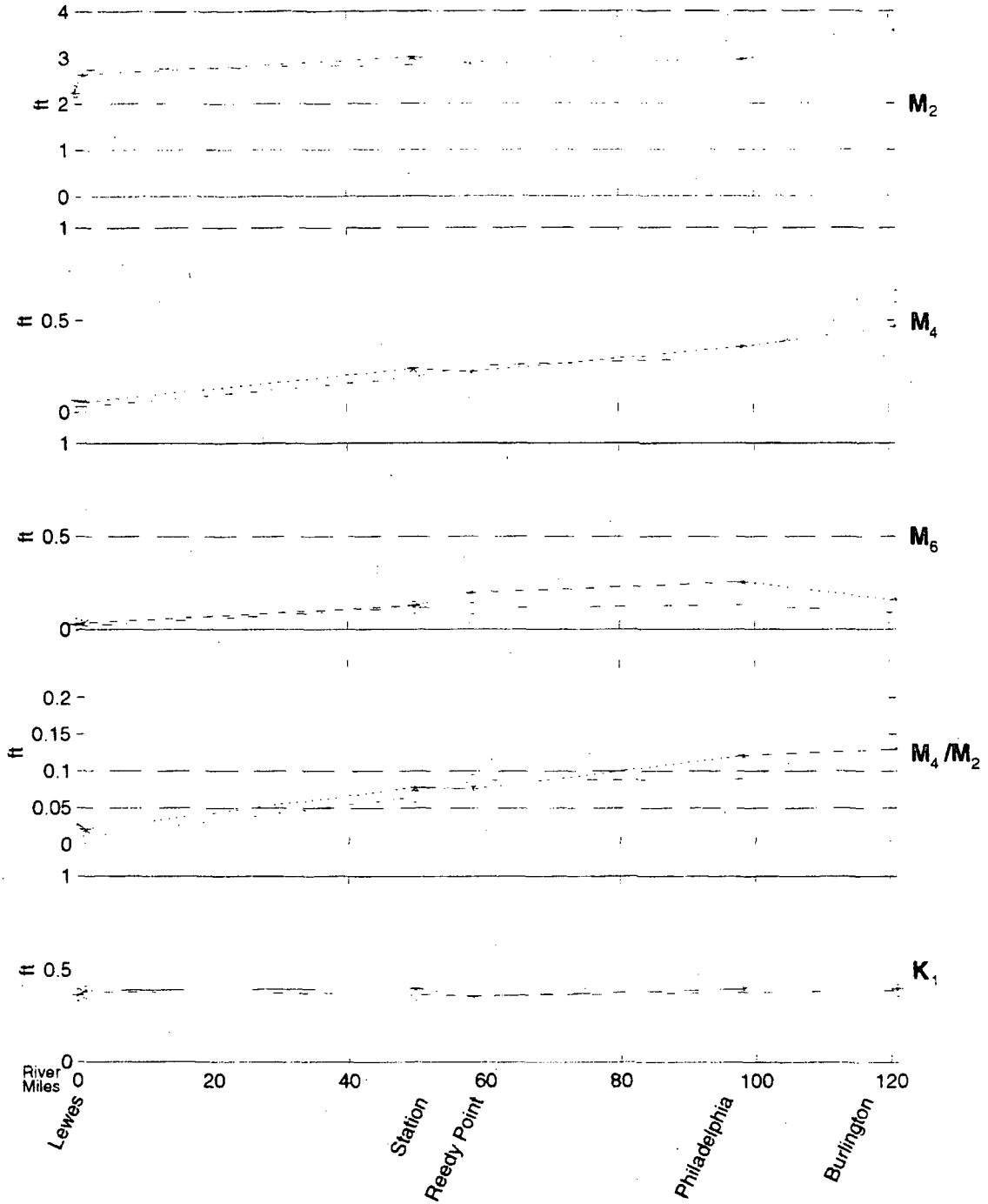


E-2 Figure III-121. Comparison of TTM results with observed bottom water temperatures at Mooring 21 (04 October 1998 through 17 October 1998).



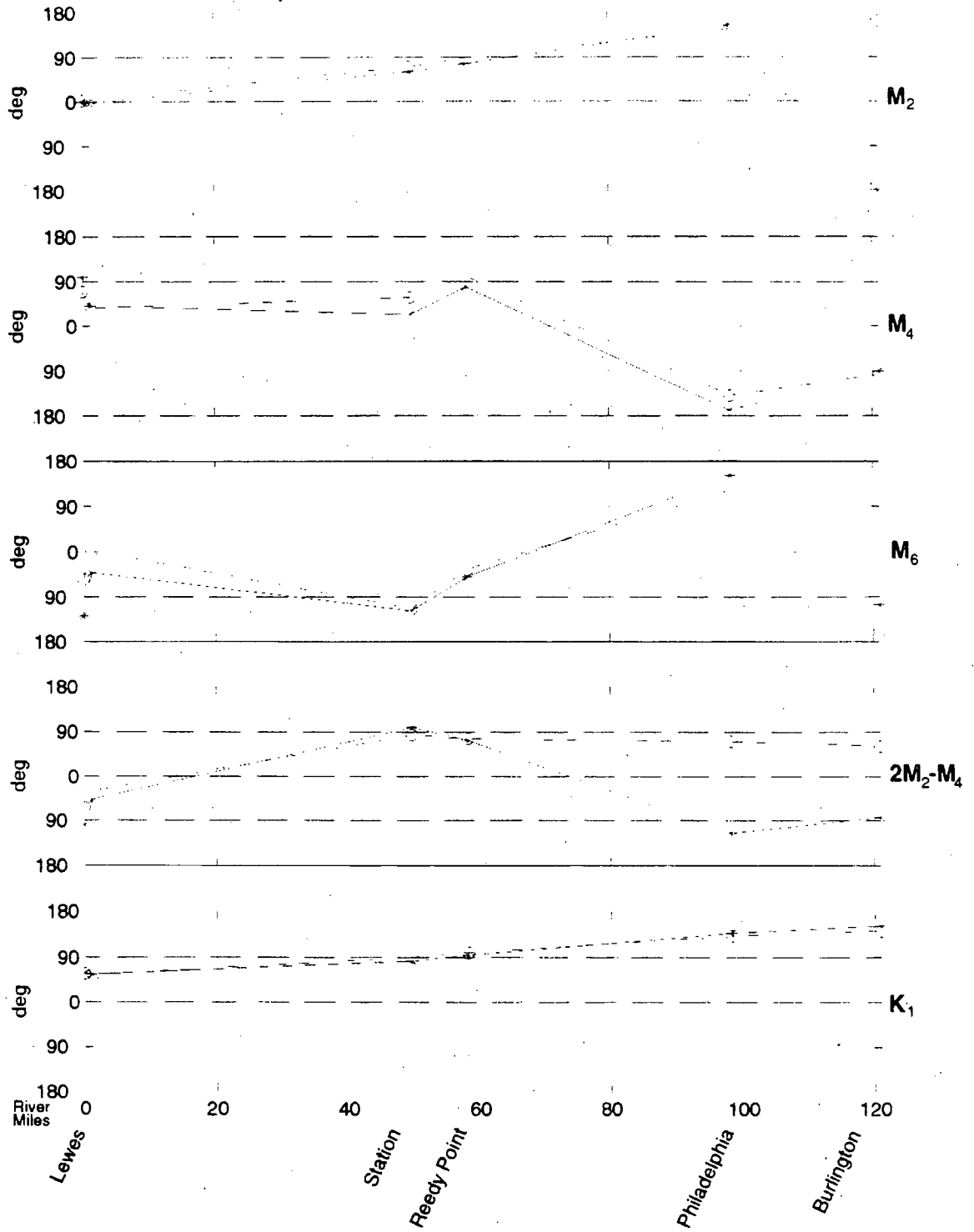
E-2 Figure IV-1. Map of Delaware Bay showing moored instrument station locations occupied during the Two-Unit Survey May-June 1998 (Exhibit E-1-3).

Comparison of Observed and Modeled Amplitude

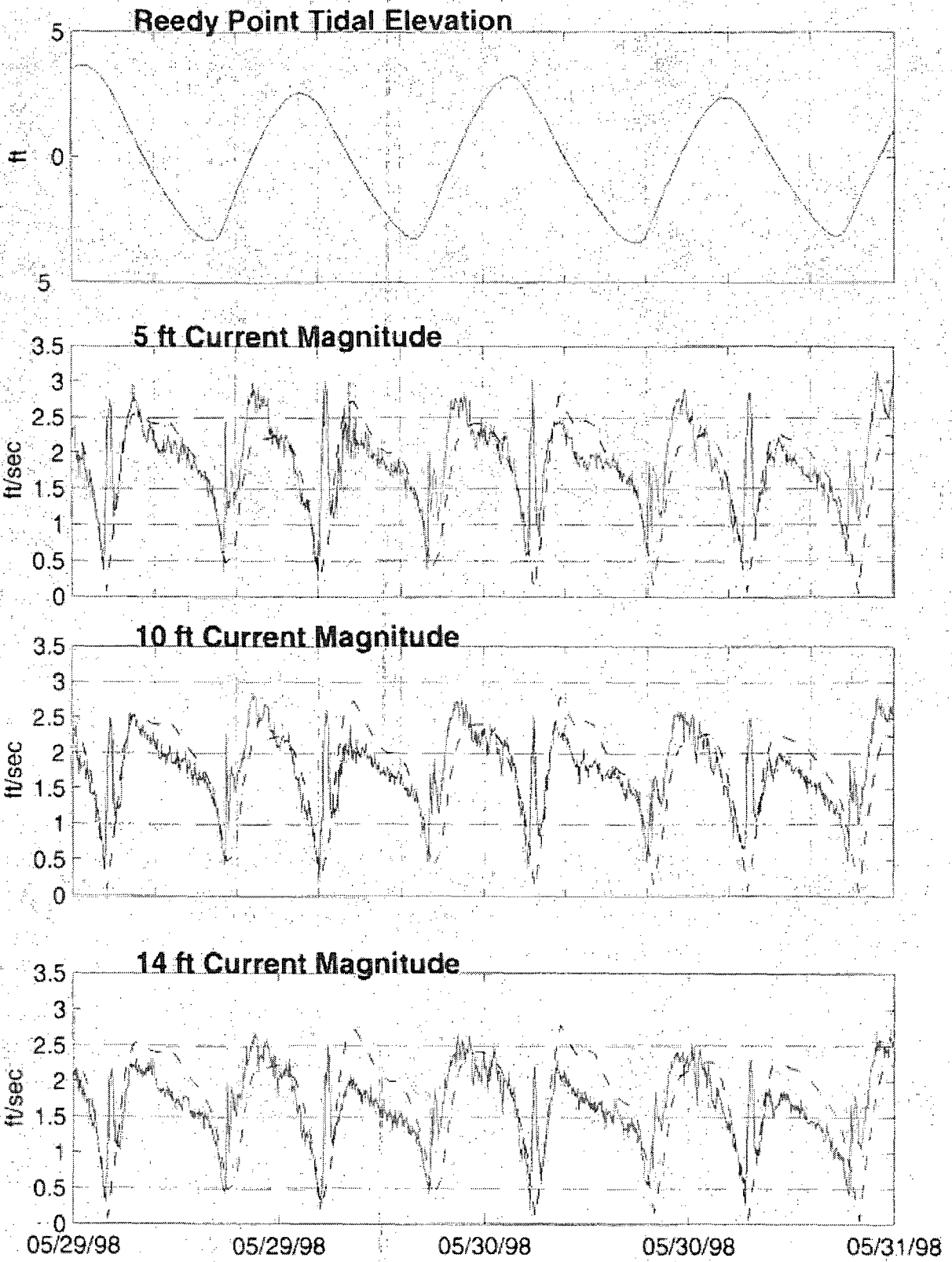


E-2 Figure IV-2a. Longitudinal variation of tidal harmonic constituents and nonlinear components along Delaware Bay: amplitudes.

Comparison of Observed and Modeled Phase

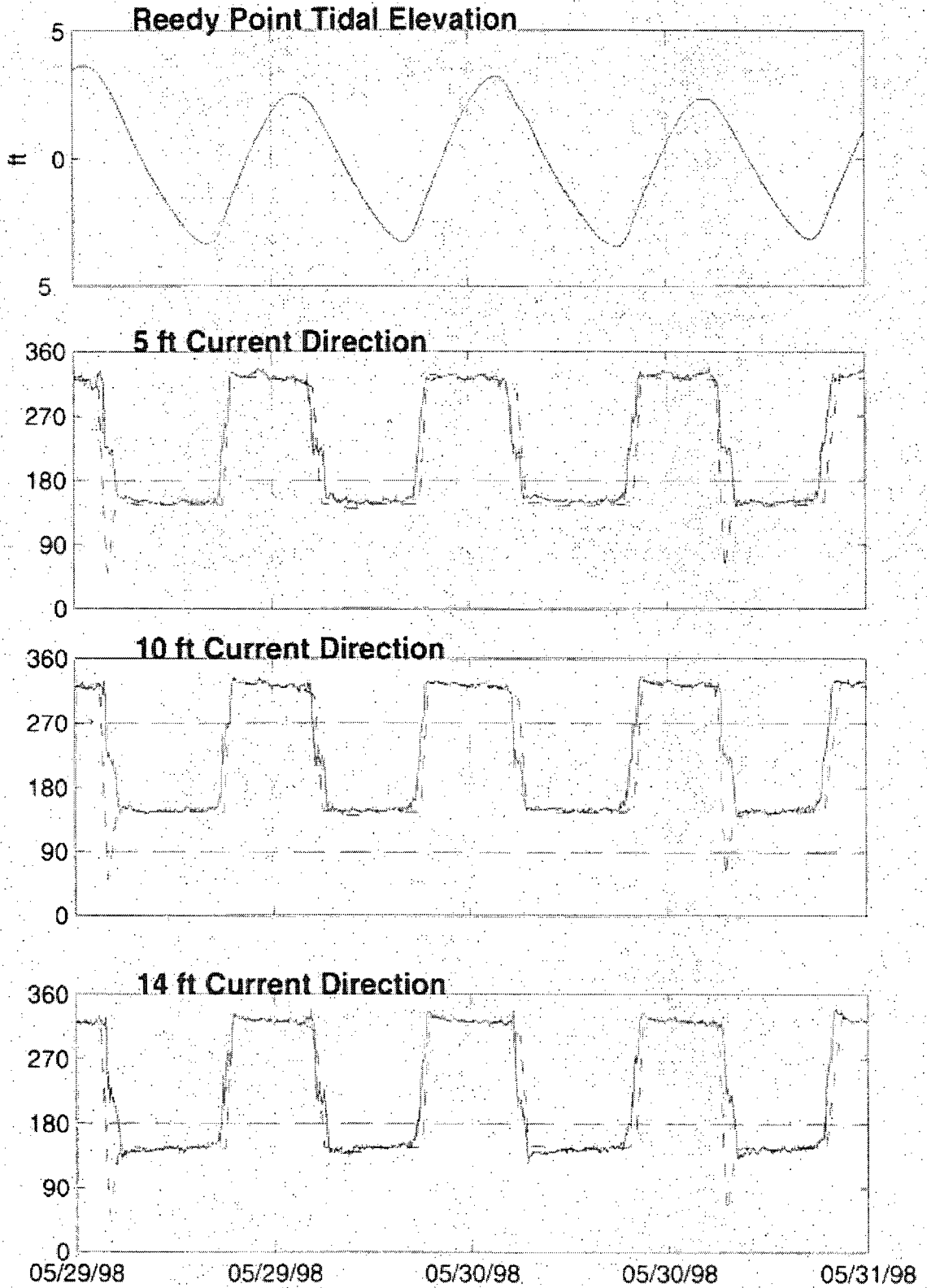


E-2 Figure IV-2b. Longitudinal variation of tidal harmonic constituents and nonlinear components along Delaware Bay: phases

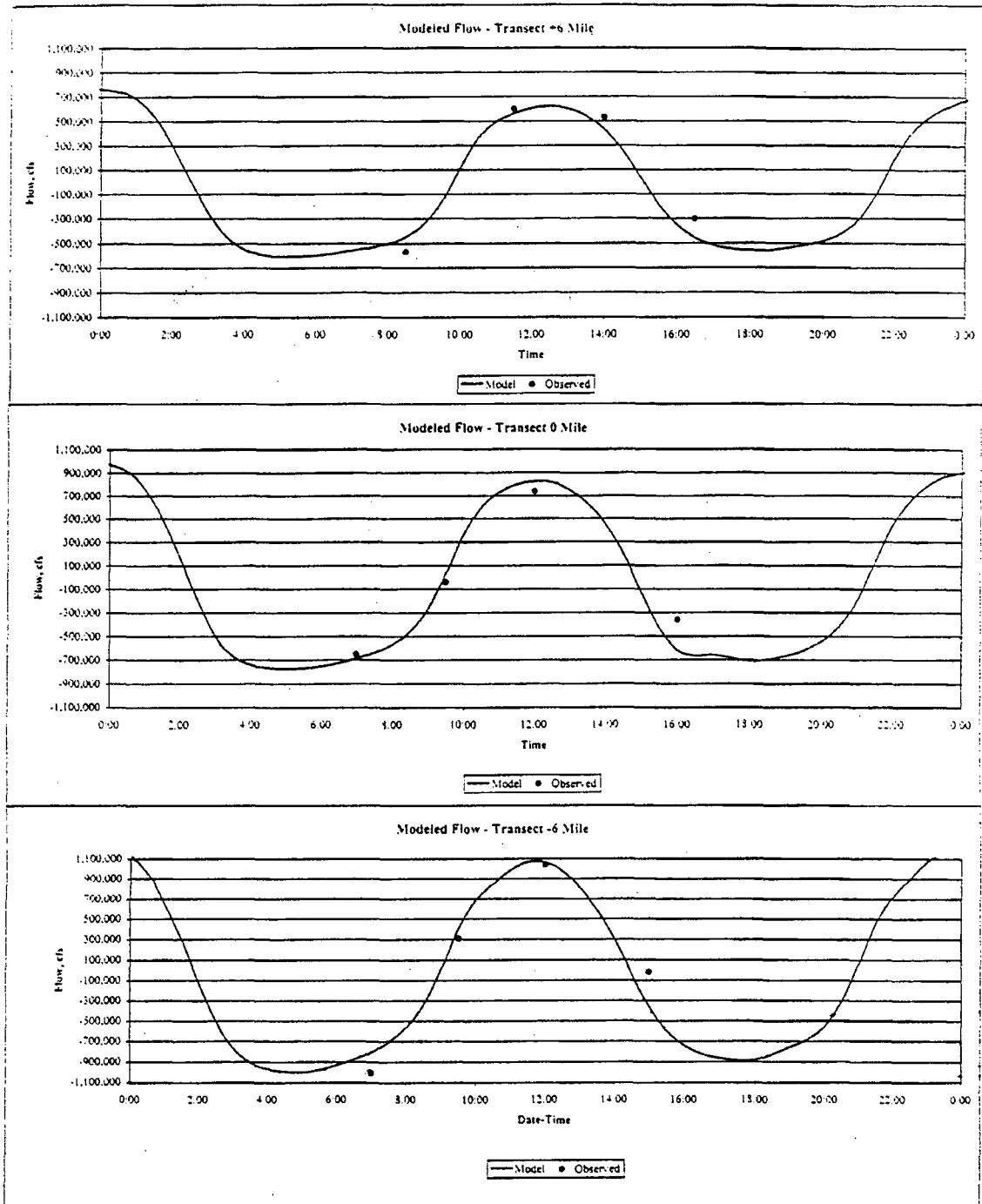


E-2 Figure IV-3a. Current time-series at near-surface, mid-depth, and near-bottom levels measured with an ADCP at mooring V (red), compared with model-predicted currents (black). a: Current Speed. Sea level measured at Salem Barge Slip is also shown.

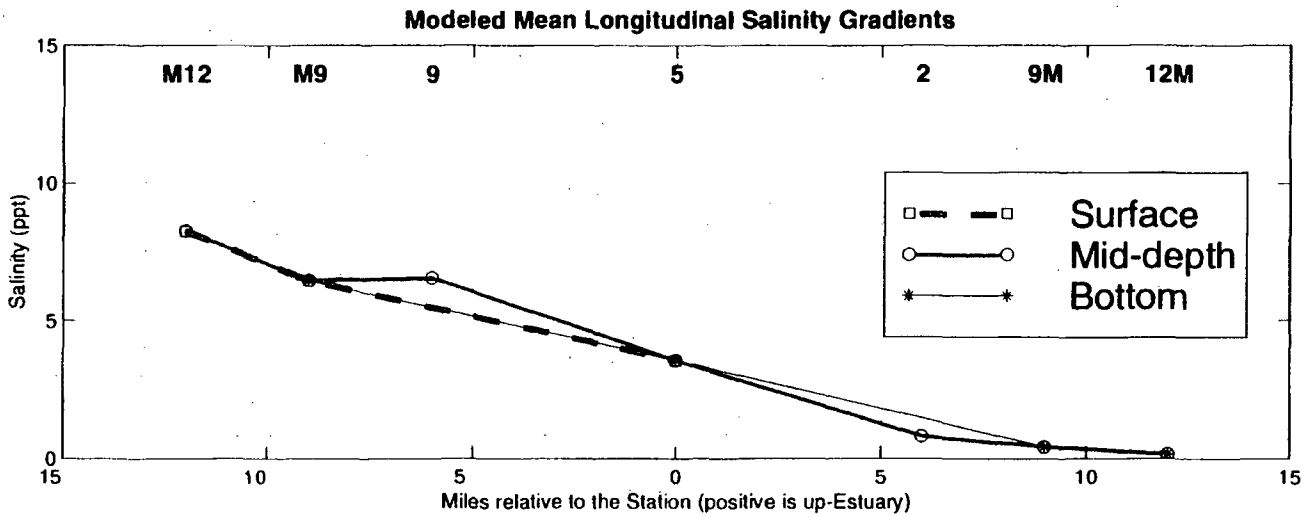
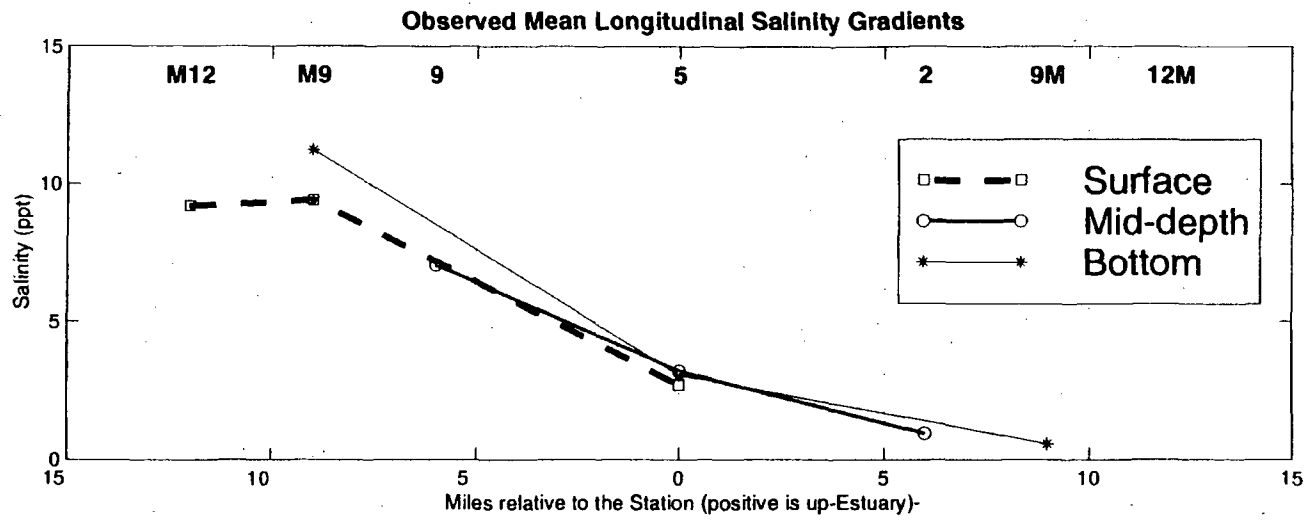
Bottom ADCP Currents



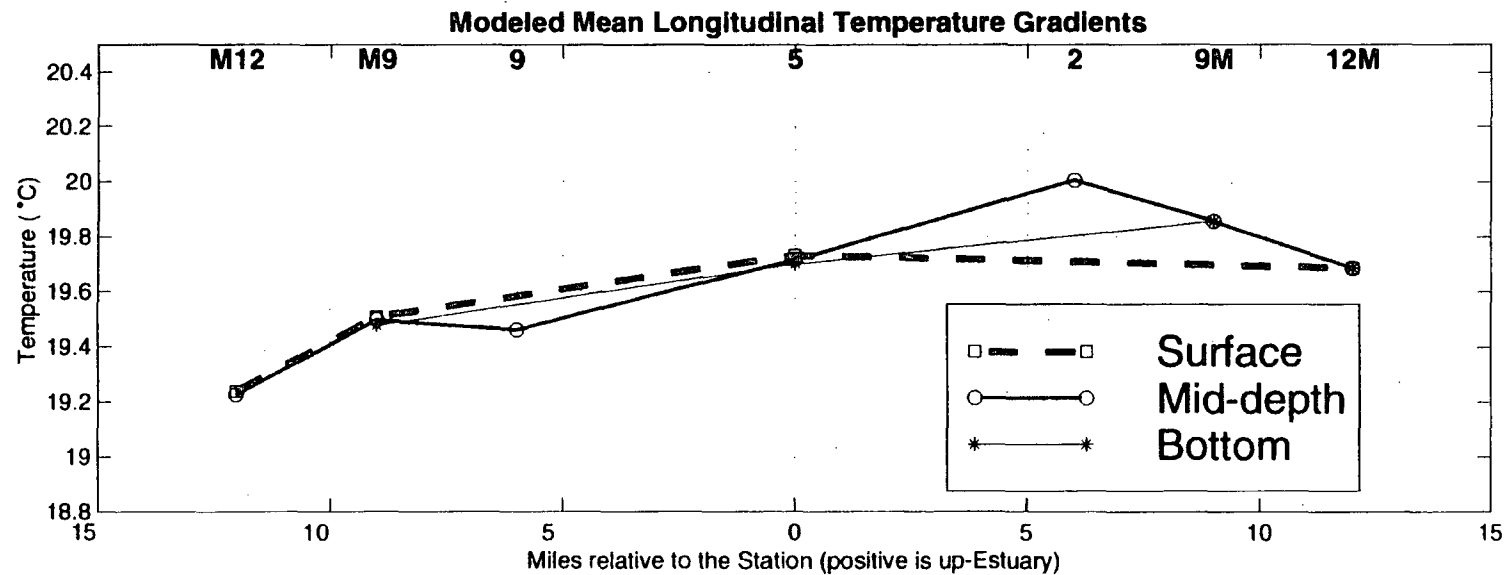
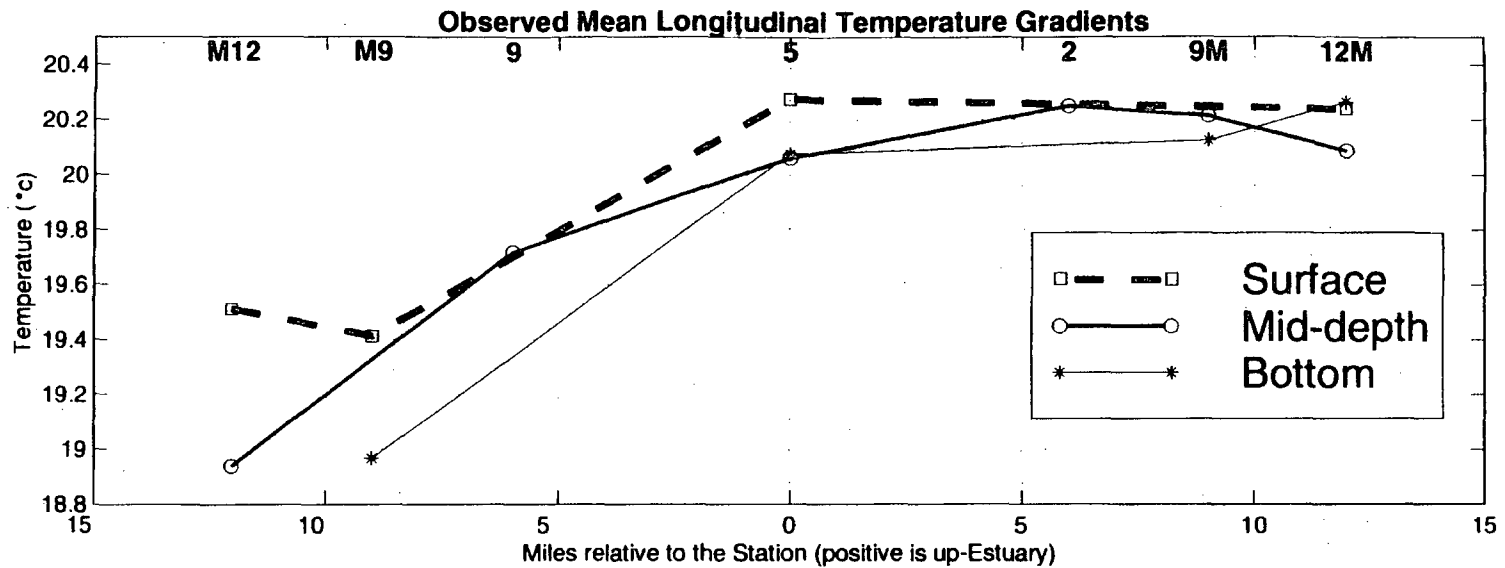
E-2 Figure IV-3b. Current time-series at near-surface, mid-depth, and near-bottom levels measured with an ADCP at mooring V (red), compared with model-predicted currents (black). b: Current Direction. Sea level measured at Salem Barge Slip is also shown.



E-2 Figure IV-4. Comparison of modeled and observed flow on 29 May 1998 at three cross-river transects located six miles upstream and downstream of the Station and at the Station. The curves show smoothed model predictions, and the plotted points are observed volume transport measurements from the vessel ADCP surveys (Exhibit E-1-3).

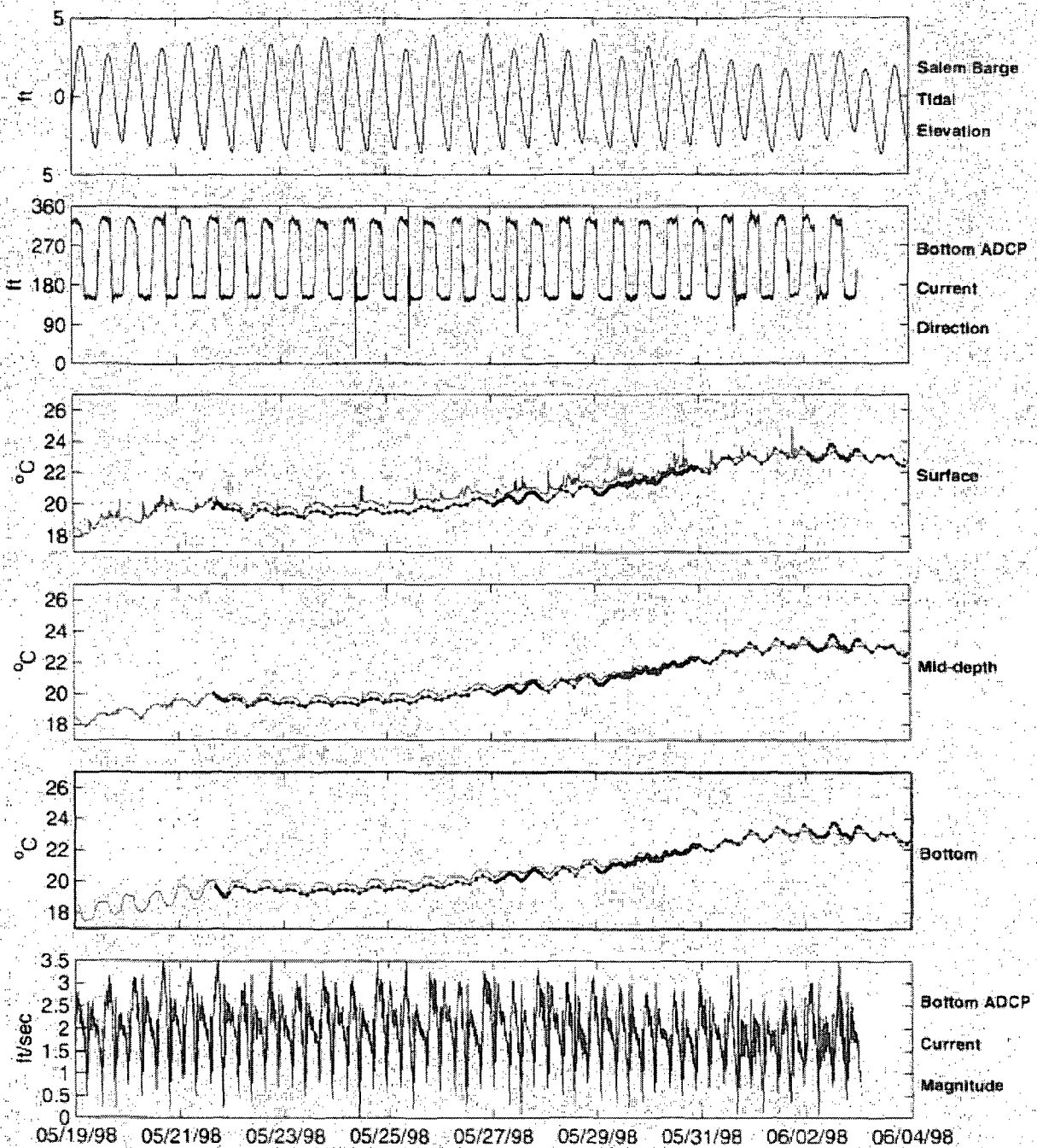


E-2 Figure IV-5. Observed (upper panel) and modeled (lower panel) mean longitudinal salinity structure of Delaware Bay. Mile 0 on this plot represents the location of the Station. The moorings shown are located at the east side of the main channel.

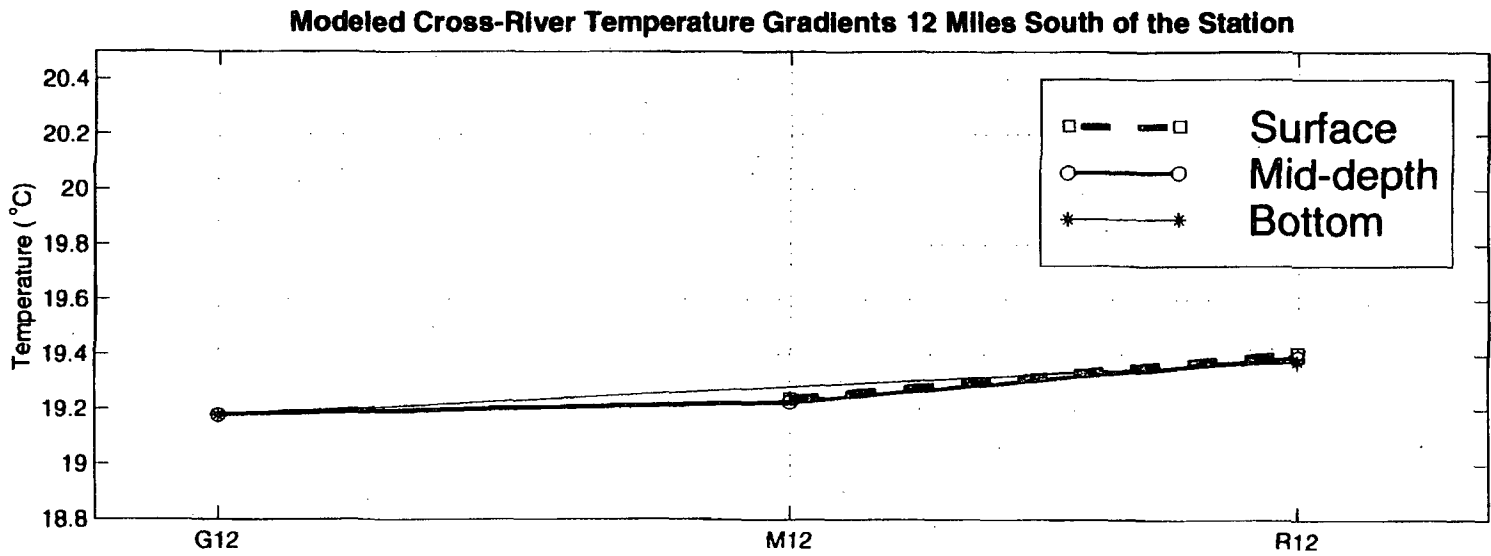
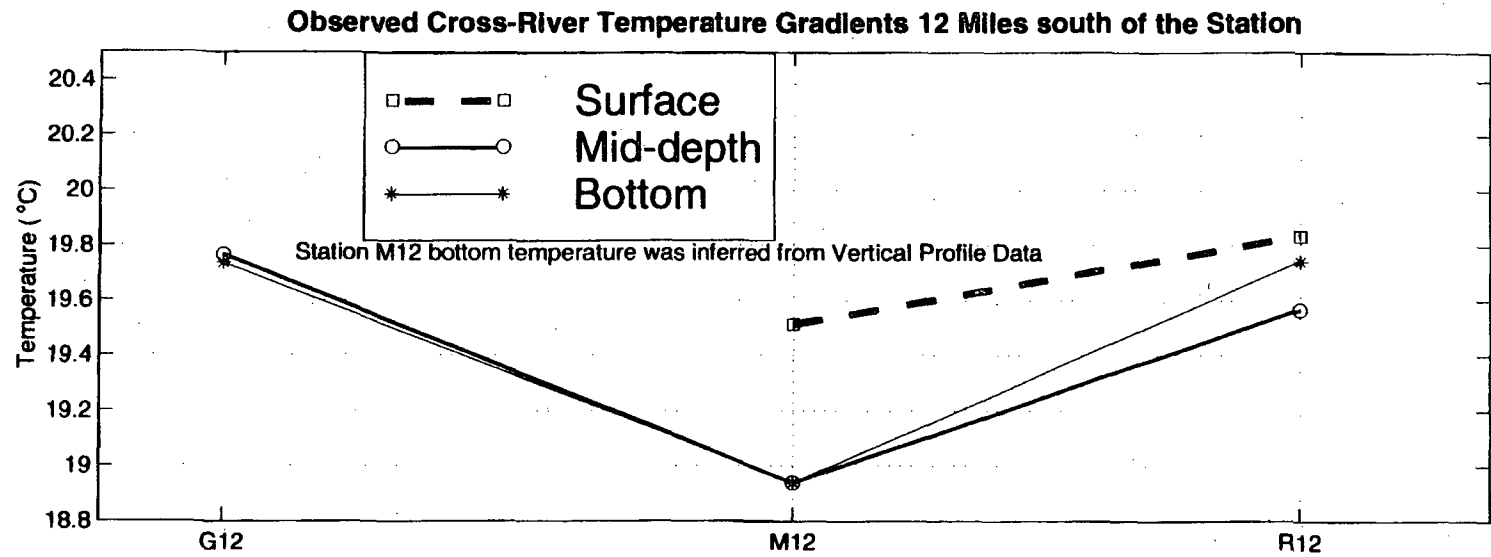


E-2 Figure IV-6. Observed and modeled mean longitudinal temperature structure of Delaware Bay. Mile 0 on this plot represents the location of the Station. The moorings shown are located at the east side of the main channel.

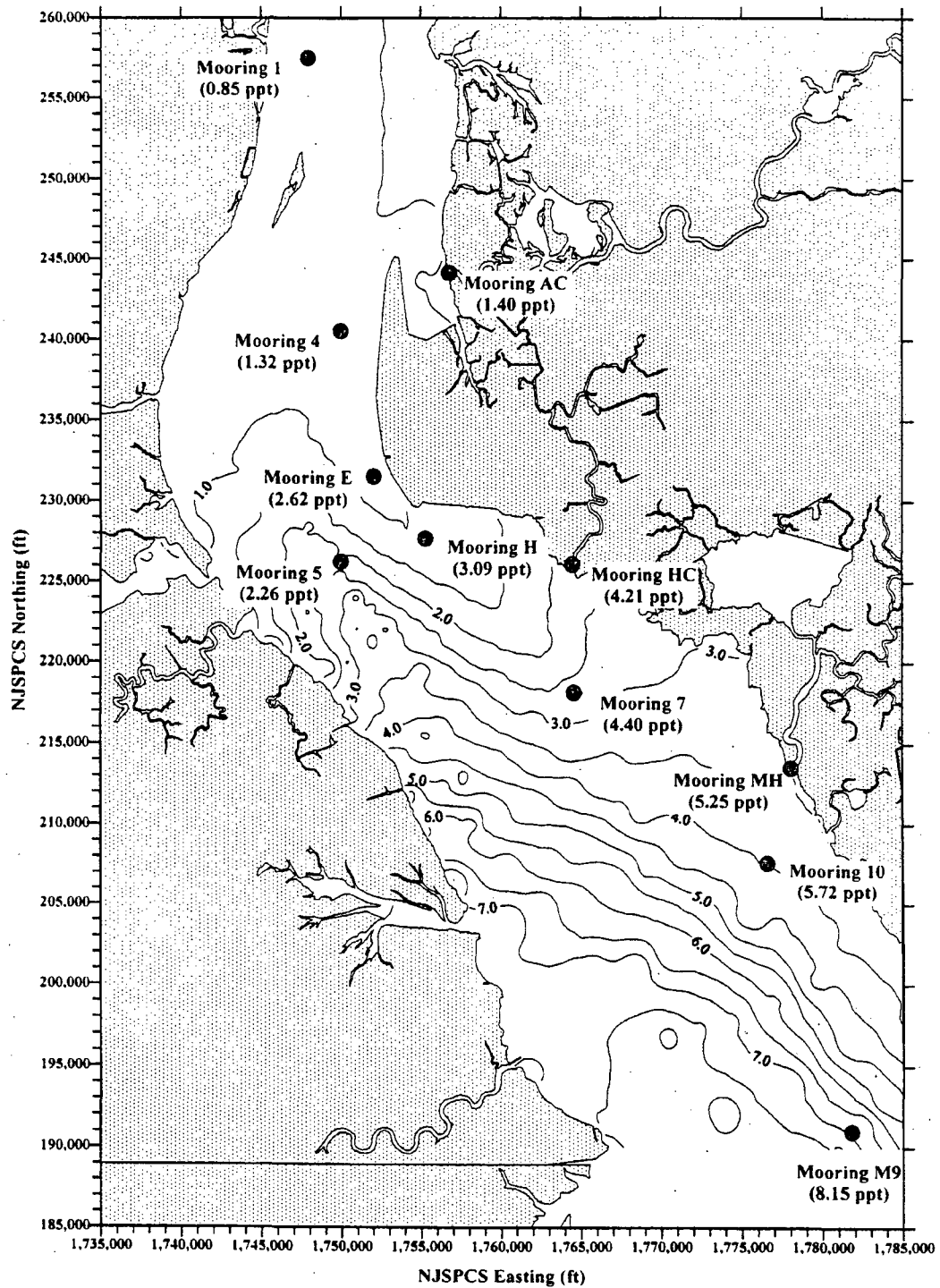
Mooring 5 (West of the Station) Temperature Time-series



E-2 Figure IV-7. Observed (red) and modeled (black) time-series of surface, mid-depth, and bottom temperatures at mooring 5, also showing tide height at Salem Barge Slip and ADCP current speed and direction.

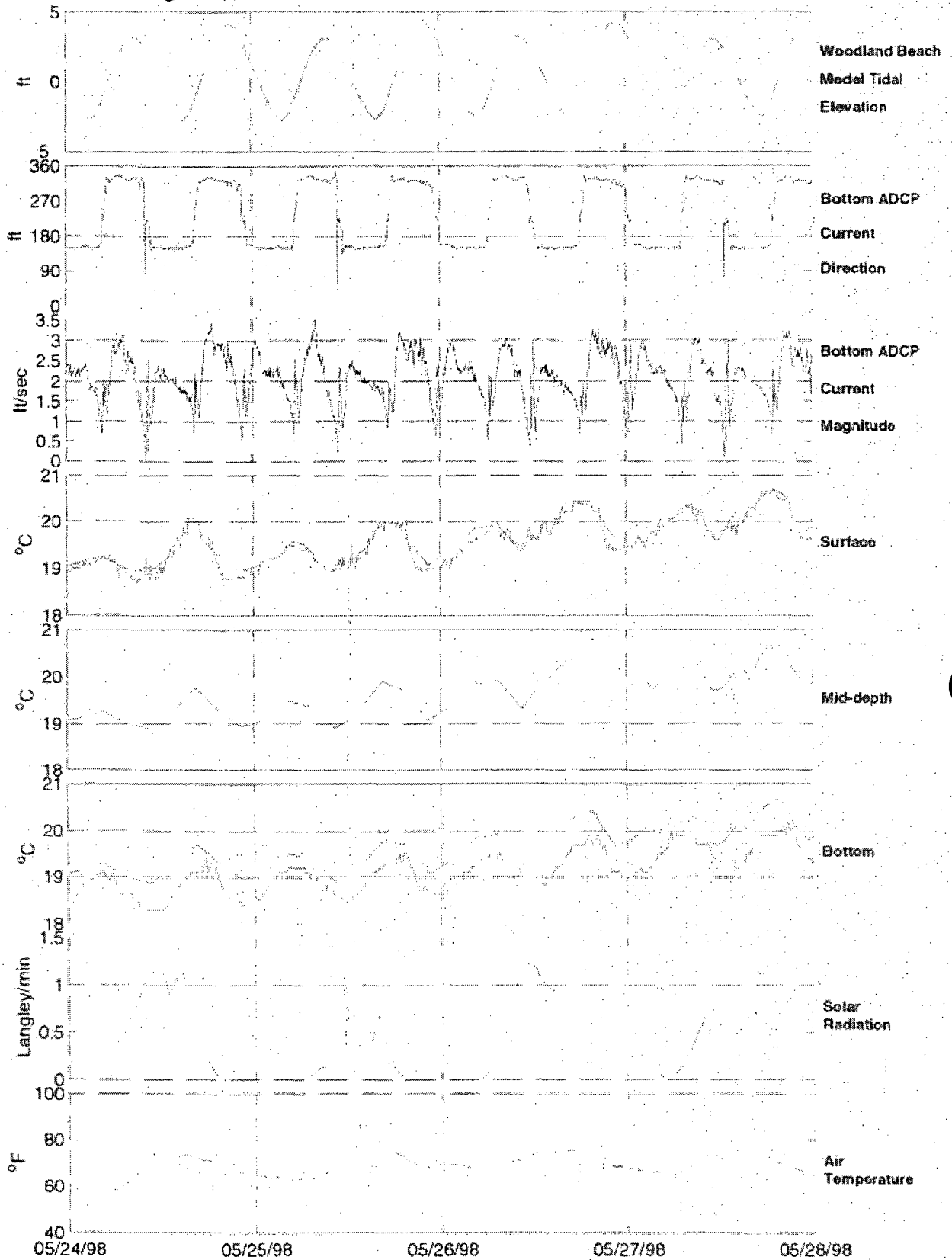


E-2 Figure IV-8. Observed and modeled cross-river structure of mean temperature and salinity. The bottom observed temperature at mooring M9 is extrapolated from the mid-depth observation (due to lack of moored data).



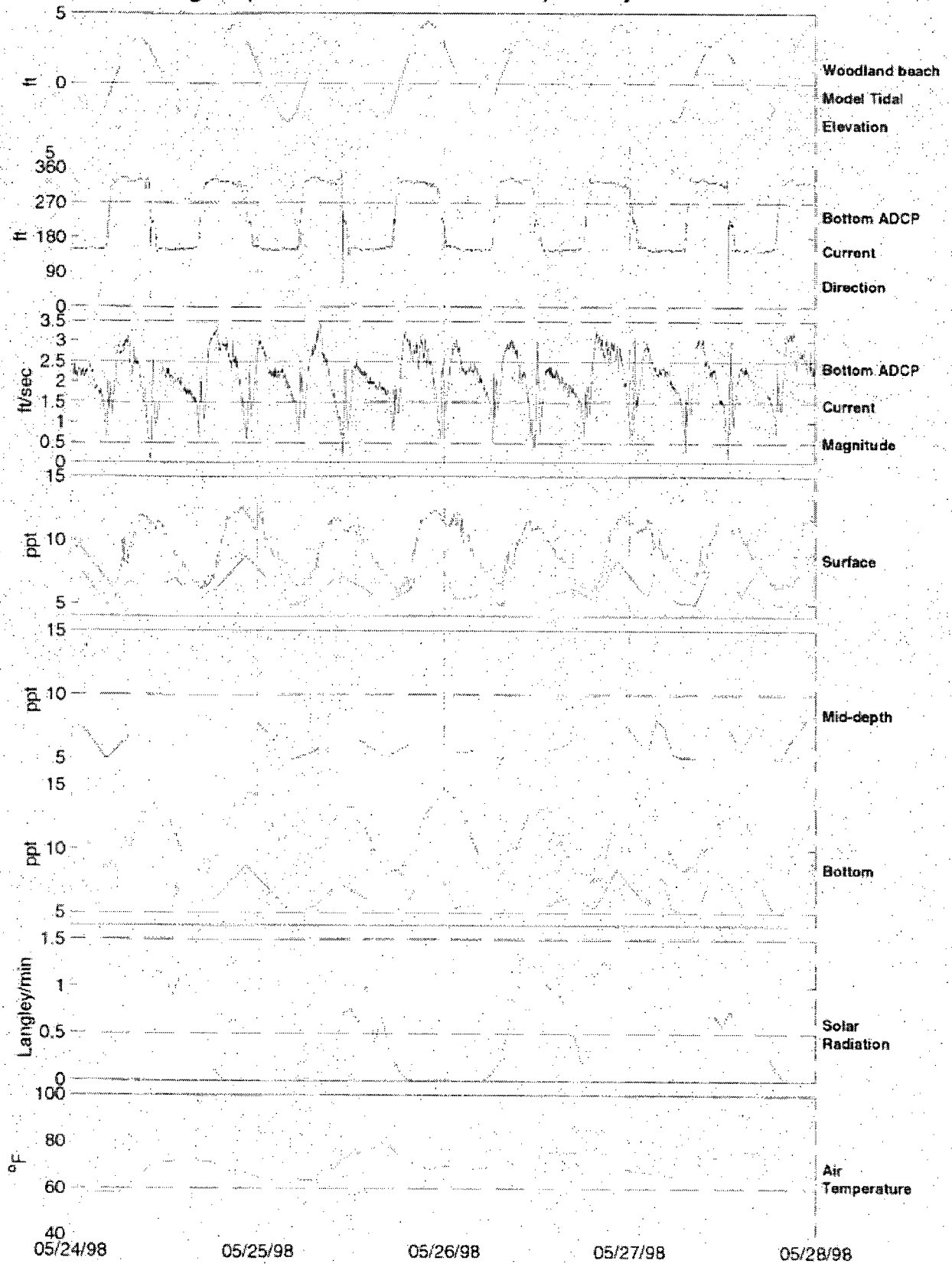
E-2 Figure IV-9. Tidally-averaged surface salinity predicted by RMA-10 during 12.5 hour period centered on 1200 hrs, 29 May 1998, also showing tidally-averaged mean salinities measured with moored instruments.

Mooring M9 (9 miles south of the Station) Temperature Time-series



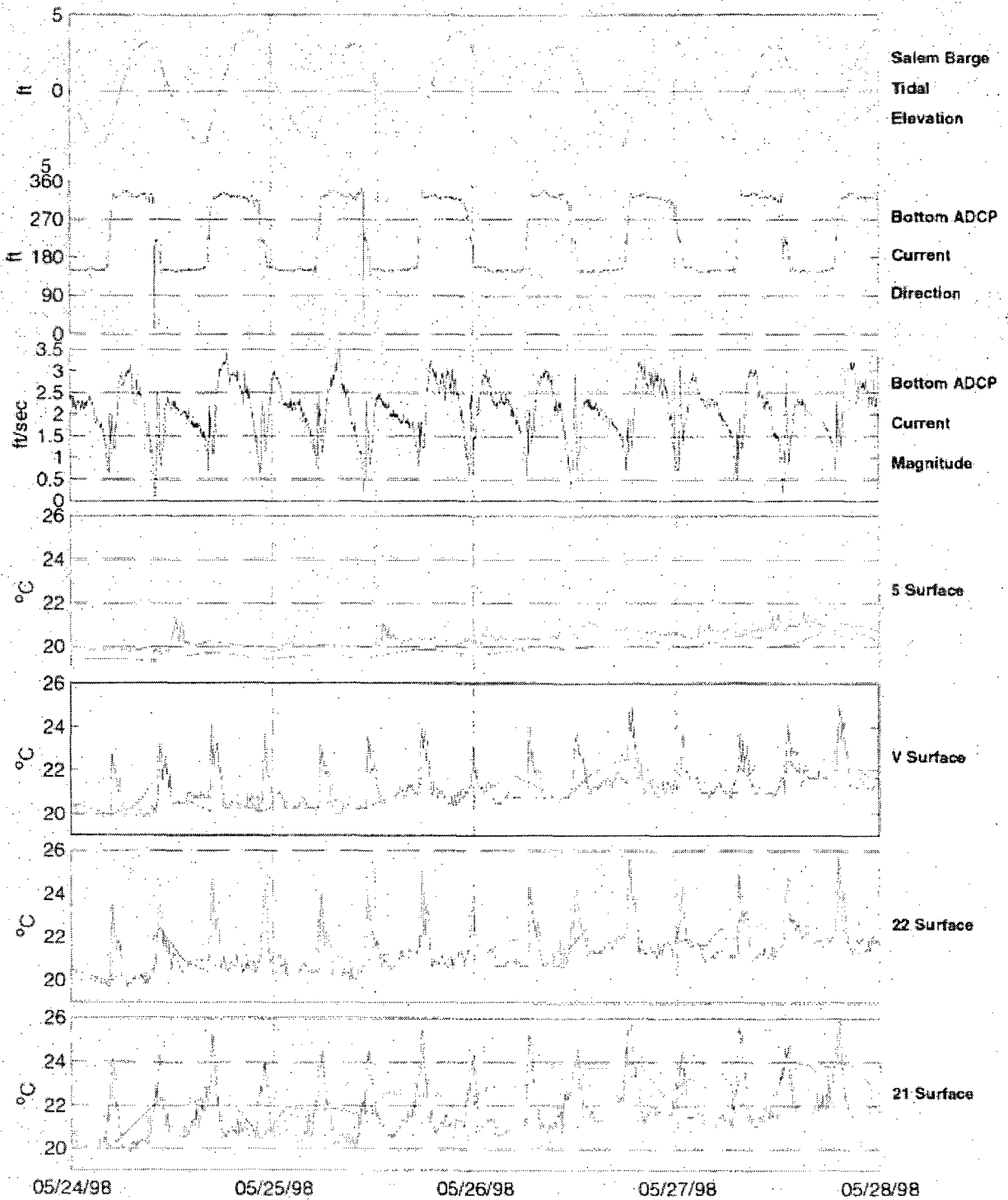
E-2 Figure IV-10. Observed (red) and modeled (black) temperature time-series at station M9 at surface, mid-depth, and bottom levels, also showing modeled tide height at Woodland Beach, solar insolation, and air temperature.

Mooring M9 (9 miles south of the Station) Salinity Time-series

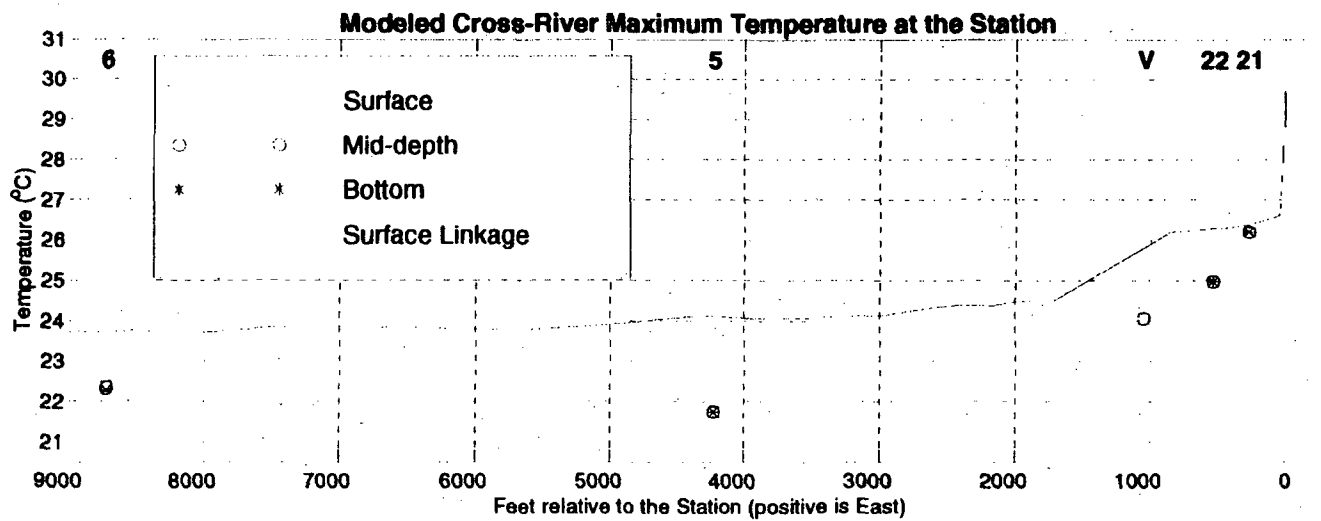
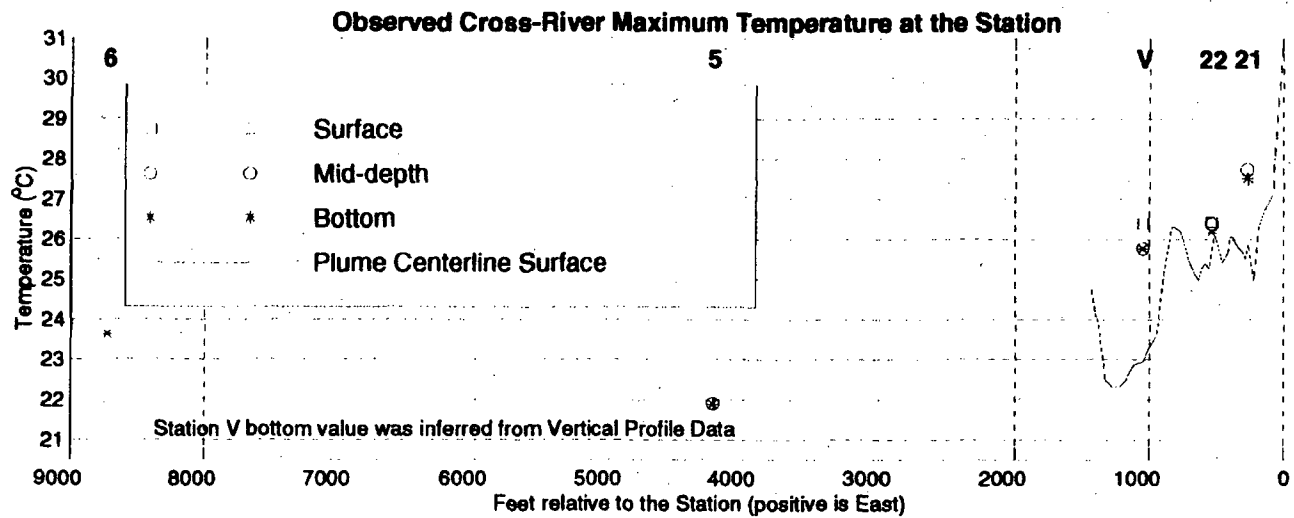


E-2 Figure IV-11. Observed (red) and modeled (black) salinity time series at mooring M9 at surface, mid-depth, and bottom levels, also showing modeled tide height at Woodland Beach, solar insolation, and air temperature.

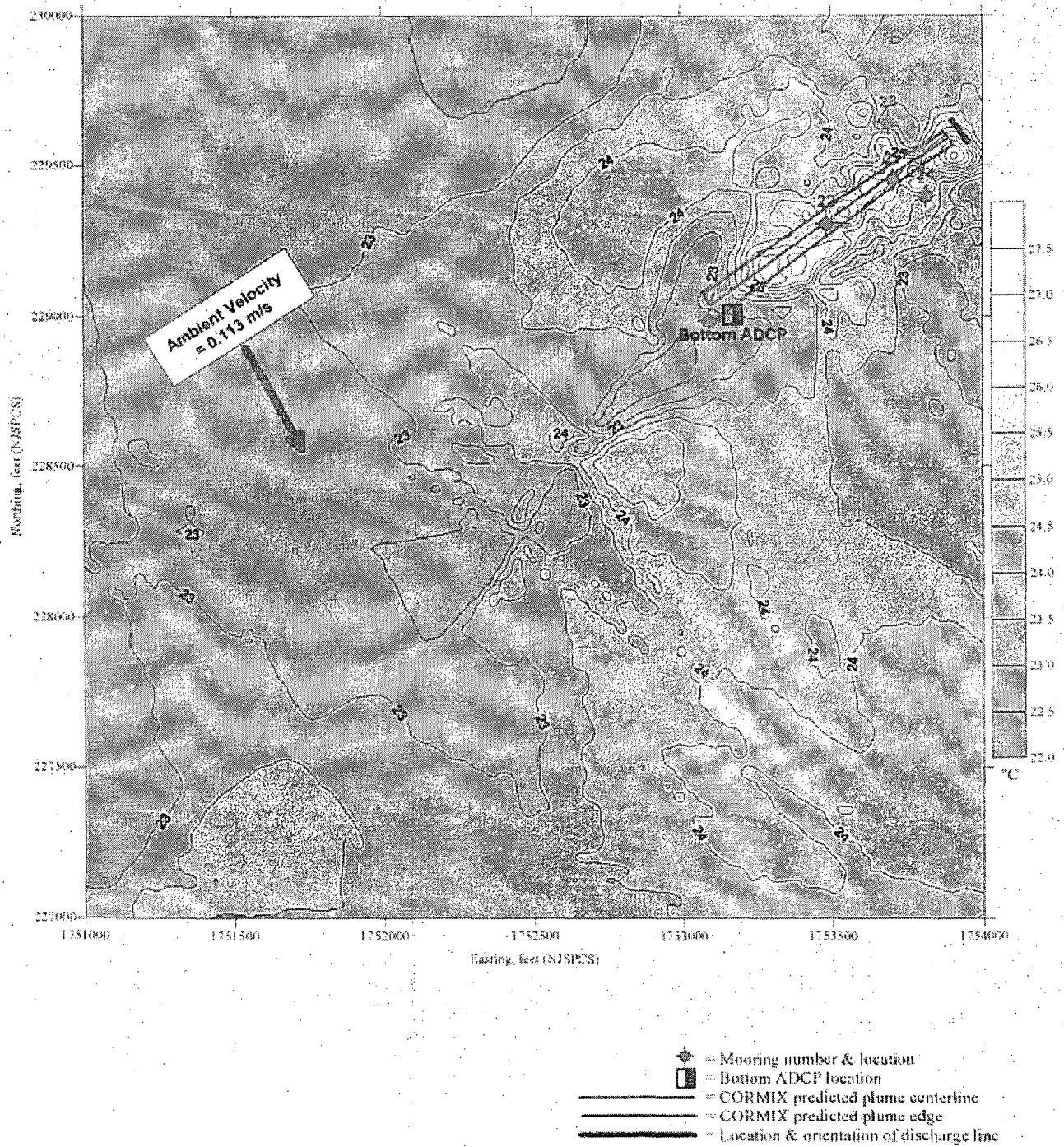
Surface Temperature Time-series Cross-river at the Station



E-2 Figure IV-12. Observed (red) and modeled (black) surface temperature time series along a line extending offshore through the Station's discharge. From east to west, the moorings plotted are 21, 22, V, and 5. Also shown is tide height at the nearest point, the Salem Barge Slip.

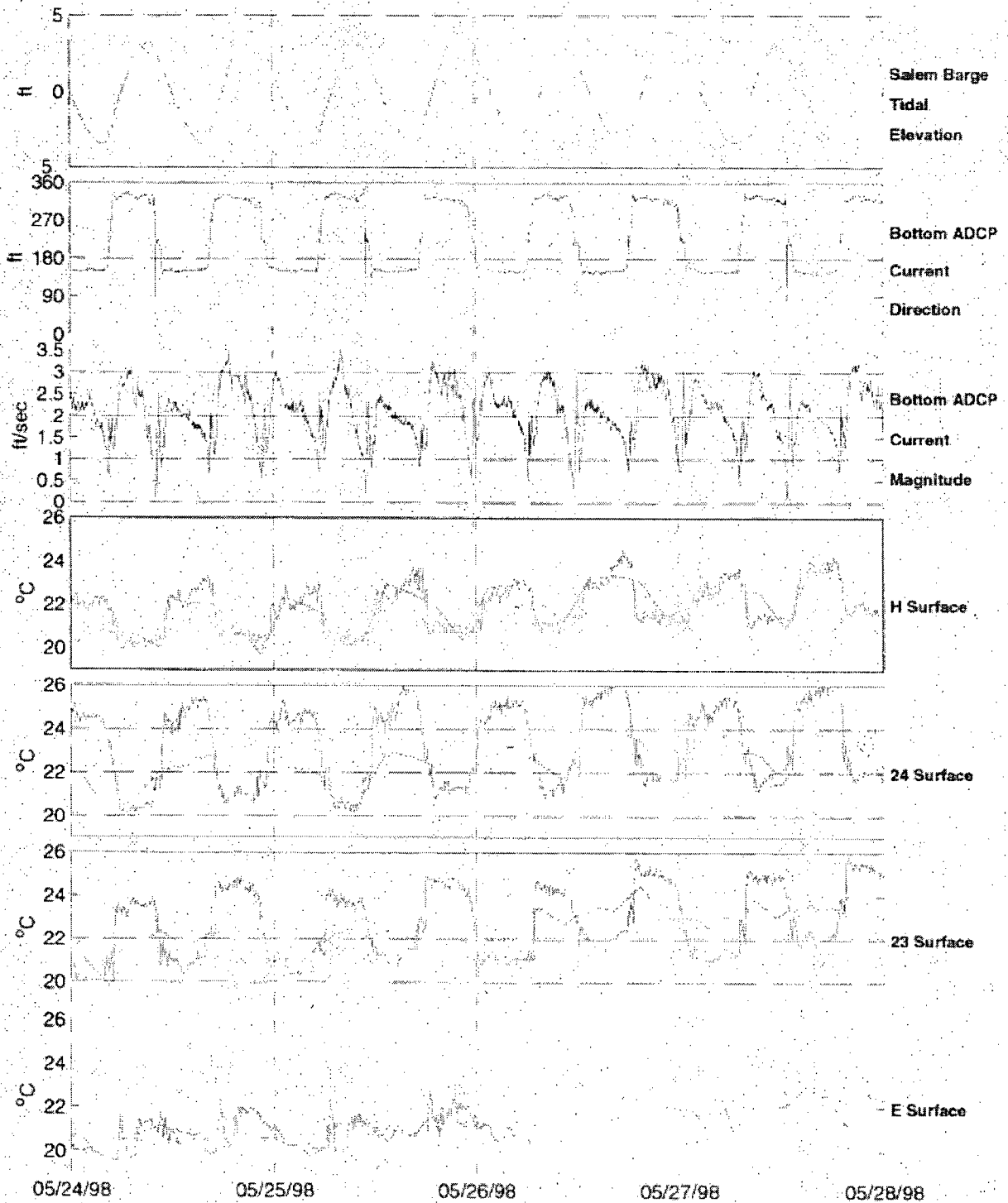


E-2 Figure IV-13. Peak observed (upper panel) and modeled (lower panel) temperatures at surface, mid-depth, and bottom at stations 21, 22, V, 5, and 6 on a cross-river line through the Station's discharge. Shown on the upper panel (solid line) is observed surface temperature from a vessel survey following the plume. Shown on the lower panel (solid line) is the combined model-predicted temperature following the centerline of the predicted plume.

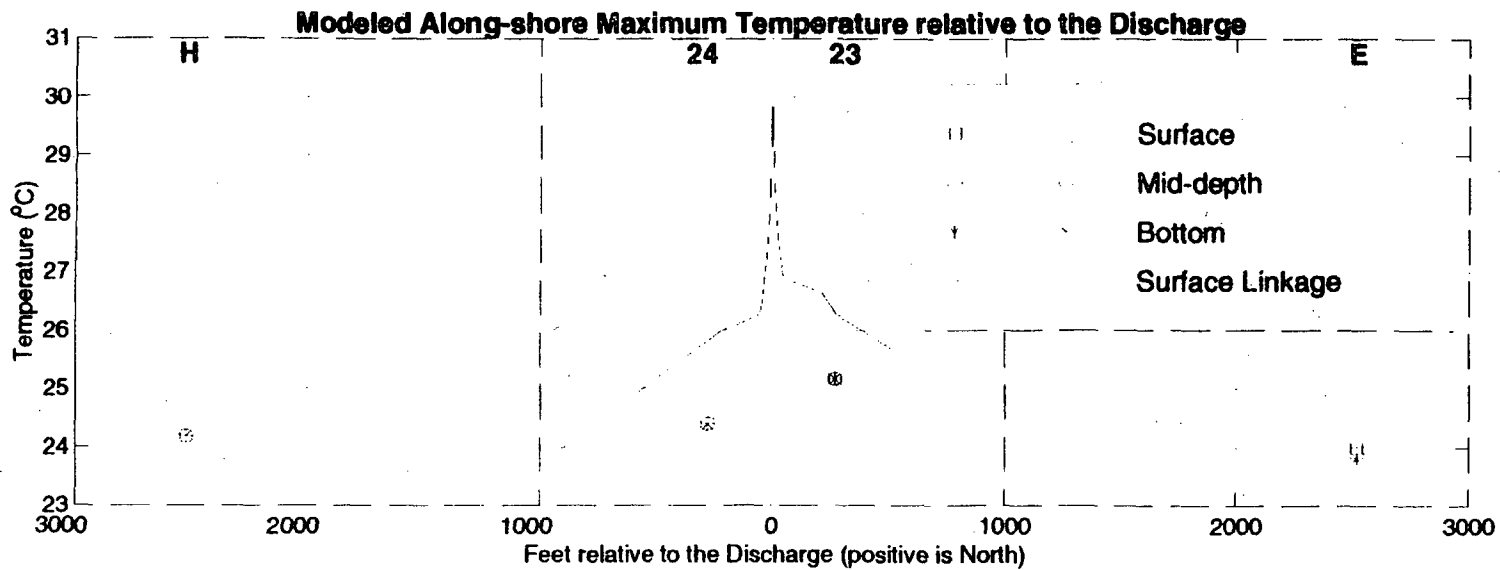
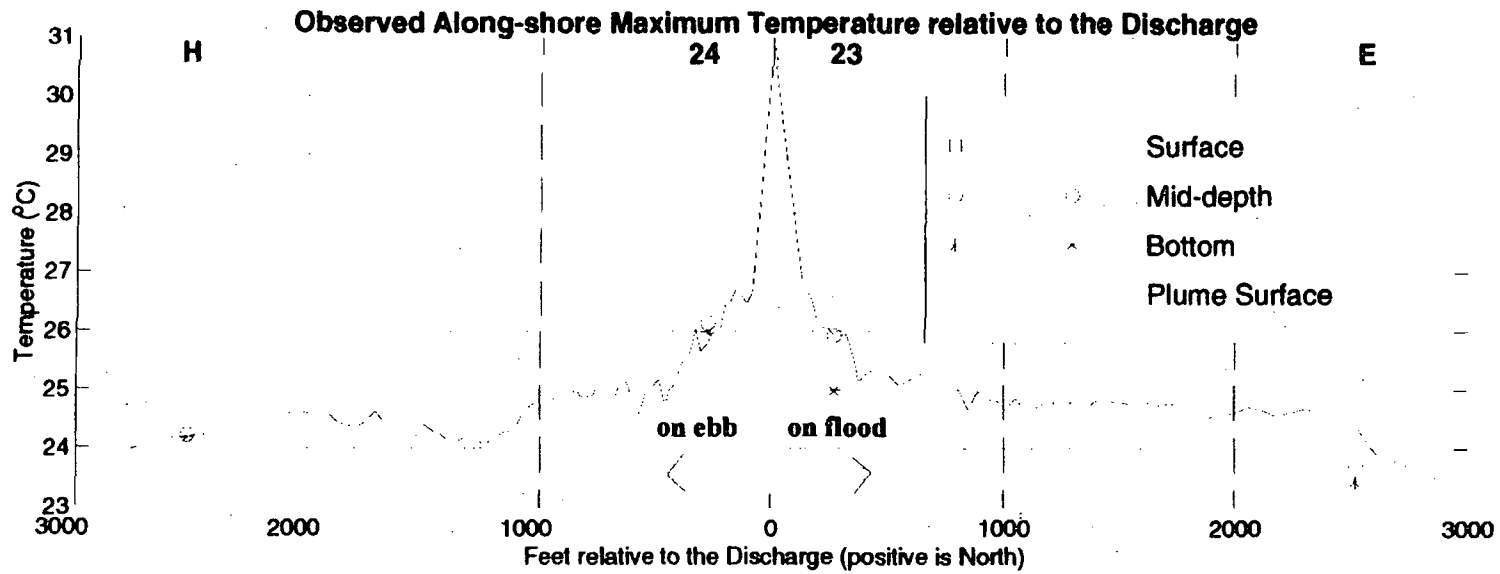


E-2 Figure IV-14.
 Observed surface plume temperature during the EOF slack period from the
 Two-Unit Survey, 29 May 1998 (Exhibit E-1-3), overplotted with CORMIX model results.

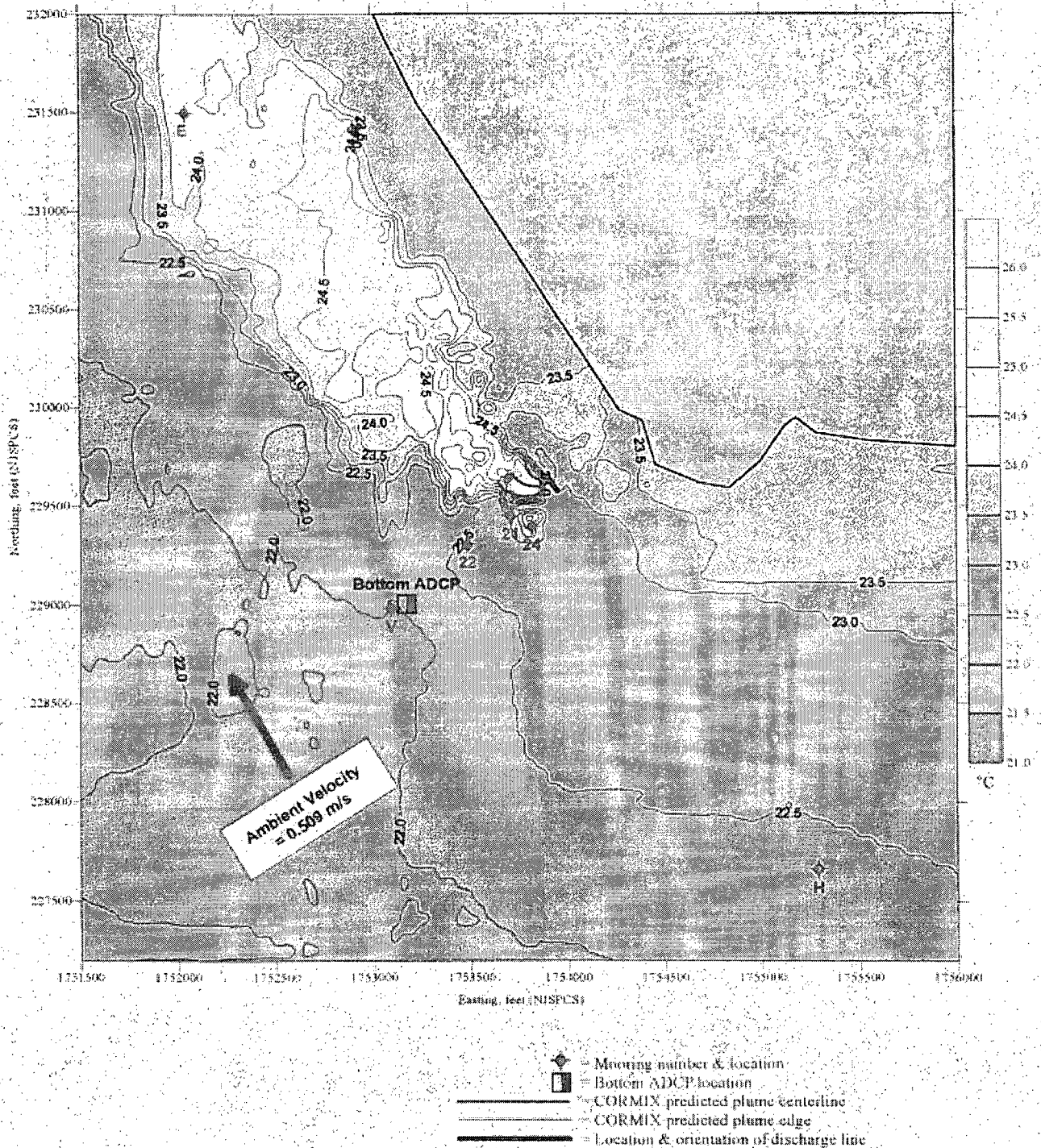
Surface Temperature Time-series Along-river relative to the Station



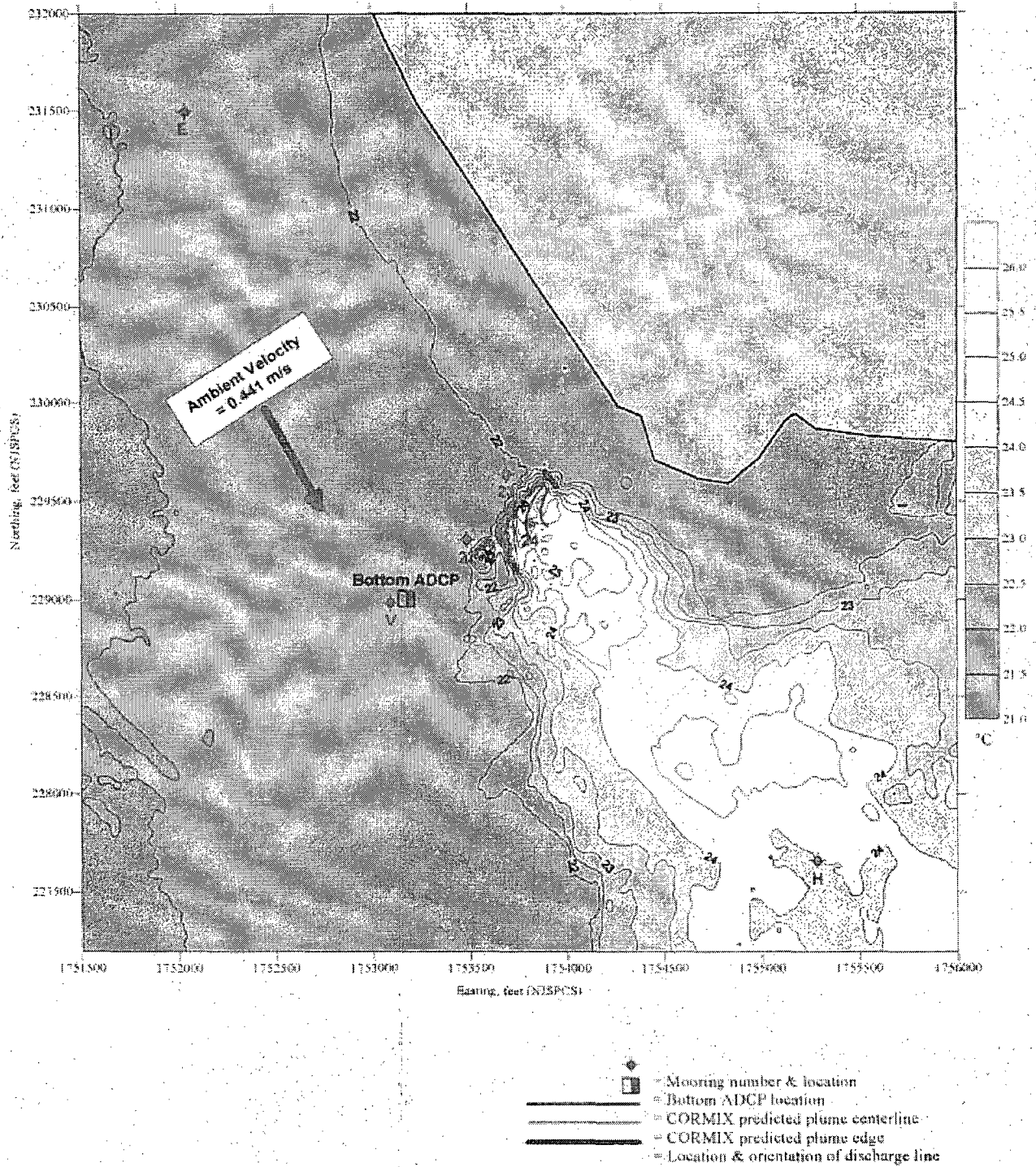
E-2 Figure IV-15. Observed (red) and modeled (black) surface temperature time-series along a shore-parallel line through the Station discharge. From south to north, the moorings plotted are H, 24, 21, 23, and E. Also shown is tide height at the nearest point, the Salem Barge Slip.



E-2 Figure IV-16. Peak observed (upper panel) and modeled (lower panel) temperatures at surface, mid-depth, and bottom at moorings H, 24, 23, and E on an along-shore line through the Station's discharge.

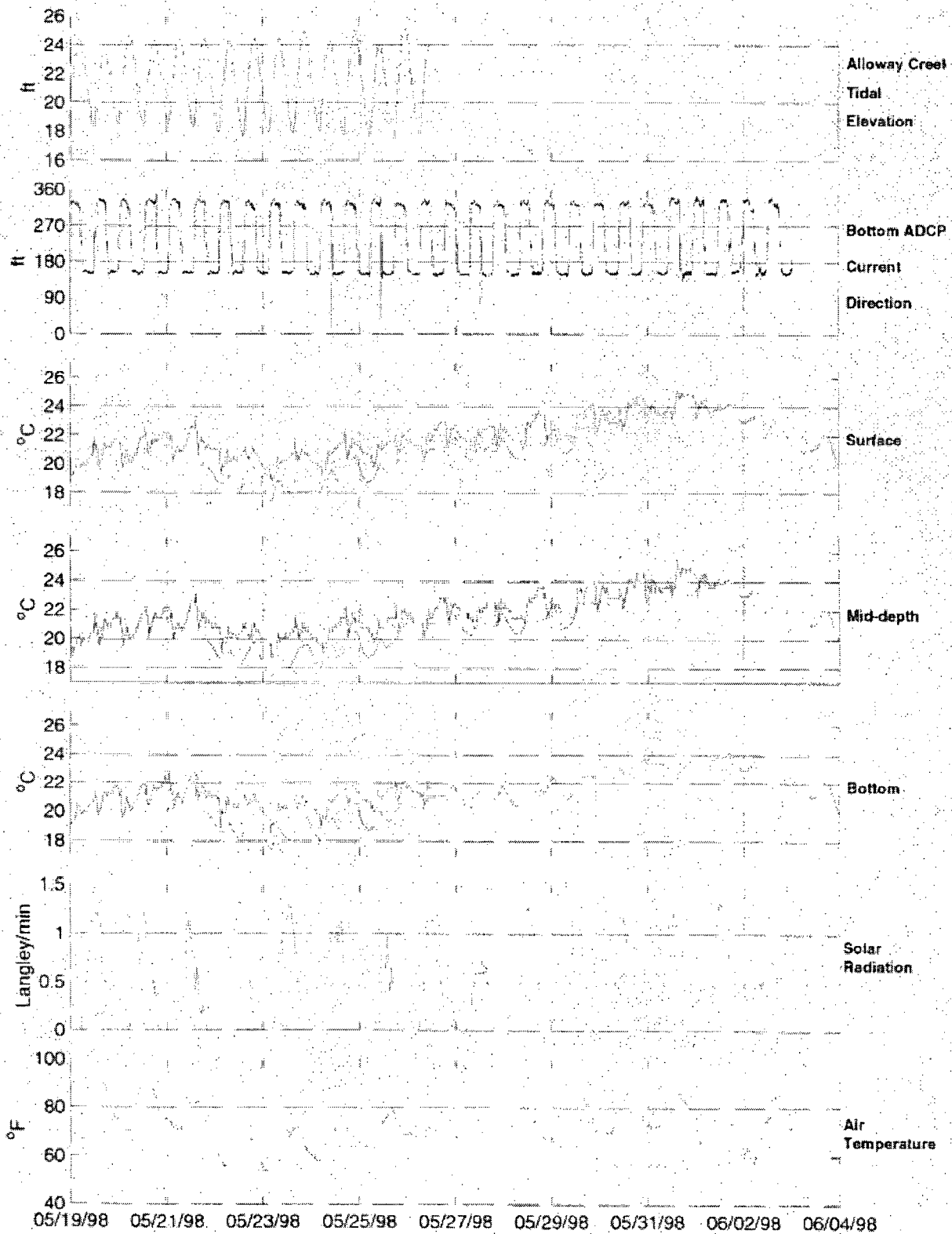


E-2 Figure IV-17. Observed surface plume temperature during flood phase from the Two-Unit Survey, 29 May 1998 (Exhibit E-1-3), overplotted with CORMIX model results.



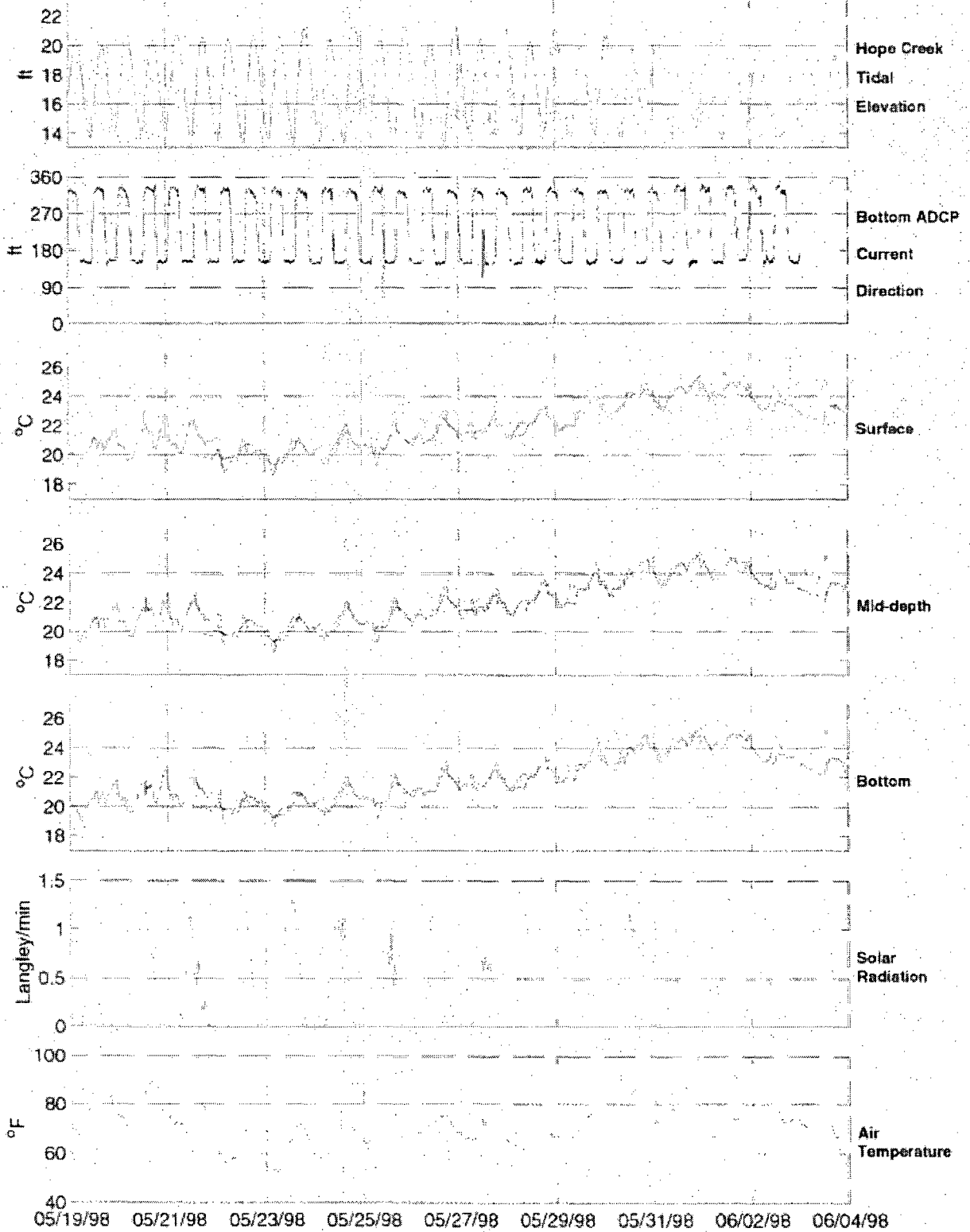
E-2 Figure IV-18. Observed surface plume temperature during ebb phase from the Two-Unit Survey, 29 May 1998 (Exhibit E-1-3) overlaid with CORMIX model results.

Alloway Creek Temperature Time-series



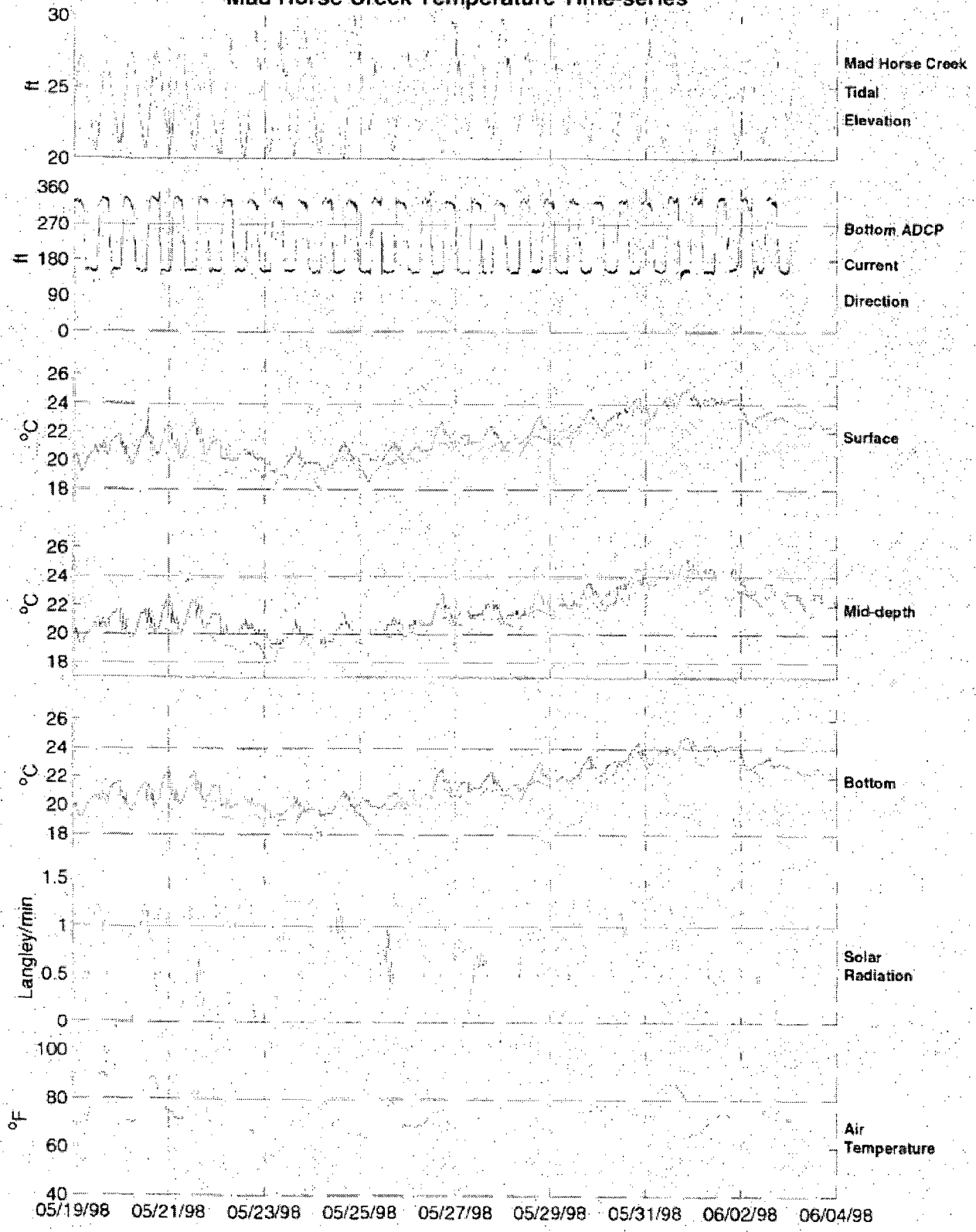
E-2 Figure IV-19. Observed (red) and modeled (black) temperature time-series at Alloway Creek. Also shown; tide height at Alloway Creek, current direction from the bottom-mounted ADCP near the Station, and solar insolation and air temperature at the Station.

Hope Creek Temperature Time-series



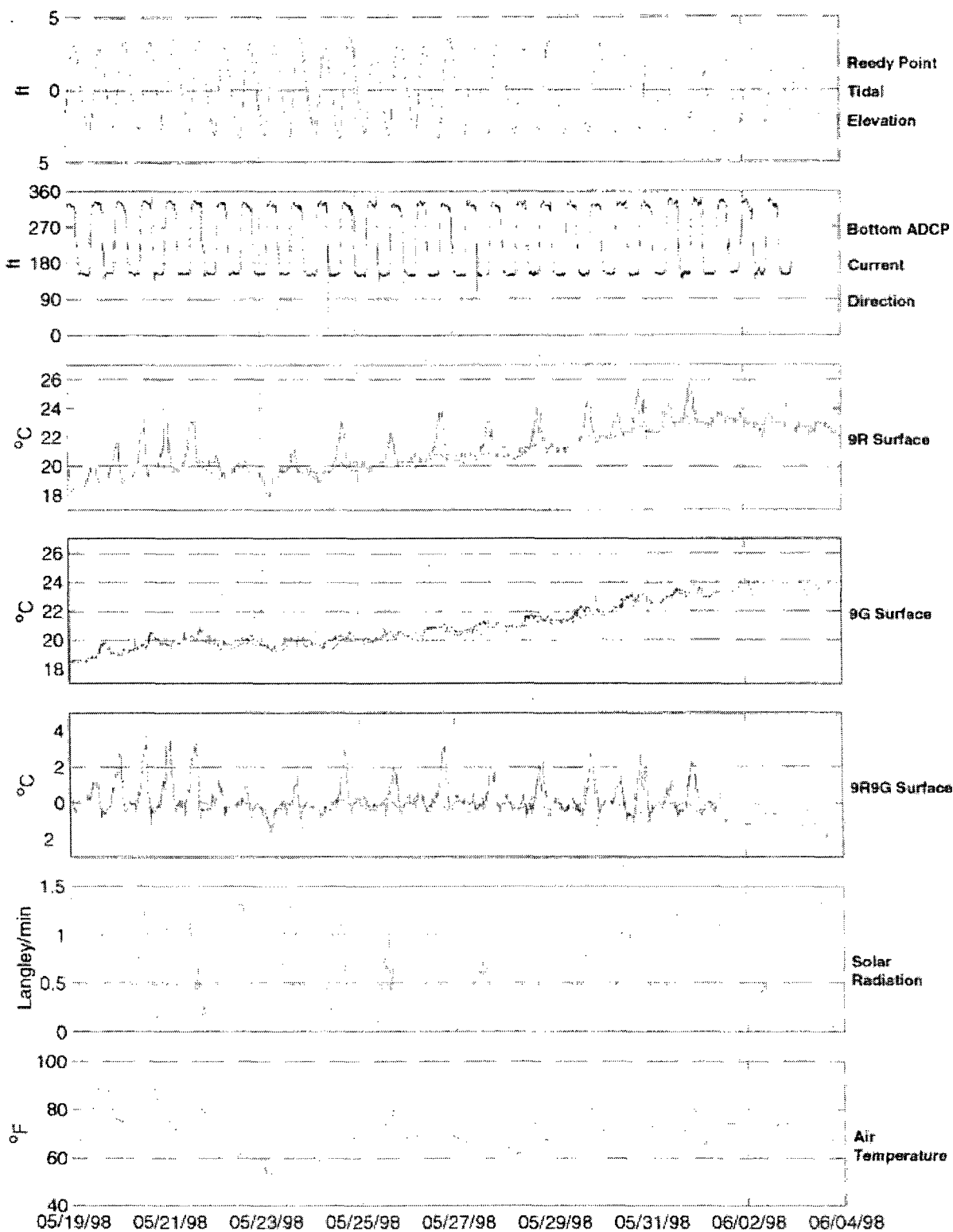
E-2 Figure IV-20. Observed (red) and modeled (black) temperature time-series at Hope Creek. Also shown; tide height at Hope Creek, current direction from the bottom-mounted ADCP near the Station, and solar insolation and air temperature at the Station.

Mad Horse Creek Temperature Time-series



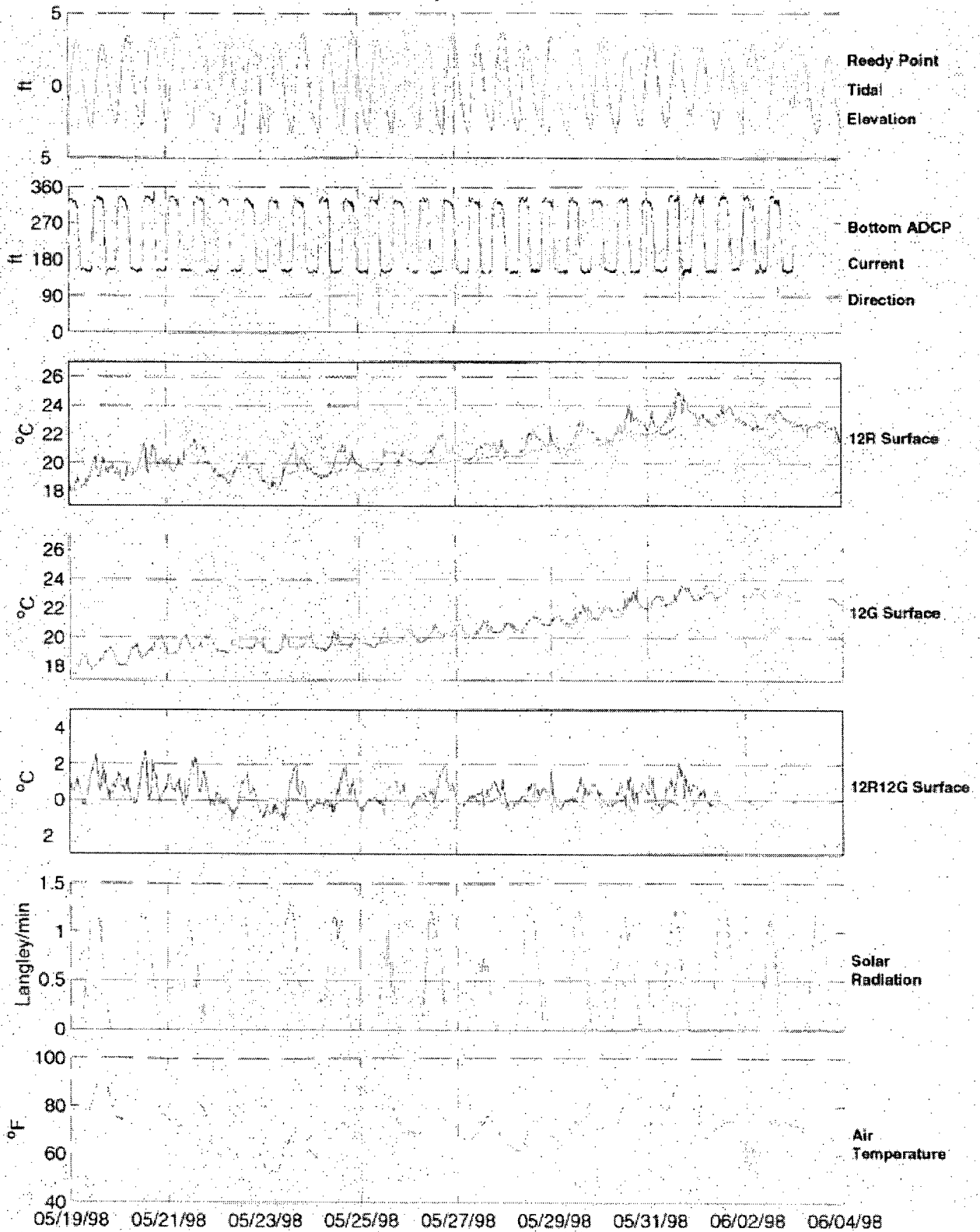
E-2 Figure IV-21. Observed (red) and modeled (black) temperature time-series at Mad Horse Creek. Also shown, tide height at Mad Horse Creek, current direction from the bottom-mounted ADCP near the Station, and solar insolation and air temperature at the Station.

9R and 9G Temperature Time-series

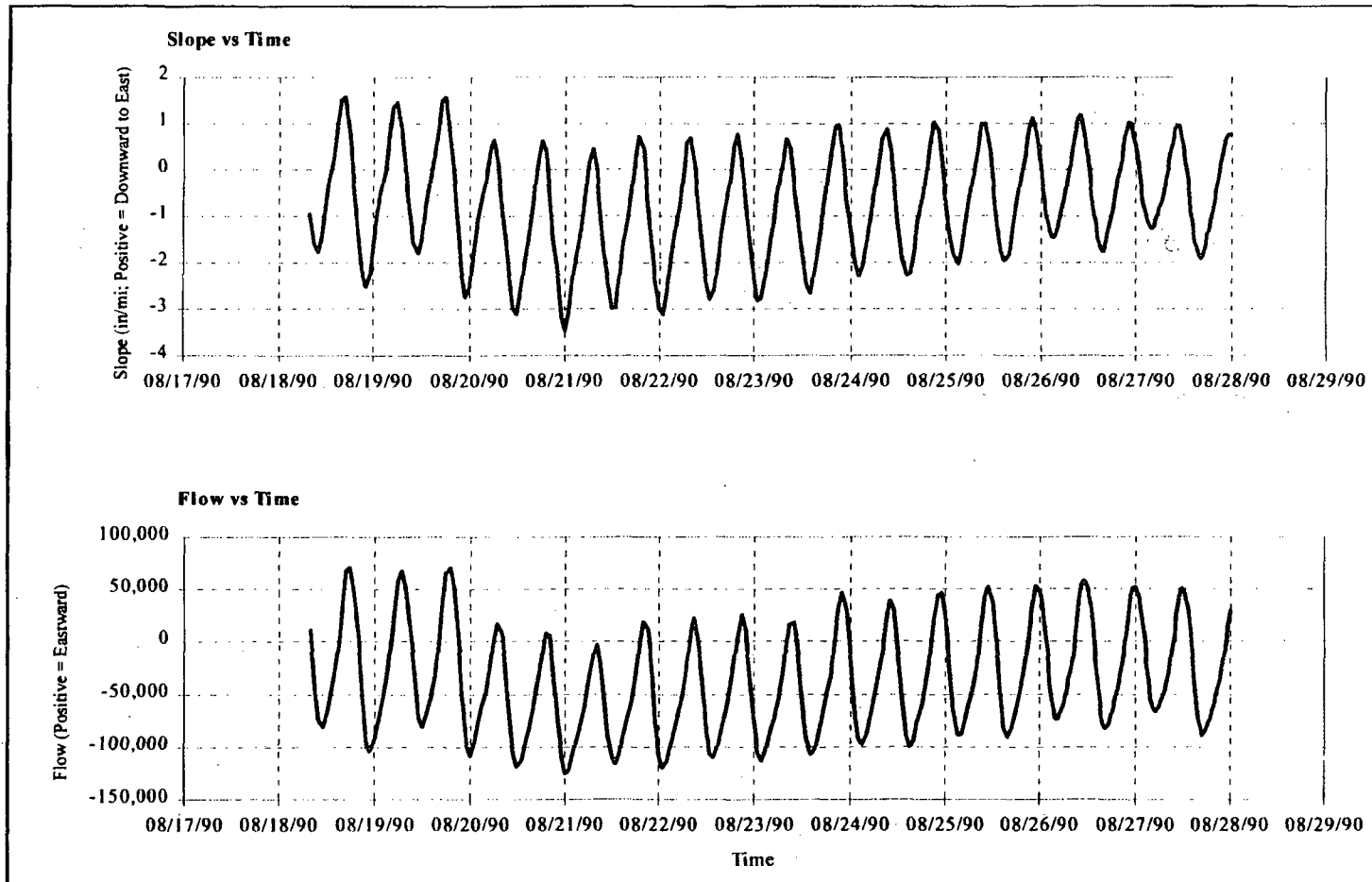


E-2 Figure IV-22. Observed (red) and modeled (black) time-series of surface temperature at moorings 9G and 9R, located 9 miles north of the Station off the Salem River. Also shown are Reedy Point tide height, current direction from the bottom-mounted ADCP at the Station, and solar insolation and air temperature from the Station.

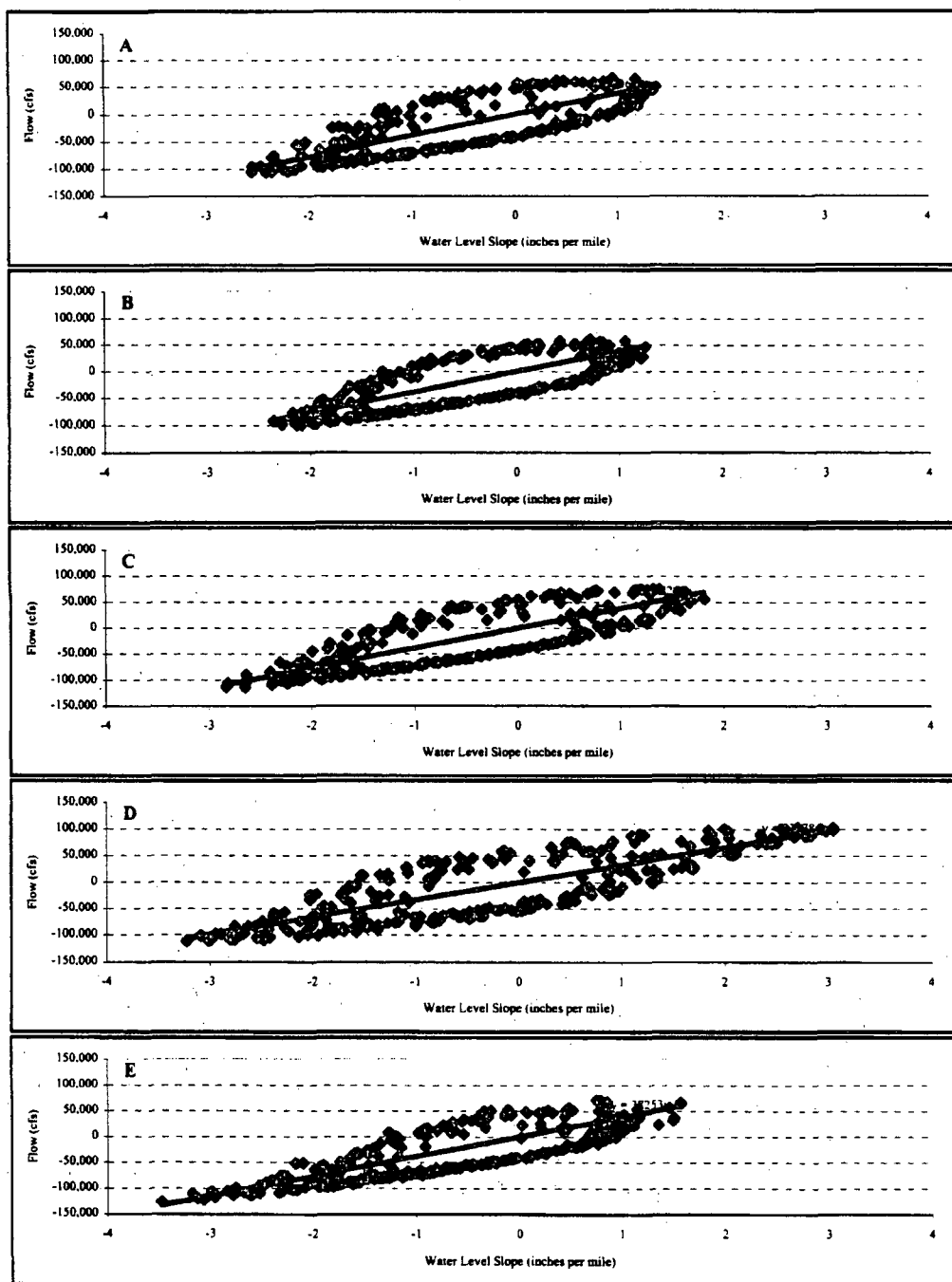
12R and 12G Temperature Time-series



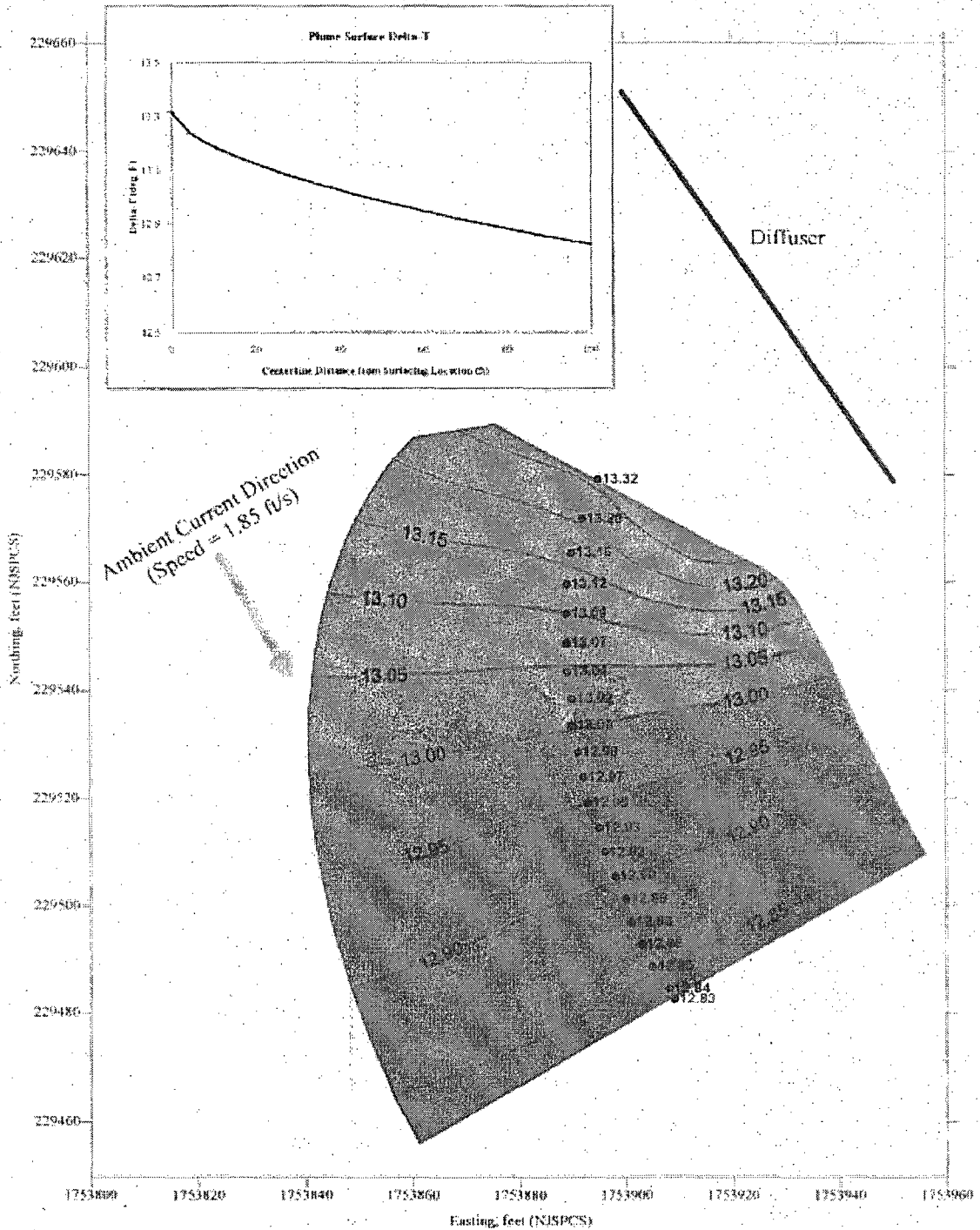
E-2 Figure IV-23. Observed (red) and modeled (black) time-series of surface temperature at moorings 12G and 12R, located 12 miles north of the Station off the Salem River. Also shown are Reedy Point tide height, current direction from the bottom-mounted ADCP at the Station, and solar insolation and air temperature from the Station.



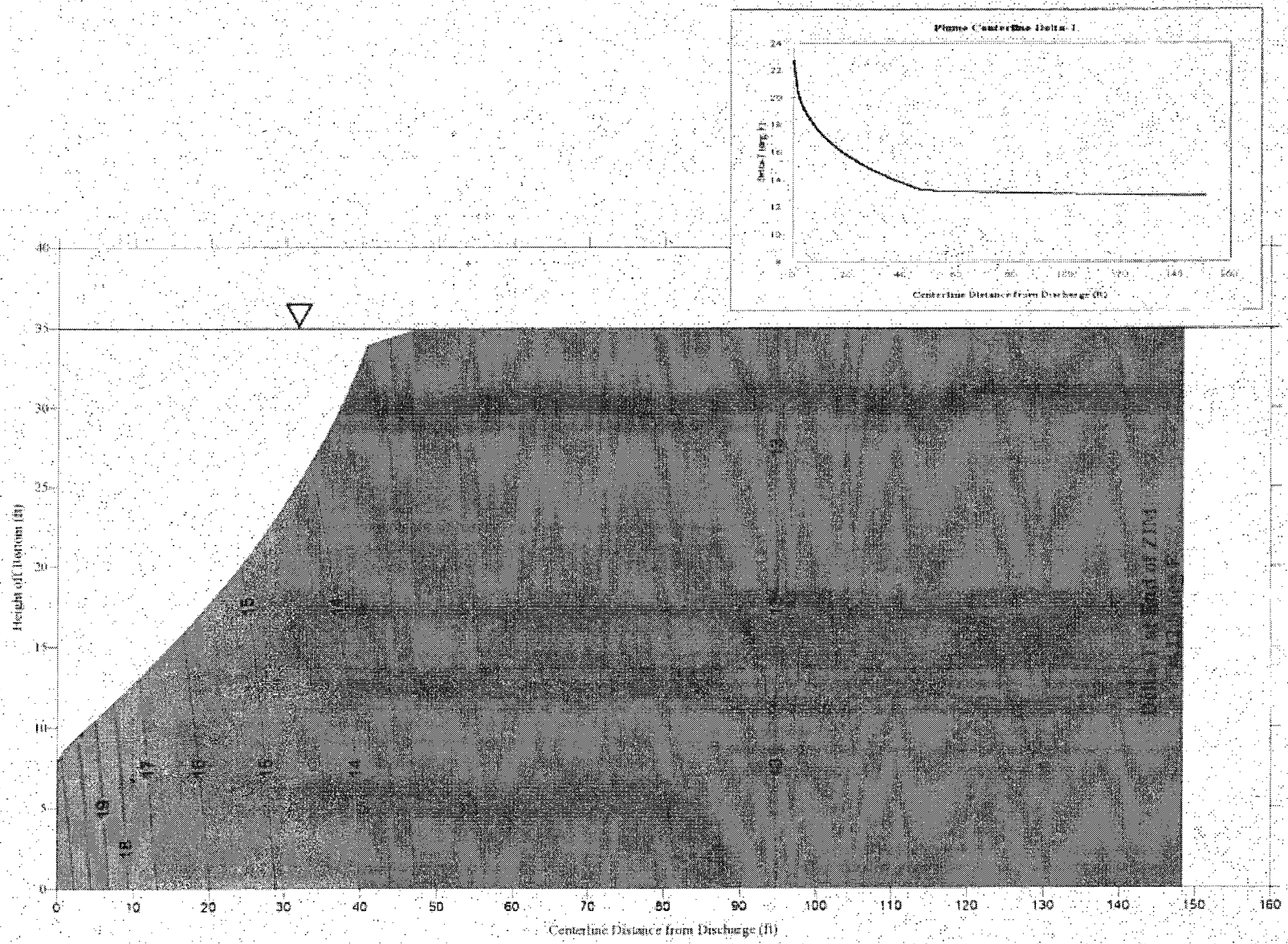
E-2 Figure IV-24. Time-series of water surface slope along the C&D Canal (upper trace) and modeled flow in the Canal (lower trace) for sample Simulation E.



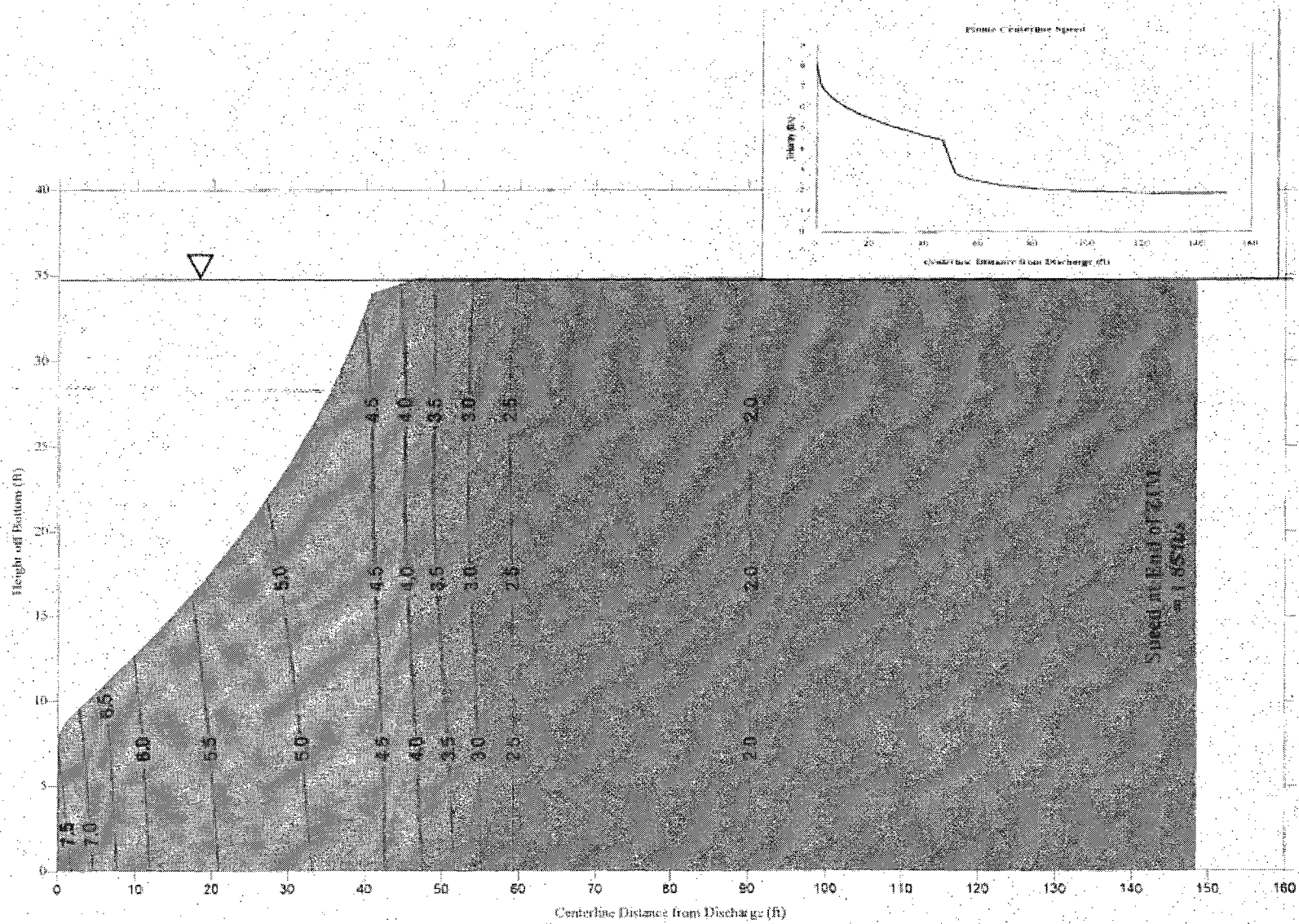
E-2 Figure IV-25. Relationship of flow to slope in modeled C&D Canal for projection sample Simulations A-E. Data points are hourly values; lines are linear least squares regressions.



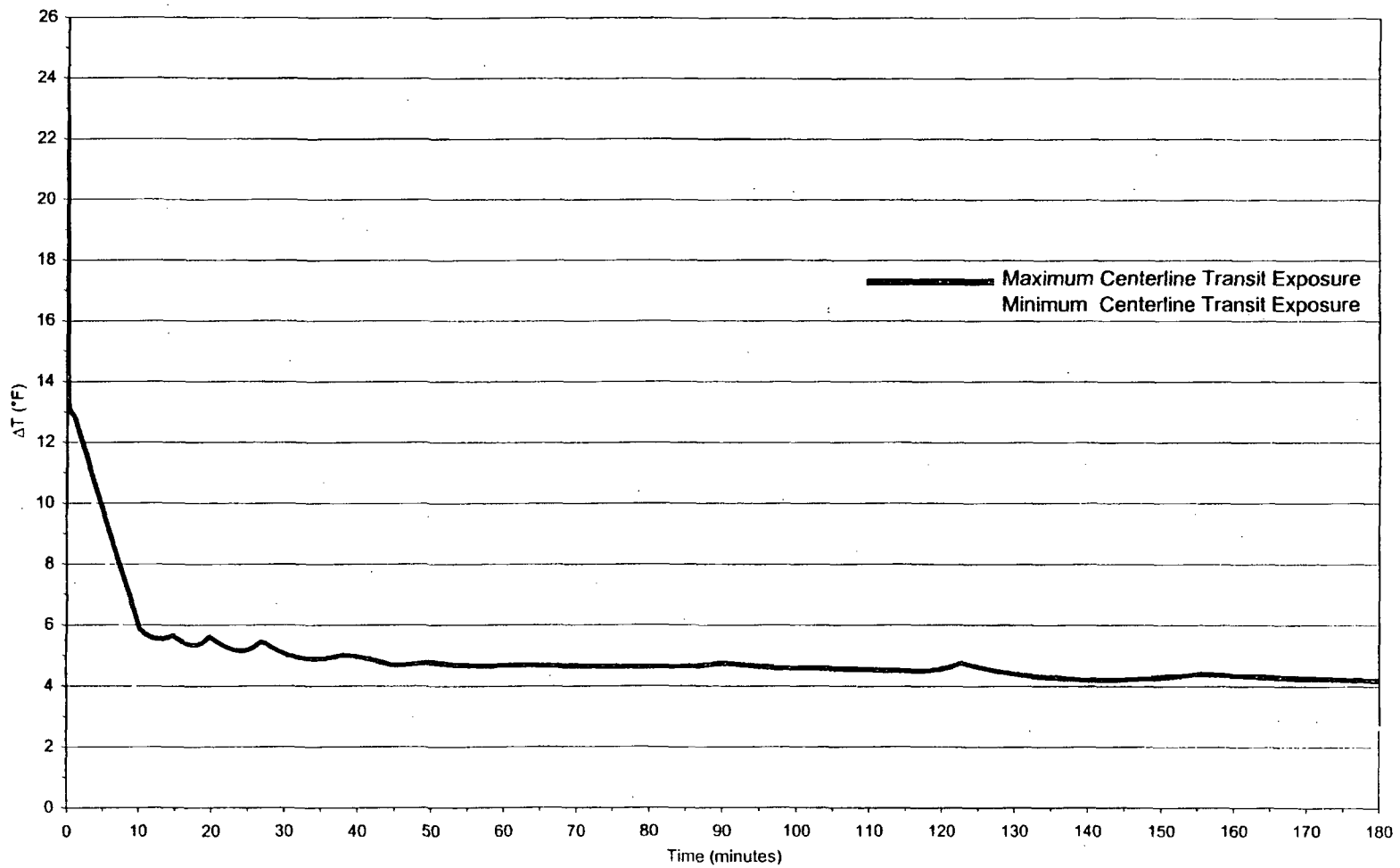
E-2 Figure V-1. Plume Surface Delta-T Contours Ebb Tidal Phase, 6/2/98 0830 hrs
 Discharge Delta-T = 22.7 deg.F (Relative to Ambient Temperature).



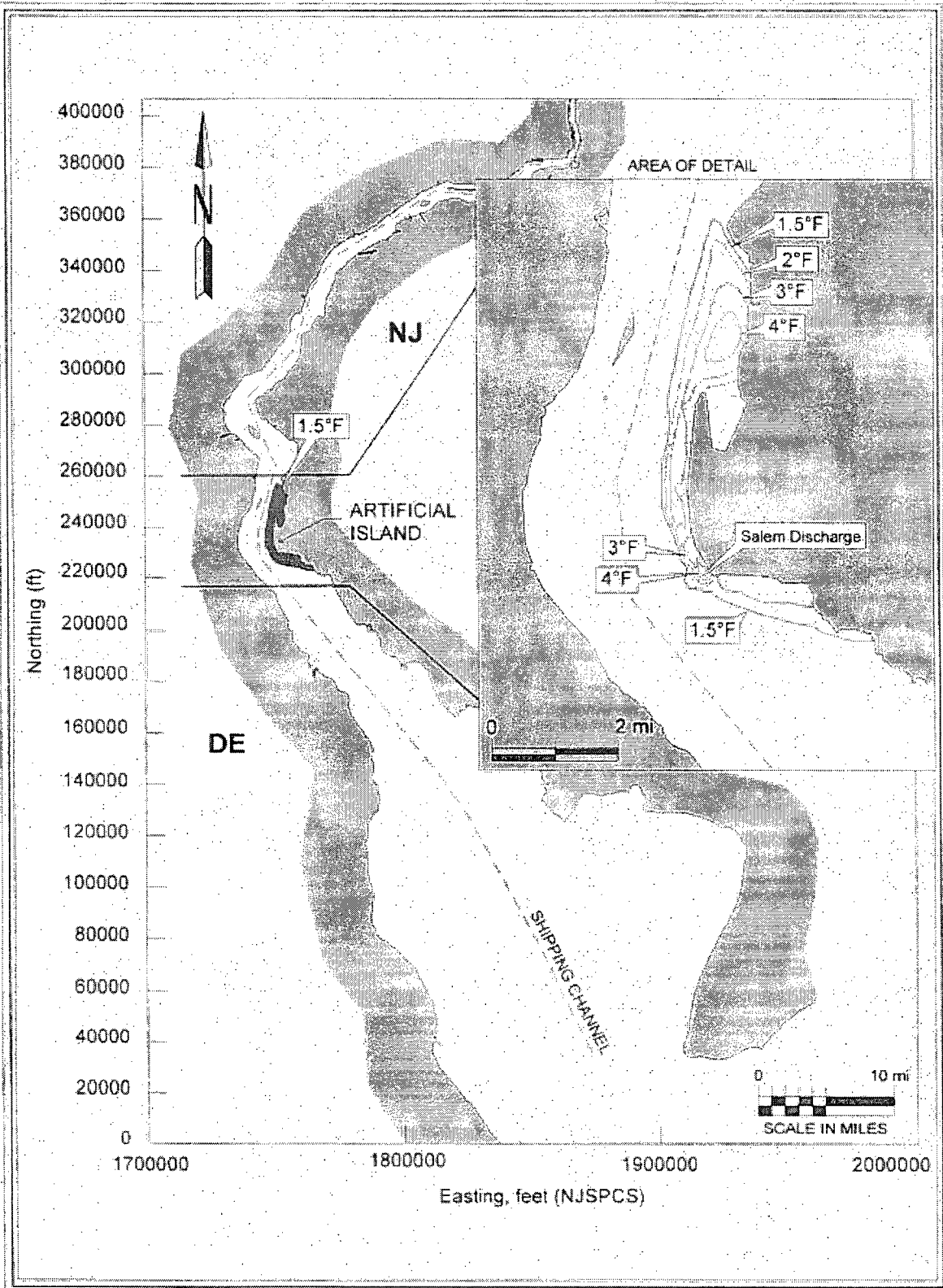
E-2 Figure V-2. Plume Centerline Delta-T (degrees F) Ebb Tidal Phase, 6/2/98 0830 hrs
 Discharge Delta-T = 22.7 deg.F (Relative to Ambient Temperature).



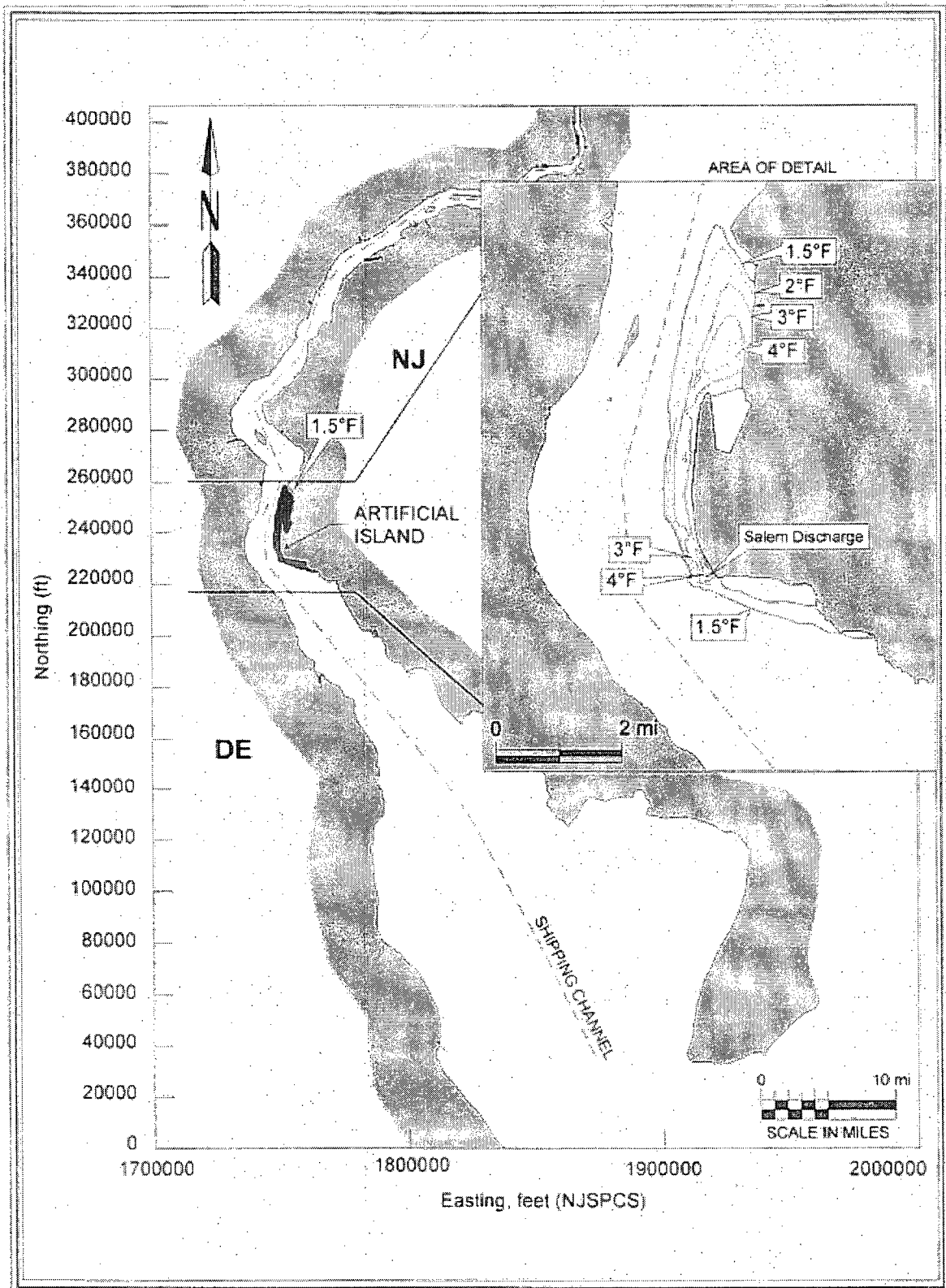
E-2 Figure V-3. Plume Centerline Velocity (feet per second) Ebb Tidal Phase, 6/2/98 0830 hrs
 Ambient Velocity = 1.85 ft/s.



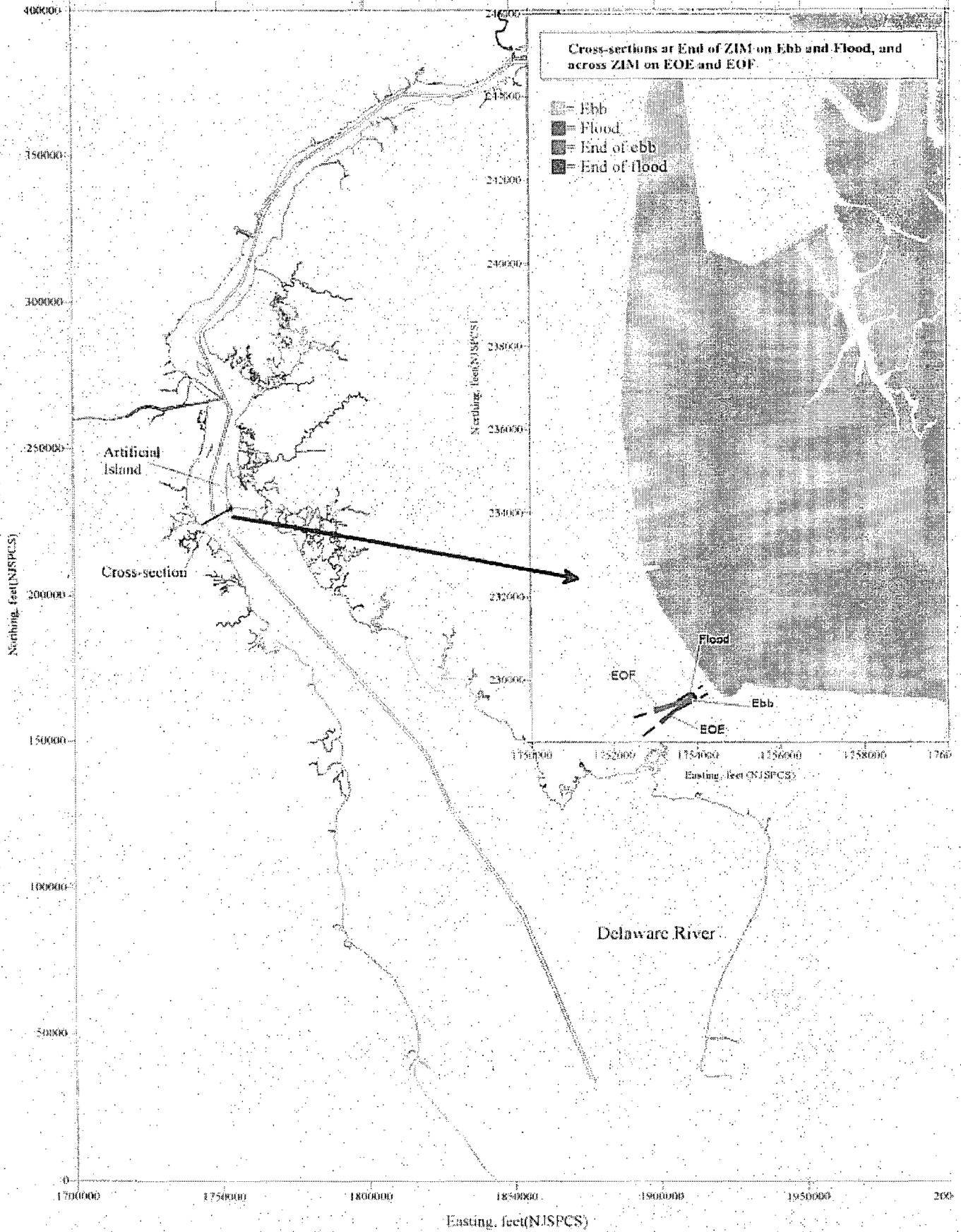
E-2 Figure V-5. Sample Time-Delta-Temperature History, Ebb Phase (2 June 1998, 0830 hrs.).



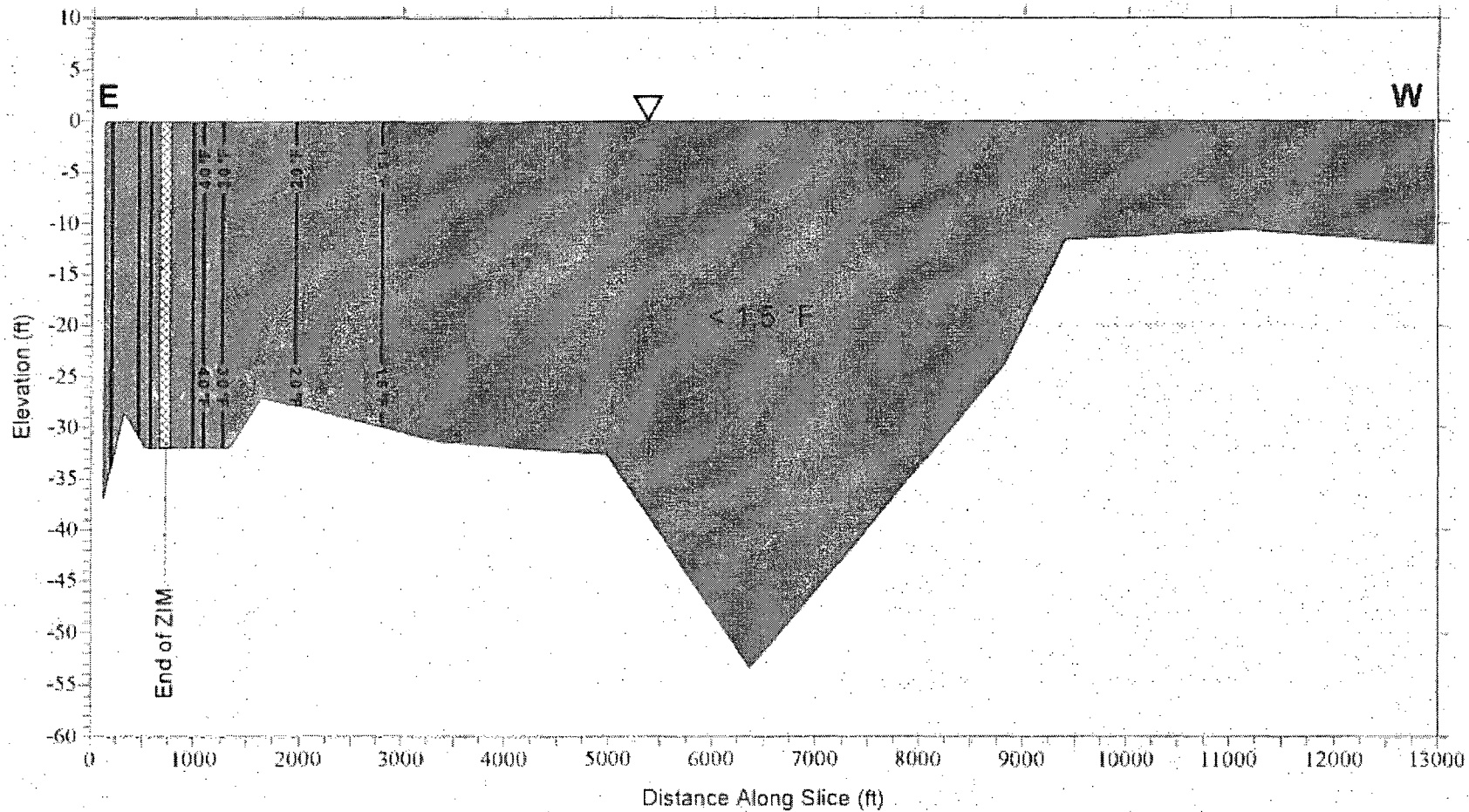
E-2 Figure V-6. Surface ΔT isotherms for Salem's longest plume at end-of-flood on 31 May 1998.



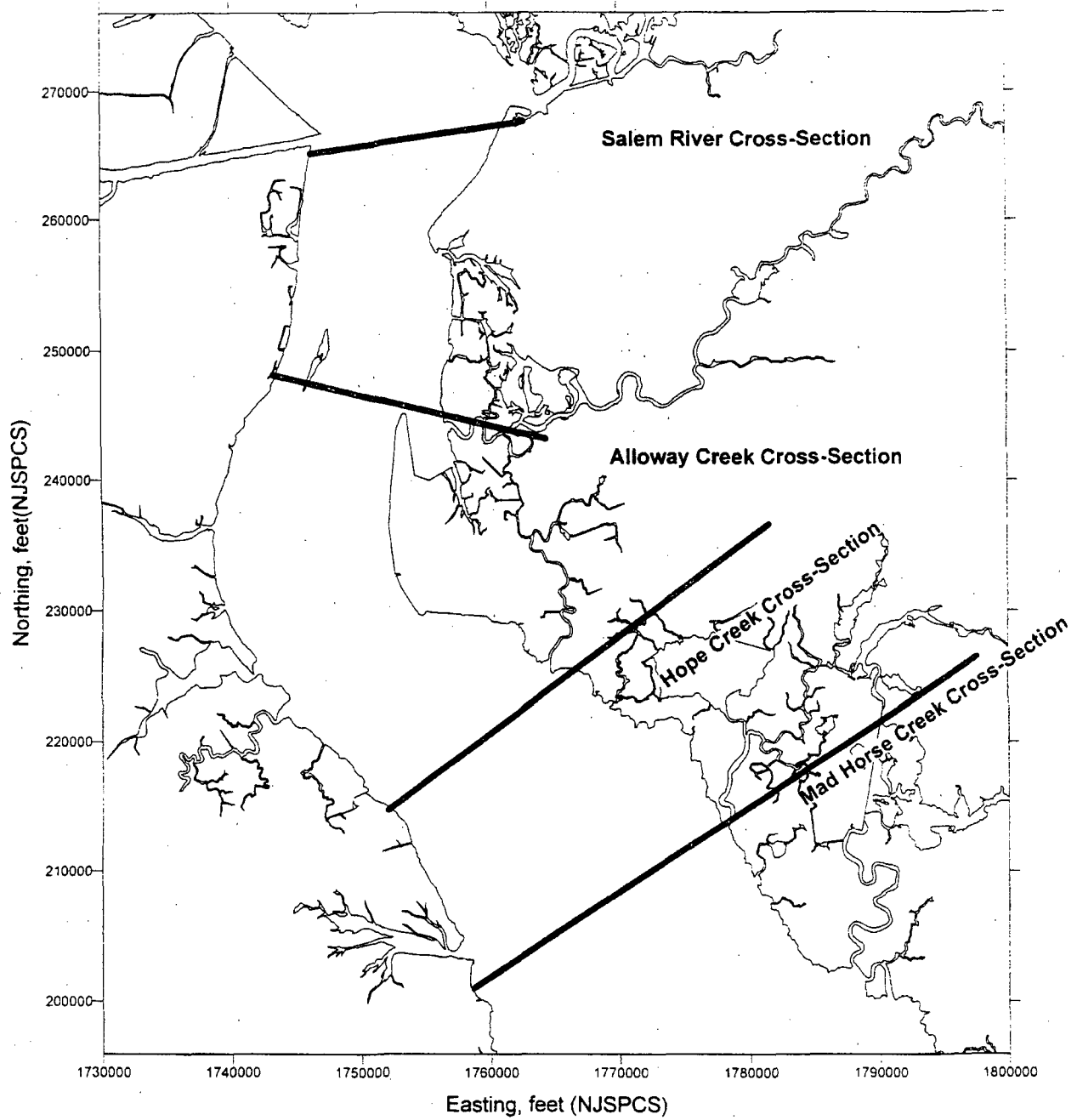
E-2 Figure V-7. Bottom ΔT isotherms for Salem's longest plume at end-of-flood on 31 May 1998.



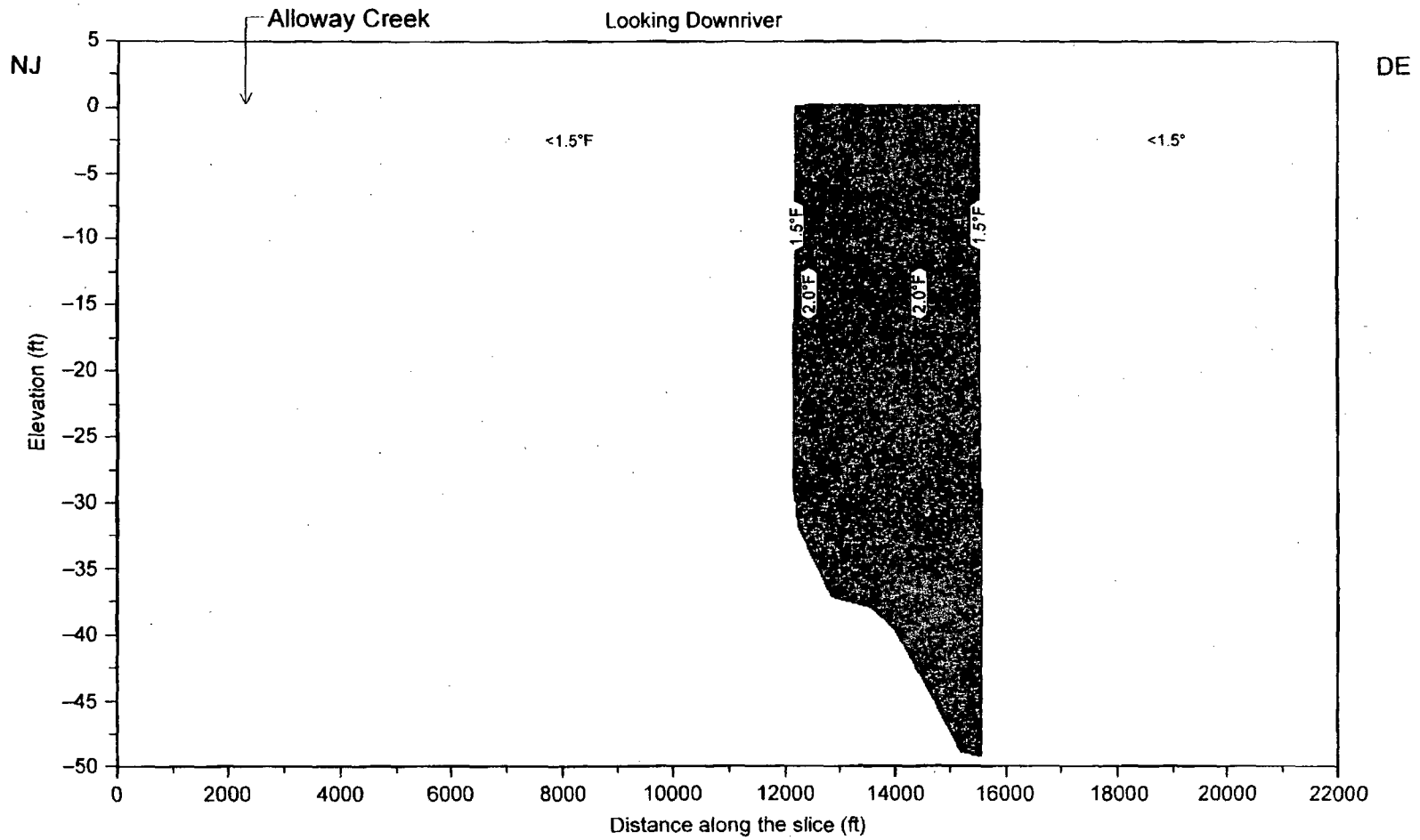
E-2 Figure V-8. Cross-section locations for the Delaware Estuary in the vicinity of the Salem Thermal Discharge



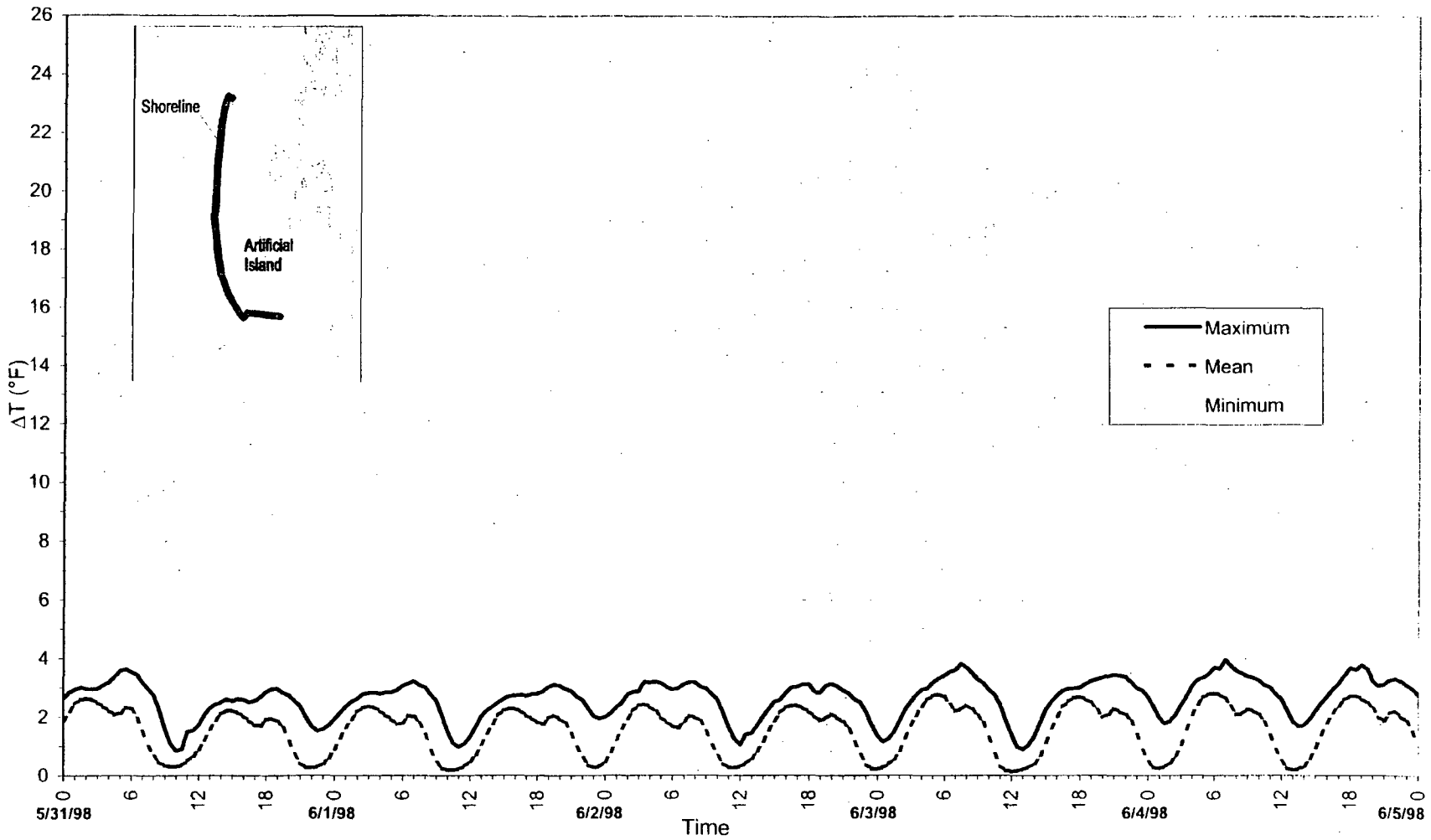
E-2 Figure V-9. Delaware River delta-T cross-section looking down-river at end of ZIM on ebb tide, 2 June 1998, 0830 hrs.



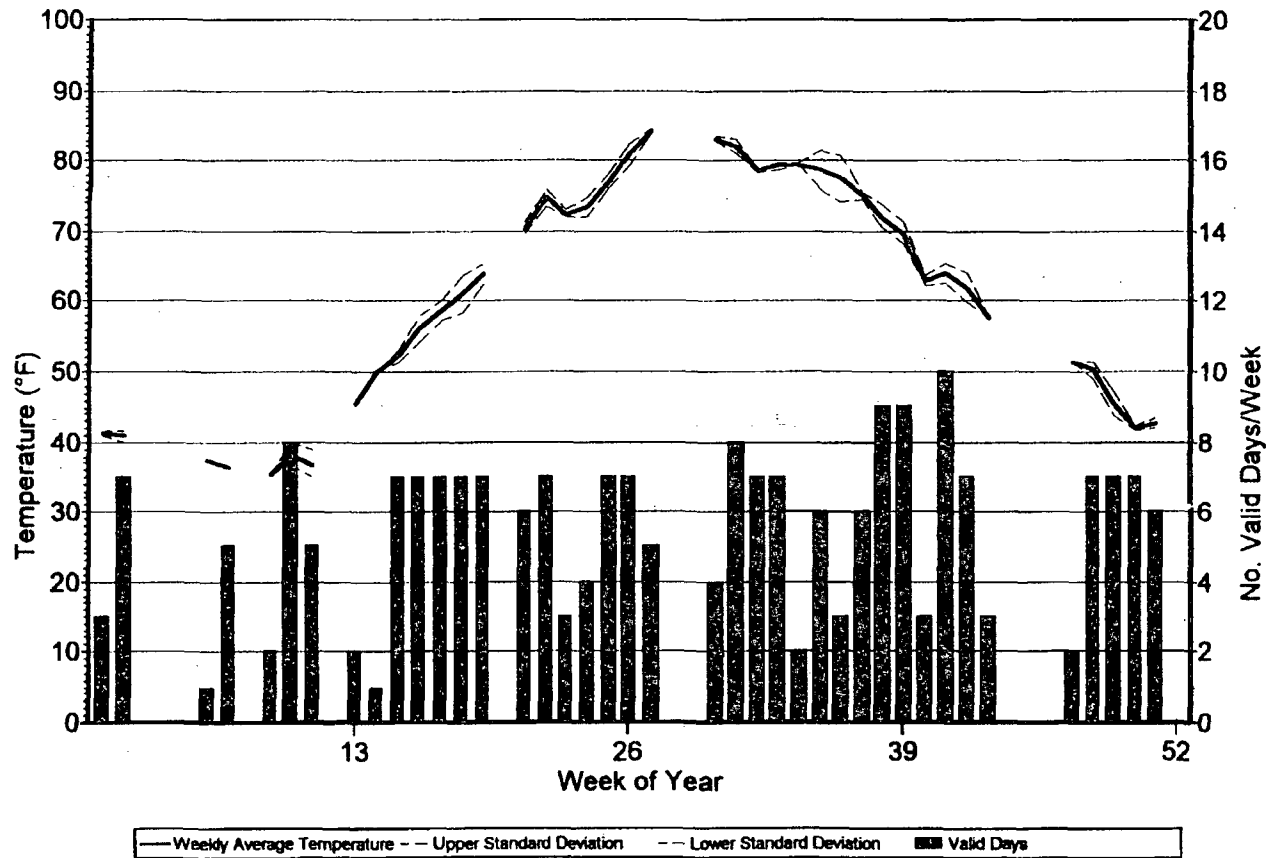
E-2 Figure V-10. Locations of Delaware River cross-sections at mouths of tributaries.



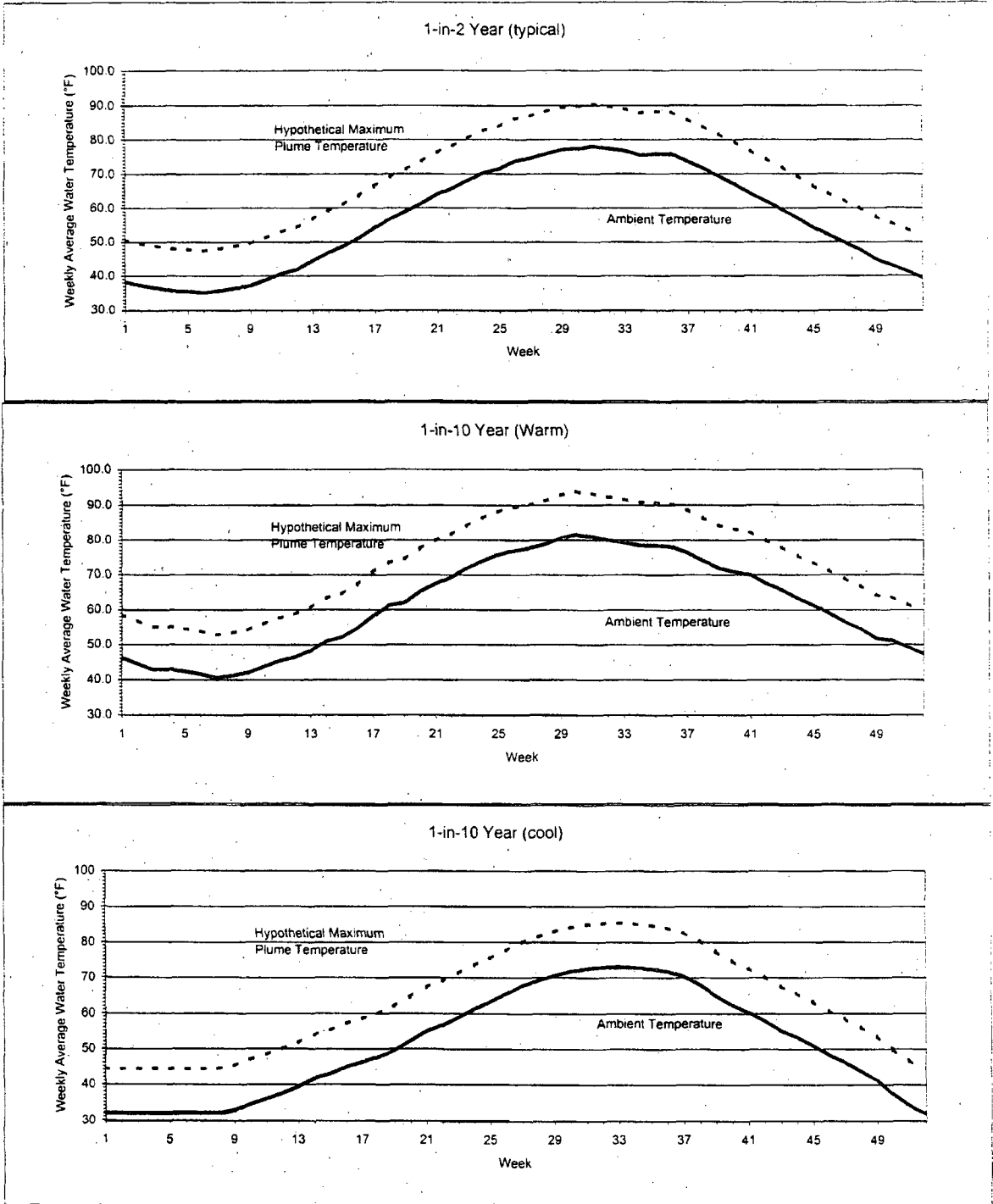
E-2 Figure V-11. Cross-section of ΔT : Delaware River at Alloway Creek on ebb, 2 June 1998, 0830 hrs.



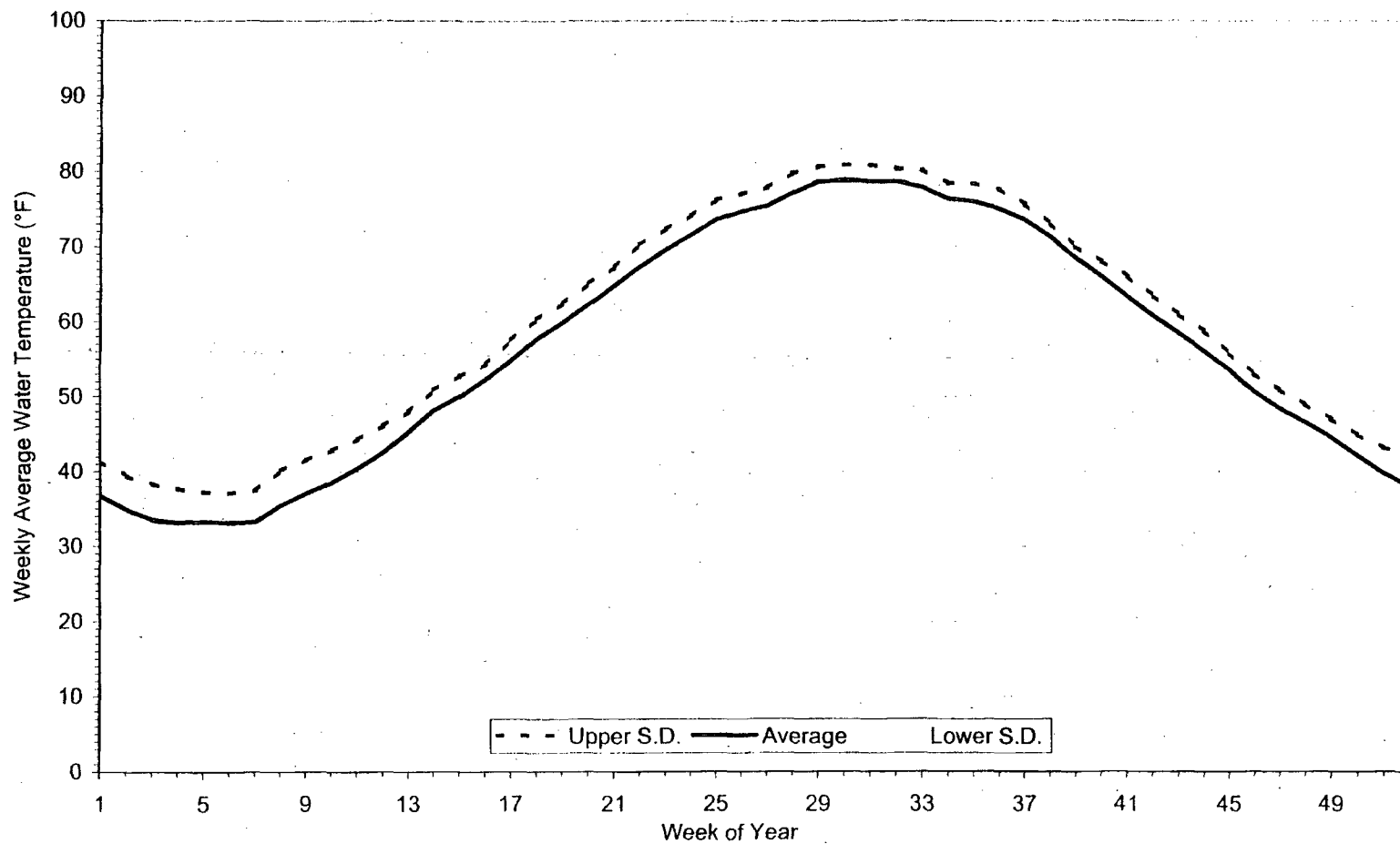
E-2 Figure V-12. Example of Time series of shoreline ΔT along Artificial Island (31 May - 4 June 1998).



E-2 Figure V-13. Weekly Mean Observed Water Temperature at Plant Intake 1992-1998
 Plant at or above 90% Thermal Power for 7 or More Consecutive Days.



E-2 Figure V-14. Ranked Weekly Average Temperatures.



E-2 Figure V-15. 20-Year Average Weekly Ambient Water Temperatures (1978-1997) from ATM Modeling.

**APPENDIX E
ATTACHMENT E-3**

ANALYSIS OF DISSOLVED OXYGEN IN THE VICINITY OF THE STATION

**SPONSOR: DR. DAVID G. AUBREY
PSE&G RENEWAL APPLICATION
SALEM GENERATING STATION
PERMIT NO. NJ0005622
4 MARCH 1999**

ATTACHMENT E-3

**ANALYSIS OF DISSOLVED OXYGEN
IN THE VICINITY OF THE STATION**

TABLE OF CONTENTS

I. INTRODUCTION	6
II. REGULATORY FRAMEWORK	6
III. DISSOLVED OXYGEN DYNAMICS IN ESTUARIES	7
IV. HISTORICAL DO TRENDS NEAR THE STATION	11
V. RECEIVING WATER DISSOLVED OXYGEN LEVELS NEAR THE STATION..	12
V.A. Two-Unit Survey, 2 September to 8 October 1998	13
V.B. Ambient Survey 11 to 14 July 1997	15
VI. MODEL OF DISSOLVED OXYGEN CONTENT IN THE ESTUARY	18
VI.A. Modeling Approach	18
VI.B. The Dissolved Oxygen Model	19
VI.C. Results	21
VII. DISSOLVED OXYGEN IN SALEM'S CIRCULATION WATER SYSTEM	22
VIII. CONCLUSIONS	24

ATTACHMENT E-3
ANALYSIS OF DISSOLVED OXYGEN IN THE VICINITY OF THE STATION

LIST OF TABLES

Table No.	Title
E-3 Table IV-1	Historic and Recent Dissolved Oxygen Concentrations at Appoquinimink River/Liston Pt., DE
E-3 Table V-1	Dissolved Oxygen Meter Depths (Two-Unit Survey)
E-3 Table V-2	Temperatures (°C) During the Two-Unit Survey
E-3 Table V-3	Salinity Data (Two-Unit Survey) (Results in ppt)
E-3 Table V-4	Dissolved Oxygen Concentration (Two-Unit Survey) (Results in mg/L)
E-3 Table V-5	Measured Variations in Temperature, Salinity, and Dissolved Oxygen and Calculated Maximum Oxygen Variation (Two-Unit Survey)
E-3 Table V-6	Dissolved Oxygen Concentration (Two-Unit Survey) (Results in Percent of Air Equilibration)
E-3 Table V-7	Dissolved Oxygen Meter Depths (Ambient Survey)
E-3 Table V-8	Temperature (°C) During the Ambient Survey
E-3 Table V-9	Salinity During the Ambient Survey

- E-3 Table V-10 Dissolved Oxygen During the Ambient Survey (mg L)
- E-3 Table V-11 Measured Variations in Temperature, Salinity, and Dissolved Oxygen and Calculated Maximum Oxygen Variation (Ambient Survey)
- E-3 Table V-12 Dissolved Oxygen Saturation During the Ambient Survey
- E-3 Table VII-1 Sources of Data for Mechanistic Analysis of the Potential Dissolved Oxygen Reduction Through the Station

LIST OF FIGURES

- | Figure No. | Title |
|--------------|---|
| E-3 Fig IV-1 | Historical summer dissolved oxygen concentration. |
| E-3 Fig IV-2 | Dissolved oxygen concentration for annual and summer 1995-1997. |
| E-3 Fig IV-3 | Dissolved oxygen concentrations at Appoquinimink River (RM 51) and Liston Point (RM 49) near Salem. |
| E-3 Fig V-1 | Mooring map (Two-Unit and Ambient surveys). |
| E-3 Fig V-2 | Times series of surface temperature and salinity for the main stem river (9M), Estuary at the Station (21), and Mad Horse Creek. |
| E-3 Fig V-3 | Time series of temperature, salinity, dissolved oxygen concentration, and saturation for the three locations shown in E-3 Figure V-2, for the surface moorings. |

- E-3 Fig V-4 Time series of temperature, salinity, dissolved oxygen concentration, and saturation for the mid-depth moorings.
- E-3 Fig V-5 Frequency distribution of dissolved oxygen concentrations for Two-Unit Survey, at mooring 9M.
- E-3 Fig V-6 Frequency distribution of dissolved oxygen concentrations for Two-Unit Survey, at Mad Horse Creek.
- E-3 Fig V-7 Time series of temperature, salinity, dissolved oxygen concentration, and saturation for three locations: main stem River (E), and two creek mouths.
- E-3 Fig V-8 Frequency distribution of dissolved oxygen concentrations for Ambient Survey, at Delaware location E.
- E-3 Fig V-9 Frequency distribution of dissolved oxygen concentrations for Ambient Survey, at Mad Horse Creek.
- E-3 Fig VI-1 Time-temperature history, worst case scenario
- E-3 Fig VI-2 Dissolved oxygen calculation for the Delaware River.
- E-3 Fig VI-3 Dissolved oxygen calculations (expanded scale).
- E-3 Fig VII-1 Pressure/Temperature/Time Profile for the Station's Circulation Water System.
- E-3 Fig VII-2 Absolute pressure distribution through the Station.

E-3 Fig VII-3 Potential DO reduction through the Station under Ambient Survey
(July 1997) conditions.

E-3 Fig VII-4 Potential DO reduction through the Station under One-Unit Survey
(October 1997) conditions.

E-3 Fig VII-5 Potential DO reduction through the Station under Two-Unit Survey
(Sept. 1998) conditions.

ATTACHMENT E-3 ANALYSIS OF DISSOLVED OXYGEN IN THE VICINITY OF THE STATION

I. INTRODUCTION

In addition to assessing direct thermal effects on the protection and propagation of a balanced indigenous community (BIC), Section 316(a) Guidance requires that the Demonstration present an assessment of indirect effects of heat discharged from the Station, including interactive effects with dissolved oxygen (DO) and other pollutants. This attachment addresses Salem Station's indirect thermal effects on DO. Dissolved oxygen concentrations can change by means of in-pipe physical and biochemical processes in the Station CWS, and as a result of thermal effects on receiving waters or on Estuary biological processes.

In order to address these potential effects, the following analyses were performed: (1) an evaluation of effects on DO levels within the CWS at the Station through a mechanistic analysis of DO concentration fluctuations with varying temperature and pressure; and (2) an evaluation of direct thermal effects on DO levels in the Estuary through two types of analysis. In order to assess direct thermal effects on DO concentrations in the Estuary, historical data, including new sources of data acquired by PSE&G, were analyzed for spatial trends and differences. Second, processes controlling oxygen dynamics in the Estuary were modeled to investigate the effects of thermal discharge on biogeochemical rates in the Estuary.

This attachment is organized as follows. Section II provides the regulatory framework for this analysis of the presence of DO in the Estuary. Section III is an overview discussion of DO dynamics in estuaries, including a brief review of trends in DO concentrations in the Delaware Estuary. The DO trends analysis shows no relationship to Station operations. Section IV summarizes the historical DO trends near the Station. Section V is a review of DO data from measurements made as part of this submittal. This review demonstrates that the data support the finding of no effect on DO from Station operations. Section VI presents results of a modeling analysis of DO within the Estuary. The modeling demonstrates that the Station has no measurable effect on River DO levels. Section VII presents an analysis of DO dynamics within the Station itself. This analysis demonstrates that temperature and pressure changes within the Station CWS have no effect on DO in the river. Finally, Section VIII presents summary conclusions, including the conclusion that DO in the Delaware Estuary is not adversely affected by Station operations.

II. REGULATORY FRAMEWORK

DRBC regulatory standards for DO levels vary by location, season, and averaging interval. The DRBC criteria (DRBC 1996) for dissolved oxygen in Zone 5 of the Delaware Estuary (extending from RM 48.2 at Liston Point to RM 78.8, including the

region fronting the Station) state that the 24-hour average DO concentration shall be not less than:

- 3.5 mg/L at River Mile 78.8
- 4.5 mg/L at River Mile 70.0
- 6.0 mg/L at River Mile 59.5

The regulatory threshold oxygen concentration for the seasonal intervals from 1 April to 15 June and from 16 September to 31 December, developed by the DRBC, must not average less than 6.5 mg/L throughout Zone 5. NJDEP has adopted and incorporated DRBC's water quality standards for the Delaware Estuary, as stated at NJAC 7:9B - 1.14(d).

III. DISSOLVED OXYGEN DYNAMICS IN ESTUARIES

In estuarine environments, water column oxygen content is a key determinant in defining water quality. This respiratory gas is essential to virtually all aquatic life. Through its role in various biogeochemical processes, oxygen plays a major part in the maintenance of the vitality of coastal environments and of the health of its abundant resources.

Estuaries are coastal ecosystems ranging from large open bays to smaller embayments and coastal ponds. Many are riverine, meaning that freshwater transported by rivers meets the saline waters of the coastal ocean. Estuaries exhibit a gradient of increasing salinity from the headwaters to the open ocean. This gradient may influence a variety of ecological processes that occur within the estuarine system, including nutrient dynamics, cycles of biological production and decomposition, and the density stratification of the water column. The nature of these processes in concert with other physical processes such as circulation, tidal flushing, and wind-driven mixing can have significant effects on oxygen concentrations within the system.

Because of their relatively shallow depth, periodic flushing, and proximity to naturally-occurring nutrient sources, most estuaries are nutrient-rich and highly productive, creating an ideal environment for the growth and survival of many ecologically and economically important species of finfish and shellfish. A readily available supply of oxygen to support this growth is fundamentally important to the ecological health of these systems.

Oxygen conditions in estuarine environments at any given moment are the result of complex interactions between both biological and physical processes. Major biological contributions to the cycling of oxygen are production through photosynthesis by phytoplankton and benthic algae and plants, and consumption via respiration by these same algae and plants, by animals, and by microorganisms during decomposition of organic matter within the water column and in the sediments. In an estuary, oxygen production and consumption are in approximate balance with each other. In Chesapeake Bay for example, photosynthesis over the whole water column accounts for 50 percent of the oxygen inputs while respiration accounts for 43 percent of the losses (Kemp et al. 1992).

In the upper water column where light effectively penetrates and photosynthesis occurs, there is often a net increase in oxygen; whereas below the level where light effectively penetrates, there is net oxygen loss due to dominance by respiration. So while the whole system is roughly in oxygen balance, there are local spatial differences in oxygen conditions because of differences in the rates of biological processes that produce and consume oxygen. Since photosynthetic oxygen production is a light-driven process, there is also a day/night temporal disparity between the biological supply and removal of oxygen, with oxygen biologically supplied and consumed during the day, but only consumed at night.

In nearly all coastal embayments, the minimum oxygen levels occur near dawn, after the period of darkness. From the post-dawn minimum, oxygen conditions improve during the day. Therefore measurements of oxygen concentrations conducted only during daylight hours may overestimate average oxygen concentrations over a daily basis. Understanding these processes is important for interpreting oxygen monitoring data for assessment of water quality.

Physical factors that influence oxygen conditions in estuaries are bathymetry, wind-driven mixing, hydrodynamics, temperature, and salinity. These processes act in concert with biological activities, and can have major influences on estuarine oxygen conditions. Under normal circumstances, the exchange of oxygen with the atmosphere and with external waters via the tides is the more influential regulator of estuarine oxygen concentrations compared to biological supply and removal processes. These physical processes alone can account for more than half of the flux of oxygen in and out of estuarine systems. Near Salem, these physical processes are even more dominant due to low bathymetry, or bottom depth, can profoundly influence the ability of oxygen to mix within the water column. Isolated deep basins, cut off from photosynthetic activity, can affect overlying DO concentrations both through their accumulation of organic matter (which results in bottom-water oxygen consumption by decomposition processes within the sediments), and through the inability of wind to mix oxygen physically from surface layers into deeper basins. This vertical separation of water masses is called stratification. During periods of low wind conditions and strong salinity gradients, such stratification of the water column can occur, especially in deep basins and in circulation-restricted areas of rivers and estuaries.

Other physical features of estuaries influence stratification as well. The orientation of the estuary in relation to prevailing winds can affect stratification, either enhancing or inhibiting wind-driven mixing of the water column. A storm can completely overturn a stratified water column in less than an hour, equalizing oxygen concentrations between upper and lower depths. However, the water column may quickly re-stratify after the storm event ends.

Stratification due to salinity gradients can periodically occur in coastal water bodies. It results from a combination of physical and chemical parameters in the estuary whereby

denser, saltier, and colder water settles beneath less dense, fresher, and warmer water. In well-mixed estuaries, tidal forces are sufficient to mix the water column and the system is nearly vertically homogeneous. Tidally-induced vertical mixing is most dramatic during spring tides. The Delaware Estuary is well-mixed by tides and winds, so this stratification process is not a significant contributor to oxygen dynamics in the Bay and Transition Zones.

Seasonal stream-flow events can influence oxygen dynamics in these estuaries. High stream flow can contribute to prolonged stratification and low oxygen levels. These freshwater inputs often carry high suspended solid loads leading to turbid conditions which can significantly reduce photosynthesis and cause net oxygen loss. Conversely, low stream flow can result in less stratification and, when combined with wind-driven circulation, can result in earlier and quicker turnover of the water column. A secondary but attenuating effect occurs due to the relationship between salinity and low stream flow. Because the saturation concentration of DO decreases with higher salinity, low river flow can decrease oxygen content as well.

Water temperature is another important factor that influences oxygen concentration in estuarine ecosystems. At higher temperatures, the solubility of oxygen is lower; as water cools, oxygen capacity in the water increases independent of biological activity (cold water holds more dissolved gas than does warm water). A decrease in DO concentration is frequently observed in conjunction with increasing temperatures from spring to summer. In many instances, the decrease can be accounted for solely by physical processes influencing the solubility of the gas.

Because estuaries are generally shallow, having large surface-to-volume ratios relative to oceanic systems, temperature variations are generally large, reflecting changes in atmospheric conditions through heat exchange at the air-water interface. Exchanges across the sediment-water interface can also affect temperature fluctuations in overlying water columns, with sediments moderating extremes through the storage and release of heat with time. Factors such as tidal and wind-driven mixing can reduce heat storage and aid the exchange of heat from estuarine waters to the atmosphere. As water temperatures increase, biological processes such as photosynthesis and respiration are also affected. Temperature rise causes increases in biological respiration which in turn potentially leads to oxygen-depleted conditions in the water column.

The above discussion has focused on natural processes that influence oxygen conditions in all estuaries. However, during the last 100 to 200 years, human activities have played an increasing role in the health of estuarine ecosystems, including oxygen status (Sutton et al. 1996). Coastal areas have become more heavily populated during this time period and today are sites of intense domestic, agricultural, and industrial activities. Estuaries have historically been recipients of directly discharged domestic and industrial wastes and fertilizers via storm runoff. Studies of sediment cores from several estuaries show that oxygen stress has been steadily increasing during the last 200 years and has been particularly acute during the last 50 years.

The nutrients associated with sewage and fertilizers have a very important effect on estuarine health in general and on oxygen conditions in particular. Nutrients are an important component of the production of phytoplankton and benthic algae and plants, collectively called primary producers. Absence of a key nutrient may limit primary production in a marine ecosystem. Addition of nutrients to estuarine waters commonly stimulates the growth of primary producers, much like fertilizer does to a garden. Freshwater systems are often nitrogen- or phosphorus-limited. Because estuaries typically exhibit gradients in salinity, there may exist a transition from phosphorus limitation in the upper reaches of estuaries to nitrogen limitation near the mouth of the embayment. Seasonal variations in freshwater flow to these systems may result in a temporary shift in nutrient limitation in parts of the estuary. In some estuaries, primary production is limited not by nutrients but by light availability due to high concentrations of suspended particulate matter which negate any stimulatory effect of nutrients. This is the situation in the Transition Zone of the Delaware Estuary where the Station is located (Appendix C).

Increased nutrient inputs from anthropogenic sources stimulate increased rates of primary production, a process called eutrophication. Sources of anthropogenic nutrient inputs to coastal waters are generally classified into two types: point sources, which tend to be discrete and easily quantifiable, and non-point sources, which are more widespread, more difficult to identify and measure, and frequently reach estuarine waters through groundwater transport both directly into embayments and into the tributaries that feed them. Point sources such as storm sewer outfalls, discharge pipes from sewage treatment plants, and waste outfalls from factories and industrial plants have historically been regulated and quantified, whereas non-point sources such as precipitation, surface runoff, and groundwater inputs are more recent issues of concern. Non-point source inputs can originate within a watershed at a considerable distance from the estuary itself and flow to the estuary via streams, rivers, or groundwater.

With increased levels of primary production, there is an increased oxygen demand from respiration, both by the larger populations of algae and plants and by the increased abundance of decaying organic matter. When production of organic matter becomes excessive, physical exchange and biological oxygen production cannot keep up with the ecosystem's respiratory demand, or with biochemical oxygen demand (BOD). BOD is frequently used as an indicator of oxygen stressors and eutrophication in aquatic ecosystems. Sewage and industrial discharges are significant contributors to BOD. In general, the higher the organic matter production, the higher the BOD. Such an imbalance between oxygen production and consumption results in the degradation of water quality and the disappearance of valuable ecosystem resources. The physiological stress associated with low oxygen concentrations can result in the loss of stable, economically valuable populations of finfish and shellfish, and their replacement with undesirable opportunistic species which take advantage of nutrient-rich, oxygen-poor habitats. Although this deterioration may be driven by nutrient loading, it is the depletion of oxygen due to nighttime respiration of these plants combined with microbial

decomposition of organic matter that is the proximate cause. When an ecosystem is severely eutrophic and on the border of failing in oxygen maintenance, the concentrations in the water can swing repeatedly between supportive of life and stressfully low in a short time. During heavier periods of organic matter production, as during summer planktonic algal blooms, coupled with prolonged water column stratification, the oxygen content can be reduced for periods of several weeks to levels having an adverse effect on biological activity. Fortunately, eutrophication is not prevalent in this region of the Delaware Estuary (Sutton et al. 1996).

Although most of the respiration and nutrient regeneration in estuaries takes place in the water column, sediments can also play an important role in the nutrient and oxygen economy of coastal ecosystems. Marine sediments receive dead organic matter from the water column and are sites of active decomposition. As organic matter decomposes, nutrients are released and BOD increases. The amount of nutrient regeneration and oxygen consumption is directly proportional to the amount of organic matter produced. The re-release of nutrients after algae and phytoplankton (whose growth has been stimulated by the initial availability of nitrogen) die and decompose makes nutrients once again available for production in the water column. Thus, the sediments may act as a "storage battery" for nutrients, continuing to provide nutrients for biological production even though the original nutrient inputs may have diminished or ceased. Nutrients regenerated from the sediments can supply almost half of the total nutrients used in primary production. The number of times the nutrients cycle between sediments and the water column before being flushed out to the ocean or buried permanently is directly related to the degree of eutrophication and oxygen depletion.

IV. HISTORICAL DO TRENDS NEAR THE STATION

Examination of the historical trends requires an averaging period that is long enough to remove unrepresentative, short-term variability, yet short enough to reveal significant long-term trends. Hydrological, physical, biochemical, and meteorological variations can be given as an example of short-term variability.

Figure IV-1 presents historical DO profile trends along the main stem of the Estuary for the periods 1968-1970, 1978-1980, 1983-1985, 1988-1990, and 1995-1997 based on DRBC's biweekly boat surveys. There is a dramatic increase in historical DO concentrations over time, specifically from RM 60 to RM 120. This change can be quantified approximately as 3.5 mg/L for a maximum increase around RM 90 - RM 95 from the 1968-1970 period to the 1995-1997 period.

The average DO concentrations for the 1995-1997 period is compared with summer data for the same period in Figure IV-2. A decrease of about 1 mg/L can be observed between overall average and summer concentrations due to high concentrations during the winter season when colder water holds more oxygen.

Table IV-1 provides summaries of historic and recent DO data near the Station (specifically for Appoquinimink River (Rm 50.9) and Liston Pt., (Rm 49.0), DE). During

the historical 1971–1997 sampling period, the average concentration of all DO data was 7.9 mg/L. Occasionally, measurements below 5 mg/L were observed (Figure IV-3). The average DO concentration from 1995 to 1997 was 7.0 mg/L (Table IV-1), with a summer average of 6.1 mg/L and a minimum observation of 4.4 mg/L.

At the Appoquinimink/Liston Point station, about 10% of the historical summer DO concentrations were less than 6 mg/L. Over the entire monitoring period (1971-1997, Figure IV-3), no significant trends in DO were found for either the summer seasons or for all seasons combined (Attachment C-15).

V. RECEIVING WATER DISSOLVED OXYGEN LEVELS NEAR THE STATION

Two sets of field data were examined to quantify relationships between DO concentrations close to and away from the Station. One is the most continuous set of oxygen data available from the Two-Unit Survey, obtained during the late summer/early fall of 1998 (Exhibit E-1-3). The second set is from a five-day interval when the Station was not operating (Ambient Survey, 11 to 16 July 1997, Exhibit E-1-2). Comparisons of data quantify differences in DO concentrations due to a variety of factors, including the thermal discharge from the Station.

The present analysis complements the other sections of this Appendix. The previous section addressed the historical trends of oxygen in the Estuary. The present section addresses a limited set of field measurements taken in the Estuary within 10 miles of the Station. The next two sections represent modeling efforts of DO in the Estuary fronting the Station, and within the Station.

The objective of this Section is to evaluate what differences, if any, occur in short-term (week-to-month time scale) measurements of dissolved oxygen in the vicinity of the Station. The comparisons are made here not only for the mean levels of oxygen (which may vary along the Estuary as described in the previous section), but also for the magnitude of diurnal (daily) and tidal (twice daily) changes in oxygen levels. These diurnal and tidal time scales mirror the dominant processes that control oxygen in the estuary. The diurnal time scale represents the biological processes associated with respiration and photosynthesis, which respond to the daily solar cycle. To a lesser extent, the diurnal time scale is representative of oxygen variations due to heating and cooling of the atmosphere and water, and to daily land-sea breezes. The tidal time scale represents the movement (advection) of waters past the fixed moorings, bringing alternately more or less oxygenated waters from adjacent portions of the Estuary.

The changes in DO in the Estuary possibly attributable to Station operations is placed in context of the other contributors to temperature fluctuations and its influence on oxygen dynamics. In particular, the Station is surrounded by marshes, most proximately the Mad Horse Creek marsh, the Hope Creek marsh, and the Alloways Creek marsh. In the twenty miles surrounding the Station (10 miles upstream and 10 miles downstream), the area of

marsh is 70.9 square miles, more than the area of the main stem River (65.2 square miles, Exhibit E-1-5).

V.A. Two-Unit Survey, 2 September to 8 October 1998

The "Two-Unit Survey" conducted in the fall of 1998 involved the deployment of multiple oxygen, temperature, and salinity recording instruments during the operation of both of the Station's generating units. These instruments, attached to moorings, made measurements at 10-minute intervals at fixed depths (Exhibit E-2-2). The high frequency of data collection was needed to capture variations in the dissolved oxygen field associated with tidal and diurnal cycles, and other periodic influences (e.g., thermal discharge, storms, wetland discharges, etc). Even short-term depletions of dissolved oxygen can be significant to biota, and consequently the ecological health of the receiving waters. The focus of the evaluation of the high-frequency measurements is to determine the natural baseline conditions in the estuarine waters and the potential effects of thermal discharges from the Station on that baseline.

Dissolved oxygen concentrations in the Estuary were measured directly (using pulsed polarographic electrodes) while obtaining parallel measurements of temperature and salinity to aid in the interpretation of the DO data. Dissolved oxygen concentrations are controlled, in part, by the temperature and salinity of the water. As water temperature and salinity increase, the DO saturation value decreases. These physical parameters determine the amount of oxygen in estuarine water that is in thermodynamic equilibrium with the overlying atmosphere (air). Biological processes are typically responsible for the oxygen deficit or excess within estuarine waters (measured as DO concentration in air-equilibrated water minus actual DO concentration).

The mooring locations for the Two-Unit Survey are indicated in Figure V-1. The Two-Unit Survey of DO was conducted while both power generating Units were in operation. The three mooring stations were: mooring 9M (271940 Northing and 1751713 Easting), midstream, and in the far field of the discharge; mooring 21 (229451 Northing and 1753707 Easting), near the discharge of Salem Station off Artificial Island; and mooring MHC (213522 Northing and 1778204 Easting), at the mouth of Mad Horse Creek. Depths at which the dissolved various meters were deployed are shown in Table V-1. Examples of the measured temperatures and salinities representative of the deployment period are shown in Figure V-2.

Water temperatures during the Two-Unit Survey period are summarized in Table V-2. This time interval of September to early October was one of high water temperatures, with maxima ranging up to 30.2 °C (86.4 °F), and minima of 17.4 °C (63.3 °F). Temperature ranges in the main-stem River were up to about six degrees at the surface and mid-water. Temperature ranges in the Estuary near the Station varied up to 9.3 °C (48.7 °F). Finally, temperatures within Mad Horse Creek ranged up to 8 °C (46.4 °F).

Salinity during the Two-Unit Survey period is summarized in Table V-3. Salinities are higher than normal at this time since river flow in the Fall typically is low (Appendix C).

Mean salinities vary from a low of 5.9 ppt in the River north of the Station, and a high of 13 ppt in Mad Horse Creek. Salinity ranges are greater at mooring 21 opposite the Station, reflecting the normal flow of the tide on flood and ebb.

Dissolved oxygen concentrations measured during the Two-Unit Survey are summarized in Table V-4. Mean DO concentration varies from just under 6 mg/L to a high of just under 7 mg/L. Ranges in dissolved oxygen are much higher in the marsh than in the main stem River (3-4 mg/L versus 1-3 mg/L).

There was a seasonal increase in both oxygen concentration and percent saturation at all three mooring stations from September to October as water temperatures declined (Table V-4). This pattern is associated with the seasonal temperature cycle and is typical of temperate estuaries. The autumnal temperature decline increases the capacity of the water to hold oxygen, and also decreases the rate of biological processes controlling oxygen uptake in shallow estuarine systems.

Summaries of variations in measured water temperature, salinity, and dissolved oxygen are presented in Table V-5. The calculated maximum oxygen change due to variations in salinity and water temperature is also shown. The calculated variation due to physical factors are nearly the same as the measured values, except at Mad Horse Creek, where the natural variation is larger by 2 to 3 mg/L than that caused solely by changes in salinity and water temperature.

DO content is dependent on a number of factors, both biological and physical (for example, wind speed, vertical mixing). The maximum concentration of DO is normally limited by the air equilibration value, also referred to as air saturation. This saturation value decreases as temperature and salinity increase. DO concentrations are commonly compared to the saturation value, since this measure will indicate how undersaturated or oversaturated the water is. Percent saturation is the measure of the ratio of DO concentration to its saturation value.

Table V-6 shows the percent saturation for the different moorings at different levels. The maximum saturation for the one-month period varies from about 85 percent to just above 100 percent. Minimum saturation varies from 40 percent (in the marsh) to a value of 80 percent (in the River). The range of percent change in saturation is greatest in the marshes (39 to 52 percent) and lowest in the River (8 to 28 percent).

Figure V-3 overlays the time series of temperature, salinity, and dissolved oxygen concentration at the surface moorings. Figure V-4 overlays these same parameters for the mid-depth moorings. Figure V-3 demonstrates that the fluctuations in dissolved oxygen concentrations are river-wide in occurrence, and vary not only with salinity and temperature but also with tidal transport. There is a pattern of diurnal oxygen level variations at mooring stations 9M and 21, whereas the pattern at MHC at the mouth of the creek is distinctly tidal. The greatest drops in oxygen occur within the marshes. The River diurnal variation reflects daily solar insolation patterns, whereas the marsh

semidiurnal variation reflects tidal export processes. Figure V-4 shows a similar result for the mid-depth. Despite the slightly higher temperatures near the Station, the mean salinities are not depressed compared to the main stem River mooring (9M). The data are consistent with the absence of a Station effect on Estuary DO levels.

The main oxygen story lies with the marshes. Mad Horse Creek is shallow and its waters are warmer than Estuary waters during the summer months. Warm water holds less oxygen than cooler water. Moreover, oxygen supply in creek waters is further depleted by biological respiration in both the water column and sediments of the creek and connected wetlands. The BOD in bottom sediments of shallow creeks and wetlands, combined with the large surface-to-volume ratio, causes a greater oxygen sink than is present in the adjacent bay system. The effect is a greater biochemical oxygen demand per unit surface area within the creek system.

When warmer, oxygen-depleted creek water enters the River during tidal ebb, oxygen concentrations decrease. Oxygen levels in the marshes rise as Estuary waters enter the creek during flood tides. The pattern at this time of year indicates that the creek acts as an oxygen sink, delivering low-oxygen water to the Estuary, in spite of the high biological productivity. This finding is consistent with the fact that detrital loads in the marsh creeks are high this time of year, creating oxygen demand. At mooring station 21 at mid-depth (20 feet) in late September, there is evidence of only a weak effect of the thermal discharge on dissolved oxygen level during ebb tide; this is a much smaller response than observed from natural oxygen fluctuations in ebbing creek waters at MHC. Marsh dissolved oxygen concentrations decrease slightly (less than 1 mg/L) during this ebb tide period but increase again during flood tide with better oxygenated River water. Mad Horse Creek acts, in a sense, as an effluent conduit, delivering warm, oxygen-depleted water to the Estuary at this time of year.

This concept of strong marsh influence is demonstrated in Figures V-5 and V-6. Figure V-5 shows the frequency of occurrence of dissolved oxygen concentration at both the surface and mid-depth sensors. The values all lie between 5.5 and 7.5 mg/L, with the vast majority between 6.0 and 7.0 mg/L. By contrast, Figure V-6 shows the frequency distribution of DO concentration at Mad Horse Creek. The DO in the marsh covers a much broader range of values, from 3 to 7.5 mg/L. These figures show the strong influence of marshes on the DO content in its vicinity. Since marshes cover an area of 70.9 square miles within a distance of 10 miles to either side of the Station, compared to the 65.2 square miles covered by open water in this same stretch, the marshes contribute to the overall DO balance within the Estuary.

V.B. Ambient Survey 11 to 14 July 1997

Moored oxygen, temperature, and salinity sensors were deployed on moorings for a 5-day interval from 11 to 16 July 1997. During this interval, there was no thermal circulation water discharge from the Station. The moored instruments recorded water-column conditions in a similar manner to the Two-Unit Survey of the fall of 1998. The data are comparable except that no post-survey instrument calibration data are available for the

Ambient Survey. Generally, instruments are calibrated before and after every deployment to evaluate instrument performance. The results are used in this analysis even absent these post-survey calibrations, because the instruments were calibrated pre-survey, and were deployed for only a limited interval (5 days). Two instruments, one at mooring HC mid-depth and one at mooring MHC surface, were not used in this analysis due to data inconsistencies characteristic of instrumentation difficulties.

These data are explained and presented in greater detail in Exhibit E-1-2, the report on the Ambient and One-Unit surveys. The five mooring stations used for this July 1997 Ambient Survey were mooring E (231497 Northing, 1752044 Easting); mooring H (227658 Northing, 1755286 Easting); mooring Alloways Creek (AC, 244142 Northing, 1756769 Easting); mooring Hope Creek (HC, 226067 Northing, 1764500 Easting); and mooring Mad Horse Creek (MHC, 213491 Northing, 1778076 Easting). Table V-7 lists the water depths at which the instruments were deployed during the Ambient Survey.

Water temperatures during the Ambient Survey period are summarized in Table V-8. This time interval of July was one of high water temperatures, with maxima ranging up to 29.1 °C (84.4 °F), and minima of 25.5 °C (77.9 °F). Temperature ranges throughout the Estuary varied from 1° to 2 °C (1.8° - 3.6 °F) in the River, to up to 4 °C (7.2°F) in the marshes. Marsh moorings exhibited the highest temperatures as well as the lowest temperatures, illustrating their contribution to the heat balance of the river (Exhibit E-1-5).

Salinity during the Ambient Survey period is summarized in Table V-9. Mean salinities vary from a low of 4.3 ppt in the River, and a high of 9.7 ppt in Mad Horse Creek. Salinity ranges are greatest in the River, reflecting the normal flow of the tide on flood and ebb, and lower in the marshes.

Dissolved oxygen concentrations measured during the Ambient Survey are summarized in Table V-10. Mean DO concentration varies from 6.3 to a high of 7.6 mg/L. Ranges in dissolved oxygen are much higher in the marsh than in the main stem River (2.5 to 6 mg/L versus 1.5 to 2.2 mg/L).

Summaries of variations in measured water temperature, salinity, and dissolved oxygen are presented in Table V-11. The calculated maximum oxygen change due to variations in salinity and water temperature is also shown. In contrast to the September 1998 data, the measured maximum oxygen variation exceeded that calculated from salinity and temperature dependence. This suggests a higher level of biological activity during this time interval compared to the September 1998 interval. The largest differences between measured and calculated were observed in the marshes, further evidence of the enhanced biogeochemical oxygen processes in these shallow marshes.

Table V-12 shows the percent saturation for the different moorings at different levels. In the River, saturation varies from 80 percent up to 111 percent (surface values at both River moorings). In the marshes, percent saturation ranged from 53 percent up to 144

percent, a much greater range than in the River. Marsh oxygen saturations display a much larger range than present in the River moorings.

Figure V-7 overlays the time series of temperature, salinity, and dissolved oxygen concentration at the surface moorings. The marshes show a much stronger DO concentration signal than the River. The marshes show a significant tidal variability modulated by a diurnal variability, whereas the River shows a strong diurnal variability, reflecting the different processes controlling the DO concentration. The distinct diurnal variation of 0.9°C (1.6°F) to 1.9°C (3.4°F) at all stations suggests that the greatest influences on water temperatures in the summer are solar radiation and the ambient air temperature. In the marshes, tidal import/export processes contribute strongly to DO fluxes.

Figure V-8 and Figure V-9 demonstrate the effect of marshes on the oxygen dynamics. Figure V-8 shows the frequency distribution of dissolved oxygen concentrations measured in the River during the Ambient Survey. The range of DO is narrow, from 6.0 to 8.5 mg/L. Once the River water enters the marshes, various processes spread the DO concentrations markedly. Mad Horse Creek has DO concentrations ranging from 3.5 to 10. Marsh processes therefore add and take away DO from the water, depending on time of day and tidal stage. These observations suggest that, similar to mooring station MHC in the Two-Unit Survey of 1998, the creek systems act as oxygen sinks, delivering oxygen-depleted water to the Estuary under certain conditions of solar insolation, tidal phase relative to daylight hours, and possibly season.

These field studies permit several conclusions. The first is that oxygen measurements at the mouths of the creeks (mooring stations AC, HC, and MHC) consistently indicate that these marsh creeks act as natural conduits, delivering an effluent that is oxygen-depleted by biological respiration during certain conditions.

The second conclusion results from comparing the variations of these natural marsh creek conduits to the variations near the Station discharge. This comparison shows no evidence of any discernable, consistent effect of the Station's thermal effluent on dissolved oxygen concentrations in receiving waters.

The DO data from each of the three sites measured in fall (Two-Unit Survey) show similar average depletion of oxygen relative to atmospheric equilibrium. The lack of a strong spatial pattern in relative oxygen depletion supports the contention that biological and physical processes operating within the Estuary are the dominant controls on oxygen levels, and that the effect of the thermal discharge on oxygen is small even within the near-field of the Station's thermal discharge.

All measurements show DO concentrations adjacent to the Station that are consistent with the DO concentrations in the River away from the Station. The DO concentrations off the Station are at levels that support aquatic life, according to USEPA guidelines.

These results suggest that any DO level changes due to thermal discharge from the Station during September and early October 1998 are small, periodic, and short-term. The variation in DO concentrations in receiving Estuary waters due to the thermal discharge is substantially smaller than variations due to other naturally occurring processes, such as biological photosynthesis and respiration within the creeks and marshes adjoining the main stem River.

VI. MODEL OF DISSOLVED OXYGEN CONTENT IN THE ESTUARY

VI.A. Modeling Approach

Physical processes that affect the concentration of DO in estuarine waters include exchange with the atmosphere at the surface (reaeration), and changes in temperature, salinity, and pressure. Biogeochemical processes that affect DO levels include consumption of oxygen via respiration and microbial decomposition of organic matter, and production of oxygen via photosynthesis.

This analysis assesses the effects of the Station's discharge on DO levels under full two-unit operation, based on thermal modeling results and accepted relationships that describe temperature effects on mechanisms that affect DO.

Mechanisms that relate temperature increases in a water body to a change in DO concentrations include (1) a decrease in the saturation concentration of DO with rising temperatures, which lowers the tendency for reaeration, and (2) an increase in the reaction rates for specific DO mechanisms: BOD deoxygenation, reaeration, photosynthesis and respiration, and sediment oxygen demand (SOD).

The saturation of DO is a well-known function of temperature and salinity. Although reaction rate coefficients have typical ranges (based on the Arrhenius relationship), the effect of temperature on those rates can vary from water body to water body. The best source for the local, Delaware Estuary-specific reaction rates is the DO model of the Delaware Estuary recently developed for DRBC by HydroQual (1998). The DRBC model is a three-dimensional, hydrodynamic and time-variable water quality model of the Delaware Estuary between Liston Point (RM 48) and Trenton (RM 133). This study area includes the site of Salem Station (RM 50). The underlying equations employ reaction kinetics to describe the interactions between nutrients (carbon, nitrogen, phosphorus), phytoplankton, and DO. The report provides data on the DO, nitrogen, and phosphorus concentrations, and the BOD, in the Estuary, along with applicable model parameter values as a result of the model calibration and verification. Together with time-temperature history curves from the thermal modeling with and without Station discharge, this rate information can be used to estimate the effect of the elevated temperature regime on DO.

VI.B. The Dissolved Oxygen Model

The sources and sinks of DO can be mathematically expressed by the DO equation in the HydroQual Report. This equation provides the values used in the analysis.

DissolvedOxygen =

$$k_a \theta_a^{(T-20)} \times ([DO_{sat}] - [DO]) \quad \text{Atmospheric Reaeration}$$

$$- a_r \times k_{pr} (Gp) \times P_c \quad \text{Algal Respiration}$$

$$- a_{on} \times k_{9,10} \theta_{9,10}^{(T-20)} \times [NH_3] \times \frac{[DO]}{k_{nitr} + [DO]} \quad \text{Nitrification}$$

$$- k_{12,0} \theta_{12,0}^{(T-20)} \times BOD_s \times \frac{[DO]}{k_{DO} + [DO]} \quad \text{BOD Oxidation}$$

$$- SOD \quad \text{Sediment Oxygen Demand}$$

where :

$K_a = 0.15 \text{ day}^{-1}$ = reaeration coefficient at 20°C at RM 48 to 50

k_{pr} = endogenous respiration rate = 0.04 day^{-1}

$k_{9,10}$ = nitrification rate at 20°C = 0.5 day^{-1}

k_{nitr} = half saturation constant for nitrification limitation = 1 mg/L/day

k_{DO} = BOD oxidation; half saturation constant for DO = mg/L/day

$k_{12,0}$ = BOD oxidation rate constant at 20°C = 0.05 day^{-1}

BOD_s = Soluble ultimate BOD fraction

$$= \frac{1}{2} \times 4.5 \times BOD_s = 2.25 BOD_s$$

θ_a = atmospheric reaeration temperature coefficient = 1.024

$\theta_{9,10}$ = nitrification temperature coefficient = 1.080

$\theta_{1.2,0}$ = BOD/oxidation temperature coefficient = 1.047

SOD = sediment oxygen demand = 0.5 g/m²/day

$a_{oc} = 2.67 [O_2] / [C]$

$a_{on} = 4.57 [O_2] / [NH_3]$

P_c = Phytobiomass = 0.003 mg Chl/L × 40 [C]/[Chl] (carbon-to-chlorophyll ratio)

[DO] = concentration of dissolved oxygen from previous time step; mg/L

[DO_{sat}] = concentration of DO saturation (Thomann & Mueller 1987)

[NH₃] = concentration of NH₃ at RM 48 to 50; 0.02 mg/L

The focus of this analysis is on temperature-dependent reactions that affect DO concentration. The dependence of a reaction rate (symbolized by certain subscripted k terms in the DO equation) on water temperature follows the Arrhenius relationship:

$$k_T = k_{20} \theta^{(T-20)}$$

in which

k_T = rate coefficient at temperature T (day⁻¹)

k_{20} = rate coefficient at 20°C (day⁻¹)

T = temperature (°C)

θ = temperature correction coefficient (unitless)

The terms in the DO equation that have this Arrhenius relationship are evaluated at two Estuary temperature conditions: with Station operation and without Station operation (ambient). The incremental difference in the computed DO concentration is a prediction of the effect of the Station thermal discharge on DO in the Estuary.

The first term on the right side of the DO equation expresses atmospheric reaeration, which increases with increasing temperature. The second term is algal respiration, which is dependent partially on the algal biomass and associated photosynthesis. Although HydroQual's model includes a term for algal photosynthesis, the effect of photosynthesis is negligible downstream of RM 70 to about RM 48 (the Transition Zone). Therefore, algal photosynthesis is not included in this analysis of the Station's thermal discharge (located at approximate RM 50) although algal respiration is included in the model.

The third term is nitrification, which also increases with increasing temperature. The fourth term, oxidation of soluble biochemical oxygen demand (BOD), includes two factors. The first factor (1/2) is the portion of the total BOD that is soluble; the second

factor (4.5) is the ratio of ultimate BOD to 5-day BOD. The fast- and slow-reacting dissolved BOD are combined in the term BOD_5 because Delaware Estuary-specific empirical reaction coefficients for both forms are identical, according to Appendix B-2 of the HydroQual Report. The ammonia (NH_3/NH_4) and BOD_5 concentrations were estimated based on August and September 1995 data presented for RM 48 to RM 53 of the HydroQual model. These concentrations remain constant in time (and space) for both conditions analyzed.

The fifth term is for sediment oxygen demand (SOD), which is temperature-dependent, but is not modeled as such for the Delaware Estuary by the HydroQual Report. Although the DO reduction due to SOD is computed in this analysis, there is no difference between the results of the two conditions evaluated because of the lack of temperature dependence.

The magnitude of the temperature increase and the duration of this increase as simulated by the hydrothermal model (RMA-10), are used in this mechanistic analysis of DO. The release of water in the Station's thermal discharge at various tidal times was simulated under operational and non-operational conditions (Appendix E Section V.E). The release that resulted in the maximum sustained, elevated ΔT during the three hours following Station discharge is taken as the worst-case time-temperature history of a parcel of water flowing from the discharge. In this simulation, as the thermal plume rises to the surface, the parcel of water analyzed for DO follows the centerline of the plume. The ΔT for this worst case is approximately $3.9^\circ C$ ($7^\circ F$) during the half hour following release and decreases to approximately $2.2^\circ C$ ($4^\circ F$) after three hours (Figure VI-1). Although the decrease is not monotonic, an exponential decay was assumed in order to extrapolate the ΔT beyond the hydrothermal model simulation period.

The ambient temperature, salinity, and initial DO concentration values for the analysis were taken from data collected at mooring station 9M for 4 to 17 September 1998. This period coincides with the seasonally warm Estuary temperatures that pose relatively severe conditions for attaining adequate DO concentrations. An ambient temperature of $26^\circ C$ ($78.8^\circ F$), salinity of 6.9 ppt, and an initial DO concentration of 6.5 mg/L (averages of the data) were used.

VI.C. Results

The computations of the change in DO concentration associated with each term of the DO equation were performed. A computational timestep of 0.5 hours was set to compute DO concentration for a total interval of 70 hours.

The computed DO concentrations for operational and non-operational conditions are shown graphically along with the DO saturation concentration when the plant is operational (Figure VI-2). The DO saturation point for ambient condition is 7.80 mg/L. The maximum difference in DO of 0.05 mg/L occurs between 19 and 43 hours following discharge, and is shown on an expanded DO scale in Figure VI-3. This maximum

difference is less than the accuracy of DO measurements in natural waters (generally considered to be 0.1 mg/L).

The difference in DO levels decreases with time after hour 43 because change in DO levels attributable to reaeration increases with decreasing DO concentration, whereas the rates of change due to nitrification and BOD oxidation decrease with decreasing temperature. The net effect is that the difference in the rate of change in DO levels between the two temperature conditions decreases and hence the change in oxygen levels diminishes.

The effects on DO below the water surface due to increased stratification associated with the thermal discharge are not assessed by this analysis of the worst-case release. This vertical variation in DO levels is small because the Estuary is generally well-mixed in salinity and temperature. Vertical profiles of temperature in the near-field plume showed less than 1°C (1.8°F) difference over depth. Analysis of field observations supports this conclusion.

The mechanistic analysis of the effect on DO in the Delaware Estuary demonstrates that the Station's thermal discharge does not reduce the DO concentration in the receiving waters.

VII. DISSOLVED OXYGEN IN SALEM'S CIRCULATION WATER SYSTEM

In addition to salinity and elevated temperature, other factors can also affect DO concentration. Among these is variation in absolute pressure. The purpose of this analysis is to evaluate the effect of in-pipe DO reductions as the cooling water passes through the Station's CWS.

The results were modeled using standard relationships for DO concentration as a function of temperature, salinity, and nonstandard pressures. The American Public Health Association provides a relationship describing dissolved oxygen saturation concentration at nonstandard pressures resulting from atmospheric conditions as a function of the partial pressure of water vapor, valid for absolute pressures ranging between 0.0 and 2.0 atm (USEPA 1985). Equilibrium of DO saturation with changing pressures is assumed to be instantaneous. The equation governing the relationship is:

$$C_{sp} = C_{so}P \left[\frac{[(1 - P_{wv} / P)](1 - \theta P)}{(1 - P_{wv})(1 - \theta)} \right]$$

C_{sp} = DO saturation (mg/L) at pressure P

C_{so} = DO saturation at sea level as function of temperature and salinity

C_{st} = DO saturation at sea level as a function of temperature only

$$\ln C_{so} = \ln C_{st} - S \left(1.7674 \times 10^{-2} - \frac{1.0754 \times 10^1}{T} + \frac{2.1407 \times 10^3}{T^2} \right)$$

and

$$\ln C_{st} = -139.34411 + \frac{1.575701 \times 10^5}{T} - \frac{6.642308 \times 10^7}{T^2} + \frac{1.243800 \times 10^{10}}{T^3} - \frac{8.621949 \times 10^{11}}{T^4}$$

S = salinity in ppt

T = temperature Kelvin (K)

P = nonstandard pressure in atm; standard pressure is 1 atm

P_{wv} = partial pressure of water vapor, atm, calculated from:

$$\ln P_{wv} = 11.8571 - (3840.70/T) - (216961/T^2)$$

$$\theta = 0.000975 - (1.426 \times 10^{-5}t) + (6.436 \times 10^{-8}t^2)$$

t = temperature °C

The DO concentration of the intake water was taken from available data collected during the ambient (July 1997), One-Unit (October 1997), and Two-Unit (September 1998) Surveys. Table VII-1 summarizes the sources of data used in this analysis. The delta temperature and pressures of cooling water at representative points in the cooling system were provided by PSE&G as illustrated in the 1994 Salem 316(b) Demonstration (Figure VII-1). The absolute pressure measurements at various points in the CWS are presented in Figure VII-2. The saturation concentration of DO was then calculated as a function of temperature, salinity (assumed constant throughout the CWS), and the absolute pressures presented.

The CWS undergoes pressure changes at various points throughout the system, which affect the partial pressure of dissolved gases in the water. In all scenarios, however, the predicted saturation concentration of DO at the condenser and discharge pipe outlet is greater than the measured Estuary water concentration of DO. Figures VII-3, VII-4, VII-5 present the saturation concentration profile through the CWS at various intake temperatures and salinity concentrations. The figures reveal that DO concentration within the condenser unit may be low (less than 4 mg/L) due to decreasing absolute pressure within the unit. However as the absolute pressure increases through the condenser outlet, the saturation concentration of DO increases. This enables the released oxygen to redissolve in the circulating water. Because measured Estuary water DO levels are lower than the saturation concentration in the discharge pipe outlet, there is no DO reduction in the circulating water system.

This analysis is consistent with the expected DO transfer within a closed system. The transfer of oxygen from the dissolved phase to the gaseous phase is expected because of varying pressure, although the application of the pressure term in the DO equation assumes barometric non-standard pressures, not applied pressures. Because the system is a closed one under pressure, the oxygen can not escape in the gaseous phase from the system. As pressure is applied to the system, oxygen that had entered the gaseous phase

under the low pressure encountered within the condenser is forced back into the dissolved state because the saturation concentration within the CWS is higher than the measured Estuary water DO concentration.

VIII. CONCLUSIONS

The potential for interaction of the thermal discharge from the Station with dissolved oxygen in the Estuary was investigated in this Attachment. This analysis followed several parallel paths:

- Review of historical DO data
- Analysis of DO data acquired by PSE&G in 1997 and 1998
- Model of DO dynamics in the Estuary
- Model of DO dynamics within the Station CWS

These analyses lead to conclusions about the behavior of DO in the Estuary. This study included consideration of the contributions of the marshes adjoining the Station and potential effects associated with the Station discharge.

Marshes make up the majority of the area of the Estuary within a 10-mile radius of the Station. These marshes affect the heat budget of the Estuary (Exhibit E-1-5) which, in turn, affects the DO concentrations. Marshes have another effect on DO concentrations: their enhanced biogeochemical oxygen demand reduces the DO concentrations emanating from them on ebbing tides. Major conclusions about marsh contributions to the Estuary DO balance include:

- Marshes are net consumers of oxygen under certain solar, tidal, and seasonal conditions. Field observations of marsh DO concentrations show that marshes can either reduce, or increase DO concentrations, depending on the physical and biological conditions. In general, during portions of the hot summer and fall, marshes are net consumers of oxygen, returning oxygen-depleted waters to the Estuary.
- Marsh oxygen demand contributes to lower oxygen levels near the marsh creeks. Because of the large volume of flow emanating from the marshes, they create an as-yet-unquantified oxygen load on the Estuary during times when marsh outflow has depleted DO. Because the depletion can reach up to 4.5 mg/L of DO, the oxygen load from the marshes is high at certain periods.

Conclusions reached about DO concentrations in the 10-mile radius from the Station include:

- Historical information on DO levels in the River stretch near the Station show no long-term trends, either declining or increasing. The oxygen sag that used to affect the Delaware River prior to massive improvements to the sewage treatment in the region was located tens of miles to the north of the Station.
- During recent years, the DO concentrations in the upper Delaware Bay Zone have declined, slightly reducing the DO up into the Transition Zone. This reduction was during a time when the Station was not operational, and there was no heat discharge from the circulation water.

- Measurements of DO concentrations near the Station, by the DRBC and others, consistently show levels elevated enough to support estuarine life.
- Marshes surrounding the Station create a net DO load to the River at certain periods during the summer. The exact magnitude of this load has not been quantified.
- A simple spreadsheet model of dissolved oxygen in the River near the Station, relying on DRBC-sponsored DO model parameters, and using as input actual Station discharge at times when the River was monitored under hot summer conditions, shows no potential for oxygen depletion due to the Station's thermal load.
- A spreadsheet model of Station pressure and temperature variation within the Circulating Water System shows no evidence of oxygen loss within the Station cooling water system.
- All these lines of evidence support the absence of Station impact on Estuary DO levels, which are controlled by Estuary-wide natural processes rather than by the Salem thermal discharge.

E-3 Table IV-1. Historic and Recent Dissolved Oxygen Concentrations at Appoquinimink River/Liston Pt., DE

	Parameter	N ^a	Mean	Median	Min	Max	Standard Deviation
Historic (1971-1997)	DO	477	7.9	7.6	1.4	13.7	1.8
Recent (1995-1997)	DO	49	7.02	6.9	4.4	11.6	1.4
	Summer DO	21	6.07	6.1	4.4	7.5	0.76

^a Number of observations

E-3 Table V-1. Dissolved Oxygen Meter Depths (Two-Unit Survey)

Mooring	Water Depth^a	Surface^b	Mid-Depth^b
9M	29 feet	5 feet	17 feet
21	39 feet	3 feet	20 feet
MHC	26 feet	n/a	14 feet

^a Water depth is the mean depth of water (tidally corrected).

^b Depths are measured from the water surface (i.e., a depth of 17 feet refers to a meter located 17 feet below the water surface).

E-3 Table V-2. Temperatures (°C) During the Two-Unit Survey

Dates	Mooring	Level	Mean	SD	Max	Min	Range
Sept 2 - 17	9M	Surf ^a	25.1	1.1	26.9	23.5	3.4
Sept 18 - Oct 8	9M	Surf	23.0	1.7	25.4	19.5	5.9
Sept 2 - 17	9M	Mid ^b	25.1	1.1	26.9	23.5	3.4
Sept 18 - Oct 8	9M	Mid	23.1	1.7	25.4	19.6	5.8
Sept 2 - 17	21	Surf	26.1	1.3	29.1	23.5	5.6
Sept 18 - Oct 8	21	Surf	24.9	2.0	29.3	20.0	9.3
Sept 2 - 17	21	Mid	26.3	1.5	30.2	23.1	7.2
Sept 18 - Oct 8	21	Mid	24.2	1.8	28.3	20.1	8.2
Sept 2 - 17	MHC	Surf	24.4	1.4	26.6	21.3	5.3
Sept 18 - Oct 8	MHC	Surf	22.6	2.0	25.7	17.4	8.3

^a Surface
^b Mid-water

E-3 Table V-3. Salinity Data (Two-Unit Survey) (Results in ppt)

Dates	Mooring	Level	Mean	SD	Max	Min	Range
Sept 2 - 17	9M	Surf ^a	5.9	1.1	8.5	3.7	4.8
Sept 18 - Oct 8	9M	Surf	5.9	1.0	8.6	4.0	4.6
Sept 2 - 17	9M	Mid ^b	5.9	1.0	8.3	4.6	3.8
Sept 18 - Oct 8	9M	Mid	6.4	1.1	9.3	4.3	5.0
Sept 2 - 17	21	Surf	10.0	1.4	12.7	7.3	5.4
Sept 18 - Oct 8	21	Surf	6.9	0.9	11.6	5.3	6.4
Sept 2 - 17	21	Mid	9.6	1.3	11.9	7.1	4.9
Sept 18 - Oct 8	21	Mid	10.4	1.3	13.0	7.1	5.9
Sept 2 - 17	MHC	Surf	12.1	0.6	14.1	10.9	3.1
Sept 18 - Oct 8	MHC	Surf	13.0	0.6	14.8	11.6	3.2

^a Surface

^b Mid-water

E-3 Table V-4. Dissolved Oxygen Concentration (Two-Unit Survey) (Results in mg/L)

Dates	Mooring	Level	Mean	SD	Max	Min	Range
Sept 2 - 17	9M	Surf ^a	6.3	0.2	6.8	5.8	1.0
Sept 18 - Oct 8	9M	Surf	6.6	0.5	7.5	4.6	2.9
Sept 2 - 17	9M	Mid ^b	6.6	0.3	7.1	6.1	1.0
Sept 18 - Oct 8	9M	Mid	6.6	0.3	7.3	6.1	1.2
Sept 2 - 17	21	Surf	6.8	0.5	7.5	5.7	1.8
Sept 2 - 17	21	Mid	5.9	0.2	6.3	5.0	1.3
Sept 18 - Oct 8	21	Mid	5.7	0.6	7.2	4.7	2.5
Sept 2 - 17	MHC	Surf	5.7	1.0	7.3	3.0	4.3
Sept 18 - Oct 8	MHC	Surf	6.7	0.7	7.8	4.6	3.3

^a Surface

^b Mid-water

E-3 Table V-5. Measured Variations in Temperature, Salinity, and Dissolved Oxygen and Calculated Maximum Oxygen Variation (Two-Unit Survey)

Date	Mooring	Level	Maximum Temperature Variation (°C)	Maximum Salinity Variation (ppt)	Measured Maximum Oxygen Variation (mg/L)	Calculated Maximum Oxygen Variation (mg/L)
Sept 2 - 17	9M	Surf ^a	0.55	4.7	0.3	0.3
Sept 18 - Oct 8	9M	Surf	0.50	3.9	0.5	0.3
Sept 2 - 17	9M	Mid ^b	0.36	4.0	0.2	0.2
Sept 18 - Oct 8	9M	Mid	0.45	4.1	0.3	0.3
Sept 2 - 17	21	Surf	2.35	2.4	0.5	0.4
Sept 18 - Oct 8	21	Surf	3.46	2.7	0.6	0.6
Sept 2 - 17	21	Mid	3.45	4.1	0.6	0.6
Sept 18 - Oct 8	21	Mid	3.09	4.7	0.8	0.6
Sept 2 - 17	MHC	Surf	1.73	2.0	2.6	0.3
Sept 18 - Oct 8	MHC	Surf	0.65	2.2	2.0	0.2

^a Surface
^b Mid-water

E-3 Table V-6. Dissolved Oxygen Concentration (Two-Unit Survey) (Results in Percent of Air Equilibration)

Dates	Mooring	Level	Mean	SD	Max	Min	Range
Sept 2 - 17	9M	Surf ^a	79	2	84	75	9
Sept 18 - Oct 8	9M	Surf	79	5	90	58	32
Sept 2 - 17	9M	Mid ^b	84	2	88	80	9
Sept 18 - Oct 8	9M	Mid	80	2	84	76	8
Sept 2 - 17	21	Surf	89	5	101	76	25
Sept 2 - 17	21	Mid	77	4	86	62	25
Sept 18 - Oct 8	21	Mid	73	6	89	61	28
Sept 2 - 17	MHC	Surf	73	11	92	40	52
Sept 18 - Oct 8	MHC	Surf	84	8	98	59	39

^a Surface

^b Mid-water

E-3 Table V-7. Dissolved Oxygen Meter Depths^a (Ambient Survey)

Mooring	Water Depth^b	Surface Meter^c	Mid-Depth Meter	Bottom Meter
Alloway Creek	21	2.0	11.0	16.0
Mooring E	22	2.0	11.0	16.0
Mooring H	17	2.0	8.0	11.0
Mad Horse Creek	13.4	2.0	6.5	9.5
Hope Creek	12.9	2.0	6.5	10.5

^a All depths are in feet.

^b Local water depth is approximate.

^c All sensor depths are relative to the uncorrected sea surface.

E-3 Table V-8. Temperature (°C) During the Ambient Survey

Mooring	Level	Mean	SD ^a	Max	Min	Range
AC	Surf ^b	27.2	0.8	29.1	25.7	3.4
AC	Mid ^c	27.1	0.7	28.5	25.6	2.9
AC	Bot ^d	27.2	0.7	28.5	25.7	2.8
E	Surf	26.9	0.5	27.9	25.9	2.0
E	Mid	26.9	0.5	27.9	26.0	1.9
E	Bot	26.8	0.4	27.8	26.0	1.8
H	Surf	26.9	0.5	28.1	26.0	2.1
H	Mid	26.8	0.5	27.7	26.0	1.7
H	Bot	26.8	0.4	27.7	26.0	1.7
HC	Surf	27.3	0.8	29.1	25.5	3.6
HC	Mid	27.2	0.8	29.0	25.5	3.5
HC	Bot	27.2	0.8	28.9	25.5	3.4
MHC	Surf	27.2	0.7	28.7	25.7	3.0
MHC	Mid	27.2	0.7	28.6	25.8	2.8
MHC	Bot	27.1	0.7	28.4	25.7	2.7

- ^a Standard deviation
- ^b Surface
- ^c Mid-water
- ^d Bottom

E-3 Table V-9. Salinity During the Ambient Survey (ppt)

Mooring	Level	Mean	SD	Max	Min	Range
AC	Surf ^a	4.7	0.7	6.5	3.7	2.8
AC	Mid ^b	4.3	0.6	6.0	3.4	2.6
AC	Bot ^c	4.5	0.6	6.2	3.6	2.6
E	Surf	6.9	1.1	9.2	4.9	4.3
E	Mid	7.4	1.1	9.5	5.2	4.3
E	Bot	7.8	1.1	10.1	5.2	4.9
H	Surf	6.3	0.9	8.0	4.5	3.5
H	Mid	7.4	0.9	9.4	5.2	4.2
H	Bot	8.3	1.0	10.5	5.6	4.9
HC	Surf	8.3	0.4	9.5	7.7	1.8
HC	Mid	7.6	0.3	8.8	7.1	1.7
HC	Bot	9.1	0.4	10.3	8.5	1.8
MHC	Surf	9.7	0.5	10.9	9.1	1.8
MHC	Mid	9.2	0.5	10.3	8.6	1.7
MHC	Bot	9.0	0.5	10.0	8.4	1.6

^a Surface
^b Mid-water
^c Bottom

E-3 Table V-10. Dissolved Oxygen During the Ambient Survey (mg/L)

Mooring	Level	Mean	SD ^a	Max	Min	Range
AC	Surf ^b	6.7	0.6	8.0	5.5	2.4
AC	Mid ^c	6.7	0.6	8.0	5.5	2.4
AC	Bot ^d	6.5	0.6	7.8	5.4	2.3
E	Surf	7.0	0.4	8.3	6.1	2.3
E	Mid	6.8	0.3	7.8	6.2	1.7
E	Bot	6.7	0.3	7.5	6.0	1.5
H	Surf	7.3	0.4	8.4	6.5	2.0
H	Mid	6.7	0.3	7.6	6.1	1.5
H	Bot	6.7	0.3	7.5	5.9	1.6
HC	Surf	7.6	1.2	10.7	4.8	5.8
HC	Mid	14.9	3.4	25.9	7.8	18.0
HC	Bot	6.8	1.1	9.4	4.2	5.2
MHC	Surf	5.3	2.0	9.5	2.2	7.3
MHC	Mid	7.5	1.1	9.9	4.6	5.3
MHC	Bot	7.0	1.3	9.1	3.9	5.2

- ^a Standard Deviation
- ^b Surface
- ^c Mid-water
- ^d Bottom

E-3 Table V-11. Measured Variations of Temperature, Salinity, and Dissolved Oxygen and Calculated Dissolved Oxygen Variation (Ambient Survey)

Mooring	Level	Maximum Temperature Variation °C	Maximum Salinity Variation ppt	Measured Maximum Oxygen Variation (mg/L)	Calculated Maximum Oxygen Variation (mg/L)
AC	Surf ^a	1.6	2.6	2.5	0.3
AC	Mid ^b	1.6	2.2	2.4	0.3
AC	Bot ^c	1.6	2.3	2.3	0.3
E	Surf	1.8	3.9	1.7	0.4
E	Mid	1.3	3.6	1.1	0.3
E	Bot	0.7	4.0	1.0	0.3
H	Surf	1.5	3.0	1.5	0.3
H	Mid	0.9	3.3	1.1	0.3
H	Bot	0.9	3.5	1.1	0.3
HC	Surf	1.9	1.0	4.6	0.3
HC	Mid	NA	NA	NA	NA
HC	Bot	1.9	1.1	3.7	0.3
MHC	Surf	NA	NA	NA	NA
MHC	Mid	1.3	1.5	2.6	0.2
MHC	Bot	1.3	1.5	2.1	0.2

^a Surface
^b Mid-water
^c Bottom

E-3 Table 12. Dissolved Oxygen Saturation^a During the Ambient Survey

Mooring	Level	Mean	SD ^b	Max	Min	Range
AC	Surf ^c	87	9	105	71	34
AC	Mid ^d	86	8	105	71	34
AC	Bot ^e	84	8	102	70	32
E	Surf	91	6	111	80	31
E	Mid	90	4	104	82	22
E	Bot	88	4	99	80	19
H	Surf	95	6	111	84	27
H	Mid	88	4	100	80	20
H	Bot	88	5	99	78	21
HC	Surf	101	16	144	65	79
HC	Bot	91	14	126	57	69
MHC	Mid	100	15	133	63	70
MHC	Bot	93	16	123	53	70

^a Results expressed as percent saturation

^b Standard deviation

^c Surface

^d Mid-water

^e Bottom

E-3 Table VII-1. Sources of Data for Mechanistic Analysis of the Potential Dissolved Oxygen Reduction Through the Station.

Figure No.	Description	Sources of Data/News	
1	Absolute Pressure Distribution Through the SGS	Pressure (atm)	PSE&G Fig 3.3.6
2	Potential for DO Reduction Through the SGS Under Ambient Survey Conditions	Temperature (°C) ΔTemperature (°C) Pressure (atm) Salinity (ppt) DO (mg/L)	1 ^a PSE&G Fig 3.3.6 PSE&G Fig. 3.3.6 1 1
3	Potential for DO Reduction Through the SGS Under One-Unit Survey Conditions	Temperature (°C) ΔTemperature (°C) Pressure (atm) Salinity (ppt) DO (mg/L)	2 ^b PSE&G Fig 3.3.6 PSE&G Fig. 3.3.6 2 2
4	Potential for DO Reduction Through the SGS Under Two-Unit Survey Conditions	Temperature (°C) ΔTemperature (°C) Pressure (atm) Salinity (ppt) DO (mg/L)	3 ^c PSE&G Fig 3.3.6 PSE&G Fig. 3.3.6 3 3

^a Ambient Survey Data (Exhibit E-1-2); 11-16 July 1997; Mooring H average of surface mid-depth and bottom measurements.

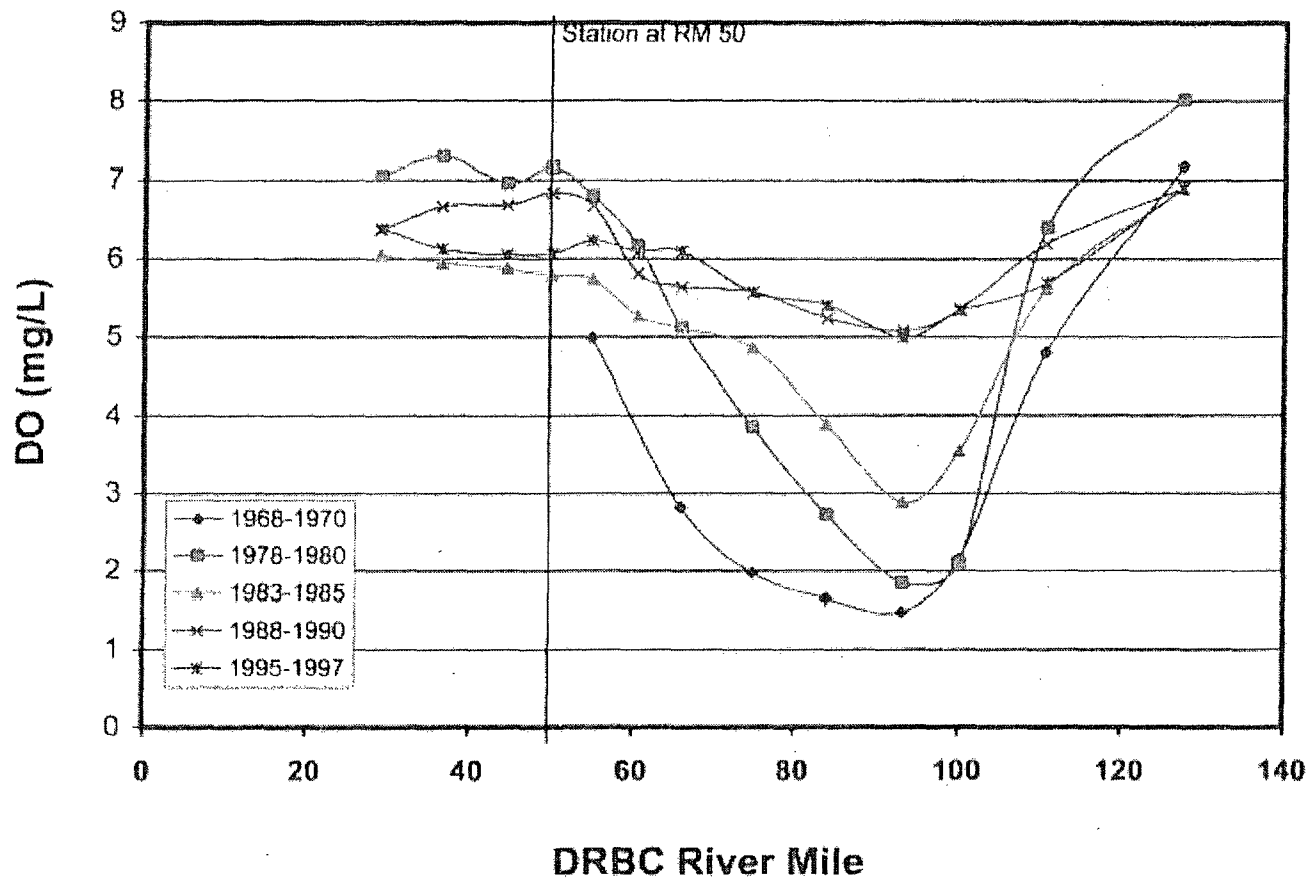
^b One-Unit Survey Data (Exhibit E-1-2); 10-31 October 1997; Mooring H average of surface and bottom measurements.

^c Two-Unit Survey Data (Exhibit E-1-3); 1-30 September 1998. Excludes mid-depth data from 4-9 September 1998.

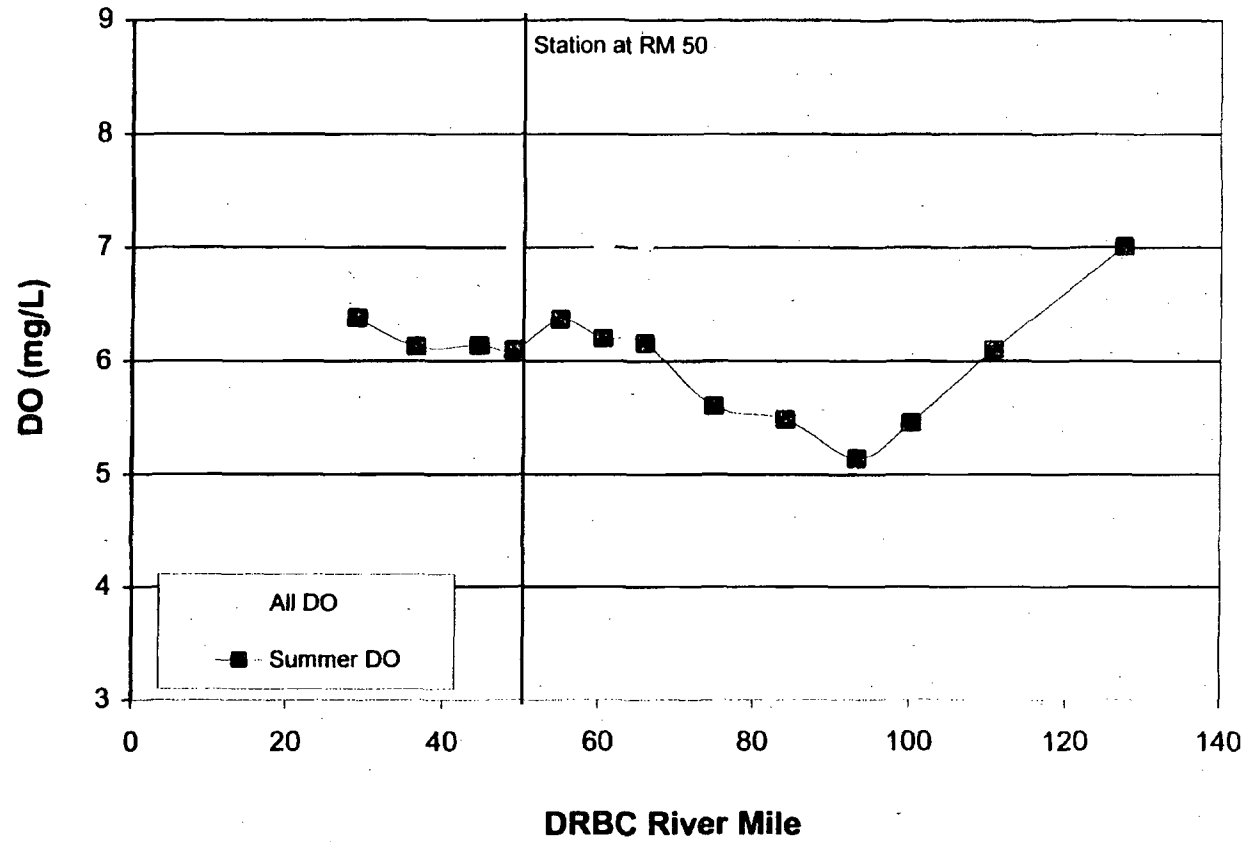
ATTACHMENT E-3
ANALYSIS OF DISSOLVED OXYGEN IN THE VICINITY OF THE STATION

REFERENCES

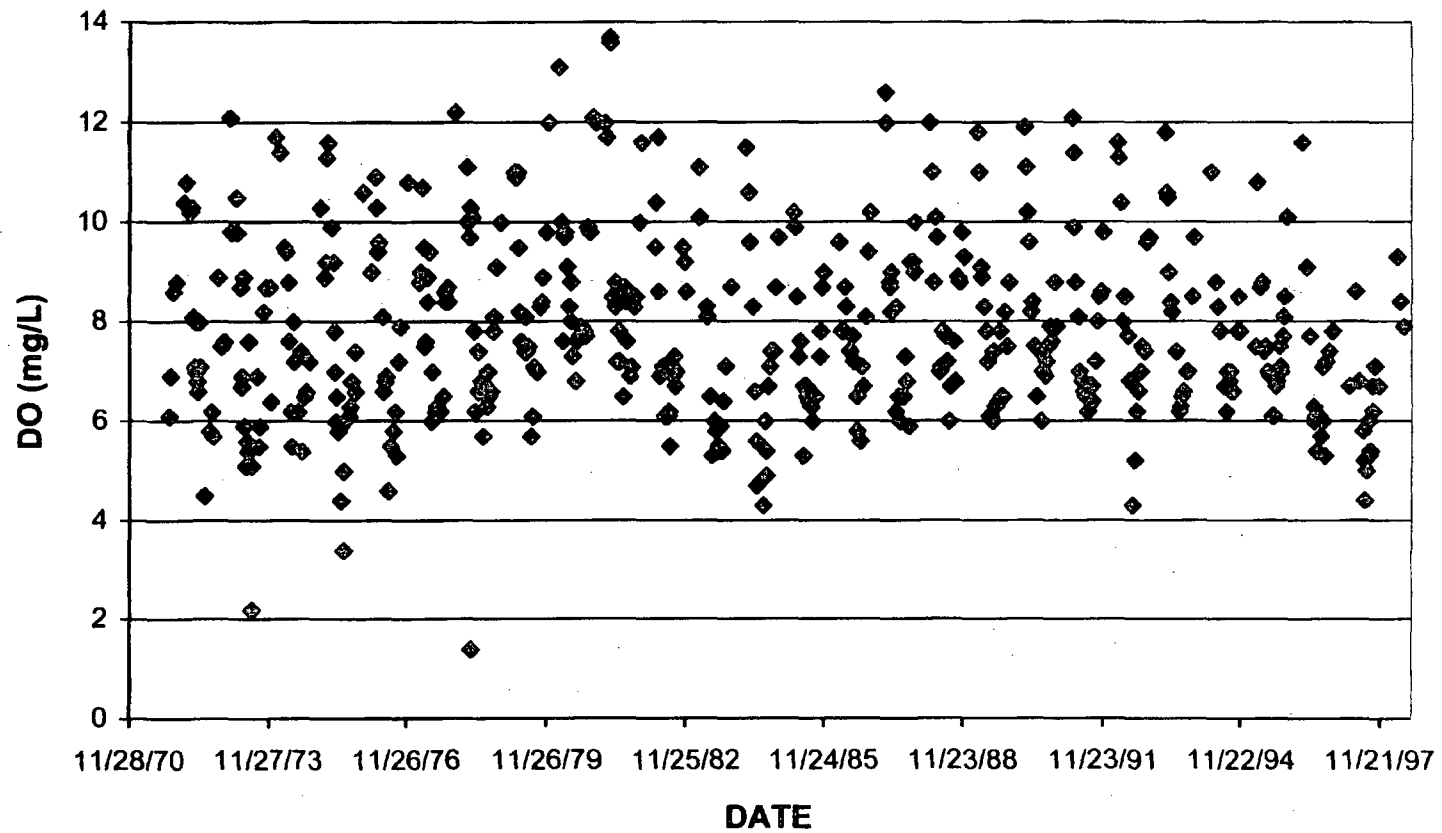
- Delaware River Basin Commission. 1996. Delaware River and Bay Water Quality Assessment: New Jersey.
- HydroQual, Inc. 1998. Delaware River Basin Commission. *Development of a Hydrodynamic Model for the Delaware River*.
- Kemp, W.M., P.A. Sampou, J. Garber, J. Tuttle and W.R. Boynton. 1992. Seasonal depletion of oxygen from bottom waters of Chesapeake Bay: roles of benthic and planktonic respiration and physical exchange processes. *Marine Ecology Progress Series*, 85:137-152.
- Sutton, C.C., J.C. O'Herron II, and R.T. Zappalorti. 1996. The Scientific Characterization of the Delaware Estuary. DRBC Project No. 321. The Delaware Estuary Program. Herpetological Associates, Inc., Forked River, New Jersey.
- Thomann, R.V. Mueller, J.A.. 1987. Principles of Surface Water Quality Modeling and Control, Harper & Row.
- U.S. Environmental Protection Agency (USEPA). 1985. Rates, Constants, and Kinetics Formulations in Surface Water Quality Modeling (Second Editions). Athens, Georgia. June.



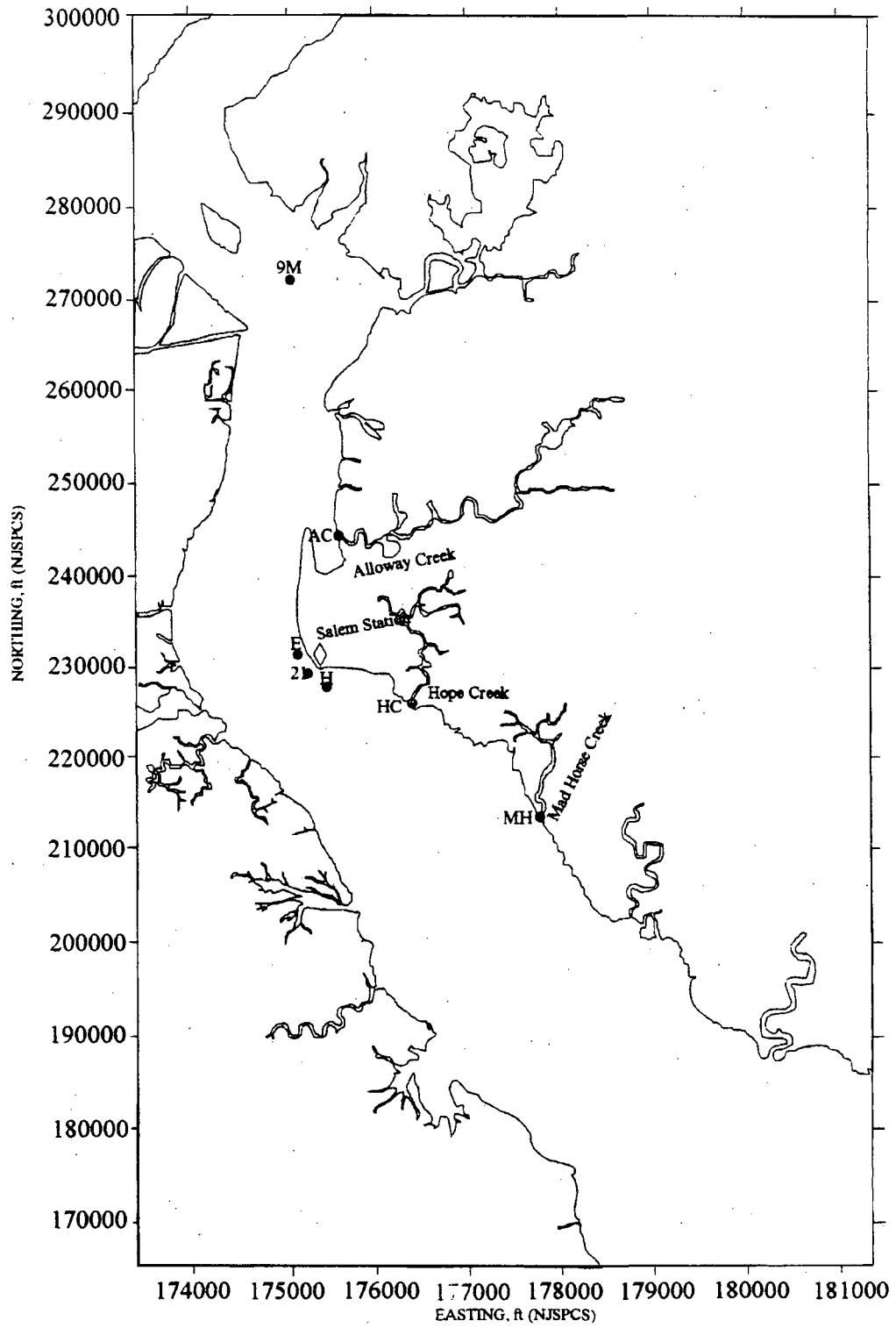
E-3 Figure IV-1. Historical Summer Dissolved Oxygen Concentration.



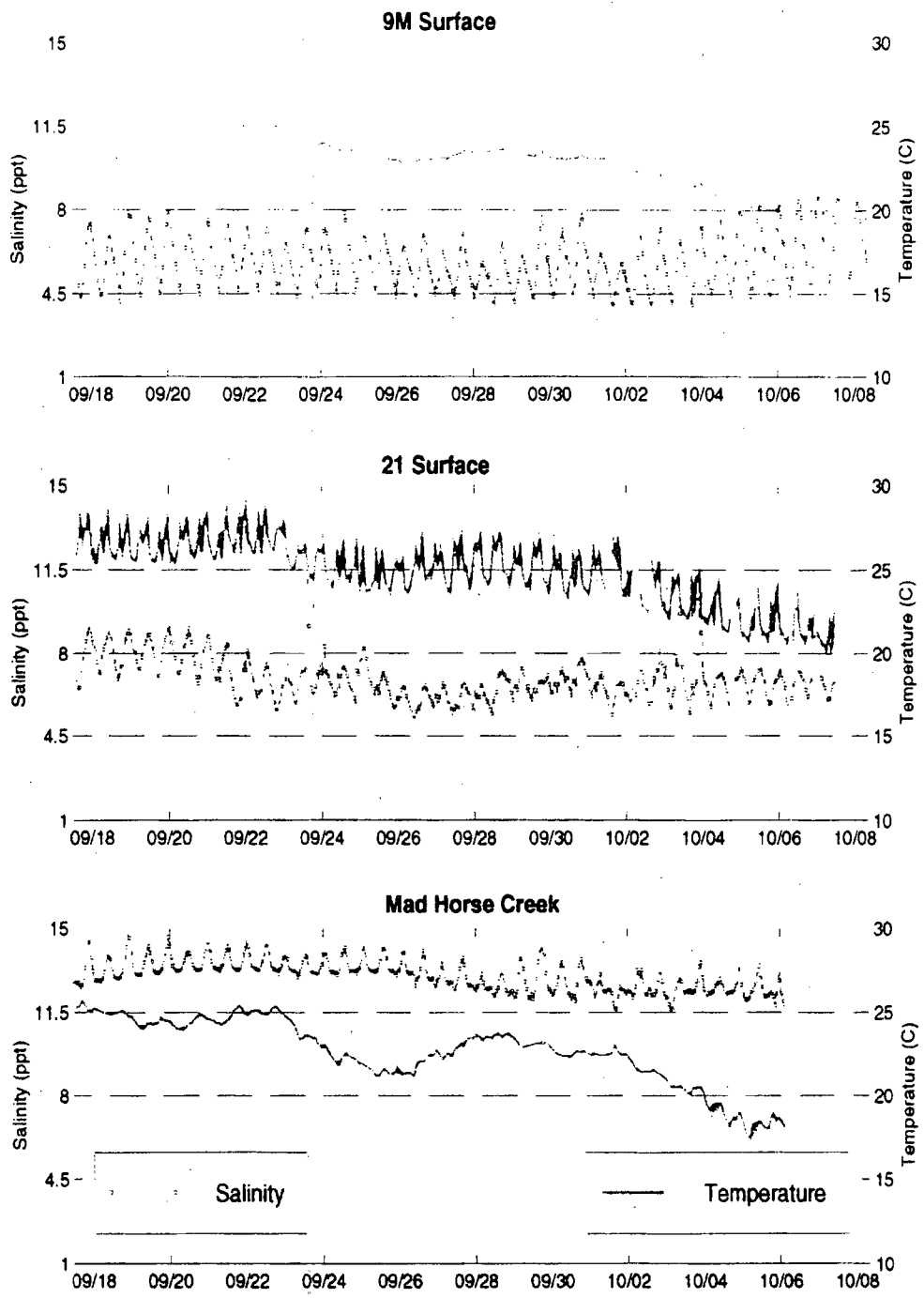
E-3 Figure IV-2. Dissolved Oxygen Concentration for annual and summer 1995-97.



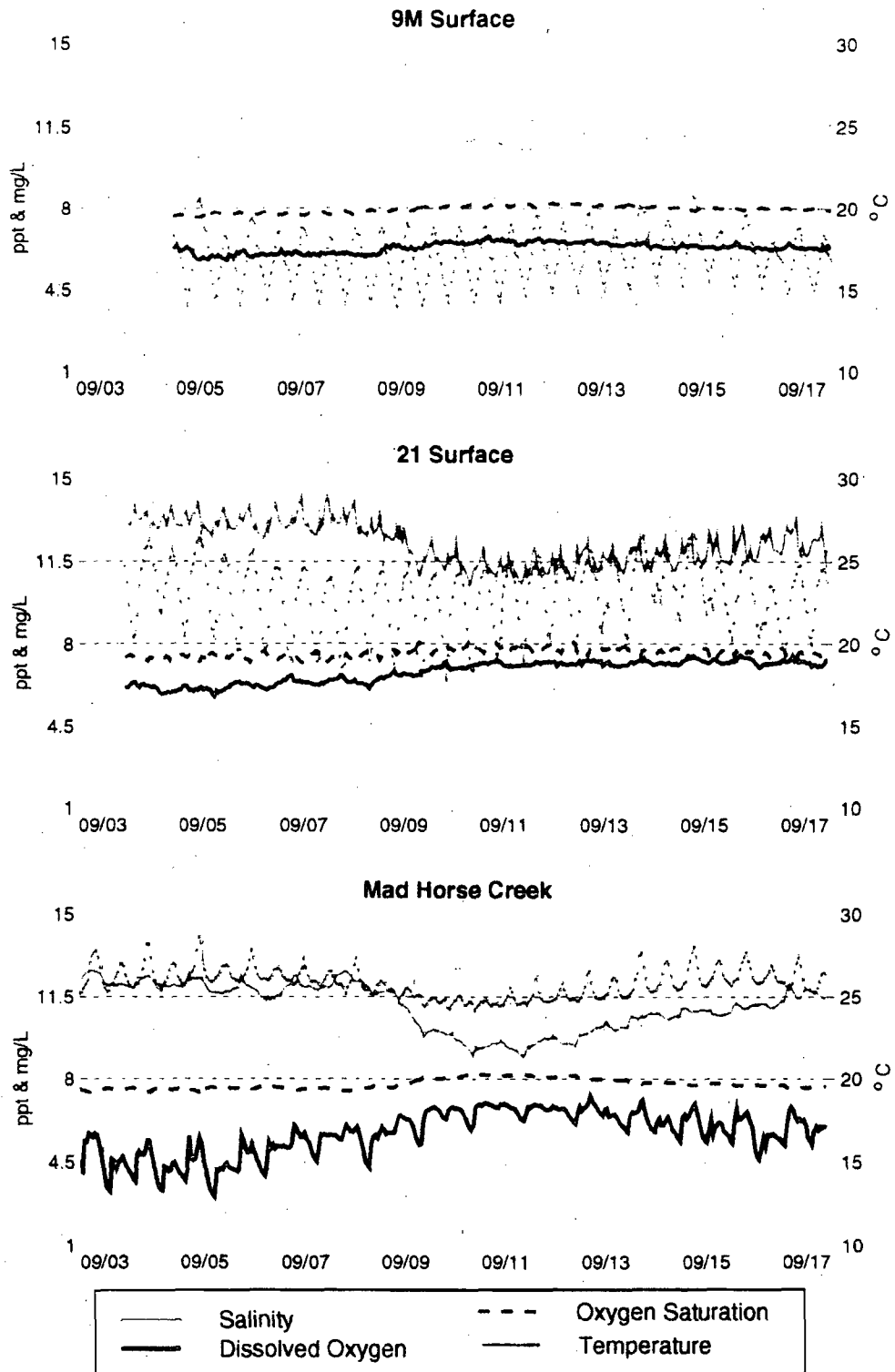
E-3 Figure IV-3. Dissolved oxygen concentrations at Appoquinimink River (RM 51) and Liston Point (RM 49) near Salem.



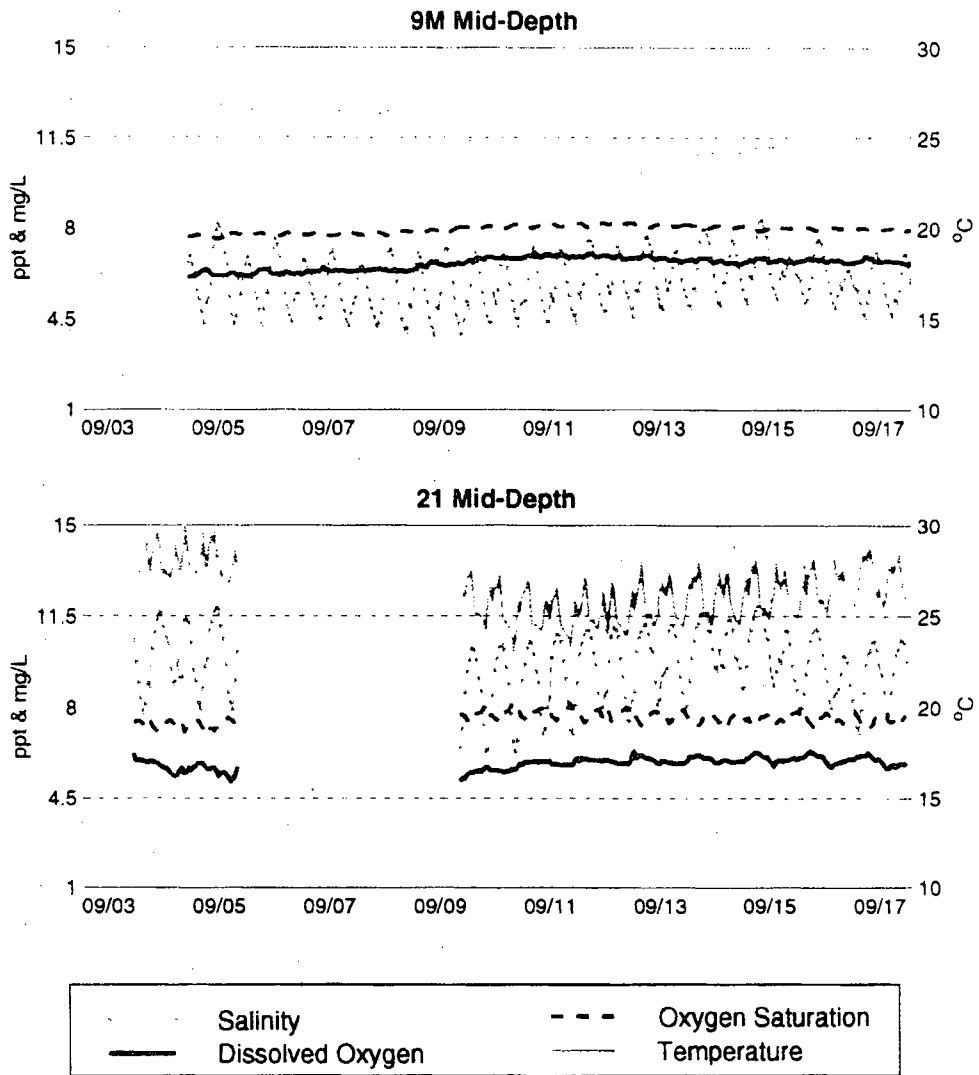
E-3 FigureV-1. Mooring map (Two-Unit and Ambient surveys).



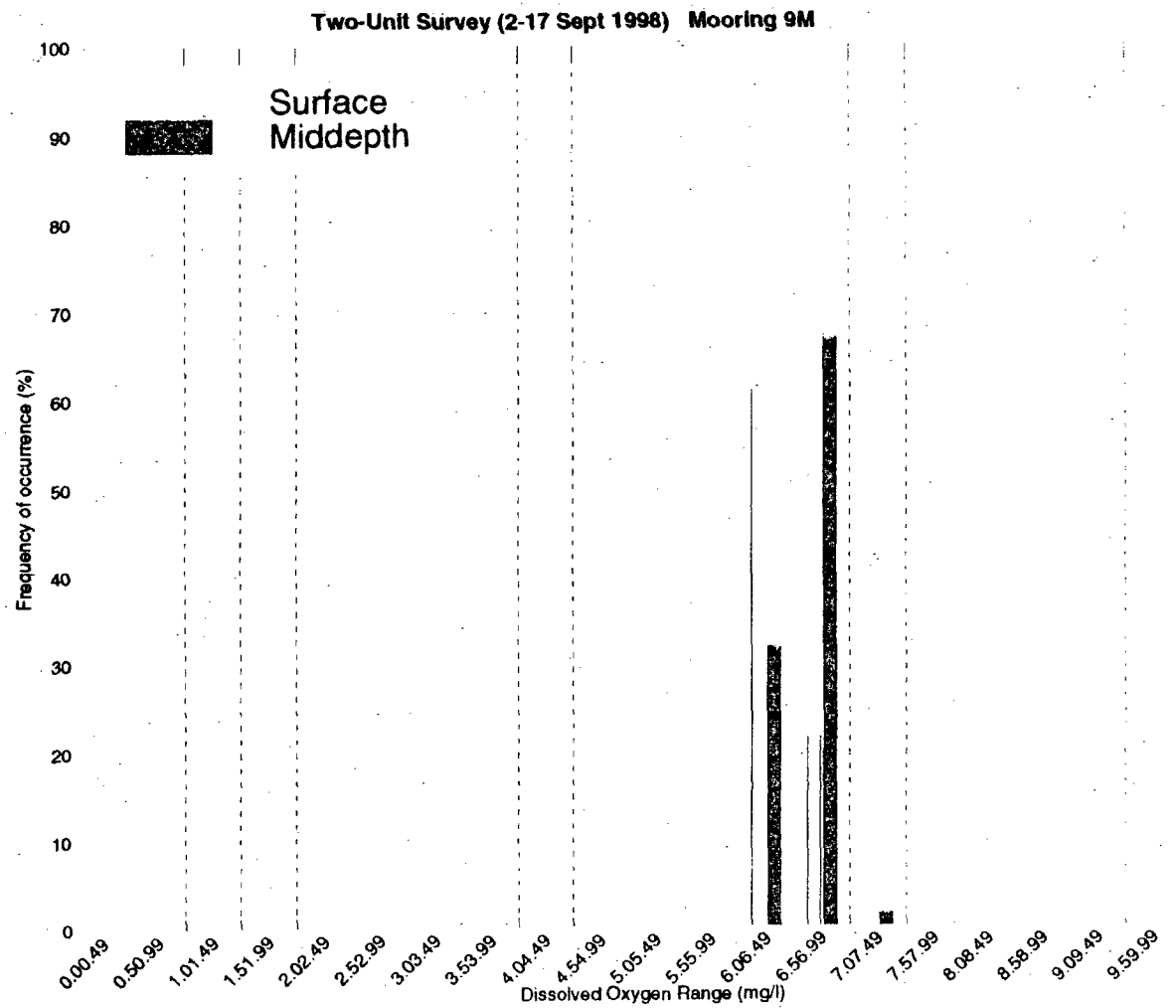
E-3 Figure V-2. Time series of surface temperature and salinity for the main stem river (9M), Estuary at the Station (21), and Mad Horse Creek.



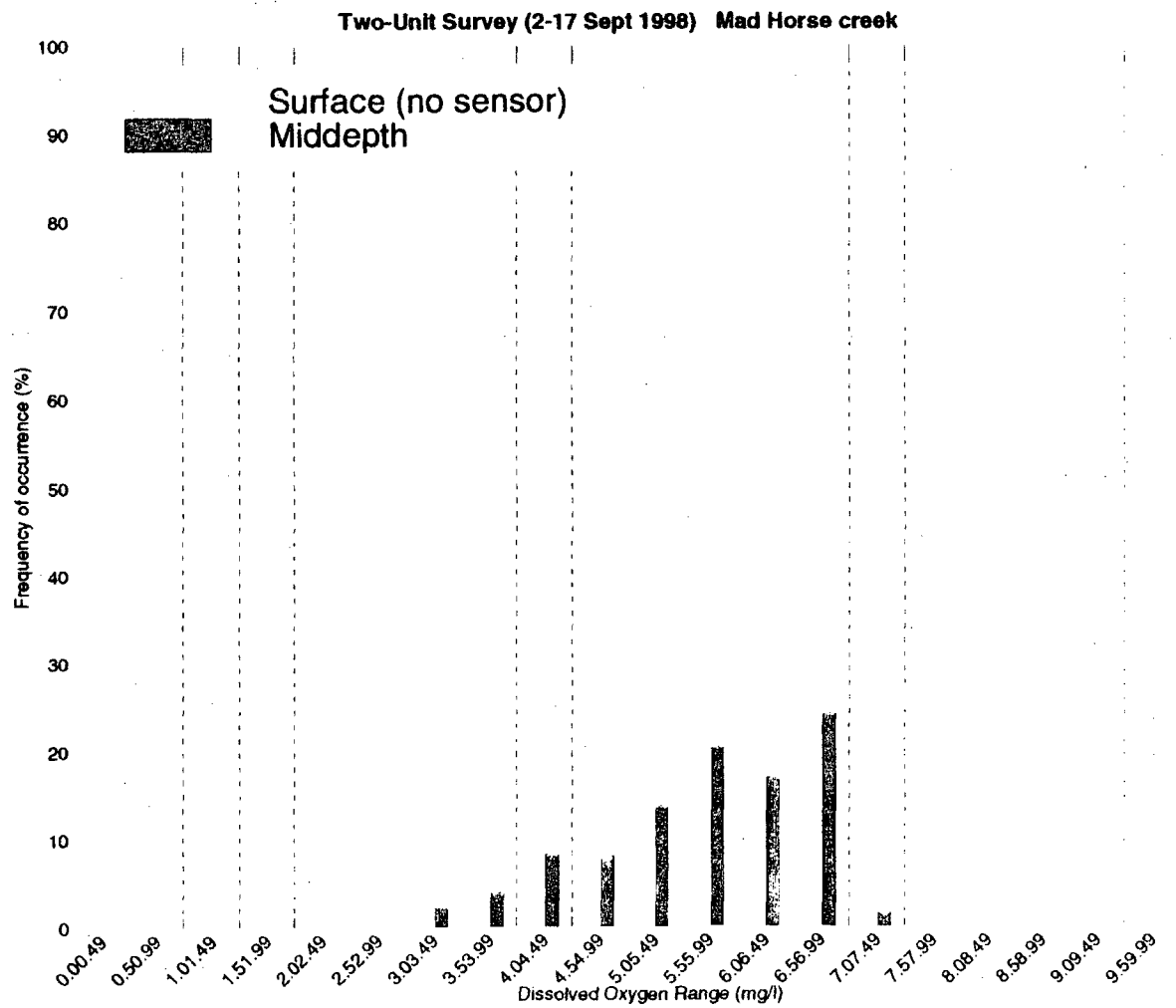
E-3 Figure V-3. Time series of temperature, salinity, dissolved oxygen concentration, and saturation for the three locations shown in E-3 Figure V-2, for the surface moorings.



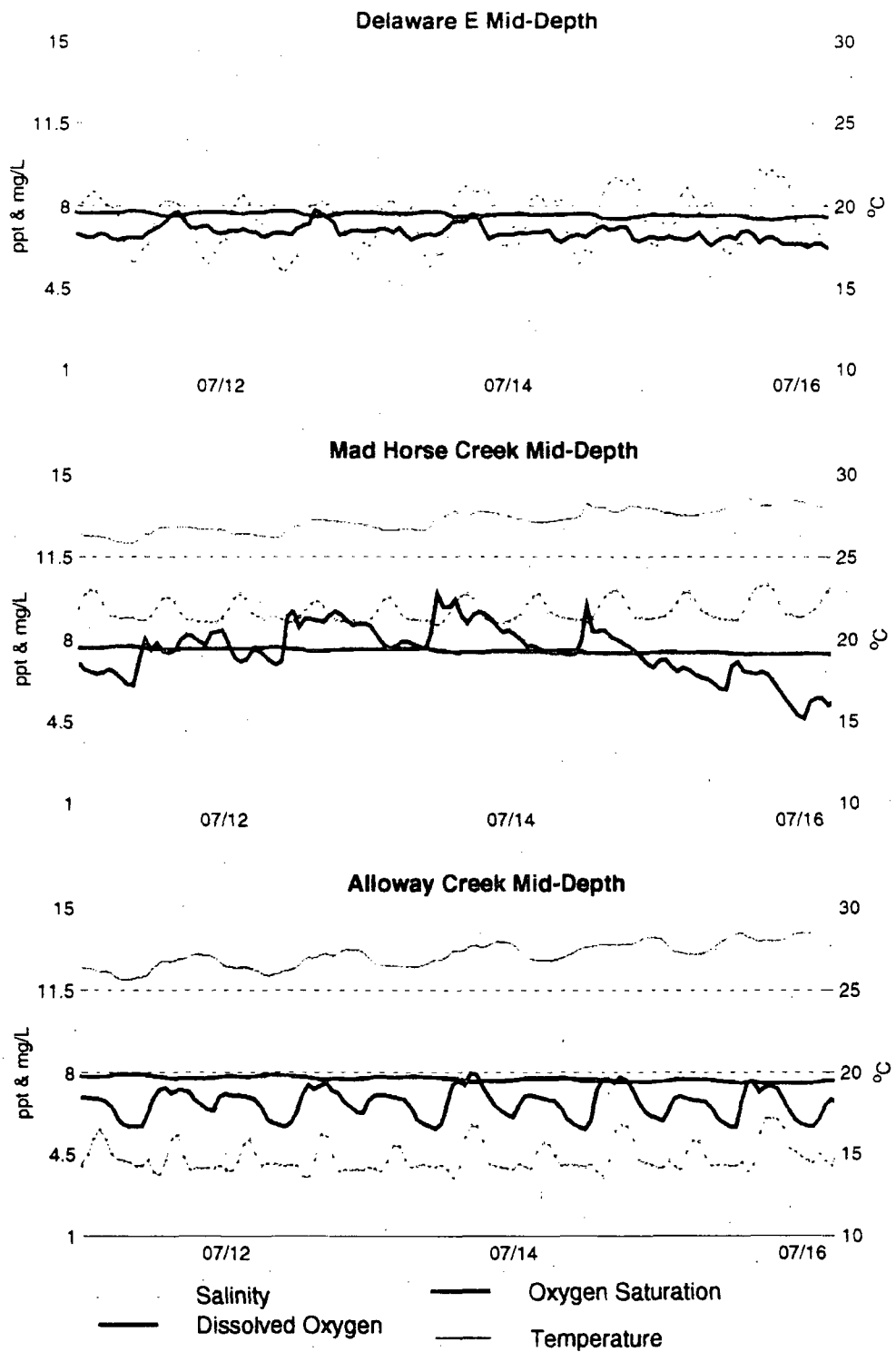
E-3 Figure V-4. Time series of temperature, salinity, dissolved oxygen concentration, and saturation for the mid-depth moorings.



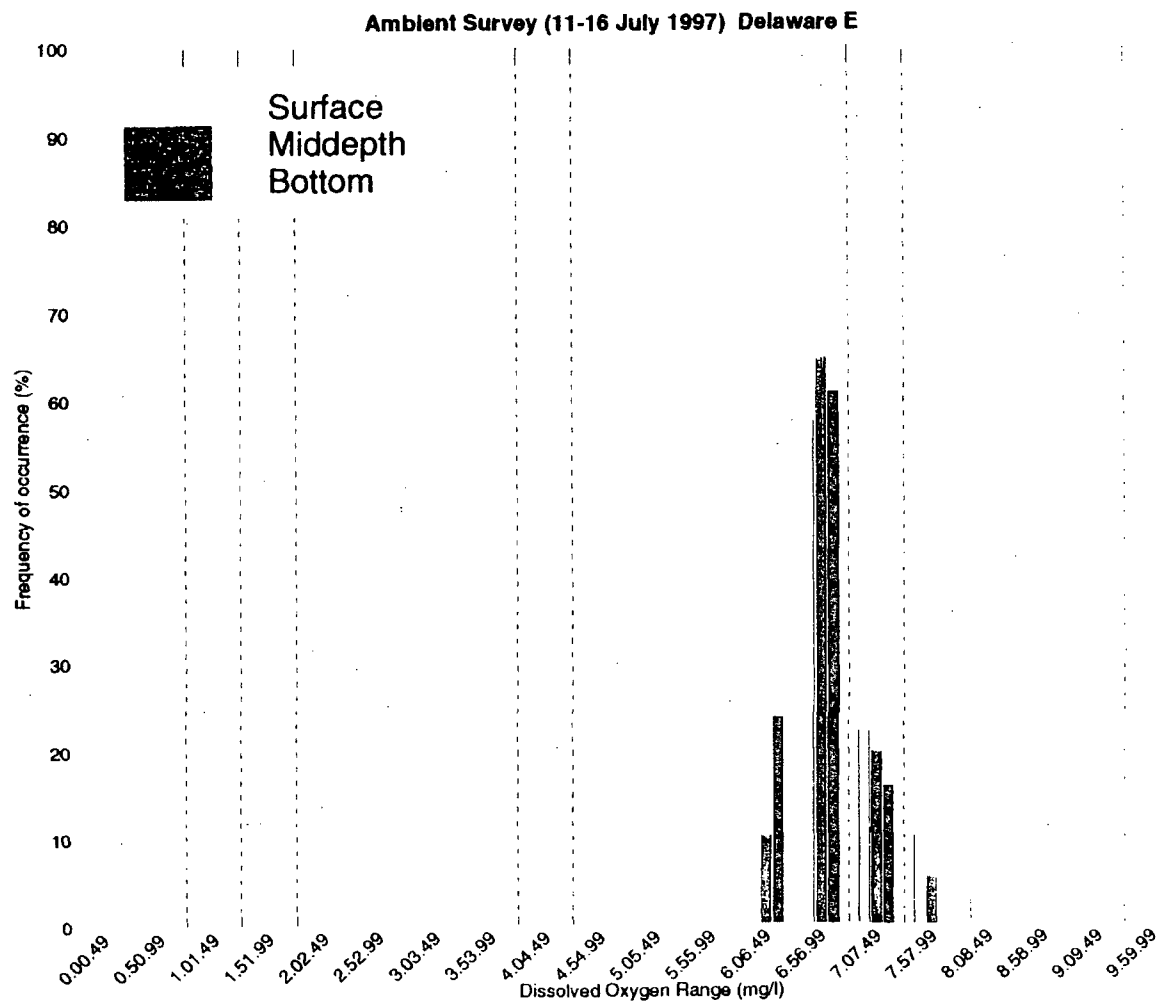
E-3 Figure V-5. Frequency distribution of dissolved oxygen concentrations for Two-Unit Survey, at mooring 9M.



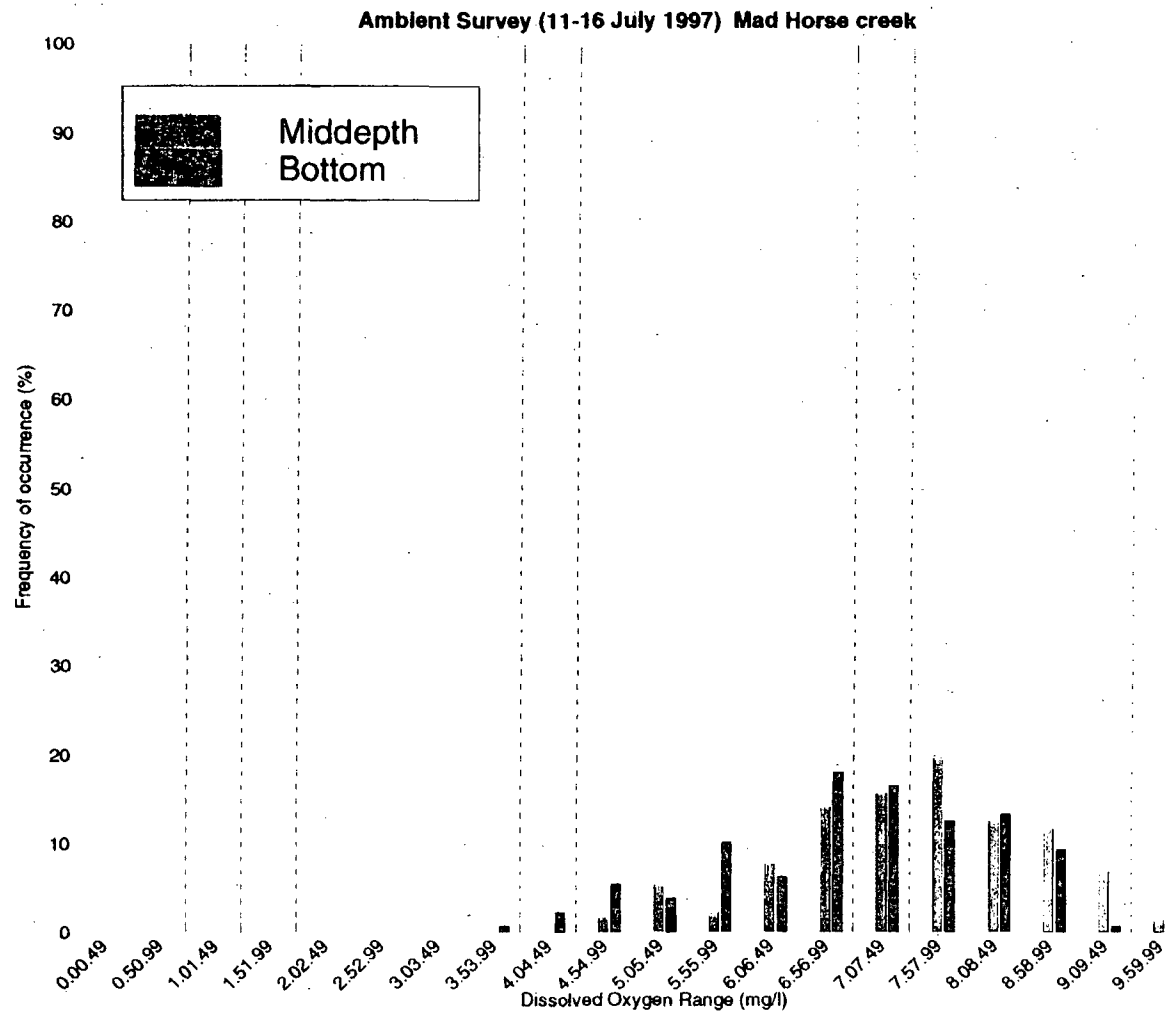
E-3 Figure V-6 Frequency distribution of dissolved oxygen concentrations for Two-Unit Survey, at Mad Horse Creek.



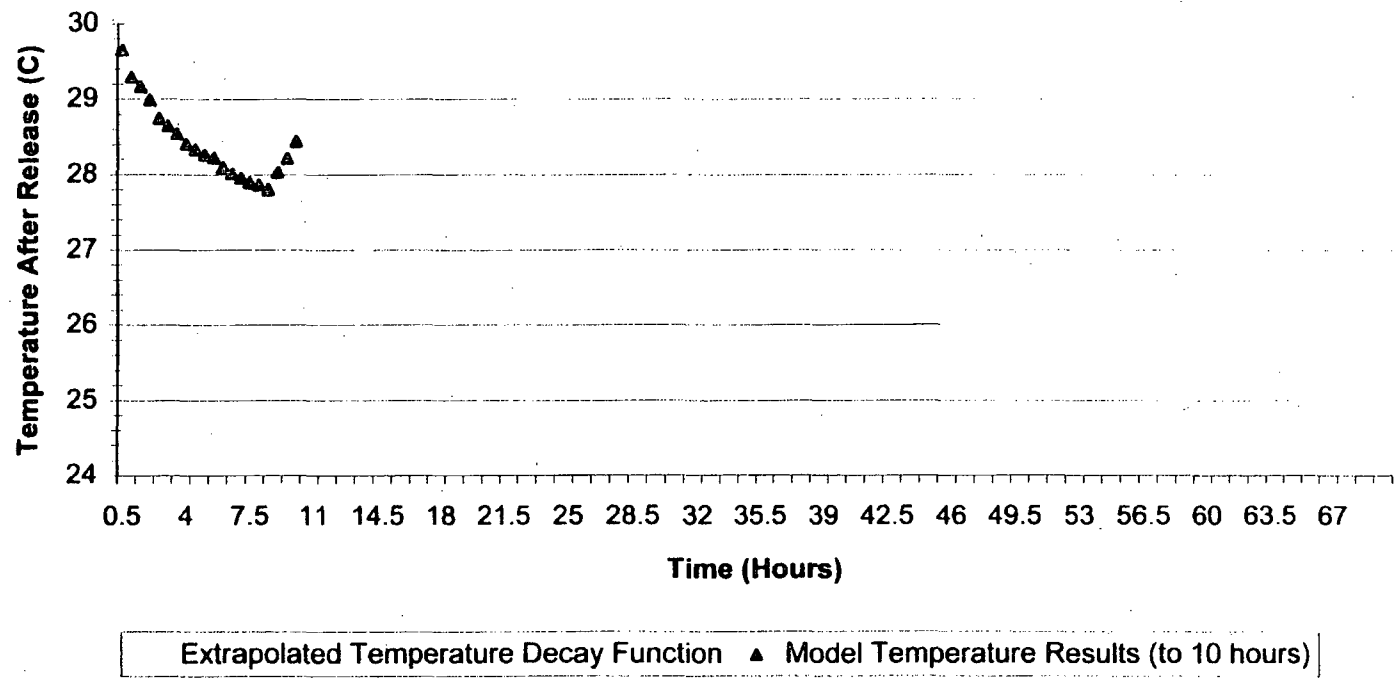
E-3 Figure V-7. Time series of temperature, salinity, dissolved oxygen concentration and saturation for three locations: main stem river (E), and two creek mouths.



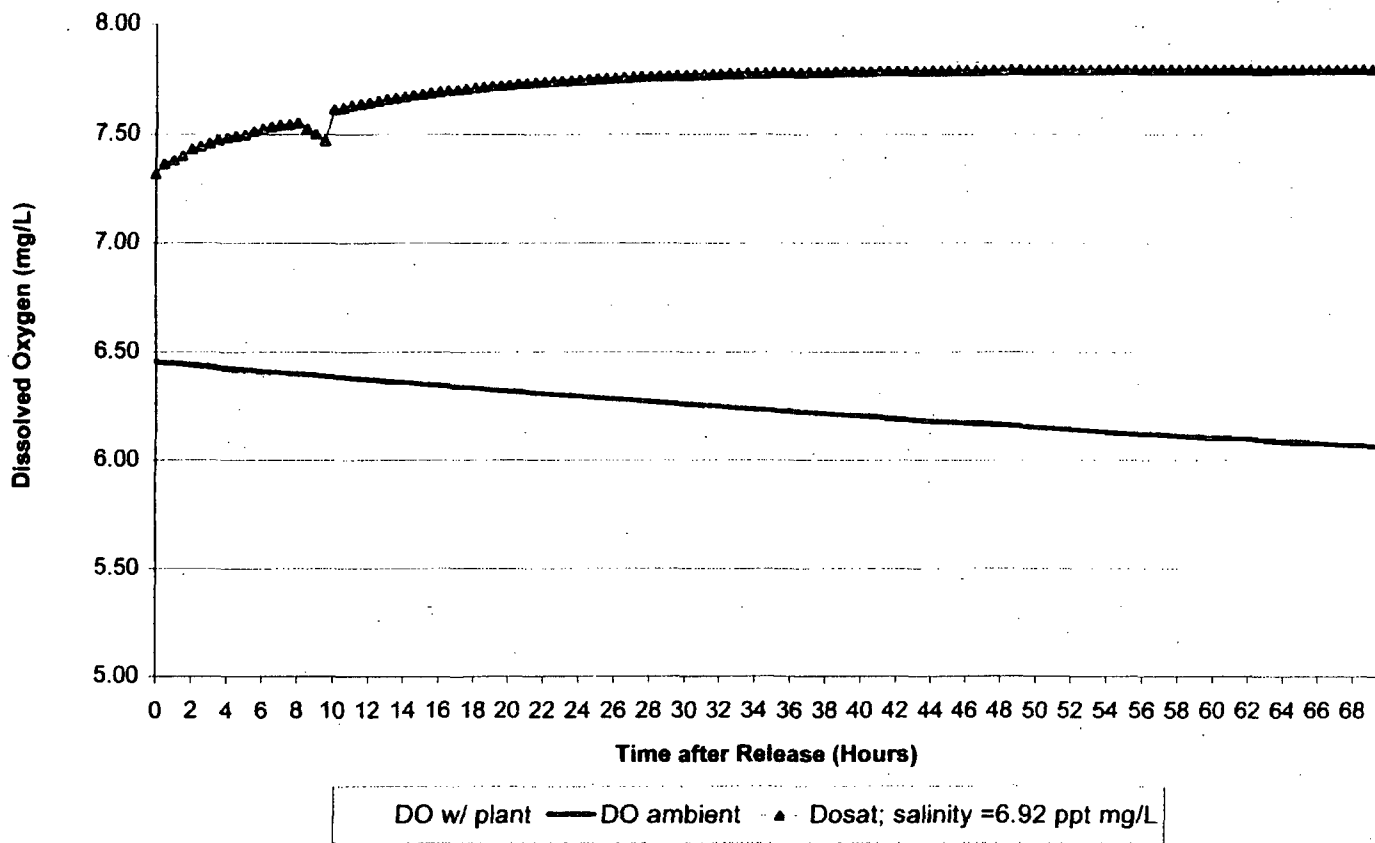
E-3 Figure V-8. Frequency distribution of dissolved oxygen concentrations for Ambient Survey, at Delaware location E.



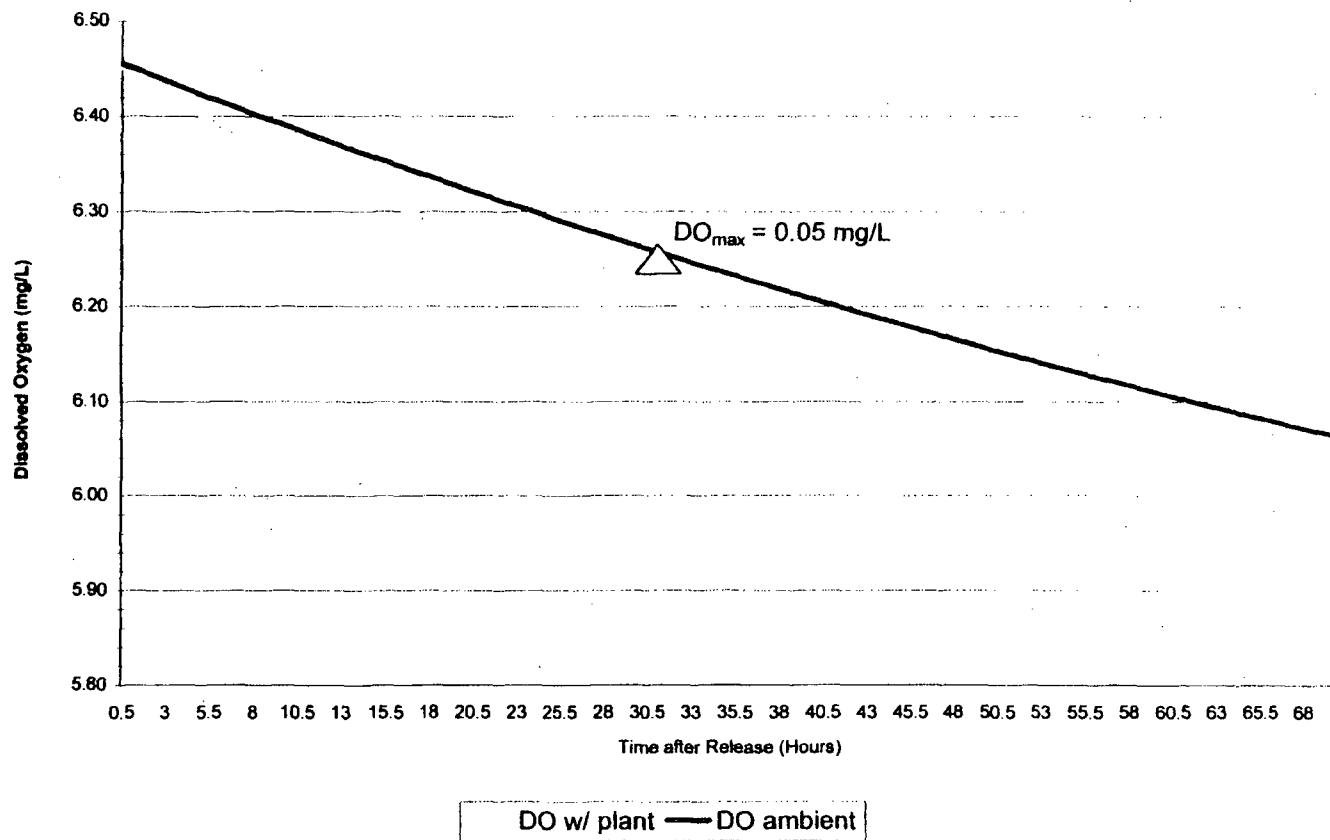
E-3 Figure V-9. Frequency distribution of dissolved oxygen concentrations for Ambient Survey, at Mad Horse Creek.



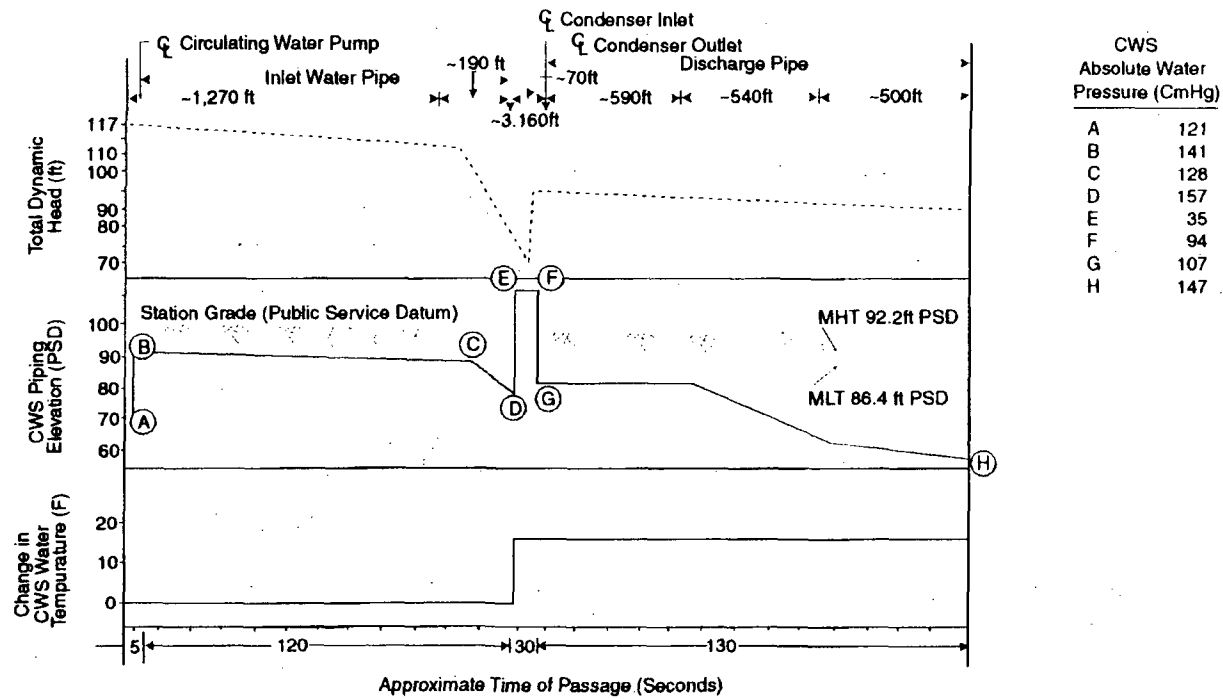
E-3 Figure VI-1. Time-temperature history, worst case scenario.



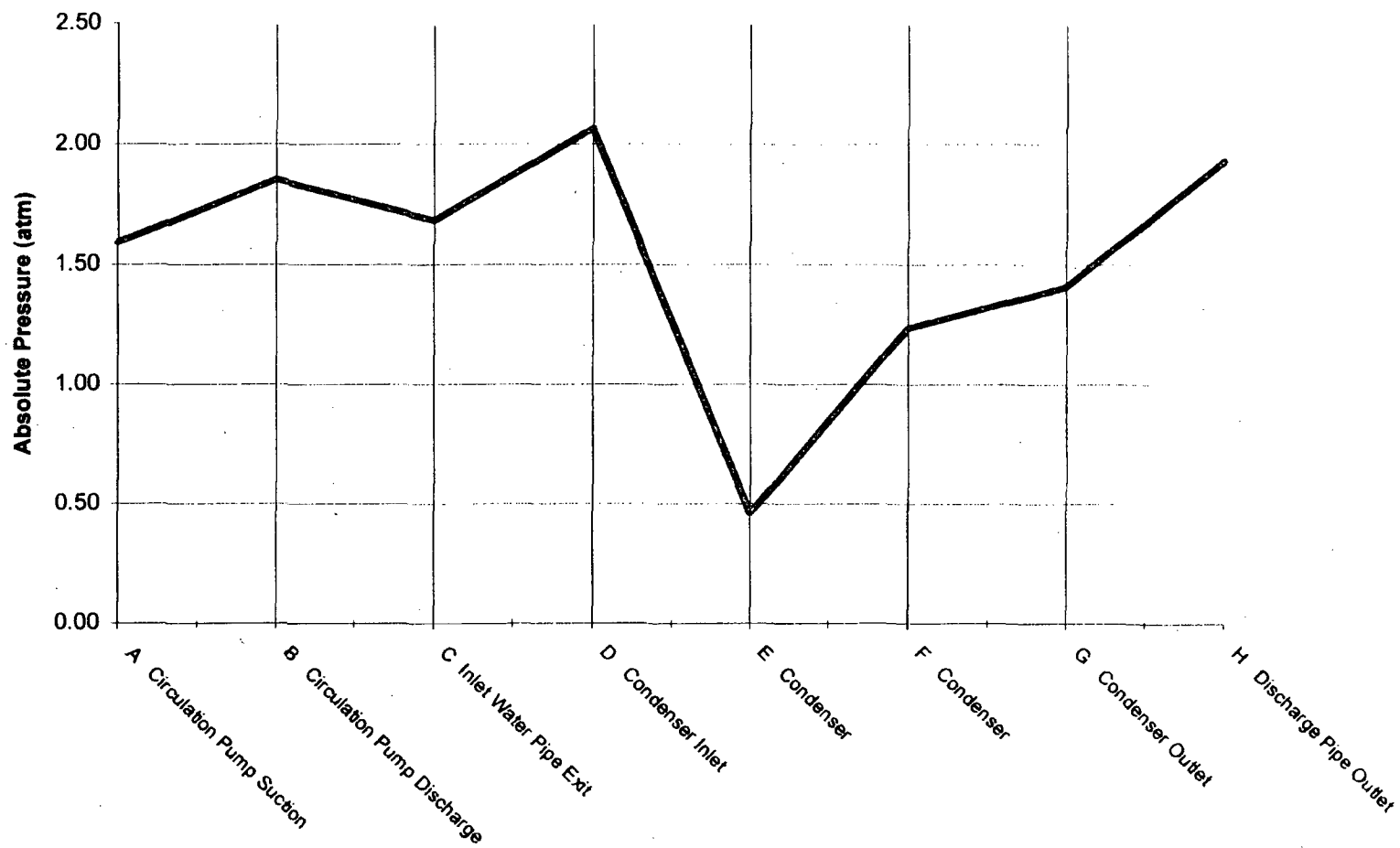
E-3 Figure VI-2. Dissolved oxygen calculation for the Delaware River.



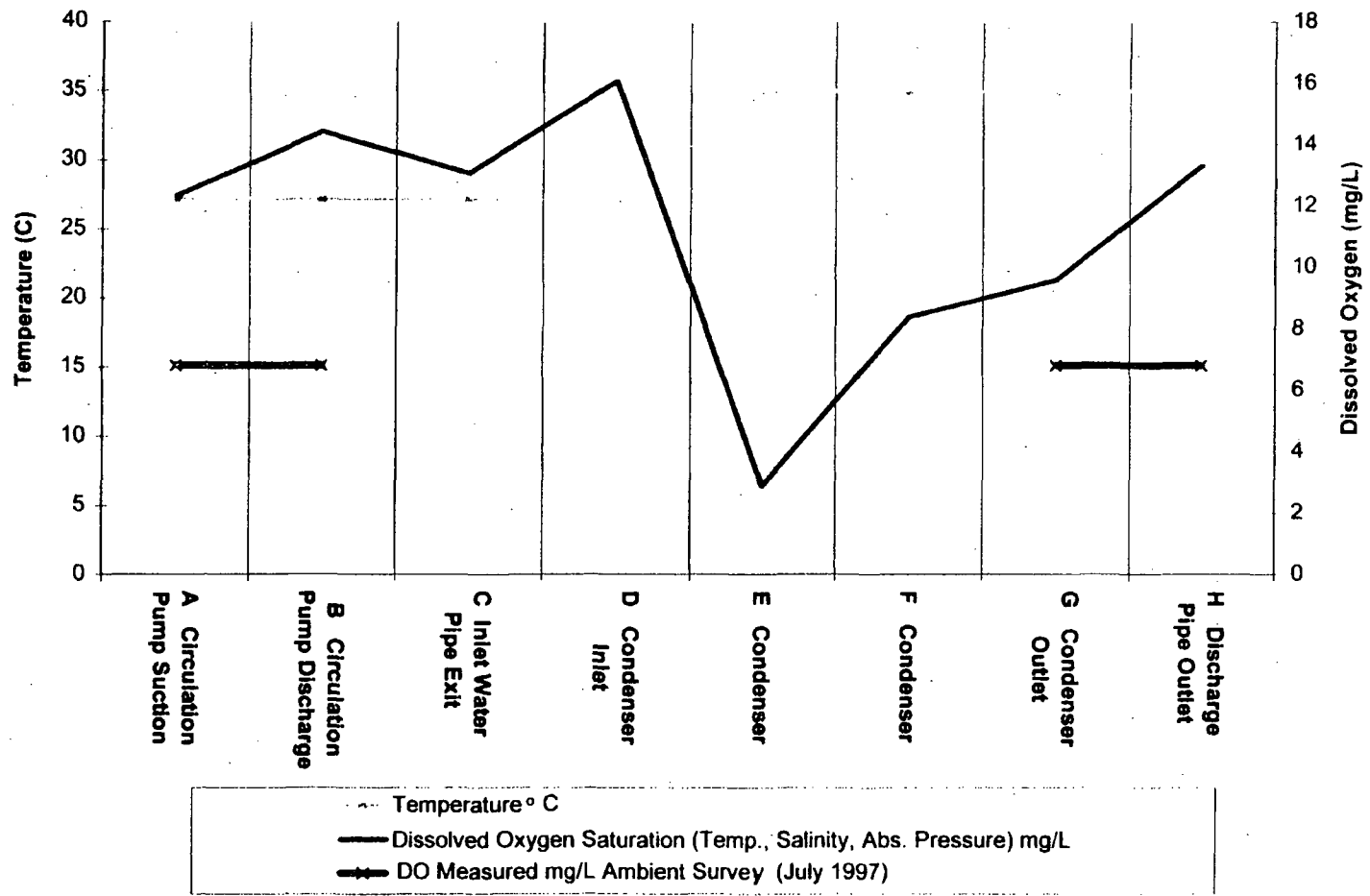
E-3 Figure VI-3. Dissolved Oxygen Calculations (expanded scale).



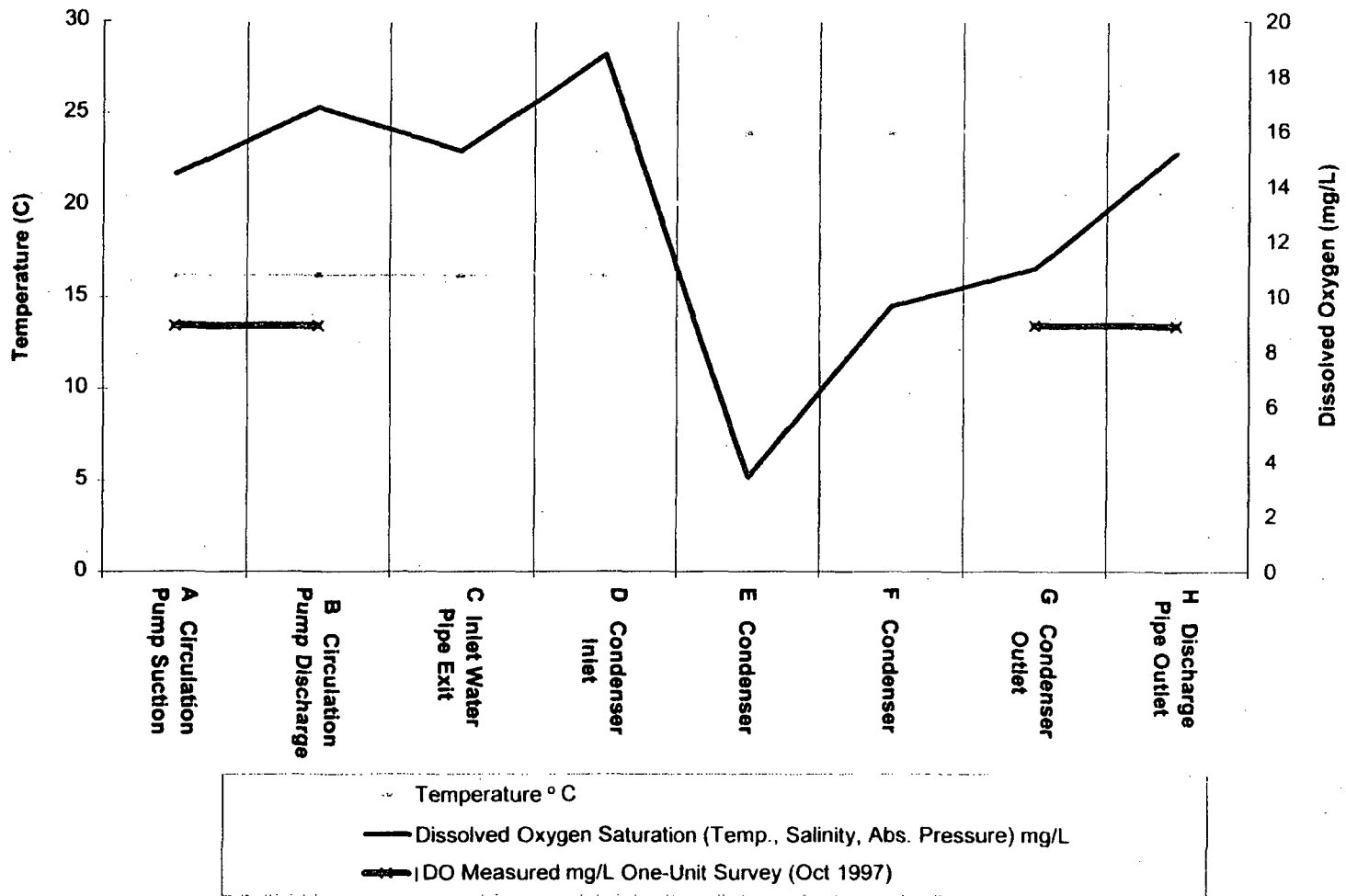
E-3 Figure VII-1. Pressure/ Temperature/ Time Profile for the Station's Circulation Water System.



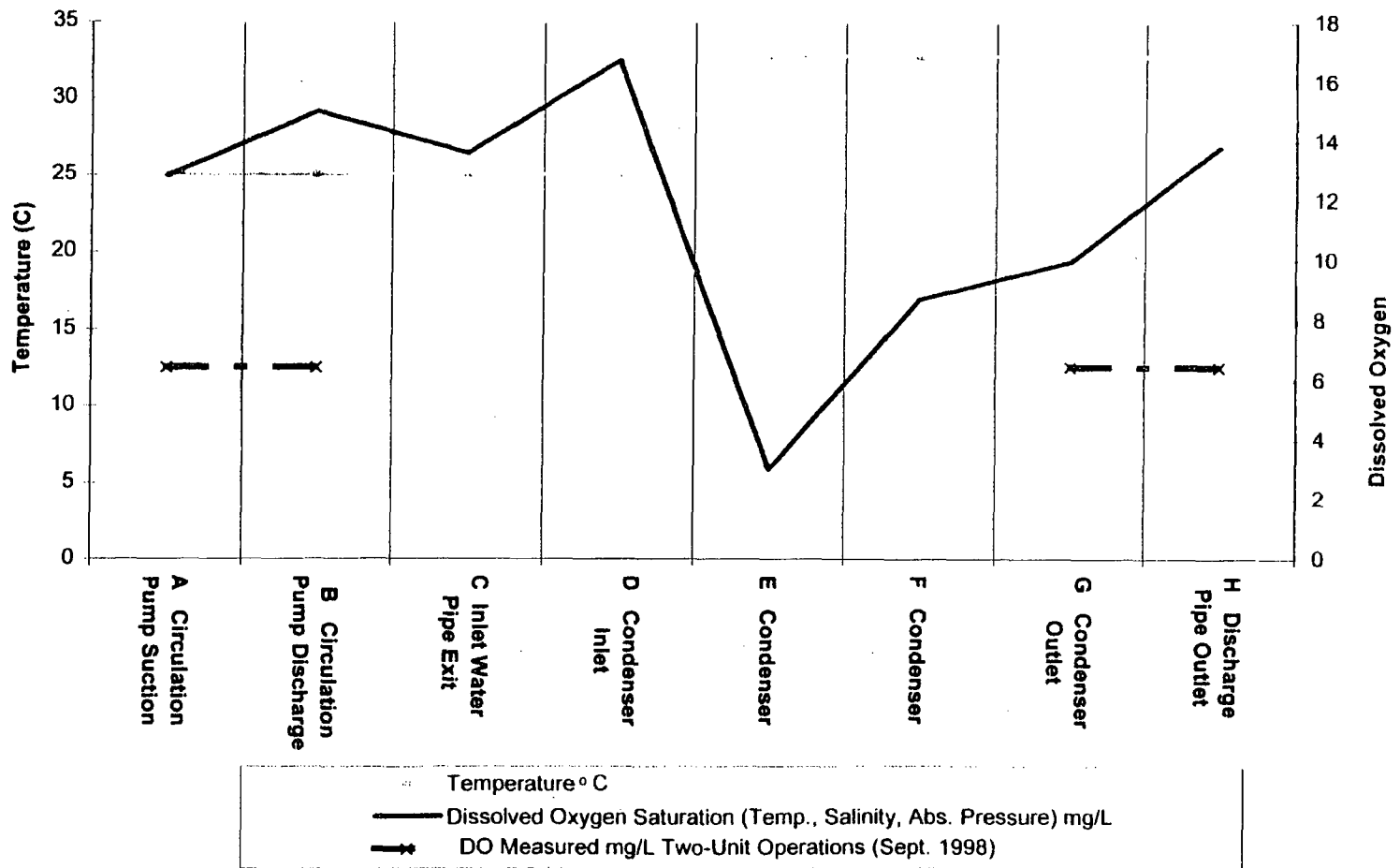
E-3 Figure VII-2. Absolute Pressure Distribution Through the Station.



E-3 Figure VII-3. Potential DO Reduction through the Station under Ambient Survey (July 1997) conditions.



E-3 Figure VII-4. Potential DO Reduction through the Station under One-Unit Survey (1997 October) conditions.



E-3 Figure VII-5. Potential DO reduction through the Station under Two-Unit Survey (Sept. 1998) conditions.

**APPENDIX E
EXHIBIT E-3-1**

6-MONTH MOORING DISSOLVED OXYGEN CALIBRATION PROTOCOL

**SPONSOR:
PSE&G RENEWAL APPLICATION
SALEM GENERATING STATION
PERMIT NO. NJ0005622
4 MARCH 1999**

EXHIBIT E-3-1
6-MONTH MOORING DISSOLVED OXYGEN CALIBRATION PROTOCOL
LIST OF TABLES

Figure No.	Title
Table 1	YSI 6000 calibrations for the first deployment
Table 2	YSI 6000 calibrations for the second deployment
Table 3	Linear regression corrections for YSI 6000s

EXHIBIT E-3-1 6-MONTH MOORING DISSOLVED OXYGEN CALIBRATION PROTOCOL

Ten dissolved oxygen sensors were calibrated with the procedures outlined by the manufacturer and deployed to their specific sites for data collection. The sensors used were YSI 6000 series instruments. The calibration procedure is summarized below including the resulting tables of pre- and post-deployment calibration:

Pre-Deployment:

1. Conductivity cells were calibrated according to YSI instructions.
2. The Oxygen Electrode was calibrated and verified in air according to YSI instructions.
3. Electrode response was determined throughout full concentration range: 100% air saturation, 50% air saturation, and 0% air saturation.
4. Precision temperature test chamber equilibration was verified with standardized gases using high precision (Radiometer) Winkler titrations.
5. Pre-deployment calibration values were determined and are presented in Tables 1 and 2 for deployments 1 and 2, respectively (measured saturation values vs. actual saturation values).
6. With the accuracy of YSI data capture protocols confirmed, data collection was started.

On-site water samples were collected during instrument deployment for Winkler DO titrations to confirm electrode performance. All Winkler samples were titrated with a potentiometric end-point method, calibrated with certified bi-iodate standards.

Post-Deployment:

1. Oxygen Electrode calibration was verified and electrode response was determined throughout full concentration range: 100% air saturation, 50% air saturation, and 0% air saturation.
2. Test chamber equilibration was verified with standardized gases using Winkler titrations.
3. Post-deployment calibration values were determined and are presented in Tables 1 and 2 for deployments 1 and 2, respectively (measured saturation values vs. actual saturation values).
4. Dissolved oxygen data were retrieved from instruments, and then corrected by pre- and post-calibration values (Table 3).
5. The corrected data were transformed to concentrations using the Benson-Krause equation, based on measured salinity and temperature data and standard atmospheric pressure.
6. Finally, the agreement between corrected data, pre/post deployment standards and in-situ samples were confirmed.

Table 3 shows the linear regression calculated from the values in pre- and post-calibration tables. The raw data were corrected for electrode drift by linearly interpolating between the pre- and post- calibration curves. These curves were weighted through time.

Quality checks were made before the deployment of each instrument to assure the accuracy of the measurements. Any necessary instrument adjustments, changes, and repairs were made before the deployment of instruments. The instruments used were of high quality and fully appropriate for this survey.

Based on this quality procedure, only the instrument deployed at mooring 21 surface during the second deployment showed possible inaccurate behavior. Data from this instrument were not used in the analysis of dissolved oxygen.

E-3-1 Table 1. Summary of YSI 6000 calibration for the first deployment.

Deployment 1: Pre-Calibration

Site	Instrument ID	Deployment/ Recovery Date	Concentration 1		Concentration 2		Concentration 3	
			Actual Calibration % DO Saturation	Measured Probe Response % DO Saturation	Actual Calibration % DO Saturation	Measured Probe Response % DO Saturation	Actual Calibration % DO Saturation	Measured Probe Response % DO Saturation
Mad Horse Creek	93B02260	2 Sept 1998	100	100.1	47.2	52.1	0	10.1
21 Surface	95C30809	2 Sept 1998	100	99.8	47.2	51.1	0	8.2
21 Mid-Depth	95L43268	2 Sept 1998	100	99.8	47.1	53.4	0	13.8
9M Surface	95H35847	2 Sept 1998	100	100.0	47.1	53.4	0	14.6
9M Mid-Depth	96D48108	2 Sept 1998	100	99.8	47.1	50.5	0	4.8

Deployment 1: Post-Calibration

Site	Instrument ID	Deployment/ Recovery Date	Concentration 1		Concentration 2		Concentration 3	
			Actual Calibration % DO Saturation	Measured Probe Response % DO Saturation	Actual Calibration % DO Saturation	Measured Probe Response % DO Saturation	Actual Calibration % DO Saturation	Measured Probe Response % DO Saturation
Mad Horse Creek	93B02260	17 Sept 1998	100	110.7	47.1	54.6	0	4.8
21 Surface	95C30809	17 Sept 1998	100	94.8	47.1	46.5	0	1.9
21 Mid-Depth	95L43268	17 Sept 1998	100	126.5	47.1	62.1	0	0.7
9M Surface	95H35847	17 Sept 1998	100	99.1	47.1	41.8	0	-12.6
9M Mid-Depth	96D48108	17 Sept 1998	100	120.6	47.1	57.1	0	-1.4

E-3-1 Table 2. Summary of YSI 6000 calibration for the second deployment.

Deployment 2: Pre-Calibration			Concentration 1		Concentration 2		Concentration 3	
Site	Instrument ID	Deployment/ Recovery Date	Actual Calibration % DO Saturation	Measured Probe Response % DO Saturation	Actual Calibration % DO Saturation	Measured Probe Response % DO Saturation	Actual Calibration % DO Saturation	Measured Probe Response % DO Saturation
Mad Horse Creek	93G07332	17 Sept 1998	100	100.6	47.1	48.7	0	1.8
21 Surface	96J0893AB	17 Sept 1998	100	100.0	47.1	62.3	0	28.5
21 Mid-Depth	95J38607	17 Sept 1998	100	100.0	47.1	47.9	0	0.8
9M Surface	96G48109	17 Sept 1998	100	100.0	47.1	51.9	0	6.36
9M Mid-Depth	93H07680	17 Sept 1998	100	99.3	47.1	48.6	0	1.9

Deployment 2: Post-Calibration			Concentration 1		Concentration 2		Concentration 3	
Site	Instrument ID	Deployment/ Recovery Date	Actual Calibration % DO Saturation	Measured Probe Response % DO Saturation	Actual Calibration % DO Saturation	Measured Probe Response % DO Saturation	Actual Calibration % DO Saturation	Measured Probe Response % DO Saturation
Mad Horse Creek	93G07332	8 Oct 1998	100	98.3	47.1	46.2	0	1.1
21 Surface	96J0893AB	8 Oct 1998	100	95.8	47.1	51.1	0	11.2
21 Mid-Depth	95J38607	8 Oct 1998	100	51.1	47.1	26.6	0	1.1
9M Surface	96G48109	8 Oct 1998	100	119.1	47.1	66.4	0	19.1
9M Mid-Depth	93H07680	8 Oct 1998	100	97.6	47.1	47.5	0	0.3

E-3-1 Table 3. The actual linear regressions calculated from numbers in Pre- and Post-Calibration tables for both deployments 1 and 2.

Deployment 1: Pre-Calibration

Site	Instrument ID	Deployment Date	Pre-Calibration Linear Regression	R ²
Mad Horse Creek	93B02260	2 Sept 1998	Actual % Sat. = (1.10 * Measured % Sat.)-10.11	0.999
21 Surface	95C30809	2 Sept 1998	Actual % Sat. = (1.08 * Measured % Sat.)-8.20	0.998
21 Mid-Depth	95L43268	2 Sept 1998	Actual % Sat. = (1.14 * Measured % Sat.)-13.78	0.998
9M Surface	95H35847	2 Sept 1998	Actual % Sat. = (1.13 * Measured % Sat.)-14.44	0.997
9M Mid-Depth	96D48108	2 Sept 1998	Actual % Sat. = (1.05 * Measured % Sat.)-4.66	0.998

Deployment 1: Post-Calibration

Site	Instrument ID	Recovery Date	Post-Calibration Linear Regression	R ²
Mad Horse Creek	93B02260	17 Sept 1998	Actual % Sat. = (0.94 * Measured % Sat.)-4.52	0.999
21 Surface	95C30809	17 Sept 1998	Actual % Sat. = (1.08 * Measured % Sat.)-2.35	0.999
21 Mid-Depth	95L43268	17 Sept 1998	Actual % Sat. = (0.79 * Measured % Sat.)-1.13	0.998
9M Surface	95H35847	17 Sept 1998	Actual % Sat. = (0.79 * Measured % Sat.)+12.70	0.999
9M Mid-Depth	96D48108	17 Sept 1998	Actual % Sat. = (0.82 * Measured % Sat.)-0.85	0.998

Deployment 2: Pre- Calibration

Site	Instrument ID	Deployment Date	Pre-Calibration Linear Regression	R ²
Mad Horse Creek	93G07332	17 Sept 1998	Actual % Sat. = (0.97 * Measured % Sat.)-1.20	0.999
21 Surface	96J0893AB	17 Sept 1998	Actual % Sat. = (1.40 * Measured % Sat.)-39.91	0.999
21 Mid-Depth	95J38607	17 Sept 1998	Actual % Sat. = (1.01 * Measured % Sat.)-0.98	0.999
9M Surface	96G48109	17 Sept 1998	Actual % Sat. = (1.07 * Measured % Sat.)-7.26	0.999
9M Mid-Depth	93H07680	17 Sept 1998	Actual % Sat. = (1.03 * Measured % Sat.)-2.24	0.999

Deployment 2: Post-Calibration

Site	Instrument ID	Recovery Date	Post-Calibration Linear Regression	R ²
Mad Horse Creek	93G07332	8 Oct 1998	Actual % Sat. = (1.01 * Measured % Sat.)-0.94	0.999
21 Surface	96J0893AB	8 Oct 1998	Actual % Sat. = (1.18 * Measured % Sat.)+13.27	0.999
21 Mid-Depth	95J38607	8 Oct 1998	Actual % Sat. = (1.93 * Measured % Sat.)-3.35	0.998
9M Surface	96G48109	8 Oct 1998	Actual % Sat. = (1.00 * Measured % Sat.)-19.17	0.999
9M Mid-Depth	93H07680	8 Oct 1998	Actual % Sat. = (1.03 * Measured % Sat.)-0.79	0.999

**APPENDIX E
ATTACHMENT E-4**

ANALYSIS OF TOTAL RESIDUAL CHLORING IN THE VICINITY

**SPONSOR: DR. DAVID AUBREY
PSE&G RENEWAL APPLICATION
SALEM GENERATING STATION
PERMIT NO. NJ0005622
4 MARCH 1999**

**ATTACHMENT E-4
TABLE OF CONTENTS**

I. REGULATORY FRAMEWORK.....3

II. STATION OPERATIONS.....4

III. CHLORINE DEMAND.....5

IV. ASSESSMENT APPROACH.....7

IV.A. Chlorine Demand Studies7

IV.B. End-of-Pipe Calculations8

IV.C. Riverine Processes Affecting TRC9

V. CONCLUSIONS9

**ATTACHMENT E-4
LIST OF FIGURES**

Figure No.	Title
Figure II-1	Schematic of Service Water System chlorination flow.
Figure II-2	Non-contact Cooling Water System (DSN 481-486).
Figure IV-1	Chlorine demand at Salem (from MBC 1988).

ATTACHMENT E-4 ANALYSIS OF TOTAL RESIDUAL CHLORINE IN THE VICINITY OF THE STATION

I. REGULATORY FRAMEWORK

In addition to assessing potential direct effects of the Salem thermal plume on the protection and propagation of a balanced indigenous community (BIC), 316(a) Guidance (USEPA 1974, 1977) also requires assessment of indirect effects of heat discharged from the Station, including effects of its influence, if any, on DO and other pollutants. Assessment of the effects of TRC levels contributed by Salem operations are considered in this Attachment to the 316(a) Demonstration.

Although Delaware River Basin Commission (DRBC) Water Quality Regulations (revised to include amendments through October 23, 1996) address chlorine under the disinfection requirements for wastewater treatment facilities, DRBC has no water quality criteria for TRC or Chlorine-Produced Oxidants (CPO) in the Estuary. The original DRBC Salem Docket in 1970 permitted chlorination of the Station's condenser tubes, imposing an effluent limit of 0.1 ppm (i.e., 100 µg/L) for chlorine residual in the circulating cooling water. Subsequent to that time (mid-1980s), PSE&G ceased chlorinating the Circulating Water System (CWS), and in recognition of this fact, the DRBC Revised Docket (dated 29 September 1995) no longer set an effluent limit. The DRBC recognized that "The Station's chlorine discharges are now regulated by the NJDEP PERMIT [sic]."

The current discharge standards for Salem Station are included in the 1994 New Jersey Pollutant Discharge Elimination System (NJPDDES) permit for Salem (NJ0005622). The Permit states: "Samples taken in compliance with the specified monitoring requirements shall be taken at the outfalls of discharges 481, 482, 483, 484, 485, and 486, and reported monthly." The discharges refer to PSE&G Discharge Serial Numbers (DSN). Three discharge limitations apply for chlorine: (1) when only service water system (SWS) non-contact cooling water is discharged, monthly average TRC shall not exceed 0.3 mg/L, daily maximum TRC shall not exceed 0.5 mg/L, and sampling will occur three times per week, using a grab sample; (2) when circulating water system (CWS) non-contact cooling water is discharged as well, the TRC discharge limitation is 0.2 mg/L daily maximum; and (3) if chlorination is required for the CWS, "TRC shall not be discharged from any single generating unit for more than two hours per day," and specific requirements and approval prior to sodium hypochlorite addition are required. However, as indicated, chlorine is no longer added to the CWS itself.

Besides the regulatory requirement for TRC outlined in the Permit, additional consideration is given in this Demonstration to the potential interactive biological effects of TRC discharged from the SWS through the combined CWS/SWS discharge pipes into the Estuary. These potential biological effects are considered as part of the Demonstration's assessment of potential acute and chronic effects.

USEPA water quality criteria include both acute and chronic toxicity criteria for TRC in marine waters. USEPA (1985) states that, "except possibly where a locally important species is very sensitive, saltwater aquatic organisms and their uses should not be affected unacceptably if the four-day average concentration of chlorine-produced oxidants does not exceed 7.5 $\mu\text{g}\cdot\text{L}$ more than once every three years on the average and if the one-hour average concentration does not average 13 $\mu\text{g}\cdot\text{L}$ more than once every three years on the average." The acute aquatic life protection criterion is a one-hour average of 13 $\mu\text{g}\cdot\text{L}$, and the chronic life protection criterion is a four-day average of 7.5 $\mu\text{g}\cdot\text{L}$. New Jersey Department of Environmental Protection (NJDEP) Water Quality Standards for Class SE waters use USEPA's acute/chronic criteria for TRC/CPO (NJAC 7:9B-1.14). End-of-pipe concentrations of TRC at the Station's discharge are evaluated in light of these criteria.

II. STATION OPERATIONS

The SWS is the only chlorinated cooling-water system at the Station. Sodium hypochlorite (NaOCl) is added in order to prevent biofouling of critical heat exchanger surfaces and other components in the SWS, which has smaller-diameter flow paths than the CWS, and thus could be more adversely affected by fouling. Because the SWS is essential to Station nuclear safety, it is constructed with redundant equipment. For instance, there are two heat exchangers, both of which are susceptible to fouling unless chlorinated or otherwise maintained to prevent fouling. However, because only one of these heat exchangers is in operation at any time, the water in the redundant system is more stagnant, and consequently the redundant system is more susceptible to biofouling.

Liquid sodium hypochlorite is added at the intake of each operating service water pump by variable displacement pumps (E-4 Figure 1). This addition is carefully controlled manually to maintain a TRC concentration of 300 $\mu\text{g}\cdot\text{L}$ (with a maximum of 500 $\mu\text{g}\cdot\text{L}$) at the outlet of the last heat exchanger in the header (the Component Cooling Heat Exchanger). The chlorine concentration going into the pumps is not monitored; instead, the TRC concentration at the outlet of the heat exchangers is monitored and manually adjusted to compensate for changes in the natural chlorine demand and ambient temperature of the SWS water. Control of chlorine addition is based on readouts of TRC from an Orion 1770 (chlorine analyzer) located near the outlet of the SWS heat exchangers.

The SWS effluent joins the combined CWS/SWS discharge pipes. The combined CWS and SWS discharge to the Estuary at the end of twelve 10-ft diameter pipes extending along the river bottom about 500 feet from shore (Exhibit E-1-4). Flow rates and transit times have been calculated for this piping from the juncture of the SWS and CWS to the discharge location (Appendix B).

The CWS residual chlorine monitor (also an Orion 1770), located at the CWS standpipes (E-4 Figure 1) between the point where the SWS joins the CWS and the system discharges to the Estuary, electronically signals the sodium hypochlorite injection pumps

to halt the addition of sodium hypochlorite before the maximum permitted TRC discharge level is exceeded. Therefore, if the manual control of chlorine injection fails, the CWS chlorine monitor will automatically stop the chlorination process before the discharge limits are exceeded.

During Station operation, the service water combines with the circulating water from the condensers and is discharged to the Estuary. There is a cross-feed discharge so that each Unit will discharge part of its SWS into the CWS servicing that Unit as well the CWS servicing the companion Unit. A diagram of the circulating and service water systems (E-4 Figure 2) demonstrates how non-contact cooling water flows through the Station, and where the SWS and CWS commingle.

Volumes for the CWS discharge under full two-unit operation range from 1.68 million gpm to 2.1 million gpm, depending upon the operating conditions at the time. The SWS discharges between 28,500 gpm and 41,200 gpm, depending on operating conditions (its discharge rate is lower when the CWS is not operating). The CWS discharges approximately 40 to 50 times the volume of the SWS when the Station is operating both Units.

Approximate transit times for the SWS can be calculated based on flow rates, pipe diameters, and flow path lengths. Transit time from the SWS heat exchanger header (the outlet of the last heat exchanger where TRC is monitored) to the confluence with the CWS, a distance of 250 feet, is approximately one minute. From the SWS/CWS confluence to the discharge point, a distance of 800 feet, transit time is one minute when the CWS is at full flow.

No permit exceedences have occurred for the TRC discharge between January 1994 and September 1998, as reported in Discharge Monitoring Reports (DMRs) using measurement methods with a practical quantitation limit of 100 $\mu\text{g/L}$. The discharge sampling points for TRC (DSNs 481 through 486) are located downstream of the confluence of the service and circulation water flows, and downstream of the confluence with the non-radioactive liquid waste discharge system (E-4 Figure 2, and Appendix B to this submittal). The Station is permitted to use sodium hypochlorite to treat chemical wastes prior to discharge in the non-radioactive liquid waste disposal system (DSN 48C). This treatment process leaves a residual chlorine concentration in the effluent from DSN 48C. DSN 48C discharges with the CWS effluent after entering upstream of the TRC monitoring location; therefore, its effects are also monitored.

III. CHLORINE DEMAND

Chlorine behavior in estuarine waters is complex, and related to the chemistry of the saline water. Chlorine added to water in the hypochlorite form undergoes hydrolysis to form free chlorine consisting of aqueous molecular chlorine, hypochlorous acid, and hypochlorite ions. The relative proportions of these forms of chlorine are dependent on pH and temperature. Hypochlorous acid and hypochlorite ion will predominate for the pH range 6 to 9. The free chlorine will react with bromide to form hypobromous acid and

perhaps bromite. Both the chlorine and bromine can react with amines (ammonia and other nitrogenous compounds) to form chlorinated brominated amines. Certain analytical methods for groups of chlorine compounds will also reflect concentrations of the bromine compounds, particularly in estuarine or marine waters. Depending on the analytical method, results may include various forms of chlorine (e.g., free available chlorine, total residual chlorine, etc.). These tests essentially determine levels of oxidants, and different tests may detect different oxidants. In comparing different studies, care must be taken to discriminate between these various forms of chlorine.

Chlorine reaction rates are a function of inorganic and organic processes, as well as pH, water temperature, and other factors. Inorganic processes (commonly but not exclusively associated with iron or other metals) are relatively rapid; organic processes are in general less rapid. Chlorine demand, which is high in estuarine waters, generally refers to the rapid reduction of chlorine to chloride as the sodium hypochlorite reacts with and is reduced by chemical species in the cooling water. This chlorine reduction occurs on the order of a few seconds. Following this rapid chlorine decay, a more gradual decay process takes place. Helz et al. (1984) provide a description of this process as it occurs in estuarine waters. Chlorine demand in different environments will vary in a complex fashion depending on the water chemistry.

Total Residual Chlorine is commonly divided into two forms: free residual chlorine (FRC) and combined residual chlorine (CRC). Free Residual Chlorine is relatively susceptible to rapid reduction through chlorine demand processes, whereas the rates for reduction of CRC are somewhat slower. The chemical reactions and their rates are dependent on, among other things, the ratio of nitrogen to chlorine; at high ratios the chlorine is in the form of trichloramine, which is instantaneously reduced to nitrogen and water. At low ratios, the chlorine is present as monochloramine and dichloramine, which are more slowly reduced and more available.

Chlorine demand slows as organic reduction processes dominate inorganic reduction processes. The exact rates and processes vary from water body to water body. Therefore, TRC demand should be measured on a sample from the specific water body of interest. The rapid portion of chlorine demand typically is estimated from laboratory experiments on field samples. The slower period can be modeled using either in situ or laboratory measurements.

Reintroduction of new waters having a high chlorine demand to a chemically reduced chlorinated waste stream will not create the same high initial chlorine demand. A chlorinated cooling water discharge to a river, for instance, will not be able to take advantage of high chlorine demand when mixed with new river waters because the forms of chlorine in the chlorinated stream differ from the sodium hypochlorite that was introduced in the Station.

IV. ASSESSMENT APPROACH

IV.A. Chlorine Demand Studies

In 1984 and 1985, PSE&G conducted a chlorine minimization and decay study (Burton and Garey 1986). Chlorine demand was evaluated on water samples from the SWS and CWS of one Unit during each sampling episode at a frequency of 5 days per month from July through November 1984. Sampling was performed for 10 days per month from May to November 1985 at certain locations in the CWS. Immediately following sampling, FRC and TRC were measured on all samples by the forward amperometric titration procedure. Thirty-second (0.5 minute) and three-minute laboratory chlorine demands were determined for ambient water at the CWS intake. Both FRC and TRC decay in the SWS and CWS were analyzed statistically. Temperature, conductivity, salinity, pH, dissolved oxygen, total suspended solids, various nitrogen compounds, and phosphate were measured in the ambient intake water, and a limited number of measurements were taken at the discharge standpipe (in the combined CWS/SWS discharge approximately 500 feet before the end-of-pipe).

For the SWS in 1984, the yearly average 0.5-minute chlorine demand was 410 $\mu\text{g/L}$ TRC, and the yearly average 3-minute chlorine demand was 560 $\mu\text{g/L}$ TRC. The dose rate for these tests was approximately 1000 $\mu\text{g/L}$. These levels of demand were different in 1985, which had a reported 3-minute chlorine demand average of 470 $\mu\text{g/L}$. Assuming a first-order decay process, a first-order rate constant can be determined from the two chlorine demand endpoints, and an initial chlorine concentration (dose rate) of 1000 $\mu\text{g/L}$. This first-order decay rate is representative not of initial rapid chlorine demand, but rather the later and slower chlorine demand associated with chlorine interaction with organics. This resulting model can then provide a decay rate for any transit period.

A second study performed for PSE&G, by Marine Biocontrol Corporation (MBC) in 1988, provided slightly more conservative values (slower consumption) for chlorine demand than the Burton and Garey (1986) study; therefore, the modeling below relies on the MBC study (E-4 Figure2).

A first order decay model was selected to represent the decay of chlorine in the SWS and CWS (Helz et al. 1984):

$$dC/dt = -\lambda C_0$$

where:

C = Chlorine concentration for any point in time (mg/L or $\mu\text{g/L}$)

t = time in minutes

λ = first order rate constant, in units of min^{-1}

C_0 = Initial value of chlorine concentration (mg/L or $\mu\text{g/L}$)

Based on data from the study performed by MBC (1988), λ is calculated to be equal to 0.0825 min^{-1} , the average of the rate constants calculated from the MBC work. This is

faster than the chlorine demand obtained by Helz et al. (1984) for the Patuxent Estuary in Maryland which yielded a value of about 0.014/min, about six times lower than at Salem. This difference is to be expected because of the differing chemical make up of the two water bodies. Delaware Estuary water has a higher bromine content, which has faster reaction kinetics; the Patuxent Estuary has high levels of nitrogen, resulting in the formation of intermediate compounds with the chlorine and slowed decay processes. Therefore, the MBC study provides a reasonable estimate of decay rate for the slow chlorine demand period for the Station. This calculation is conservative in that the value for the ratio constant represents the average of values from MBC, which is slower than values derived from the Burton and Garey study (1986; 0.1173 min^{-1}) and those used in the 1973 Final Environmental Statement of the USAEC (1973).

IV.B. End-of-Pipe Calculations

Two processes are important for the evaluation of end-of-pipe concentrations of TRC emanating from treatment of the Salem SWS using sodium hypochlorite. The first process is chlorine demand, represented here as TRC demand. The second process is dilution of the SWS by the combination with the CWS discharge prior to reaching the end of the combined discharge pipes.

Chlorine demand data are taken from the study by MBC (1988) at Salem Station. Pipe flows and distances were taken from Appendix B, as discussed above.

Total residual chlorine concentration in the SWS at the outlet from the last heat exchanger is $300 \mu\text{g/L}$ on average, and should not exceed $500 \mu\text{g/L}$ (Burton and Garey 1986 recommendation; Appendix B). For the purposes of these calculations, the higher value of $500 \mu\text{g/L}$ is applied ($C_0 = 500 \mu\text{g/L}$). This assumption is conservative in the sense that the end-of-pipe TRC concentration estimates will be higher than actual average concentrations.

Assuming a one-minute transit time in the SWS piping, the TRC concentration (C) in the SWS at the point where the SWS and the CWS meet is:

$$C = C_0 e^{(-\lambda t)} = 460 \mu\text{g/L}$$

The CWS dilutes the SWS by a factor of 40 to 50. Assuming the lower dilution of 40, the concentration immediately after dilution is:

$$C = 460/40 = 11.5 \mu\text{g/L}$$

This calculation is conservative in the sense that the lower dilution factor (40) is applied. It takes another minute for this water to reach end-of-pipe, during which decay continues:

$$C = 11.5 e^{(-\lambda t)} = 10.6 \mu\text{g/L}$$

This estimated value is well below the NJPDES discharge limitations and also below the USEPA acute criterion of 13 $\mu\text{g/L}$. The value is far below the practical quantitation level of 100 $\mu\text{g/L}$. Although the estimated value exceeds the USEPA chronic criterion, the discharge mixes extremely rapidly after entering the river, diluting the TRC concentration a further 50 percent after 7 seconds (Appendix E Section V). No organism stays in this high-velocity effluent for any length of time, therefore consideration of the chronic criterion does not appear to be appropriate.

IV.C. Riverine Processes Affecting TRC

In addition to the chlorine demand processes listed above, other processes such as phototransformation and volatilization will further decrease chlorine concentrations when TRC reaches the river. First-order phototransformation rates (e.g., rate constant of 0.0004 min^{-1}) and volatilization rates (e.g., 0.0019 min^{-1}) quoted in the literature (Lee et al. 1982) are much lower than the rates derived from the in situ measurements of TRC decay from Burton and Garey and MBC. In one study of discharge through a cooling canal (Helz et al. 1984), photochemical decomposition mechanisms appeared relatively unimportant overall; they may be similarly insignificant in this case as natural river turbidity is high and light penetration is low.

The major factor decreasing discharged TRC concentration at the Station is dilution by river water. For full-power operations, the discharge velocity is approximately 10 ft/sec. Near-field modeling performed as part of this 316(a) Demonstration (Attachment E-2 Section III.B) shows dilution of the Station discharge of 50 percent within 7 seconds of discharge.

V. CONCLUSIONS

The NJDEP has established a discharge limitation for TRC from the Station. Since the permit was issued in 1994, measured TRC discharge concentrations have not exceeded that limitation. In situ measurements of chlorine demand in CWS and SWS waters at the Station in 1984, 1985, and 1988 provide a basis for estimating end-of-pipe TRC concentrations resulting from chlorination of the SWS (the only chlorinated non-contact cooling water discharged to the Estuary). Based on chlorine demands for periods ranging from 0.25-minute to 15-minute intervals, a first-order decay model was derived to estimate chlorine demands for different flow conditions.

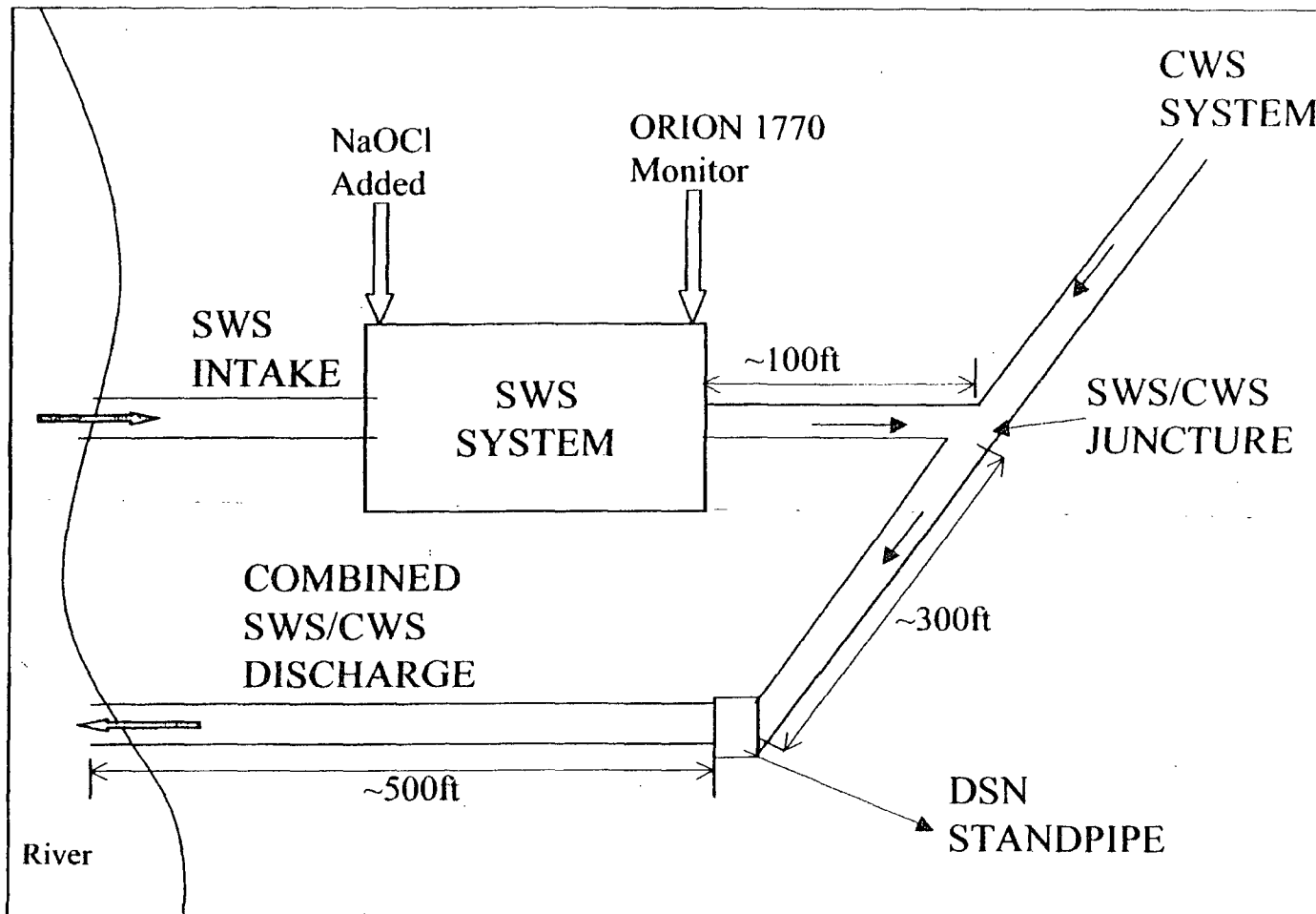
The design chlorination rate for the SWS is based on a chlorine minimization study conducted in 1984 and 1985, and the rate is monitored continually using two in-line chlorine measurement systems. During Station operation, the circulating water dilutes the service water about 800 feet from the combined CWS/SWS discharge, lowering TRC concentrations to well below the Permit's discharge limits and below regulatory acute biological effects levels. Although these conservative estimates may indicate an end-of-pipe maximum concentration exceeding the USEPA chronic criterion, rapid dilution in the Estuary following discharge (Appendix E, Section V) reduces the level to below such a criterion in less than seven seconds after discharge.

This calculation is conservative in several respects:

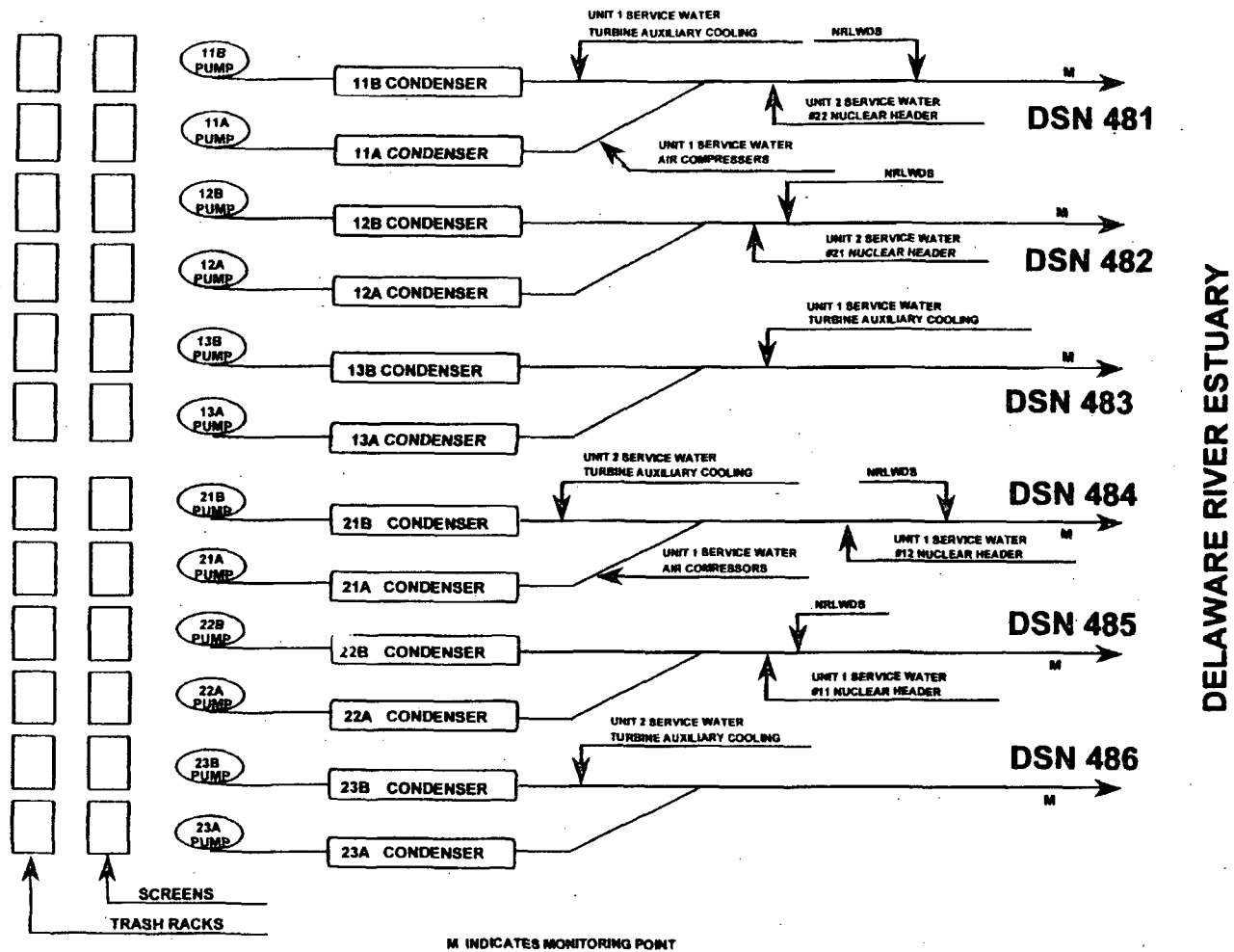
- (1) the maximum TRC concentration entering the SWS was used for the calculations, rather than the average value, causing calculated end-of-pipe concentrations to be higher than the actual average values;
- (2) the chlorine demand data were consequently taken from the study showing the lowest chlorine demand, even though two other studies at the Station showed higher demand; and
- (3) the lowest dilution factor relating CWS flow to SWS flow was used (a dilution of 40 rather than 50).

A less conservative series of assumptions would produce end-of-pipe concentrations below the USEPA chronic level. There are no measurements suggesting exceedence of the USEPA chronic criteria. The practical quantitation level is 100 μL , well above the USEPA criteria.

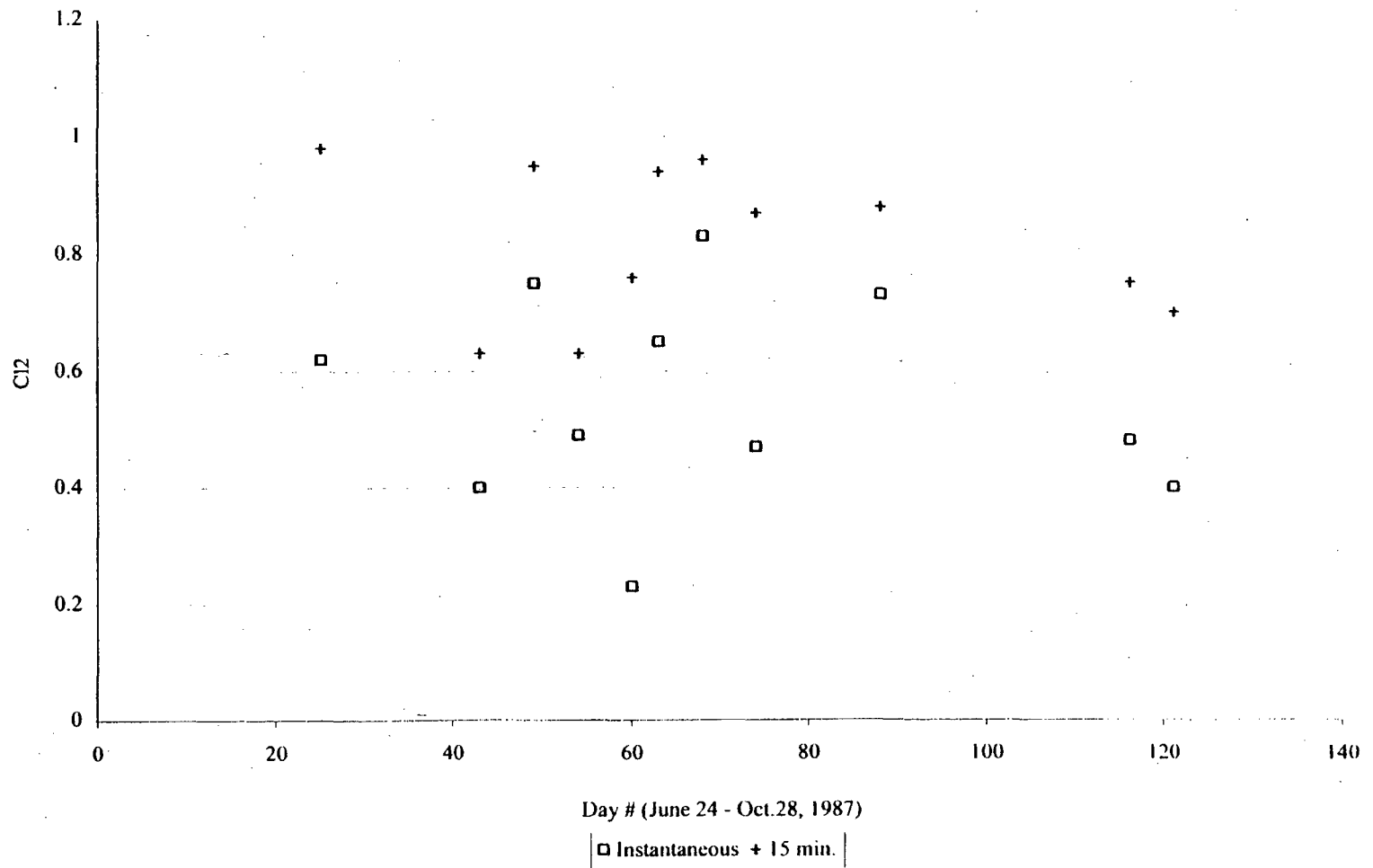
Chlorine-produced oxidant concentrations at the end-of-pipe, related to full Station operations, are below regulatory acute toxicity levels and well below applicable Permit discharge limitations. The regulatory chronic levels are theoretically exceeded under only the most conservative assumptions, and only within a small volume. Because the assumptions behind these calculations are conservative at several levels, the likelihood of exceedence of even chronic toxicity limits is small.



E-4 Figure II-1. Schematic of Service Water System chlorination flow.



E-4 Figure II-2. Non-contact Cooling Water System (DSN 481 - 486).



E-4 Figure IV-1. Chlorine demand at Salem (from MBC, 1988).